University of Liège
Faculty of Civil Engineering
ArGEnCo Department

The cyclic behaviour of sand, from the Prevost model to offshore geotechnics

A thesis submitted for the degree of
Philosophiae Doctor in Applied Sciences by

Benjamin Cerfontaine

June 2014, version 08/2015

This research was funded by: FRIA-F.R.S.-F.N.R.S.

Fonds pour la formation à la Recherche dans l'Industrie et dans l'Agriculture
Rue d'Egmont, 5
B-1000, Bruxelles

Jury

Frédéric Collin	Université de Liège	(President)
Robert Charlier	Université de Liège	(Supervisor)
Hervé Degée	Universiteit Hasselt	(Co-supervisor)
Alain Holeyman	Université catholique de Louvain	
Séverine Levasseur	Université de Liège	
Jean-Philippe Ponthot	Université de Liège	
Bruno Stuyts	Cathie Associates	
Claudio Tamagnini	Università degli Studi di Perugia	

Remerciements

Accoucher d'une thèse est le fruit d'un long cheminement personnel mais certainement pas solitaire. Je voudrais remercier chaleureusement tous ceux, qui par leur soutien logistique, scientifique, spirituel ou stylistique ont contribué à rendre cette aventure possible.

Je voudrais tout d'abord remercier André Plumier et Robert Charlier, qui sont conjointement à l'origine de ce projet. J'espère toujours bénéficier de la grande sympathie d'André Plumier, même si l'objet de cette thèse a considérablement dérivé de son objectif premier. Je suis également reconnaissant envers Robert Charlier de m'avoir permis de travailler en grande indépendance et de m'avoir laissé toute latitude pour orienter mes recherches. Ses questions pertinentes ont toujours été source de questionnement et donc de progrès.

Cette thèse n'aurait pu éclore hors de cet environnement de recherche extraordinaire, offert par toute l'équipe présente et passée : Arnaud, Bertrand, Elnaz, Georgia, Gwendal, Marc, Noémie, Pierre, Séverine, Simon. L'excellent esprit qui règne parmi nous fut un moteur essentiel durant les mornes journées de piétinement scientifique. Je félicite Benoît d'avoir placidement supporté toute la ménagerie du bois de quatre sous à deux pas de ses oreilles.
Je voudrais également remercier Jean-Pol, qui symbolise à lui seul notre bonne entente. A la manière d'un grand-papa canard, il nous a pris sous son aile et montré la voie. Il a en permanence une oreille compatissante et ouverte aux questions, mais surtout, il a toujours une réponse pertinente.
Ce travail n'aurait pu aboutir sans Frédéric. Bien que (sur)chargé de cours, il m'a toujours écouté et aiguillé. Son art socratique de poser les questions qui font mal m'a permis d'avancer. Sa relecture assidue de la plupart de mes écrits leur a permis de gagner en qualité. Enfin, son inoxydable bonne humeur et son rire surpuissant m'ont permis de dépasser bien des ennuis.
Enfin je voudrais remercier Anne-Catherine pour nos multiples discussions scientifiques ou non, notre émulation graphique et linguistique, ses relectures pertinentes, sa collaboration dans l'organisation du LAGASHOP et son rire communicatif. Je suis ravi d'avoir rencontré une collègue et gagné une amie.

Les voyages sont nécessaires et toujours profitables. Les rencontres avec d'autres scientifiques et le changement d'environement permettent de modifier son point de vue sur les choses. Les problèmes cachés dans l'ombre se révèlent à la lumière d'un jour nouveau et deviennent plus simples à résoudre. Je voudrais donc remercier l'ensemble de mes hôtes madrilènes, Manuel Pastor, Pablo Mira, Miguel Stickle, Paola Dutto et Jose Antonio Fernandez Merodo. Francisco-Javier Montans m'a également apporté des éclaircissements sur un certain nombre de questions sans réponses. *A todos, muchas gracias por el buen tiempo que pasé con vosotros.*
Chaque conférence ou voyage scientifique est l'occasion de découvrir des idées inédites mais également de faire de nouvelles rencontres, au détour d'un buffet de conférence ou devant une Chartreuse. Aussois reste l'exemple type de cette mise au vert, tant au bar qu'à la montagne.
Je voudrais citer mes amis d'un soir ou d'une semaine, Stéphane, Coralie, Valentina, Sophie et Cédric, qui connaissent la chanson.
Je voudrais remercier les collaborateurs de Cathie Associates pour l'aide qu'ils m'ont apportée et particulièrement Hendrik Versteele pour son travail de fin d'études qui m'a mis sur la voie de la géotechnique offshore.

Cette thèse n'aurait pu voir le jour sans tous mes amis, qui m'ont soutenu et aidé. Je les remercie de ne pas m'en vouloir de les avoir abandonnés pendant plusieurs mois d'écriture. Je remercie spécifiquement Quentin pour sa théière, qui m'a abreuvé pendant les mois d'hiver doux comme de printemps polaire. Merci à Nicolas, Noémie, Julien, Aurélie, Grégory, Sébastien, Alexandre, Nicolas, Valérie, Manu et Constance. J'ajoute également une petite pensée pour le futur joueur d'échec. Je n'oublie pas non plus mes parents sans qui je ne serais pas là, ni mes grands-parents sans qui mes parents ne seraient pas là, sans oublier leurs parents et grands-parents...
Quand il s'agit d'anglais, il est toujours utile d'avoir de bons amis pour débusquer les faux. Ce manuscrit a gagné en style grâce à la relecture acérée de Thomas. Bien plus que le relecteur, je remercie ici le binôme avec lequel je travaille depuis bien des années et l'ami de longue date avec qui j'ai partagé tant d'idées. Nos longues discussions bigarrées et ses saillies drolatiques me ravissent depuis que j'ai posé le pied à l'université.

Finalement, je remercie Maud, pour m'avoir soutenu stoïquement et avoir permis à ma thèse de lui voler la prééminence dans mon esprit au cours de ces derniers mois. Le point final de ces remerciements lui rendra la primauté.

Contents

List of symbols and notations

If units are complex or manifold, the symbol [!] is used.

Latin symbols

$\mathcal{B}$	Solid volume	[-]
$\partial\mathcal{B}$	Boundary of $\mathcal{B}$	[-]
$\mathbb{C}$	Tangent stiffness operator	[!]
Dr	Relative density	[%]
D	Diameter of the suction caisson	[m]
e	Thickness of the suction caisson	[m]
e	Void ratio	[-]
e_{min}	Minimum void ratio	[-]
e_{max}	Maximum void ratio	[-]
E	Young modulus	[Pa]
$\mathbb{E}$	Fourth order tensor of linear elastic coefficients	[Pa]
f	Yield criterion	[Pa,Pa^2]
g	Acceleration of gravity	[m/s^2]
g_N	Gap function (minimum distance between walls of the interface)	[m]
$\mathbf{g}_T$	Tangential displacement at the interface	[m]
G	Shear modulus	[Pa]
G_{ref}	Reference shear modulus	[Pa]
H	Height of the suction caisson	[m]
H'^i	Plastic modulus associated to surface i	[Pa]
$\bar{H}^i$	Modified plastic modulus associated to surface i	[Pa]
$H^{*,i}$	Projected modified plastic modulus associated to surface i	[Pa]
J	Jacobian matrix	[-]
$\mathbf{K}$	Stiffness matrix	[..]
k, k_l	Intrinsic permeability	[m^2]
K	Bulk modulus	[Pa]
K_0	Coefficient of earth pressure at rest	[-]
K_{ref}	Reference bulk modulus	[Pa]
K_N, K_T	Normal and tangential penalty coefficients	[N/m^3]
M	Half opening (radius) of a conical surface	[-]
M_{el}	Half opening (radius) of the first yield surface	[-]
n	Porosity	[-]
n	Exponent of the confinement dependency relation	[-]

$\mathbf{n}$	Normal vector	[Pa,-]
$\hat{\mathbf{n}}$	Normal unit vector	[-]
p'	Mean effective stress	[Pa]
$\mathrm{p}'_0, \mathrm{p}'_c$	Initial mean effective stress stress	[Pa]
p_N	Total normal stress within the interface	[Pa]
p'_N	Effective normal stress within the interface	[Pa]
p_{ref}	Reference pressure for the confinement dependency	[Pa]
$\mathbf{P}$	Direction of plastic deformation	[-]
$\mathbf{P'}$	Deviatoric component of the direction of plastic deformation	[-]
P''	Volumetric component of the direction of plastic deformation	[-]
P_{load}	Total load pressure applied to the caisson	[Pa]
q	Invariant of deviatoric stress tensor	[Pa]
$\mathrm{q}_s, \mathrm{q}_{off}, \mathrm{q}_{init}$	Initial invariant of deviatoric stress tensor	[Pa]
q_{cycl}	Cyclic amplitude of invariant of deviatoric stress tensor	[Pa]
$\mathbf{Q}$	Unit normal to the yield surface	[-]
$\mathbf{Q'}$	Deviatoric component of the unit normal to the yield surface	[-]
Q''	Volumetric component of the unit normal to the yield surface	[-]
r_i	Residual of the local iterative process	[-]
$\mathbf{R}$	Rotation matrix	[-]
S_{QSS}, S_{PT}	Quasi-steady state shear resistance	[Pa]
S_{SS}	Steady state shear resistance	[Pa]
$\dot{S}$	Storage fluid flux	[kg/s]
$\mathbf{s}$	Deviatoric stress tensor/vector	[Pa]
t	Time	[s,h]
$\mathbf{t}^{\alpha}$	Traction load on the interface	[Pa]
t_N	Normal components of traction load	[Pa]
$\mathbf{t}_T$	Tangent components of traction load	[Pa]
T_w^t	Transversal transmissivity	[$\mathrm{mPa^{-1}s^{-1}}$]
$\mathbf{u}$	Generalised coordinates vector	[m,Pa]
u_w	Pore water pressure	[Pa]
W_G	Gauss Weight	[-]
$\mathbf{x}$	Coordinates describing a solid volume in its current position	[m]
X	Coordinates describing a solid volume in its reference position	[m]

Greek symbols

α	Parameter of the line search algorithm	[-]
α	Triaxial backstress of a conical surface	[-]
$\boldsymbol{\alpha}$	Backstress tensor (Position of the centre of a conical surface)	[-]

$\boldsymbol{\alpha}_{n+1}$	Discretised backstress tensor (end of the step)	[-]
γ	Shear deformation	[-,%]
$\delta_{i,j}$	Kronecker delta	[-]
$\boldsymbol{\delta}$	Second order identity matrix	[-]
$\delta g_N, \delta \mathbf{g}_T$	Admissible virtual variation of gap function	[m]
δu_w	Admissible virtual variation of water pore pressure	[Pa]
$\delta W_E, \delta \dot{W}_E$	Exterior virtual work/power	[J,W,!]
$\delta W_I \delta W_I$	Interior virtual work/power	[J,W,!]
$\delta \mathbf{x}$	Admissible virtual displacement	[m]
ΔF_{tot}	Variation of total load applied to the caisson	[N]
ΔF_{ext}	Variation of total outer friction along the skirt	[N]
ΔF_{int}	Variation of total inner friction along the skirt	[N]
ΔF_{tip}	Variation of total reaction at the tip	[N]
ΔF_{top}	Variation of total reaction at the top	[N]
ΔF_{uw}	Variation of total pore pressure under the top	[N]
Δt	Time step	[s]
ΔP_{load}	Variation of total pressure applied to the caisson	[Pa]
Δu_w	Variation of pore water pressure	[Pa]
Δy	Variation of vertical displacement at the centre of the caisson	[m]
$\Delta \boldsymbol{\alpha}$	Discrete variation of the backstress tensor/vector	[-]
$\Delta \boldsymbol{\epsilon}$	Discrete variation of the deformation tensor/vector	[Pa]
$\Delta \lambda$	Discrete variation of the plastic multiplier	[-]
$\Delta \lambda_{n+1}$	Discrete variation of the plastic multiplier (end of the step)	[-]
$\Delta \lambda^i_{n+1}$	Component of the discrete variation of the plastic multiplier associated to surface i (end of the step)	[-]
$\Delta \boldsymbol{\sigma}$	Discrete variation of the stress tensor/vector	[Pa]
$\boldsymbol{\epsilon}$	Deformation tensor/vector	[-]
$\dot{\boldsymbol{\epsilon}}$	Deformation tensor/vector rate	[s^{-1}]
$\dot{\boldsymbol{\epsilon}}^e$	Elastic component of deformation tensor/vector rate	[s^{-1}]
$\dot{\boldsymbol{\epsilon}}^p$	Plastic component of deformation tensor/vector rate	[s^{-1}]
ϵ_q	Deviatoric deformation	[-]
$\dot{\epsilon}_q$	Deviatoric deformation rate	[s^{-1}]
ϵ_v	Volumetric deformation	[-]
$\dot{\epsilon}_v$	Volumetric deformation rate	[s^{-1}]
η	Reduced deviatoric stress ratio	[-]
$\bar{\eta}$	Phase transformation ratio	[-]
$\eta_{f,c}$	Reduced deviatoric stress ratio at failure (compression)	[-]
$\eta_{f,e}$	Reduced deviatoric stress ratio at failure (extension)	[-]
$\dot{\lambda}$	Continuous plastic multiplier	[-]
$\lambda_N, \boldsymbol{\lambda}_T$	Lagrange multipliers in normal and tangential directions	[Pa]
μ	Friction coefficient	[-]
$\boldsymbol{\mu}$	Deviatoric hardening direction of surface i	[Pa]
$\hat{\boldsymbol{\mu}}$	Deviatoric unit hardening direction of surface if	[-]
ν	Poison's ratio	[-]
$\boldsymbol{\xi}, \xi^1, \xi^2$	Convective coordinates of a boundary surface/Isoparametric coordinates	[m]

ρ	specific mass of the porous medium	[kg/m^3]
ρ_f	specific fluid mass	[kg/m^3]
ρ_s	specific mass of the grains	[kg/m^3]
$\boldsymbol{\sigma}$	Cauchy stress tensor/vector	[Pa]
$\boldsymbol{\sigma}'$	Effective Cauchy stress tensor/vector	[Pa]
$\dot{\boldsymbol{\sigma}}$	Cauchy stress tensor/vector rate	[Pa/s]
$\tilde{\boldsymbol{\sigma}}$	Objective Jaumann stress tensor/vector rate	[Pa/s]
$\boldsymbol{\sigma}_c^1$	Contact stress vector at point $\bar{\mathbf{x}}^1$	[Pa]
$\boldsymbol{\sigma}_{n+1}$	Discretised stress tensor (end of the step)	[Pa]
$\sigma_y, \sigma_1, \sigma_v$	Vertical stress component	[Pa]
$\sigma_x, \sigma_2, \sigma_h$	Horizontal stress component	[Pa]
σ_0	Initial confining stress	[Pa]
σ_0'	Initial Effective stress	[Pa]
τ_s	Initial shear stress	[Pa]
τ_{cycl}	Cyclic amplitude of shear stress	[Pa]
$\varphi(\mathcal{B})$	Mapping of $\mathcal{B}$ from reference to current configuration	[-]
ϕ_i	Shape function associated to node i	[-]
χ_f	Fluid compressibility	[Pa^{-1}]
ψ	Volumetric parameter of the non associated volumetric hardening rule	[-]

Chapter 1

Introduction

The only true wisdom is in knowing you know nothing.

Socrates

Contents

1.1 Motivations and context

From the cyclic behaviour of soils...

Nowadays civil engineering is continuously evolving. More and more, architects and engineers push the limits *citius*, *altius*, *fortius*. New constructions are taller, slender and lighter, built in inhospitable environments and subject to the assaults of nature (earthquakes, wind, waves...). These extreme conditions coupled with the increasing complexity of structures require an accurate understanding of underlying phenomena and a detailed modelling for the design.

Classic design standards and guidelines are sometimes limited when complex loadings are involved. Security must be ensured in each circumstance, during and after the building of a structure. Computational power has also increased for the last decades and allows to perform detailed analyses. Structural engineering has already taken the plunge and complex simulations are already common. Soil mechanics follows closely, but it is faced with its inherent difficulties. Soils are non-homogeneous media, have a strongly non-linear behaviour and impossible to inspect entirely.

Engineers and researchers have always resorted to physical modelling and laboratory experiments to understand what they ignore. However, it is not conceivable to perform costly scale modelling for each project. Therefore, numerical modelling is gathering momentum since it is flexible, suitable for parametric studies and it allows many cheap computations.

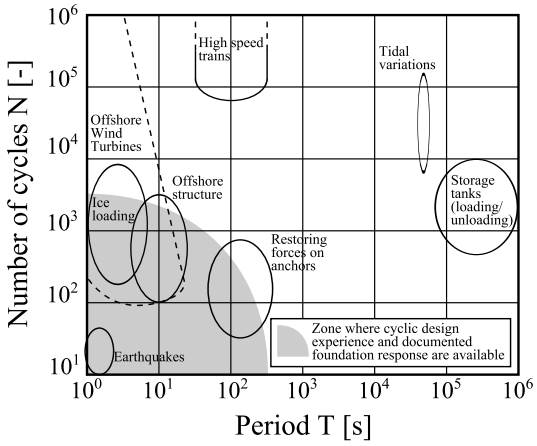

FIGURE 1.1: Cyclic loading types, after [Andersen et al., 2013].

Constitutive laws are the centre of gravity of this work. Indeed, a suitable model is the basic component of a finite element code since it represents the behaviour of a material whatever the loadings and the boundary conditions. This work principally aims at modelling the cyclic behaviour of soils with the finite element code `LAGAMINE`. Although it is not as famous as commercial FE codes, `LAGAMINE` is used and developed around the world.

Cyclic loading belongs to a family of loading processes, encompassing distinct realities and timescales (see in Figure 1.1). High speed trains induce small amplitude and moderate period cycles, but the number of cycles encountered over the lifetime of the foundation is very large. On the other hand, earthquakes engender a small number of very large amplitude at high frequency. Offshore loading lies in between. Obviously the consequences of such loadings are not identical, although they share similar features.

Cyclic loading of soil gives birth to very particular behaviours and failure modes. Whatever the type of loading, the deformation is progressively or sharply accumulated, with regard to the number of cycles. Soil stiffness tends to decrease accordingly. Very brutal and disastrous failure might occur where the so-called *liquefaction* is triggered. All these phenomena are not taken into account by classic soil constitutive laws.

Numerical methods must be used very cautiously. Indeed, numerical simulations, if not endorsed by experimental backup, can demonstrate anything. With a little imagination, they could even prove the existence of god(s). Therefore, it is of uttermost importance to evaluate the quality of the results. Two principal steps of control for any model should be considered, [Brinkgreve, 2013].

1. **Validation :** *process of determining the degree to which a model (including the set of parameters selected) is an accurate representation of the real world from the perspective of the intended use of the model.* This encompasses the selection of the model and its parameters that better calibrate the application to be modelled.

2. **Verification :** *process of determining that a computational model accurately represents the underlying mathematical model and is capable of reproducing the theoretical solution.*

... to offshore geotechnics.

The name of the scholarship endorsing this work is FRIA, i.e. "Research foundation for industry and agriculture". Therefore, the development of a theoretical constitutive law should not be the only motivation of the thesis. It should contribute to improve the knowledge of a field of engineering beneficial to Belgian industry.
Offshore engineering provides many interesting and relevant case studies, where cyclic modelling is involved. For instance, offshore wind energy is developing exponentially. Wind turbine of 5GW capacity were installed within the EU at the end of 2012, mainly in UK. A 40GW installed capacity is expected by 2020 and 150GW by 2030 [Caprace et al., 2012]. Indeed, the EU climate and energy package targets three main objectives :

- 20% reduction of EU greenhouse gas emissions from 1990 levels;
- 20% of the EU energy consumption produced from renewable resources;
- 20% improvement in the EU's energy efficiency.

Seven concession areas in Belgian North Sea are devoted to wind farms, representing $9-10\%$ of the total electricity consumption in Belgium [Verkest, 2013]. The C-Power project is already installed and consists of six 5MW and forty-eight 6MW windturbines, 30km off the coast. Such structures face both technical and economical challenges.
Indeed, competitive electricity costs is the *sine qua non* condition to ensure the viability of offshore projects. The cost of foundations represents up to a third of the total cost of a project [Senders, 2008]. Wind turbine structures are very light and subject to a large overturning moment. They must be designed to resist extreme storm events. Furthermore, offshore wind turbines are growing in size and implanted in deeper water.
Therefore, offshore foundations are a leading-edge technology. A compromise must be found between these technical and economical constraints, creating a large scientific emulation. However, this very ongoing topic and competition between private companies create a lack of available data in the literature, since they are often jealously guarded.
Fortunately, geotechnical conditions in the North Sea are remarkably uniform (see Figures 1.2a and 1.2b). Most of the deposit encountered are very dense layers, of the order of 100%. Therefore, data available from previous projects can be reused.

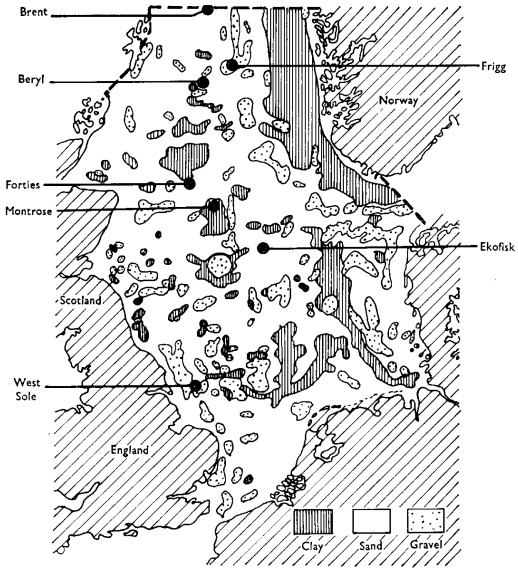

(a) Map of the North Sea with distribution of bottom sediments, [Bjerrum, 1973]

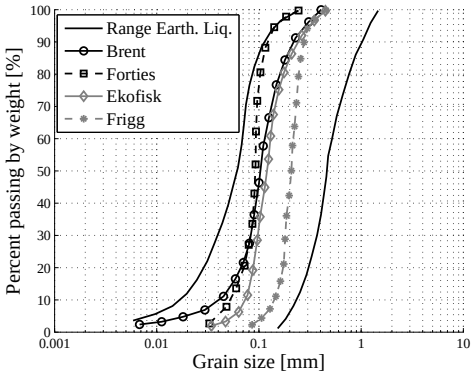

(b) Grain-size distributions of soil samples obtained at shallow depths at different sites in North Sea, [Bjerrum, 1973].

FIGURE 1.2

1.2 Objectives

The objectives of any thesis can be summed up in two single words : "why" and "how". The former answer is to provide the finite element code `LAGAMINE` the capability of modelling cyclic behaviour of cohesionless soils and to illustrate it with a suitable case study. How this objective is completed lies in a much longer sequence of intermediate goals.

1. **What happens ?** Initially, the salient features of the cyclic behaviour of soil must be identified through laboratory experiments. Pertinent characteristics are the basic requirements any constitutive law must fulfil.

2. **How to represent it ?** Among many possibilities, a constitutive law must be adopted to numerically reproduce the cyclic behaviour of sands.

3. **Which parameters ?** Parameters representative of the studied materials must be determined from experimental data. This step allows to understand the capabilities and limitations of the constitutive law adopted. The sensitivity of the response to these parameters must also be assessed.

4. **How to use it ?** The constitutive law must be implemented into the finite element code `LAGAMINE`. An integration scheme must be adopted and the algorithm must be verified with regards to the analytical model. Accuracy, efficiency and robustness of the algorithm must be ensured.

5. **Additional tools ?** An interface finite element must be updated to take into account the hydro-mechanical soil structure interaction. Its efficiency and robustness must be verified to ensure the global convergence of numerical simulations.

6. **Which application ?** The selected application is dissected to highlight the contribution of the model to the physics of observed phenomena. This last step emphasises the key issues of the functioning of an offshore foundation and draws attention to crucial parameters.

1.3 Outline

The backbone of this thesis consists of five main chapters briefly described hereafter. They are organised in a logical sequence, from the laboratory to a numerical application.

Chapter 3 presents an overview of the experimental behaviour of sand. Monotonic and cyclic experimental results are described and discussed. Salient features that are pertinent for the modelling of offshore foundations are highlighted. They consist of the minimum requirements a numerical model has to take into account.

Chapter 4 summarises the main constitutive models that are able to reproduce the cyclic behaviour of sands. The Prevost model is finally adopted and its basic equations are developed. The last part of this Chapter deals with the validation step. Indeed, the model must be able to reproduce real behaviour of a given material. Three calibrated sets of parameters are calibrated.

Chapter 5 fills the gap between an analytical constitutive model and its practical implementation in the finite element code `LAGAMINE`. A closest point projection algorithm is adopted involving an implicit integration of the constitutive law. Consequently, a special hardening rule must be adopted and a non-linear set of equations must be iteratively solved. A verification step is performed to ensure the discrete integration procedure corresponds to the analytical constitutive law. Convergence and accuracy of the model are illustrated.

Chapter 6 displays the theory related to hydro-mechanical interface finite elements. The element developed manages sliding, fluid flow through and along the interface as well as suction effect created by unsticking of both sides. The full derivation of energetically equivalent nodal forces and stiffness matrix as well are provided. Finally, numerical simulations illustrate performance of the element and emphasises the partially drained behaviour of soils.

Chapter 7 concludes this work in dissecting an offshore case study. The response of a vertically loaded suction caisson is deeply studied. Monotonic push and pull simulations are investigated under drained and partially drained conditions. The final example consists of a pseudo-random and a sinusoidal-equivalent loadings acting on the caisson. Consequences on pore pressure settlement accumulations are explored.

Chapter 2

Mechanical modelling of geomaterials

Le conformisme commence à la définition.
(Conformism starts with a definition.)

Georges Braque

Contents

2.1 Mathematical notations

The main *mathematical* beings that populate this work are vectors and tensors. They are denoted in bold characters, e.g. $\mathbf{X}$. A particular treatment is given to fourth order tensor, which are denoted in blackboard bold characters, e.g. $\mathbb{X}$. $\boldsymbol{\delta}$ is the identity tensor and δ_{ij} is the special Kronecker delta,

$$\delta_{ij} = \begin{cases} 1 & \text{if} \quad i = j \\ 0 & \text{if} \quad i \neq j \end{cases} \tag{2.1}$$

Indicial (or Einstein) notation convention is adopted in the following in order to increase readability. This system of notations adopts the summation convention, i.e. dummy indices replace the summation symbol if they appear exactly twice in each term of a sum, e.g.

$$a_i \, b_i = \sum_{i=1}^{n} a_i \cdot b_i. \tag{2.2}$$

The transpose of a vector or matrix is denoted $(\cdot)^T$.

The dot product is designated by ":". It represents a two-indice contraction between two tensors

$$\mathbf{a} : \mathbf{b} = a_{ij} \cdot b_{ij}. \tag{2.3}$$

Consequently, it represents a scalar if $\mathbf{a}$ and $\mathbf{b}$ are second-order tensors. It follows that the norm of that tensor is defined as

$$\|\mathbf{a}\| = \sqrt{\mathbf{a} : \mathbf{a}} \tag{2.4}$$

Finally the Macauley brackets $\langle\rangle$ are defined according to

$$\langle\beta\rangle = \frac{1}{2} \cdot (\beta + |\beta|) \tag{2.5}$$

2.2 Referential, stress and strain

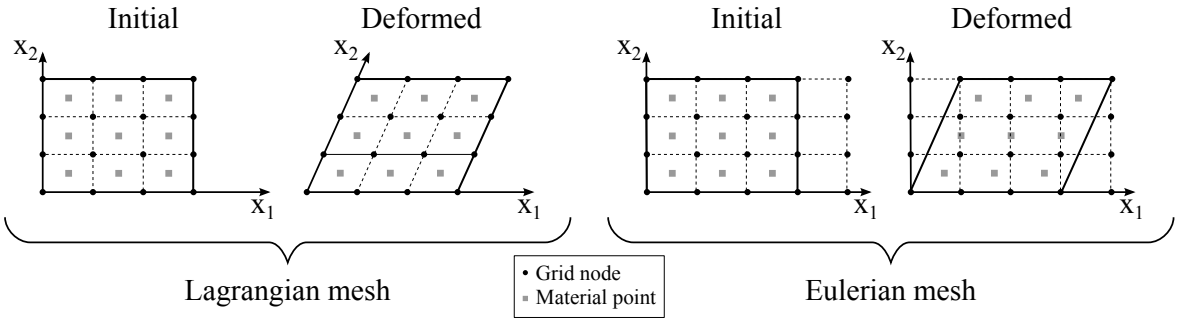

FIGURE 2.1: Difference between Eulerian and Lagrangian meshes, inspired by [Donea et al., 2004].

The finite element code `LAGAMINE` was initially devoted to the modelling of metal forming [Charlier, 1987]. Thence, large strains and/or displacements as well as rigid body motions had to be taken into account. Equilibrium equations of any body $\mathcal{B}$ stand whatever its configuration. These equilibrium equations hold over a volume and are stated in an orthonormal basis. Different possibilities are available but the possible formulations divide roughly into two families [Malvern, 1969].

1. **Lagrangian description.** The equilibrium is formulated with respect to the reference configuration but the basis evolves with the deformed body $\mathbf{e}_i$. Lagrangian mesh is linked to the material points and moves with it (see Figure 2.1).

2. **Eulerian description.** The equilibrium is formulated with respect to the deformed configuration but in the reference fixed basis $\mathbf{E}_i$. Eulerian mesh is fixed in the space and material points move through it (see Figure 2.1).

Let us now consider a deformable body $\mathcal{B}$. At time $t \in \mathbb{R}^+$, $\boldsymbol{\varphi}_t : \mathcal{B} \to \mathbb{R}^{n_{dim}}$ is the mapping[1] that associates a point $\mathbf{X}$ of the reference configuration $\mathcal{B}$ onto its current position $\mathbf{x} = \boldsymbol{\varphi}_t(\mathbf{X})$. This transformation is characterised by the deformation gradient $\mathbf{F}$ (Jacobian tensor) which relates tangent vectors in the initial configuration to tangent vectors in the deformed one, i.e. a material line element $d\mathbf{X}$ in $\mathcal{B}$ is associated to the line element $d\mathbf{x}$ in $\varphi(\mathcal{B})$, such as

$$\mathrm{d}\mathbf{x} = \mathbf{F} \cdot \mathrm{d}\mathbf{X}. \tag{2.6}$$

Components of the deformation gradient are given in indicial notations by

$$F_{i,j} = \frac{\partial x_i}{\partial X_j}. \tag{2.7}$$

Conditions on $\mathbf{F}$ hold to preserve uniqueness of the mapping and prevents self-penetration of the body, i.e.

$$J = \det\mathbf{F} > 0. \tag{2.8}$$

Thence, transformation of area from reference configuration $\mathcal{B}$ (dA) to current configuration $\varphi(\mathcal{B})$ (da) can be derived [Wriggers, 2006] from the Nanson formula

$$d\mathbf{a} = \mathbf{n}\, da = J \cdot \mathbf{F}^{-1} \cdot \mathbf{N}\, dA = J \cdot \mathbf{F}^{-1} \cdot d\mathbf{A} \tag{2.9}$$

where $\mathbf{n}$ is the normal vector associated to da in the current configuration and $\mathbf{N}$ is the normal associated to dA in the reference configuration. A similar relation associates reference volume to current one

$$dv = J \cdot dV. \tag{2.10}$$

In this work, the updated Lagrangian formulation is adopted (see Figure 2.2):

- the mesh is Lagrangian and moves with material particles;
- stress and strain measurements are Eulerian, i.e. they refer to the current configuration;
- derivatives and integrals are computed with respect to the Eulerian coordinates $\mathbf{x}$;
- the orthonormal basis is related to the body $\mathcal{B}$ evolution in space. However, in the finite element code `LAGAMINE`, the direction of unit vectors remains constant.

The updated Lagrangian formulation can be related to the Lagrangian one by stating that stresses and strains refer to the reference configuration that evolves at every step, i.e. the reference configuration becomes $\varphi(\mathcal{B})$.

The velocity of a material point $\mathbf{x}$ in the current configuration $\varphi(\mathcal{B})$ reads

$$\mathbf{v} = \frac{d\mathbf{x}}{dt}. \tag{2.11}$$

[1] n_{dim} is the number of dimension of the space considered.

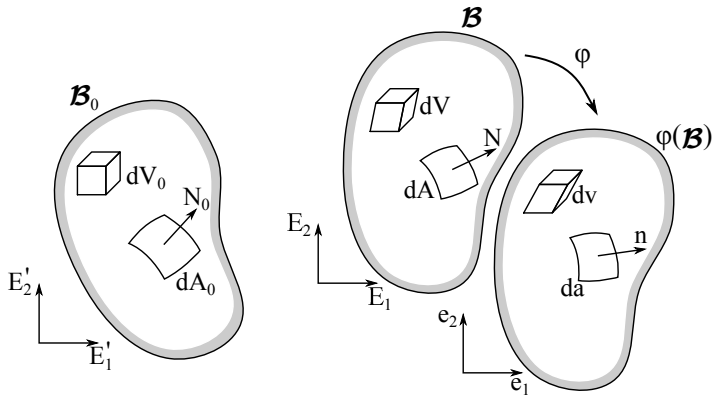

FIGURE 2.2: Updated Lagrangian formulation : $\mathcal{B}_0$ and (E_1', E_2') are the initial configuration and basis respectively; $\mathcal{B}$ and (E_1, E_2) are the updated reference configuration and basis; $\mathcal{B}$ and (e_1, e_2) are the current configuration and basis; dA_0, dA, da and dV_0, dV, dv are the elementary surfaces and volumes associated to each configuration; φ is the mapping of the reference configuration $\mathcal{B}$ to the current configuration $\varphi(\mathcal{B})$.

Consequently, the velocity gradient $\mathbf{L}$ in the current configuration is given by

$$\mathbf{L} = \frac{\partial \mathbf{v}}{\partial \mathbf{x}} = \frac{\partial \mathbf{v}}{\partial \mathbf{X}} \frac{\partial \mathbf{X}}{\partial \mathbf{x}}, \tag{2.12}$$

which can be split into a symmetrical and anti-symmetrical part

$$\mathbf{L} = \frac{1}{2}\left(\mathbf{L} + \mathbf{L}^T\right) + \frac{1}{2}\left(\mathbf{L} - \mathbf{L}^T\right). \tag{2.13}$$

The rate of strain tensor (or stretching tensor) is defined as the symmetrical part of $\mathbf{L}$

$$\mathbf{D} = \frac{1}{2}\left(\mathbf{L} + \mathbf{L}^T\right), \tag{2.14}$$

and the spin rate is the anti-symmetrical one

$$\boldsymbol{\omega} = \frac{1}{2}\left(\mathbf{L} - \mathbf{L}^T\right). \tag{2.15}$$

The definition of the rate of the stretching tensor, Equation (2.14), is meaningless in the field of large rotations and deformations. In others words this equation holds only for small deformations. Thence natural deformation tensor $\mathbf{G}$ is used instead,

$$\mathbf{G} = \ln \mathbf{U}, \tag{2.16}$$

where $\mathbf{U}$ is the stretching tensor obtained from the polar decomposition of the Jacobian tensor $\mathbf{F}$, [Charlier, 1987]

$$\mathbf{F} = \mathbf{R} \cdot \mathbf{U}, \tag{2.17}$$

where $\mathbf{R}$ is the rigid body rotation tensor, i.e. which implies no deformation. Furthermore, $\mathbf{D}$ is an approximation of the tensor $\mathbf{U}$ for small rotations. It is noteworthy that the strain measure $\mathbf{G}$ coincides with the integral of Equation (2.14) in principal axes if they remain unchanged.

In the following, the rate of the stretching tensor is termed $\dot{\boldsymbol{\epsilon}}$ irrespectively of its definition. Moreover, the local integration of the constitutive law requires a hypothesis on the evolution of this tensor over a time step. In this work, it is assumed the velocity gradient $\mathbf{L}$ is constant

over step. The detailed justification of the method is out of the scope of this work, but interested reader should refer to [Charlier, 1987; Cescotto, 1992; De Montleau et al., 2008].

The large displacement/deformation process requires an objective stress rate computation, i.e. independent of rigid body rotation. Therefore, the Jaumann objective stress rate $\tilde{\boldsymbol{\sigma}}$ is adopted in the following

$$\tilde{\boldsymbol{\sigma}} = \dot{\boldsymbol{\sigma}} - \boldsymbol{\omega} \cdot \boldsymbol{\sigma} - \boldsymbol{\sigma} \cdot \boldsymbol{\omega}^T. \tag{2.18}$$

Other schemes can be used instead, as shown in [Ponthot, 2002].

Finally, the sign convention of soil mechanics is adopted, *i.e.* compression stress and compaction strains are positive.

2.3 Granular medium, effective stress

In the field of soil mechanics, modelled media are most of the time composed of several phases : solid, fluid and gas, [Coussy, 1991; Detournay and Cheng, 1993; Lewis and Schrefler, 1998]. Therefore, if a representative elementary volume of soil $d\Omega$ is considered (see Figure 2.3), the porous medium can be considered as a juxtaposition of

- the soil skeleton, which is a continuous arrangement of solid grains. The volume of this medium $d\Omega_s$ is equal to the volume of the grains. Their specific mass is noted ρ_s and they are most of the time deemed incompressible. Consequently, the global behaviour of the medium is not due to the deformation of the grains but to the relative slip between them.
- the void medium, noted $d\Omega_v$, which can be filled with fluid(s) and/or gas. Void volume can be filled either by a liquid phase only or by liquid and gas phases. The soil is referred as saturated in the former case and partially saturated in the latter. In this work, only water is considered for either fluid or gas phases.

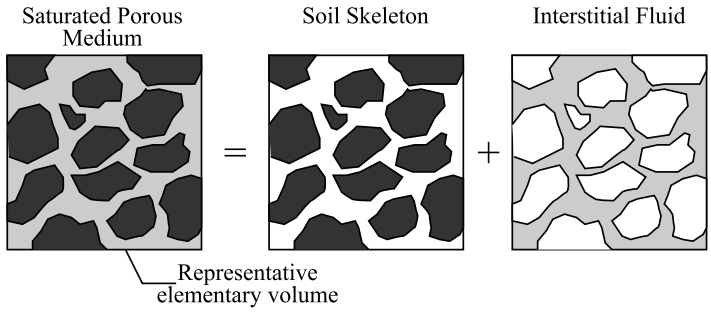

FIGURE 2.3: Description of a porous medium : cross-section of a representative elementary volume $d\Omega_e$, after Barnichon [1998]

Homogenisation at a macroscopic scale allows to define an equivalent continuous medium Ω. Thence, solid Ω_s and fluid Ω_f phases are superimposed and defined at any geometrical point of the represented volume. The open porosity n is defined as

$$n = \frac{\Omega_v}{\Omega} = \frac{\Omega_v}{\Omega_s + \Omega_v} \qquad \in [0, 1]. \tag{2.19}$$

Thence, the specific mass of the porous medium ρ is obtained from

$$\rho = (1 - n) \cdot \rho_s + n \cdot \rho_f, \tag{2.20}$$

where ρ_f is the specific mass of the fluid.

Solid kinematic description defined in Section 2.2 can be applied to the solid skeleton of the continuum porous medium. However, these concepts cannot be applied to the fluid phase straightforwardly. Indeed, the major difference with classic continuum description is that any elementary volume $d\Omega$ might exchange fluid or gas with its environment. Moreover, the mechanical behaviour, e.g. the relative slip of the grains, might reduce or increase the void volume Ω_v and influences fluid behaviour. This effect of one phase to another is defined as a "coupling". Eulerian and Lagrangian descriptions are both available.

1. **Eulerian description**. The Eulerian relative flow of fluid mass vector $\mathbf{f}_w$, [Coussy, 1991; Bourgeois and Dormieux, 1996], is defined as

$$\mathbf{f}_w = \rho_f \cdot \mathbf{v}^d, \tag{2.21}$$

where $\mathbf{v}^d$ is the Darcy velocity, i.e. the relative velocity of the fluid with respect to the solid skeleton. It is written

$$\mathbf{v}^d = n \cdot (\mathbf{v}^w - \mathbf{v}^s) \tag{2.22}$$

where $\mathbf{v}^w$ is the average spatial velocity of water phase and $\mathbf{v}^s$ is the spatial velocity of the solid phase. $\mathbf{v}^d$ is insensitive to rigid body motion. Let us consider an infinitesimal surface da, whose the normal is $\mathbf{n}$. At time t and per unit of time, a fluid mass J_f^m flows through da such as

$$J_f^m = \mathbf{f}_w \cdot \mathbf{n}\, da. \tag{2.23}$$

2. **Lagrangian description.** The Lagrangian relative flow fluid vector $\mathbf{F}_w$ is equivalent to $\mathbf{f}_w$. Thence, the fluid mass J_f^m flows through an infinitesimal surface in reference configuration dA of normal $\mathbf{N}$ reads

$$J_f^m = \mathbf{F}_w \cdot \mathbf{N}\, dA. \tag{2.24}$$

Vectors $\mathbf{f}_w$ and $\mathbf{F}_w$ become equivalent if displacement velocity is much smaller than the fluid one, [Barnichon, 1998].
In the finite element code `LAGAMINE`, the description may be qualified as hybrid. Indeed the mesh follows the solid skeleton that deforms while the description of the fluid is Eulerian inside this solid framework.

The interstitial fluid is characterised by its pressure p_f. In presence of water, the so-called *pore water pressure* is referred as u_w. Thence, total $\boldsymbol{\sigma}$ and effective $\boldsymbol{\sigma}'$ Cauchy stress tensors must be distinguished thanks to the Postulate of Terzaghi which states generally

$$\boldsymbol{\sigma} = \boldsymbol{\sigma}' + p_f \cdot \boldsymbol{\delta}, \tag{2.25}$$

where $\boldsymbol{\delta}$ is the second order identity tensor.

2.4 Problem statement

2.4.1 Mechanical part

The full description of the mechanical problem requires the statement of boundary conditions. The reference boundary $\partial\mathcal{B}$ of the body $\mathcal{B}$ can be decomposed into non overlapping parts

- $\partial\mathcal{B}_f$, which is load free ;
- $\partial\mathcal{B}_{\bar{x}}$, where displacements ($\bar{\mathbf{x}}$) are imposed ;
- $\partial\mathcal{B}_{\bar{t}}$, where traction loads ($\bar{\mathbf{t}}$) are imposed;

such that

$$\partial\mathcal{B} = \partial\mathcal{B}_f \cup \partial\mathcal{B}_{\bar{t}} \cup \partial\mathcal{B}_{\bar{x}} \qquad \text{and} \qquad \partial\mathcal{B}_f \cap \partial\mathcal{B}_{\bar{t}} \cap \partial\mathcal{B}_{\bar{x}} = \varnothing. \tag{2.26}$$

Consequently, the strong form of the initial boundary value problem under quasi static conditions consists in finding the field of displacement $\Delta\mathbf{x}$ for all $\mathbf{x} \in \varphi(\mathcal{B})$ such that

$$\begin{aligned} \mathrm{div}\boldsymbol{\sigma} + \bar{\mathbf{f}} = &\quad 0 \quad \text{in}\, \varphi(\mathcal{B}), && (2.27)\\ \mathbf{x} = &\quad \bar{\mathbf{x}} \quad \text{on}\, \varphi(\partial\mathcal{B}_{\bar{x}}), && (2.28)\\ [\boldsymbol{\sigma}]^T \cdot \mathbf{n} = &\quad \bar{\mathbf{t}} \quad \text{on}\, \varphi(\partial\mathcal{B}_{\bar{t}}), && (2.29) \end{aligned}$$

where $\mathbf{n}$ is the unit normal vector to $\varphi(\partial\mathcal{B}_{\bar{t}})$ and $\bar{f}$ are the volume body forces, e.g. the gravity forces. The equilibrium equations hold within the current configuration, *i.e.* $\varphi(\mathcal{B})$ since the approach is updated Lagrangian. In addition, it is assumed that initial field of displacement $x_0 = x(t=0)$ verifies Equation (2.27), (2.28) and (2.29). Up to that point, no hypothesis has been formulated on the behaviour of the material. However, a constitutive relation has to be stated in order to relate stress rate and strain rate, i.e.

$$\tilde{\boldsymbol{\sigma}}' = \mathbf{f}(\dot{\boldsymbol{\epsilon}}, \boldsymbol{\sigma}', \boldsymbol{\kappa}) \tag{2.30}$$

where $\boldsymbol{\kappa}$ are internal parameters of the law.

Finite element codes such as `LAGAMINE` are derived from a weak formulation of the equilibrium equations [Borja, 2013; Zienkiewicz and Taylor, 2000]. Let us consider an admissible virtual velocity field $\delta\dot{\mathbf{x}}$, i.e. a field of velocities that verifies solid continuity and boundary conditions. Therefore, the principle of virtual power implies that, for any $\delta\dot{\mathbf{x}}$, the solid is in equilibrium if internal virtual power $\delta\dot{W}_I$ is equal to external one $\delta\dot{W}_E$, i.e.

$$\underbrace{\int_{\varphi(\mathcal{B})} \boldsymbol{\sigma} \cdot \boldsymbol{\epsilon}[\delta\dot{\mathbf{x}}]\, \mathrm{d}V}_{\delta\dot{W}_I} = \underbrace{\int_{\varphi(\mathcal{B})} \bar{\boldsymbol{f}} \cdot \delta\dot{\mathbf{x}}\, \mathrm{d}V + \int_{\varphi(\partial\mathcal{B}_{\bar{t}})} \bar{\boldsymbol{t}} \cdot \delta\dot{\mathbf{x}}\, \mathrm{d}\Gamma}_{\delta\dot{W}_E}. \tag{2.31}$$

2.4.2 Hydraulic part

Since fluid flow occurs inside a porous medium, additional boundary conditions are necessary to fully describe the boundary value problem. Thence, from a hydraulic point of view, the boundary $\partial\mathcal{B}^f$ of the body $\mathcal{B}$ can be decomposed into non overlapping parts

- $\partial\mathcal{B}^f_f$, which is free;
- $\partial\mathcal{B}^f_{\bar{q}}$, where fluid fluxes ($\bar{\mathbf{q}}$) are imposed ;
- $\partial\mathcal{B}^f_{\bar{u}_w}$, where fluid pressures ($\bar{u}_w$) are imposed;

such that

$$\partial\mathcal{B}^f = \partial\mathcal{B}^f_f \cup \partial\mathcal{B}^f_{\bar{q}} \cup \partial\mathcal{B}^f_{\bar{u}_w} \qquad \text{and} \qquad \partial\mathcal{B}^f_f \cap \partial\mathcal{B}^f_{\bar{q}} \cap \partial\mathcal{B}^f_{\bar{u}_w} = \varnothing. \tag{2.32}$$

Thence, the strong form of the initial boundary value problem consists in finding the field of variations of pore water pressure Δu_w for all $\varphi(u_w \in \mathcal{B})$ such that

$$\dot{S} + \operatorname{div} \mathbf{f}_w = \bar{Q} \quad \text{in } \varphi(\mathcal{B}), \tag{2.33}$$

$$u_w = \bar{u}_w \quad \text{on } \varphi\left(\partial\mathcal{B}^f_{\bar{u}_w}\right), \tag{2.34}$$

$$\mathbf{f}_w^T \cdot \mathbf{n} = \bar{q} \quad \text{on } \varphi\left(\partial\mathcal{B}^f_{\bar{q}}\right), \tag{2.35}$$

where $\bar{Q}$ is the source term, $\dot{S}$ the rate of variation of stored fluid mass and $\mathbf{n}$ is the unit normal vector to $\varphi(\partial\mathcal{B}_{\bar{u}_w})$. This variation of fluid mass content is given by [Biot, 1977]

$$\Delta S = (J \cdot \rho_f \cdot n)|_{t+\Delta t} - (\rho_f \cdot n)|_t, \tag{2.36}$$

where J is defined in Equation (2.8) and n is the porosity. It must be pointed out that this variation stems from both the deformation of solid skeleton (coupling term) and the compressibility of the fluid. Indeed, considering an isotherm evolution, the fluid state equation relates its specific mass ρ_f to its pressure u_w. The linearised fluid state equation is obtained from [Burger, 1985]

$$\rho_f^{t+\Delta t} = \rho_f^t \cdot \left(1 + \frac{u_w^{t+\Delta t} - u_w^t}{\chi_f}\right), \tag{2.37}$$

where χ_f is the fluid compressibility. The determinant of the Jacobian matrix J is related to the volumetric strain $\epsilon_v = \mathrm{tr}\boldsymbol{\epsilon}$ by[2]

$$J = 1 + \epsilon_v, \tag{2.38}$$

which is the origin of the coupling solid-fluid, since ϵ_v depends on the constitutive law adopted to describe the solid behaviour.

A relation similar to the constitutive law, Equation (2.30), for the solid skeleton has still to be determined. THe Darcy's law derives from the balance of momentum equation for the pore water [Lewis and Schrefler, 1998]. The interaction force between the skeleton and the fluid is proportional to the relative motion between the two phases. This law is only valid in case of laminar fluxes, which is verified in many geotechnical applications.

$$\mathbf{v}^d = -\frac{k}{\mu_f}\left(\boldsymbol{\nabla} u_w + \rho_f \cdot g \cdot \boldsymbol{\nabla} z\right), \tag{2.39}$$

where k is the intrinsic permeability (unit $[L^2]$) and μ_f is the fluid dynamic viscosity (unit $[ML^{-1}T^{-1}]$), equal to 10^{-3} $Pa.s$ for water at 20°C.

Considering an admissible virtual displacement of pore pressure δu_w, the principle of virtual power can be derived from equilibrium Equations (2.33), (2.34) and (2.35). Thence, the weak formulation of the problem can be stated in the updated configuration

$$\underbrace{\int_{\varphi(\mathcal{B})} \left(\dot{S} \cdot \delta u_w - \mathbf{f}_w \cdot \boldsymbol{\nabla}(\delta u_w)\right) \mathrm{d}V}_{\delta W_I} = \underbrace{\int_{\varphi(\mathcal{B})} \bar{Q} \cdot \delta u_w \,\mathrm{d}V + \int_{\varphi\left(\partial\mathcal{B}^f_{\bar{q}}\right)} \bar{q} \cdot \delta u_w \,\mathrm{d}\Gamma}_{\delta W_E} \tag{2.40}$$

2.5 Discretisation

In the classic finite element method, each continuum body is discretised by n_e finite elements of volume Ω_e. The approximate body $\mathcal{B}^h$ is defined such that (see Figure 2.4)

$$\mathcal{B}^h = \bigcup_{e=1}^{n_e} \Omega_e. \tag{2.41}$$

[2]This relation only holds in case of small deformations.

For the sake of simplicity, equations and pictures are provided for a 2D formulation but the transition to 3D is straightforward. Primary unknowns are the nodal coordinates (either mechanical or hydraulic). They are interpolated over the element using shape functions. In the finite element code `LAGAMINE`, isoparametric elements are extensively employed. This concept is developed and discussed extensively in many books devoted to finite element method, see for instance [Zienkiewicz and Taylor, 2000] or [Schrefler and Lewis, 1998]. Thence the author feels free to avoid theoretical developments that could only be less elegantly presented.
Coordinates and pore water pressures are computed over a single element using the same shape functions $\phi_i(\boldsymbol{\xi})$ (see Figure 2.4)

$$\mathbf{u}^e(\boldsymbol{\xi}) = \sum_{i=1}^{n_n} \phi_i(\boldsymbol{\xi}) \cdot \mathbf{u}_i \qquad \text{and} \qquad \boldsymbol{\Delta}\mathbf{u}^e(\boldsymbol{\xi}) = \sum_{i=1}^{n_n} \phi_i(\boldsymbol{\xi}) \cdot \boldsymbol{\Delta}\mathbf{u}_i, \tag{2.42}$$

where

- n_n is the number of nodes of the element Ω_e ;
- $\mathbf{u}^e(\boldsymbol{\xi})$ is the generalised coordinate vector of any point belonging to Ω_e. Each node has 3 degrees of freedom : two global coordinates (x_1, x_2) and a pore water pressure u_w. The element has an equal order of interpolation for both mechanical and hydraulic degrees of freedom. They do not mathematically fulfil the inf-sup condition, but oscillation problems within the results. Further developments about this condition might be found in [Mira et al., 2003] ;
- $\boldsymbol{\Delta}\mathbf{u}^e(\boldsymbol{\xi})$ are the generalised displacements corresponding to $\mathbf{u}^e(\boldsymbol{\xi})$;
- $\mathbf{u}_i$ are the nodal generalised coordinates of the ith node of element Ω^e ;
- ϕ_i are the shape functions associated to the local coordinates ;
- $\boldsymbol{\xi} = (\xi_1, \xi_2)$ are the local isoparametric coordinates.

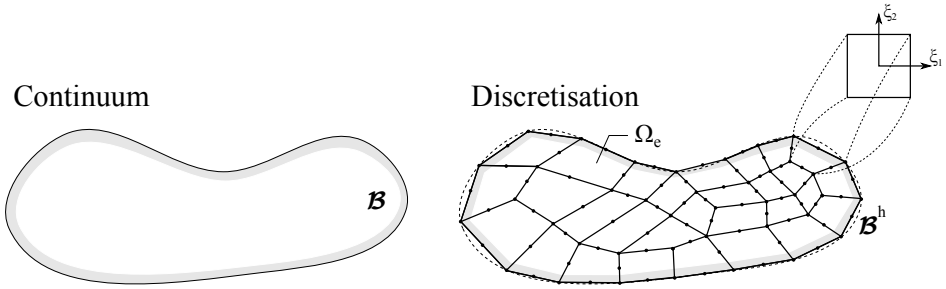

FIGURE 2.4: Discretisation of the continuum. $\mathcal{B}$ stands for the continuum volume . $\mathcal{B}^h$ is its discrete counterpart composed by n_e finite elements Ω^e. (ξ_1, ξ_2) are the isoparametric local coordinates.

Let us consider $\delta\dot{\mathbf{x}}^{\Omega^e}$ a vector that contains the velocities $\delta\dot{\mathbf{x}}_i^{\Omega^e}$ associated to each node i of the of the n_n nodes composing the single element Ω^e. Following Equation (2.31), the

virtual internal power can be written for that element

$$\begin{aligned}
\delta\dot{W}_I^{\Omega_e} &= \int_{\varphi(\Omega_e)} \boldsymbol{\sigma}\cdot\boldsymbol{\epsilon}[\delta\dot{\mathbf{x}}^{\Omega_e}]\,\mathrm{d}V \\
&= \sum_{i=1}^{n_n}\left[\int_{\varphi(\Omega_e)} \boldsymbol{\sigma}\cdot\boldsymbol{\epsilon}[\phi_i]\,\mathrm{d}V\right]\cdot\delta\dot{\mathbf{x}}_i^{\Omega_e} \\
&= \sum_{i=1}^{n_n}\left[\mathbf{F}_{I,i}^{\Omega_e}\right]^T\cdot\delta\dot{\mathbf{x}}_i^{\Omega_e} \qquad (2.43)\\
&= \left[\mathbf{F}_I^{\Omega_e}\right]^T\cdot\delta\dot{\mathbf{x}}^{\Omega_e}, \qquad (2.44)
\end{aligned}$$

where Equation (2.44) is the vectorial form of Equation (2.43). $\mathbf{F}_i^{\Omega_e}$ is the vector of internal energetically equivalent nodal forces associated to node i of the element Ω_e. Since the global discretised body is composed of n_e elements, they must be assembled together according to Equation (2.41). Thence, the global vector of mechanical nodal forces reads

$$\mathbf{F}_I = \bigcup_{e=1}^{n_e}\mathbf{F}_I^{\Omega_e}. \qquad (2.45)$$

Equation (2.44) only defines the mechanical internal nodal forces. However, hydraulic nodal forces can be derived similarly, considering the expression of internal virtual work Equation (2.40). Hydraulic and mechanical nodal forces can be grouped together in the same vector $\mathbf{F}_I$, which becomes the generalised equivalent nodal forces of different natures (mechanical and fluxes). External energetically equivalent nodal forces $\mathbf{F}_E$ are derived in the same way from external virtual power, i.e. Equations (2.31) and (2.40).

The last step is the numerical integration of $\mathbf{F}_i^{\Omega_e}$. The integration over the deformed element can be carried out numerically using Gauss quadrature. The result of the integral is the sum of the evaluation of each integrand at the integration point (IP), i.e.

$$\int_{\varphi(\Omega_e)} \boldsymbol{\sigma}\cdot\boldsymbol{\epsilon}[\phi_i]\,\mathrm{d}V = \sum_{IP}\left[\boldsymbol{\sigma}\cdot\boldsymbol{\epsilon}[\phi_i]\right]_{IP}\cdot J^t\cdot t\cdot W_G \qquad (2.46)$$

where IP is the number of integration points, t is the thickness of the element Ω_e (in case of plane state), J^t is the determinant of the Jacobian matrix (corresponding to the transformation of the isoparametric element) and W_G is the Gauss weight corresponding to the integration point IP.

2.6 Solving the global problem

Equilibrium is reached when energetically equivalent internal nodal forces $\mathbf{F}_I$ are equal to external ones $\mathbf{F}_E$. However, due to the evolution of the loading or the transient behaviour of the studied solid, these nodal forces are probably not balanced at the beginning of an arbitrary time step. Therefore, the so-called out of balance forces are defined such that [Borja, 2013]

$$\mathbf{F}_{OB} = \mathbf{F}_E - \mathbf{F}_I, \qquad (2.47)$$

which are a measurement of the imbalance within the system. A numerical criterion has to be adopted in order to differentiate between equilibrium and no equilibrium. Indeed the out of balance forces will never be exactly equal to zero and are different in nature (forces or fluid

fluxes), so they cannot be summed roughly. This discussion is out of the scope of this thesis but can be found in [Charlier, 1987].
The out of balance forces are expanded in a Taylor series, limited to the first order,

$$\mathbf{F}_{OB}^{(t+\Delta t)} = \mathbf{F}_{OB}^{(t)} + \frac{\partial \mathbf{F}_{OB}^{(t)}}{\partial \Delta \mathbf{u}} \cdot \Delta \mathbf{u}, \tag{2.48}$$

where $\Delta \mathbf{u}$ gathers the generalised displacements, either mechanical or hydraulic. The equilibrium is reached at time $t + \Delta t$, if out of balance forces are null, i.e.

$$\mathbf{F}_{OB}^{(t+\Delta t)} = 0. \tag{2.49}$$

Generalised degrees of freedom are corrected by $\Delta \mathbf{u}$, that is derived from a rearrangement of Equations (2.48) and (2.49).

$$\Delta \mathbf{u} = -\left[\frac{\partial \mathbf{F}_{OB}^{(t)}}{\partial \mathbf{u}}\right]^{-1} \cdot \mathbf{F}_{OB}^{(t)} = -\left[\mathbf{K}^{(\mathbf{t})}\right]^{-1} \cdot \mathbf{F}_{OB}^{(t)}, \tag{2.50}$$

$$\mathbf{u}^{(t+\Delta t)} = \mathbf{u}^{(t)} + \Delta \mathbf{u}, \tag{2.51}$$

where the stiffness matrix $\mathbf{K}^{(t)}$ at time step t naturally appears. Each component of the stiffness matrix is then computed as the variation of equivalent nodal forces at node i, $\mathbf{F}_{OB,i}$, due to a variation of generalised coordinates at node j, $\mathbf{u}_j$,

$$[\mathbf{K}]_{i,j} = -\frac{\partial \mathbf{F}_{OB,i}}{\partial \mathbf{u}_j}. \tag{2.52}$$

The apparently trivial inverse operation of the stiffness matrix in Equation (2.50) is one of the most CPU time consuming operation in a finite element code, especially for very large systems. Algorithms and numerical tricks, adapted to contact mechanics or not are the theme of many books and won't be developed here. Interested reader should refer to [Simo and Taylor, 1985].

The ordinary differential equation governing the motion of the discretised medium is written in a canonical form as [Canor, 2014; Bathe et al., 1975]

$$\mathbf{M} \cdot \Delta \ddot{\mathbf{u}} + \mathbf{C} \cdot \Delta \dot{\mathbf{u}} + \mathbf{K} \cdot \Delta \mathbf{u} + \Delta \mathbf{g}(\mathbf{u}, \dot{\mathbf{u}}) = \Delta \mathbf{f}(t) \tag{2.53}$$

where $\mathbf{M}$ is the mass matrix, $\mathbf{C}$ is the damping matrix, $\Delta \mathbf{g}$ gathers non-linear forces and $\Delta \mathbf{f}(t)$ is the vector of external forces. In case of dynamic or viscous analyses, the temporal integration is ruled by a particular integration scheme, for instance the Newmark algorithm. In this work, the analysis is quasi-static, viscous effects are neglected and there are no additional non-linear forces. Thence the equation (2.53) reduces to

$$\mathbf{K} \cdot \Delta \mathbf{u} = \Delta \mathbf{f}(t). \tag{2.54}$$

This equation holds for any time t. The temporal variable must also be discretised in order to solve the problem. All the variables are known at discrete moments, termed t^n. The amount of time elapsed between two successive discrete moments t^n and t^{n+1} is termed *time step*.

Equilibrium equations are established for any time t. Therefore the out of balance forces can be written for any time t, $\mathbf{F}_{OB}(t)$. It is unlikely that these out of balance forces are continuously equal to zero between two successive moment t^a and t^b. Thence, it can be written

$$\int_{t^a}^{t^b} P(t) \cdot \mathbf{F}_{OB}(t)\, \mathrm{d}t = \mathbf{0} \tag{2.55}$$

where $P(t)$ is a weighting function. In the `LAGAMINE` code, $P(t) = \delta(t - t^\theta)$ reduces to a collocation and the equilibrium is established for a given time t^θ such that

$$t^\theta = (1 - \theta) \cdot t^a + \theta t^b. \tag{2.56}$$

If $\theta = 0$, the equilibrium equations are written using configuration at the beginning of the time step and the integration is explicit since all the matrices $\mathbf{M}, \mathbf{C}, \mathbf{K}$ are known. If $\theta \neq 0$, the scheme is implicit are requires an iterative scheme since the matrices are not known *a priori*. The scheme is proved to be unconditionally stable if $\theta \geq 1/2$. Finally, solving the problem consists in solving Eq.(2.50) and (2.51) at a given discrete time.

2.7 Stress representation

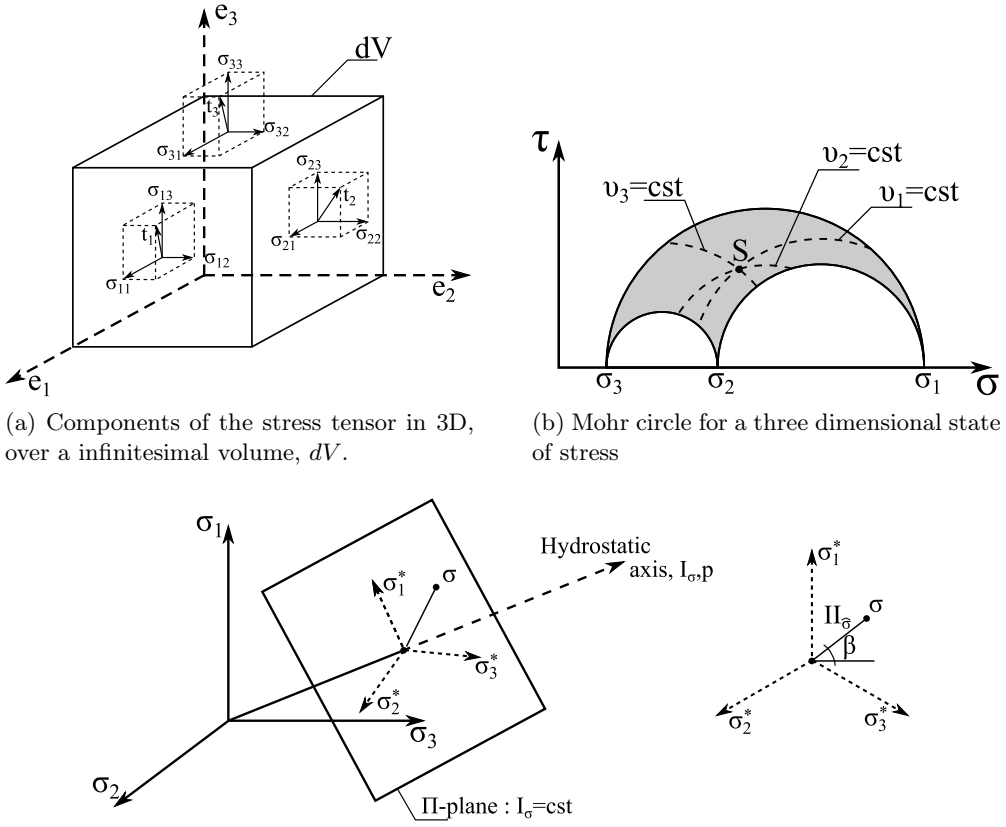

(a) Components of the stress tensor in 3D, over a infinitesimal volume, dV.

(b) Mohr circle for a three dimensional state of stress

(c) Position of a stress state in the principal stress space (left) and the deviatoric plane (right). σ_i^* are the traces of the principal stress directions in the deviatoric plane.

FIGURE 2.5

In this work, the geomechanics sign convention is adopted, i.e. compressive stress and strains are positive. In the general case, the stress tensor $\boldsymbol{\sigma}$ is composed of 6 non-zero components, i.e.

$$\boldsymbol{\sigma} = \boldsymbol{\sigma} = \begin{bmatrix} \sigma_{11} & \sigma_{12} & \sigma_{13} \\ & \sigma_{22} & \sigma_{23} \\ Sym. & & \sigma_{33} \end{bmatrix}. \tag{2.57}$$

The principal stresses are defined such that

$$\boldsymbol{\sigma} = \begin{bmatrix} \sigma_1 & 0 & 0 \\ 0 & \sigma_2 & 0 \\ 0 & 0 & \sigma_3 \end{bmatrix}. \tag{2.58}$$

The stress state is thus decomposed into three components perpendicular to the principal planes in a new coordinate system. Each principal stress is associated to a principal vector. A physical representation of this tensor is illustrated in Figure 2.5a for an infinitesimal volume dV. The Mohr circle was proposed by [Mohr, 1882] in order to geometrically represent possible stress states (see Figure 2.5b). Three circles are bounded by the principal stress values $[\sigma_1, \sigma_2, \sigma_3]$. The admissible stress states lie within the greyed zone.
Let us consider the stress state corresponding to a facet $\mathrm{d}\mathbf{A} = \mathrm{d}A \cdot \mathbf{n}$, i.e. an infinitesimal plane surface $\mathrm{d}A$ perpendicular to the vector $\mathbf{n} = [\nu^1, \nu^2, \nu^3]$, where ν^i are the direction cosine of the vector. All the stress states corresponding to a constant component ν^i are depicted by a dashed line in Figure 2.5b. Therefore, the stress state corresponding the combination of three fixed components $[\nu^1, \nu^2, \nu^3]$ is univocally defined at point S. However this formulation is not very adapted to the development of modern constitutive laws.
The stress tensor can be conveniently described by a triplet of stress invariants $[I_\sigma, II_s, III_s]$. The first one is described as

$$I_\sigma = \sigma_{ii}, \tag{2.59}$$

which is the trace of the stress tensor. The deviatoric stress can then be defined as

$$\mathbf{s} = \boldsymbol{\sigma} - \frac{I_\sigma}{3} \cdot \boldsymbol{\delta}. \tag{2.60}$$

The second invariant of the stress tensor thus reads

$$II_s = \sqrt{\frac{1}{2} s_{ij} \cdot s_{ij}} = \sqrt{\frac{1}{2} \cdot \mathbf{s} : \mathbf{s}}. \tag{2.61}$$

The third invariant is computed according to

$$III_s = \frac{1}{3} \cdot s_{ij} \cdot s_{jk} \cdot s_{ki}. \tag{2.62}$$

Therefore, this triplet of invariants acts as a new polar coordinate system. The Π-plane, or *deviatoric plane*, encompasses all the stress states that lead to an identical first invariant I_σ. In this plane, the second invariant II_s described how far from the hydrostatic axis is the stress state. The third invariant is used to compute the Lode angle β, which determines a "direction" from a reference (see Figure 2.5c). The Lode angle is obtained from

$$\beta = -\frac{1}{3} \sin^{-1}\left(\frac{3\sqrt{3}}{2} \frac{III_s}{II_s^3}\right), \qquad \beta \in [-30°, 30°]. \tag{2.63}$$

The first two invariants are frequently reformulated into the mean and deviatoric stress invariant (p,q)

$$\mathrm{p} = \frac{I_\sigma}{3} \tag{2.64}$$

$$\mathrm{q} = \sqrt{3} \cdot II_s \tag{2.65}$$

Chapter 3

Experimental characterisation of undrained behaviour of sands

In theory there is no difference between theory and practice. In practice there is.

Yogi Berra

Contents

3.1 Introduction

Saturated cohesionless soil layers are frequently encountered in geotechnical engineering. In many fields, especially in offshore or earthquake engineering, the behaviour of the soil is undrained or partially drained. Therefore an accurate understanding of several phenomena is a prerequisite for the design of foundations. *In situ* experiments (field trials or reduced scale) are most of the time expensive and impractical. However, it has been shown that similarities exist between *in situ* stress states and laboratory experiments, which are more convenient [Youd and Idriss, 2001].

The monotonic undrained behaviour of sands has been studied for many years in laboratories across the world [Seed et al., 2003]. It strongly depends on many factors such as the relative density, the initial mean effective stress, the fine content, the orientation of principal axes... Loose and medium sands might exhibit instabilities and softening behaviour after a peak resistance. The state of local minimum shear resistance is termed quasi-steady state and is characterised by a change of volumetric behaviour (=phase transformation) from contractive to dilative. The steady state differs from the quasi-steady state by the large deformation encountered. It consists in a continuous deformation of a soil sample for constant shear stress. It appears that all these states lie on a unique straight line in the p'-q plane, called the phase transformation line [Ishihara et al., 1975].
From an engineering point of view, it is interesting to predict the triggering of instabilities. The collapse boundary surface is used to delimit the states of soil samples in the e-p'-q space, where instabilities start [Sladen et al., 1985; Alarcon-Guzman et al., 1988]. It is extended to different orientations of principal axes in [Symes et al., 1984]. Seemingly, instabilities are strongly dependent on the structure of the soil sample. For instance, loose sands are metastable and prone to collapse.
Different phenomena, such as collapse of sand structure and steady state, involve large deformations and pore pressure increase within the soil sample. The *liquefaction* ragbag word is frequently used to encompass many phenomena [Marcuson, 1978]. It was firstly used in [Hazen, 1920] to describe the failure of a dam. The interest of engineers for this behaviour arose after the earthquakes of Nigata and Alaska in 1964 that highlight its potentially disastrous consequences [Seed and Lee, 1966].

Cyclic loading is used generically to characterise variable loads that have clearly repeated patterns and a degree of regularity in amplitude and return period [Andersen et al., 2013]. These loads can be essentially of environmental origin : seasons, waves, tides, earthquakes. Wave periods and number of cycles are very different. In offshore engineering, periods of large sea waves lie between 5-15s while the number of cycles is very high [Rahman et al., 1977]. On the other hand, in earthquake geotechnics, few cycles of high amplitudes and periods around 0.1-3s have to be taken into account [Ishihara, 1996]. In this work, laboratory tests presented are applicable to earthquake and offshore engineering. Few cycles are considered and induced deformations may reach 10 to 20 per cent. Therefore, these tests are not applicable to all cyclic loadings, such as railway or road solicitations, that involve million of cycles of very small amplitude.
The main feature of cyclic loading of sands is the progressive pore pressure accumulation with the number of cycles. As a corollary effect, the stiffness of the soil sample decreases and deformation may accumulate. Cyclic mobility is a liquefaction phenomenon typical of cyclic loading. It involves the accumulation of deformation and pore pressure during cycles [Vaid and Sivathayalan, 2000]. It has been shown that monotonic stress paths can be used as collapse boundary surfaces for cyclic stress paths [Alarcon-Guzman et al., 1988]. This allows a unifying interpretation framework of cyclic tests, especially regarding with the influence of initial deviator and cyclic amplitude.

In this chapter, main features of the undrained monotonic behaviour of sand are defined and described. The essential characteristics of steady state, quasi-steady state and phase transformation are developed. Collapse surfaces are used to analyse the initiation of liquefaction and extended to the interpretation of cyclic loading. Finally a brief review of *in situ* methods is proposed for an insight into practical methods.
This chapter is consistent although non exhaustive. Many topics are not tackled despite their inherent interest. For example all the tests are provided without distinction between direct shear or triaxial experiments. The drained behaviour of sand is not addressed even if it is related to the undrained one. Moreover it seems that early researchers tried to build a Babel tower at the beginning since many terms seem to have divergent definitions. Finally it must be pointed out that science is continuously evolving. Therefore concepts and interpretations described hereinafter might be invalidated by new findings or technical methods in the future, or even in the present.

3.2 *In situ* stress state

3.2.1 Seismic loading

Triaxial apparatuses are frequently used in soil and rock mechanics (see Figure 3.1b). They allow to model a broad range of engineering issues. This flexible device is adapted to drained or undrained as well as monotonic or cyclic loading experiments. The purpose of this section is to demonstrate the similarity between *in situ* and laboratory conditions.

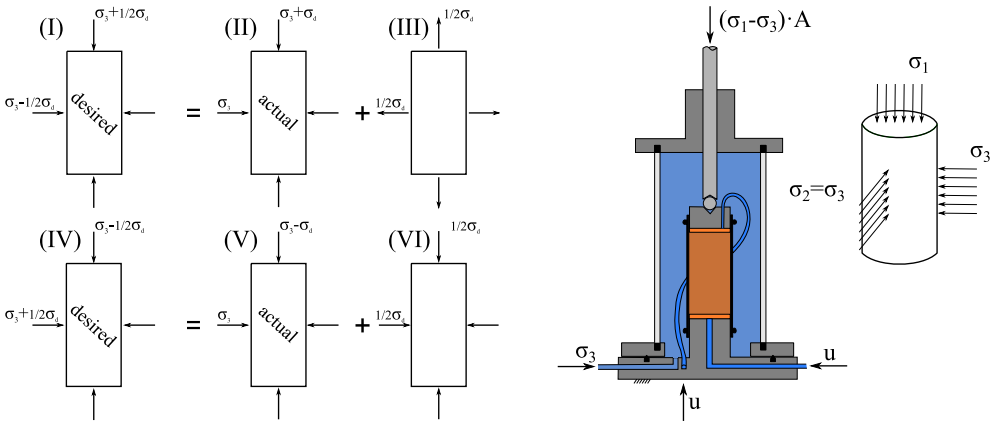

(a) Stress state applied to a soil sample during a triaxial test, after [Das and Ramana, 2010; Seed and Lee, 1966].

(b) Schematic representation of a triaxial apparatus.

FIGURE 3.1: Triaxial test

Let us consider a plane stress state before an earthquake. The stress state is readily depicted by a Mohr circle in Figure 3.2, if it is assumed isotropic ($K_0 = 1$) for the sake of simplicity. There is no tangential stress acting on the representative element of soil.
Seismic loading mainly consists of vertically propagating shear waves, which modify the initial stress state. If the effect of pressure waves is deemed negligible, the stress state within a soil sample can be modelled by adding shear stresses acting on its faces [Seed and Lee, 1966], as shown in Figure 3.2.

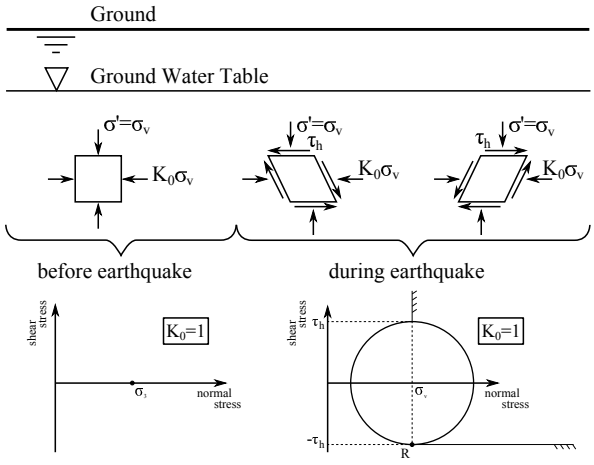

FIGURE 3.2: Stress state within the soil before and during an earthquake, after [Das and Ramana, 2010; Seed and Lee, 1966].

By definition, in a soil sample subject to isotropic consolidation, the stress state is identical whatever the plane considered within the specimen (see Figure 3.3a). If a compressive axial load is added ($\frac{1}{2}\sigma_d$), the stress state is modified and shear stress $\tau = \frac{1}{2}\sigma_d$ appears on planes XX and YY, inclined of 45° to the vertical axis (see Figure 3.3b). Identical conclusion holds if the total vertical load decreases (see Figure 3.3c), but the sense of the shear stress reverses. These stress states existing on a diagonal plane in the soil sample are identical to those occurring during an earthquake on horizontal planes previously described in Figure 3.2. Therefore, the *in situ* seismic behaviour of a soil can be studied in laboratory.

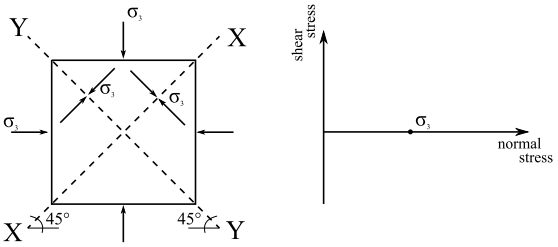

(a) Isotropic stress conditions.

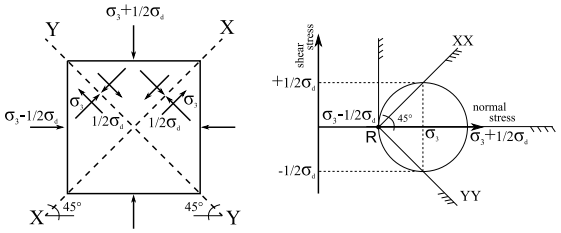

(b) Induced total stress state in an undrained soil sample in compression.

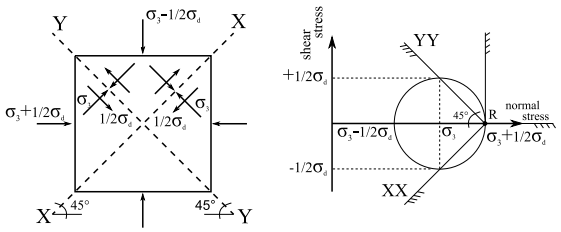

(c) Induced total stress state in an undrained soil sample in extension.

FIGURE 3.3: Total stress state in an undrained soil sample for simulating earthquake loading, after [Das and Ramana, 2010; Seed and Lee, 1966].

From a practical point of view, the total stress state desired is illustrated in Figures 3.3b and 3.3c on a plane oriented of 45° to the vertical axis, which induces a variation of both vertical and horizontal total stresses applied to the soil sample : $\sigma_3 \pm 1/2\sigma_d$ and $\sigma_3 \mp 1/2\sigma_d$ (3.1a(I,IV)). These boundary conditions should be achieved by changing simultaneously vertical and horizontal stresses, which is cumbersome.
Classically, only the vertical stress changes (see Figures 3.1a(II,V)). The desired stress state might be recovered from the applied one by readily adding or subtracting $1/2\sigma_d$ (see Figures 3.1a(III,VI)). However, due to the undrained nature of the test, this change of confinement only induces a change of internal pore pressure, without affecting the effective stress path, then the deformations. Therefore, the test can be carried out under vertical stress change only. The measured pore pressure has just to be corrected afterwards to correspond to earthquake induced loading [Seed and Lee, 1966].

3.2.2 Offshore loading

Similarly, offshore facilities are subject to waves and wind, which induce a cyclic loading of the superstructure, then of the foundations. The combination of vertical, horizontal and moment loads produces a complex stress distribution within the soil. An example of a potential failure surface under an offshore gravity based foundation is provided in Figure 3.4.
Stress conditions vary along this failure surface and loading approaches either triaxial compression and extension or direct shear stress experiments. Therefore a wise design of offshore foundations can be deeply studied in laboratory through the aforementioned experiments.

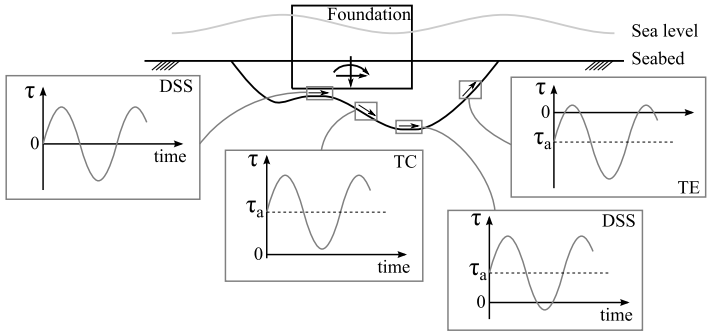

FIGURE 3.4: Simplified stress conditions along a potential failure surface in the soil beneath a gravity structure under cyclic loading [Andersen, 2009]. DSS, direct shear test; TC, triaxial compression; TE, triaxial extension.

3.3 Monotonic undrained behaviour of sand

3.3.1 Contractancy/dilatancy of the sand

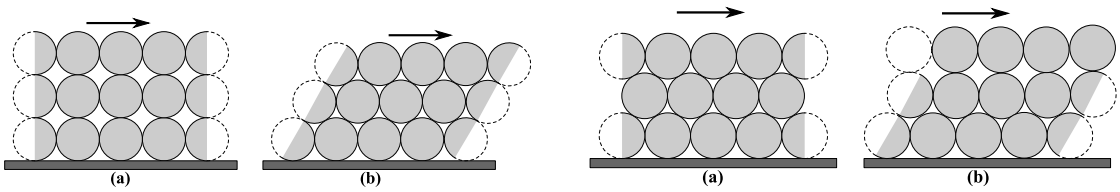

(a) Contractancy of a sand upon shearing (b) Dilatancy of a sand upon shearing

FIGURE 3.5: Volumetric behaviour of a soil sample, after [Reynolds, 1885; Charlier, 1987]

Although they are mainly modelled as continuum media, sands are inherently an assembly of discrete particles. The macroscopic behaviour of a soil sample is strongly dependent on the nature of these particles and on their arrangement. It can be distinguished between [Been et al., 1991]

1. the state of a sand which is the description of the physical conditions under which it exists : void ratio, stress, fabric (= arrangement of grains at particle scale)...
2. the intrinsic material properties of a sand, which are independent of its state : grain size distribution, grain shape, mineralogy ...

If sand grains are sharp and angular, their resistance to sliding is higher than for rounded grains. If they are poorly packed, the volume of void is high compared to the volume of grains, the soil sample is called *loose*. On the other hand, a very packed volume of grains is deemed *dense*.
Let us consider an assembly of rounded grain particles (see Figure 3.5) without water. If a shear loading is applied to an initially poorly packed soil sample (see Figure 3.5a), grains are prone to slip, to rearrange and the soil sample contracts. The behaviour is termed *contractant* and the total volume of the sample decreases. On the other hand, a dense soil sample subject to a similar loading tends to dilate and the total volume expands (see Figure 3.5b), [Bolton, 1986; Vaid and Sasitharan, 1992]. It is called *dilatant*.
Dilatancy of granular media was coined by Reynolds [1885] that carried out experiments on rigid spherical particles. It was defined in the second half of the twentieth century as the ratio of plastic volumetric strain increment $\mathrm{d}\epsilon_v^p$ to plastic deviatoric strain increment $\mathrm{d}\epsilon_v^p$ in the triaxial space, i.e.

$$d = \frac{\mathrm{d}\epsilon_v^p}{\mathrm{d}\epsilon_q^p} \tag{3.1}$$

where $\mathrm{d}\epsilon_v = \mathrm{d}\epsilon_1 + 2\mathrm{d}\epsilon_3$ and $\mathrm{d}\epsilon_q = 2\left(\mathrm{d}\epsilon_1 - \mathrm{d}\epsilon_3\right)/3$ [Roscoe and Burland, 1968; Li and Dafalias, 2000]. Both Taylor [1948] and Rowe [1962] have demonstrated that the dilatancy is a unique function of the stress ratio η and intrinsic material constants (C), i.e.

$$d = d\left(\eta, C\right) \tag{3.2}$$

The consequences of contractancy/dilatancy are obvious when considering saturated soils, e.g. the undrained shear loading of a contractive soil sample. The solid skeleton tends to contract upon shearing, however an undrained test is synonym of no volumetric deformation. Therefore, fluid pressure inside rises to compensate the tendency to contract and the mean

effective stress decreases. On the other hand, the shearing of a dilative sand involves a drop of pore pressure and an increase of mean effective stress. These two notions are of paramount importance, since they underlie most of the analyses of this chapter.

3.3.2 First observations of monotonic undrained tests

Undrained monotonic test on Toyoura sand, proposed in [Ishihara, 1993], are depicted in Figure 3.6. It must be pointed out that the material is identical (Toyoura sand) but the arranging differs (increasing relative density). Different initial confining pressures are also taken into account. For each void ratio, results in the deviatoric (q)-mean effective stress (p') and deviatoric-axial deformation (ϵ_y) planes are provided.

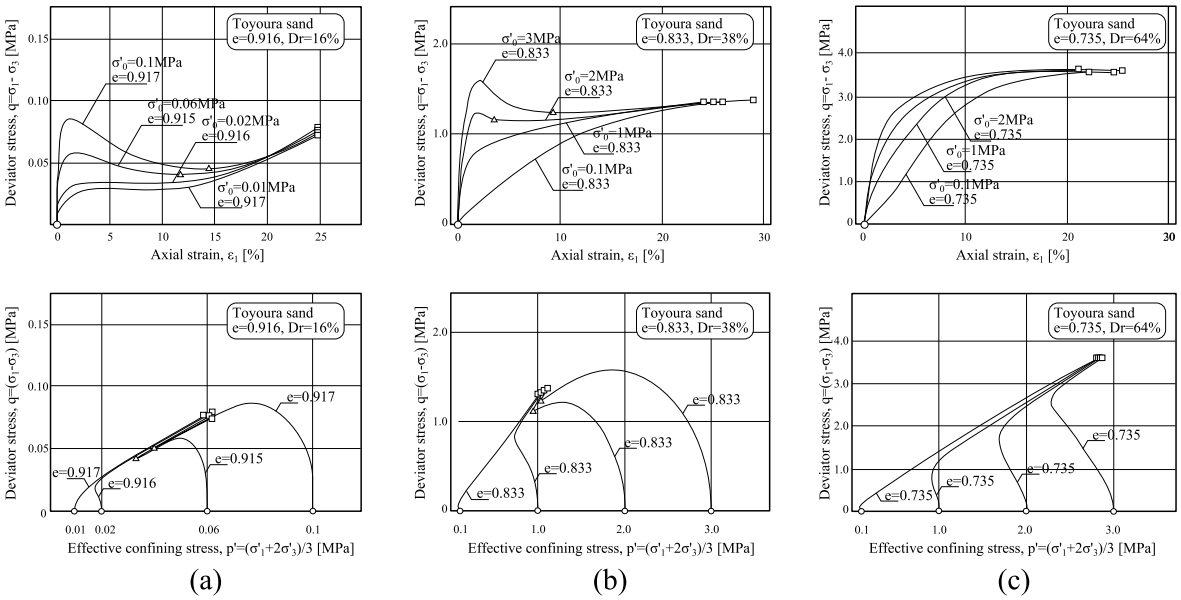

FIGURE 3.6: Compressive triaxial tests on Toyoura sand prepared by moist placement (see in section 3.3.8.1 for the sample reconstitution method). ◯ = initial state ; □ = final state ; triangle △= intermediate state. [Ishihara, 1993]

Let us consider first a loose Toyoura sand (see Figure 3.6(a)). Results are strongly initial confinement dependent and three different shapes curves are depicted hereafter[1].

1. $p' = 0.06/0.1$MPa : the stress strain relationship exhibits a peak of deviatoric stress, followed by a softening[2] behaviour down to a local minimum and then hardening[3] again for large deformations. The stress path shows that the beginning of the test and the softening part as well are contractive. The interstitial fluid pressure increases (then p' decreases) and the stress path moves towards the left.

2. $p' = 0.02$MPa : the stress strain relationship is continuously hardening, even if a plateau spans over around 10 % of deformation. The stress path can also be decomposed between

[1]The range of confining pressures considered here is relatively low, since most of the cases studied involve shallow foundations. However, for higher confining stress greater than 5MPa, a new phenomenon termed particle crushing influences results [Hyodo et al., 2002; Toyota et al., 2004].

[2]In this chapter, softening is characterised by a decrease of shear resistance with increasing deformation.

[3]In this chapter, hardening is characteristed by an increase of shear resistance with increasing deformation.

firstly contractive and secondly dilative behaviours. The plateau observed in the first figure corresponds to the transformation of a contractive phase to a dilative one.

3. $p' = 0.01$MPa : the stress strain relationship is similar to those observed in the $p' = 0.02$MPa case. However, the behaviour is only dilative

It is noteworthy that all the curves finally merge at very high vertical deformation.

Results presented for a relative density of 38% are similar (see Figure 3.6). However the peaks of resistance are smoother (the difference between peak value and local minimum value) and the final state seems to reach a final constant deviatoric resistance. This latter effect is more highlighted when considering the test on 64% relative density curves. In such case, all the soil samples experience only dilative phases and reach an identical deviatoric stress.
Experimental work produces a large amount of curves and results that must be synthesised. For instance, peak and residual resistances as well are interesting pieces of information for engineers designing foundations. Therefore, experimenters have applied themselves to elaborate concepts that summarise and describe different behaviours observed as a function of engineer parameters. These concepts are described hereafter.

3.3.3 Steady state

An idealisation of two types of behaviour is reproduced in the Figure 3.7. It was previously pointed out that in a large deformation state, typically an axial deformation of 20-25 %, the deviatoric stress remains constant while deformation keeps increasing. The *steady state of deformation* of a soil is referred as *a state in which a mass of particles is continuously deforming at constant volume, constant normal effective stress, constant shear stress and constant velocity* [Castro and Poulos, 1977; Poulos, 1981]. This state is similar to the critical state defined in clays [Roscoe et al., 1958; Schofield and Wroth, 1968].

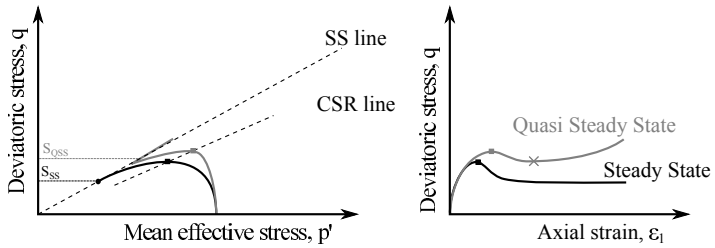

FIGURE 3.7: Idealisation of steady and quasi-steady states, after [Vaid et al., 1990], at constant relative density. SS line = steady state line ; CSR line = critical state ratio line.

This behaviour may occur in sands and clays as well, for any drainage and loading conditions. Actually the shear deformation leads to a total breakdown of the initial structure. When the steady state eventually starts, the soil is reworked into a new "flow structure", described by [Casagrande, 1971]. Physically, the contractive behaviour of sand and pore water pressure that occurs during shearing allow the reorientation of sand particles. Steady state starts when grains reach a final flow structure that offers the minimum resistance to shearing. It was demonstrated that the angle of friction mobilised at the steady state is constant [Mohamad and Dobry, 1986; Vaid et al., 1990]. Moreover, the state of stress and the residual resistance of a sand at this state is only a function of the void ratio and lies on the steady state line in the p'-e plane [Verdugo and Ishihara, 1996], (see Figure 3.8). Thence, void ratio and

mean effective stress at the critical state cannot be independently imposed and the relation between them is unique for a given material.

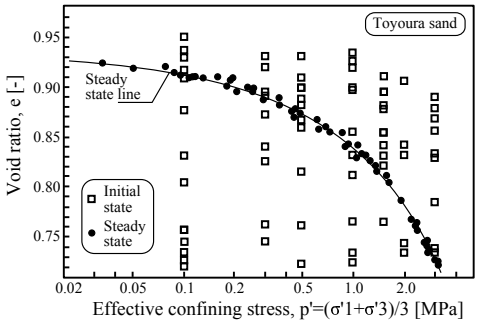

FIGURE 3.8: Steady state line and initial states for a Toyoura sand, [Verdugo and Ishihara, 1996].

Riemer and Seed [1997]; Yoshimine and Ishihara [1998] also proved that steady state lines are different in compression and extension triaxial tests in the e-p' plane. The steady state strength is actually lower in this case and the soil exhibits a more contractive behaviour. The explanation might lie within the inherently anisotropy of the material or in a stress path effect, [Riemer and Seed, 1997]. Indeed, strain path and deformation modes are different between compression and extension tests.
Recent advances from [Li and Dafalias, 2012] based on DEM (discrete element method) seem to question the classic definition of the critical state (and then of the steady state) based only on a isotropic measurement (void ratio). In this paper, a fabric tensor is introduced to take into account the anisotropic structure of the soil sample created by the loading.

3.3.4 Quasi-steady state

It was highlighted in Figure 3.6 that some of the tests encounter a drop in resistance after a peak in $q - \epsilon_y$ plane. This contractive softening behaviour ends when the soil becomes dilative and is marked by an elbow of the parent curve in p'-q plane. This state of minimum strength was termed *quasi-steady state*, [Alarcon-Guzman et al., 1988; Been et al., 1991]. It is different from the steady state because it appears for much lower strains. The choice of steady state or quasi-steady state friction angles as residual strength is a major concern in geotechnical engineering.

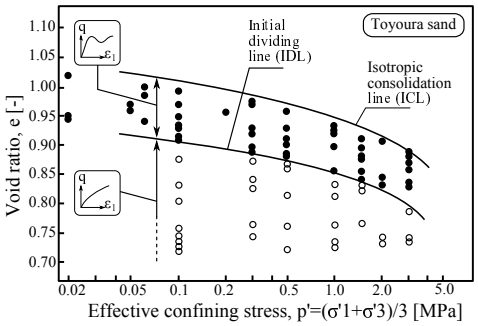

(a) IDL for moist placed samples of Toyoura sand. Solid markers indicate that a QSS was observed. Open markers denote QSS-free tests.

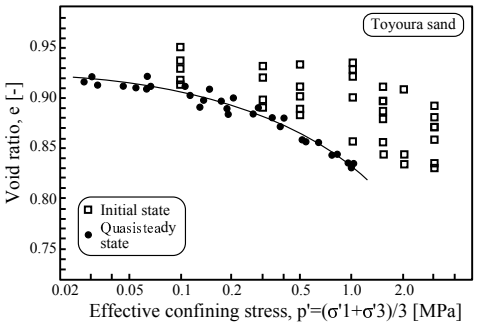

(b) quasi-steady state line.

FIGURE 3.9: The quasi-steady state of Toyoura sand, [Ishihara, 1993].

The quasi-steady state (QSS) does not occur in each experiment. Actually the occurrence or non occurrence of this state depends on the void ratio and the initial confining stresses, Verdugo and Ishihara [1996]. An initial dividing line (IDL) separates initial states that lead to QSS from those which do not (see Figure 3.9a). This state is particularly a feature of loose soil samples sheared from large initial confining stresses, [Ishihara, 1993]. Similarly to the steady state, a quasi-steady state line can be drawn in the e-p' plane (see Figure 3.9b). The QSS strength is strongly dependent on the initial mean effective stress, [Verdugo and Ishihara, 1996] and on the loading mode. Indeed, the strength in extension is lower than in compression, [Vaid et al., 2001].

3.3.5 Phase transformation line

If the stress states that characterise steady and quasi-steady states are plotted together, it appears that they all lie on a straight line in the p'-q plane (see Figure 3.10). Moreover, the change of behaviour from contractive to dilative in case of continuously hardening soil sample (see Figure 3.6(c)) lies also on this line. This outcome is remarkably similar in compression and extension. However, the uniqueness of such a straight line is still an open topic. Indeed, some authors recently distinguish between phase transformation and failure or steady state lines, [De Gennaro et al., 2004; Hyodo et al., 2002]

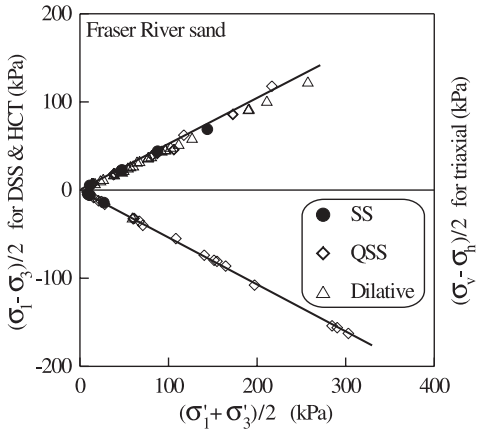

FIGURE 3.10: Effective stress state at SS, QSS (softening) and phase transformation (hardening) in triaxial compression, extension, simple shear (DSS) and torsional shear (HCT) tests, [Vaid and Sivathayalan, 2000].

This line was termed *phase transformation line* by [Ishihara et al., 1975] referring to the change of behaviour from contractive do dilative. This concept was largely adopted within the scientific community [Mohamad and Dobry, 1986; Alarcon-Guzman et al., 1988; Vaid et al., 1990; Hyodo et al., 1994; Verdugo and Ishihara, 1996] and unifies previous concepts. The quasi-steady state degenerates in a particular case of phase transformation where the shear strength temporarily drops over a limited interval of deformation. Interestingly, the phase transformation line is identical to the characteristic line defined for drained tests [Lade and Yamamuro, 1997].

A summary of the aforementioned concepts is described in Figure 3.11. The ultimate steady state is the steady state that is finally attained, for a given void ratio, irrespective of the initial stress conditions, [Yoshimine and Ishihara, 1998]. The critical steady state occurs when phase transformation and ultimate steady state are merged. Thus, no hardening occurs after the minimum strength resistance is reached (see Figure 3.11(a)). Interested reader should refer to [Yoshimine and Ishihara, 1998] for more information about the influence of parameters on curves presented in Figure 3.11.

3.3.6 CSR line - collapse line

The description of the peak resistance during shearing is a major concern in design. Indeed the drop of resistance after the peak may lead to unstable behaviour. The locus of peak states in the p'-q plane was denoted *critical state ratio line* by [Vaid and Chern, 1985]. Contrary to the phase transformation line, this CSR line has different slopes in compression and extension [Vaid and Thomas, 1995].
This line depends on the density of the sand [Alarcon-Guzman et al., 1988; Been and Jefferies, 1985]. The shape of the locus of peaks was found to be a straight line [Mohamad and Dobry, 1986] but it might deviates especially for low confinements of loose sands [Yamamuro and Lade, 1997].

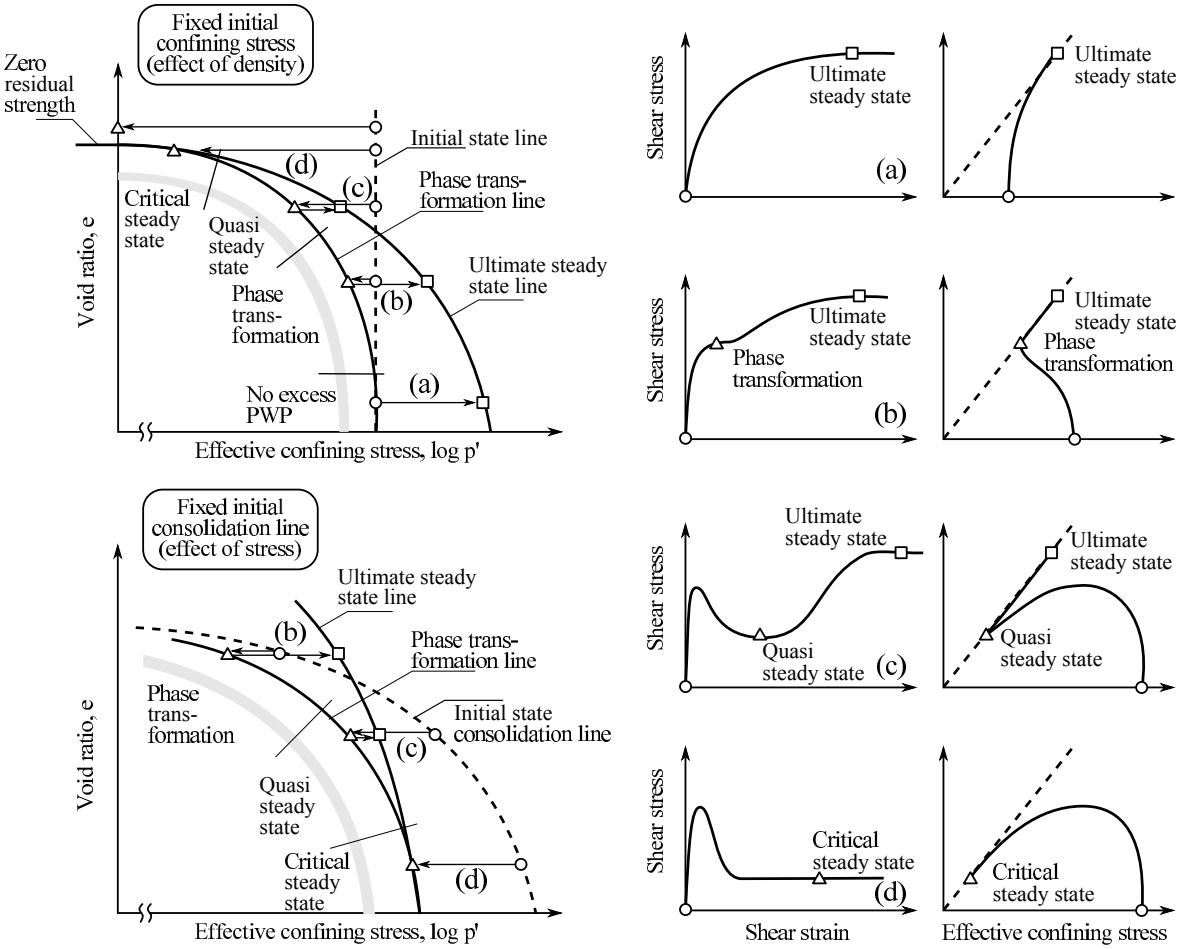

FIGURE 3.11: General undrained shear behaviour of sand under large deformations, [Yoshimine and Ishihara, 1998]. ◯ = initial state ; □ = final state ; triangle △= intermediate state.

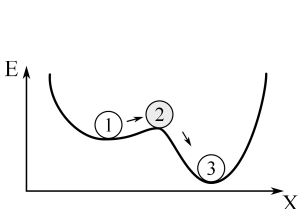

(a) Energy of an arbitrary body as a function of its position. (1) metastable position; (2) transient position; (3) absolutely stable position

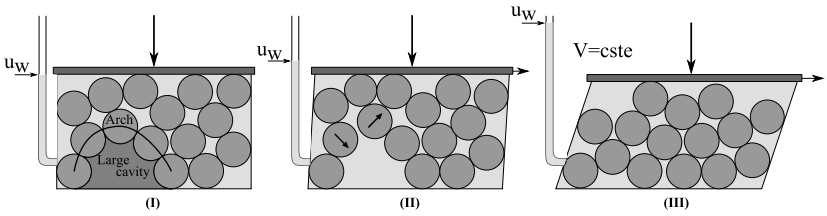

(b) Idealisation of an undrained sand specimen.

FIGURE 3.12: Structural collapse

This particular undrained behaviour of sand is related to the structural collapse concept, defined by [Alarcon-Guzman et al., 1988]. As a matter of fact, the structure of contractive sands is metastable. An example of this concept is given in Figure 3.12a, in which the energy function of an arbitrary body is depicted as a function of its position. Initially, the body is at rest and stable in position (1) because any slight variation of displacement δX brings it to a higher energy level. However, if it gains a sufficient amount of energy, it is allowed to reached

a new position of equilibrium (3) by overpassing the (2) local maximum of energy.
In collapsive skeletons of some contractive sands, small shear strains are sufficient to create a sudden rearrangement of the grains and a loss of contact points between them. Therefore, the collapse results in a sharp transfer of the total load from the solid grains to the interstitial pressure. For instance, let us consider the metastable collapsive skeleton presented in Figure 3.12b. The arrangement of grains creates a large cavity and grains around resist by vault effect (I). A small shearing of the soil samples lead to a loss of contact of sand grains (II) and eventually to a sudden rearrangement of the grains inside (III). Since the test is undrained, the pore water pressure rises up to bear the total load. It must be pointed out that collapse behaviour can also be observed during drained tests and is marked by a volumetric contraction. This was demonstrated by [Skopek et al., 1994] for loose sands.

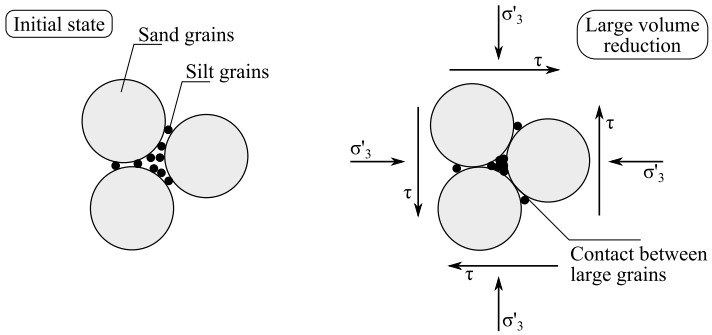

FIGURE 3.13: Silty sands structure, [Yamamuro and Lade, 1997]

Similarly, the addition of fines affects the behaviour behaviour of a soil sample (see Figure 3.13). Some of them affect the density of the soil sample, but they do not change its resistance which is mainly borne by sand grains. On the other hand, particles might lie near contact points between larger grains. Upon shearing or isotropic compression, these particles might easily slide towards the inner void. This increases the contractive behaviour of the soil and then the pore pressure rising was demonstrated for very loose sands [Yamamuro and Lade, 1997]. However, recent studies demonstrate that the fine content effects are much more complex and depend on the nature of the fines (plasticity index,...), their concentration, the relative density and the confinement [Tsukamoto et al., 2004; Boulanger and Idriss, 2006; Bray and Sancio, 2006; Sadrekarimi, 2013].

For a given relative density of a soil sample, Sladen et al. [1985] define the CSR line as a collapse line that delimits the states of stable and unstable behaviours. The concept is extended to the state space where the collection of all the collapse lines for each void ratio gives birth to a collapse surface (see Figure 3.14b). Actually Alarcon-Guzman et al. [1988]; De Gennaro et al. [2004] prove that the actual limit is delineated by a monotonic stress path in p'-q plane (see Figure 3.14a). Sasitharan et al. [1993] eventually conclude that the CSR line is an acceptable approximation of the actual collapse line. Symes et al. [1984] extended the boundary surface to non vertically applied stresses.
However it must be mentioned that Been and Jefferies [2004] refute the concept of collapse surface for very loose sand, which proves that the interpretation of such behaviours is still an ongoing research topic !

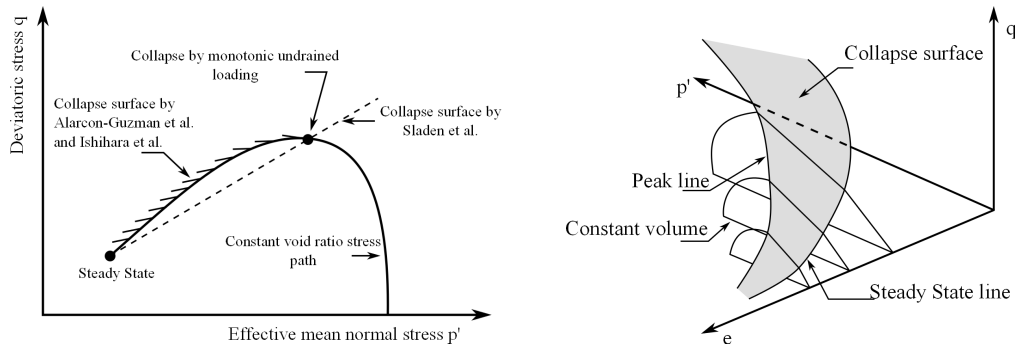

(a) Comparison of state boundary and collapse surfaces proposed by [Alarcon-Guzman et al., 1988] and [Sladen et al., 1985]

(b) Typical collapse surface in effective mean normal stress (p') - deviator stress (q) - void ratio space (e).

FIGURE 3.14: Definitions of state boundary and collapse surfaces, [Sasitharan et al., 1993]

3.3.7 Liquefaction

Liquefaction is not a recent topic and has been widely studied for the late thirties [Casagrande, 1936]. However the term "liquefaction" encompasses a large variety of behaviours and its definition is not unique. All the phenomena covered have in common an increasing interstitial fluid pressure and large deformations, [Castro, 1975; Castro and Poulos, 1977].
Some authors relate liquefaction to the steady state previously defined, [Castro and Poulos, 1977; Hyodo et al., 1994]. Thence the soil sample undergoes very large deformation and a constant resistance to shearing. The liquefaction is total since the shear resistance is very low and the sand flows like a liquid, [Castro and Poulos, 1977]. However, this true liquefaction is limited to a range of relative densities. They are more frequent in silty sands, [Yoshimine and Ishihara, 1998].
Initial or static liquefaction also occurs, i.e. the soil sample reaches a null state which means both effective and deviatoric stresses are null. This behaviour was defined in [Seed and Lee, 1966] and also represented in [Yamamuro and Lade, 1997] for loose sands.
The concept of flow failure was described by [Casagrande, 1976; Castro, 1969]. It consists in a sharp pore pressure build up and a sudden increase in deformation. This flow failure is not properly a state of deformation but it triggers it. Alarcon-Guzman et al. [1988] proposed the structural collapse concept to explain this phenomenon and Sladen et al. [1985] relate its triggering to a collapse surface in the void ratio - stress plane.
A transient state of partial liquefaction is also mentioned by [Lee and Seed, 1967; Vaid and Sivathayalan, 2000] when the soil reaches the quasi-steady state, before hardening. It defines the sharp increase of deformation encountered after the peak of strength. This definition is identical to the flow failure.
A unifying definition is provided in [National Research Council, 1985; Vaid and Thomas, 1995]: *the terms liquefaction and liquefaction failure encompass all phenomena involving excessive deformations of saturated cohesionless soils.* Thence, the definition of failure should better refer to a fixed amount of plastic deformation accumulated irrespective of the phenomenon causing it, [Ishihara et al., 1975].

Figure 3.15 proposed by [Yamamuro and Lade, 1997] for a loose sand illustrates the instabilities that might occur during the triaxial compression test, related to liquefaction concept. Low confining pressures samples are prone to static liquefaction, i.e. $(p', q) = (0, 0)$. A temporal liquefaction is also observed, i.e. a loss of shear stress accompanied by an sudden increase of pore pressure and deformation. Higher confining pressures exhibit either a temporal instability or an instability, i.e. the steady state is reached and no hardening occurs. For a given

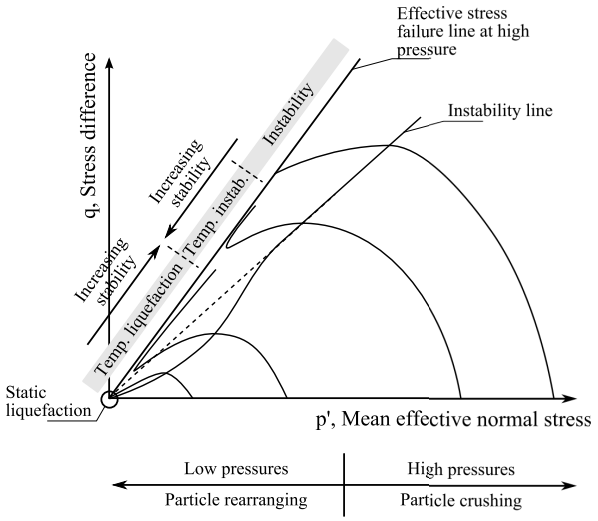

FIGURE 3.15: Four distinct general types of undrained effective stress paths of loose silty sands, [Yamamuro and Lade, 1997]

loose relative density, the actual behaviour strongly depends on the initial confining stress. It must also be pointed out that the instability line, equivalent to CSR line, deviates from the straight line for low confining pressure.
Liquefaction is a very complex phenomenon involving many parameters. For example, Eliadorani and Vaid [2005] also prove that a partially drained behaviour is more damageable than drained or undrained ones. Small expansive volumetric strains might transform an initially dilative sand to a contractive one. Finn et al. [1970]; Nemat-Nasser and Takahashi [1985] studied the effect of pre-liquefaction and demonstrate that the weakening effect of a preliquefaction is not mandatory. The fabric of the soil plays a very important role in this resistance.

3.3.8 Remarks on the experiments

3.3.8.1 Sample reconstitution method

Generally, granular soil samples tested in laboratory are reconstituted from a virgin material. Three methods of reconstitution are illustrated in Figure 3.16

- moist tamping/placement (MT) : wet sand is poured in successive layers ;
- air-pluviating/dry deposition (AP) : dry sand is poured in successive layers ;
- water pluviating/sedimentation (WP) : sand is poured under water in successive layers.

In each of these methods, a hammer can be used to increase the density.

The choice of a reconstituting method is not neutral. Indeed, a soil sample described by identical void ratio and initial stress state might lead to very different behaviours (see Figure 3.17a). The moist tamped method creates sample much more prone to contactive and quasi-steady state behaviours than the two others. As a matter of fact, this method tends to create honeycomb structure, described in [Casagrande, 1976], which is likely to collapse. Evidence of such a collapse as soon as the sample is saturated was reported in [Sladen et al., 1985].
The method that better represents the *in situ* soil conditions is the water pluviated one, [Oda

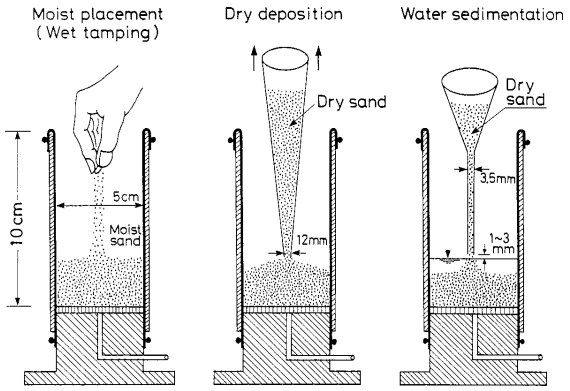

FIGURE 3.16: Method of sample preparation, [Ishihara, 1996]

et al., 1978]. Actually this method mimics the natural way of sand deposition. A comparison between laboratory reconstituted and *in situ* frozen samples is carried out (see Figure 3.17b). Moreover, the water pluviated method leads to a better void ratio distribution uniformity over the height of the soil sample [Vaid and Sivathayalan, 2000].

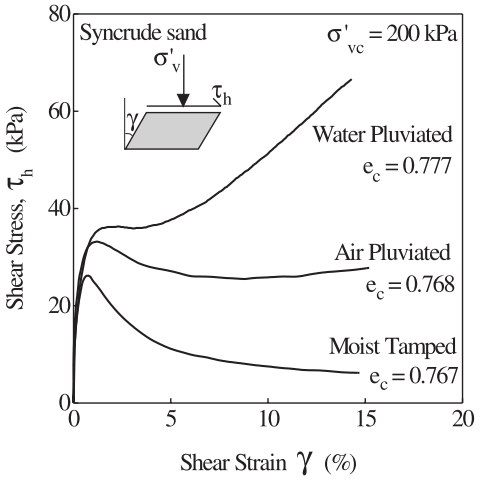

(a) Effect of reconstitution technique (fabric) on the undrained simple shear response of Syncrude sand, after Vaid and Thomas [1995]. e_c, void ratio; σ'_v and σ'_{vc}, vertical effective stress and vertical consolidation stress, respectively.

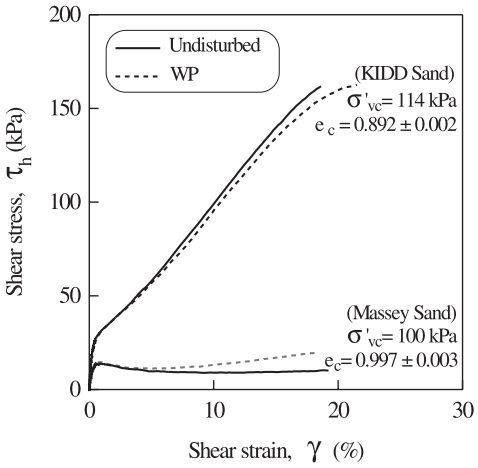

(b) Comparison of undrained simple shear response of undisturbed in situ frozen and equivalent water-pluviated sand at essentially identical states, Vaid and Sivathayalan [2000].

FIGURE 3.17

3.3.8.2 Direction of principal stress

The direction of principal stress has an important influence on the results measured [Yoshimine et al., 1998; Vaid and Sivathayalan, 2000; De Gennaro et al., 2004]. It can be described by two parameters

- α is the inclination of the major principal stress σ_1 to the specimen axis (deposition direction);

- $b = (\sigma_2 - \sigma_3)/(\sigma_1 - \sigma_3)$ describes the intermediate principal stress σ_2. Thence, $b = 0$ and $\alpha = 0$ stand for triaxial compression while $b = 1$ and $\alpha = 90°$ stem for triaxial extension.

The influence of these parameters is illustrated in Figure 3.18 where a loose Fraser sand was subject to various loading conditions. The sample exhibits a dilative response for the compressive triaxial test. In contrast, a softening compressive behaviour is observed for the triaxial extension tests. This divergence highlights the inherent anisotropy of sand, already recognised in [Miura and Toki, 1982].
If compression and extension tests start from an identical hydrostatic state ($q_{init} = 0$), the softening triggers earlier in extension than in compression, since the slope of the QSS line is weaker in extension [Vaid and Sivathayalan, 2000]. As a matter of fact, deformation modes are different in both cases. The greater deformability in horizontal plane is the main cause of the divergences observed. The deformation path is of greater importance than the stress path [Riemer and Seed, 1997; Vaid and Sivathayalan, 2000; De Gennaro et al., 2004]. Similar difference was early demonstrated between triaxial and direct shear tests [Peacock and Seed, 1968]. This inherent shortcoming of triaxial tests can be overcome by the use of torsional tests. The advantage of such a method is the similar form of the results in both direction of loading, which better approach natural cyclic shear loading [Georgiannou et al., 2008].

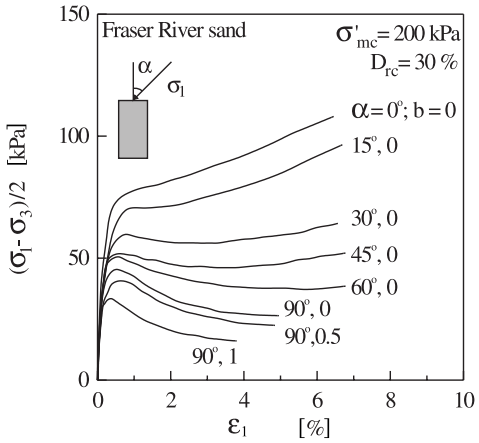

FIGURE 3.18: Dependence of undrained response on the direction of principal stress and the intermediate stress parameter. σ'_{mc}, mean consolidation stress [Vaid and Sivathayalan, 2000]. Triaxial compression: (α,b)=(0°,0) ; Triaxial extension: (α,b)=(90°,1)

3.3.8.3 Non-homogeneities

The aforementioned state concepts implicitly induce the hypothesis of uniform fields of deformation, stresses and pore pressure within the soil sample. Consequently, if the steady state is achieved, an identical void ratio can be measured within the whole specimen.
Strain localisation was coined to describe the concentration of deformation into thin zones of intense shearing (also shear banding) [Desrues and Viggiani, 2004]. These bands can be of different shapes and depend on density, grain size or perturbations due to the test apparatus. Thus, it is always an imperfection of the test (from sample and/or apparatus) that triggers the localisation. Consequently, the unknown is not the likelihood of localisation occurrence but its geometry. The main outcome of this particular phenomenon is the loss of uniformity of deformation and stress distribution within the soil sample tested.

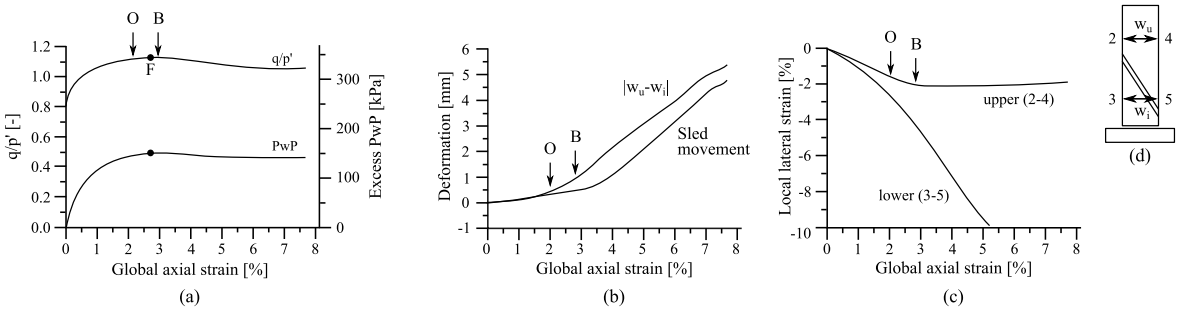

FIGURE 3.19: Strain localisation during undrained plane strain shearing [Finno et al., 1996].

Shear banding is strongly associated with failure and post-peak drained softening behaviours in sands [Wang and Lade, 2001]. Therefore, steady state and quasi-steady state can be reinterpreted in the light of this phenomenon. An example of results is illustrated in Figure 3.19 for a plane strain shearing test of a loose sand.
The global stress-strain response obtained by boundary measurements is provided in Figure 3.19(a). The final result should be interpreted as liquefaction or steady state since the deformation seems to continue at constant deviatoric stress. However, considering measurements of deformation at the top and the bottom of the sample (see positions of w_u and w_i in Figure 3.19(d)), it can be seen that the deformation is not uniform. The function $|w_u - w_i|$ should have been equal to zero if vertical deformation were uniform, i.e. upper and lower deformation are identical. On the contrary, the non-zero values indicate that deformation is not uniform. The triggering of localisation is marked by point O and is considered ended at point B. Finally, local lateral deformations in the Figure 3.19(c) depict the consequences of the shear band. After localisation has been fully developed, the upper part of the sample slides along the shear band as a rigid body (there is no additional lateral deformation of the upper part). However, the lateral deformation of the lower part is still increasing, since the measure gauge encompasses the shear band.
In short, consequences of steady state are globally observed, but the conditions of steady state (constant volume, constant rate of shear strain...) hold only in the shear band [Finno et al., 1996]). Identical conclusion was drawn for drained tests about the critical state, occurring within the shear band [Desrues et al., 1996; Mooney et al., 1998].

It was also demonstrated that the increase of shearing resistance after a local minimum might also come from non uniformities [Finno et al., 1996]. Moreover, Zhang and Garga [1997] pointed out the effect of friction between the soil and the test apparatus that induces end restraint. This behaviour is insignificant for loose sand but gains more importance for denser sands. They finally postulated that the quasi-steady state might be a test-induced behaviour. All the previously described concepts, such as steady or quasi-steady states, implicitly make the hypothesis that the state of the soil specimen was homogeneous. This section demonstrates it is probably not. However, the macroscopic behaviour reflects the local physics, which has to be kept in mind for the development of constitutive laws and calibration of parameters. Fortunately, the range of deformation that is of particular interest in this work lies far before the failure. Thence the behaviour is still homogeneous and can be adequately modelled by classic continuum mechanics.

3.4 Cyclic undrained behaviour of sands

3.4.1 Insight into the cyclic undrained behaviour of sands.

The cyclic loading of a soil is characterised by the variation of shear stress q_{cycl} around a mean value q_s which denotes an initial anisotropic consolidation state. A reversal exists if the cyclic amplitude is greater than the initial mean value, i.e. compressive deviatoric stresses coexist with extensive ones. The stress path and potential failure mode depend prominently on the initial stress state, void ratio states and cyclic amplitude. Four different modes of failure are presented in Figure 3.20.

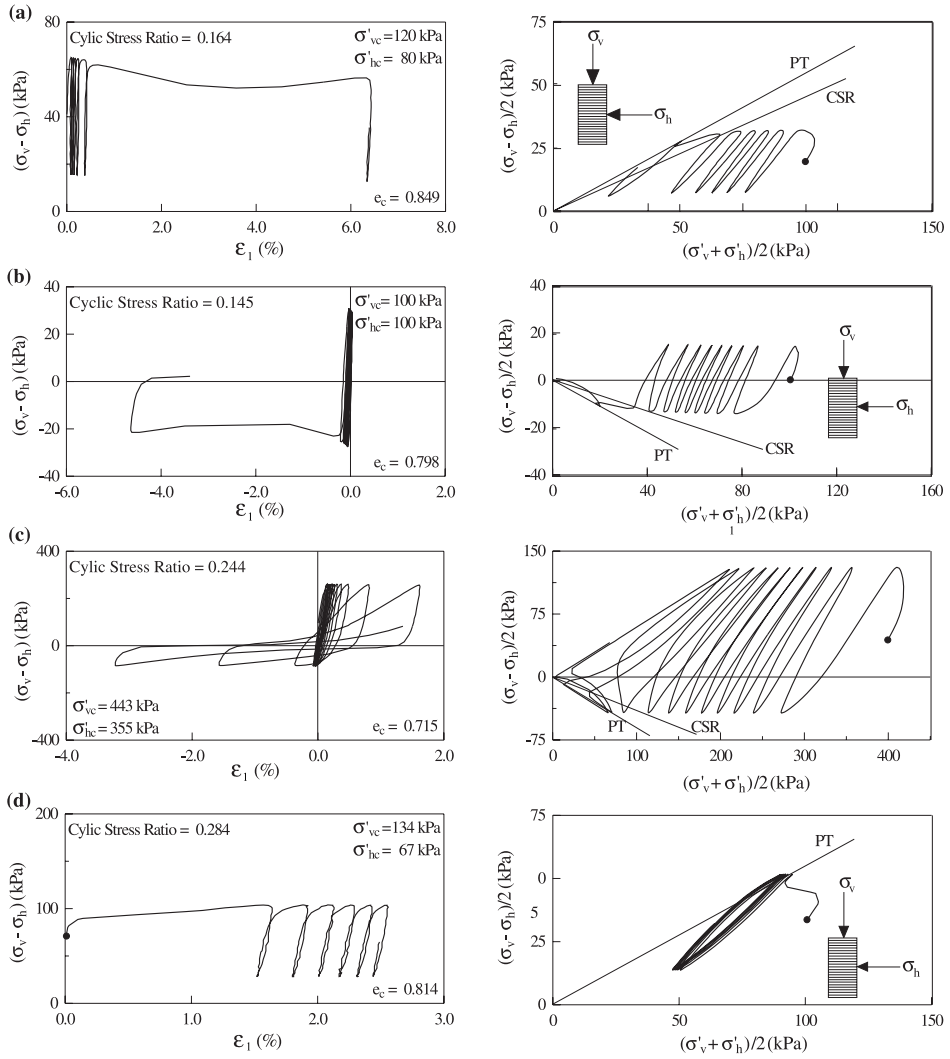

FIGURE 3.20: Liquefaction due to (a) contractive deformation in compression during cyclic loading; (b) contractive deformation in extension during cyclic loading; (c) cyclic mobility with transient states of zero effective stress during cyclic loading; (d)cyclic mobility without transient state of zero effective stress during cyclic loading; [Vaid et al., 2001]. Fraser river sand : $e_{min} = 0.605, e_{max} = 0.926$.

Figure 3.20(a) illustrates a cyclic loading without reversal. A common feature of cyclic loading is the pore pressure build up, due to the contractive behaviour of tested soil samples. This tendency is marked by a continuous decrease of the mean effective stress within the soil

specimen, i.e. cycles move towards the left in the p'-q plane. Finally, the stress path crosses the CSR line, which triggers a flow deformation [Vaid and Chern, 1983], i.e. an instability coupled with a sudden increase in deformation.
A cyclic loading with reversal is represented in Figure 3.20(b). Similar conclusions can be drawn, but in this case the stress path reaches the initial liquefaction, i.e. a state of null mean effective and deviatoric stresses. An identical flow deformation occurs but on the extension side. It was shown in [Seed and Lee, 1966] that an alternate loading with reversal leads frequently to initial liquefaction.
Figure 3.20(c) exhibits another common feature of cyclic loading, butterfly wing stress path. The reversal loading triggers a nearly initial liquefaction state. However, the soil sample starts hardening before the next reverse loading. This pattern is replicated and higher plastic deformation are accumulated for each cycle each time the stress path crosses the hydrostatic axis, either in compression and extension. This phenomenon is termed *cyclic mobility*.
Finally, Figure 3.20(d) denotes a combination of the two previous modes of failure. The stress path initially encounters a limited flow deformation, i.e. the soil sample exhibits a large deformation accumulation but cycles stabilise later on. However, even if the cycles are stabilised in the p'-q plane, they accumulate axial deformation. This *ratcheting effect* is also a type of cyclic mobility.

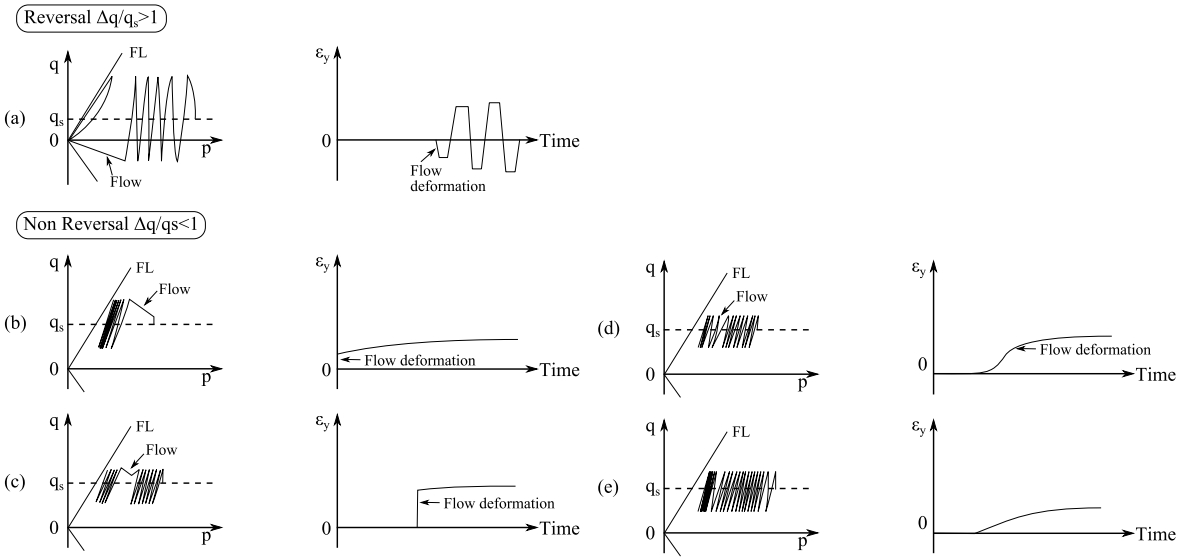

FIGURE 3.21: Schematic diagram for sveral stress path and axial displacements Hyodo et al. [1994].

These different behaviours are summarised in Figure 3.21. The different patterns of accumulation of axial strain are highlighted between reversal and non reversal loading types. It must be reminded that liquefaction is not a well-defined state but a matter of convention. However, most of the results provided show the importance of the flow deformation in the triggering of the liquefaction. Therefore the description of a triggering surface is of major concern.

3.4.2 Cyclic mobility

The cyclic mobility phenomenon was previously mentioned. Once again, this denomination includes several distinct phenomena. Some authors consider that cyclic mobility is the progressive degradation of the stiffness of the soil sample due to the progressive increase of pore pressure [Casagrande, 1976; Castro and Poulos, 1977; Pecker, 1984; Yoshimine and Ishihara, 1998]. Some others used cyclic mobility to characterise the state of a soil subject to a transient state of (nearly) null mean effective and deviatoric stress [Alarcon-Guzman et al., 1988; Hyodo et al., 1994; Castro, 1975; Vaid and Thomas, 1995].
According to [Hyodo et al., 1994], liquefaction is peculiar to contractive soil while cyclic mobility occurs in dilative ones. On the other hand, Castro [1975] assesses that cyclic mobility may appear in any type of soil, independently of its initial state. Vaid and Sivathayalan [2000] conclude in differentiating between cyclic mobility with or without initial liquefaction. In each of the presented cases, the common feature is the degradation of the stiffness due to the accumulated pore pressure coupled with a continuous increase of residual deformation.

3.4.3 Link between monotonic and cyclic loadings

It was previously demonstrated that a collapse surface could be established, that delineates a zone of instability triggering. Alarcon-Guzman et al. [1988] represented on the same graph a monotonic stress path and the stress at the beginning of flow deformation (see Figure 3.22). It appears that the monotonic stress path for an identical initial mean effective stress acts as a boundary surface of flow deformation triggering for a cyclic test.

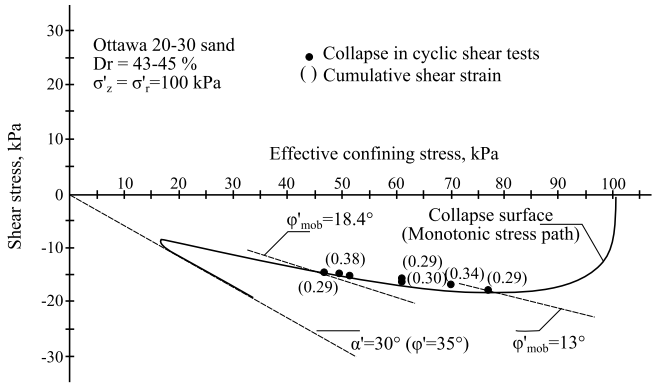

FIGURE 3.22: Stress conditions at initiation of strain softening behaviour under cyclic loading Alarcon-Guzman et al. [1988].

This was confirmed by experiments carried out in [Hyodo et al., 1994], represented in Figure 3.23. The main outcome induced by this conclusion is that many cycles can be accumulated even if the stress path crosses the CSR-line (see Figure 3.23b).
Figure 3.23 illustrates two modes of failure previously described. In Figure 3.23a, the stress reversal leads to initial liquefaction of the soil sample. The specimen encounters few deformation accumulation up to reach the unstable point that triggers a flow deformation, on the extension side. Hardening is observed afterwards coupled with very high deformation. In Figure 3.23b, flow deformation occurs on the compression side and cycles stabilise in the end.

The condition *sine qua non* to observe a flow deformation is that the maximum (or mini-

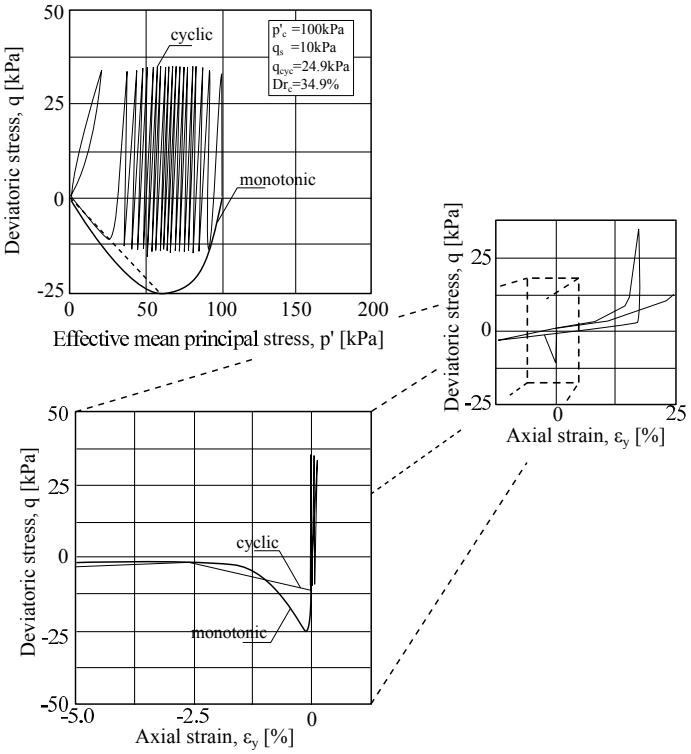

(a) Flow deformation occurs on the extension side. Zoom on the deviatoric-axial strain.

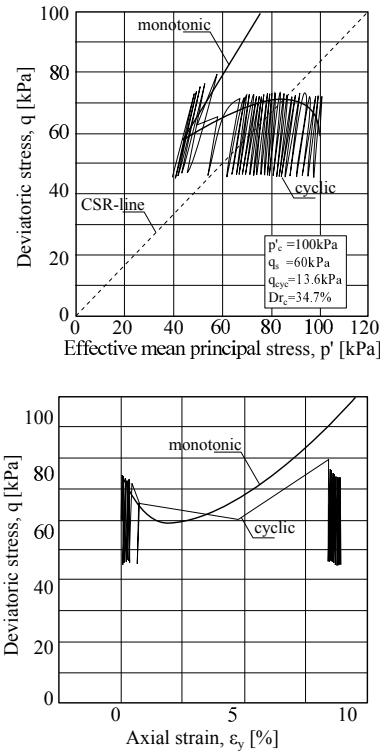

(b) Flow deformation occurs in the midle of the cycle on the compression side.

FIGURE 3.23: Comparison between monotonic and cyclic test results on Toyoura sand [Hyodo et al., 1994]. (a) instability and flow failure; (b) temporary instability; (c) Cyclic mobility.

mum) cyclic shear stress is greater than the residual shear resistance (S_{SS} or S_{QSS}), i.e.

$$q_s + q_{cycl} > S_{SS} \text{ or } S_{QSS}, \tag{3.3}$$

$$|q_s - q_{cycl}| > S_{SS} \text{ or } S_{QSS}, \tag{3.4}$$

where S_{SS} and S_{QSS} are respectively the residual resistance at the steady state and quasi-steady state in compression or extension. These conditions are illustrated in Figure 3.24. If the critical state is reached after the flow failure, a total instability occurs which can be assimilated to total liquefaction, as shown in Figure 3.24(a). In case of quasi-steady state, the crossing of the monotonic stress path triggers a temporary instability coupled with a high deformation accumulation, but stabilises later (see Figure 3.24(b)). If the variation of cyclic loading lies below the monotonic envelop, no flow deformation appears (see Figure 3.24(c)). However, failure may be attained by cyclic mobility.

It must be pointed out that this schematic representation of possible failure modes does not encompass all the possibilities. As a matter of fact, the actual failure mode depends on the initial state of the soil (relative density, mean effective stress, initial deviatoric stress) and on the cyclic applied loading. However, considering the monotonic stress path as a boundary surface unifies the interpretation of flow deformation triggering under a unique concept.

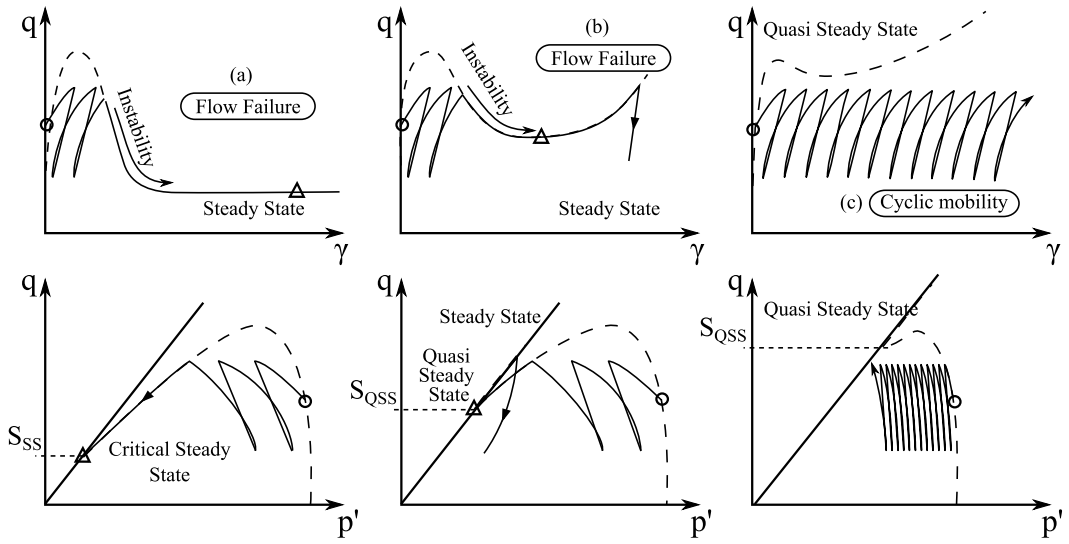

FIGURE 3.24: Flow failure and cyclic mobility [Yoshimine and Ishihara, 1998]. Stress path and deviatoric-shear strain results. ◯ = initial state; △ = quasi/critical steady state.

3.4.4 Initial and cyclic deviatoric amplitudes

Many researches have undertaken experiments to address the effect of initial deviatoric stress q_s and cyclic deviatoric amplitude q_{cycl} on the occurrence of flow deformation [Lee and Seed, 1967; Castro, 1975; Seed and Booker, 1977; Castro and Poulos, 1977; Vaid and Chern, 1983; Mohamad and Dobry, 1986; Hyodo et al., 1991]. They conclude either that an initial deviatoric stress improve or deteriorate the resistance towards flow deformation.

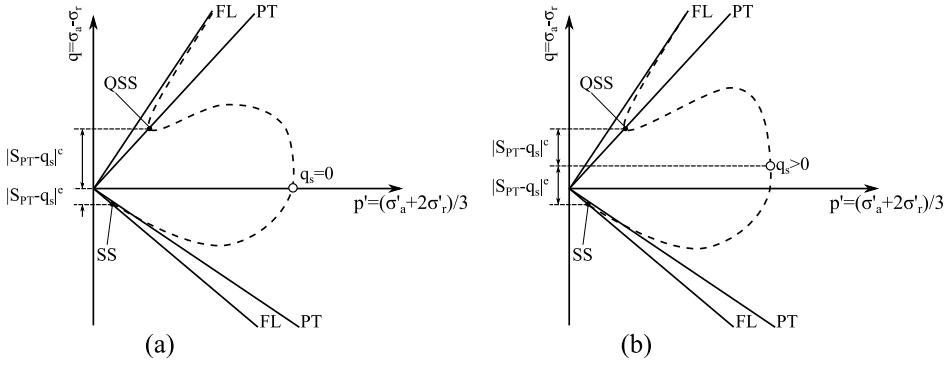

FIGURE 3.25: Monotonic undrained triaxial test from non zero initial deviatoric stress q_s. PT, phase transformation line; FL, failure line; S_{PT}, residual strength; ◯, initial state.

First, let us consider a monotonic undrained triaxial test starting from an initial deviatoric stress q_s, resulting from an anisotropic consolidation of the soil sample (see Figure 3.25). If $q_s = 0$, the residual resistance S_{PT} in compression is likely to be greater than in extension. Therefore, the difference $|S_{PT} - q_s|^c$ in compression is greater than $|S_{PT} - q_s|^e$ in extension (see Figure 3.25(a)).
If q_s is shifted up, the stress path followed and the residual strengths S_{PT} in extension and compression slightly change (see Figure 3.25(b)). However, the difference $|S_{PT} - q_s|^c$ decreases as q_s approaches S_{PT}. On the other hand, $|S_{PT} - q_s|^e$ increases, since q_s moves away from S_{PT}. This explains Figure 3.26a, where $|S_{PT} - q_s|^e$ (extension) increases with q_s and $|S_{PT} - q_s|^c$

(compression) decreases. Moreover, if q_S becomes too high, anisotropic consolidation might directly lead to the failure of the soil sample and $|S_{PT} - q_s|^c$ tends to zero.

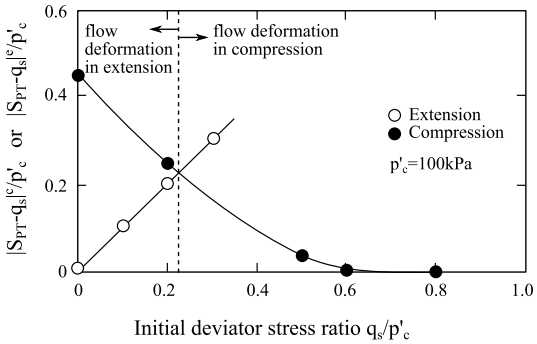

(a) Relationship between $|S_{PT} - q_s|/p'_c$ and initial deviator stress ratio for a monotonic undrained test. S_{PT} is the phase transformation strength, corresponding to the quasi-steady state, it is positive for the compression side and negative either.

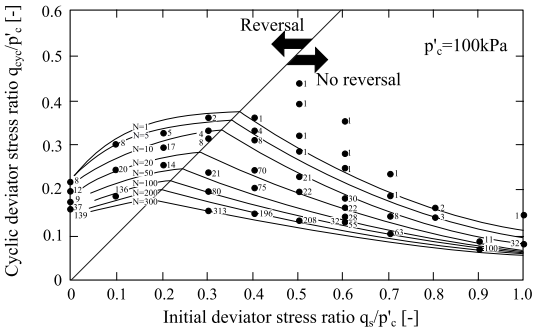

(b) Relationship between cyclic deviator stress ratio and initial static deviator stress ratio to induce flow deformation in each specified number of cycles.

FIGURE 3.26: Flow deformation occurrence for monotonic and cyclic test on saturated loose Toyoura sand [Hyodo et al., 1994]. Fl = failure line ; PT = phase transformation line; q_s mean deviatoric stress; p'_c effective initial confining stress.

It was previously displayed that the monotonic stress path defines a collapse boundary surface [Alarcon-Guzman et al., 1988; Ishihara et al., 1991; Sasitharan et al., 1993]. Therefore, it can be stated that a flow deformation might occur during a cyclic test if $|q_s - q_{cycl}| > |S_{PT} - q_s|$, i.e. the stress path intersects the unstable part of the monotonic path for an identical initial q_S (see Figures 3.27(a) and (b)).

Results in Figure 3.26a represent the maximum cyclic amplitude that can be applied without triggering flow deformation. For an initial stress ratio q_s/p'_c a cyclic amplitude greater than $|S_{PT} - q_s|$ in compression or extension, indicates that the cyclic stress path crosses the monotonic stress path, which acts as a collapse surface. Therefore, if $q_s/p'_c < 0.2$ the flow deformation intersects the collapse surface on the extension side and flow deformation occurs on that side. The flow deformation holds on the compression side if $q_s/p'_c > 0.2$.

Figure 3.26b depicts the combination of initial and cyclic deviatoric stresses that lead to a flow deformation after N cycles. If $q_{cycl} > q_s$, a reversal occurs and the flow deformation lies in the extension side. It is the opposite provided no reversal occurs. These results are consistent with Figure 3.26a. Initially, q_{cycl} that can be applied without flow deformation increases with q_s, since the stress path is shifted up and escapes from the unstable part of the extension collapse surface (see Figure 3.27(a)). However, it starts decreasing afterwards because it gets closer to the collapse surface in compression (see Figure 3.27(b)).

Actually, this collapse envelop is very flat and the behaviour is thus very sensitive to the combination (q_s, q_{cycl}). A small variation of initial deviatoric stress or cyclic amplitude may strongly affect the final behaviour and therefore the safety factors that should be adopted.

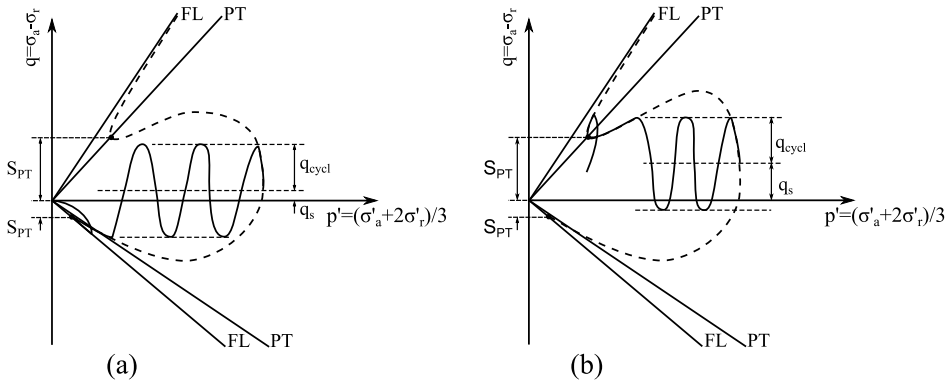

FIGURE 3.27: Schematic diagram explaining the initiation of flow deformation in the effective stress space during cyclic test [Hyodo et al., 1994]. PT = phase transformation line; FL = failure line; S_{PT} = residual strength.◯ = initial state

3.4.5 Density effect

As previously discussed, the relative density of a soil sample rules its failure behaviour. The relation between initial and cyclic deviatoric stress amplitudes required to reach a given deformation in 10 cycles is given in Figure 3.28. Loose sand shows parabolic shape curves which indicate a kind of optimum mean deviatoric stress associated to cyclic variations. For a given cyclic amplitude, any other τ_s considered would lead more quickly to a given deformation threshold.
The medium dense sand exhibits a similar behaviour even if the position of the optimum varies. The divergence of the curves appears in a non-reversal zone, where deformation accumulation rate is lower. Therefore a small variation of cyclic amplitude significantly affects the accumulated deformation. The dense sand behaviour is characterised by a continuously increasing τ_{cycl}, which indicates a greater resistance to liquefaction.

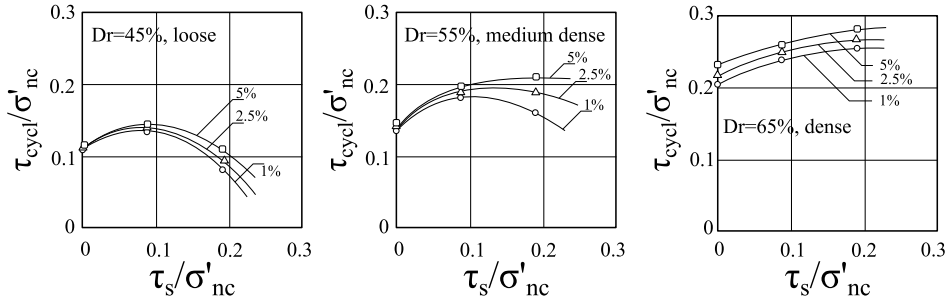

FIGURE 3.28: Effect of initial static shear stress on cyclic stress ratio required to cause various levels of axial strain [1%,2.5%,5%] in 10 stress cycles. Toyoura sand [Vaid and Chern, 1983]. σ'_{nc} is the static consolidation stress on the plane inclined at 45° to σ'_1 plane.

3.4.6 Cyclic behaviour vocabulary

In addition to the previously described behaviours, some other concepts are frequently used to described results, in the field of soil mechanics or merely mechanics. Three particular concepts may appear during cyclic tests, sometimes for a very large number of cycles. They are defined since they are employed in the following.

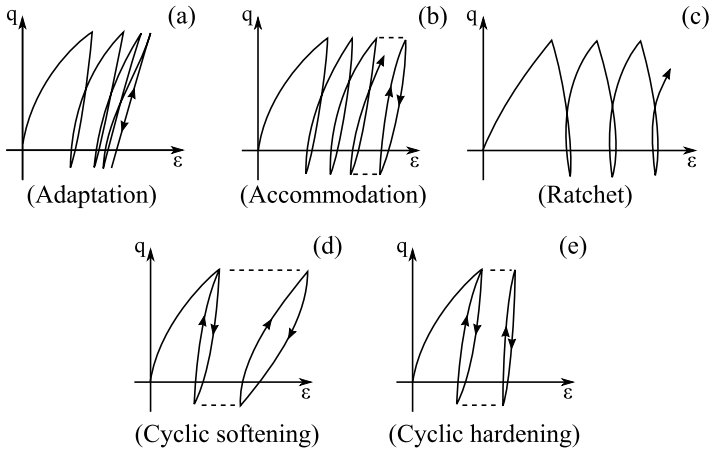

FIGURE 3.29: Particular cyclic behaviours, after [Rascol, 2009].

There is *adaptation* if the cyclic stress path converges to a new elastic state (see Figure 3.29(a)). When this state is reached, a new cycle does not involve any dissipation and the path is linear. This true state is never reached practically. A more likely effect is the *accommodation* (also plastic shakedown, see Figure 3.29(b)). The stress path accommodate to the loading and follow a closed loop. Therefore it does not accumulate more plastic deformation, but is still dissipating energy.
Ratcheting is the continuous accumulation of deformation for each new cycle (see Figure 3.29(c)). It is worth noting that a continuous ratcheting leads to infinite deformation. Therefore this phenomenon cannot hold for ever.
Depending on the material tested, the effect of cycling might be an increase or a decrease of the average stiffness of a loop (see Figure 3.29(d) and (e)). The former case is termed cyclic softening and the latter cyclic hardening.

3.5 Evaluation of *in situ* resistance to liquefaction

Laboratory experiments are mainly an academic luxury. Indeed, *in situ* stress states are not easily reproducible and specimens of soils obtained from typical drilling and sampling techniques are most of the time disturbed, [Youd and Idriss, 2001]. Ground freezing technique can provide undisturbed soil samples but the cost of such a technique is prohibitive.
Several field tests have become a common practice for evaluation of liquefaction resistance in most of the day-to-day projects. Among many techniques, the standard penetration test (SPT), the cone penetration test (CPT), the shear wave velocity measurement (V_s) and the Becker penetration test (BPT) are currently employed. The purpose of these tests is not to obtain parameters describing the complex cyclic behaviour of the soil but to assess the likelihood of liquefaction triggering. Correlations have been elaborated for the last decades, based on observations of sites where liquefaction occurred during earthquakes. Recent advances aim at assessing the available post liquefaction strength and induced deformation. The exact methodology for liquefaction potential assessment is out of the scope of this study but interested reader should refer to [Ishihara, 1993, 1996; Youd and Idriss, 2001; Seed et al., 2003] for a deep insight into practical methods.

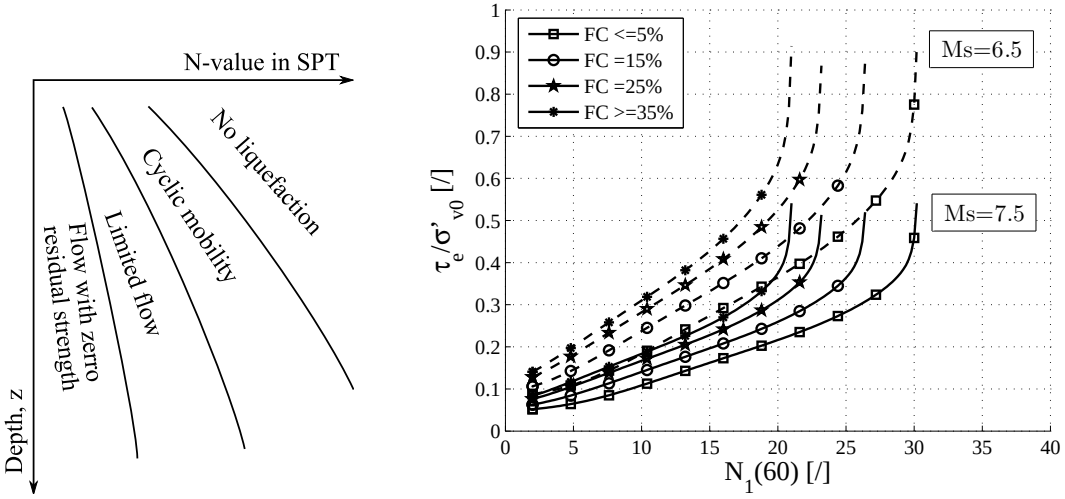

(a) Categorisation of liquefaction phenomena [Yoshimine and Ishihara, 1998]

(b) SPT based curves for the cyclic resistance ratio available, adapted from [Youd and Idriss, 2001] and [European Committee for Standardization, 2003].

FIGURE 3.30: *In situ* potential resistance to liquefaction.

SPT are widely used across the world and highly normalised. Roughly, the procedure consists in the penetration of a thick walled sample tube due to the falling of a hammer. The N-SPT value, i.e. the standard penetration resistance, is the number of blows required to drive the sample to a given depth of penetration [Skempton, 1986]. Normalisation takes into account many corrections in order to unify results obtained from different standards. For instance, the blow count number is adjusted to encompass the effect of the test apparatus, the borehole diameter and the hammer energy efficiency.
Many correlations have been elaborated based on this test. Figures 3.30a relates the N-value of the standard penetration test to a likely liquefaction phenomenon. This might occur if the residual strength after flow deformation is lower than the initial stress state within the soil [Yoshimine and Ishihara, 1998]. However, a triggering effect is necessary to overcome the onset resistance, i.e. to cross the collapse surface. This effect may be materialised by an

earthquake event for example.

One of the oldest correlations was proposed in [Seed et al., 1985]. It relates a liquefaction potential (or a cyclic resistance ratio, CRR) to the normalised[4] blow count $N_1(60)$. This CRR represents the cyclic resistance available at a given depth.
This relation was strongly improved throughout the last decades, benefiting of experience gained after recent earthquakes, [Seed and Idriss, 1971; Seed, 1979; Seed et al., 1985; Youd and Idriss, 2001]. Thence, effects of fine content and magnitude-duration of earthquakes are taken into account. An example of deterministic criterion is presented in Figure 3.30b. The proposed curve, for a given magnitude and fine content, describes the maximum available resistance at a given depth. If the applied load is lower than the curve for a given $N_1(60)$, liquefaction does not occur. Recent advances introduce the notion of *probabilistic liquefaction* triggering correlation (see Figure 3.31). Uncertainties are introduced in the computation of the available strength, which is more consistent with recent design methods. Similar correlation curves have been developed for CPT-based methods.

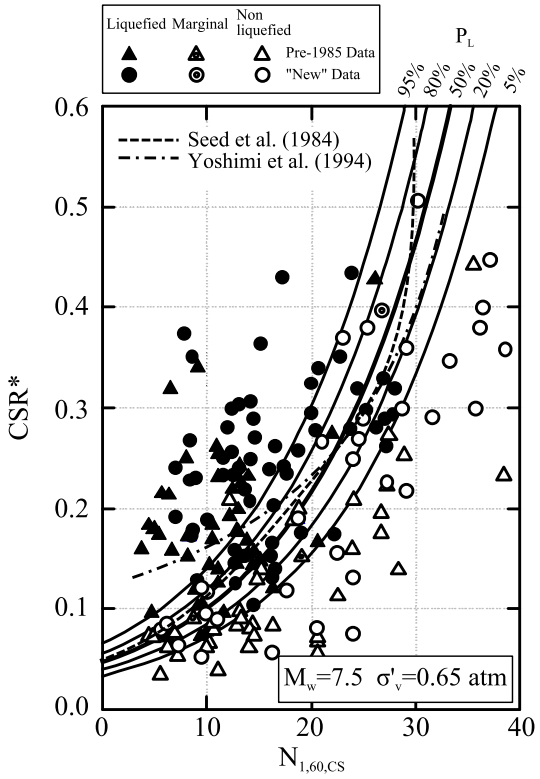

FIGURE 3.31: Recommended probabilistic SPT-based liquefaction triggering correlation (for $M_w = 7.5$ and $\sigma'_v = 0.65$atm, after [Seed et al., 2003]. P_L stands for probability of liquefaction.

In earthquake engineering, a safety factor against liquefaction can be derived from the ratio of the resistance (CRR) to the excitation termed cyclic stress ratio (CSR). This latter can be deduced from

$$CSR = 0.65 \cdot \left(\frac{a_{max}}{g}\right) \cdot \left(\frac{\sigma_v}{\sigma'_v}\right) \cdot r_d \tag{3.5}$$

where a_{max} is the peak ground surface acceleration, g is the acceleration of gravity, σ_v and σ'_v

[4] $N_1(60)$ is the SPT blow count normalised to an overburden pressure of approximately 100 kPa and a hammer efficiency of 60%.

are the total and effective vertical stresses and r_d is the non-linear shear mass participation factor. This factor is a non-linear function modulating the shear loading and depending on the depth, the earthquake magnitude, the shaking intensity and the site stiffness [Seed and Idriss, 1971; Cetin et al., 2002].
However, despite correlations are more and more complex, they are still not able to provide enough information to adequately calibrate convoluted constitutive models. Too complicated models or too low budget allocated to soil investigations are both facets of an identical reality: soils are really difficult to model.

3.6 Conclusion

This chapter consists in a review of the principal features of the undrained behaviour of soils, for both monotonic and cyclic loading. A large amount of papers and experiments exist on numerous distinct sands. However, many common phenomena were identified. During the last decades, concepts were developed to interpret and unify experiments on sands. These are the basic ingredients that should be represented by any numerical model.
Contractancy and dilatancy are obviously crucial since they underlie most of the other phenomena. The phase transformation line is one of the most important approach and allows to unify steady state, quasi-steady state and phase transformation. Although steady state is very important in experimental work, it is less essential from a numerical point of view. Indeed, it is related to very large deformations, which most of the time correspond to a post-failure behaviour of structures and is of lower interest for the design.
On the other hand, the quasi-steady state and the peak descriptions of stress paths are very relevant since they correspond to threshold and residual resistances. This residual resistance appears for a limited amount of deformation and can be followed by hardening. Therefore any numerical model should be able to reproduce temporal instabilities and peak resistances. Coherence between monotonic and cyclic loading must also be reproducible since it was demonstrated that a monotonic test represents a collapse surface for cyclic ones. Cyclic mobility and typical butterfly wings are also deemed indispensable.
It must be kept in mind that failure and post-failure behaviours mainly correspond to non-homogeneous soil samples. Therefore the macroscopic measurements indicate a change of behaviour of the soil sample, but the physics of deformation might be localised.
Additional phenomena such as the initial mean effective stress dependency, the variation of the results with orientation of principal axes or the relative density effect are important.

We shall keep in mind that the laboratory experiment is only an idealisation of reality. Initial stress state and fabric of the sand are reconstituted. The method of sample preparation has therefore a crucial impact on the results observed and might not correspond to actual behaviour. On the other hand, *in situ* tests are the only ones that truly represent the actual behaviour of the soil. However, they most of the time do not provide enough information to characterise a complex cyclic behaviour of a soil, then to calibrate complex models. The main purpose of these tests is to elaborate correlations between *in situ* measurements and potential of liquefaction. Researchers may act as an interface between laboratory and *in situ* experiments, between science and practitioners. Their knowledge of complex behaviours is necessary to summarize comprehensive design charts for day-to-day projects.

Chapter 4

From experiments to numerical modelling

If the facts don't fit the theory, change de facts.

Albert Einstein

Contents

4.1 Introduction

4.1.1 General introduction

Development and use of complex constitutive models has become widespread for he past decades. However it appears talented scientists did not wait the advent of personal computers to think about mechanics of materials. A short review of the developments in this domain is provided hereafter. It is probably incomplete, but includes most of the principal contributors. Advances and scientists are classified chronologically. However, it is interesting to note that they are roughly classified by country. Indeed, the history of sciences seems to follow golden ages of nations. Therefore Italian scientists dominated the Renaissance, French school was born during the Enlightenment and endured afterwards, many English researchers hatched out with industrial revolution and finally Prussian/German Universities arose in the late 19th century.
The history of strength material and solid mechanics starts with the famous Leonardo da Vinci and Galileo Galilei. The former carried out first experiments on wires, beams and columns. However, his notes were buried into his huge written production that was not published during his lifetime. Galileo Galilei is accepted as the originator of contemporary mechanics [Osakada, 2010][1]. He introduced modern experiments in his book "Two new sciences"[2] [Galilei, 1638], e.g. the strength of a stone beam (see Figure 4.1a), and had a great influence on scientists of his time.

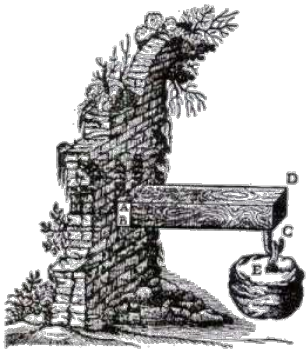

(a) Galileo illustration of a bending test, from [Lemaitre, 2001].

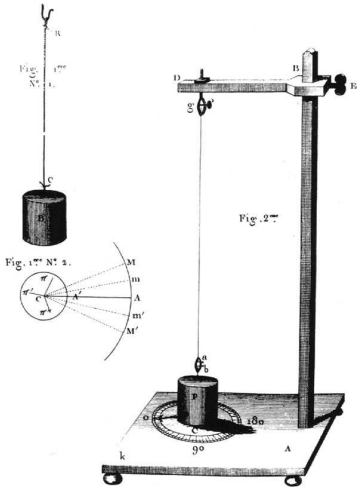

(b) Torsion test by Coulomb, in [Bell and Truesdell, 1984]

FIGURE 4.1

The next step forward was achieved by Robert Hooke who laid the foundations of the further elasticity theory. His major outcome in this field lies in the sentence "*ut tensio sic vis*"[3], literally "as the extension, so the force", published in the book "Of spring" [Hooke, 1678].
He was followed by Charles Augustin Coulomb who measured the shear modulus of an iron

[1]The backbone of the historic part of this introduction is based on this paper. For a review of the history of strength materials, focusing more on the structural aspect, interested reader should refer to [Timoshenko, 1983].

[2]This book was published by Lodewijk Elzevir, originated from Leuven, who founded a small print house, active up to 1712. The modern Elsevier founded in 1880 took its name in reference to this historic house, http://www.elsevier.com/about/history.

[3]Firstly published under the anagram *ceiiinosssttuv* in order to keep it secret, scientists are a bit of a tease!

wire. He also studied the recoverable and irrecoverable angle of that wire under successive rotations (see Figure 4.1b). In 1773, he submitted his first paper on the fracture of sandstone [Coulomb, 1773]. *He concluded that fracture of sandstone occurred when the shear stress reached a certain value, similarly to the yield condition due to maximum shear stress* [Osakada, 2010].
The *École Polytechnique of Paris* revealed a series of geniuses in the early 19th century. Simeon Denis Poisson introduced the famous coefficient bearing his name [Poisson and Garnier, 1838]. Henri Navier distinguished between yield and strength limits. Augustin Cauchy and Gabriel Lamé described the law of elasticity in a mathematical and usable form [Lamé, 1866]. Simultaneously, on the other side of the Channel, Thomas Young and George Green also developed the concept of elasticity [Young, 1845]. The latter is still present in every mechanical book since the Young modulus is termed after his name.
The work of Henri Tresca interested Barré de Saint-Venant who wrote in 1871 a paper on the partly plastic problems treating the bending of rectangular beams. He assumed that [Osakada, 2010]

- the volume of material does not change during plastic deformation ;
- the directions of principal strains coincide with those of the principal stresses ;
- the maximum shear stress at each point is equal to a specific constant (Y) in the plastic region. This last assumption is known as the Tresca criterion,

$$\sigma_1 - \sigma_3 = Y \tag{4.1}$$

  where σ_1 is the maximum principal stress and σ_3 the minimum one.

The second half of the 19th marked the advent of German schools in the fields of plasticity. Johann Bauschinger installed a compression tension testing machine and carried out numerous tests on the stress-strain relations of materials. He noticed that the yield stress in compression after plastic extension was lower than the initial yield stress in tension [Bauschinger, 1886]. This phenomenon is now termed Bauschinger effect. Otto Mohr presented a graphical representation of the stress state at a point [Mohr, 1882]. This method is now widespread as Mohr's circle. He suggested that the envelop of those circles was a yield condition and gave birth to the Mohr yield condition. In France the brothers Cosserat also developed a complex theory of elasticity [Cosserat and Cosserat, 1896].
Ludwig von Mises presented a yield criterion that would become largely used up to now [von Mises, 1913]. He also elaborated an incremental formulation that related increments of plastic strain to deviatoric stresses. Ludwig Prandtl[4] [Prandtl, 1920] and Reuss [Reuss, 1930] showed that in the plastic range, elastic and plastic deformation should be handled separately, which preluded the advent of modern elastoplastic theory. The first book in English[5] tackling plasticity was written in 1931 by Arpad Nadai [Nadai, 1931].
The era of modern mechanics opened with the remarkable book on the theory of plasticity [Hill, 1950] and the advent of finite element and computers [Zienkiewicz and Cheung, 1967]. Afterwards the number of models and researchers started increasing continuously and exponentially, which closes this historic digression.

The following chapter opens with definitions of concepts widely used in elastoplasticity. This first section aims at ensuring a unique definition for each term. The next part is a review of existing models developed in the last decades that aims at describing cyclic modelling of

[4] Ludwig Prandlt was the teacher of eminent scientists such as Theodore von Karman, Stephen Timoshenko, Arpad Nadai and William Prager
[5] Translated from German.

geomaterials, although this review is closer to philology than to applied sciences. Some models have different designation but a common basic idea, while some others share vocabulary but are mathematically different. Therefore, a subjective ordering was adopted which is not a ranking but a presentation of popular families of models.
A developed formulation of the adopted model is presented afterwards. Only the continuous formulation is presented since the numerical integration is the purpose of the next chapter. The basic model equations are stated as well as recently published variants. Parameters required for the model are developed further on, based on a simplified triaxial formulation. Drained and undrained monotonic triaxial tests on Nevada and Lund sands are presented and parameters are calibrated. Cyclic tests are then modelled based on this calibration. Sensitivity analyses are provided to test the influence of the model parameters.

4.1.2 Concepts of the elastoplasticity framework

Constitutive laws compose a particular field of engineering mechanics that requires clear premises and definitions. Most of the models described in the following, lie within the framework of elastoplasticity that possesses its own *jargon*. Therefore, some major concepts have to be introduced before any review of the literature. They were established many years ago and did not change a lot. Therefore references to pioneering researchers endorse them.

1. **Elasticity/Plasticity**
   Elasticity means that the current stress is a function of the current strain, i.e. it does not depend on the stress or deformation path [Kolymbas, 1991]. The material can always recover its original configuration, i.e. it is reversible, and does not dissipate energy during deformation.
   Plasicity characterises the non elasticity of the material. It is characterised by irreversible deformations. Moreover the current stress state depends on the previous stress/strain path.

2. **Elastoplasticity**
   Elastoplasticity is a conjunction of elasticity and plasticity [Kolymbas, 1991]. The basic hypothesis admitted hereafter is the decomposition of the total strain ($\boldsymbol{\epsilon}$) between elastic ($\boldsymbol{\epsilon}^e$) and plastic components ($\boldsymbol{\epsilon}^p$) [Prager, 1949],i.e.

   $$\boldsymbol{\epsilon} = \boldsymbol{\epsilon}^p + \boldsymbol{\epsilon}^e. \tag{4.2}$$

   It means that the current deformation is the addition of a recoverable and irrecoverable components. It must be pointed out that the multiplicative formulation should be adopted to rigorously model large elastoplastic deformations. The total deformation gradient $\mathbf{F}$ is decomposed into elastic $\mathbf{F}^e$ and plastic $\mathbf{F}^p$ components, such that

   $$\mathbf{F} = \mathbf{F}^e\mathbf{F}^p. \tag{4.3}$$

   For example, this formulation is adapted to the modelling of crystalline plasticity. In this case, $\mathbf{F}^p$ is caused by dislocation motion of the material, while $\mathbf{F}^e$ stretches and rotates the crystal lattice [Simo and Hughes, 1998]. This decomposition was also used in the developments of inelastic constitutive equations for soils, see for instance [Armero, 1999].

3. **Yield surface**
   The domain of the stress states, within a stress space, where no yielding occurs, is termed *elastic domain* [Koiter, 1953]. The boundary of this region is called *yield surface*,

which is a hyper-surface in a general stress space (6 dimensions for a symmetric stress tensor) or a 2D surface in the principal stress space (3 dimensions). If it is continuously differentiable, it can be described by

$$f(\boldsymbol{\sigma}, \boldsymbol{\kappa}) = 0. \tag{4.4}$$

where $\boldsymbol{\kappa}$ is the vector of internal variables characterising the state of the material. The sign of $f(\boldsymbol{\sigma}, \boldsymbol{\kappa})$ is chosen in order to be negative within the elastic domain. Therefore a stress state can only be twofold : elastic or plastic. The former lies within the yield surface and the latter on it. Thence, stress states out of the yield surface are not admissible (see Figure 4.2). Furthermore, Prager [1949] demonstrated the condition of irreversibility that holds for the particular case of work-hardening materials (defined hereafter)

$$\dot{\boldsymbol{\sigma}} : \dot{\boldsymbol{\epsilon}}^p > 0, \tag{4.5}$$

i.e. the second order work is positive, whenever a change of plastic strain occurs ($\|\dot{\boldsymbol{\epsilon}}^p > 0\|$). Thence, the angle between the vector pointing to any stress state on the yield surface $\boldsymbol{\sigma}$ and the exterior normal of the yield surface must be acute. Therefore, the yield surface enclosing the origin must be convex. This requirement can be extended to each material, as good practice rule.

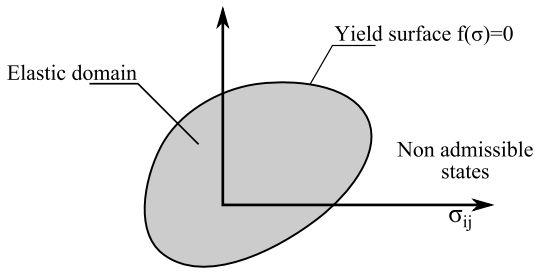

FIGURE 4.2: Definition of a yield surface in the stress space.

4. **Consistency condition**
The loading from a plastic state verifying Equation (4.4) might lead to another plastic state that must verify again Equation (4.4). Thence the so-called *consistency condition* holds between these states

$$\dot{f} = 0. \tag{4.6}$$

This condition ensures that the stress state always lies on the yield surface during a plastic loading.

5. **Plastic multiplier**
The variation of plastic deformation $\dot{\boldsymbol{\epsilon}}^p$ between two plastic states can be decomposed into a scalar ($\dot{\lambda}$) and a tensor ($\mathbf{n}_{\dot{\boldsymbol{\epsilon}}^p}$). The mathematical formulation of the evolution of the deformation is termed flow rule,

$$\dot{\boldsymbol{\epsilon}}^p = \dot{\lambda} \cdot \mathbf{n}_{\dot{\boldsymbol{\epsilon}}^p}. \tag{4.7}$$

The scalar $\dot{\lambda}$ characterises the amount of plastic strain rate and $\mathbf{n}_{\dot{\boldsymbol{\epsilon}}^p}$ its direction. $\dot{\lambda}$ is determined from the consistency condition, i.e. it represents the necessary plastic deformation that must occur to enforce a stress state lying on the yield surface. It is termed the *plastic multiplier* $\dot{\lambda}$. It is positive if the stress state is plastic and null if it is elastic. Therefore, definitions of consistency equation and plastic multiplier can

be grouped together in the so called Karush-Kuhn-Tucker condition [Simo and Hughes, 1998; Borja, 2013]

$$f(\boldsymbol{\sigma}, \boldsymbol{\kappa}) \leq 0 \qquad \dot{\lambda} \qquad \dot{\lambda} \cdot f(\boldsymbol{\sigma}, \boldsymbol{\kappa}) = 0. \tag{4.8}$$

In case of plastic loading, $f = 0$ and $\dot{\lambda} \neq 0$. If $f < 0$ and $\dot{\lambda} = 0$, the final state is elastic (unloading from plastic state).

6. **Plastic potential**
In the previous developments, the direction of plastic deformation remained arbitrary. The derivative to a surface termed *plastic potential* $\mathbf{g}$ at the current stress state gives the direction of the plastic deformation, i.e.

$$\mathbf{n}_{\dot{\boldsymbol{\epsilon}}^p} = \frac{\partial g}{\partial \boldsymbol{\sigma}} \tag{4.9}$$

If plastic potential and yield surface are merged, the variations of stresses and strains have identical direction and the deformation is denominated *associated*. Conversely, deformation is called *non-associated* [Koiter, 1953].

7. **Hardening/Softening**
In case of perfect plasticity, the shape of the yield surface remains constant. However, it was previously shown that a material can harden or soften (see Chapter 3). Odqvist [1933] firstly introduced isotropic hardening of a yield surface. The size of this surface expands to represent soil hardening (see Figure 4.3a). This effect is due to the accumulation of plastic deformation. On the other hand, the soil might also experience a peak followed by a decrease in resistance, which might be modelled by a contraction of the yield surface (softening).
Another type of hardening was introduced to take into account the Bauschinger effect: the *kinematic hardening*. The yield surface is translated into the stress space without any modification of its shape (see Figure 4.3a). In that case, the *back-stress* tensor is an internal variable memorising the position of the centre of the surface. Whatever the hardening type, the so-called *hardening rule* must be elaborated in order to describe the evolution of the yield surface size, of its position or both of them.
It must be noticed that hardening is differently interpreted from experimental and

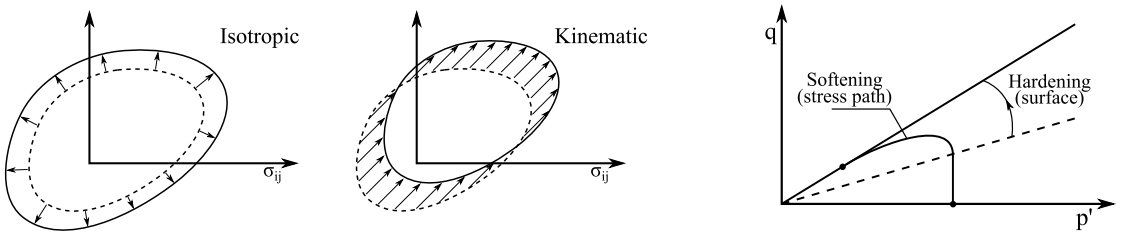

(a) Isotropic (left) and kinematic (right) hardening.

(b) Hardening yield surface, softening behaviour.

FIGURE 4.3

numerical points of view. Undrained stress paths for loose sands are typical of such behaviours (see Figure 4.3b). From a physical point of view, the deviatoric stress decreases with deformation, there is softening of the material. However, from a numerical point of view, the surface size expands, i.e. it hardens.
Mathematically the hardening/softening corresponds to the evolution of the internal variables characterising the yield surface. Thence, the hardening rule reads

$$\dot{\boldsymbol{\kappa}} = \dot{\lambda} \cdot \mathbf{h}(\boldsymbol{\sigma}, \boldsymbol{\kappa}) \tag{4.10}$$

where $\mathbf{h}$ is a vectors or functions defined by the model adopted describing the direction of evolution of internal variables.

4.1.3 Mathematical formulation of elastoplasticity

The mathematical formulation of elastoplasticy gathers the aforementioned concepts. All the following equations give birth to a system of equations that can be solved for a given increment of deformation $\dot{\boldsymbol{\epsilon}}$.

1. Decomposition of deformation rate
$$\dot{\boldsymbol{\epsilon}} = \dot{\boldsymbol{\epsilon}}^e + \dot{\boldsymbol{\epsilon}}^p \tag{4.11}$$

2. Stress-strain relation
$$\dot{\boldsymbol{\sigma}}' = \mathbb{E} : (\dot{\boldsymbol{\epsilon}} - \dot{\boldsymbol{\epsilon}}^p) \tag{4.12}$$
where $\mathbb{E}$ is an fourth-order elastic stiffness tensor

3. Flow rule
$$\dot{\boldsymbol{\epsilon}}^p = \dot{\lambda} \cdot \frac{\partial g}{\partial \boldsymbol{\sigma}} \tag{4.13}$$

4. Elastic domain (E), yield function and Karush-Kuhn-Tucker condition
$$\mathrm{E} = f\,\{\,(\boldsymbol{\sigma}, \boldsymbol{\kappa}) \,|\, f(\boldsymbol{\sigma}, \boldsymbol{\kappa}) \leq 0\} \tag{4.14}$$
$$f \leq 0 \qquad \dot{\lambda} \geq 0 \qquad \dot{\lambda} \cdot f = 0 \tag{4.15}$$

5. Hardening rule
$$\dot{\boldsymbol{\kappa}} = \dot{\lambda} \cdot \mathbf{h}(\boldsymbol{\sigma}, \boldsymbol{\kappa}) \tag{4.16}$$

6. Consistency condition
$$\dot{f} = 0 \tag{4.17}$$

This set of equations represents the general framework of elastoplasticity. It is established here for arbitrary yield functions, plastic potentials... Moreover, the consistency condition Eq.(4.17) can be expanded as
$$\frac{\partial f}{\partial \boldsymbol{\sigma}} \cdot \dot{\boldsymbol{\sigma}} + \frac{\partial f}{\partial \boldsymbol{\kappa}} \cdot \dot{\boldsymbol{\kappa}} = 0.$$
Introducing Eq.(4.12), Eq.(4.13) and Eq.(4.16) yields
$$\frac{\partial f}{\partial \boldsymbol{\sigma}} \cdot \mathbb{E} : \left(\dot{\boldsymbol{\epsilon}} - \dot{\lambda} \cdot \frac{\partial g}{\partial \boldsymbol{\sigma}} \right) + \dot{\lambda} \cdot \frac{\partial f}{\partial \boldsymbol{\kappa}} \cdot \mathbf{h} = 0 \tag{4.18}$$
which can be rearranged to isolate $\dot{\lambda}$
$$\dot{\lambda} = \frac{\overbrace{\dfrac{\partial f}{\partial \boldsymbol{\sigma}} \cdot \mathbb{E} : \dot{\boldsymbol{\epsilon}}}^{>0}}{\underbrace{\dfrac{\partial f}{\partial \boldsymbol{\sigma}} \cdot \mathbb{E} : \dfrac{\partial g}{\partial \boldsymbol{\sigma}} \underbrace{- \dfrac{\partial f}{\partial \boldsymbol{\kappa}} \cdot \mathbf{h}}_{H^p}}_{K^p}} \tag{4.19}$$

In this equation, H^p is termed plastic modulus

$$H^p = -\frac{\partial f}{\partial \boldsymbol{\kappa}} \cdot \mathbf{h}. \tag{4.20}$$

There is no restriction on its sign, thence it can be positive, null or negative. However, it is necessary the denominator K^p is positive. Indeed, it mus be ensured the plastic multiplier $\dot{\lambda}$, if it exists, is positive. The numerator is always positive if the trial state $\mathbb{E} : \dot{\boldsymbol{\epsilon}}$ lies outside the yield surface and the yield surface is convex. Therefore the choice of a suitable $\mathbf{h}$ ruling the evolution of the internal variables must fulfil this condition.

4.1.4 Inappropriate isotropic hardening models

Classic isotropic hardening models are unable to capture the main features of cyclic loading [Prevost, 1977]. Let us consider the cyclic loading of a soil sample described by the classic isotropic hardening Mohr-Coulomb conical yield surface in Figure 4.4.
The stress path starts from the point A, for a given initial mean effective stress. Initially, the behaviour is elastic since the stress state lies within the yield surface. The stress path crosses the initial position of the yield surface in B and the behaviour becomes elastoplastic. It is assumed that the plastic potential is non associated and the plastic volumetric behaviour is contractive. Therefore, the pore pressure rises and the stress path moves towards the left. The yield surface hardens up to reach the reversal point C.
This first loading part can be modelled adequately by an isotropic hardening model. However, when the stress path reverses, the behaviour is elastic again as it evolves within the yield surface. The elastic state remains up to the point D, which is the symmetric of the point C on the yield surface. However, D is a reversal point and no plasticity occurs. Therefore, the loading continues without plasticity effect between C and D in the p'-q plane unless the amplitude increases. This outcome is definitely inappropriate since it was previously shown in Chapter 3 that a non-linear stress path is observed both in loading and unloading.

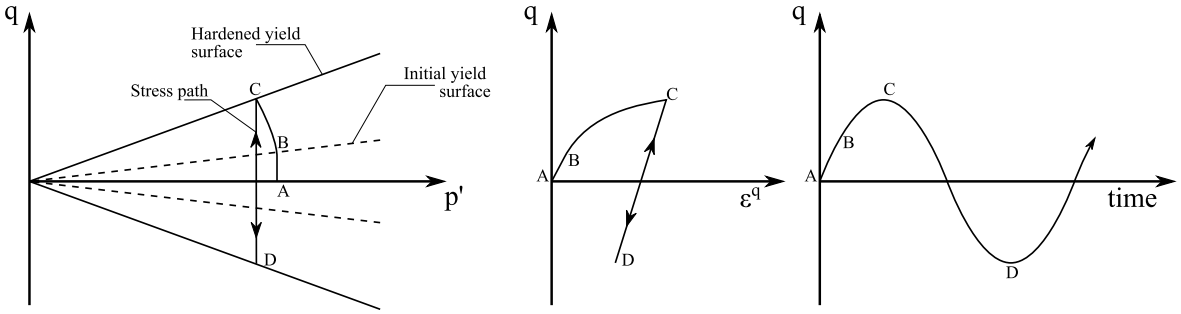

FIGURE 4.4: Cyclic loading and isotropic hardening of a classic Mohr-Coulomb yield surface. A : initial stress state ; B : initial crossing of the yield surface ; C : unloading ; D : symmetric stress state to C.

4.2 Cyclic models

4.2.1 Multi-surfaces

The multi-surface concept is one of the first attempts conceived to overcome limitations of classic isotropic hardening problems [Mroz, 1967; Iwan, 1967]. The concept is illustrated for a uniaxial loading in Figure 4.5.

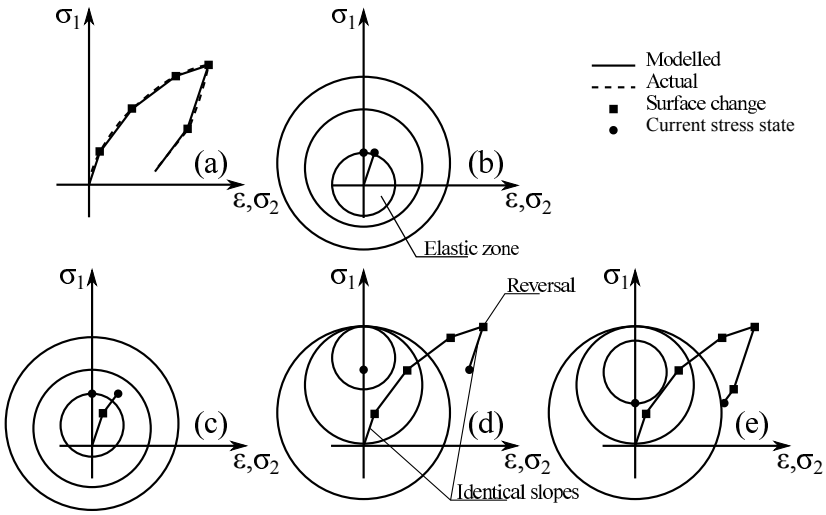

FIGURE 4.5: Idealised stress-strain behaviour with multi-surface plasticity, inspired by [Yu, 2006].

Let us consider an actual loading-unloading stress-strain relation presented in Figure 4.5(a). The actual (dashed) curve can be idealised by a succession of straight segments (solid lines), each associated to a given slope. The squared markers denote the transition from one segment to another. Each segment is associated to a yield surface and all of these surfaces are nested and homothetical.
Initially the stress path lies within the first surface, the behaviour of the modelled material is elastic (see Figure 4.5(b)) and the position of the surfaces remains constant. When the stress path crosses the first surface, the behaviour becomes plastic and the slope of the $\sigma - \epsilon$ curve changes (see Figure 4.5(c)). The surface is subject to kinematic hardening. The stress state lies on it and they are translated together up to get into contact with the next surface. Therefore, the slope changes again, the two first surfaces are tangent at the stress space and move together. This continues up to the reversal point.
When the unloading part of the curve takes place, the behaviour is elastic again since the stress path lies within the first surface (see Figure 4.5(d)). Therefore, the slope of the first unloaded segment is elastic. Then the stress path reaches the first yield surface, the slopes changes again (see Figure 4.5(e)) and so on.

The multi-surface concept is a way of discretising the field of plastic moduli which has been recognised [Dafalias and Popov, 1975], as the main factor inducing softening, hardening, ratcheting... It has been adapted to the modelling of clay behaviour in [Prevost, 1977, 1978]. The multiaxial formulation of the model involves Von Mises type yield surfaces. Their trace in the deviatoric plane is circular, but their section is constant along the hydrostatic axis (see Figure 4.6a). The $\boldsymbol{\alpha}$ value is the back-stress tensor locating the centre of each yield surface in the deviatoric plane (see Figures 4.6a and 4.6b). In last decades, one of the main drawbacks of the multi-surfaces method was the large amount of computational memory required to

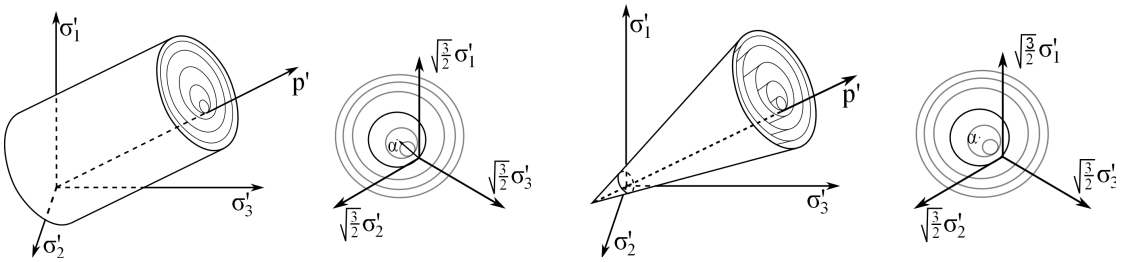

(a) Von Mises yield surfaces in principal effective stress space.

(b) Conical yield surfaces for the Prevost model in principal effective stress space, after [Prevost, 1985; Yang et al., 2003].

FIGURE 4.6: Multi-surface models.

store information about each surface [Prevost, 1982]. Nowadays this argument ceases to be pertinent, since the storage capacity of computers has grown exponentially.
The extension of such a model to cohesionless soils is not straightforward [Prevost, 1985]. One of the main feature of granular materials is the dependence of their resistance to the mean effective stress. Consequently, the yield surface family is of the Drucker Prager type, i.e. conical [Drucker and Prager, 1952]. However, the trace of the considered surfaces in the deviatoric plane is still circular (see Figure 4.6b).
The second major change to represent sand behaviour is the non-associated volumetric plastic potential. As it was previously described, the volumetric behaviour of the soil might be either contractive or dilative. Within the framework of elastoplasticity, the dilatancy reads

$$d = \frac{\mathrm{d}\epsilon_v^p}{\|\mathrm{d}\boldsymbol{\epsilon}_q^p\|}, \tag{4.21}$$

where ϵ_v^p is the volumetric component of the plastif deformation and $\mathrm{d}\boldsymbol{\epsilon}_q^p$ is its deviatoric part [Li and Dafalias, 2000]. Furthermore, Rowe [1962] demonstrate that the dilatancy rate depends on the stress ratio $\eta = q/p'$. The original formulation of the Prevost model separates the p'-q plane into contractive and dilative zones. The limit between them corresponds to the phase transformation line, defined in Section 3.3.5. The original model is extended in [Elgamal et al., 2002, 2003] to better take into account the cyclic mobility at low confinement. Further improvements adapt the model to the Lode angle dependence [Lade and Duncan, 1975; Yang and Elgamal, 2008; Zerfa and Loret, 2003].

4.2.2 Generalised plasticity

Generalised plasticity was originally introduced in [Zienkiewicz and Mroz, 1984] and extended later in [Pastor and Zienkiewicz, 1986; Pastor et al., 1990] to the modelling of soils. This model is an hybrid between hypoplasticity and elastoplasticity. It lies within the framework of the latter, but neither yield surfaces nor plastic potential are defined. Loading ($\mathbf{n}$) and plastic flow ($\mathbf{m}$) directions are postulated *a priori* for any given stress state $\boldsymbol{\sigma}$. It is worth noting that classic surfaces (yield or plastic potential) could be established *a posteriori* by integration of $\mathbf{n}$ and $\mathbf{m}$.
This formulation assumes distinct behaviours in loading and unloading. Therefore a criterion has to be adopted to distinguish between both states. The sign of $\mathbf{n} : \mathrm{d}\boldsymbol{\sigma}^e$, where $\mathrm{d}\boldsymbol{\sigma}^e$ is the elastic increment of stress, separates loading (> 0) from unloading (< 0). Plastic flow directions and their associated plastic moduli are then differentiated between loading ($\mathbf{m}_L, H_L$) and unloading ($\mathbf{m}_U, H_U$). The flow rule is non associated since $\mathbf{m}$ is different from $\mathbf{n}$. If $\mathbf{n} : \mathrm{d}\boldsymbol{\sigma}^e = 0$ the behaviour is termed neutral and corresponds to a reversible stress path.

Finally the tangent elastoplastic compliance tensor reads [Mira et al., 2009]

$$\left(\mathbf{D}_{t,L/U}\right)^{-1} = \left(\mathbf{D}_t^e\right)^{-1} + \frac{1}{H_{L/U}} \cdot \left[\mathbf{m}_{L/U} \otimes \mathbf{n}\right] \tag{4.22}$$

where $\mathbf{D}_t^e$ is the tangent fourth order elastic stiffness tensor and L/U distinguished between loading and unloading. Since flow direction and plastic moduli are continuously defined over the stress state, the generalised plasticity model can be viewed as a generalisation of multi-surface models with an infinite number of surfaces.

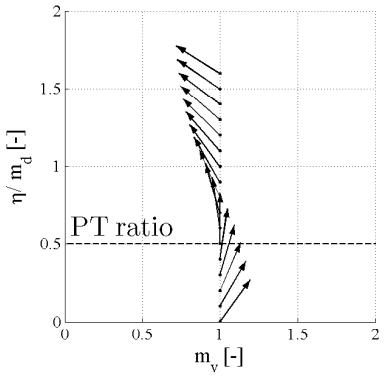

(a) Components of the flow direction $\mathbf{m} = (m_v, m_d)$ as a function of η. The PT ratio corresponds to the slope of the phase transformation or critical state line in the p'-q plane.

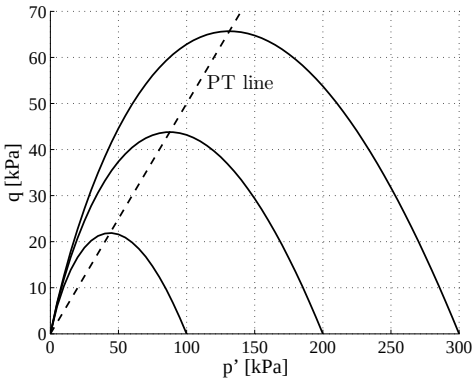

(b) Reconstituted family of yield surfaces. The PT line is the phase transformation line also termed critical state line.

FIGURE 4.7

The dilatancy was assumed to be linearly dependent on the stress ratio $\eta = q/p$ [Pastor et al., 1990]. The generalised plasticity model takes into account the phase transformation line delimiting the contractive zone from dilative ones. An example of the plastic flow deformation direction as a function of η is illustrated in Figure 4.7a. The phase transformation (PT) ratio delimits arrows that point to the right (contractive) from those which point to the left (dilative). The shape of plastic potential surfaces corresponding to $\mathbf{m}$ in a classic elastoplastic framework is depicted in Figure 4.7b [Pastor et al., 1990].
The last component of the model is the plastic modulus $H_{L/U}$. It allows the representation of the softening post peak behaviour in drained tests and critical state as well. A discrete memory factor is introduced to take into account the degradation of the plastic modulus with plastic shear deformation [Mira et al., 2009].

4.2.3 Bounding surface

Bounding surface models were introduced in the seventies by Dafalias and Popov [1975]. An example for triaxial compression and extension is illustrated in Figure 4.8a, where four surfaces are drawn

1. The *bounding surface* (slope M_c^b) has the shape of an open wedge and separates admissible from non admissible stress states.

2. The *critical state surface* (slope M_c^c) was previously defined in Section 3. It is unique for a given material in the e-p' plane and is defined from material parameters. This state is characterised by a continuous deformation at constant volume and shear strength.

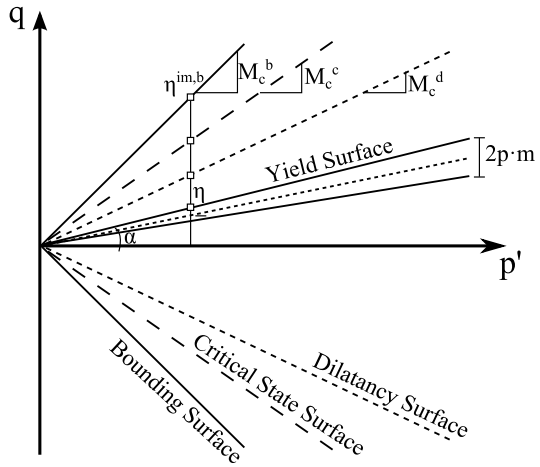

(a) Bounding surface concept, after [Papadimitriou et al., 2001]. η is the current stress state and $\eta^{im,b}$ is its projection on the bounding surface. M_c^b, M_c^c and M_c^d are the slopes of the bounding, critical and dilatancy surfaces.

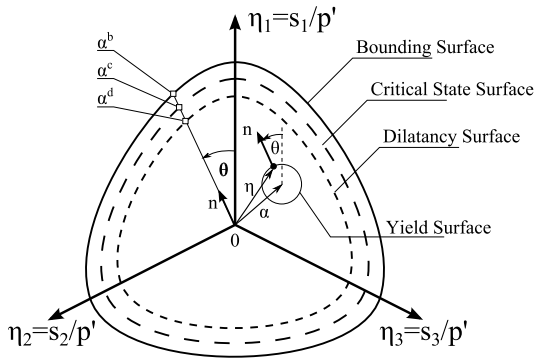

(b) Generalisation of the bounding surface model to multiaxial formulation, after [Papadimitriou and Bouckovalas, 2002].

FIGURE 4.8: Bounding surface models.

3. The *dilatancy surface* (slope M_c^d) delimits contractive from dilative zones.

4. The *yield/loading surface* (opening m, back-stress α) encompasses the elastic zone. This latter can be translated within the bounding surface by kinematic hardening [Dafalias, 1986]. Therefore, the back-stress $\boldsymbol{\alpha}$ acts as a memory variable.

The critical state surface is univoquely defined for a given material and relates the current void ratio to the mean effective stress. On the other hand, bounding and dilatancy surfaces are dependent on the state of the material [Papadimitriou et al., 2001]. They are function of the critical state surface and on the so called state parameter defined in [Been and Jefferies, 1985] such that

$$\Psi = e - e_c, \tag{4.23}$$

where e_c is the void ratio at the critical state for a given mean effective stress p'. The state parameter is a measurement of how far the current state e is from the critical state e_c. A tendency for contraction is expected for positive ψ and a tendency for dilation otherwise. Therefore, bounding surface models take into account the critical state theory [Li et al., 1999].
The plastic modulus and the volumetric behaviour are ruled by the distance between the current stress state on the yield surface and the dilatancy or bounding surfaces. An image point is computed on these surfaces through a mapping rule. For instance, the current state in Figure 4.8a is denoted by η and its image point on the bounding surface by $\eta^{im,b} = M_c^b$. Therefore, in this simplified triaxial representation, the distance is readily computed

$$d^b = M_c^b - \eta. \tag{4.24}$$

The plastic modulus is a function of the distance d^b and is null when the yield surface reaches the bounding surface (= failure). Therefore the hardening rule of the yield surface is easily obtained. The extension to multiaxial case is not trivial and requires more complex developments [Andrianopoulos et al., 2010] (see Figure 4.8b). Similarly, a distance to the dilatancy surface is computed and the flow rule that describes the volumetric behaviour is derived

$$d^d = M_c^d - \eta. \tag{4.25}$$

Thus, $d^d < 0$ indicates a contractive volumetric plastic behaviour.
The boundary surface model formulation was extended to multiaxial formulation [Wang et al., 1990; Papadimitriou and Bouckovalas, 2002]. Surfaces considered are still of wedge type but their trace in the deviatoric plane is a function of the Lode angle (see Figure 4.8b). The scalar back-stress variable becomes a tensor $\boldsymbol{\alpha}$ and the scalar distances describing hardening and flow rules are given by

$$d^{b,d} = \left(\boldsymbol{\alpha}^{b,d} - \boldsymbol{\alpha}\right) : \mathbf{n}, \tag{4.26}$$

where $\boldsymbol{\alpha}^{b,d}$ are the "image" back-stresses associated to the boundary and dilatancy surfaces respectively ; $\mathbf{n}$ is the deviatoric component of the normal to the yield surface at the current stress state.
Bounding surface models incorporate other refinements such as an hypoelastic formulation in which moduli depend on the mean effective stress [Wang et al., 1990]. The effect of sand fabric during cyclic loading is taken into account through a modification of the dilatancy rule, which allows the modelling of classic butterfly wing stress paths [Dafalias and Manzari, 2004]. Among recent alternative formulations, Oka et al. [1999] propose a description based on a generalised flow rule and non-linear kinematic hardening. Khalili et al. [2005] take into account the plasticity that can appear for an hydrostatic compression, due to the grain crushing, by modifying the shape of the bounding surface in the p'-q plane. Yu et al. [2007] develop a model based on Cam-clay like shape function unified for both sands and clays. Recently Wang et al. [2014] modify the classic formulation to take into account the post liquefaction behaviour of sand.

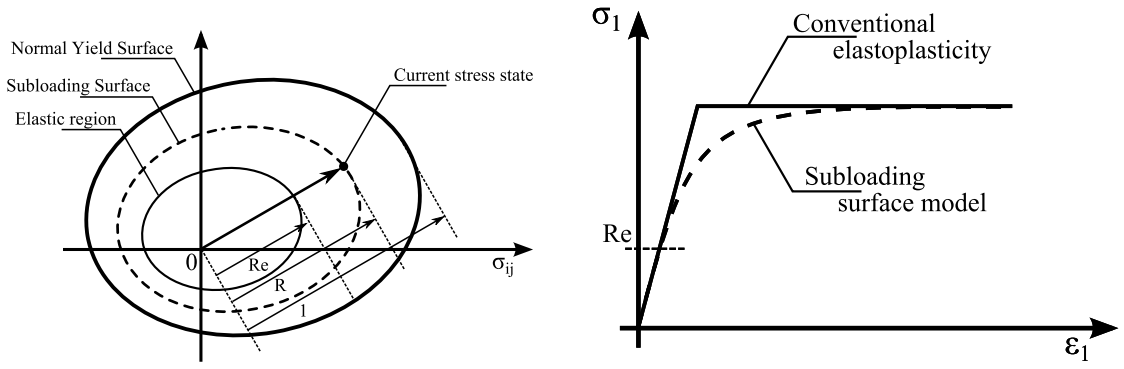

(a) Subloading surface model concept.

(b) Application to elastic perfectly plastic behaviour.

FIGURE 4.9: Subloading surface model after [Hashiguchi, 2009].

Another family of bounding surface models deserves attention. The *subloading surface* model was coined in [Hashiguchi and Ueno, 1977]. This model is a kind of bounding surface model or as it is claimed by the author [Hashiguchi, 2009], the bounding surface model is a kind of subloading model[6]. The formulation is based on an elastic region, a subloading surface and a normal yield surface (see Figure 4.9a). All of them are homothetic in such a way that if the outer surface can be written

$$f(\boldsymbol{\sigma}) = F(\mathbf{H}), \tag{4.27}$$

where $\mathbf{H}$ is a collection of internal variables, then the subloading surface can be computed as

$$g(\boldsymbol{\sigma}) = R \cdot F(\mathbf{H}), \tag{4.28}$$

[6]This hot topic is not settled here.

where $R \in [0, 1]$. Elastic region is described by the special case $R = R_e$. Contrary to previous models in which the yield surface is translated due to kinematic hardening, the subloading surface expands or contracts. In the special case $R = 1$, subloading and normal yield surfaces are merged and the classic theory of elastoplasticity holds. The aims of such a technique, among many advantages underlined in [Hashiguchi, 2009], is that result curves are smoothed and do not encounter sharp changes of slopes. This salient feature is illustrated in Figure 4.9b in the case of perfect plasticity. Classic theory assumes an elastic behaviour up to reach the yield surface, then a perfectly plastic behaviour. On the other hand, subloading surface model involves a smooth divergence starting from the elastic limit R_e and finally a convergence to the plateau. The model has been extended to cyclic modelling [Hashiguchi and Chen, 1998; Hashiguchi, 2009]

4.2.4 Explicit accumulation

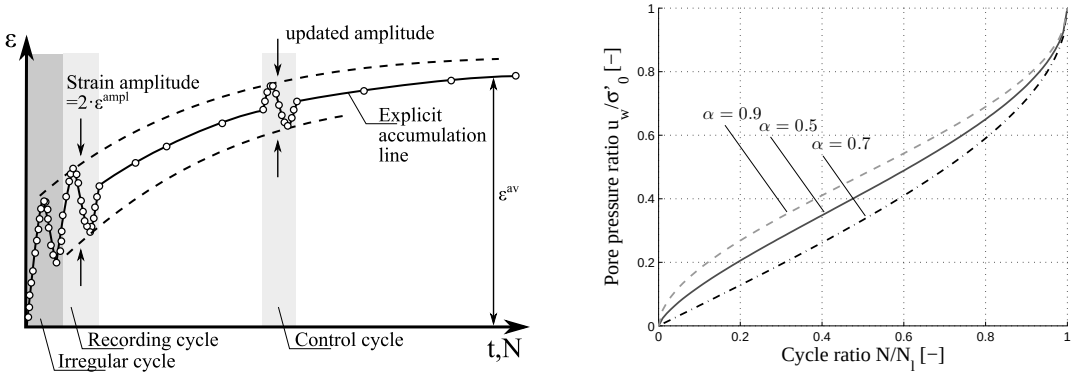

(a) Explicit calculation strategy of the cumulative deformation, after [Niemunis et al., 2005].

(b) Rate of pore water pressure buildup, after [Seed and Booker, 1977]

FIGURE 4.10: Explicit accumulation models.

Cyclic loading may involve a very large number of cycles of constant or variable amplitude, e.g. modelling of an offshore foundation subject to a storm (undrained case) or progressive settlement of railways due to high speed train vibrations (drained case). In such cases, models developed previously describing accurately the complex behaviour of the soil, suffer two drawbacks. The former is the cost of a simulation for a very high number of cycles. The latter is the loss of accuracy that may arise from the numerical implementation, the non conservative reversible part of the stress-strain relation, the forward Euler scheme... [Niemunis et al., 2005].
The evolution of the deformation can be decomposed into a trend and a transient signals (ϵ^{av} and ϵ^{ampl} respectively in Figure 4.10a) [Wichtmann et al., 2011]. If the cyclic amplitude is low ($\epsilon < 10^{-3}$), the transient part of the deformation becomes negligible with respect to the accumulated one for a large number of cycles. Therefore, the backbone idea of explicit formulation is to describe the trend of the deformation accumulation rather than the exact deformation signal.
The accumulation model does not replace a complex model, but it allows to extrapolate its results to a very large number of cycles. Therefore, according to [Niemunis et al., 2005], the algorithm proceeds in several steps.

1. Computation of the initial stress field within the boundary value problem using a conventional model.

2. For any integration point, the "exact" deformation for the two first cycles is computed. Indeed, the first cycle is most of the time irregular (see Figure 4.10a) and not suitable for the computation of a trend. The cyclic amplitude applied during the first cycle is assumed constant up to a control cycle, where it is computed "exactly" again.

3. The accumulation strain rate $\mathbf{D}^{acc}$ is computed from the second cycle previously recorded. This trend depends on many factors that can be separated through

$$\mathbf{D}^{acc} = \mathbf{m} \cdot f_{ampl} \cdot \dot{f}_N \cdot f_p \cdot f_Y \cdot f_e \cdot f_\pi, \tag{4.29}$$

   where $\mathbf{m}$ is the direction of accumulation, f_{ampl} depends on the cyclic amplitude ϵ^{acc}, $\dot{f}_N$ takes into account the number of cycles N, f_p encompasses the influence of the mean effective stress and f_Y of the stress ratio, f_e is a function of the void ratio and f_π reflects the consequence of the polarisation of the cycles.

4. Finally the variation of the stress distribution caused by N additional cycles is computed.

Wichtmann et al. [2010] demonstrate that the sequence of application of the cycles is of minor importance, i.e. the *Miner rule* [Miner, 1945], known from fatigue mechanics in metal, is applicable. Despite its accuracy, it must be pointed out this method requires experimental data based on tests involving very large number of cycles [Wichtmann et al., 2005].

Rahman et al. [1977] develop a similar method that accounts for the pore pressure build-up during earthquakes. It is based on the pore pressure evolution described in [Seed and Booker, 1977], as shown in Figure 4.10b,

$$\frac{u_w}{\sigma'_0} = \frac{2}{\pi} \arcsin \left[\left(\frac{N}{N_l} \right)^{1/2\alpha} \right], \tag{4.30}$$

where u_w is the current pore water pressure, σ'_0 is the initial mean confining stress, N_l is the number of cycles of a given amplitude required to reach liquefaction, N is the current number of cycles and α is a material parameter. This equation accounts for the development of plastic deformation and non-linear pore pressure generation and has to be coupled with a classic model, such as Mohr-Coulomb [Taiebat and Carter, 2000; Versteele et al., 2013]. Therefore, the ratio u_w/σ'_0 is equivalent to a damage index. When the pore water pressure attains the initial mean effective stress, initial liquefaction occurs and the soil looses its stiffness.
A shortcoming of the method is the necessity of converting an actual signal to equivalent cycles. As a corollary, many experimental results are also required. Instead of N_l, Green et al. [2000]; Polito et al. [2008] adopt a criterion based on the energy dissipated per unit volume of soil during the loading.

This idea was also adopted by Pecker et al. [2001] who decouple the pore pressure evolution between the fast time and the slow time phenomena. The former is modelled as a linear elastic problem for an incompressible medium and the second as a non-linear poroelastic problem with a strain source term. This latter one requires an evolution curve similar to Figure 4.10b. Similarly, Di Prisco and Zambelli [2003] elaborate two decoupled plastic mechanisms. The former is associated to the global evolution of the fabric and the latter one to small strains and small size cyclic loads disturbance.

4.2.5 Others

Other models have been developed and used all around the world for the cyclic modelling of soils. Some of them may have deserved a longer explanation and some other may have been

displaced to one of the previously described families. Whether a model has been described is a subjective choice and may depends on the ease to be explained without complex mathematical framework.

1. **Hypoplasticity**
   According to [Kolymbas, 1991] hypoplasticity includes *all plastic (*i.e. *path dependent and dissipative) constitutive models which do not use any yield surface.* Constitutive equations are referred as rate type, i.e.

   $$\dot{\boldsymbol{\sigma}} = h(\boldsymbol{\sigma}, \dot{\boldsymbol{\epsilon}}, ...) \tag{4.31}$$

   where the function h must be non-linear with respect to $\dot{\boldsymbol{\epsilon}}$. It means that a relationship is defined for every stress state between deformation and stress rates [Gudehus, 1996]. This formulation assumes *a priori* this relation. A factorised representation of this basic equation was adopted by [Bauer, 1996] to ease the comprehension and the calibration of the model. This consists in separating the basic Equation (4.31) into independent factors that are only function of physical variables such as density. These kinds of models incorporate classic concept such as critical state or Drucker-Prager limit state [von Wolffersdorff, 1996].
   Among the close cousins of this kind of models Darve and Labanieh [1982] develop an incremental constitutive law that already incorporates the absence of yield surface and relates increments of deformation to increment of stresses.
   Hypoplasticity was sometimes related to bounding surface models [Dafalias, 1986; Wang et al., 1990], despite the use of yield and bounding surfaces seems to contradict the aforementioned definition. The key difference between them is that hypoplasticity does not introduce a decomposition of the strain between reversible and irreversible components.

2. **Multi-mechanism**
   Hujeux [1985] introduced an elastoplastic constitutive law containing three deviatoric mechanisms and one isotropic. Each deviatoric mechanism represents a specific plane of the space and might be activated or not. In the deviatoric plane associated to each mechanism, yield functions are represented by concentric circles [Hicher and Shao, 2002]. It was adapted to cyclic loading by adding a cyclic yield surface that becomes active when a reversal occurs [Foucault, 2010] and is subject to kinematic hardening.
   Iai and Ozutsumi [2005] introduce a multiple mechanism models in the strain space relating the micromechanical structure to macroscopic deformation. It consists of a multitude of simple shear mechanisms oriented in arbitrary directions. Stress distribution is computed locally from the projection of the macroscopic strain field. The local stress tensors are then averaged over a representative elementary volume to reconstruct a macroscopic stress field. Dilatancy is taken into account through a fabric tensor and allows to cyclic simulations [Iai et al., 2011].

3. **Disturbed state concept**
   This model basically combines different states of the material, the relatively intact and fully adjusted states [Park and Desai, 2000]. The former state is modelled using a classic plastic hardening model. The fully adjusted state characterises the final state of the material, for example the critical state. The principal idea of this model is to couple them. Thence, observed behaviour tends asymptotically to the fully adjusted state. The transition from one to the other is ruled by the disturbance function D. Its formulation is close to damage model. If $D = 0$ the state is relatively intact and if $D \to 1$ it is fully adjusted. However, contrary to damage model, considering the cracks such as a non-resistant part of the domain, the disturbed state concept involves a fully adjusted state, that is not necessarily a zero resistance state.

4.2.6 Choice of the model

Many models are able to reproduce salient features of the cyclic modelling of soils. Therefore it is not easy to make a choice between one and the others. Several criteria have to be taken into account

1. the capability of reproducing pertinent cyclic features for a given application;
2. the number of parameters that must be calibrated (including the initial conditions of internal variables) ;
3. the practical implementation of the model in a finite element code.

The first two criteria must be combined. As a matter of fact, the model adopted must correspond to the actual need of the designer. For instance, if the purpose is to avoid the failure of a foundation, it is not useful to truly describe the post-liquefaction behaviour of a soil. Indeed, liquefaction will probably induce very large deformation and the objective is to avoid them. However, this might be convenient if failure occurs only locally. Therefore, post-failure modelling is necessary to allow a redistribution of the stress state within the soil.
The number of parameters is very important in practice. Many models well-fitting experimental data require from ten to fifteen parameters. Their calibration is a luxury of science and research but is not applicable to day-to-day projects. On the other hand, practitioners would rather describe highly non-linear complex problems using two parameters models, which is impossible. Therefore a balanced approach should be found to bridge the gap between practitioner and researcher practices.
The ease of implementation of a model is the dark side of computational mechanics. The elegance of a theoretical formulation does not mandatory imply an easy implementation. Many issues such as stability, robustness and accuracy have to be considered. Models are mostly developed on the basis of laboratory tests, such as the triaxial ones. However, general finite element codes require tensorial formulations that are less straightforwardly derived.
In computational modelling and in poker game as well, the price must be paid to see behind the cards. A sufficient experience can only be acquired in programming and implementing models which is the only way to reveal the drawbacks of a formulation. The Prevost model was chosen in this work mainly for the simplicity of its formulation and its relation with physical parameters. In its basic formulation, extension and compression triaxial tests are sufficient to calibrate the parameters.

4.3 The Prevost model

The aforementioned Prevost model is a member of the multi-surfaces family. All of the nested surfaces considered are homothetic. Therefore, the description of yield functions and hardening rules as well is limited to one single surface hereafter and identical for the other ones. Practical implementation is the purpose of the next chapter which better describes how to manage the succession of yield surfaces.

4.3.1 Constitutive equations

The Prevost model is based on the already mentioned assumption that the total strain rate $\dot{\boldsymbol{\epsilon}}$ can be split into elastic $\dot{\boldsymbol{\epsilon}}^e$ and plastic $\dot{\boldsymbol{\epsilon}}^p$ components. Therefore, Equation (4.32) is stated and relates the stress rate[7] $\dot{\boldsymbol{\sigma}}'$ to the elastic strain rate $\dot{\boldsymbol{\epsilon}} - \dot{\boldsymbol{\epsilon}}^p$

$$\dot{\boldsymbol{\sigma}}' = \mathbb{E} : (\dot{\boldsymbol{\epsilon}} - \dot{\boldsymbol{\epsilon}}^p), \tag{4.32}$$

where $\mathbb{E}$ is the fourth-order tensor of elastic coefficients (linear elasticity), that can be written in the simplified formulation

$$[\mathbb{E}]_{ijkl} = \left(K - \frac{2}{3} \cdot G\right) \cdot \delta_{ij} \cdot \delta_{kl} + G \cdot (\delta_{ik} \cdot \delta_{jl} + \delta_{il} \cdot \delta_{jk}), \tag{4.33}$$

where K and G are respectively the bulk and shear moduli. The flow rule $\dot{\boldsymbol{\epsilon}}^p$ is factorised into [Lubliner, 1975],

$$\dot{\boldsymbol{\epsilon}}^p = \mathbf{P} \cdot \langle \dot{\lambda} \rangle, \tag{4.34}$$

where $\mathbf{P}$ is a symmetric second-order tensor defining the direction of plastic deformation. The plastic loading function $\dot{\lambda}$ (= plastic multiplier), is a scalar depicting the variation of plastic deformation and is defined in [Lubliner, 1975] as

$$\dot{\lambda} = \frac{1}{\mathrm{H}'} \cdot \mathbf{Q} : \dot{\boldsymbol{\sigma}}', \tag{4.35}$$

where $\mathbf{Q}$ is a second-order tensor defining the unit outer normal to the active yield surface and H' the plastic modulus associated to this surface. Therefore, combining Equations (4.32), (4.34) and (4.35) leads to

$$\dot{\boldsymbol{\sigma}}' = \mathbb{E} : \dot{\boldsymbol{\epsilon}} - \mathbb{E} : \mathbf{P} \langle \dot{\lambda} \rangle, \tag{4.36}$$

which is the basic continuous equation of elastoplasticity. Thus, the variation of stress state associated to an arbitrary variation of deformation can be viewed as an elastic predictor ($\mathbb{E} : \dot{\boldsymbol{\epsilon}}$) reduced by a plastic corrector ($\mathbb{E} : \mathbf{P} \langle \dot{\lambda} \rangle$) to bring the stress state back to the yield surface.

4.3.2 Yield functions

4.3.2.1 Basic model

The Prevost model belongs to the J_2 plasticity family, i.e. plasticity occurs when the second invariant of the stress tensor reaches a threshold. It means that the trace of that criterion in the deviatoric plane is a circle. The shear strength of cohesionless soils is mean effective stress dependent. Therefore, the family of considered nested surfaces is composed

[7] Objective Jaumann stress rate.

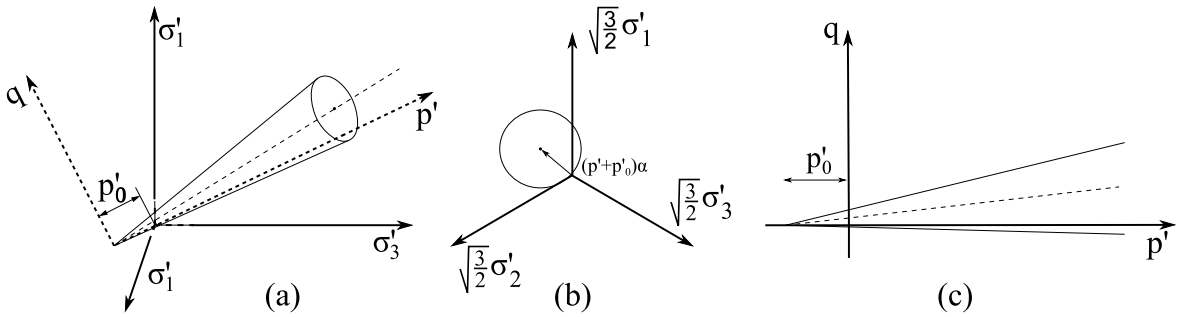

FIGURE 4.11: Three views of a Prevost conical yield surface : (a) principal stresses space, (b) deviatoric plane, (c) p'-q plane.

of conical yield surfaces in the principal stress space. Their apex is fixed at the origin of the axes and their mathematical formulation reads

$$\mathrm{f}^i \equiv \left(\mathbf{s} - \mathrm{p}' \cdot \boldsymbol{\alpha}^i\right) : \left(\mathbf{s} - \mathrm{p}' \cdot \boldsymbol{\alpha}^i\right) - \frac{2}{3} \cdot \left(\mathrm{p}' \cdot \mathrm{M}^i\right)^2 = 0 \tag{4.37}$$

where p' is the mean effective stress, $\boldsymbol{\alpha}^i$ is the back-stress tensor and M^i is a material parameter denoting the half-aperture of the surface. A representation of this surface is provided in Figure 4.11(a) in the principal stresses space. The back-stress tensor points to the centre of the surface in the deviatoric space (see Figure 4.11(b)). The trace of this surface in a p'-q plane is denoted by two straight lines (see Figure 4.11(c)).
It must be pointed out that the surface is conical, but is not a true cone in the principal stress plane. If the back-stress tensor $\boldsymbol{\alpha}$ is null, the surface is centred on the hydrostatic axis and its trace in the deviatoric plane is a circle, i.e. the axis of the surface and the perpendicular to the deviatoric plane are collinear. If the back-stress tensor is not null, the trace of the surface in the deviatoric plane remains a circle even if the central axis ceases to be collinear.
The normal to the surface at the stress state $\boldsymbol{\sigma'}$ is computed through

$$\frac{\partial f}{\partial \boldsymbol{\sigma'}} = 2 \cdot \left(\mathbf{s} - \mathrm{p}' \cdot \boldsymbol{\alpha}^i\right) + \frac{2}{3} \cdot \left[\mathrm{p}' \cdot \left(\boldsymbol{\alpha}^i : \boldsymbol{\alpha}^i - \frac{2}{3} \cdot \left(M^i\right)^2\right) - \mathbf{s} : \boldsymbol{\alpha}^i\right] \cdot \boldsymbol{\delta}.$$

Finally the corresponding unit-norm normal tensor is derived and is decomposed into deviatoric ($\mathbf{Q}'$) and volumetric (Q") parts

$$\mathbf{Q} = \frac{\dfrac{\partial f}{\partial \boldsymbol{\sigma'}}}{\left\| \dfrac{\partial f}{\partial \boldsymbol{\sigma'}} \right\|} = \mathbf{Q}' + \mathrm{Q}^{"} \cdot \boldsymbol{\delta}. \tag{4.38}$$

4.3.2.2 Variants

Most of the time, actual materials are not truly cohesionless, e.g. silty sands. On the other hand cohesion is sometimes necessary for numerical purpose, in order to facilitate convergence or to avoid spurious local or superficial failure. Thence, cohesion is simply taken into account through a shift p'_0 of the apex from its actual position to the origin of the axis (see Figure 4.12a). Computations are carried out for shifted surfaces and stress paths, and then brought back to initial configuration.

It was also shown that the direction of principal stresses has a great importance on the sand behaviour and shear resistance [Lade and Duncan, 1975]. Therefore, it is possible to adapt

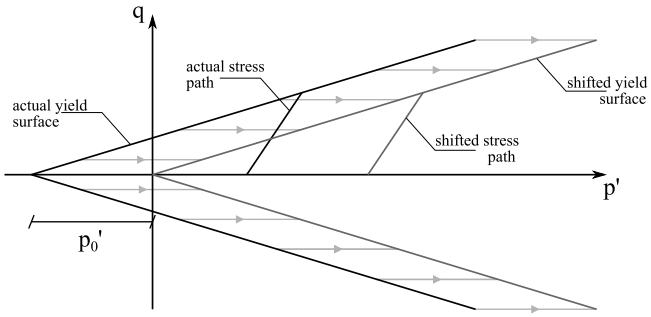

(a) Shift of the yield surface along the hydrostatic axis.

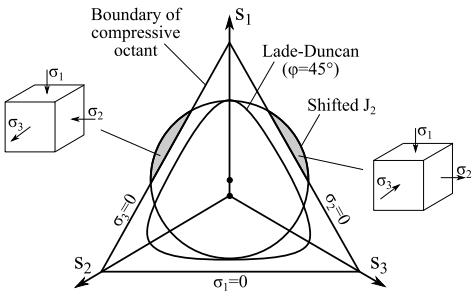

(b) Lade-Duncan failure criterion for a friction angle of 45°, and comparison with a centre-shifted J_2 function, [Yang and Elgamal, 2008] citing [Lade, 1984].

FIGURE 4.12: Variants of the basic Prevost model

the yield criterion to take into account the effect of Lode angle. Several criteria encompass the Lode angle dependency of the yield surface. They are smooth approximation of the Mohr-Coulomb criterion. The Lade-Duncan criterion is presented in Figure 4.12b. It is worth noting that other formulations such as Van Eekelen [Van Eekelen, 1980] or Matsuoka-Nakai [Matsuoka and Nakai, 1974] criteria can be adopted.
The classic J_2 plasticity surface can be shifted to coincide with the Lade-Duncan criterion for a particular stress path, e.g. triaxial. However, the shear resistance is then poorly approximated for other loading paths (see Figure 4.12b). Although a Lode-dependent surface was shown to improve accuracy, it was chosen not to take it into account for the sake of simplicity of the developments.

4.3.3 Flow rule

4.3.3.1 Basic model

The tensor $\mathbf{P}$ indicates the direction of plastic deformation in the flow rule Equation (4.34). It can be decomposed into its deviatoric $\mathbf{P'}$ and volumetric P" components

$$\mathbf{P} = \mathbf{P'} + \mathrm{P}^{"} \cdot \boldsymbol{\delta}. \tag{4.39}$$

The deviatoric component is associated, i.e. its direction in the principal stress space is identical to the deviatoric component of the normal at the current stress state

$$\mathbf{P'} = \mathbf{Q'} = \frac{2 \cdot (\mathbf{s} - \mathrm{p'} \cdot \boldsymbol{\alpha})}{\left\| \dfrac{\partial f}{\partial \boldsymbol{\sigma}} \right\|}. \tag{4.40}$$

On the other hand, the volumetric part is non-associated in order to take the dilatancy/contractancy of the material into account and reads

$$\mathrm{P}^{"} = \frac{1}{3} \cdot \frac{\bar{\eta}^2 - \eta^2}{\bar{\eta}^2 + \eta^2} \qquad \text{where} \qquad \eta = \frac{\sqrt{3/2 \cdot \mathbf{s} : \mathbf{s}}}{\mathrm{p'}} = \frac{\mathrm{q}}{\mathrm{p'}}. \tag{4.41}$$

The PT ratio $\bar{\eta}$ takes into account the aforementioned phase transformation line. This parameter rules the volumetric behaviour and separates the p'-q plane into two zones. Stress ratios (η) lower than $\bar{\eta}$ indicate a plastic contractive behaviour, whilst the other zone depicts a dilative plastic behaviour (see Figure 4.13a). The amount of volumetric dilation or contraction

is also a function of η. Contraction is maximum for $\eta = 0$ and dilation tends asymptotically to $-1/3$ for high η values (see Figure 4.13b). This parameter does not depend on the state parameter, contrary to the previously described bounding surface model [Dafalias and Popov, 1975]. Thence, the model is not able to reproduce the critical state conditions.

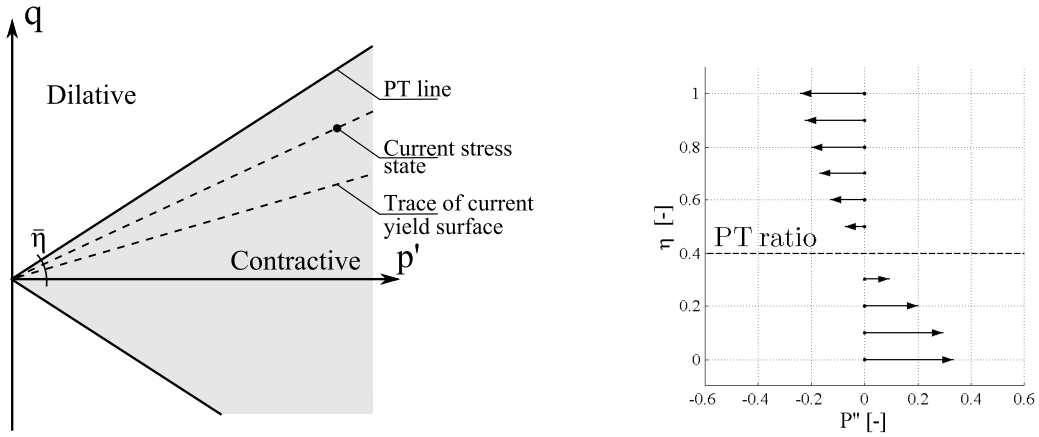

(a) Limit between contractive and dilative zones, PT line = phase transformation line

(b) Volumetric component of the plastic potential P" as a function of η, PT ratio = slope of the PT line.

FIGURE 4.13

4.3.3.2 Variants

The original volumetric plastic potential is not very accurate since it depends only on a unique parameter $\bar{\eta}$. Once the phase transformation ratio is defined, the magnitude of dilatancy is not adjustable. Thence, a constant scale parameter ψ can be readily introduced

$$P" = \frac{\psi}{3} \cdot \frac{\bar{\eta}^2 - \eta^2}{\bar{\eta}^2 + \eta^2}, \tag{4.42}$$

which might be sufficient to fit monotonic curves. However, a more elaborated formulation is necessary to represent more accurately cyclic mobility, especially at low confinement and ψ depends on the state of the soil. Elgamal et al. [2003] presented such an improvement (see Figure 4.14). This potential allows the shear stress-shear strain relation to mark a plateau when the stress phase reaches the phase transformation line (phases 1-2, 6-5, 7-8 in Figure 4.14). The length of this plateau increases at each loops and is ruled by a damage-like law. However, this yield phase is only significant at low confinement $<$ 10kPa, [Elgamal et al., 2003]). Obviously, the cost of this formulation is the addition of new parameters that must be calibrated. The applicability to complex stress paths is much more intricate than to triaxial tests. Therefore, this special plastic potential is not employed in the following.

4.3.4 Hardening rule

A hardening rule is necessary to describe the kinematic translation of each of the yield surfaces. Indeed, each of them hardens up to get into contact with the next one. A purely deviatoric hardening rule is adopted in the basic model [Prevost, 1985], which reads

$$\mathrm{p}' \cdot \dot{\boldsymbol{\alpha}} = a \cdot \boldsymbol{\mu} \tag{4.43}$$

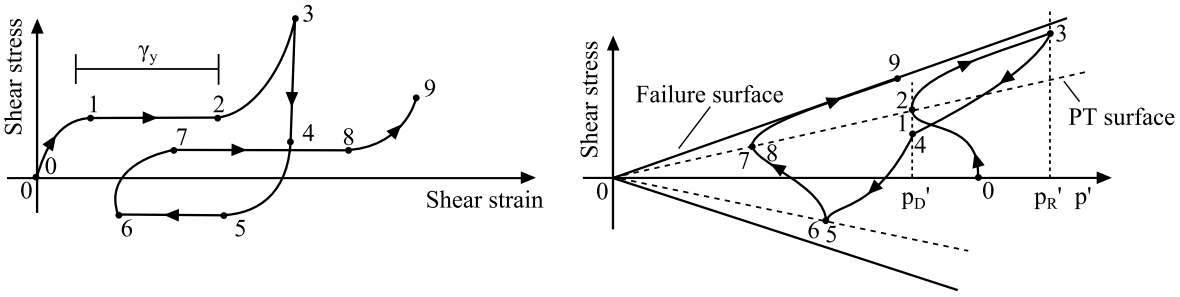

FIGURE 4.14: Shear stress - shear strain and effective stress path under undrained shear loading conditions, [Elgamal et al., 2003].

where $\boldsymbol{\mu}$ is a deviatoric tensor defining the direction of hardening of the yield surface and a is its "amount" of translation. The consistency condition then reads

$$\begin{aligned} & \dot{f} && = 0 \\ \Leftrightarrow \quad & \frac{\partial f}{\partial \boldsymbol{\sigma}'} : \dot{\boldsymbol{\sigma}}' + \frac{\partial f}{\partial \boldsymbol{\alpha}} : \dot{\boldsymbol{\alpha}} && = 0 \\ \Leftrightarrow \quad & \mathbf{Q} : \dot{\boldsymbol{\sigma}}' - \mathrm{p}' \cdot \mathbf{Q}' : \dot{\boldsymbol{\alpha}} && = 0. \end{aligned} \tag{4.44}$$

Introducing Equations (4.35) and (4.43) into Equation (4.44) allows to compute the variable a

$$a = \frac{H'}{\mathbf{Q}' : \boldsymbol{\mu}} \cdot \dot{\lambda} \tag{4.45}$$

and finally the amount of translation of the yield surface

$$\mathrm{p}' \cdot \dot{\boldsymbol{\alpha}} = \frac{\mathrm{H}'}{\mathbf{Q}' : \boldsymbol{\mu}} \cdot \langle \dot{\lambda} \rangle \cdot \boldsymbol{\mu}. \tag{4.46}$$

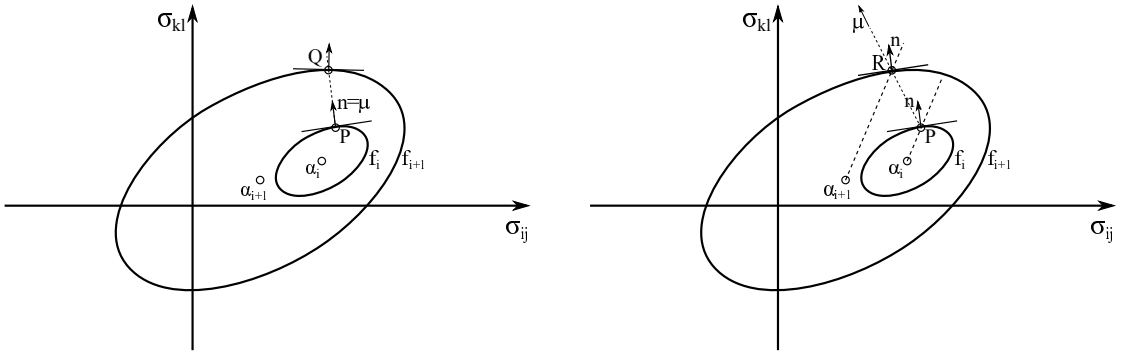

(a) Iwan translation rule of the yield surface f_i.

(b) Mroz translation rule of the yield surface f_i.

FIGURE 4.15: Hardening rules after [Yu, 2006]. $\boldsymbol{\alpha^i}$ and $\boldsymbol{\alpha}^{i+1}$ are respectively the centres of surfaces f_i and f_{i+1}; P is the current stress state, Q and R are the projection of the point P on the next yield surface along the hardening direction $\boldsymbol{\mu}$.

Up to that point, the direction of translation remains arbitrary. However it is one of the basic ingredients of the model and its choice is crucial. Furthermore, it must be kept in mind that the translation rule, despite described with regard to a single surface, is constraint by the set of nested surfaces. Indeed, each surface is supposed to be enclosed by the next one and its possibilities of translation are then limited. Therefore, explicit and implicit integration schemes may lead to different results during integration.

Iwan [1967] assumes that current yield surface translates in a direction parallel to the the increment of plastic strain, which is formulated as

$$\boldsymbol{\mu} = \frac{\partial f}{\partial \boldsymbol{\sigma}'}. \tag{4.47}$$

A geometric interpretation of such a criterion is illustrated in Figure 4.15a. Two successive nested surfaces (f_i and f_{i+1}) are represented. The former surface translates up to get into contact to the next one, which in turn moves. The point P is the current stress state. The hardening rule leads to a contact point Q, where outer normal tensors are not identical. Therefore, two successive surfaces might intersect, which is not admissible.

Mroz [1967] introduce a hardening direction ensuring no possible crossing of two successive surfaces. The normal at the current stress state on the surface f_i is denoted $\mathbf{n}$ (see Figure 4.15b). The hardening direction is defined by the vector that relates the point P with the point R of identical normal vector $\mathbf{n}$. It makes the surfaces align gradually along the current stress path direction.
The point R is straightforwardly identified since it can be shown that direction $\overrightarrow{\alpha^i P}$ is parallel to $\overrightarrow{\alpha^{i+1} R}$, which can be written in the deviatoric plane

$$\frac{\mathbf{s}^R - \mathrm{p}' \cdot \boldsymbol{\alpha}^{i+1}}{\mathbf{s}^P - \mathrm{p}' \cdot \boldsymbol{\alpha}^i} = \frac{M^{i+1}}{M^i} \tag{4.48}$$

where $\mathbf{s}^P$ and $\mathbf{s}^R$ are respectively the deviatoric stress tensors at the current and projected stress states. *Mutatis mutandis*, one obtains

$$\boldsymbol{\mu} = \frac{M^{i+1}}{M^i} \cdot \left(\mathbf{s}^P - \mathrm{p}' \cdot \boldsymbol{\alpha}^i\right) - \left(\mathbf{s}^P - \mathrm{p}' \cdot \boldsymbol{\alpha}^{i+1}\right) \tag{4.49}$$

4.4 Parameters calibration

Surprisingly, the hardest step of the calibration of parameters is the finding of data to be calibrated. Indeed, graphs and figures of many triaxial tests are available in the literature, but rough numerical data are much scarcer. The main quality of the Nevada and Lund sands calibrated in the following is the existence of freely available data reports that allow an exact description of the test results.

4.4.1 Nevada Sand

Triaxial tests on Nevada sand are part of an extended report on the VELACS (VErification of Liquefaction Analyses by Centrifuge Studies) program. This freely available database was already used to calibrate the Prevost model in [Elgamal et al., 2002; Yang et al., 2004]. General properties of that material are provided in Table 4.1. Permeability of the soil is also measured and varies between 6.6×10^{-5}m/s for a relative density of 40% and 2.3×10^{-5}m/s for a relative density of 90%.

γ_s [kN/m^3]	$\gamma_{d,max}$ [kN/m^3]	$\gamma_{d,min}$ [kN/m^3]	e_{max} [-]	e_{min} [-]
26.7	17.33	13.87	0.511	0.887

TABLE 4.1: Properties of the Nevada sand : γ_s, density of the solid grains ; $\gamma_{d,max}$, maximum dry density ; $\gamma_{d,min}$, minimum dry density ; e_{max}, maximum void ratio ; e_{min}, minimum void ratio.

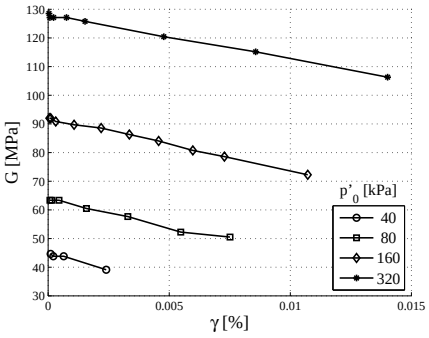

(a) Evolution of the shear modulus with shear deformation (Dr= 40%).

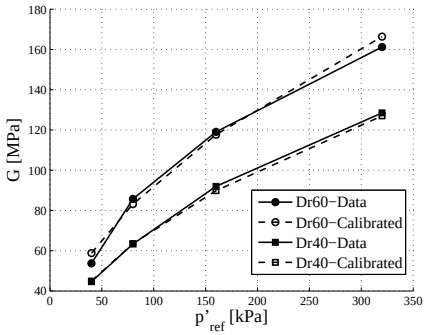

(b) Confinement dependency of the shear modulus at very low shear deformation.

FIGURE 4.16: Resonant column tests on soil samples at different confinements p'_0, after [Arulmoli et al., 1992].

Figures 4.16a and 4.16b present results on resonant column tests on Nevada sand at Dr= 40% or Dr= 60%. The former figure illustrates the evolution of the shear modulus with shear deformation, at different confinements. Measured data are only constant at a very low shear strain and decrease linearly with increasing shear deformation afterwards. Therefore, it calls into question the definition of a true elastic zone and the choice of its size is a key issue. The evolution of the shear modulus with the confinement is illustrated in Figure 4.16b. The represented G values correspond to the data measured at the lowest strain deformation in Figure 4.16a. A calibrated relationship was superimposed to the measured data for both relative densities, i.e.

$$G(\mathrm{p}') = G_{ref} \cdot \left(\frac{\mathrm{p}'}{\mathrm{p}_{ref}} \right)^{0.5}, \tag{4.50}$$

where p_{ref} is a reference pressure ($100kPa$) and G_{ref} is the corresponding shear modulus. Estimated and measured data coincide very well. Therefore it is assumed in the following that both elastic (G, K) and plastic (H') moduli are confinement dependent, i.e. they verify

$$X(\mathrm{p}') = X_{ref} \cdot \left(\frac{\mathrm{p}'}{\mathrm{p}_{ref}} \right)^{0.5}, \tag{4.51}$$

where X is either G, K or H'. It must be pointed out that for numerical stability, the ratio $\mathrm{p}'/\mathrm{p}_{ref}$ is limited to a lower bound $\mathrm{p}'_{lim}/\mathrm{p}_{ref}$ in order to avoid $H' \to 0$ in numerical simulations.

4.4.2 Nevada sand Dr= 40%

4.4.2.1 Experimental results

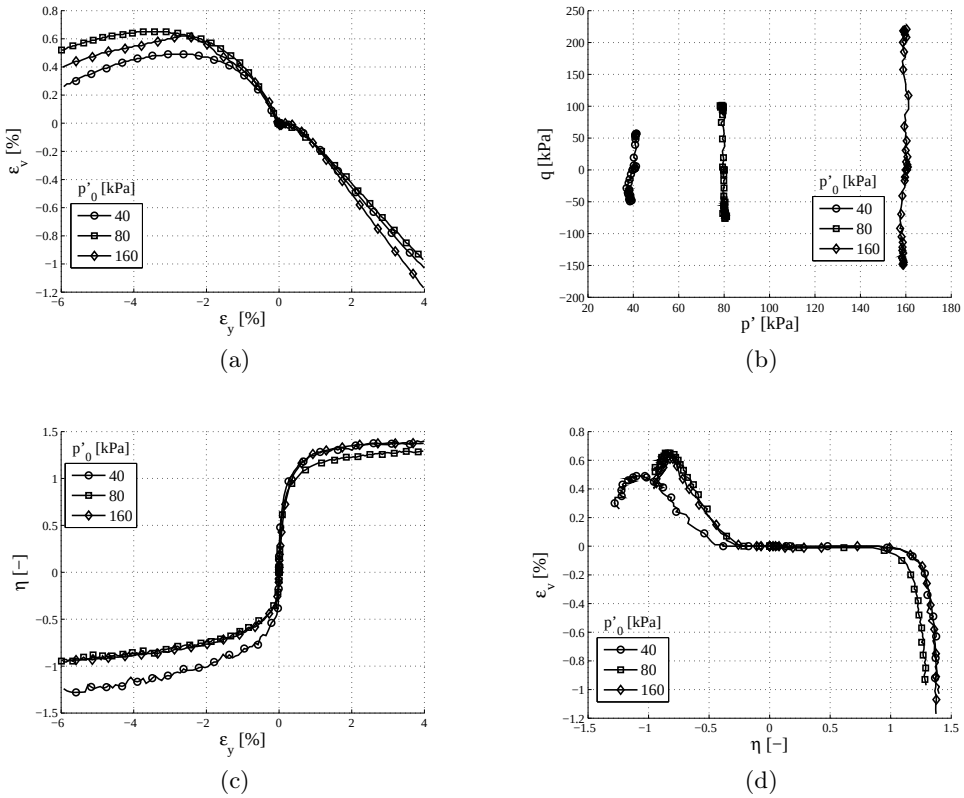

FIGURE 4.17: Monotonic drained triaxial test (p'=cst) on Nevada sand, Dr= 40%, after [Arulmoli et al., 1992]. p'_0, initial mean effective stress.

Special drained triaxial tests (p'=constant) on Dr= 40% Nevada sand are provided in Figure 4.17. They consist of six tests at three distinct initial mean effective stresses $p'_0 = [40, 80, 160]$kPa. Initial data provided in [Arulmoli et al., 1992] reach up to 20% of axial deformation. However, the tests fail after much less vertical deformation. It is clear in Figure 4.17c that the shear stress is bounded and deformation continues. This might be the sign of a loss of uniformity along the sample. As a matter of fact, shear band occurrence was observed between 10% and 15% of the test.
Compressive and extensive samples exhibit different behaviours (see Figure 4.17a). For instance, extensive tests encounter a strong contractive phase while compressive are nearly dilative from the beginning. Compressive result curves in Figure 4.17c indicate a nearly unique failure friction angle that corresponds to a slope of around 1.4 (friction[8] angle= 35°). The failure slope of extensive tests is roughly 2/3 lower.
The phase transformation slope corresponds to the maximum of volumetric deformation in drained triaxial test, i.e. $\dot{\epsilon}_v = 0$. This behaviour is clear for extensive results but is absent for compressive test (see Figure 4.17d). Therefore, additional information is required to overcome scatter of the data.

On the other hand, undrained tests, at least compressive tests, show remarkably similar behaviours (see Figure 4.19). Moreover, the phase transformation can be more easily located by identifying a maximum of pore water pressure, i.e. $\dot{u}_w = 0$. However, it is worth noting

[8] $\sin\phi' = (3\eta)/(6+\eta)$ if cohesion is equal to 0.

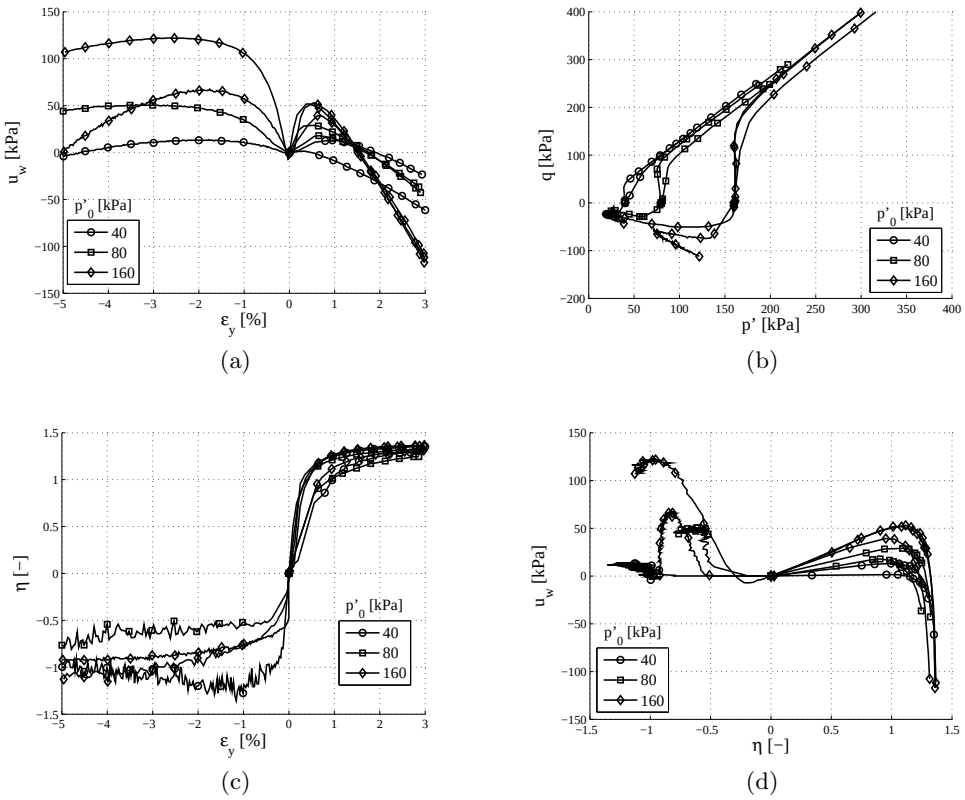

FIGURE 4.18: Monotonic undrained triaxial test on Nevada sand, Dr= 40%, after [Arulmoli et al., 1992]. p'_0, initial mean effective stress.

that results are scattered, especially in extension. For instance, two tests starting from an identical state (p'_0 = 160kPa) exhibit distinct pattern of pore pressure accumulation (diamond markers, in Figure 4.19a). However, their stress path are similar in the sense that they overcome a peak of shear strength followed by an unstable part (decreasing q) and a final hardening (see Figure 4.18b). This example exhibits the large scatter that might exist between laboratory tests.
It is also interesting to note that during the unstable part of the stress path, the deviatoric stress q decreases (see Figure 4.18b) with increasing deformation, i.e. the soil softens. However, the reduced deviatoric stress η monotonically increases (see Figure 4.18c). Therefore, from a numerical point of view, the stress state is supposed to lie on a hardening yield surface, since η increases.

Two undrained cyclic triaxial tests are provided in Figure 4.19. These tests are theoretically identical. The initial mean effective stress p'_0 is equal to 160 kPa, the deviatoric offset q_{cycl} is equal to approximately 21kPa and the deviatoric cyclic amplitude q_{cycl} to 28kPa. The final behaviour of the soil sample is identical, i.e. cyclic mobility occurs, but the stress path is distinct.
During the first test, there is initially a strong accumulation of deformation followed by the so-called butterfly wing shape cycles. Each cycle accumulates more vertical deformation up to a maximum positive vertical deformation of about 12%. On the other hand, the second test encounters seven close cycles before triggering a strong accumulation of deformation up to 28%.
Thence, it is illusory to succeed in modelling exactly a cyclic test from a unique set of parameters. Results are scattered and difficult to analyse. However, experimenters should not be blamed. Indeed, such tests are not easy to carried out, since they involve unstable phases

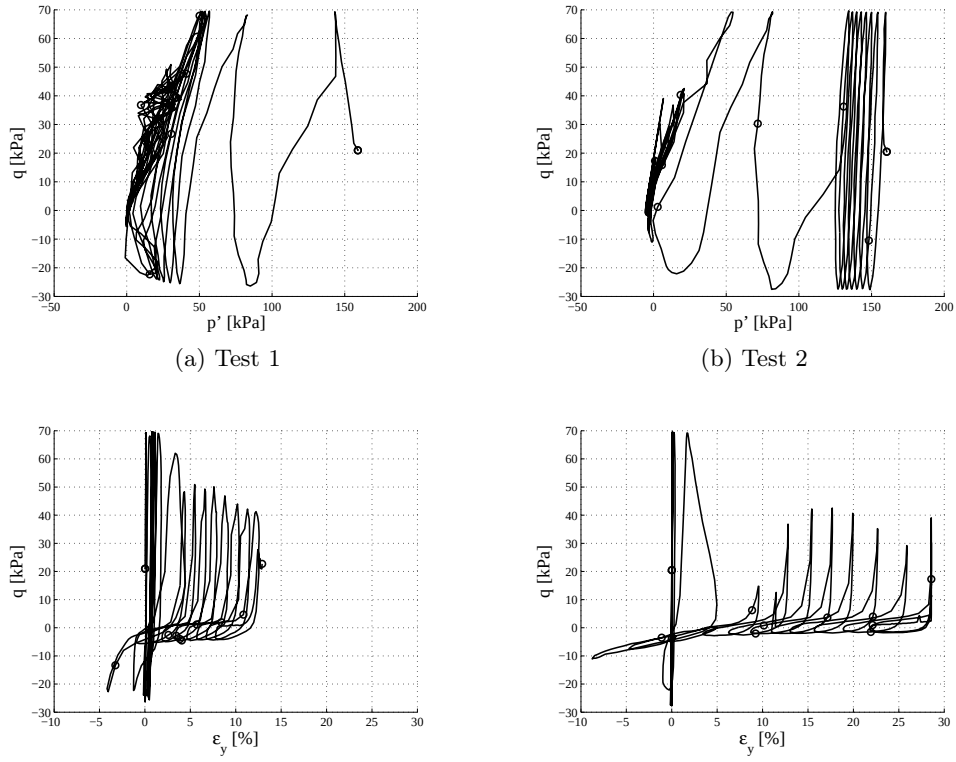

(a) Test 1 (b) Test 2

(c) Test 1 (d) Test 2

FIGURE 4.19: Cyclic undrained triaxial test on Nevada sand, Dr= 40%, after [Arulmoli et al., 1992]. $p'_0 = 160$kPa, initial mean effective stress ; $q_{off} = 21$kPa and $q_{cycl} = 28$kPa.

and are very sensitive to imperfections and small variations of the loading. Therefore, the calibration task becomes difficult and unrewarding since it is not possible to find a unique set of parameters that perfectly depicts experimental data. Moreover, a choice must be made to distinguish acceptable from unacceptable results of simulations.

4.4.2.2 Calibration of drained/undrained tests

Simplified equations describing the model in the simple triaxial case are provided in Appendix A. An explicit integration of these equations was carried out in Matlab in order to "simply" calibrate parameters.
An arbitrary monotonic test can be readily calibrated to obtain a set of parameters. Figure 4.20 represents the calibration of both drained and undrained triaxial test on a Dr= 40% Nevada sand, at $p'_0 = 80$kPa. Calibrating independently drained and undrained experiments leads to the definition of two distinct sets of parameters. Therefore, an iterative procedure of calibration should be followed to ensure a good average fitting of the two sets of data.

	G_{ref}[MPa]	K_{ref}[MPa]	$\bar{\eta}$[-]	Ψ[-]	M_{el}[-]	$\eta_{f,c}$[-]	$\eta_{f,e}$[-]
Drained (S1)	40	-	0.85	0.60	0.10	1.28	-0.95
Undrained (S2)	40	40	0.75	0.19	0.125	1.40	-0.80

TABLE 4.2: Drained and undrained sets of parameters for the calibration of Dr= 40% Nevada sand. G_{ref}, reference shear modulus; K_{ref}, reference bulk modulus; M_{el}, opening of the elastic yield surface; $\bar{\eta}$ and Ψ, parameters of the volumetric flow rule; $\eta_{f,c}$ and $\eta_{f,e}$, failure slope.

Both of them are given in Table 4.2. Thirteen nested surfaces are used in each case but the corresponding parameters are omitted for the sake of readability and would be summarised afterwards. A common elastic shear modulus was adopted for both simulation types. Its order of magnitude is consistent with data obtained from resonant column tests (see Figure 4.16a). However, its determination is uneasy since few data are measured at the early beginning of the test, when the behaviour is truly elastic. It must be pointed out that bulk modulus cannot be determined with the drained test since the mean effective stress is kept constant. Therefore the elastic component of the volume change is null. Thence, the volumetric drained behaviour is theoretically the consequence of plastic deformation only.

Calibrated parameters of the volumetric flow rule diverge for both tests. Indeed, $\bar{\eta}$ parameters are close but results are very sensitive (see in the next Section). Ψ parameters are clearly divergent, but it is worth noting that K_{ref} and Ψ have a similar influence on the results and are therefore uneasily calibrated together.
Elastic yield surfaces have similar opening in both cases. On the other hand, the Prevost model implemented does not explicitly take into account a failure, since no bounding surface is implemented. However, if the plastic modulus of the last surface is low enough, the result is similar to a null modulus. Therefore a failure line can be distinguished. These limits are not identical in drained and undrained cases, which is probably due to the scatter of the results.

It is interesting to know if both sets of parameters previously calibrated are equivalent or lead to distinct results. Thence, both sets of parameters obtained from drained (S1, in Table 4.2) and undrained (S2, in Table 4.2) are compared in Figure 4.21. Drained and undrained triaxial tests are reproduced for three initial mean effective stresses $p'_0 = [40, 80, 160]$kPa. They clearly lead to dissimilar results from volumetric and deviatoric points of view. In the latter case, the slopes of the failure envelopes are distinct (see Figure 4.21d and 4.21b), which only reflects the divergences observed in the laboratory tests. As a consequence, a unique set of parameter can be obtained solely by averaging the calibrated data. Nevertheless, a study of their respective influence is firstly carried out in the next section.

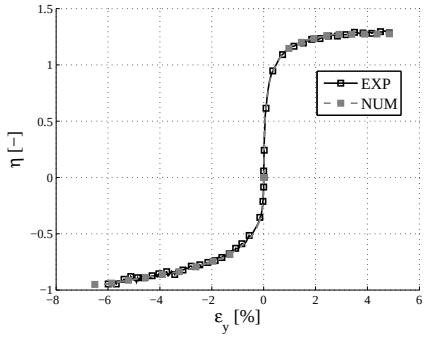

(a) Drained

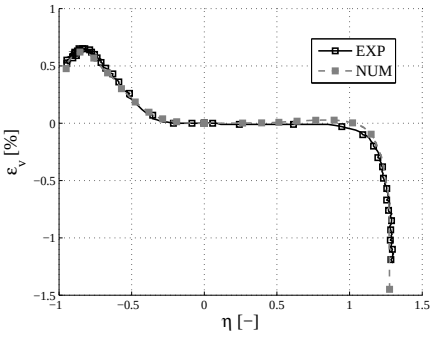

(b) Drained

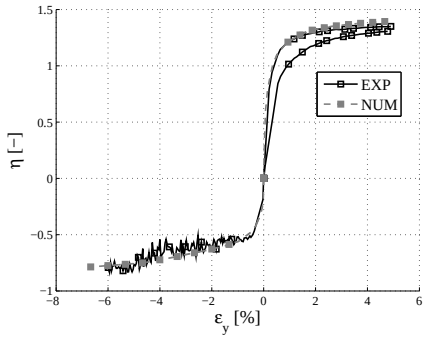

(c) Undrained

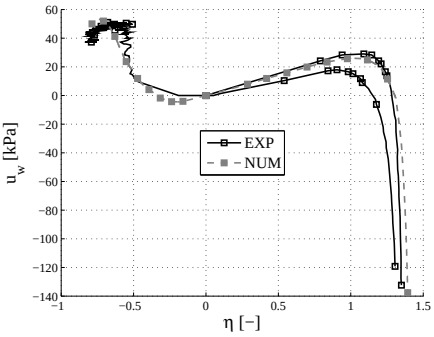

(d) Undrained

FIGURE 4.20: Comparison of measured and calibrated results for a Nevada sand (Dr= 40%) and an initial mean effective stress p'$_0$ = 80kPa, after [Arulmoli et al., 1992].

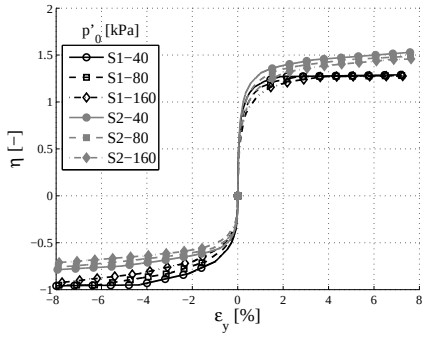

(a) Drained

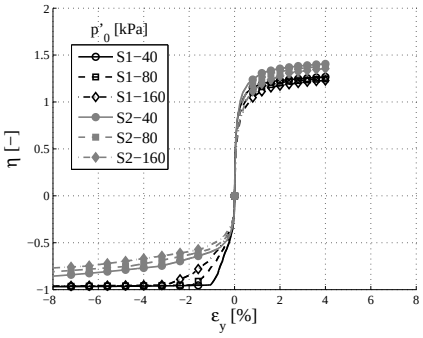

(b) Undrained

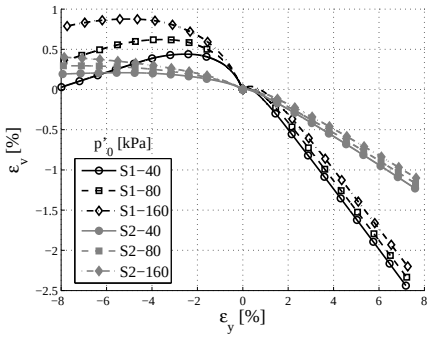

(c) Drained

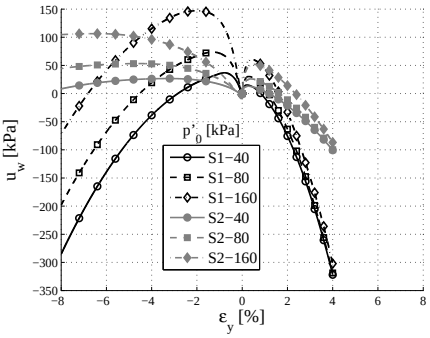

(d) Undrained

FIGURE 4.21: Comparison of the two sets of data (S1 and S2, in Table 4.2) for simulated drained and undrained tests.

4.4.2.3 Influence of parameters

Parameters obtained from undrained tests (S2, in Table 4.2) are modified in this section to highlight their influence. Only those altering the volumetric behaviour are investigated in Figure 4.22. Thence, it must be pointed out that the influence of each parameter on the $\epsilon_y - \eta$ curve is nearly null. As a matter of fact, the flow rule is split into associated deviatoric and non associated volumetric parts. Therefore, volumetric parameters have nearly no effect on this curve, but they have on $q - \epsilon_y$.
First of all, it can be observed in Figure 4.22 that all the results present similar patterns. In compression, the behaviour is firstly contractive and dilative afterwards after the stress path has crossed the phase transformation line. On the other hand, extensive tests are not so easily analysed. From the volumetric point of view, they are composed of three phases :

Phase 1 The rate of pore pressure variation is negative. As a matter of fact, the elastic effects dominate and $\dot{u}_w < 0$ since the test is extensive. The stress path (not represented) translates towards the left, i.e. $\dot{\mathrm{p}}' < 0$ since $\dot{\sigma}_1 < 0$. It is interesting to note that this phase spans over a clear range of η, for instance $\eta \in [-0.18, 0]$ (see Figure 4.22b) but only corresponds to a tiny range of $\epsilon_y \in [-0.016, 0]\%$[9] (see Figure 4.22a).

Phase 2 Afterwards, a classic plastic contractive phase takes place since $\eta < \bar{\eta}$ (see Figure 4.22b). The stress path continues to be translated towards the origin of the axes (not represented).

Phase 3 The maximum of pore water pressure is then reached when the stress path crosses the phase transformation line. A plastic dilative phase takes place and pore water pressure becomes negative.

The influence of the reference bulk modulus K_{ref} is illustrated in Figures 4.22a and 4.22b. It does not affect the initial slope of the $\epsilon_y - u_w$ curve since it only depends on the shear modulus. Therefore the slopes of $\epsilon_y - u_w$ and $\eta - u_w$ are symmetric at the origin.
Its influence is less obvious to understand afterwards since equations governing the undrained behaviour of the soil are complex. Mathematically, it is demonstrated in Appendix A that for a loading part ($\dot{\mathrm{q}}$) of the stress path, the following equation holds

$$\frac{\dot{\mathrm{q}}}{\dot{\mathrm{p}}'} = \eta - \frac{H'}{K} \cdot \frac{\sqrt{6}}{2} \cdot \frac{1 + (\eta/\bar{\eta})^2}{1 - (\eta/\bar{\eta})^2} \cdot \sqrt{1 + \frac{2}{9}\eta^2}. \tag{4.52}$$

Let us assume that elastic yield surface vanishes, i.e. $M_1 \to 0$ (soil behaviour is directly elastoplastic), and initial stress state is on the hydrostatic axis, i.e. $\eta = 0$. Therefore, Equation 4.52 can be reorganised as

$$\dot{\mathrm{p}}' = -\dot{q} \cdot \frac{K}{H'} \cdot \frac{2}{\sqrt{6}}. \tag{4.53}$$

The influence of K is then easy to understand for the beginning of the test, and then to extrapolate. For a given positive $\dot{\mathrm{q}}$, the mean effective stress decreases, since the stress state lies within the contractive zone. Therefore, the higher the bulk modulus, the higher the variation of $\dot{\mathrm{p}}'$ and the higher the pore pressure accumulated.
It can also be observed that a higher K_{ref} involves a higher rate of pore water pressure decrease during the dilative phase. It also slightly shifts the η value corresponding to the

[9] This strong change of behaviour and variation of η over a very small range of deformation will be of uttermost importance for the numerical implementation of the model.

maximum u_w, at least in compression. It means that the phase transformation line is not ruled only by $\bar{\eta}$. It must also be kept in mind that the current bulk modulus depends on the mean effective stress, accentuating the divergence.

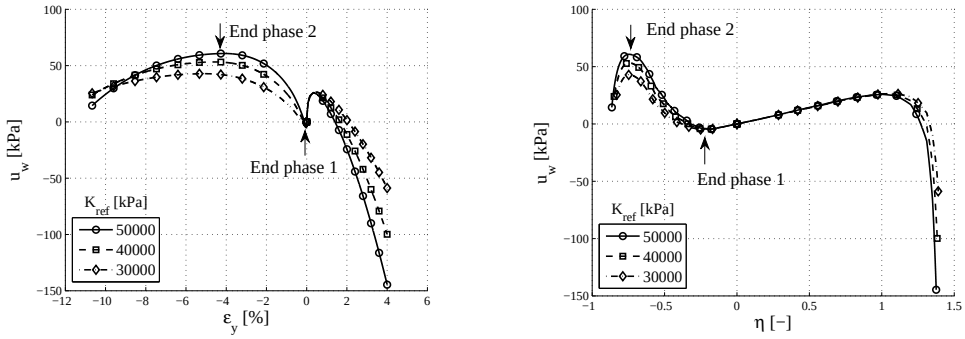

(a) Influence of K_{ref} (b) Influence of K_{ref}

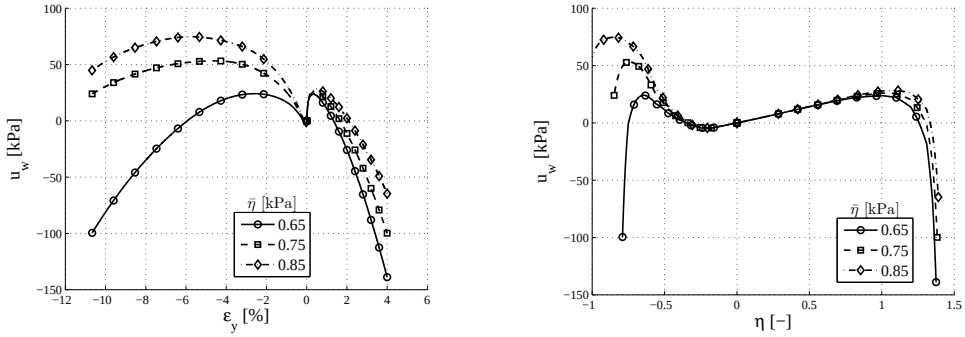

(c) Influence of $\bar{\eta}$ (d) Influence of $\bar{\eta}$

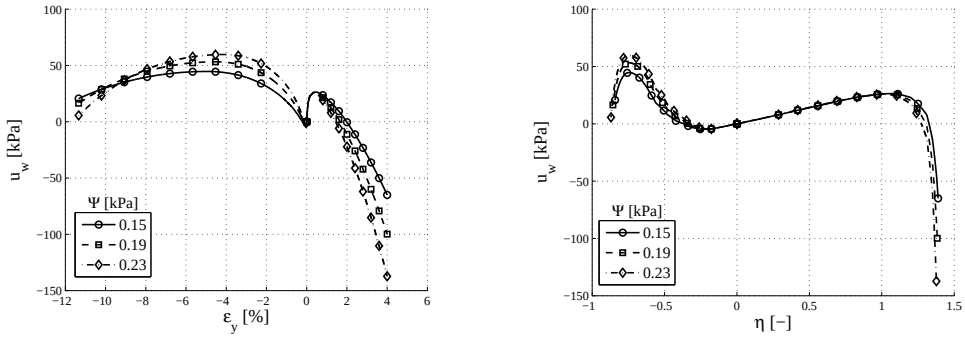

(e) Influence of Ψ (f) Influence of Ψ

FIGURE 4.22: Influence of parameters related to volumetric behaviour for Nevada sand, Dr= 40%, $p'_0 = 80$kPa.

The effect of $\bar{\eta}$ is more straightforward (see Figures 4.22c and 4.22d). All the aforementioned phases still hold but the difference between the curves is more significant. Obviously, a change of $\bar{\eta}$ strongly affects the position of the maximum pore water pressure, since the transition from contractive to dilative is ruled by

$$P\text{”} = \frac{\Psi}{3} \cdot \frac{\bar{\eta}^2 - \eta^2}{\bar{\eta}^2 + \eta^2}. \tag{4.54}$$

The maximum accumulated u_w is higher for higher $\bar{\eta}$. Indeed, if $\bar{\eta}$ is higher, yield surfaces of lower plastic moduli are reached, which increases the rate of pore water pressure. Finally, a

constant Ψ parameter has an effect similar to K_{ref} (see Figures 4.22e and 4.22f). It is worth noting the extreme sensitivity of this parameter since a slight change induces non negligible variations of the results.

4.4.2.4 Final calibration

A final set of parameters was adopted which is an averaging of the two previously calibrated sets (see in Table 4.2). The number of yield surfaces is a key issue. It could be defined at the beginning of the calibration process, but if there is no memory limitation, it can be adapted to each material. It must be kept in mind that surfaces discretise the evolution of the hardening modulus over the stress space. Therefore, the higher the number of surfaces, the higher the precision. However, too many surfaces can decrease the convergence rate of the algorithm during the integration of the constitutive law, since the number of active surfaces oscillate.
A minimum number of surfaces must be ensured at low $\eta = q/p$ in order to ensure a plastic contractancy even at low deviatoric stress, which corroborates experimental tests. On the other hand, more surfaces might be added at high $\eta = q/p$. Indeed, during the dilative phase, the increase of the confinement, coupled with the confinement dependency of the modulus, can introduce spurious hardening. In this calibration, thirteen yield surfaces are defined and characterised by their opening M, their plastic modulus H' and their backstress α (see in Appendix A.4 to convert triaxial scalar backstress into a tensorial variable).

G_{ref}[MPa]	K_{ref}[MPa]	$\bar{\eta}$[-]	Ψ[-]	$\eta_{f,c}$[-]	$\eta_{f,e}$[-]
40	40	0.85	0.40	1.28	-0.95

TABLE 4.3: Dr= 40% Nevada sand parameters (elastic and volumetric). G_{ref} and K_{ref}, reference shear and bulk moduli; $\bar{\eta}$ and Ψ, parameters of the volumetric flow rule; $\eta_{f,c}$ and $\eta_{f,e}$, failure slopes.

N° surf	1	2	3	4	5	6	7			
M [-]	0.1	0.175	0.245	0.325	0.44	0.55	0.615			
H' [MPa]	400	200	80	20	12	7	3			
α [-]	0.05	0.105	0.155	0.175	0.21	0.25	0.265			
N° surf					8	9	10	11	12	13
M [-]					0.695	0.775	0.835	0.93	1.025	1.11
H' [MPa]					2.3	1.4	0.9	0.4	0.2	0.01
α [-]					0.255	0.275	0.265	0.23	0.195	0.16

TABLE 4.4: Dr= 40% Nevada sand parameters (surface description). M, opening of the yield surface; H', plastic modulus; α, back stress in triaxial format.

The comparison of laboratory results and calibrated simulations is provided in Figure 4.23 for drained and undrained monotonic tests as well. Adopted parameters lead to reasonable discrepancies for both types of tests. From a volumetric point of view, variation of volumetric strain is a bit not steep enough during the dilative phase (see Figure 4.23a). On the other hand, the pore pressure generation seems to be too sharp during the dilative phase (see Figure 4.23b). However the difference is kept acceptable.
The slope of the failure surface has the expected order of magnitude, with regard to the scatter observed in laboratory experiments (see Figures 4.23c and 4.23d). The main features of the stress paths are correctly represented. They present distinct undrained behaviours in

compression and extension, i.e. an unstable stress path (decreasing q) in extension and a continuously increasing shear strength in compression (see Figure 4.23f).
Finally, the phase transformation line is an averaging of experimental values. Then the fitting does not represent exactly each test but the general trend of volumetric features is well captured (see Figures 4.23g and 4.23h).

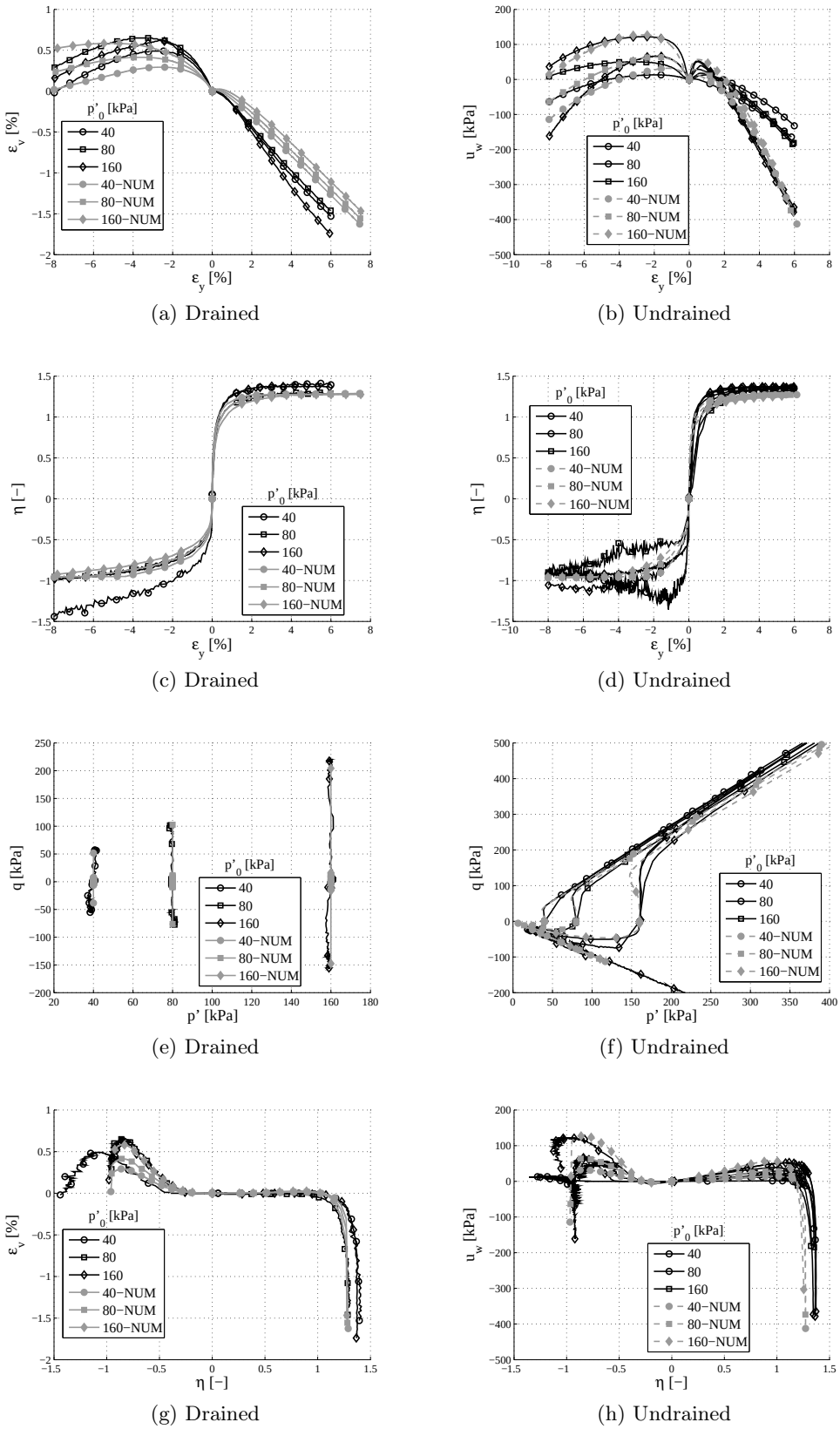

(a) Drained (b) Undrained

(c) Drained (d) Undrained

(e) Drained (f) Undrained

(g) Drained (h) Undrained

FIGURE 4.23: Comparison of drained and undrained simulations for a unique set of parameters, Nevada sand, Dr= 40%. NUM stands for numerical simulation.

4.4.2.5 Cyclic tests

For the given set of parameters, the comparison of undrained cyclic laboratory results and numerical simulations is provided in Figure 4.24. The initial mean effective stress is equal to 160kPa and the deviatoric stress varies within the range $q = 21 \pm 48.4$ kPa.
Obviously, the pre-failure pattern is similar but not identical when comparing measured and simulated data (see Figure 4.24a). However, the stress path follows the right tendency towards the origin of the axes and initial liquefaction. A flow failure/deformation occurs on the extension side (see Figure 4.24a), creating an instability (sudden decrease of q).
This flow is marked by a sudden increase of negative vertical plastic deformation (extension), that can be observed in Figure 4.24c. There is then a clear distinction between laboratory and numerical results. In the former case, positive vertical deformation is quickly accumulated and rises up at a constant rate. In the latter case, there is a slow accumulation of vertical settlement after a minimum value. Moreover, the butterfly wing pattern seems to stabilise and vertical deformation is accumulated at a constant rate of deformation, which is typical of ratcheting.

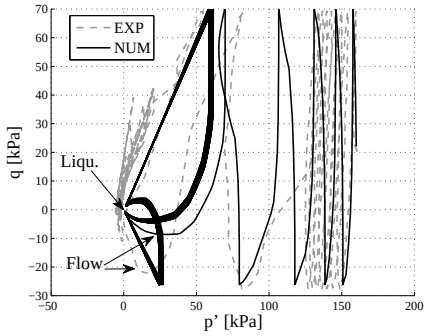

(a) Flow deformation and liquefaction in the p'-q plane.

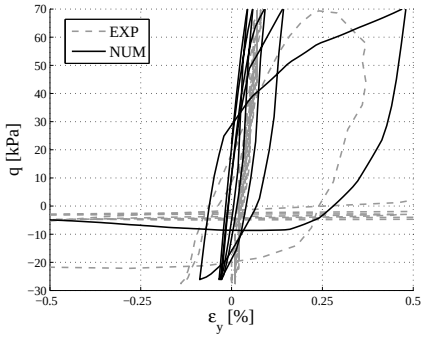

(b) Vertical deformation - deviatoric stress for the 5 first cycles. Zoom of Figure 4.24d

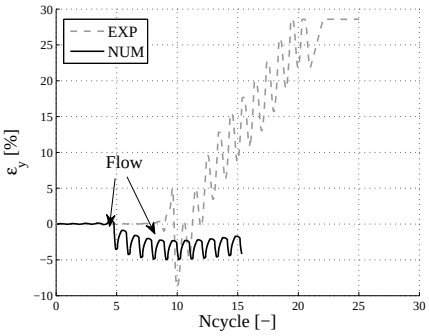

(c) Accumulation of deformation with the number of cycles (30cycles).

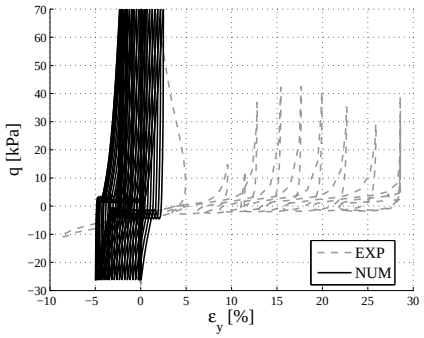

(d) Vertical deformation - deviatoric stress for the 15 first cycles.

FIGURE 4.24: Comparison of laboratory results (EXP) and numerical simulations (NUM) of an undrained test at Dr= 40%.

A zoom on early cycles exhibits a positive accumulation of vertical deformation, i.e. a settlement which is consistent with laboratory observations (see Figure 4.24b). However, the flow deformation on the extension side involves a great accumulation of negative deformation which does not exist in laboratory measurements (see Figure 4.24d).
Nevertheless, experiments are load-controlled. Thus, instabilities are not easy to manage since large deformation is accumulated for a load lower than the applied one. Moreover, the

zone of initial liquefaction (origin of the axes in Figure 4.24a) is prone to accumulate large deformation. It is also clear that experimenter loses the mastery of the test since it behaves strangely after initial liquefaction, e.g. the deviatoric shear stress varies a bit anarchically and does not reach any more the theoretically imposed extreme values of -27kPa or 70kPa.

On the other hand, the Matlab routine used to simulate the test has a mixed control. The integration of the constitutive law is deformation controlled. At each step, the algorithm verifies if the stress path lies within the imposed boundaries $q_{off} \pm q_{cycl}$ and modifies the sense of loading if necessary. The instability is then "mastered". Consequently, one of the possible explanation of these huge discrepancies observed between numerical and experimental results might be the control of the tests.
Additional comments should be formulated. The basic Prevost model only reproduces roughly post-liquefaction behaviour, e.g. cyclic mobility. Unfortunately, the main part of laboratory experiments actually lies typically in the zone of initial liquefaction (measured p' can reach -5kPa). Simulated stress path approaches very close to the initial liquefaction zone and describes the butterfly wing pattern. This close proximity and the following ratcheting is only possible with numerical simulations. In practice, imperfections break the regularity of the pattern and liquefaction is reached.
However, the homogeneity of the sample after liquefaction is doubtful. Consequently, comparisons between macroscopic measurements obtained from a soil specimen and numerical simulation of a homogeneous soil becomes specious. Furthermore, there is probably a distinct failure mode between triaxial test and in the field behaviour. As a consequence, the important information that has to be modelled is the likelihood of the liquefaction and flow deformation, which is correctly captured.

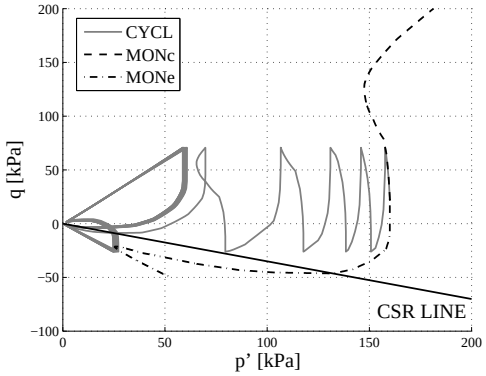

FIGURE 4.25: Comparison between cyclic (CYCL) and monotonic (compression MONc, extension MONe) triaxial tests from an identical initial state.

It was stated in the previous chapter that the monotonic stress path and/or the CSR line could be viewed as a failure surface for a cyclic test, starting from the identical initial state. A numerical comparison between cyclic and monotonic stress paths from an identical initial state $(p', q) = (160, 21.4)$kPa is illustrated in Figure 4.25. It is carried out to verify the model is able to reproduce the failure surface. The instability is triggered when the stress path crosses the CSR line. However, both monotonic and cyclic stress paths are quite close.

For a given distribution of yield surfaces, parameters that mostly influence the cyclic stress path are the related volumetric ones, i.e. $K/\bar{\eta}/\Psi$. Their effect is synthesised in Figure 4.26. The evolution of the total vertical deformation and the normalised pore pressure accumulation with the number of cycles applied are illustrated. All results present similar features.

Phase A a slow accumulation of vertical deformation ϵ_y with the number of cycles (pictures on the left) coupled with the increase of normalised pore water pressure u_w/p'_0 (pictures on the right).

Phase B a sudden increase of vertical deformation coupled with a jump of pore water pressure. This is the consequence of the instability previously observed and corresponds to a flow failure.

Phase C a repeated pattern of pore water pressure variations (which corresponds to the butterfly wing pattern in the p'-q plane) coupled with an accumulation of plastic vertical deformation (either negative or positive).

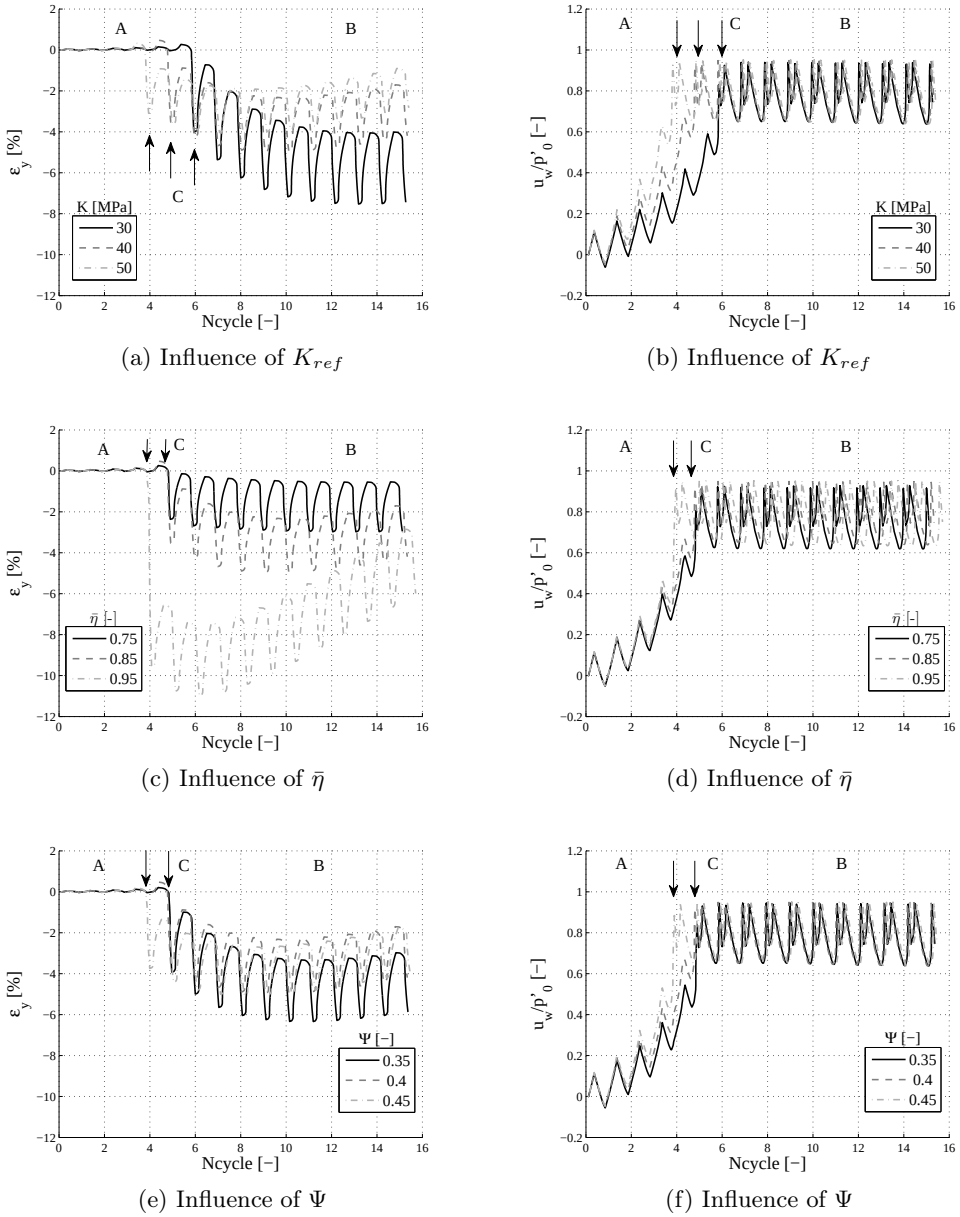

(a) Influence of K_{ref}

(b) Influence of K_{ref}

(c) Influence of $\bar{\eta}$

(d) Influence of $\bar{\eta}$

(e) Influence of Ψ

(f) Influence of Ψ

FIGURE 4.26: Influence of parameters on the cyclic stress path. ϵ_y is the vertical deformation and u_w/p_0 is the initial mean effective stress. A, slow accumulation; C, sharp increase; B, butterfly wing pattern.

Influence on K_{ref} is depicted in Figures 4.26a and 4.26b. The higher the bulk modulus the lower the number of cycle to reach instability (see Figure 4.26a). It means that pore water

pressure is accumulated more slowly, when the soil has a lower elastic compressibility, which can be observed in Figure 4.26b. This modulus also influences the number of cycles required to reach the minimum ϵ_y. After this minimum, the rate of vertical deformation becomes positive again. The consequences of a change in K_{ref} can be derived from Equation (4.53) as well.

A higher $\bar{\eta} = 0.95$ parameter enlarges the contractive zone and creates a stronger flow deformation that appears slightly before two others results ($\bar{\eta} = 0.75$ and $\bar{\eta} = 0.85$, see Figure 4.26c). However, the post flow deformation behaviour marks a greater rate of positive accumulation of deformation.

Finally, Ψ does not strongly affect the behaviour. Nevertheless its effect on the rate of accumulation of pore water pressure increases with the number of cycles (see Figure 4.26f), i.e. it increases for a stress path approaching liquefaction.

Furthermore, undrained cyclic simulations are very sensitive to a modification of the parameters of the constitutive law. Indeed, a slight variation of one of them affects the position or the value of the peak strength, which controls the triggering of the instability.

4.4.3 Nevada sand Dr= 60%

4.4.3.1 Experimental results : comparison Dr= 40%

A comparison between drained and undrained laboratory tests for Dr= 40% and Dr= 60% is provided in Figure 4.27. Once again, the range of represented deformations is limited since shear bands were observed. Undrained triaxial tests especially become meaningless when very large negative pore pressures and deformations are measured. Results presented span over three initial mean effective stresses : $p'_0 = [40, 80, 160]$kPa.
The natural trend is the increasing of the strength with relative density, which can be clearly observed in compression in Figure 4.27a. There is also a little increase in compression in Figure 4.27b for undrained experiments. However, the trend in extension is dubious in both figures. Final strength is equal or lower than those measured for Dr= 40%. Moreover, there is a large dispersion of the results. Nevertheless, a ratio of 2/3 can be accepted between shear strength in extension and compression.
The contractive phase is weaker for the Dr= 60% soil samples, i.e. maximum positive volume or pore water pressures are lower. This is clearer on the extension side of the tests in Figures 4.27c and 4.27d. Once again, the dispersion of the data makes the determination of the phase transformation line uneasy.

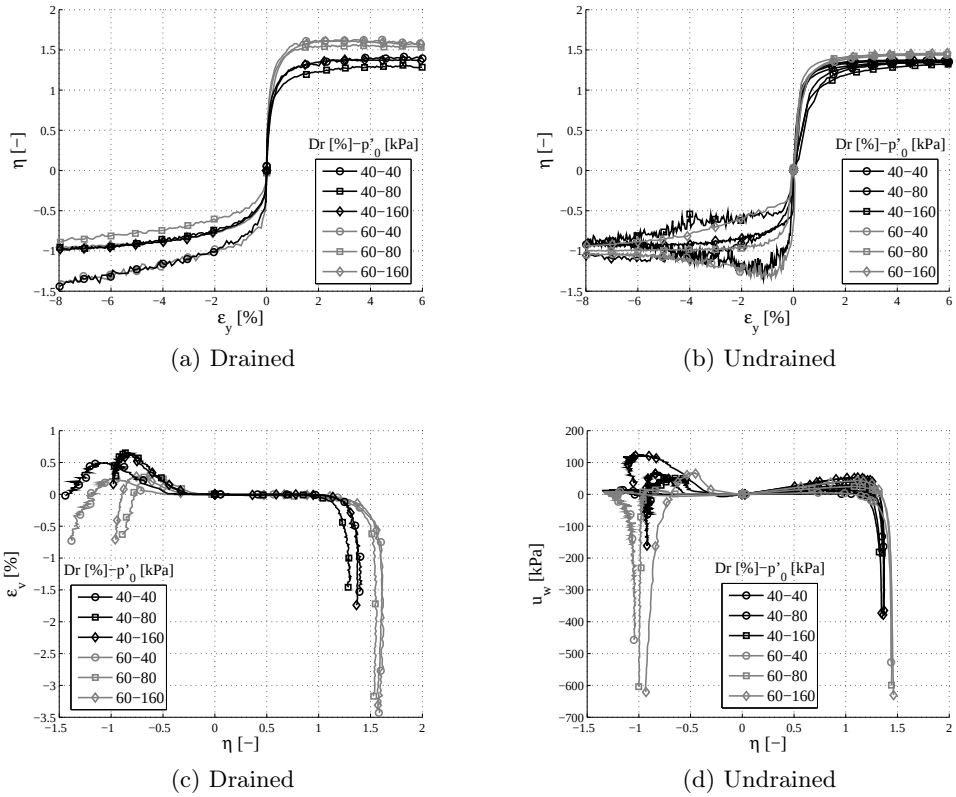

(a) Drained (b) Undrained

(c) Drained (d) Undrained

FIGURE 4.27: Monotonic drained and undrained triaxial test on Nevada sand, comparison between Dr= 40% and Dr= 60%, after [Arulmoli et al., 1992]. p'_0, initial mean effective stress.

4.4.3.2 Calibration of monotonic tests

The set of parameters adopted to simulate Nevada sand behaviour at Dr= 60% is provided in Tables 4.5 and 4.6. Elastic parameters are consistent with resonant column tests provided in [Arulmoli et al., 1992]. The reference moduli are higher than in the Dr= 40% case, which is obvious. The failure envelope has a final friction angle of 39°. This limit is only reached after several per cent of deformation. The failure limit in extension is just slightly lower than in the Dr= 40% case. The model is composed of thirteen yield surfaces. This number of yield surface might be distinct from the Dr= 40% Nevada sand since parameters for each density range of a given material must be independently calibrated. The identical number of surfaces is then purely fortuitous.
Comparison between laboratory and simulated tests is illustrated in Figure 4.28 for both drained and undrained triaxial tests. Results finally match reasonably even if a large dispersion might be observed, especially for extension tests (see Figures 4.28c and 4.28d). Similarly, the phase transformation line slope is an averaging of the scattered values.
The fitting of the experimental data is not easy in this case since there is only few measurements at the beginning of the test. Therefore, elastic properties and first yield surfaces are more idealised than calibrated. Moreover, results are very sensitive to parameters such as $\bar{\eta}$, Ψ or K_{ref}. As a matter of fact, a $K_{ref} = 60.5$MPa leads to a better fit of monotonic tests but a weaker of cyclic. Finally, the large dispersion of data does not facilitate the process.

G_{ref}[MPa]	K_{ref}[MPa]	$\bar{\eta}$[-]	Ψ[-]	$\eta_{f,c}$[-]	$\eta_{f,e}$[-]
54.5	30	0.9	0.6	1.6	-1.01

TABLE 4.5: Final set of parameters used for the modelling of Dr= 60% Nevada sand (elastic and volumetric). G_{ref}, reference shear modulus; K_{ref}, reference bulk modulus; $\bar{\eta}$ and Ψ, parameters of the volumetric flow rule; $\eta_{f,c}$ and $\eta_{f,e}$, failure slopes in compression and extension.

N° surf	1	2	3	4	5	6	7				
M [-]	0.15	0.25	0.37	0.5	0.65	0.775	0.9				
H' [MPa]	200	100	40	20	10	5	3				
α [-]	0.05	0.1	0.13	0.2	0.2	0.225	0.25				
N° surf						9	10	11	12	13	
M [-]						1.0	1.075	1.14	1.18	1.21	
H' [MPa]						1.5	0.6	0.3	0.15	0.05	
α [-]						0.25	0.245	0.26	0.24	0.23	

TABLE 4.6: Dr= 60% Nevada sand parameters (surface description). M, opening of the surface; H', plastic modulus; α back stress in triaxial format.

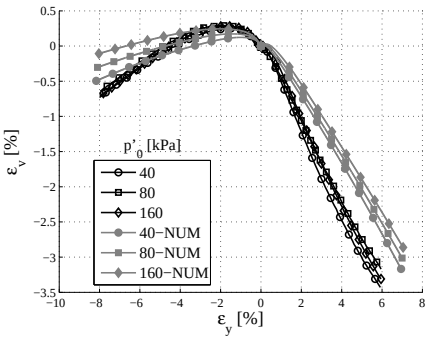

(a) Drained

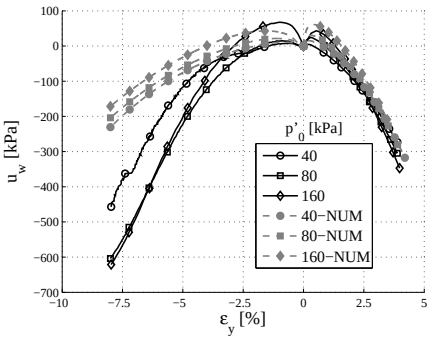

(b) Undrained

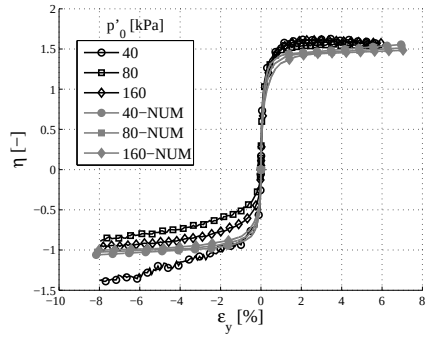

(c) Drained

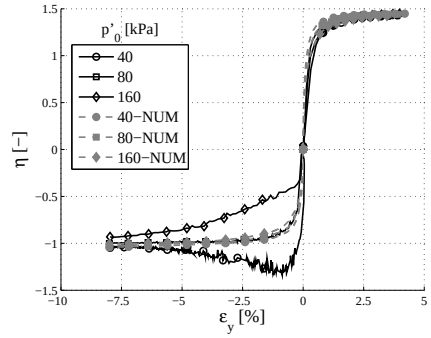

(d) Undrained

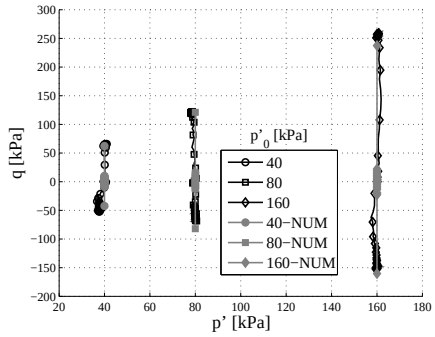

(e) Drained

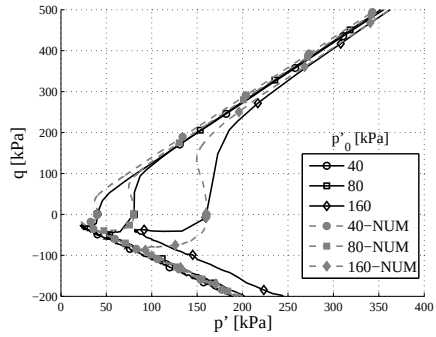

(f) Undrained

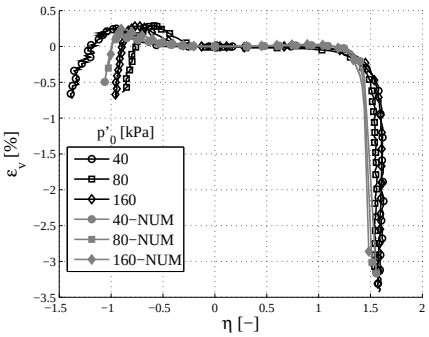

(g) Drained

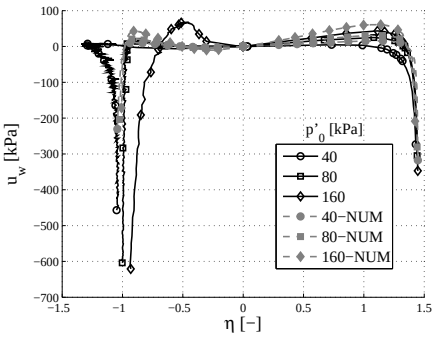

(h) Undrained

FIGURE 4.28: Comparison of drained and undrained simulations for a unique set of parameters, Nevada sand, Dr= 60%. NUM stands for numerical simulation. p'_0, initial mean effective stress.

4.4.3.3 Cyclic tests

A cyclic test was simulated using this set of parameters (see Figure 4.29). The mode of failure is different between laboratory experiments and simulated results. In the latter, a flow failure is triggered while laboratory test seems to exhibit cyclic mobility. Moreover, numerical results show a ratcheting effect. It is possible to artificially better fit the results by decreasing the bulk modulus. However, this operation deteriorates the monotonic match.

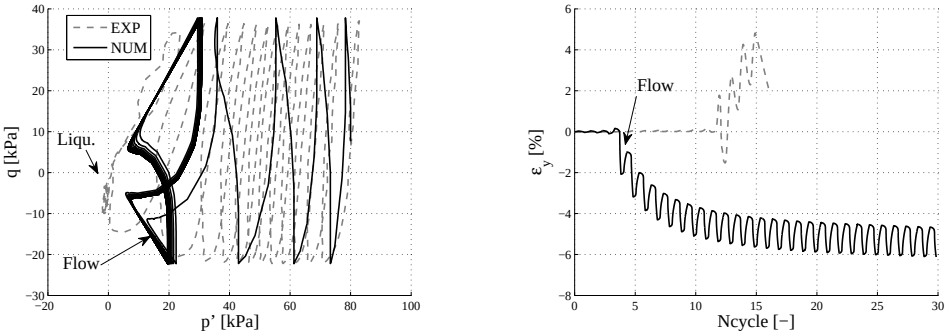

(a) Drained (b) Undrained

FIGURE 4.29: Comparison experimental (EXP) and simulated (NUM) triaxial tests, Nevada sand, Dr= 60%.

4.4.4 Lund sand Dr= 90%

4.4.4.1 Properties

Sandy soils in the North Sea are very uniform and might reach very high densities [Bjerrum, 1973]. Therefore, data for such a dense material are necessary. The Lund sand comes from Denmark where it is obtained from a gravel pit near Horsens and open source data are available for high densities. Main properties of this material are provided in Table 4.7.

γ_s [kN/m^3]	e_{max} [-]	e_{min} [-]	d_{50} [mm]	C_u [-]
26.5	0.889	0.524	0.35	1.7

TABLE 4.7: Properties of Lund sand, from [Ibsen and Jacobsen, 1996; Ibsen, 1998]

4.4.4.2 Calibration

Drained triaxial tests for a relative density equal to 90% were calibrated and parameters are provided in Tables 4.8 and 4.9. Unfortunately, only compressive tests are available in [Ibsen and Jacobsen, 1996]. It is assumed that initial lower trace of the yield surface in the p'-q plane was 2/3 of the upper trace (see Figure 4.30). A complete set of parameters can then be deduced.

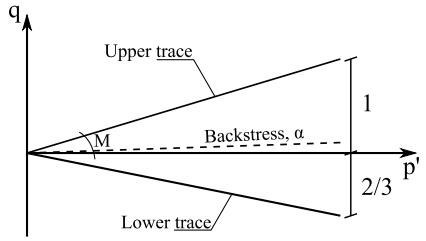

FIGURE 4.30: Extrapolation of the extensive strength of the Lund sand, Dr= 90%.

The calibrated phase transformation parameter $\bar{\eta}$ corresponds to an angle of 28.8°, which is very close to the angle of 30° described in [Ibsen, 1998] for the Lund sand, irrespectively of the density.

G_{ref}[MPa]	K_{ref}[MPa]	$\bar{\eta}$[-]	Ψ[-]	$\eta_{f,c}$[-]	$\eta_{f,e}$[-]
47	65	1.15	1.0	1.7	-1.25

TABLE 4.8: Final set of parameters used for the modelling of Dr= 90% Lund sand (elastic and volumetric). G_{ref}, reference shear modulus; K_{ref}, reference bulk modulus; $\bar{\eta}$ and Ψ, parameters of the volumetric flow rule; $\eta_{f,c}$ and $\eta_{f,e}$, failure slopes in compression and extension.

N° surf	1	2	3	4	5	6	7	8		
M [-]	0.05	0.10	0.167	0.292	0.458	0.667	0.792	0.875		
H' [MPa]	700	500	100	70	50	30	20	12		
α [-]	0.01	0.02	0.033	0.58	0.092	0.133	0.158	0.1750		
N° surf			9	10	11	12	13	14	15	16
M [-]			1.00	1.125	1.23	1.292	1.367	1.4251	1.475	1.517
H' [MPa]			5	2.5	1.2	0.8	0.4	0.3	0.1	0.025
α [-]			0.2	0.225	0.247	0.258	0.273	0.285	0.295	0.303

TABLE 4.9: Final set of parameters used for the modelling of Dr= 90% Lund sand (surface description). M : opening of the surface ; H' : plastic modulus ; α back stress in triaxial format.

Superposition of experimental tests and simulations is provided in Figure 4.31 for compressive drained triaxial tests. In this case, triaxial tests are classic drained tests, i.e. the slope of the stress path in the p'-q plane is equal to 3. It can be observed that the failure slopes tend to increase with decreasing mean effective stress (see Figure 4.31c). Despite this is not explicitly modelled by the Prevost model, such a behaviour can also be simulated. Final shear strength corresponding to lower p'_0 are slightly shifted. However the distribution of maximum η spans over a narrower range of failure slopes $\eta_{f,c}$ than observed during experiments.
From the volumetric point of view, simulations are in very good agreement with experiments (see Figure 4.31a). Results presented in Figure 4.31d are scattered due to the aforementioned p' dependency of $\eta_{f,c}$.

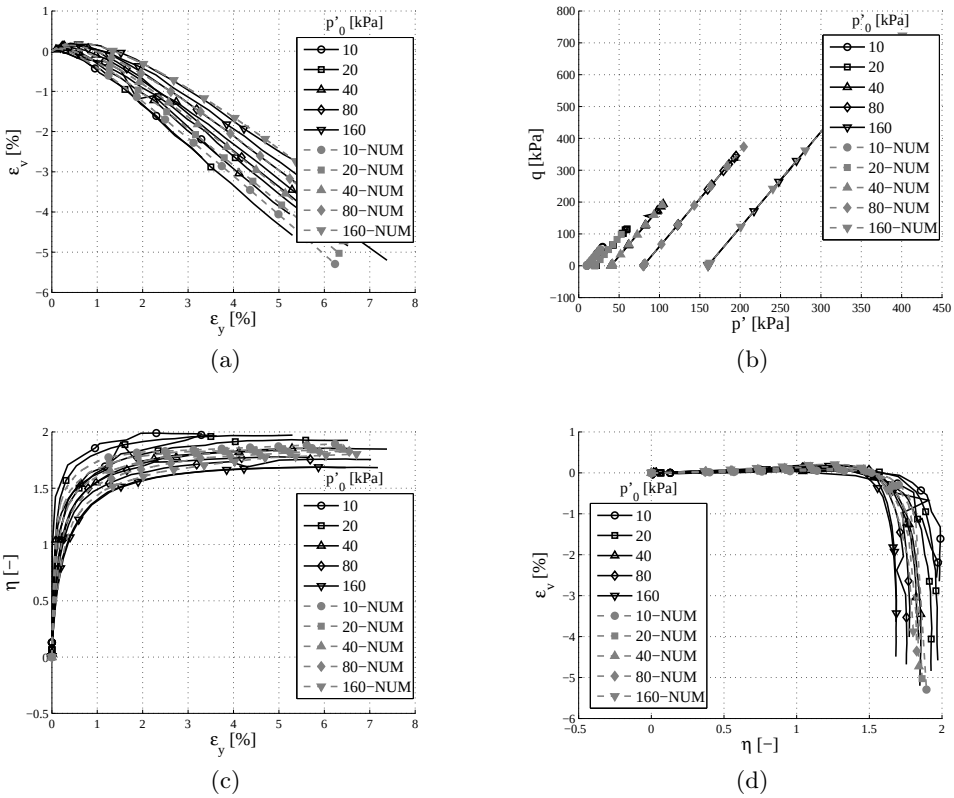

FIGURE 4.31: Monotonic drained triaxial tests on Lund sand, Dr= 90%, after [Ibsen and Jacobsen, 1996]. Comparison of laboratory tests and numerical simulations (NUM).

Results of simulations of undrained triaxial tests are illustrated in Figure 4.32. They are just provided to depict the global trend of undrained tests since they cannot be compared to experimental results. Actually few undrained tests are available in [Ibsen, 1998] but they are not accurate enough at the early beginning of the test to be exploited. Observed stress paths are classic (see Figure 4.32b) and asymmetric in compression and extension.

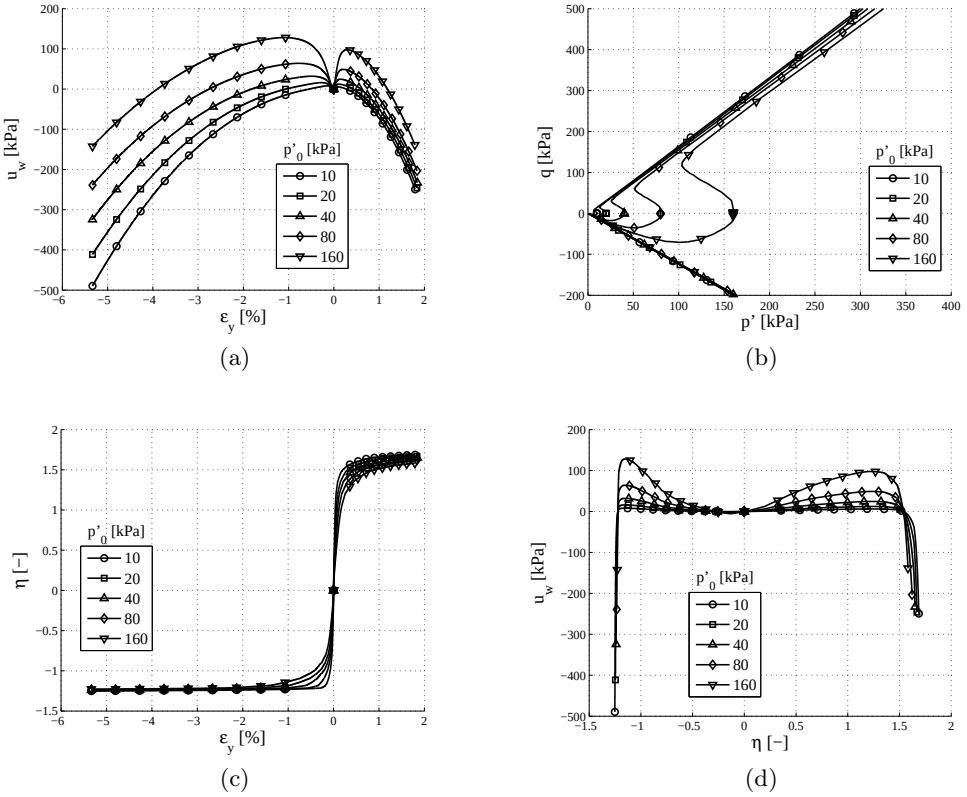

FIGURE 4.32: Simulations of monotonic undrained triaxial tests on Lund sand, Dr= 90%.

4.4.4.3 Cyclic tests

Synthetic cyclic tests ($q_{cycl} = 20$kPa) for three initial deviatoric stresses ($q_{off} = [5, 25, 45]$kPa) are provided in Figure 4.33. All the simulations exhibit similar very contractant first cycles and the stress paths moves towards the left. However, the modes of failure are different.
In the former case (see Figures 4.33a and 4.33b), where reversal occurs, a flow failure is triggered on the extension side and a negative vertical deformation holds. It is followed by a butterfly wing pattern of the stress path and an accumulation of settlement.
In two other cases, there is no flow deformation since the stress path never moves to extension side. However, if the failure is defined by a maximum deformation, it can be reached by accumulation of deformation. Interestingly, the highest deviatoric offset simulation accommodates more quickly, i.e. deformation and stress path stabilise.

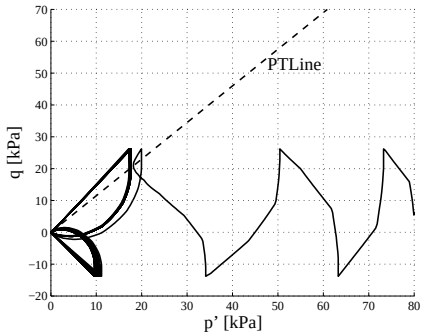

(a) Undrained cyclic test, $q = 5 \pm 20$kPa

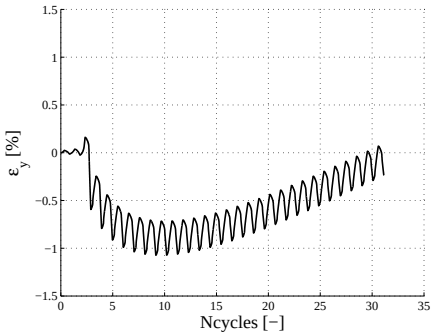

(b) Undrained cyclic test, $q = 5 \pm 20$kPa

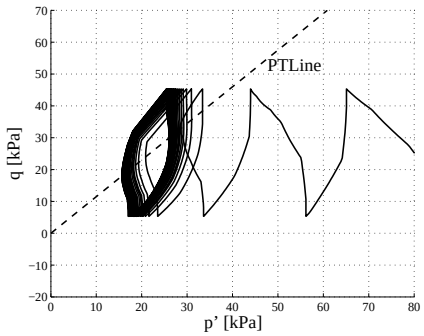

(c) Undrained cyclic test, $q = 25 \pm 20$kPa

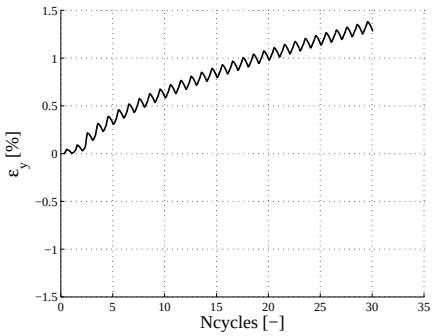

(d) Undrained cyclic test, $q = 25 \pm 20$kPa

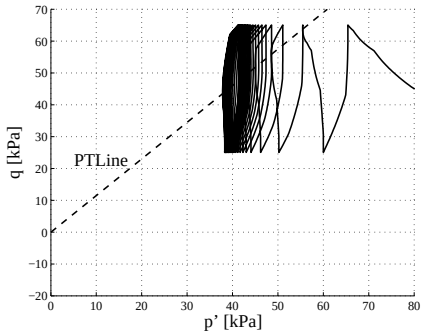

(e) Undrained cyclic test, $q = 45 \pm 20$kPa

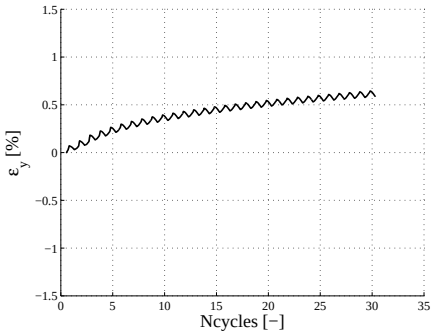

(f) Undrained cyclic test, $q = 45 \pm 20$kPa

FIGURE 4.33

4.4.5 All together

Monotonic drained (p'=cst) and undrained simulations corresponding to the three sets of parameters (Nevada 40%, Nevada 60%, Lund 90%) are compared in Figure 4.34. They correspond to an initial isotropic state of 80kPa and illustrate a range of variation of the results. Obviously, the higher the density, the higher the failure stress ratio η (see Figures 4.34c and 4.34d).
Volumetric behaviour is much divergent (see Figures 4.34a and 4.34b). The Lund sand exhibits variation of volumetric deformation and pore pressure much sharper than the Nevada sand Dr= 40%. Finally, all of the soil samples present an elbow and a non symmetric extension/compression behaviour in the p'-q plane, during undrained simulations (see Figure 4.34f).

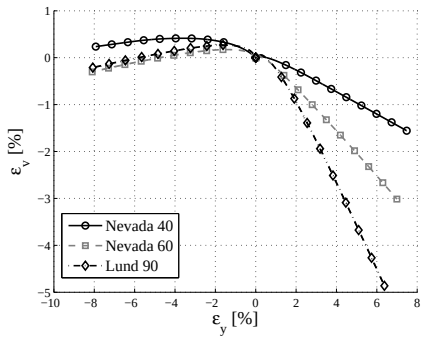

(a) Drained

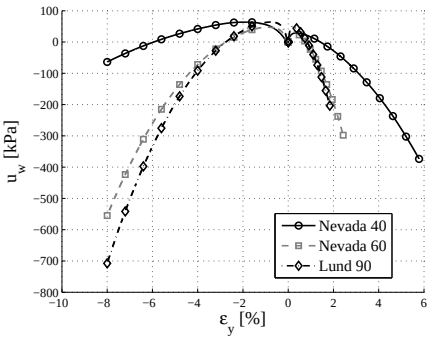

(b) Undrained

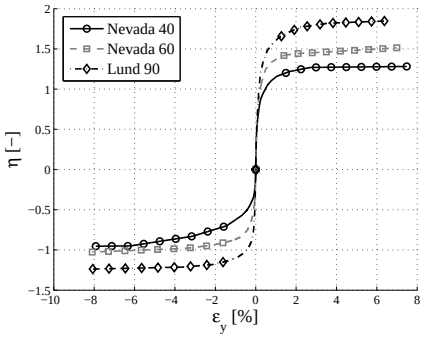

(c) Drained

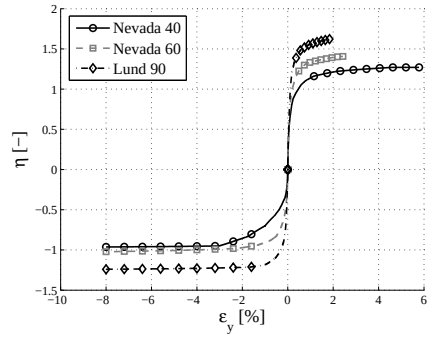

(d) Undrained

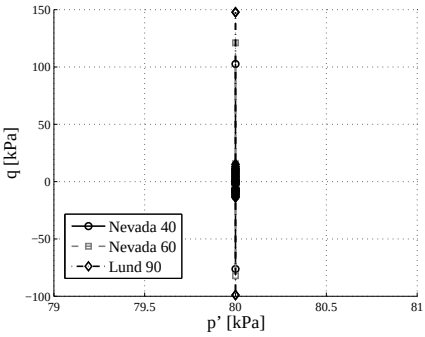

(e) Drained

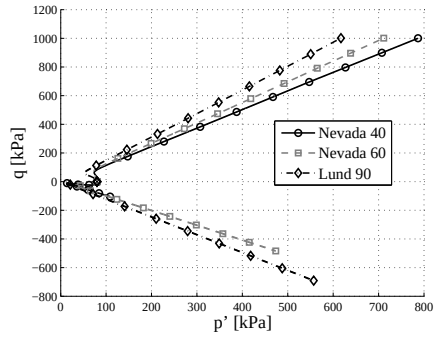

(f) Undrained

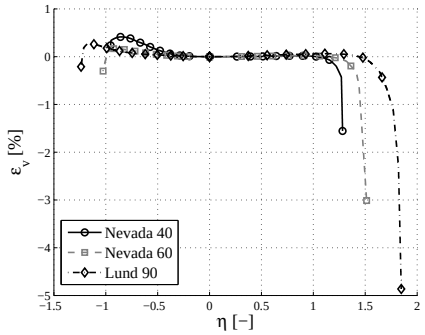

(g) Drained

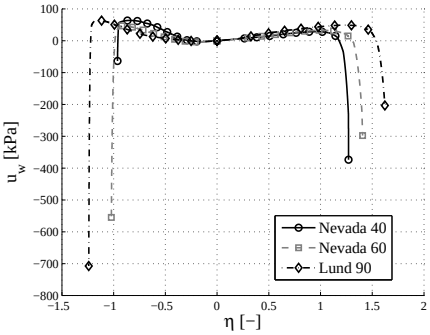

(h) Undrained

FIGURE 4.34: Comparison of drained and undrained simulations for Nevada sand (Dr= 40% or Dr= 60%) and Lund sand (Dr= 90%).

4.5 Conclusion

Elastoplasticity offers a robust framework for the constitutive modelling of soils. Many conceptual ways of representing cyclic loading of soils have been investigated in the past decades since the advent of personal computers and the generalisation of finite element codes. Among all of them, the Prevost model was adopted for its conceptual simplicity and its physically related parameters.
This model is able to reproduce monotonic drained and undrained behaviours of cohesionless soils. It includes contractive and dilative behaviours, hardening and softening, failure... The trend of the cyclic behaviour is also represented. Pore water pressure accumulates during triaxial tests due to the plastic contractive zone. Therefore the stress path is translated towards the left and the origin of the axes in p'-q plane. It is most of the time impossible to exactly simulate stress paths obtained from laboratory, but simulations and laboratory experiments are in good agreement.
On the other hand, the Prevost model is not able to reproduce post-failure behaviour and accurate cyclic mobility. However this shortcoming is not really relevant. Firstly, post-cyclic failure is out of the scope of this study. Secondly, failure might involve the loss of homogeneity of the samples which lapses the continuum modelling of the soil.
Parameters of the Prevost model do not depend on the density. Therefore, a unique set of parameters for a given material does not exist. They must be calibrated independently for each sample of different density. Phase transformation line has a constant slope. The shape of the yield surfaces belongs to the J_2 family. Therefore, its trace in the deviatoric plane is a circle, which is not exact for representing cohesionless soil behaviours. Though not negligible, the use of such a criterion is not critical to a first approximation.
Calibration of parameters is not an easy task. The first difficulty is the finding of accurate data. Afterwards, the calibration process is not so complex if adequate simplified routines are available, e.g. simplified triaxial routine on Matlab. However, the definition of a unique set of parameters is not obvious. Indeed, results might be very sensitive to plastic potential parameters. Furthermore, the low-deformation behaviour of the soil sample is very important, since it accumulates large variations of stresses over a narrow range of deformation. However, measures are often scarce in this zone and the calibration looses its accuracy.
The Prevost model does not takes into account plastic effects for hydrostatic stress path, i.e. grain crushing is not taken into account. It was shown that this effect holds for confinement on the order of 3-5MPa, which is out of concern in this work.
All the recognised drawbacks of this model are known or of minor importance. Therefore, the model was adopted to represent cyclic behaviour of a cohesionless soil in the following.
In this chapter, the calibration of parameters for two sands and distinct densities was carried out. They allow to model various soil conditions and accurate data are available in the literature. A systematic comparison of laboratory tests and simulations has highlighted the possibilities and the limitations of the model. Globally, monotonic tests match reasonably well in both cases. The fitting of cyclic tests is much less obvious. The trend of increasing pore water pressure and the flow deformation on the extension sides are well reproduced. However, an exact correspondence of stress path was never reached. The relative complexity of such experiments, their sensitivity to imperfections and the difference between deformation and load control tests are factors that might explain the discrepancies between them.
Finally, even if a numerical simulation perfectly represents a laboratory experiment, it reflects only the ability of the model to reproduce experiments. This does not induce straightforwardly the ability to reproduce actual *in situ* field behaviour which is inherently heterogeneous. Consequently, there is no need to be very strict on the fitting of data. Finally, a strong conclusion about the ability of the model to reproduce the behaviour of a geotechnical structure could only be drawn if experimental data were available for that particular material.

Chapter 5

Numerical integration of the constitutive law

Das Zeichnen ist die Sprache des Ingenieurs.
(Drawing is the language of engineers).

Karl Culmann

Contents

5.1 Introduction

Only few letters separate *model* and *modelling*. However, there is a large gap between them. For scientists, a model is a physical, mathematical or conceptual representation of reality[1]. Many sub-definitions are encompassed in this word, inducing a neverending ambiguity. A model can be a small scale physical representation of an object (e.g. centrifuge small scale tests) or a set of numerical data defining a real body (e.g. a mesh which relates physical properties to each material point it depicts) or a mathematical relation describing a particular phenomenon (e.g. constitutive law that describes a material). In this work, the term *model* only defines the latter case and especially a constitutive law.
A model is amorphous, it exists, it is. The modelling is the animation of the model. It implies other actions from the researcher such as measurements of acceleration in a centrifuge test, introduction of a time dependent loading that distorts a geometric mesh or the integration of the constitutive law. The modelling is a way to obtain a result that corresponds to a given situation. In the previous chapter, results are provided for a very simple loading case, i.e. triaxial test. However, if real situations have to be represented, e.g. designing a foundation, a mathematical model ceases to live by itself and must be included into a more general entity, e.g. a finite element code. This step, moving from an analytical model to its discrete counterparts, is termed *implementation*.
Most of the time the hurried researcher acts such as a Frankenstein doctor. It uses a model from X, a finite element code from Y, an algorithm from Z and tries to give birth to a functional suitable usable routine. However many traps and ambushes lie on the long way to convergence. Sources of mistakes and discrepancies are numerous, pernicious and hidden in details. Continuous models are transformed into discrete ones, variables have to be defined according to a given precision, many subroutines have been used and coded by previous old-timer scientists who forget their functioning, iterative processes accumulate error, the researcher had a party the night before and so on.
Starting from a known stress state $\boldsymbol{\sigma}_n$, corresponding to a material point, the purpose of implementation is to elaborate a robust, efficient and accurate method able to compute the new stress state $\boldsymbol{\sigma}_{n+1}$ corresponding to a discrete increment of deformation $\Delta\boldsymbol{\epsilon}$. This chapter deals with salient features related to this target.
The first objective presented is the transformation of a continuous description of the model to a discrete scheme. Equations are linearised, since a computer can only solve this type of equations. The return mapping algorithm class is described and two families of integrations schemes are presented. An implicit closest point projection is adopted in this work, enforcing the choice of a suitable hardening rule. Indeed, the multi-surface approach requires that they never intersect. A final set of linearised equations can finally be solved, which is practically achieved by using a Newton procedure.
The second part of the chapter is dedicated to paradoxical numerical experiments. Implicit algorithm eventually implemented in the `LAGAMINE` code is compared to exact simplified equations of triaxial conditions. A multiaxial test is carried out as an illustration and compared to an *exact* solution, consisting in applying the algorithm for very small time steps. Finally isoerror maps are generated to illustrate the accuracy of the algorithm and an insight into convergence of the local problem is given.

[1] Actually some fashion models are also a truncated representation of reality and not the reality.

5.2 Discrete formulation : generalities

5.2.1 General integration schemes

The continuum formulation of the constitutive law has been defined incrementally in the previous chapter. The objective Jaumann effective stress rate $\tilde{\boldsymbol{\sigma}}$ is a function of the current stress state[2] $\boldsymbol{\sigma}$, current internal plastic variables $\boldsymbol{\kappa}$ and the deformation rate $\dot{\boldsymbol{\epsilon}}$, *i.e.*

$$\tilde{\boldsymbol{\sigma}} = \mathbf{g}(\boldsymbol{\sigma}, \boldsymbol{\kappa}, \dot{\boldsymbol{\epsilon}}). \tag{5.1}$$

Let us consider that the evolution of $\boldsymbol{\sigma}$ is studied over the time interval $t \in [0, T]$. The integration of the constitutive laws requires the discretisation of the time into N steps such that[3]

$$t_0 = 0 \quad , \quad \Delta t = \frac{T}{N} \quad \text{and} \quad t_{n+1} = t_n + \Delta t. \tag{5.2}$$

The Prevost model is rate independent. Therefore, the time is a fictitious variable and the deformation rate does not really matter. Let us assume the stress state $\boldsymbol{\sigma}_n$ of the material at time step t_n is known. Basic Euler scheme assumes that its variation $\Delta\boldsymbol{\sigma}$ is linear between t_n and t_{n+1}. Therefore, Equation (5.1) is discretised for a given finite variation of deformation $\Delta\boldsymbol{\epsilon}$ corresponding to a time step Δt

$$\Delta\boldsymbol{\sigma} = g(\boldsymbol{\sigma}_{n+\theta}, \boldsymbol{\kappa}_{n+\theta}, \Delta\boldsymbol{\epsilon}) \tag{5.3}$$

$$\boldsymbol{\sigma}_{n+\theta} = (1-\theta)\cdot\boldsymbol{\sigma}_n + \theta\cdot\boldsymbol{\sigma}_{n+1} \qquad \theta \in [0,1] \tag{5.4}$$

$$\boldsymbol{\kappa}_{n+\theta} = (1-\theta)\cdot\boldsymbol{\kappa}_n + \theta\cdot\boldsymbol{\kappa}_{n+1} \qquad \theta \in [0,1] \tag{5.5}$$

which is termed the generalised midpoint rule, since the increment of stress depends on variables evaluated in $n+\theta$. The integration is termed *explicit* if all the variables required to compute g are known at the beginning of the step. On the other hand, if variables have to be computed in $n+1$, they are unknown at the beginning of the step and the integration scheme is called *implicit*. Particular values of θ lead to classic integration schemes

$\theta = 0$, forward (explicit) Euler scheme, i.e. the slope of the assumed linear variation between t_n and t_{n+1} is computed in t_n;

$\theta = 1$, backward (implicit) Euler scheme, i.e. the slope of the assumed linear variation between t_n and t_{n+1} is computed in t_{n+1};

$\theta = 1/2$, midpoint rule (implicit), i.e. the slope of the assumed linear variation between t_n and t_{n+1} is computed in $t_{n+1/2}$.

The first explicit method is straightforward since variables used to compute the slope are already known. Conversely, the two other methods require an iterative process. A second order accuracy of the integration is only obtained for $\theta = 1/2$ (in case of small time steps) and unconditional linearised stability requires that $\theta \geq 1/2$, [Simo and Hughes, 1998].

5.2.2 Discretised constitutive equations

Equation (4.36) can be recast, taking into account the midpoint rule. This equation is true for a yield surface, whatever the kinematic or isotropic hardening rule adopted. However

[2] Either effective or total stresses can be used. Therefore, the ' symbol is dropped for the sake of generality.
[3] Time steps are not necessarily equal.

in this case, internal plastic variables $\boldsymbol{\kappa}$ are identified to the backstress tensors $\boldsymbol{\alpha}$, as

$$\Delta\boldsymbol{\sigma} = \mathbb{E} : \Delta\boldsymbol{\epsilon} - \mathbb{E} : \mathbf{P}_{n+\theta} \cdot \Delta\lambda, \tag{5.6}$$

where $\mathbb{E}$ is the elastic fourth order tensor, $\mathbf{P}_{n+\theta}$ is the direction of plastic deformation and $\Delta\lambda$ is the discrete plastic multiplier. The evolution of the backstress tensor can be established without any loss of generality such as

$$\Delta\boldsymbol{\alpha} = \Delta\lambda \cdot \mathbf{h}(\boldsymbol{\sigma}_{n+\theta}, \boldsymbol{\alpha}_{n+\theta}), \tag{5.7}$$

where $\mathbf{h}$ is a function describing the hardening of internal plastic variables. The final state has to verify the Karush-Kuhn-Tucker condition at the end of the step, i.e.

$$f(\boldsymbol{\sigma}_{n+1}, \boldsymbol{\alpha}_{n+1}) \leq 0, \quad \Delta\lambda \geq 0, \quad f(\boldsymbol{\sigma}_{n+1}, \boldsymbol{\alpha}_{n+1}) \cdot, \Delta\lambda = 0 \tag{5.8}$$

where $f(\boldsymbol{\sigma}_{n+1}, \boldsymbol{\alpha}_{n+1})$ denotes the yield criterion at step $n+1$. Thence, if the stress state is elastic, no plastic deformation occurs and $\Delta\lambda = 0$. The evolution of the plastic deformation can then be established such that

$$\boldsymbol{\epsilon}^p_{n+1} = \boldsymbol{\epsilon}^p_n + \Delta\lambda \cdot \mathbf{P}_{n+\theta}. \tag{5.9}$$

5.2.3 Return mapping algorithm

Solution of this set of Equations 5.6-5.9 is based on a two-step algorithm, termed *return mapping*. The **first step** consists of the computation of an elastic predictor state $(\boldsymbol{\sigma}_{tr}, \boldsymbol{\alpha}_{tr}, \boldsymbol{\epsilon}^p_{tr})$ for a given $\Delta\boldsymbol{\epsilon}$, as

$$\boldsymbol{\sigma}_{tr} = \boldsymbol{\sigma}_n + \mathbb{E} : \Delta\boldsymbol{\epsilon} \tag{5.10}$$
$$\boldsymbol{\epsilon}^p_{tr} = \boldsymbol{\epsilon}^p_n \tag{5.11}$$
$$\boldsymbol{\alpha}_{tr} = \boldsymbol{\alpha}^p_n, \tag{5.12}$$

which is the variation of stress corresponding to a zero plastic deformation. Thence the yield criterion is evaluated at this state and there are two distinct possibilities (see in Figure 5.2)

$$f(\boldsymbol{\sigma}_{tr}, \boldsymbol{\alpha}_{tr}) \leq 0 \quad \Rightarrow \quad \text{Elastic step} \tag{5.13}$$
$$f(\boldsymbol{\sigma}_{tr}, \boldsymbol{\alpha}_{tr}) > 0 \quad \Rightarrow \quad \text{Elastoplastic step.} \tag{5.14}$$

If the first condition holds, the trial state lies within the yield surface. It means that the final state is elastic and equal to the trial stress, as shown in Figure 5.1. If the second condition is verified, the stress state is out of the yield surface, which is not admissible. Then the **second step** consists of a plastic corrector that brings back the final state onto the yield surface, i.e. it restores the consistency condition $f(\boldsymbol{\sigma}_{n+1}, \boldsymbol{\alpha}_{n+1}) = 0$.

The plastic corrector emerges naturally from Equation (5.6) after reorganisation

$$\boldsymbol{\sigma}_{n+1} - \cancel{\boldsymbol{\sigma}_n} = \boldsymbol{\sigma}_{tr} - \cancel{\boldsymbol{\sigma}_n} - \mathbb{E} : \mathbf{P}_{n+\theta} \cdot \Delta\lambda. \tag{5.15}$$

A geometric interpretation of this equation is illustrated in Figure 5.2. Starting from a converged stress state $\boldsymbol{\sigma}_n$, the direction of the return mapping $\mathbf{P}_{n+\theta}$ can be viewed as a combination of the normal vector at the beginning $\mathbf{P}_n$ and at the end $\mathbf{P}_{n+1}$ of the step.

Therefore, integrating the constitutive law for a given increment of deformation $\Delta\boldsymbol{\epsilon}$ reduces to finding $\Delta\lambda$ that verifies Equations (5.7), (5.8) and (5.15). Most of the time, this set of

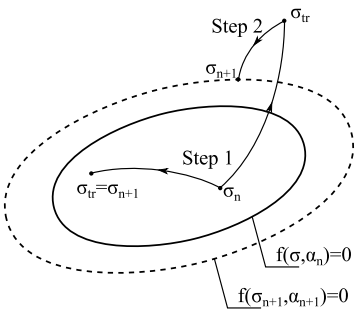

FIGURE 5.1: Geometric interpretation of trial stress state $\boldsymbol{\sigma}_{tr}$ and plastic corrector.

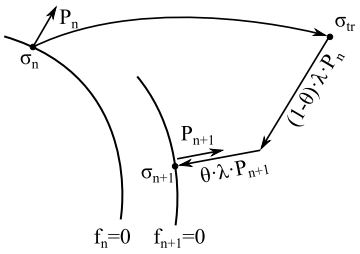

FIGURE 5.2: Geometric interpretation of the trapezoidal rule, after [Ortiz and Popov, 1985]. $\boldsymbol{\sigma}_n$, initial stress state; $\boldsymbol{\sigma}_{tr}$, trial stress state; $\boldsymbol{\sigma}_{n+1}$, final stress state.

equations is highly non-linear and an iterative procedure must be performed. Two families of return mapping algorithms can be distinguished[4].

These families are developed hereafter for a simplified single surface configuration. Let us denote $\boldsymbol{\sigma}^{(i)} = \boldsymbol{\sigma}^{(i)}_{n+1}$ and $\boldsymbol{\alpha}^{(i)} = \boldsymbol{\alpha}^{(i)}_{n+1}$ the stress state and backstress tensor at iteration (i). Consistency condition for this couple of variables reads $f^{(i)} = f^{(i)}(\boldsymbol{\sigma}^{(i)}, \boldsymbol{\alpha}^{(i)})$. Finally, let us assume that there is a linearised relation at iteration (i) between the variation of stress state $\Delta\boldsymbol{\sigma}$, the variation of backstress tensor $\Delta\boldsymbol{\alpha}$ and the variation of plastic multiplier $\Delta\lambda$, i.e.

$$\Delta\boldsymbol{\sigma}^{(i)} = \Delta\lambda^{(i)} \cdot \mathbf{G}^{(i)} \tag{5.16}$$

$$\Delta\boldsymbol{\alpha}^{(i)} = \Delta\lambda^{(i)} \cdot \mathbf{H}^{(i)} \tag{5.17}$$

where $\mathbf{G}^{(i)}$ and $\mathbf{H}^{(i)}$ are non linear arbitrary functions depending on $\boldsymbol{\sigma}^{(i)}$ and $\boldsymbol{\alpha}^{(i)}$. They indicate respectively the direction of the evolution of $\Delta\boldsymbol{\sigma}^{(i)}$ and $\Delta\boldsymbol{\alpha}^{(i)}$. More precisely, $\mathbf{H}^{(i)}$ is the hardening direction defined in section 4.1.2.

1. **The cutting plane algorithm**
   The consistency condition is linearised around the current variables, i.e.

$$f^{(i+1)} = f^{(i)} + \left[\frac{\partial f}{\partial \boldsymbol{\sigma}}\right]^{(i)} : \Delta\boldsymbol{\sigma}^{(i)} + \left[\frac{\partial f}{\partial \boldsymbol{\alpha}}\right]^{(i)} : \Delta\boldsymbol{\alpha}^{(i)} \tag{5.18}$$

$$= f^{(i)} + \left[\frac{\partial f}{\partial \boldsymbol{\sigma}}\right]^{(i)} : \Delta\lambda^{(i)} \cdot \mathbf{G}^{(i)} + \left[\frac{\partial f}{\partial \boldsymbol{\alpha}}\right]^{(i)} : \Delta\lambda^{(i)} \cdot \mathbf{H}^{(i)} \tag{5.19}$$

   Thence the correction $\Delta\lambda^{(i)}$ that must be applied in order to recover $f^{(i+1)} = 0$ is easily

[4] A more rigorous development of the equations that underlines these concepts can be found in [Simo and Hughes, 1998].

computed from Equation (5.19),

$$\Delta\lambda^{(i)} = \frac{-f^{(i)}}{\left[\frac{\partial f}{\partial \boldsymbol{\sigma}}\right]^{(i)} : \mathbf{G}^{(i)} + \left[\frac{\partial f}{\partial \boldsymbol{\alpha}}\right]^{(i)} : \mathbf{H}^{(i)}} \tag{5.20}$$

and iterative variables are updated

$$\boldsymbol{\sigma}^{(i+1)} = \boldsymbol{\sigma}^{(i)} + \Delta\lambda^{(i)} \cdot \mathbf{G}^{(i)} \tag{5.21}$$

$$\boldsymbol{\alpha}^{(i+1)} = \boldsymbol{\alpha}^{(i)} + \Delta\lambda^{(i)} \cdot \mathbf{H}^{(i)} \tag{5.22}$$

If $f^{(i+1)}$ is greater than a given tolerance, the procedure is started again until convergence is reached.

A geometrical interpretation is illustrated in Figure 5.3a. At every iteration, updated stresses are computed by projecting the previous iteration $\boldsymbol{\sigma}^{(i)}$ onto a hyperplane defined by the linearised equation f around the current stress $\boldsymbol{\sigma}^{(i)}$. In the limit, this plane becomes tangent to the yield surface and plastic consistency is restored at the end of the step, [Simo and Taylor, 1985; Wilkins, 1964]. This method solves linearised equations by relaxation. In case of perfect plasticity with associated flow rule, this scheme corresponds to the steepest descent path corresponding to the function f, [Simo and Taylor, 1985].

2. **The closest point projection algorithm**
The set of linearised equations can be solved by the Newton method. In the simplified configuration considered, the consistency condition is a residual function of one variable, $\Delta\lambda$.

$$f \equiv f(\underbrace{\boldsymbol{\sigma}_n + \Delta\lambda \cdot \mathbf{G}}_{\boldsymbol{\sigma}_{n+1}}, \underbrace{\boldsymbol{\alpha}_n + \Delta\lambda \cdot .\mathbf{H}}_{\boldsymbol{\alpha}_{n+1}}). \tag{5.23}$$

Therefore, the simplified sequence of solutions is given by

$$\Delta\lambda^{(i+1)} = \Delta\lambda^{(i)} - \frac{f^{(i)}}{\left[\frac{\partial f}{\partial \Delta\lambda}\right]^{(i)}} \tag{5.24}$$

A geometrical interpretation of this method is represented in Figure 5.3b. At each iteration, the trial state is projected onto a plane that is getting closer and closer to the final position of the yield surface. Thence the direction of the normal at the final state changes at each iteration and the projected stress state is identical, i.e. $\boldsymbol{\sigma}_{tr}$. It was shown in [Simo and Hughes, 1998], that for perfect plasticity and associated flow rule, the method corresponds to the closest point projection onto the yield surface in the energy norm.

The cutting plane method is an explicit method that only involves functional evaluation at the initial known iterate. On the other hand, closest point projection is an implicit formulation where the direction of return mapping is computed at the final unknown iterate. Nevertheless, one of the shortcomings of this method is the requirement of analytical derivatives. In case of normal return, it requires second order derivatives of f which can be cumbersome to obtain for complex models. However this method is known to be very powerful, [Armero and Perez-Foguet, 2002; Perez-Foguet and Armero, 2002] and is adopted hereafter.

Radial return is a special case of return mapping that is used for J_2 plasticity, i.e. for circular shape yield functions in the deviatoric plane. It belongs to the closest point projection

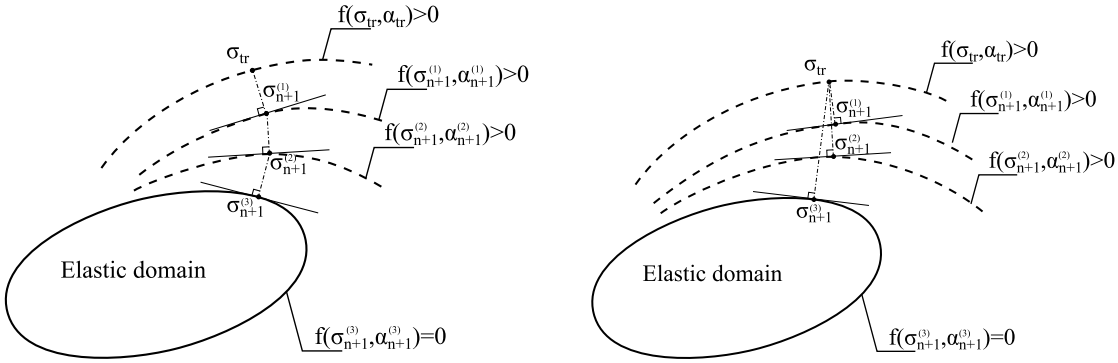

(a) Cutting plane algorithm (b) Closest point projection algorithm

FIGURE 5.3: Geometrical interpretation of two families of return mapping algorithms, after [Simo and Hughes, 1998]. $(\cdot)^{(i)}$ denotes the iteration number

family. However in this case, the elastic predictor $\boldsymbol{\sigma}_{tr}$, the final state $\boldsymbol{\sigma}_{n+1}^{(i)}$ and the centre of the surface $\boldsymbol{\alpha}_{n+1}^{(i)}$ are collinear since the surface is a circle, i.e. the normal to each point belonging to the surface passes through the centre.
A radial return algorithm is illustrated in Figure 5.4 in the case of kinematic hardening. Indeed, the size of the surface remains constant but its centre is translated. A each iteration of the algorithm, the final state $\boldsymbol{\sigma}_{n+1}^{(i)}$ only depends on the position of $\boldsymbol{\alpha}_{n+1}^{(i)}$, which simplifies the computations.

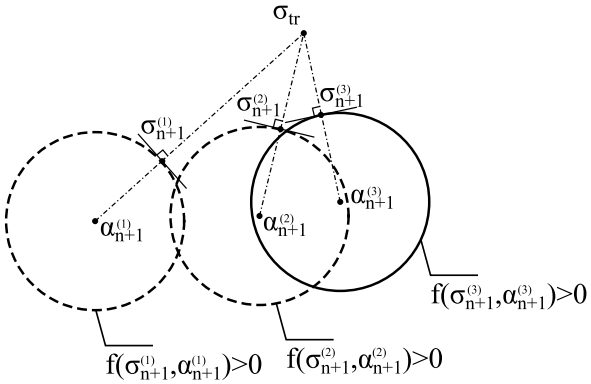

FIGURE 5.4: Closest point projection with radial return. $(\cdot)^{(i)}$ denotes the iteration number

5.3 Discrete formulation : particular case

5.3.1 Suitable hardening rule

The transition between two successive nested surfaces using the classic Mroz rule described in Section 4.3.4 is purely explicit. Firstly both surfaces must be put into contact. Secondly the next surface becomes active and starts translating. The implicit scheme adopted would overcome the splitting of the time step into different phases. Two possibilities are described hereafter to define a suitable hardening rule: the implicit Mroz translation rule and the Prager rule. Both of them are presented for a fully implicit scheme, i.e. $\theta = 1$, for the sake of simplicity.

5.3.1.1 Implicit Mroz translation rule

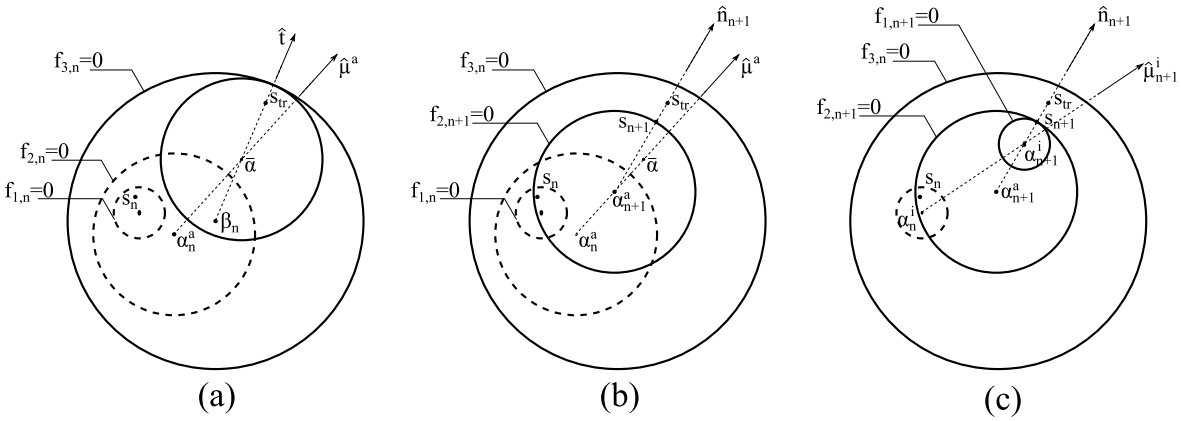

FIGURE 5.5: Hardening direction for the implicit Mroz translation rule, after [Montáns, 2000]. $f_{i,n}, \quad i = 1,3$ are the surfaces at the beginning of the step (dashed line) and $f_{i,n+1}, \quad i = 1,3$ at the end of the step (solid line); $\mathbf{s}_n$ is the initial deviatoric stress tensor; $\mathbf{s}_{tr}$ is the trial deviatoric stress tensor; $\boldsymbol{\alpha}_n$ is backstress tensor of the active yield surface; $\boldsymbol{\beta}$ is the backstress tensor of the target surface; $\boldsymbol{\mu}^i_{n+1}$ is the hardening direction of internal activated surfaces.

An implicit formulation of the Mroz rule is described in [Montáns, 2001]. A geometric interpretation is provided in Figure 5.5. Let us consider the converged configuration in Figure 5.5a. $\mathbf{s}_n$ is the converged deviatoric stress tensor and $\mathbf{s}_{tr}$ is the trial deviatoric stress tensor. The procedure for determining the hardening direction is based on the definition of

- the *active surface*, denoted by the superscript a, which is assumed *a priori* and which is the outermost surface that translates ;
- the *target surface*, which is the surface next to the active one and does not move.

In the geometric interpretation illustrated in Figure 5.5a, the second ($f_{2,n}$) and third ($f_{3,n}$) surfaces are respectively the active and target surfaces. A target tensor $\hat{\mathbf{t}}$ is then defined

$$\mathbf{t} = \mathbf{s}_{tr} - \mathrm{p}_{tr} \cdot \boldsymbol{\beta} \tag{5.25}$$

$$\hat{\mathbf{t}} = \frac{\mathbf{t}}{\|\mathbf{t}\|} \tag{5.26}$$

where $\mathrm{p}_{tr} \cdot \boldsymbol{\beta}$ is the trace of the centre of the target surface in the deviatoric plane that contains $\mathbf{s}_{tr}$. This tensor is used to compute the backstress tensor $\bar{\boldsymbol{\alpha}}$ which is the extreme position

that the active surface could occupy (see in Figure 5.5a), i.e. tangent to the target surface such that

$$\bar{\boldsymbol{\alpha}} = \boldsymbol{\beta} + \left(M^{a+1} - M^{a}\right) \cdot \sqrt{\frac{2}{3}} \cdot \hat{\mathbf{t}}, \tag{5.27}$$

where M^a and M^{a+1} are respectively the radii of the active and target surfaces. Therefore, it is assumed that active yield surface will hold a position between $\boldsymbol{\alpha}_n$ and $\bar{\boldsymbol{\alpha}}$ at the end of the step and its hardening direction can be established (see Figure 5.5a,b)

$$\boldsymbol{\mu}^a = \hat{\boldsymbol{\alpha}} - \boldsymbol{\alpha}_n^a \tag{5.28}$$

$$\hat{\boldsymbol{\mu}}^a = \frac{\boldsymbol{\mu}^a}{\|\boldsymbol{\mu}^a\|} \tag{5.29}$$

This hardening direction can be used in the consistency condition and the new backstress tensor $\boldsymbol{\alpha}_{n+1}$ can be updated (see Figure 5.5b). Therefore, direction of radial return $\hat{\mathbf{n}}_{n+1}$ can be defined

$$\mathbf{n}_{n+1} = \mathbf{s}_{tr} - \mathrm{p}_{n+1} \cdot \boldsymbol{\alpha}_{n+1}^a \tag{5.30}$$

$$\hat{\mathbf{n}}_{n+1} = \frac{\mathbf{n}_{n+1}}{\|\mathbf{n}_{n+1}\|} \tag{5.31}$$

This formulation is implicit since the direction of return $\hat{\mathbf{n}}_{n+1}$ depends on the final stress state and is not *a priori* known. Furthermore, a translation rule for each surface i such that $i < a$ must still be defined. This rule is based on the assumption that all the surfaces within the active one are finally tangent to the converged stress state $\mathbf{s}_{n+1}$. Therefore, the position of each inner surface, $\boldsymbol{\alpha}_{n+1}^i$ is aligned with $\mathbf{s}_{n+1}$ and $\boldsymbol{\alpha}_{n+1}^a$ (see Figure 5.5c), i.e.

$$\boldsymbol{\mu}_{n+1}^i = \mathbf{s}_{n+1} - \mathrm{p}_{n+1} \cdot \sqrt{\frac{2}{3}} \left(M^a - M^i\right) \cdot \hat{\mathbf{n}}_{n+1} \tag{5.32}$$

$$\hat{\boldsymbol{\mu}}_{n+1}^i = \frac{\boldsymbol{\mu}_{n+1}^i}{\|\boldsymbol{\mu}_{n+1}^i\|}. \tag{5.33}$$

In this formulation, the outermost active surface drives the algorithm, i.e. the position of all other internal surfaces are computed as a function of its position. Therefore an iterative process is necessary to solve the equations for a given assumption on this surface. Moreover, if this assumption is wrong, an additional iterative process must be superimposed to find the correct active yield surface.

5.3.1.2 Prager translation rule

The Prager rule is illustrated in Figure 5.6. The hardening $\boldsymbol{\mu}^1$ and normal $\hat{\mathbf{n}}_{n+1}$ directions are always computed in reference to the smallest yield surface. Actually, both directions are identical and computed at the end of the step, i.e.

$$\hat{\boldsymbol{\mu}}^1 = \hat{\mathbf{n}}_{n+1} = \frac{\mathbf{s}_{tr} - \mathrm{p}_{n+1} \cdot \boldsymbol{\alpha}_n^1}{\|\mathbf{s}_{tr} - \mathrm{p}_{n+1} \cdot \boldsymbol{\alpha}_n^1\|}. \tag{5.34}$$

This direction is expressed implicitly since it depends on the mean effective stress at the end of the step p_{n+1}. Once this position is updated, all surfaces that are intersected by the yield surface are updated and shifted successively. Provided a is the number of the outermost activated surface such that [Montáns, 2001]

$$\|\boldsymbol{\alpha}_n^{a+1} - \boldsymbol{\alpha}_{n+1}^1\| \leq \sqrt{\frac{2}{3}} \cdot \left(M^{a+1} - M^1\right) \quad \text{and} \quad \|\boldsymbol{\alpha}_n^a - \boldsymbol{\alpha}_{n+1}^1\| > \sqrt{\frac{2}{3}} \cdot \left(M^a - M^1\right). \tag{5.35}$$

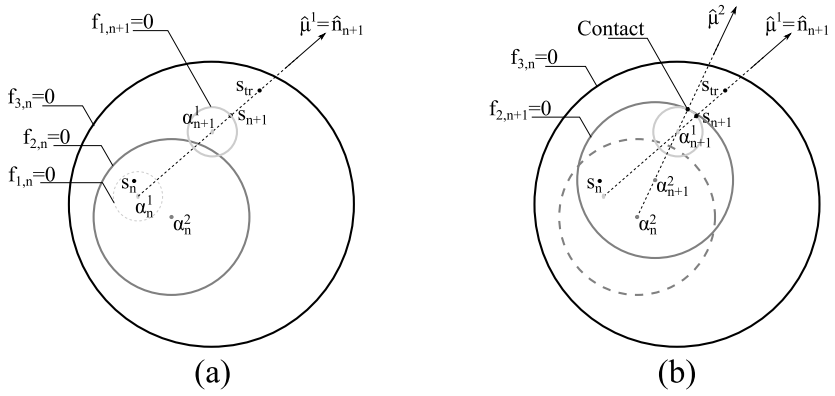

FIGURE 5.6: Hardening direction for the implicit Prager translation rule, after [Montáns, 2001]. $f_{i,n}, \quad i = 1,3$ are the surfaces at the beginning of the step (dashed line), $f_{i,n+1}, \quad i = 1,3$ are the surfaces at the end of the step (solid line), $\mathbf{s}_n$ is the initial deviatoric stress tensor, $\mathbf{s}_{tr}$ is the trial deviatoric stress tensor, $\boldsymbol{\alpha}_n^i$ is backstress tensor of the surface i.

This criterion readily identifies the outermost surface that is crossed by the first surface after its hardening. Two surfaces can not intersect if the distance between the positions of their centres is less than the difference between their radii. Thence, for each surface i such that $1 < i \leq a$, the hardening direction of the centre of the surface is given by

$$\hat{\boldsymbol{\mu}}_{n+1}^i = \frac{\boldsymbol{\alpha}_{n+1}^{i-1} - \boldsymbol{\alpha}_n^i}{\|\boldsymbol{\alpha}_{n+1}^{i-1} - \boldsymbol{\alpha}_n^i\|} \tag{5.36}$$

The geometrical interpretation of such a hardening rule is provided in Figure 5.6b. The final position is easily obtained through

$$\boldsymbol{\alpha}_{n+1}^i = \boldsymbol{\alpha}_{n+1}^{i-1} + \sqrt{\frac{2}{3}} \cdot \left(M^{i-1} - M^i\right) \cdot \hat{\boldsymbol{\mu}}_{n+1}^i. \tag{5.37}$$

One of the major difference with regard to the Mroz rule, is that the contact point between successive surfaces is not located at the final deviatoric stress state $\mathbf{s}_{n+1}$ (see Figure 5.6b). Aside, in this case, the innermost surface drives the algorithm and no hypothesis on the active solution is necessary. Furthermore, the Prager rule verifies the maximum dissipation principle, [Montáns and Caminero, 2007].

5.3.1.3 Yield/hardening surface

Nested surfaces are a key issue of the Prevost model. Up to that point, all of them were termed yield surfaces. From a theoretical point of view however, this denomination is not neutral. Elastic domain, consistency condition, flow direction and plastic modulus are dependent on the surface chosen as yield surface.
Let us assume that the last converged stress state is $\mathbf{s}_n$ (see Figure 5.7). Two different feasible stress paths exist to reach the next stress state $\mathbf{s}_{n+1}$. The first one consists of a total elastic unloading within the first surface f_1, followed by an elastoplastic part up to $\mathbf{s}_{n+1}$ (see Figure 5.7a). The active surface is then f_1 in the end. The second possibility is a virtually fully elastic stress path that follows the f_2 yield criterion (see Figure 5.7b). However, it is not admissible to reach an identical stress state, from elastic and elastoplastic stress paths, [Montáns and Caminero, 2007].

If the radial return mapping is adopted, the flow direction $\hat{\mathbf{n}}$ depends on both trial state and

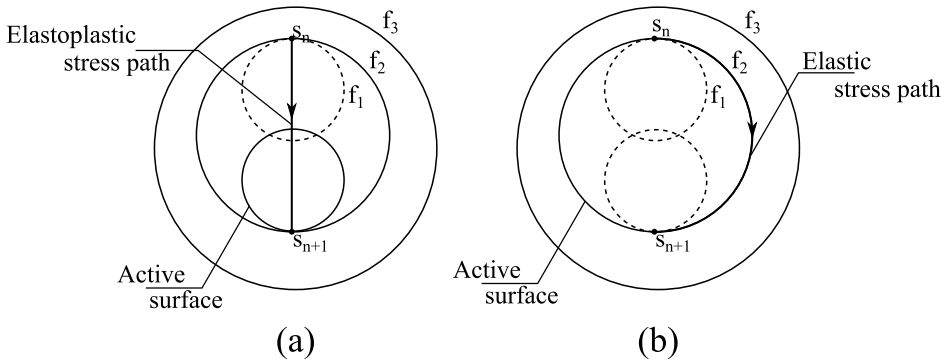

FIGURE 5.7: Possible elastic and elastoplastic stress paths from $\mathbf{s}_n$ to $\mathbf{s}_{n+1}$ after [Montáns and Caminero, 2007].

the centre of the active surface (see Figure 5.8). Therefore, let us consider two converged stress states $\mathbf{s}_n^{(1)}$ and $\mathbf{s}_n^{(2)}$ infinitesimally close. The former lies on the first smallest surface (f_1), which is very close but not tangent to the next surface (f_2). In Figure 5.7b, both surfaces are supposed tangent and the stress state lies on both surfaces.
When an infinitesimal change of the stress conditions induces a change from the first surface to the second, the flow direction changes abruptly from $\hat{\mathbf{n}}^{(1)}$ to $\hat{\mathbf{n}}^{(2)}$. This fact certainly contradicts the continuity postulate of Prager [1949]; Hashiguchi [2009], which establishes that *the stress rate changes continuously for a continuous change of the strain rate*. Moreover, there is a jump in the definition of the elastic zone that suddenly changes from the domain enclosed within f_1 to the one enclosed in f_2. Furthermore, such a change of active surface can be merely due to numerical inaccuracies and the adopted formulation should be insensitive to them.

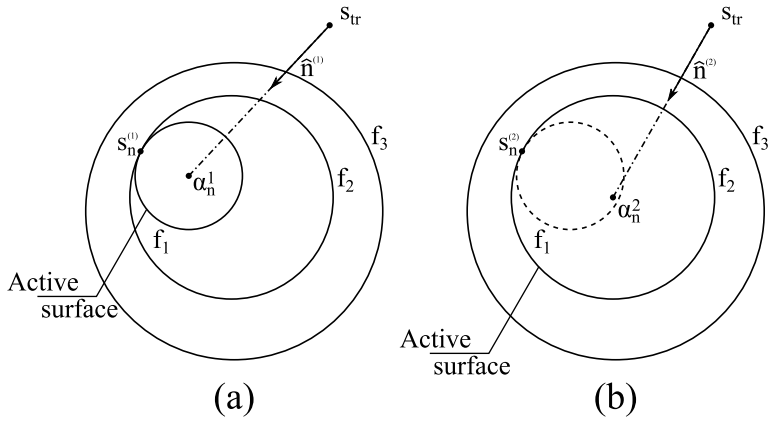

FIGURE 5.8: Discontinuity in the flow direction for two infinitesimally close stress states, after [Montáns and Caminero, 2007].

All these discrepancies disappear if yield and hardening surfaces are distinguished. The yield surface defines the elastic domain and the flow direction. In this case, it can be chosen as the innermost surface. The elastic domain is constant during the loading, i.e. it is not affected by an unloading event and a continuity in the flow direction exists within the stress space. All the other surfaces are termed hardening surfaces, i.e. they are just a numerical tool used to describe the anisotropic hardening space and to compute the hardening modulus, [Montáns and Caminero, 2007]. Therefore, the model is said to be composed of a yield and n-1 hardening surfaces, where n is the total number of surfaces.

5.3.1.4 Choice of a hardening rule

In this work, both Mroz and Prager hardening rules were successively implemented. However, it appears that the choice of the Prager rule is more judicious. Indeed, the Mroz rule corresponds to a particular case: each surface can become a yield surface. The assumption of the outermost active yield surface involves a sudden change in the elastic domain and in the flow direction. The Mroz rule in [Prevost, 1985] was introduced essentially for numerical purpose, i.e. to avoid a crossing of two successive surfaces. On the other hand, if the size of the Prager rule tends to zero, flow direction tends to the direction of deformation in the deviatoric plane, which might be more physical, [Montáns and Caminero, 2007].

Furthermore, from a practical point of view, the Mroz rule for the Prevost model was observed to be less robust. This is not inherent to the hardening rule but due to the combination with the non associated volumetric hardening. Indeed, it was shown in [Montáns and Caminero, 2007] that this rule can be very cleverly adapted to be extremely efficient, in the case of pure J_2 plasticity.
The midpoint integration scheme is adopted, i.e. directions of return are computed in the middle of the step, i.e. in $n + 1/2$. Therefore, the return direction is recast into

$$\hat{\mathbf{n}}_{n+\theta} = \frac{(1-\theta)\cdot\hat{\mathbf{n}}_n + \theta\cdot\hat{\mathbf{n}}_{n+1}}{\|(1-\theta)\cdot\hat{\mathbf{n}}_n + \theta\cdot\hat{\mathbf{n}}_{n+1}\|}. \tag{5.38}$$

5.3.2 Plastic multiplier

The computation of the plastic multiplier at the end of the step $\Delta\lambda_{n+1}$ is not a straightforward process. Indeed, plastic modulus and then plastic deformation depend on the outermost hardening activated surface. Since a multi-surface model can be viewed as a multi-mechanism model, an additive decomposition of the plastic multiplier was adopted, i.e.

$$\Delta\lambda_{n+1} = \sum_{i=1}^{a} \Delta\lambda^i_{n+1} \tag{5.39}$$

where $\Delta\lambda^i_{n+1}$ is the component of the plastic multiplier associated with the activated surface i, [Montáns, 2001]. Each of these components can be related to the amount of translation of the corresponding surface as

$$\Delta\lambda^i_{n+1} = \mathrm{p}_{n+1}\cdot\frac{\|\boldsymbol{\alpha}^i_{n+1} - \boldsymbol{\alpha}^i_n\|}{\bar{H}^i}\cdot\left\langle \mathbf{Q}'_{n+\theta} : \hat{\boldsymbol{\mu}}^i_{n+\theta}\right\rangle \tag{5.40}$$

where $\left\langle \mathbf{Q}'_{n+\theta} : \hat{\boldsymbol{\mu}}^i_{n+\theta}\right\rangle$ ensures convexity of the function $\Delta\lambda(\Delta\epsilon)$ in every condition [Montáns and Caminero, 2007]. It consists of the projection of the amount of translation of the surface i onto the deviatoric direction of flow deformation $\hat{\mathbf{n}}_{n+\theta}$. This formulation corresponds to the continuous amount of translation of an arbitrary active yield surface, (see Equation (4.46) in section 4.3.4). Equation (5.40) refers to a modified plastic modulus $\bar{H}^i$ such that

$$H'^1 = \bar{H}^1 \qquad \text{and} \qquad \frac{1}{\bar{H}^i} = \frac{1}{H'^i} - \frac{1}{H'^{i-1}}. \tag{5.41}$$

This modified plastic modulus is necessary since a duality exists between the plastic multiplier and the plastic modulus. Thence formulations associating a global plastic multiplier to the plastic modulus of the active surface, i.e. $(\Delta\lambda_{n+1}, H'^i)$ are equivalent to $(\Delta\lambda^1_{n+1}, \bar{H}^1)$, which are associated to the yield surface only.

5.3.3 Set of equations

The last step of the integration process is the elaboration of the set of equations to be solved. Firstly, the plastic correction Equation (5.15) is split into deviatoric and volumetric components, i.e.

$$\mathbf{s}_{n+1} = \mathbf{s}_{tr} - 2 \cdot G \cdot \Delta\lambda_{n+1} \cdot \mathbf{P}'_{n+\theta} \tag{5.42}$$

$$\mathrm{p}_{n+1} = \mathrm{p}_{tr} - 3 \cdot K \cdot \Delta\lambda_{n+1} \cdot P''_{n+\theta} \tag{5.43}$$

where the return mapping direction is defined such that

$$\mathbf{P}_{n+\theta} = \mathbf{P}'_{n+\theta} + P''_{n+\theta} \cdot \boldsymbol{\delta} = \mathbf{Q}'_{n+\theta} + P''_{n+\theta} \cdot \boldsymbol{\delta}. \tag{5.44}$$

The deviatoric part is associated. Thus $\mathbf{Q}'_{n+\theta}$ is the deviatoric component of the normal to the yield surface. By definition, $\hat{\mathbf{n}}_{n+\theta}$ and $\mathbf{Q}'_{n+\theta}$ have an identical direction, therefore the following equation holds

$$\mathbf{Q}'_{n+\theta} = \|\mathbf{Q}'_{n+\theta}\| \cdot \hat{\mathbf{n}}_{n+\theta}. \tag{5.45}$$

Otherwise, by definition one gets

$$\|\mathbf{Q}'_{n+\theta}\| = 2 \cdot \frac{\|\mathbf{s} - \mathrm{p} \cdot \boldsymbol{\alpha}^1\|_{n+\theta}}{\left\| \dfrac{\partial f}{\partial \boldsymbol{\sigma}} \right\|_{n+\theta}}. \tag{5.46}$$

The volumetric plastic potential is simply obtained by

$$P''_{n+\theta} = (1-\theta) \cdot P''(\eta_n) + \theta \cdot P''(\eta_{n+1}). \tag{5.47}$$

The evolution of the yield surface, i.e. the backstress variation of the first surface, is deduced from Equation (5.40)

$$\boldsymbol{\alpha}^1_{n+1} = \boldsymbol{\alpha}^1_n + \frac{\Delta\lambda^1_{n+1}}{\mathrm{p}_{n+1}} \cdot H^{*,1}_{n+\theta} \cdot \hat{\mathbf{n}}_{n+\theta} \tag{5.48}$$

where a new projected plastic modulus is introduced for the sake of readability

$$H^{*,1}_{n+\theta} = \frac{H'^1}{\mathbf{Q}'_{n+\theta} : \hat{\mathbf{n}}_{n+\theta}}. \tag{5.49}$$

Finally, the definition of the consistency condition is modified into

$$f_{n+1} = (\mathbf{s}_{n+1} - \mathrm{p}_{n+1} \cdot \boldsymbol{\alpha}_{n+1}) : \hat{\mathbf{n}}_{n+\theta} - \mathrm{p}_{n+1} \cdot \sqrt{\frac{2}{3}} \cdot M^1 = 0 \tag{5.50}$$

Equations (5.42) to (5.50) together with the Prager hardening rule and the plastic multiplier definition fully describe the model. Theoretically, they can be recast into a function of only $\Delta\lambda^1_{n+1}$, which is the plastic multiplier associated to the yield surface. However, due to the non-associated volumetric plastic potential, the computation of exact derivatives for a Newton procedure would be very cumbersome. Thus, four primal variables are chosen as primary unknowns which would be associated to four residual equations to be minimised, [de Borst and Heeres, 2002; Mira et al., 2009],

1. $\Delta\lambda^1_{n+1}$: plastic multiplier associated to the yield surface at the end of the step ;
2. p_{n+1} : mean effective stress at the end of the step ;

3. $H^{*,1}_{n+\theta}$: projected plastic modulus in $n+\theta$;
4. $\|\mathbf{Q}'_{n+\theta}\|$: the norm of the deviatoric component of the normal to the yield surface, in $n+\theta$.

The number of unknowns is unconventional with regard to other works such as [Mira et al., 2009]. Indeed, most of the time, the unknowns are the components of the final stress tensor $\boldsymbol{\sigma}_{n+1}$, the components of the backstress tensor of the yield surface $\boldsymbol{\alpha}^1_{n+1}$ and the variation of the plastic multiplier $\Delta\lambda$. Using only four unknowns considerably reduces the size of the Jacobian matrix that must be computed during the Newton-Raphson process. Thence the number of derivatives analytically computed is also reduced.

Introducing Equation (5.45) into (5.49), leads to the first residual equation

$$r_1 = \frac{H^{*,1}_{n+\theta}}{\bar{H}^1} \cdot \|\mathbf{Q}'_{n+\theta}\| - 1. \tag{5.51}$$

The second one enforces the consistency condition at the end of the step. Thus inserting Equations (5.42) and (5.43) into (5.50) reads

$$r_2 = (\mathbf{s}_{tr} - \mathrm{p}_{n+1} \cdot \boldsymbol{\alpha}_n) : \hat{\mathbf{n}}_{n+\theta} - \sqrt{\frac{2}{3}} \cdot \mathrm{p}_{n+1} \cdot M^1 - 2 \cdot G \cdot \Delta\lambda_{n+1} \cdot \|\mathbf{Q}'_{n+\theta}\| - \Delta\lambda^1_{n+1} \cdot H^{*,1}_{n+\theta}. \tag{5.52}$$

The plastic corrector Equation (5.43) and definition of $\|\mathbf{Q}'_{n+\theta}\|$ (5.46) as well are directly used as a residual equation

$$r_3 = \mathrm{p}_{n+1} - \mathrm{p}_{tr} + 3 \cdot K \cdot \Delta\lambda_{n+1} \cdot P^{"}_{n+\theta}, \tag{5.53}$$

$$r_4 = \|\mathbf{Q}'_{n+\theta}\| - 2 \cdot \frac{\|\mathbf{s} - \mathrm{p} \cdot \boldsymbol{\alpha}^1\|_{n+\theta}}{\left\| \dfrac{\partial f}{\partial \boldsymbol{\sigma}} \right\|_{n+\theta}}. \tag{5.54}$$

Residual have distinct order of magnitudes. First and fourth ones are dimensionless while second and third ones have the dimension of stresses. Therefore it is wise, for numerical purpose, to normalise r_2 and r_3 in dividing them by p_{tr}.

5.3.4 Solution

Solving of the local set of equations is performed with the iterative Newton method coupled with a line search algorithm, i.e.

$$\mathbf{x}^{k+1} = \mathbf{x}^k - \alpha^k \cdot \left[\mathbf{J}^k\right]^{-1} \cdot \mathbf{r}^k, \tag{5.55}$$

where $\mathbf{r}$ is the vector of residual equations previously defined, $\mathbf{x} = [\Delta\lambda^1_{n+1}, \mathrm{p}_{n+1}, H^{*,1}_{n+\theta}, \|\mathbf{Q}'_{n+\theta}\|]^T$ is the vector of unknowns and α is the line search parameter. It is possible to find an optimum parameter α ensuring the norm of the residual vector $\|\mathbf{r}\|$ monotonically decreases, [Borja, 2013]. The line search method is useful to overcome oscillations that might appear during the Newton algorithm. The original Newton procedure is recovered by imposing $\alpha = 1$.
A geometric interpretation of the line search algorithm is illustrated in Figure 5.9 to solve the equation $r(x) = 0$. A solution exists but the function presents a local minimum. Starting from an initial guess x_0, the Newton Method may be trapped into the local minimum (see Figure 5.9a). On the contrary, the line search algorithm searches, for a given iterate, the α

parameter that leads to a reduction of the residual. Then the process overcomes the local maximum. An example is illustrated in Figure 5.9b. At iteration 1, the slope of the Newton method $\mathbf{J}^{-1}$ is multiplied by α. The final α value adopted is the one which produces a new iterate, $\mathbf{x}^2$ corresponding to a residual function $r^2 < r^1$.
Line search methods can be very sophisticated and interested reader might refer to [Bierlaire, 2006]. However in this work, the algorithm is activated only in case of bad convergence. A secant method over the interval $\alpha \in [0, 1]$ is adopted to find an optimum α parameter[5].

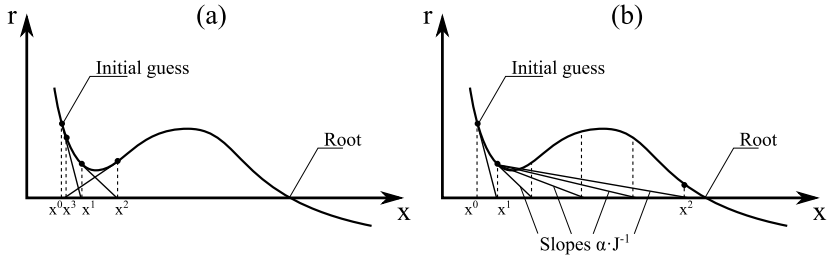

FIGURE 5.9: Illustration of Newton (a) and line search (b) algorithms.

The Newton method may be asymptotically quadratic. However the solution can oscillate or even diverge if the initial iterate is not close enough to the solution, i.e. within the radius of convergence [Rouainia and Wood, 2001]. Therefore the line search method might be essential in this case. Convergence is quadratic only if derivatives are exact. In this work, exact analytical derivatives are computed in Appendix B.
The last key feature is the convergence criterion that has to be adopted to stop the local iterative process. Convergence is deemed reached if residual equations are small enough. Another point of view is to check the primary unknowns variation with respect to their current value, i.e.

$$\frac{\|\delta \mathbf{x}\|}{\|\mathbf{x}\|}. \tag{5.56}$$

In this work, both criteria are tested simultaneously. The first one ensures residual equations are verified and the second that the current state is nearly stationary.

5.3.5 Elastoplastic tangent operator

Once the local iterative procedure is solved, the final stress state $\boldsymbol{\sigma}_{n+1}$ corresponding to the increment of deformation $\Delta\boldsymbol{\epsilon}$ is computed. However, this outcome only holds for a particular integration point. On the other hand the global finite element code requires the determination of a consistent tangent operator in order to assemble the global stiffness matrix. This is a fourth-order tensor, defined for a given integration point as

$$\mathbb{C}_{n+1} = \frac{\mathrm{d}\boldsymbol{\sigma}_{\boldsymbol{n+1}}}{\mathrm{d}\boldsymbol{\epsilon}_{n+1}}. \tag{5.57}$$

The consistent elastoplastic tangent operator must be differentiated from a classic continuum one. Indeed, the former is obtained by enforcing the consistency condition of the discrete algorithmic problem at the end of the step whereas the last results from the classic consistency condition of the continuum problem, [Simo and Taylor, 1985; Simo and Hughes, 1998].
An accurate tangent operator is necessary to ensure the convergence of the global iterative scheme, necessary to solve the boundary value problem. However a close form of $\mathbb{C}_{n+1}$ is

[5]This induces assumptions on the convexity and uniqueness of α that have not been verified.

not easily derived. This has been done for J_2 plasticity [Simo and Taylor, 1985; Montáns, 2004; Montáns and Caminero, 2007; Mira et al., 2009]. However, in this particular case of non associated volumetric flow rule and confinement dependent yield surface, $\mathbb{C}_{n+1}$ is derived by numerical perturbations. The method is described in

5.3.6 Sub-stepping

The cost of a numerical simulation is measured by the cpu time spent

1. at the local scale : updating $\boldsymbol{\sigma}_{n+1}$, computing the consistent tangent operator ;
2. at the global scale : inverting the global stiffness matrix.

The cost of the first local scale increases linearly with the number of unknowns. The growth is cubic during the global solving. Consequently, the size of the time step is a key feature to ensure an acceptable accuracy of the results. However, if deformations are localised over several elements that are part of a large mesh, it is very inefficient to reduce the global time step, only to increase the accuracy of the integration of few integration points.
Sub-stepping schemes are a solution to this shortcoming [Sloan, 1987; Manzari and Prachathananukit, 2001]. In this work, if Sub-stepping is required at a particular integration point, the deformation increments $\boldsymbol{\Delta\epsilon}$ is decomposed into a succession of N identical subincrements $\boldsymbol{\delta\epsilon}$. The hypothesis that underlines the method is that the higher the norm of deformation increment the higher the number of subincrements required to ensure a sufficient accuracy, i.e.

$$N = \max\left(\frac{\|\boldsymbol{\Delta\epsilon}\|}{DIV}, 1\right) \tag{5.58}$$

$$\boldsymbol{\delta\epsilon} = \frac{\boldsymbol{\Delta\epsilon}}{N} \tag{5.59}$$

where DIV is a user defined parameter. Indeed, more sophisticated procedures exist which can update the direction of deformation during the Sub-stepping scheme or rule the step size in controlling the error. The use of a Sub-stepping scheme might be very useful for closest point projection methods. Indeed, if the initial guess in the Newton scheme if too far from the solution, it does not converge. Therefore a Sub-stepping procedure increases the robustness of the local algorithm. The effect of Sub-stepping on the computation of consistent tangent operator is also a salient issue that is not tackled here. However, interested reader should refer to [Perez-Foguet et al., 2001].

5.3.7 Algorithm

In this work, the midpoint rule is adopted to define the plastic return direction, i.e. $\theta = 1/2$. Indeed, it has been shown that this rule provides a second order accuracy for small strain increments [Ortiz and Popov, 1985]. It was also observed during simulations that this value provides a better accuracy of the results, especially when the variation of η is large over a small deformation increment. Moreover, $\theta = 1/2$ leads to unconditionally stable schemes, [Ortiz and Popov, 1985; Mira et al., 2009]. Algorithms 1, 2 and 3 are provided in order to summarise the procedure of the implemented algorithm which the steps are previously defined. Shear, bulk and plastic moduli are updated at the beginning of each time step. Indeed, their confinement dependency is not taken into account during the integration process. Therefore, in the following algorithm, elasticity is assumed linear and plastic moduli are deemed constant over a time step.

Algorithm 1 Computation of $\Delta\boldsymbol{\sigma}(\Delta\boldsymbol{\epsilon})$

INPUT : $\Delta\boldsymbol{\epsilon}$, internal parameters
INITIALISE : $\Delta\lambda^1_{n+1}$, $H^{*,1}_{n+1/2}$, $\|\mathbf{Q}'_{n+1/2}\|$ and p_{n+1}
INITIALISE : $\mathbf{r}^k$ and $\mathbf{J}^k$
while CRIT $>$ TOL **do**
  if GOOD CONVERGENCE **then**
    $\mathbf{x}^{k+1} \leftarrow \mathbf{x}^k - \Delta\mathbf{x}$
    COMPUTE $\mathbf{r}^{k+1}$, **GO TO** Algorithm 2
  else
    $\min_{\alpha} \left\| r^{k+1}\left(\mathbf{x}^k - \alpha \cdot \Delta\mathbf{x}\right)\right\|$ **GO TO** Algorithm 2
  end if
  COMPUTE $\mathbf{J}^{k+1}$
  COMPUTE $\Delta\mathbf{x} = \left[\mathbf{J}^k\right]^{-1} \cdot \mathbf{r}^k$
  $k \leftarrow k+1$
end while
UPDATE : $\boldsymbol{\sigma}_{n+1}$,$\boldsymbol{\alpha}_{n+1}$
return

Algorithm 2 Computation of residual vector $\mathbf{r}$

INPUT : $\Delta\lambda^1_{n+1}$, $H^{*,1}_{n+1/2}$, $\|\mathbf{Q}'_{n+1/2}\|$ and p_{n+1}, internal parameters
$\boldsymbol{\alpha}^1_{n+1} = \boldsymbol{\alpha}^1_n + \dfrac{\Delta\lambda^1_{n+1}}{\mathrm{p}_{n+1}} \cdot H^{*,1}_{n+1/2} \cdot \hat{\mathbf{n}}_{n+1/2}$
$\hat{\mathbf{n}}_{n+1/2} = \dfrac{\mathbf{s}_n - \mathrm{p}_n \cdot \boldsymbol{\alpha}^1_n + \mathbf{s}_{tr} - \mathrm{p}_{n+1} \cdot \boldsymbol{\alpha}^1_{n+1}}{\|\mathbf{s}_n - \mathrm{p}_n \cdot \boldsymbol{\alpha}^1_n + \mathbf{s}_{tr} - \mathrm{p}_{n+1} \cdot \boldsymbol{\alpha}^1_{n+1}\|}$
$\mathbf{Q}'_{n+1/2} = \|\mathbf{Q}'_{n+1/2}\| \cdot \hat{\mathbf{n}}_{n+1/2}$
COMPUTE $\Delta\lambda_{n+1}$, **GO TO** Algorithm 3
$\mathbf{s}_{n+1} = \mathbf{s}_{tr} - 2 \cdot G \cdot \Delta\lambda_{n+1} \cdot \mathbf{Q}'_{n+1/2}$
$P''_{n+1/2}\left(\eta_{n+1/2}\right)$
COMPUTE $\left\|\dfrac{\partial f}{\partial \boldsymbol{\sigma}}\right\|_{n+1/2}$ and $\|\mathbf{s} - \mathrm{p} \cdot \boldsymbol{\alpha}\|_{n+1/2}$
COMPUTE $\mathbf{r}$
return $\mathbf{r}$

Algorithm 3 Computation of $\Delta\lambda_{n+1}$

$\Delta\lambda^1_{n+1}$, $H^{*,1}_{n+1/2}$, $\|\mathbf{Q}'_{n+1/2}\|$, p_{n+1} and internal parameters

$\boldsymbol{\alpha}^1_{n+1} = \boldsymbol{\alpha}^1_n + \dfrac{\Delta\lambda^1_{n+1}}{\mathrm{p}_{n+1}} \cdot H^*_{1,n+1/2} \cdot \hat{\mathbf{n}}_{n+1/2}$

i =1 ; TEST =1 ; $\bar{\boldsymbol{\alpha}} \leftarrow \boldsymbol{\alpha}^1_{n+1}$

while TEST >0 **do**

  i=i+1

  TEST $= \|\bar{\boldsymbol{\alpha}} - \boldsymbol{\alpha}^i_n\| - \left(M^i - M^{i+1}\right) \cdot \sqrt{\dfrac{2}{3}}$

  if TEST > 0 **then**

    $\hat{\boldsymbol{\mu}}^i_{n+1} = \dfrac{\bar{\boldsymbol{\alpha}} - \boldsymbol{\alpha}^i_n}{\|\bar{\boldsymbol{\alpha}} - \boldsymbol{\alpha}^i_n\|}$

    $\bar{\boldsymbol{\alpha}} \leftarrow \bar{\boldsymbol{\alpha}} + \sqrt{\dfrac{2}{3}} \cdot (M^{i-1} - M^i) \cdot \hat{\boldsymbol{\mu}}^i_{n+1}$

    $\Delta\lambda^i_{n+1} = \mathrm{p}_{n+1} \cdot \dfrac{\|\bar{\boldsymbol{\alpha}} - \boldsymbol{\alpha}^i_{n+1}\|}{\bar{H}^i} \cdot \left\langle \mathbf{Q}'_{n+1/2} : \hat{\boldsymbol{\mu}}^i_{n+1} \right\rangle$

  end if

end while

return $\Delta\lambda_{n+1}$

5.4 Examples

The purpose of this section is the verification of the integration scheme. It must be ensured that implemented algorithm corresponds to the analytical model. This step must be distinguished from the validation step, ensuring the analytical model corresponds to reality (see in previous Chapter). Therefore, the fully implicit general integration scheme implemented in the finite element code `LAGAMINE` is firstly compared to an explicit scheme devoted to simplified triaxial conditions in Matlab. A multi-axial loading is then investigated.
Unfortunately, data available in the literature about the Prevost model are scarce or even non-existent. As a matter of fact, results of simulations are often provided but parameters corresponding to nested surfaces are rarely mentioned. Therefore, it was not possible to benchmark the results.

5.4.1 Triaxial simulations

A first comparison between classic drained monotonic triaxial tests in compression and extension is provided in Figure 5.11. Parameters adopted for that comparison are provided in Tables 5.1 and 5.2. They correspond to another set of parameters calibrated for Nevada sand (Dr= 40%) that is presented in [Cerfontaine and Charlier, 2014]. The parameter n ruling the confinement dependency of the moduli has been set to zero. This ensures stiffness parameters are constant during the whole simulation and the scheme proposed is purely implicit.
The first two Figures 5.11a and 5.11b present a good concordance between explicit (dashed and solid lines) and implicit (markers) formulations. Failure and phase transformation are well represented. However, the graph of the reduced deviatoric stress ratio $\eta = \mathrm{q}/\mathrm{p}'$ is more pertinent to assess the behaviour of the algorithm (see Figures 5.11c and 5.11d). Indeed, during triaxial simulations, the stress state, backstress tensors, trial state and return deviatoric directions are aligned. Therefore a variation $\Delta\eta$ is an indication of the translation of the active surface.

G_{ref}[MPa]	K_{ref}[MPa]	$\bar{\eta}$[-]	Ψ[-]	n [-]
40	66.67	0.8	1.0	0

TABLE 5.1: Set of parameters used for numerical verification of the model. G_{ref}, reference shear modulus; K_{ref}, reference bulk modulus; $\bar{\eta}$ and Ψ, parameters of the volumetric flow rule; n, confinement dependency of the plastic moduli.

N° surf	1	2	3	4	5	6	7	8	9
M [-]	0.08	0.15	0.30	0.4250	0.64	0.775	0.92	1.045	1.14
H' [MPa]	150	100	30	10	2	1	0.4	0.15	0.01
α [-]	0	0.05	0.1	0.175	0.26	0.225	0.22	0.155	0.14

TABLE 5.2: Set of parameters used for numerical verification of the model. M, opening of the surface; H', plastic modulus; α, back stress in triaxial format.

It must be pointed out η is monotonically increasing. It means there is no unloading, nor change of direction of the yield surfaces, simplifying the integration of the constitutive law. The tricky point the algorithm has to manage is the transition from one active hardening

surface to another. Indeed, in explicit integration scheme, the stress integration might be divided into several sub-steps in order to manage the transition from one surface to another (see Figure 5.10). The implicit algorithm manages this change adequately without intermediate step.

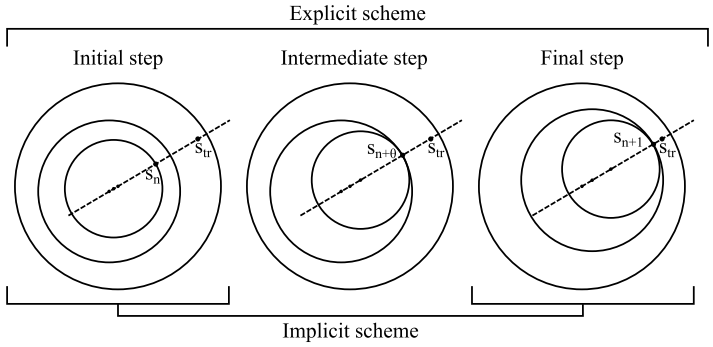

FIGURE 5.10: Comparison of explicit and implicit scheme for the surface transition.

Table 5.3 summarises the range of deformation modelled and the number of steps required to reproduce it. The average increase of deformation per step varies a bit between the tests but is around 0.3 %/step. However, the size of the step varies during the simulation. As a matter of fact, the loading process in `LAGAMINE` is ruled by an automatic strategy. The step size is increased in case of good convergence and reduced otherwise.

p'_0 [kPa]	50	150	250	50	150	250
ϵ_y [%]	8.7	8.7	8.7	-8.0	-8.0	-8.0
Nb. steps [-]	27	23	22	33	25	25
Average [%]	0.322	0.378	0.395	-0.243	-0.320	-0.320

TABLE 5.3: Number of steps necessary to reach the maximum $|\epsilon_y|$ deformation for implicit algorithm (Classic monotonic drained triaxial test).

For instance, the extension simulation for an initial $p'_0 = 50$kPa presents three step reductions. The first two occur around the maximum of ϵ_v (see Figure 5.11d). Indeed, in this case, the volumetric deformation is nearly constant and the direction of volumetric plastic deformation P'' is close to zero. Then, there is a large variation of η where ϵ_v is very flat, which is not easy to manage. Indeed, this change occurs for $P'' = 0$, might introduce some instabilities within the iterative process.
The third step reduction occurs when the last surface (Nb. 9) is activated. There is a sharp change in Figures 5.11c and 5.11d. Actually, the discretisation of plastic modulus evolution should have encompassed several additional hardening surfaces in order to smooth the failure behaviour.

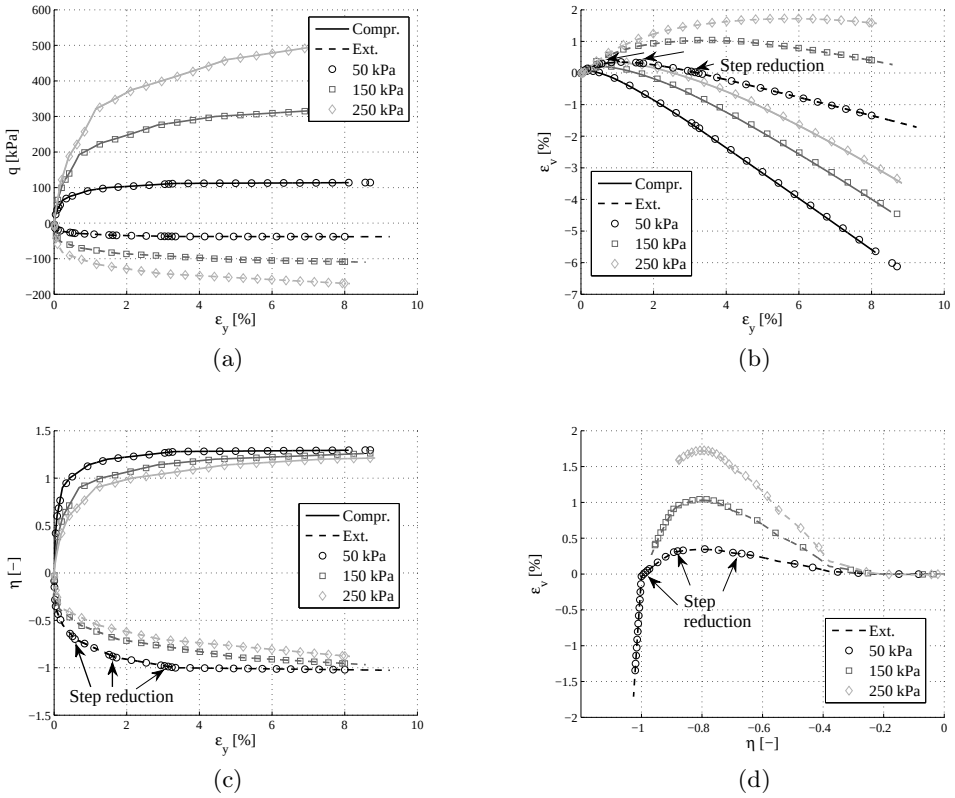

FIGURE 5.11: Monotonic classic drained triaxial test (strain-driven). Comparison between implicit and analytical (explicit) formulations. Solid lines, compressive explicit simulations ; dashed lines, extension explicit simulations ; markers, implicit simulations.

Constant mean effective stress triaxial tests are illustrated in Figure 5.12. They allow the use of larger steps from 0.4%/step to -0.7%/step and seem to encounter less step reductions. Implicit and explicit simulations match very well.

Undrained monotonic triaxial tests are provided in Figure 5.13. Classic asymmetric behaviours in compression and extension are observed. Implicit compressive tests match nicely explicit simulations and the elbow created in the p'-q plane (see Figure 5.13a).
However, extension simulations exhibit discrepancies with "exact" results. The divergence slightly starts during the contractive phase (see Figures 5.13b and 5.13d). Furthermore, the difference between explicit and implicit curves is accentuated after the maximum of pore water pressure $\delta\Delta u_w = 0$, i.e. when the behaviour switches from contractive to dilative. Actually, it can be shown that all simulations are merged in a unique curve if they are plotted in the plane $\eta - \Delta u_w/p'_0$ (see Figure 5.13d). The plateau in Figure 5.13d corresponds to a phase of quasi-liquefaction, since the ratio $\Delta u_w/p'_0$ is very close to 1. However surfaces still harden since η decreases. It can be observed in Figure 5.14b that this variation of η holds over a very small range of vertical deformation. The final divergence occurs because the implicit algorithm more slowly "escapes" from the initial liquefaction zone (see Figure 5.13d).

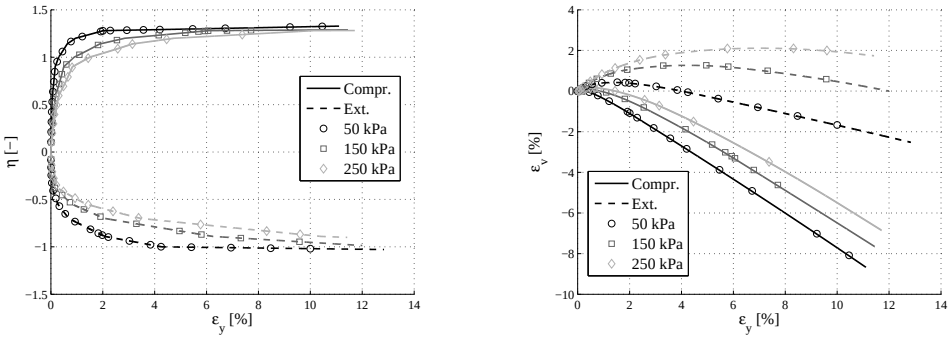

(a) (b)

FIGURE 5.12: Monotonic p'=cst drained triaxial test (strain-driven). Comparison between implicit and analytical (explicit) formulations. Solid lines = compressive explicit simulations ; dashed lines = extension explicit simulations ; markers = implicit simulations.

The only way to overcome this difficulty is to adopt a Sub-stepping scheme (see Figure 5.14). The Sub-stepping scheme decomposes the time step into smaller ones with regard to the increase of deformation encountered. Final results are of much better quality since the sharp increase of η is better captured. However, the Sub-stepping scheme based on deformation is not adapted since it is applied at each step, but it is only necessary for large variation of η. As a matter of fact, a Sub-stepping scheme based on the stress variation should be much suitable but more cumbersome to implement.

Three cyclic triaxial simulations are depicted in Figure 5.15 and in Table 5.4. They consist in two undrained stress-driven and one drained strain driven `LAGAMINE` simulations. The stress control ensures the stress path strictly varies within the bounds $q = q_{off} \pm q_{cycl}$. On the other hand, the Matlab routine is mixed controlled, i.e. increments of deformation are enforced and a correction is applied if the stress path exceeds the prescribed bounds.

	Drainage	Loading
Simulation 1	Undrained	$q = 45 \pm 40$kPa
Simulation 2	Undrained	$q = 30 \pm 40$kPa
Simulation 3	Drained	$\epsilon_y = \pm 0.083\%$

TABLE 5.4: Cyclic simulation parameters.

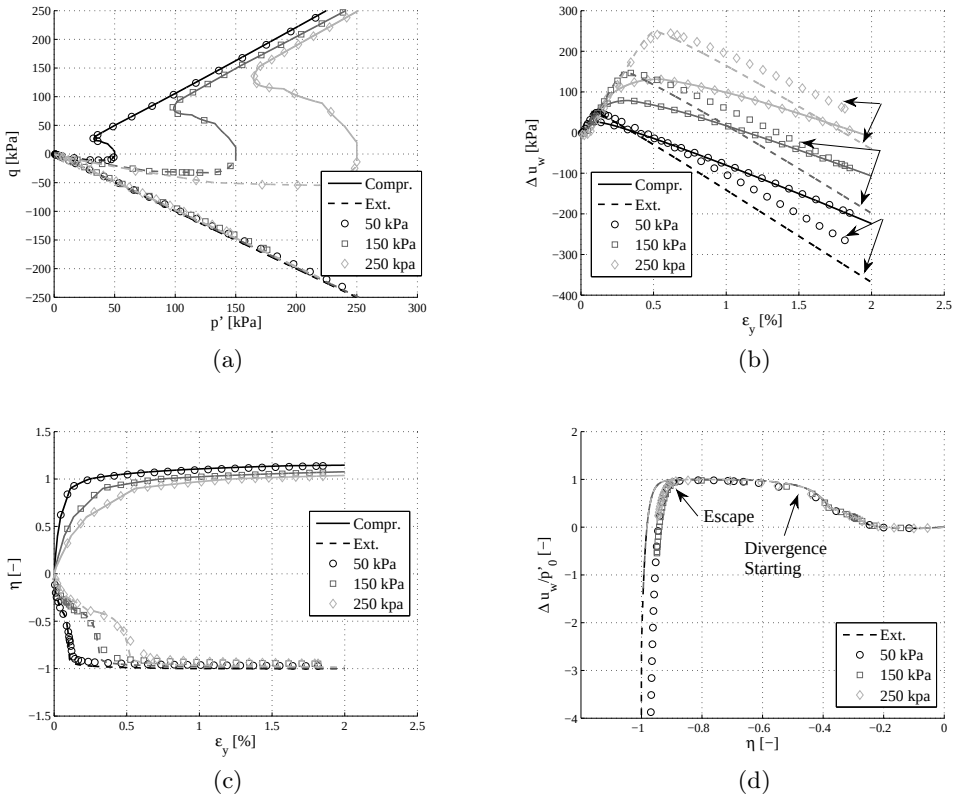

FIGURE 5.13: Monotonic undrained triaxial test (strain-driven). Comparison between implicit and analytical (explicit) formulations. Solid lines = compressive explicit simulations ; dashed lines = extension explicit simulations ; markers = implicit simulations.

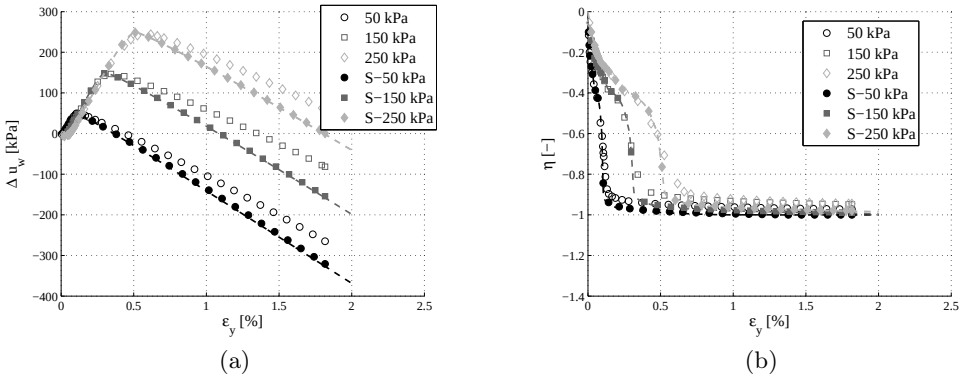

FIGURE 5.14: Monotonic undrained triaxial test (strain-driven) with subintegration (S-). Comparison between implicit and analytical (explicit) formulations. Solid lines = compressive explicit simulations ; dashed lines = extension explicit simulations ; markers = implicit simulations.

There is a very good agreement between these curves although a small error is propagated with regard to increasing number of cycles (see Figure 5.15a). Quantification of the error is not easy between two time dependent responses. An attempt to do it is illustrated in Figure 5.15d. Two stress states that share identical deviatoric stress and number of cycles are compared since they are supposed to be in the same configuration. The error measurement can be done on the mean effective stress, the deformation or the pore water pressure. This last possibility was adopted. Absolute difference on the accumulated pore water pressure is provided in Figure 5.15c with regard to the accumulated vertical deformation. The error plot alternates maximum and minimum q values. The divergence increases linearly at the beginning and starts oscillating when the stress path creates a close loop. Error observed when q is maximum is lower than the error when q is minimum

The second couple of Figures 5.15e and 5.15f presents a similar good agreement between the simulations. However, the stress path lies partially on the extension side and a flow deformation is triggered (see Figure 5.15e). This is well managed by the explicit routine, describing a butterfly wing loop before reaching initial liquefaction. On the other hand, the implicit scheme is unable to overcome the instability and simulation stops. This stop may be analysed as a failure (see Figure 5.15e) which finally also occurs for explicit simulation.

The third simulation in Figures 5.15g and 5.15h are fully strain-controlled. Pore water pressure increases gradually with the number of cycles and the envelop of deviatoric stress invariants decreases. In this case, the implicit model describes the butterfly wing pattern while the explicit model reaches initial liquefaction.
Once again, the simulations depicted prove the high sensitivity of the modelling of cyclic tests. However the major discrepancies are observed near the initial liquefaction or close to failure. Reality and numerical modelling have in common to be very sensitive, if the stress path reaches the initial liquefaction zone. Therefore it can be admitted the soil will fail and the algorithm does not need to present a surgical accuracy.

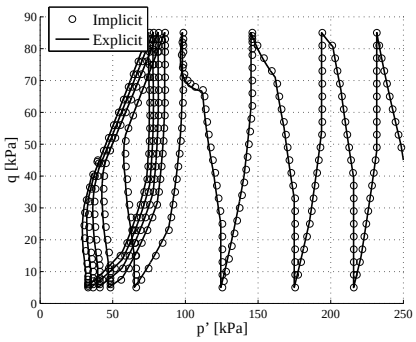

(a) Explicit mixed control/Implicit stress control (Simulation 1).

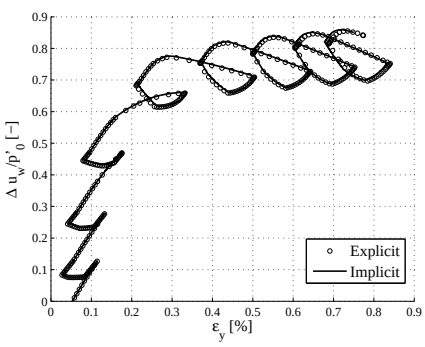

(b) Explicit mixed control/Implicit stress control (Simulation 2).

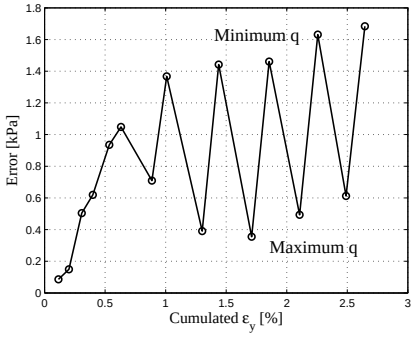

(c) Error accumulation during cyclic test described in Figures 5.15a and 5.15b (Simulation 1).

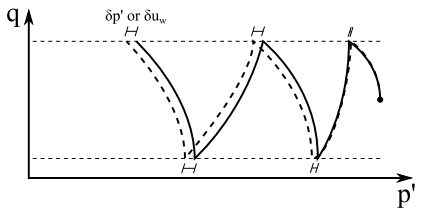

(d) Computation of the error as a variation of pore pressure or mean effective stress (Simulation 1).

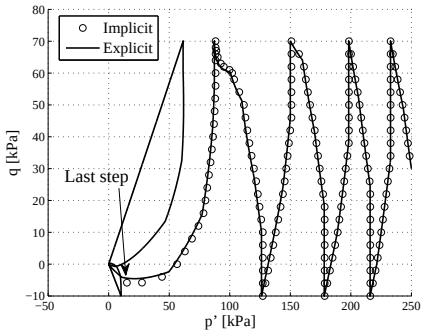

(e) Explicit mixed control/Implicit stress control (Simulation 2).

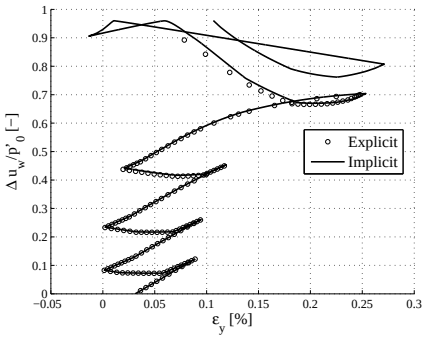

(f) Explicit mixed control/Implicit stress control (Simulation 2).

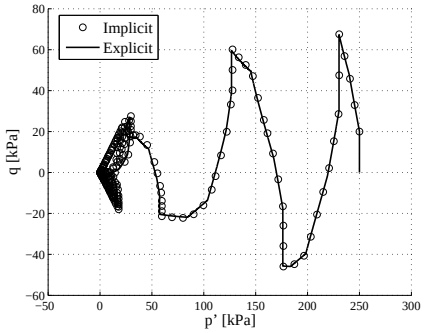

(g) Strain control (Simulation 3).

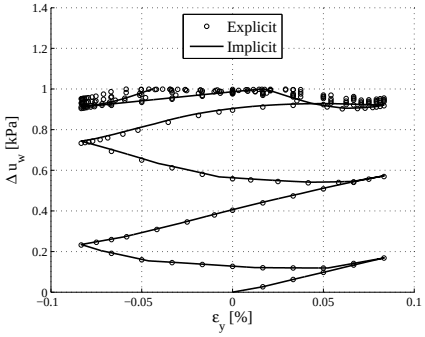

(h) Strain control (Simulation 3).

FIGURE 5.15: Cyclic undrained triaxial test. Comparison between implicit and analytical (explicit) formulations. Solid lines = compressive explicit simulations ; dashed lines = extension explicit simulations ; markers = implicit simulations.

5.4.2 Multiaxial simulations

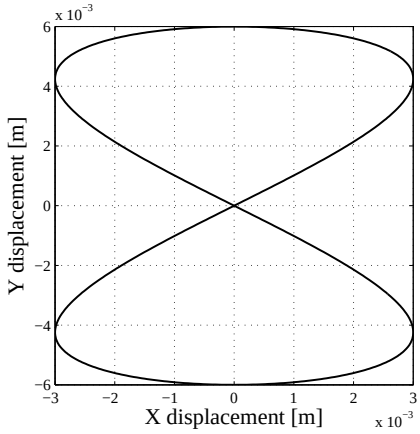

(a) Lissajous curve for shear loading $(n_\theta, \phi) = (0.5, 0)$.

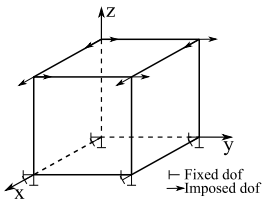

(b) Shear loading geometry

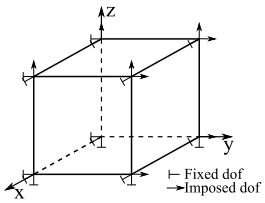

(c) Normal loading geometry

FIGURE 5.16: Prescribed displacement for complex loading.

Triaxial examples, though interesting, do not really highlight the capabilities of an integration scheme. Indeed, in this case, elastic predictor, normal and hardening directions of each surface are collinear. In this section, multiaxial drained simulations are carried out on a 3D finite element. Simulations are strain-controlled and the loading consists of a combination of two directions of displacement such that

$$x_1(\theta) = A_1 \cdot \sin\theta \tag{5.60}$$

$$x_2(\theta) = A_2 \cdot \sin(n_\theta \cdot \theta + \phi) \qquad \theta \in [0, 720]^\circ \tag{5.61}$$

where x_1 and x_2 are the two prescribed displacements, A_1 and A_2 are their amplitudes, n_θ and ϕ are parameters to be defined. The displacement imposed path describes a Lissajous curve. An example of such a displacement is provided in Figure 5.16a. In this case, imposed displacements, X and Y, of the upper face of the finite element, describe this pattern (see Figure 5.16b). In a second simulation provided hereafter, normal Y and Z displacements are imposed (see Figure 5.16c) and vary according to an identical Lissajous curve. In this section, contrary to simplified triaxial expression, the invariant of deviatoric stress is always positive, even in extension, i.e. $q \neq \sigma_1 - \sigma_3$.

A comparison of the results for different numbers of increments is provided in Figure 5.17. The first Figure 5.17a depicts variations of shear stresses, describing a hourglass shape. The loop is unclosed due to residual plastic deformation. The stress path related to this figure is not easily analysed (see Figure 5.17b). The non-associated volumetric behaviour induces variations of p producing an original stress path.
Information enclosed in this couple of figures is not sufficient to fully describe the stress state within the soil sample. Indeed, the six components of the stress state vary during the loading and a third invariant of stresses would be useful but once again difficult to interpret. A large error seems to be accumulated between D and F if only 37 load steps are used. As a matter of fact, between D and E, the variation of $\eta = q/p$ is high and therefore the volumetric behaviour is a source of error which introduces a deviation amplified between E and F. If the number of time steps is multiplied by four, the integration leads to a more acceptable accuracy.

Starting from $(x_1, x_2) = (0, 0)$, the Lissajous curve can be described in two opposite

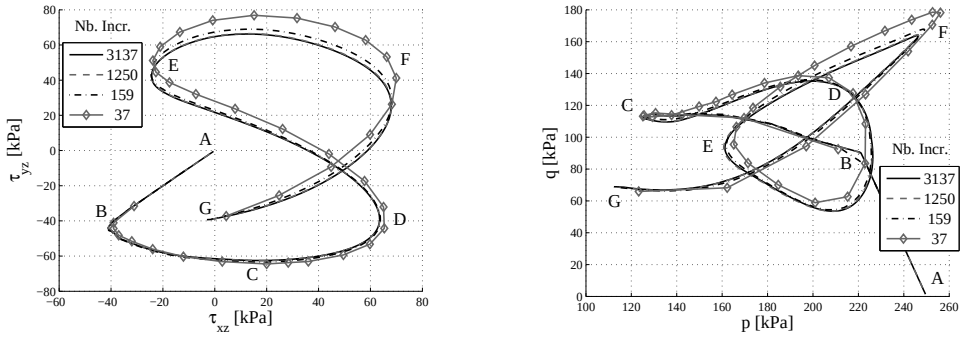

(a) (b)

FIGURE 5.17: Multi-axial simulations with imposed displacement in the X-Y plane. Starting point A, final point G. Influence of the number of time steps.

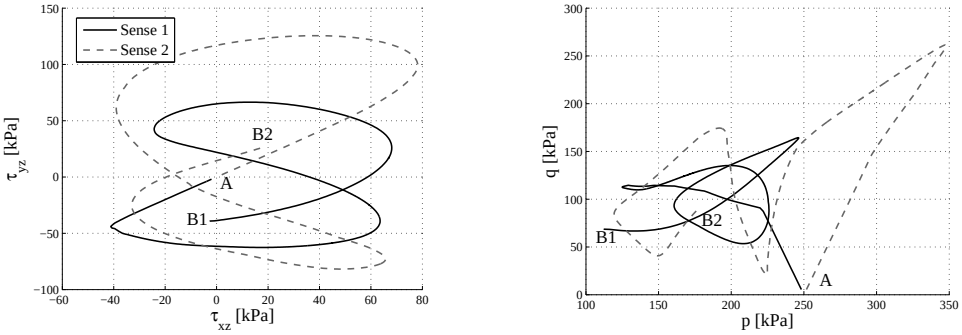

(a) (b)

FIGURE 5.18: Multi-axial simulations with imposed displacement in the X-Y plane : initially positive or negative tangential shear stresses. Starting point A, final point B1 or B2.

senses of rotation. Final results obtained are not symmetric, although a kind of scaling can be observed (see Figure 5.18a). This outcome underlines again that the volumetric plastic hardening rule strongly affects results. This is obvious in Figure 5.18b where the stress paths are definitely neither symmetric nor homothetic. Furthermore, reached final stress states are quite different.

A second example of multi-axial loading is illustrated in Figure 5.19. It consists in an identical 3D finite element but normal displacements are imposed onto two orthogonal faces (normal oriented towards Z and Y axis, see Figure 5.16c). The stress path followed by the material point is less complex than for a rotation. Thence, 36 time increments are nearly sufficient to provide its accurate representation.

It is interesting to compare the effect of the hardening translation rule, i.e. Mroz or Prager rule, on the stress path. This is done in the case of normal loading and results are provided in Figure 5.20. Initially, the results are identical but rapidly diverge. Finally the relations $\sigma_{yy} - \sigma_{zz}$ are totally distinct and the stress paths, though presenting both a V shape, are also different.
This figure shows that Mroz and Prager rule are not two ways of defining an identical hardening rule. They define two distinct models, since they do not represent the same behaviour, even for very small time steps. A comparison between two geometrical interpretations of these rules is illustrated in Figure 5.21. In this figure, hardening $\boldsymbol{\mu}$ and normal return $\hat{\mathbf{n}}$ directions are computed, as a function of an identical elastic predictor $\mathbf{s}_{tr}$. They are shown to be completely distinct from each other, especially the $\boldsymbol{\mu}^1$ direction. Therefore, results are

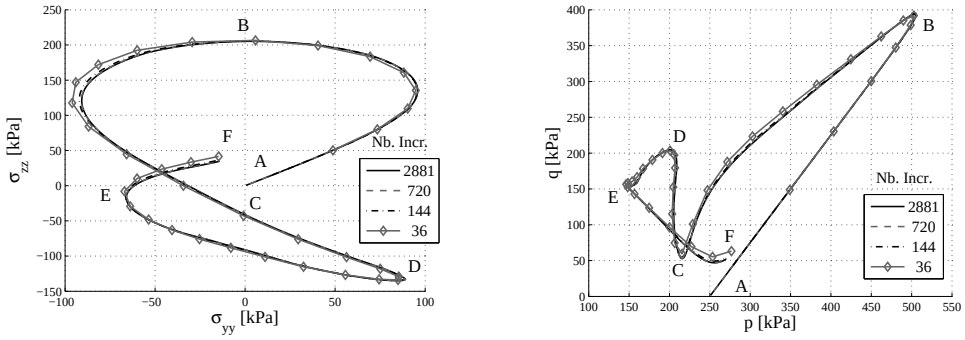

(a) (b)

FIGURE 5.19: Multi-axial simulations with imposed displacement in the Y and Z planes. Starting point A, final point F. Influence of the number of time steps.

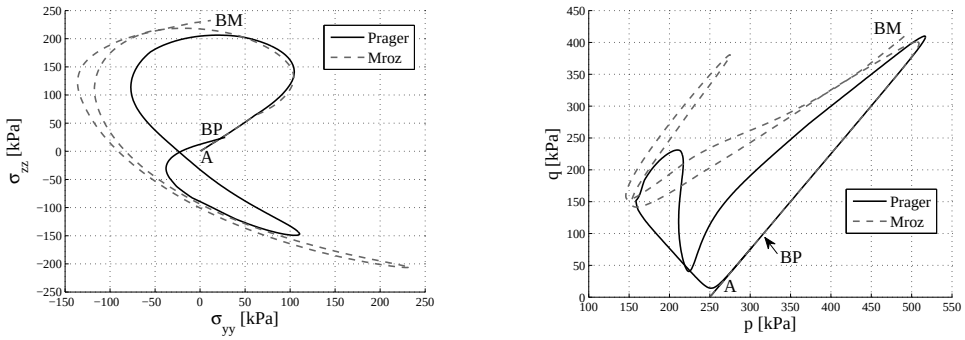

(a) (b)

FIGURE 5.20: Multi-axial simulations with imposed displacement in the Y and Z planes. Comparison between Prager and Mroz hardening rules. Starting point A, final point BM (Mroz) or BP (Prager).

obviously not identical. It must be pointed out that this divergence may only appear if a multiaxial loading path is considered. Indeed, during trixial simulations, all the aforementioned directions are collinear and both hardening rules lead to identical results.

5.4.3 Convergence of the local iterative process

The local convergence of the Newton iterative procedure can be easily checked in representing the evolution of the residual equations. Indeed, if derivatives of theses equations are correct and the initial guess of the solution is close enough, a quadratic rate of convergence is supposed to be asymptotically reached. A quadratic convergence rate induces that a residual r_i reduces between iterations k and $k+1$, such that [Mira et al., 2009]

$$r_i^{k+1} \approx C \cdot \left(r_i^k\right)^2, \tag{5.62}$$

where C is a constant. Therefore in a logarithmic space, this relation leads to

$$\log r_i^{k+1} = \log C + 2 \cdot \log r_i^k \tag{5.63}$$

which describes a straight line with a slope equal to 2 in logarithmic space. An example of such a rate of convergence is provided in Figure 5.22a for two steps of a drained triaxial test. Four residuals are represented and their tendency approaches to the quadratic convergence

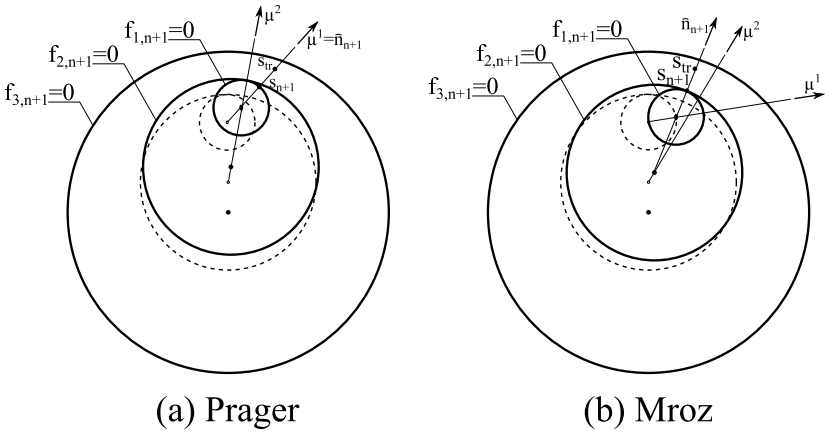

FIGURE 5.21: Comparison between Mroz and Prager hardening rules for nested surfaces. Distinct hardening directions for a similar initial stress state.

rate. Results are not straight lines but oscillate around the mean tendency. This can be due to several causes

- there are four unknowns that must be minimised together and describe a strongly non linear set of equations ;
- exact derivatives are cumbersome to obtain and some mistakes can still exist ;
- the implementation of these derivatives adds many possibilities of discrepancies ;
- the Jacobian matrix is really ill-conditioned, due to the disparity in the nature of unknowns.

However, most of the time, the algorithm converges and its efficiency is deemed acceptable. An example of divergence of the algorithm is provided in Figure 5.22b. Residuals clearly oscillate around their initial values and keep increasing. The line search algorithm is then applied to this case and finally leads to the convergence of the process (see Figure 5.22c).
The initial guess of the solution is of paramount importance. Indeed, the final solution obtained is clearly dependent on this value. For example, a non-linear set of equations possessing two unknowns (x_1, x_2) and four roots is solved for different initial conditions. The final solution provided by the Newton method as a function of the initial guess is provided in Figure 5.22d which clearly demonstrates this dependency.
However, in the Newton procedure implemented in the algorithm, this initial guess is difficult to evaluate *a priori*, which may cause the divergence of the algorithm. Demonstration of the uniqueness of a solution is a must in computational engineering. However such a mathematical demonstration is very cumbersome even for simple case, such as Von Mises surface type, [Simo and Hughes, 1998].

5.4.4 Accuracy

The accuracy of the integration algorithm might be assessed by numerical experiments. However, it does not replace a rigorous accuracy and stability analysis. Such a mathematical approach are very inaccessible especially for complex models and algorithms. The so-called *isoerror maps*, based on strain-controlled increments, are derived for that purpose, [Ortiz and Popov, 1985; Simo and Hughes, 1998]. It consists in applying a combination of increments of

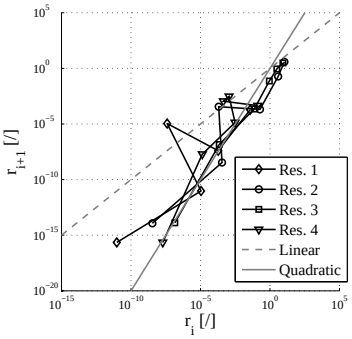

(a) Classic Newton method step 6

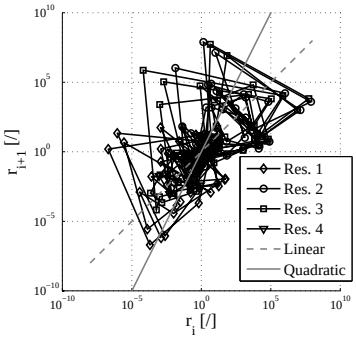

(b) Classic Newton method step 13

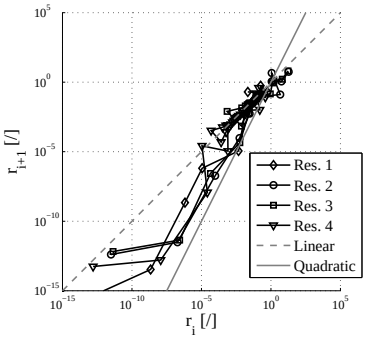

(c) Newton method with line search

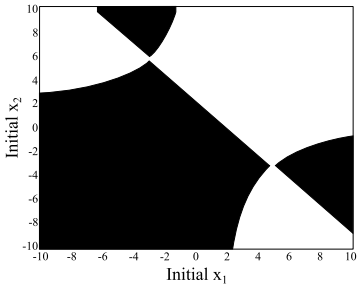

(d) Two possible solutions of a system of equations as a function of the initial guess (x_1, x_2). Solution 1 in black and solution 2 in white.

FIGURE 5.22: Local convergence of the Newton method for a drained triaxial test.

deformation in two directions $(\Delta\epsilon_1, \Delta\epsilon_2)$, from a converged stress state $(\boldsymbol{\sigma}_n, \boldsymbol{\alpha}_n)$ at step n (see Figure 5.23). Then, the updated stress state returned by the algorithm, $\boldsymbol{\sigma}_{n+1}$, is compared with an *exact* solution $\boldsymbol{\sigma}^*$, obtained from a high number of smaller steps, e.g. 200 hereafter. Thence, the error can be defined through

$$Error = \frac{\sqrt{(\boldsymbol{\sigma}^* - \boldsymbol{\sigma}_{n+1}) : (\boldsymbol{\sigma}^* - \boldsymbol{\sigma}_{n+1})}}{\sqrt{\boldsymbol{\sigma}^* : \boldsymbol{\sigma}^*}}. \tag{5.64}$$

Four isoerror maps are illustrated in Figures 5.24-5.27, in a complexifying sequence. The first two maps are obtained for a single surface model. The last two consider nested surfaces. All the surfaces are deemed to be isotropically centred at the beginning of the test and their initial mean stress is equal to 100kPa. Details of the simulations are provided in Table 5.5. Increments of deformation are applied in vertical and horizontal directions, while the deformation perpendicular to this plane is kept equal to zero. These increments are normalised by the volumetric reference strain as

$$k = \frac{p'_0}{K_{ref}} = 1.5 \cdot 10^{-3}. \tag{5.65}$$

The first isoerror map in Figure 5.24a starts from an isotropic stress state. The pattern of this figure can be explained in the light of the absolute error in Figure 5.24c, the mean stress in Figure 5.24d and the deviatoric stress in Figure 5.24d. The symmetry is obvious since the starting state is isotropic. Thence increments of deformation in both directions have an identical effect. If $(\Delta\epsilon_1, \Delta\epsilon_2) \to (0, 0)$, the error is null. In this case, the stress state lies

	Nb. surfaces [-]	Start	Active surf.	$\eta_{init.}$
Simul. 1	1	elastic	/	0.0
Simul. 2	1	plastic	/	0.448
Simul. 3	9	elastic	/	0.0
Simul. 4	9	plastic	3	0.358

TABLE 5.5: Salient parameters that define the different isoerror maps. "Nb. surfaces", is the number of surfaces that compose the model; "Start", is the state at the beginning of the algorithm; "Active surf.", is the active surface at the beginning; "$\eta_{init.}$", is the initial reduced deviatoric stress.

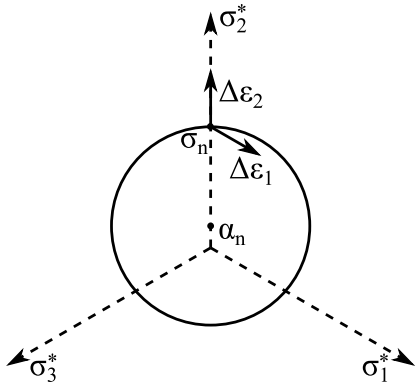

FIGURE 5.23: Isoerror map concept in the deviatoric plane. $\boldsymbol{\sigma}_n$ is the converged stress state; $\boldsymbol{\sigma}_i^*$ are the projection of the principal stress axes in the deviatoric plane; $\Delta\epsilon_1$ and $\Delta\epsilon_2$ are the directions of increments of deformation.

within the elastic zone and no error is possible.
The highest absolute error is encountered when $\Delta\epsilon_1$ and $\Delta\epsilon_2$ are maximum (see Figure 5.24b), which is expected, since the global deformation is maximum. In this case, the final deviatoric stress (see Figure 5.24d) is maximum but so is the mean stress (see Figure 5.24c). Therefore the relative error is not the highest. On the contrary, relative error is maximum when either $\Delta\epsilon_1$ or $\Delta\epsilon_2$ is maximum and the other one is null. This corresponds to a high deviatoric stress but a moderate mean stress increase, i.e. a high reduce deviatoric stress η (see Figure 5.24e). In this case, the predictor and return directions are collinear, since initial position of the yield surface $\boldsymbol{\alpha}_n$ is equal to zero, thence

$$\hat{\mathbf{n}}_{n+1} = \frac{(1-\theta)\cdot\hat{\mathbf{n}}_n + \theta\cdot\hat{\mathbf{n}}_{n+1}}{\|(1-\theta)\cdot\hat{\mathbf{n}}_n + \theta\cdot\hat{\mathbf{n}}_{n+1}\|} = \frac{\mathbf{s}_{tr}}{\|\mathbf{s}_{tr}\|}. \tag{5.66}$$

Thus, the error encountered is only due to the linearisation of the volumetric plastic variation which depends on $P''_{n+\theta}(\eta)$ and the highest error appears for the highest variation of η.

The second simulation depicted in Figure 5.25 ceases to be symmetric. Indeed, the initial stress state before tracing the map is obtained after a drained compressive triaxial test. Thence, increments $\Delta\epsilon_1$ or $\Delta\epsilon_2$ do not have a similar effect. Furthermore, the pattern is not easy to analyse in this case. An interesting observation is that the initial reduced deviatoric stress, initially equal to 0.448 decreases for a non negligible number of $(\Delta\epsilon_1, \Delta\epsilon_2)$ combinations, as shown in Figure 5.25b. This is the indication the stress state describes a rotation onto the yield surface. This spiralling effect is not easy to represent and is more accurately described with numerous substeps.
Two points near the origin of the axes have a final elastic state. Therefore, a final unloading

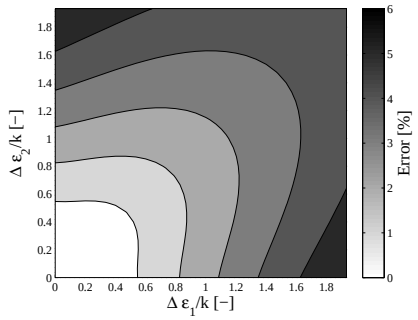

(a) Isoerror map

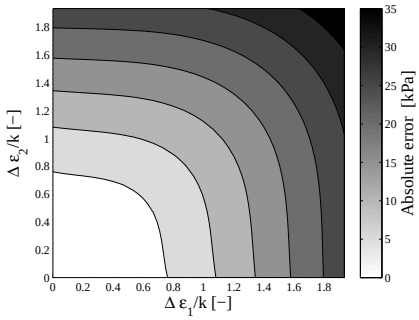

(b) Absolute isoerror map

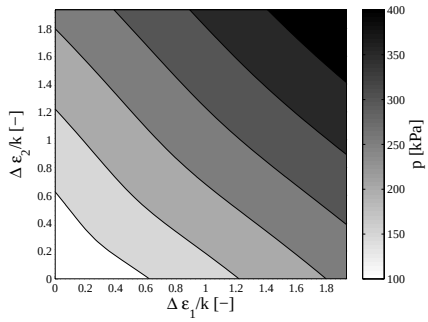

(c) Mean stress in the end

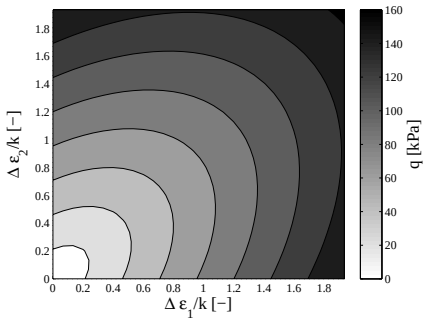

(d) Deviatoric stress in the end

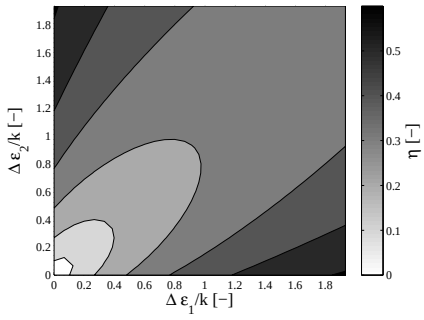

(e) Reduced deviatoric stress

FIGURE 5.24: Simul. 1, single surface model, starting point = elastic.

occurs. This unloading might only hold for a small part of the stress path over the time step and can be ignored for a unique increment. This explains the high relative error observed for $(\Delta\epsilon_1/k, \Delta\epsilon_2/k) = (0.13, 0)$. Finally, this error is relatively important where η varies a lot, as in the previous case.

The model composed of multiple surfaces provides a pattern more complex to dissect (see Figure 5.26). The initial isotropic state leads again to a symmetric map. However, the pattern is not as smooth as shown in the single surface case. Actually, a new source of error is introduced by the nested surfaces. If the final active surface is different from the reference solution, the plastic deformation is miscalculated. Figure 5.26b represents the combination of $(\Delta\epsilon_1, \Delta\epsilon_2)$ which finally activates a wrong surface with regard to the reference solution. The dispatching of the wrong final surface explains the non smooth pattern observed in Figure 5.26a.

The last isoerror map combines nested surfaces and a non-isotropic initial state (see Figure 5.27a). Once again, it presents a pattern similar to the one described for a single surface.

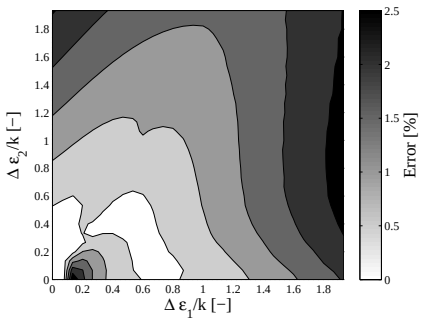

(a) Isoerror map

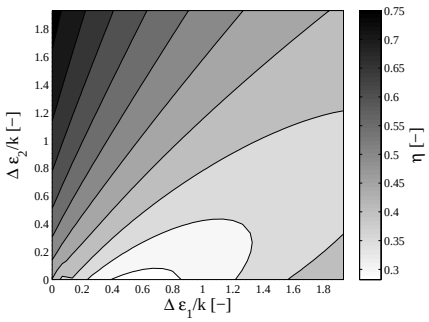

(b) Reduced deviatoric stress

FIGURE 5.25: Simul. 2, single surface model, starting point = plastic.

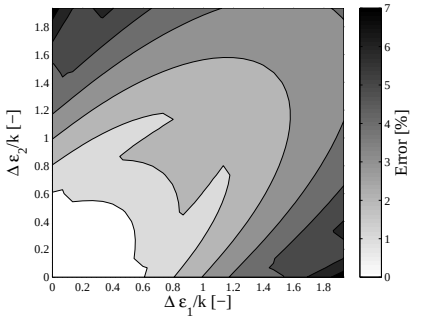

(a) Isoerror map

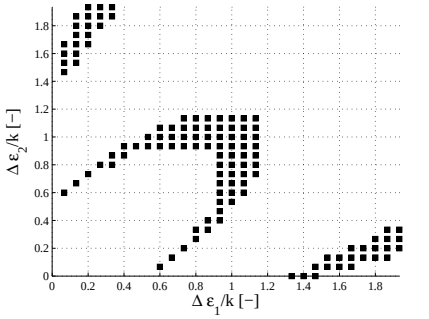

(b) Final active surface, a marker indicates a difference between reference and implicit.

FIGURE 5.26: Isoerror map for a multi-surface model : Simul. 3 (starting point = elastic)

However, the error is amplified by the wrong final activated surface (see Figure 5.27b).

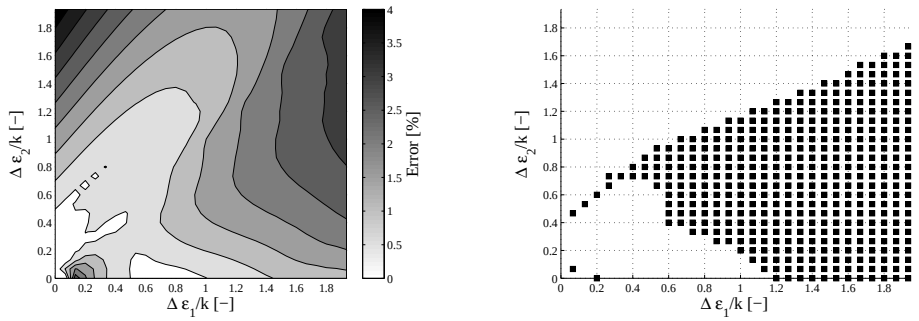

(a) Isoerror map

(b) Final active surface, marker indicate a difference between reference and implicit.

FIGURE 5.27: Isoerror map for a multi-surface model : Simul. 4 (starting point = plastic)

5.5 Conclusion

This chapter highlights salient features of the numerical implementation of the Prevost model in the finite element code `LAGAMINE`. The first part is dedicated to the choice of an integration scheme. In this work, a closest point projection algorithm is adopted. The mid-point rule is selected for the return mapping direction, i.e. it is computed at step $n + \theta$. This scheme theoretically ensures an unconditional stability and a second order accuracy as well.
In this work, the Prager implicit translation rule is adopted to rule the kinematic hardening of the surfaces. It overcomes discrepancies of the Mroz translation rule, such as the non-smooth variation of flow direction. Finally a set of non-linear equations is elaborated and solved by a Newton procedure coupled with a line search algorithm in case of bad convergence. The elastoplastic tangent operator is computed by perturbation, to avoid cumbersome derivatives.
Numerical triaxial simulations are proposed to ensure the implicit integration algorithm corresponds to the actual model. The method exhibits a satisfactory accuracy with respect to the step size. However, it is shown that it encounters sometimes step reduction due to a loss of convergence in the Newton procedure. Undrained triaxial tests highlight the requirement of Sub-stepping for extension triaxial simulations. As a matter of fact, the Sub-stepping requirement should only be necessary for few time steps, describing the well-known elbow of the stress path. In this particular case, a large variation of reduced deviatoric stress η spans over a narrow range of deformation. Therefore, a Sub-stepping strategy based on stresses rather than strains should be employed.
Cyclic triaxial undrained tests also present a good accuracy. However it is shown that error is accumulated progressively with each cycle. In one particular case, the algorithm is not able to reproduce an unstable stress path. However, this discrepancy is due to the stress-control strategy rather than to the algorithm itself.
Although they can not be compared to an explicit integration of the equations of the model, a self-comparison of results obtained for different time step sizes shows that the algorithm manage pretty well complex loading paths. A comparison between Mroz and Prager rules for such a loading highlights they finally define two distinct models. This effect is reinforced by the non associated volumetric plastic behaviour.
Convergence of the algorithm was proven to be locally of quadratic rate, even if slightly oscillating. It assumes the derivatives of the analytical local Jacobian are correct. A special case of non convergent procedure is depicted and its overcoming by a line search algorithm as well. Finally the accuracy of the method is illustrated by the mean of isoerror maps. They present complex patterns difficult to analyse. However, compared with the step size, error encountered is more than acceptable.

Chapter 6

Interfaces

The meeting of two personalities is like the contact of two chemical substances: if there is any reaction, both are transformed.

Carl Jung

Contents

6.1 Introduction

According to the Encyclopaedia Britannica, the tribology is *the study of the interaction of sliding surfaces*. This very complex interdisciplinary topic is the cross-breeding between mechanical engineering, material science and chemistry. It involves many different phenomena such as friction, wear, lubrication and spans over many fields from metal forming to medicine. Although the word *tribology* was only coined fifty years ago, empirical knowledge of the surface interaction effects is far much older [Dowson, 1998][1].

History of tribology started during the paleolithic period, when the man conquered fire and gave it birth by heating friction of wood on wood. Early Egyptian builders were known to pour water in front a wood sledge in order to reduce friction during the transportation of statues, in 2400 b.c. ! Aristotle in his book Quaestiones Mechanicae *recognized the force of friction and further observed that it was lower for round objects*. Romans and Celts also dealt with friction phenomena for their chariots, mills and other revolving wooden platforms.
However, a long time passed before the Renaissance and its brilliant torch bearer, Leonardo da Vinci, brought science out of its torpor. He theorised the first laws of friction and stated, in his Codex Atlanticus (see in Figure 6.1), that

- the force of friction is directly proportional to the applied load ;
- the force of friction is independent of the apparent area of contact.

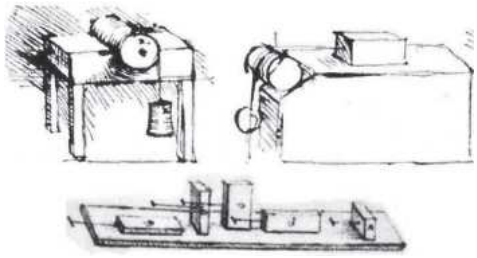

FIGURE 6.1: Extracted of codex Atlanticus, Leonardo da Vinci's notebooks.

The still unnamed tribology continued to develop, especially in the clock and machinery fields. Impulsed by Francis Bacon, the advent of modern science started stimulating researchers and great scientists worked on friction topics between 17th and 18th centuries. Guillaume Amontons rediscovered classic rules and identified the roughness of the surface as the origin of friction. Hooke worked on the rolling of a body. Euler introduced the greek letter μ to describe friction resistance and wrote the first mathematics about friction [Euler, 1750]. Newton related friction and viscosity [Newton, 1686]. All the foundations were then laid for the industrial revolution. The rise of machines increased the demand of tribology understanding and it started scattering over all fields of science which are impossible to track extensively. Charles Augustin Coulomb [Coulomb, 1821] and Charles Hatchett are two more distinguished contributors that deserve to be cited.

Afterwards, friction and mechanical contact became only a part of the tribology. Mathematicians such as Hertz, resolved analytically equations of contact mechanics [Hertz, 1881]. The advent of computer opened a new field of possibilities and the first contact finite element arose in the last sixties [Goodman et al., 1968] and after [Ghaboussi et al., 1973]. The eighties marked a big step forward in contact mechanics, see for instance [Beer, 1985],[Curnier,

[1]The major part of the historical content of this introduction is based on this reference.

1984],[Charlier and Cescotto, 1988] and [Gens et al., 1988]. An early nineties review about contact mechanics shows an already abundant literature [Zhong and Mackerle, 1992].

From that point, contact and interface should be differentiated. While the contact is restricted to a physical link between two solids, interface relates any different media. According to the Encyclopaedia Britannica the Interface is *a surface separating two phases of matter, each of which may be solid, liquid, or gaseous.* This field is much more large than the contact mechanics and tribology. However, in this chapter, the focus is restricted on the hydro-mechanical behaviour of the interface medium between two solids. An exhaustive review of literature, even limited to this particular case would be a herculean task since many topics are involved and extensively developed in many books. Therefore a subjective bibliography summary is adopted and representative references are grouped in different topics hereafter.

- **Analytic solutions.** Analytic method field is still a seething domain of research. A formulae-free review of recent advances can be consulted in [Barber and Ciavarella, 2000].

- **Geometric considerations.** Accurate and efficient search algorithms are of uttermost importance to detect contact between two solids, to compute gap distance in between, see for example [Wang and Nakamachi, 1997] and to ensure an impenetrability constraint [Belytschko and Neal, 1991].

- **Numerical formulation.** Different approaches are addressed to solve the contact problem within the finite element framework. Some authors adopt a continuum description of the interface with remeshing [Wang and Wang, 2006]. Some others use thin layer elements [Sharma and Desai, 1993] or limit models [Wang et al., 2003]. The most widespread approach is the zero-thickness interface element, see for example [Cescotto and Charlier, 1993] or [Day and Potts, 1994] for a mixed formulation.

- **Algorithmic.** Each formulation requires special tools to integrate constitutive laws [Christensen et al., 1998] and [Giannakopoulos, 1989]. Several algorithms are also available in order to ensure the contact constraint : Simo and Laursen [1992] develop an augmented Lagrangian method; Habraken et al. [1998] adopt a penalisation method; Zavarise et al. [1998] use a cross-constraint based method. A material point method has been frequently applied to the mechanical contact problem in [Ma et al., 2014].

- **Physics and constitutive laws.** Exact physical behaviour of interfaces is not yet perfectly known. The first mathematical description of the friction laws in [Coulomb, 1821] is frequently used to characterise the mechanical behaviour of interfaces. Thanks to necessary experimental back-up, many constitutive laws have been developed related to numerous materials [Wriggers, 2006]. Multiphysics couplings [Alonso et al., 2013] for example are at the leading edge of research. The cyclic behaviour of interfaces is also of paramount importance in many engineering applications [Shahrour and Rezaie, 1997].

- **Applications.** Practical use of interface modelling spans over many fields. Rock mechanics was the historical cradle of contact finite elements with the study of jointed rocks [Goodman et al., 1968]. It is still an ongoing topic with the hydro-mechanical coupling of the joints [Guiducci et al., 2002] and [Segura and Carol, 2004]. Mechanics produces many fields of interest such as metal forming, which mobilises many researchers [Charlier and Cescotto, 1988] and [Wriggers, 2006]. Soil mechanics also contributes to the diversification with pile installation [Sheng et al., 2005] or offshore foundation [Cerfontaine et al., 2014] modelling. Finally medicine and biomechanics are an expanding and very complex fields of applications [Rojek and Telega, 2001].

In this chapter, the bases of contact mechanics are briefly reviewed. Contact kinematics and geometric considerations are established. They allow the definition of the weak continuous formulation of the mechanical contact. In rock and soil mechanics, interfaces and fault offer most of the time preferential paths for fluid flow. Therefore, the contact theory is extended to hydro-mechanical couplings.
The particular case of the 1D hydro-mechanical element implemented in the finite element code `LAGAMINE` is then extensively developed, from the constitutive laws to the assembling of the stiffness matrix. A geometric storage flow is added to the mass equilibrium in order to tackle the unsticking problem. Simple 1D examples are then provided to highlight the physics hidden behind this phenomenon. A comparison between 1D and 2D geometries and a simple loading case is also addressed.

6.2 General concept of contact problem

In the following, theoretical approach is mainly based on and influenced by the prolific work of Peter Wriggers, and more precisely refers to [Wriggers, 1995; Wriggers and Zavarise, 2004; Wriggers, 2006] for the mechanical part. This section is only a humble summary and interested reader should refer to the abundant literature for more details.

6.2.1 Definition of the problem

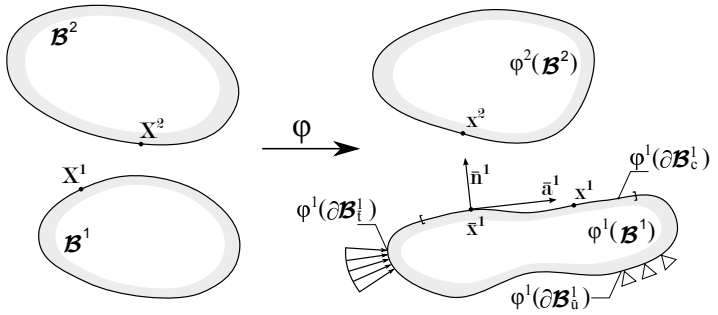

FIGURE 6.2: Statement of the problem, mapping of two deformable bodies in their current configuration, after [Wriggers and Zavarise, 2004]. $\partial\mathcal{B}^1_c$ denotes the boundary part on which contact might occur, $\partial\mathcal{B}^1_{\bar{t}}$ stands for the traction loads imposed and $\partial\mathcal{B}^1_{\bar{u}}$ stems for imposed displacements.

Mechanical part

Let us consider two deformable bodies $\mathcal{B}^\alpha$ with $\alpha = 1, 2$ (see in Figure 6.2). At time $t \in \mathbb{R}^+$, the mapping $\boldsymbol{\varphi}^\alpha_t : \mathcal{B}^\alpha \to \mathbb{R}^3$ associates the points $\mathbf{X}^\alpha$ of the reference configuration $\mathcal{B}^\alpha$ onto their current positions $\mathbf{x}^\alpha = \boldsymbol{\varphi}^\alpha_t(\mathbf{X}^\alpha)$.
Both bodies are subject to boundary conditions on $\partial\mathcal{B}^\alpha$, identical to those defined in Section 2.4.1. However, a new non-classic condition holds in addition on $\partial\mathcal{B}^\alpha_c$, where the contact occurs. The movement of solids is considered quasi-static, i.e. inertial effects can be neglected. Finally the mechanical behaviour of the solid is deemed rate independent.

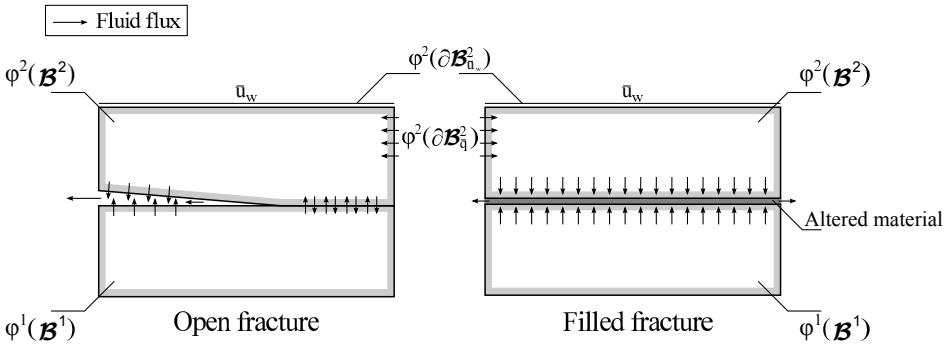

FIGURE 6.3: Example of fluid flows for an opened or a filled fracture between two rock blocs. Arrows stem for fluid flux.

Hydraulic part

In rock mechanics, fractured media are either empty or filled with altered material. Their proximity, even if they do not contact, creates a coupling between the flows that occur in both volumes (see Figure 6.3). If both walls of a fault are in contact, a head loss might occur

due to the altered material in between. Moreover, the fault creates a preferential path for fluid flow to the outer world. If the fracture is open and both sides do no contact, there is a convective exchange with ambient atmosphere. Consequently mechanical and hydraulic effects are coupled, since an opening or closing of the fracture influences the hydraulic behaviour.
In soil mechanics, the role of interfaces (soil-structure interaction) is of uttermost importance (see Figure 6.4).

(a) During the driving of a pile into the soil, a close layer of sand might be progressively altered [White and Lehane, 2004; Holeyman and Kikuchi, 2005]. The dilation or contraction of that thin layer alters its permeability properties and the normal effective stress.

(b) The horizontal loading of the pile may give birth to the unsticking between soil and pile at the interface [Stuyts et al., 2011]. Therefore, the hydraulic flow is perturbed. When dealing with offshore foundations, the void between both sides of the interface is filled with water. Moreover, if the horizontal load is cyclic, the fault opens and closes which involves a succession of contacts and losses of contact.

(c) Anticipating on the chapter 7, it can be shown that suction caissons combine these effects. The soil might be altered along the shaft, which modifies its permeability. Inside the caisson, unsticking of the soil and the structure occurs when the latter is in tension. This unsticking vertical effect causes the "suction effect" resisting to the uplift loading.

These examples endorse the need of interface boundary conditions able to reproduce the fluid flows appearing in that particular conditions. Let us consider the two previous bodies $\mathcal{B}^\alpha$ with $\alpha = 1, 2$, which are deemed sufficiently close from each other to involve hydraulic interactions. Therefore, in addition to the classic hydraulic boundary conditions defined in Section 2.4.2, a non-classic boundary condition, which is fluid pressure dependent, holds on $\partial\mathcal{B}_c^{f,\alpha}$.
The mechanical contact interface $\partial\mathcal{B}_c^\alpha$ is different from the hydraulic contact interface $\partial\mathcal{B}_c^{f,\alpha}$. Indeed, considering the case of an open fracture between two rock blocs (see Figure 6.3), mechanical contact between walls of the interface occurs only on a part of the total length of both blocks. On the other hand, hydraulic flow holds for the whole interface between the blocks, for the open and close parts of the fracture as well.

6.2.2 Contact kinematics

When dealing with contact mechanics, the concept of gap function, measuring the distance between two bodies is of uttermost importance. Every point $\mathbf{x}^2$ lying on the contact boundary $\partial\mathcal{B}^2$ can be related to a point $\bar{\mathbf{x}}^1(\bar{\boldsymbol{\xi}}) \subset \partial\mathcal{B}^1$ (see Figure 6.2), such that

$$g_N\left(\bar{\boldsymbol{\xi}}\right) = \min_{\mathbf{x}^1 \subseteq \varphi(\partial\mathcal{B}_c^1)} \|\mathbf{x}^2 - \mathbf{x}^1(\boldsymbol{\xi})\|, \tag{6.1}$$

where $\boldsymbol{\xi}$ is the vector of convective coordinates describing the surface $\partial\mathcal{B}^1$ and $\bar{\boldsymbol{\xi}} = (\bar{\xi}^1, \bar{\xi}^2)$ are the coordinates of the projected point $\bar{\mathbf{x}}^1$ in this basis. The uniqueness of that point induces the implicit hypothesis that the boundary is at least locally convex. The unit normal vector $\bar{\mathbf{n}}_1$ and the tangent (non-unit) vector $\bar{\mathbf{a}}_1$ are defined at point $\bar{\mathbf{x}}_1$. Thence, the gap function reads

$$g_N = \left(\mathbf{x}^2 - \bar{\mathbf{x}}^1\right) \cdot \bar{\mathbf{n}}^1. \tag{6.2}$$

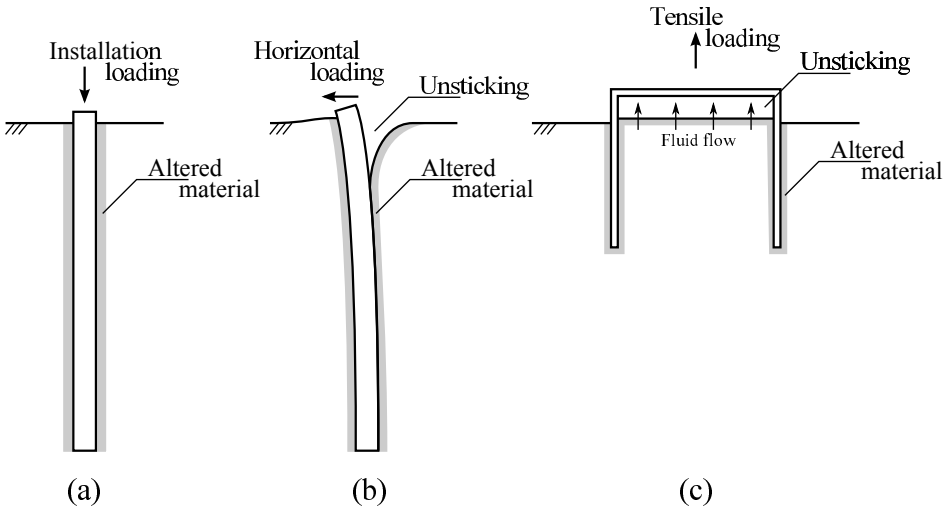

FIGURE 6.4: Examples of the role of interface in soil mechanics. (a) pile driving (b) pile horizontal loading (c) offshore suction caisson.

Equation (6.2) means that the point $\bar{\mathbf{x}}^1$ is the closest point projection of the so called "slave" point $\mathbf{x}^2$ onto the master surface $\varphi^1(\partial\mathcal{B}^1)$. Though its name, the gap function g_N defines either a gap ($g_N \geq 0$) or a penetration distance ($g_N < 0$), if interpenetration of both solids is allowed.

The partition of the two bodies into a slave and a master breaks the symmetry and attaches more importance to one of the surfaces. This difference tends to vanish when the exact non penetration condition is exactly satisfied [Wriggers and Zavarise, 2004]. Some authors propose to manage equally both sides of the interface [Habraken et al., 1998], which requires a special algorithmic treatment.

6.2.3 Ideal Mechanical contact constraint

Normal constraint

Two approaches can be adopted to ensure the contact constraint. A first low-precision contact approach readily ensures that no geometric penetration of both bodies occurs and that the stress distribution on the contact zone is accordingly computed [Wriggers, 2006]. The low-precision terminology is adopted in the sense that the contact is described on a geometric basis and is not ruled by a specific constitutive law. The second approach describes the contact phenomena with a higher precision. It involves a precise knowledge of the micro-mechanical behaviour of the interface and computes stress distribution based on a more complex constitutive law.
The former approach will be described hereafter. However this description is "ideal" and is mathematically more convenient. Indeed, it does not correspond to reality where asperities introduce non-linearities in the normal behaviour, as it would be described later on.

The condition that prevents the penetration of body $\mathcal{B}^1$ into $\mathcal{B}^2$ is stated as $g_N \geq 0$. If contact occurs ($g_N = 0$), the associated normal component ($p_N'^1$) of the effective Cauchy stress vector ($\mathbf{t}^1$) along the interface must be non-zero

$$\mathbf{t}^1 = p_N'^1 \cdot \bar{\mathbf{n}}^1 + t^1_{T,\beta} \cdot \bar{\mathbf{a}}^1_\beta \qquad \beta = 1, 2, \tag{6.3}$$

where $t^1_{T,\beta}$ are the tangential components of the stress tensor in two orthogonal directions. The action-reaction principle entails $\mathbf{t}^2 = -\mathbf{t}^1$ at the contact point. The Hertz-Signorini-

Moreau condition (Equation(6.4) [Wriggers, 2006]) is verified if the contact is frictionless, i.e. $t^1_{T,\beta} = 0$, such that

$$g_N \geq 0, \qquad p'_N \geq 0, \qquad p'_N \cdot g_N = 0. \tag{6.4}$$

If a gap exists between both solids, i.e. $g_N > 0$, the contact pressure is null. On the other side, a contact $g_N = 0$ involves positive contact pressure. This condition is referred to the Karush-Kuhn-Tucker condition in optimization theory [Luenberger and Ye, 2008].

Tangential constraint

When both sides are in contact, two cases have to be distinguished : the stick and slip states. In the former, two points in contact are not allowed to move in the tangential direction. In the latter case, they are. The first condition implies that no relative tangential motion occurs during the displacements of the bodies, meaning that the relative coordinates of the closest point projection $\bar{\mathbf{x}}^1$ does not change

$$\dot{\boldsymbol{\xi}} = \mathbf{0}. \tag{6.5}$$

The transition from stick to slip state is ruled by a criterion defining a threshold of admissible shear stress. Anticipating on constitutive law definitions, it can be defined as

$$f(\mathbf{t}^1) \leq 0. \tag{6.6}$$

If $f = 0$, the slip condition stands and a plastic relative tangential displacement occurs $\dot{g}^{sl}_T \geq 0$. Otherwise, both bodies are stuck and no relative motion occurs, i.e. $\dot{g}^{sl}_T = 0$. A formalism identical to Equation(6.4) [Laursen and Simo, 1993] might be employed to write these conditions

$$\dot{g}^{sl}_T \geq 0, \qquad f(\mathbf{t}^1) \leq 0, \qquad \dot{g}^{sl}_T \cdot f(\mathbf{t}^1) = 0. \tag{6.7}$$

Stress and deformation

In the following, normal and tangential deformation rates are grouped together in the vector

$$\dot{\mathbf{g}} = \left[\dot{g}_N \quad [\dot{\mathbf{g}}_T]^T\right]^T, \tag{6.8}$$

where $\dot{\mathbf{g}}_T$ is the vector of the variation of relative tangential displacement. It is a scalar in case of 2D geometry. Normal and tangential stresses are merged into the tensor $\mathbf{t}$ previously described in Equation(6.3)

$$\mathbf{t} = \left[p'_N \quad [\mathbf{t}_T]^T\right]^T. \tag{6.9}$$

6.2.4 Continuum description of the mechanical contact

First of all, a mechanical contact problem is nothing but a classic problem of solids mechanics with an additional constraint [Zavarise et al., 1998]. Therefore, each body $\mathcal{B}^\alpha$ verifies the classic equilibrium equations stated in Section 2.4.1, i.e.

$$\begin{aligned} \mathrm{div}\boldsymbol{\sigma} + \bar{\mathbf{f}} = \; & 0 \quad \text{in}\, \mathcal{B}, && (6.10)\\ \mathbf{x} = \; & \bar{\mathbf{x}} \quad \text{on}\, \partial\mathcal{B}_{\bar{x}}, && (6.11)\\ [\boldsymbol{\sigma}]^T \cdot \mathbf{n} = \; & \bar{\mathbf{t}} \quad \text{on}\, \partial\mathcal{B}_{\bar{t}}, . && (6.12) \end{aligned}$$

The solution of the problem consists in finding the field of displacement $\Delta\mathbf{x}$ for all $\mathbf{x} \in \mathcal{B}$ that verifies Equation(6.10)-(6.12), but is subject to the constraint inequality $g_N \geq 0$ over $\partial\mathcal{B}^\alpha_c$.

Therefore, considering a field of virtual velocities $\delta\dot{\mathbf{x}}$, the classic weak form of virtual power principle, Equation(2.31), including contributions of both solids is rewritten as

$$\sum_{\alpha=1}^{2}\int_{\varphi^\alpha(\mathcal{B}^\alpha)}\boldsymbol{\sigma}\cdot\boldsymbol{\epsilon}\left[\delta\dot{\mathbf{x}}\right]\,\mathrm{d}V \geq \sum_{\alpha=1}^{2}\left[\int_{\varphi^\alpha(\mathcal{B}^\alpha)}\bar{\boldsymbol{f}}\cdot\delta\dot{\mathbf{x}}\,\mathrm{d}V+\int_{\varphi^\alpha\left(\partial\mathcal{B}_{\bar{t}}^\alpha\right)}\bar{\boldsymbol{t}}\cdot\delta\dot{\mathbf{x}}\,\mathrm{d}\Gamma\right], \tag{6.13}$$

where the inequality in the weak formulation finds its origin in the contact constraint inequality. This latter can be removed if the contact boundary $\partial\mathcal{B}_c^\alpha$ is known. This is not trivial *a priori* since the contact zone changes during the loading. Nevertheless searching algorithm for contact area are out of the scope of this study. Then let us assume the contact zone has been previously established. Consequently, the equality Equation(6.14) stands instead of the inequality Equation(6.13).

$$\underbrace{\sum_{\alpha=1}^{2}\int_{\varphi^\alpha(\mathcal{B}^\alpha)}\boldsymbol{\sigma}\cdot\boldsymbol{\epsilon}\left[\delta\dot{\mathbf{x}}\right]\,\mathrm{d}V}_{\delta\dot{W}_{I,m}} = \underbrace{\sum_{\alpha=1}^{2}\left[\int_{\varphi^\alpha(\mathcal{B}^\alpha)}\bar{\boldsymbol{f}}\cdot\delta\dot{\mathbf{x}}\,\mathrm{d}V+\int_{\varphi^\alpha\left(\partial\mathcal{B}_{\bar{t}}^\alpha\right)}\bar{\boldsymbol{t}}\cdot\delta\dot{\mathbf{x}}\,\mathrm{d}\Gamma\right]}_{\delta\dot{W}_{E,m}}+\delta\dot{W}_{E,m}^{c} \tag{6.14}$$

where $\delta\dot{W}_{E,m}^{c}$ is the mechanical contact contribution to external virtual power. Plenty of methods are available to take this component into account. The most widely used are shortly listed hereafter but interested reader should refer to [Wriggers, 2006] for a deeper insight into science.

1. **The Lagrange multiplier method.**

   Lagrange multipliers are used to add a constraint to the weak form of the problem. This method is the only one capable of dealing with exact contact constraint[2]. The contribution of the Lagrange multipliers to virtual power reads

   $$\delta\dot{W}_{E,m}^{c,LM} = \int_{\partial\mathcal{B}_c}\left(\lambda_N\cdot\delta\dot{g}_N+\boldsymbol{\lambda}_T\cdot\delta\dot{\mathbf{g}}_T\right)\,\mathrm{d}a+\int_{\partial\mathcal{B}_c}\left(\delta\dot{\lambda}_N\cdot g_N+\delta\dot{\boldsymbol{\lambda}}_T\cdot\mathbf{g}_T\right)\,\mathrm{d}a, \tag{6.15}$$

   where (λ_N,$\boldsymbol{\lambda}_T$) are the Lagrange multipliers corresponding to ($p'_N,\mathbf{t}_T$) and ($g_N,\mathbf{g}_T$) are the normal and tangential gap functions.
   In case of sliding, tangential stresses ($\mathbf{t}_T$) have to be determined according to a constitutive law, then

   $$\boldsymbol{\lambda}_T\cdot\delta\dot{\mathbf{g}}_T \;\rightarrow\; \mathbf{t}_T\cdot\delta\dot{\mathbf{g}}_T, \tag{6.16}$$
   $$\delta\dot{\boldsymbol{\lambda}}_T\cdot\mathbf{g}_T \;\rightarrow\; 0. \tag{6.17}$$

2. **The penalty method.**

   Penalty parameters ($K_p>0$,$K_T>0$) are used to enforce the contact constraint while authorising an interpenetration $\bar{g}_N$. Thence the contribution to the external virtual power reads

   $$\delta\dot{W}_{E,m}^{c,P} = \int_{\partial\mathcal{B}_c}K_N\cdot\bar{g}_N\cdot\delta\dot{\bar{g}}_N+K_T\cdot\mathbf{g}_T\cdot\delta\dot{\mathbf{g}}_T\,\mathrm{d}a \tag{6.18}$$

   Therefore, the constraint contact ceases to be exact since both bodies intersect each other. It can be shown that the exact solution of the Lagrange multiplier method can be recovered for $(K_p,K_T)\rightarrow\infty$ [Laursen and Simo, 1993]. However, very high penalty parameters might lead to ill-conditioned systems, numerical troubles and loss of accuracy of the results [Kaliakin and Li, 1995]. Once again, if slipping occurs, the product $K_T\cdot\mathbf{g}_T\cdot\delta\mathbf{g}_T$ must be replaced by $\mathbf{t}_T\cdot\delta\mathbf{g}_T$.

[2]However it is not applicable for the modelling of a real contact, due to the non linearity that has to be taken into account for the normal stress-strain relationship

3. **The augmented Lagrange method.**

   This method combines the penalty method or the constitutive interface laws with Lagrange multipliers in order to regularise the non-differentiable normal contact and friction terms. For the normal contact, the following formulation can be adopted

$$\delta W_{E,m}^{c,AL} = \begin{cases} \displaystyle\int_{\partial\mathcal{B}_c} \left(\hat{\lambda}_N \cdot \delta\dot{g}_N + \delta\dot{\lambda}_N \cdot g_N\right) \mathrm{d}\Gamma & \text{for } \hat{\lambda_N} \leq 0, \\ \displaystyle\int_{\partial\mathcal{B}_c} -\frac{1}{K_N} \cdot \lambda_N \delta\dot{\lambda}_N \,\mathrm{d}\Gamma & \text{for } \hat{\lambda_N} > 0, \end{cases} \tag{6.19}$$

   where $\hat{\lambda}_N = \lambda_N + K_N \cdot g_N$. This functional stands also for $\hat{\lambda}_N > 0$ which means that the gap is open.

6.2.5 Hydro-mechanical continuum interface description

The strong form of the hydraulic equilibrium Equation(2.33)-(2.35) was already developed in Section 2.4.2. It can be applied to both solid porous volumes. Due to the interface that might exist between the two solid bodies, a non-classic pressure dependent boundary condition $\tilde{q}$, holds on the surface $\partial\mathcal{B}_c^{f,\alpha}$, such that

$$\mathbf{f}_{w,c}^T \cdot \mathbf{n} = \tilde{q}\left(\boldsymbol{\nabla} \boldsymbol{u_w}\right) \qquad \text{on } \partial\mathcal{B}_c^{f,\alpha}. \tag{6.20}$$

The higher the pressure gradient between the solids and the inner interface, the higher the fluid flow $\tilde{q}$. The fluid flows through the interface creates a hydraulic coupling between the two volumes.
An idealisation of an open fracture is depicted in Figure 6.5. Both sides of the fault are considered to be independent solid volumes in their current configurations : $\varphi^1(\mathcal{B}^1)$ and $\varphi^2(\mathcal{B}^2)$. The void between both solids can be either filled with altered material or empty. However whatever the actual condition, this vacuum can be modelled as a third equivalent medium $\varphi^3(\mathcal{B}^3)$ in which a fluid flow holds.
In case of empty fracture, the flow is most of the time considered as a laminar flow between two parallel plates along the coordinates $\boldsymbol{\xi}$ [Boussinesq, 1868]. Thence, the third medium $\varphi^3(\mathcal{B}^3)$ is subject to the classic equilibrium Equations(2.33), (2.34), (2.35) and to the reaction of the non-classic boundary condition Equation(6.20).

The weak form of the equilibrium equations is stated in the same way that the mechanical formulation. Starting from the Equation(2.40) of the virtual power, with δu_w an admissible field of variation of pore water pressure,

$$\underbrace{\sum_{\alpha=1}^{2}\left[\int_{\varphi^\alpha(\mathcal{B}^\alpha)} \dot{S}\cdot\delta u_w - \mathbf{f}_w\cdot\boldsymbol{\nabla}\left(\delta u_w\right)\mathrm{d}V\right]}_{\delta\dot{W}_{I,f}} + \delta\dot{W}_{I,f}^c \quad = \tag{6.21}$$

$$\underbrace{\sum_{\alpha=1}^{2}\left[\int_{\varphi^\alpha(\mathcal{B}^\alpha)} \bar{Q}\cdot\delta u_w\,\mathrm{d}V + \int_{\varphi^\alpha\left(\partial\mathcal{B}_{\bar{q}}^\alpha\right)} \bar{q}\cdot\delta u_w\,\mathrm{d}\Gamma\right]}_{\delta\dot{W}_{E,f}} + \delta\dot{W}_{E,f}^c.$$

The contribution of the interface to the internal virtual power stands for the fluid flow inside $\varphi^3(\mathcal{B}^3)$

$$\delta\dot{W}_{I,f}^c = \int_{\varphi^3(\mathcal{B}^3)} \dot{S}\cdot\delta u_w - \mathbf{f}_w^T\cdot\boldsymbol{\nabla}(\delta u_w)\,\mathrm{d}V. \tag{6.22}$$

On the other hand, if the source term inside the interface is deemed null, the contribution of the interface to the external virtual power comes from the fluid flow $\tilde{q}$ from the solid volumes $\varphi^1(\mathcal{B}^1)$ and $\varphi^2(\mathcal{B}^2)$,

$$\delta \dot{W}^c_{E,f} = \int_{\varphi^3(\mathcal{B}^3)} \bar{Q} \cdot \delta u_w \, \mathrm{d}V + \int_{\varphi^3(\partial\mathcal{B}^3)} \tilde{q} \cdot \delta u_w \, \mathrm{d}\Gamma. \tag{6.23}$$

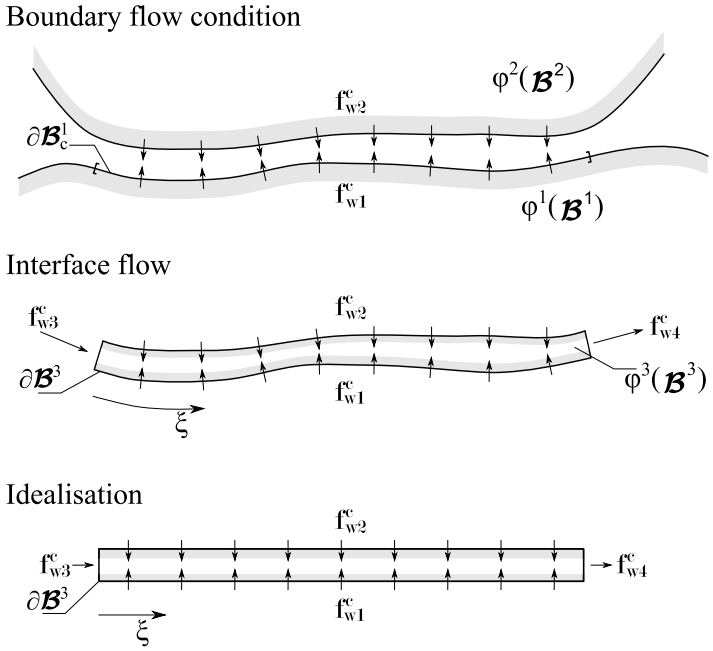

FIGURE 6.5: Hydraulic characterisation of the interface between two solid volumes in their current configurations $\varphi^1(\mathcal{B}^1)$ and $\varphi^2(\mathcal{B}^2)$. The flow is idealised to lie between two parallel plates. $f^c_{w,1}$ and $f^c_{w,2}$ are transversal fluxes from the solids to the interface. $f^c_{w,3}$ and $f^c_{w,4}$ are longitudinal fluxes inside the interface.

6.2.6 Constitutive laws for interfaces

6.2.6.1 Mechanical laws

The role of the constitutive mechanical law is to relate stress variations to displacements variations, i.e.

$$\dot{\mathbf{t}} = f(\dot{\mathbf{g}}). \tag{6.24}$$

Many distinct laws are available for any type of material and strongly depend on parameters such as roughness, adhesion and micromechanical considerations. This short review only focuses on rock and soil mechanics since they are the purpose of this thesis. However, interested reader should refer to [Wriggers, 2006] for a deeper insight into constitutive laws devoted to more mechanical topics (metal, rubber...). Most of the constitutive laws lie within the framework of elastoplasticity. On one side, there is an analogy between the stick state of the interface and classic elastic behaviour. On the other side, an analogy exists between plasticity and slip behaviour. Therefore, the constitutive law requires some basic ingredients:

- an elastic compliance tensor, which rules the stick behaviour ;
- a yield criterion, distinguishing the stick and slip states ;

- a flow rule describing the evolution of the yield surface.

The Coulomb description of friction is widely adopted [Curnier, 1984; Coulomb, 1821] for its simplicity. This model is able to take into account non-associated flow rule [Charlier, 1987]. It will be described more extensively in Section 6.3.2. Nonetheless, this formulation encounters a lack of smoothness, then existence and uniqueness can only be proved in particular cases [Oden and Pires, 1983]. Moreover the linear behaviour during the stick state and the application to cyclic loading is brought into question.

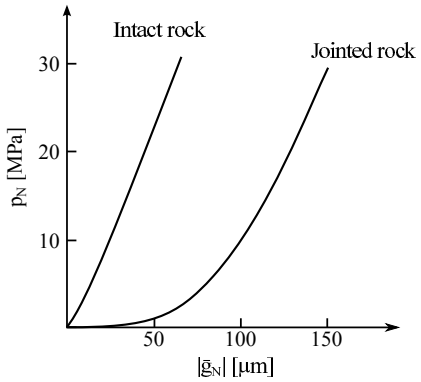

FIGURE 6.6: Normal stress-displacement behaviour in a rock joint, after [Tsang and Witherspoon, 1981] $|g_N|$ stands for the absolute value of the interpenetration function.

Some authors decide to start from the asperities level to describe the mechanical behaviour of the interface. Majumdar and Bushan [1991] develop a fractal representation of the contact surface. Tsang and Witherspoon [1981] start from the elliptical representation of a crack to derive a model describing the behaviour of jointed rocks (see Figure 6.6). Relation between normal stress and displacement ceases to be linear, which better coincides with experimental results. Oden and Pires [1983] develop a non-local friction law based on the deformation of asperities and on an averaged stress distribution.

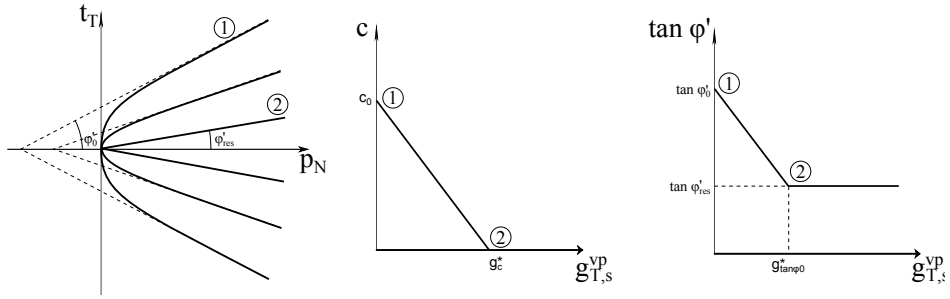

FIGURE 6.7: Hyperbolic yield criterion and softening law, after [Alonso et al., 2013]. c stands for the cohesion and φ' is the friction angle describing the yield criterion. $g_{t,s}^{vp}$ is the viscoplastic shear relative displacement.

Gens et al. [1990] propose a modified hyperbolic yield criterion as well as a hardening law for friction angle and cohesion (see Figure 6.7). They adopt a non linear normal stress-displacement relation. Such a law, called *normal law* is also described in [Bart, 2006] and involves an asymptotic closure of a rock fault.

Desai et al. [1985] and Desai and Nagaraj [1988] merge two decoupled model to take into account monotonic and cyclic behaviours of interfaces. A Ramberg-Osgood model is suggested to take into account the shearing behaviour of the interface (see Figure 6.8). The normal behaviour is also ruled by a virgin curve and allows loading/unloading non-linear

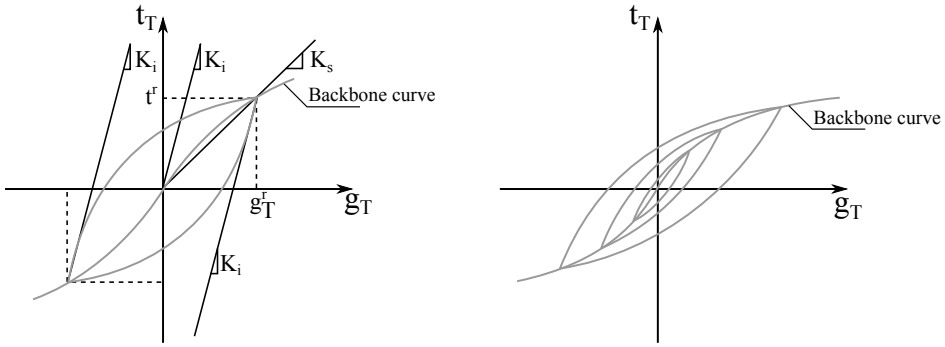

FIGURE 6.8: Ramberg-Osgood model, after [Desai et al., 1985]. K_i and K_s are respectively the initial and secant moduli. t^r and g_T^r are respectively stress and displacement that correspond to a load reversal.

behaviours (see Figure 6.9). An application is provided to model a concrete-sand interface. Mortara et al. [2002] develop a classic multi-surface model for describing cyclic behaviour of the interface (see Figure 6.10). The first elastic surface move within the bounding surface that may harden. This allows plasticity effect in both loading and unloading. Characterisation of steel or concrete sand interface is still an open ongoing research topic. For instance, DeJong et al. [2006] use particle image velocimetry in order to study localised shear band in the interface and derive simple models which could be applied to boundary value problems.

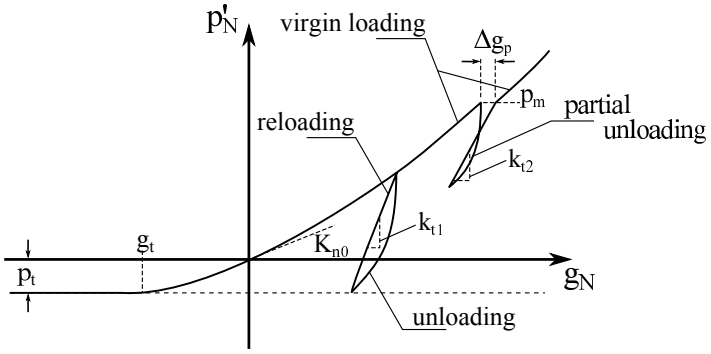

FIGURE 6.9: Normal behaviour of a thin layer interface, after [Desai and Nagaraj, 1988]. K_{n0} is the initial loading modulus. Reloading moduli k_{t1} and k_{t2} evolve with the normal displacement.

6.2.6.2 Hydraulic laws

The study of fluid flow into faults and interface media is mainly a rock mechanics concern. It is well-established that fluid flows between two sides of a fault can be described by analogy with the so called *cubic law* stated in [Boussinesq, 1868]. It is applicable to steady laminar flow of viscous incompressible fluids in a fracture composed of two smooth parallel horizontal walls and states that the flow rate is proportional to the cube of the fracture aperture [Segura and Carol, 2004; Guiducci et al., 2002; Alonso et al., 2013]. Therefore the mass flux per unit length reads

$$Q_f = \rho_w \cdot \frac{e^3}{12 \cdot \mu_w} \cdot \boldsymbol{\nabla} u_w, \tag{6.25}$$

where ρ_w is the fluid density, e is the hydraulic aperture, μ_w is the dynamic viscosity of the fluid and $\boldsymbol{\nabla} u_w$ is the gradient of pore water pressure parallel to the plates.

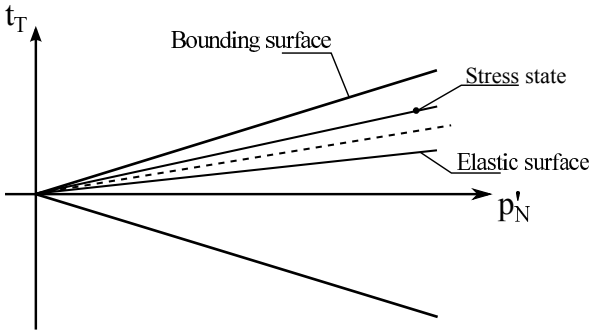

FIGURE 6.10: Bounding surface constitutive law for interface behaviour, after [Mortara et al., 2002].

However most of the time, this flow rule cannot be so straightforwardly applied. The hydraulic aperture e is different from the mechanical aperture of the fault E, due to the roughness and the tortuosity. Tsang and Witherspoon [1981] prove the validity of the cubic law in which the cube of the hydraulic aperture e^3 is computed as a weighted averaging of the cube of the variable aperture $\langle e(x,y)^3 \rangle$ over the fault. Olsson and Barton [2001] derive an empirical relation between them depending on the joint roughness (see Figure 6.11) and extend it to predict the relation between fluid flow and shearing. Many interesting papers are available about hydraulic behaviour of rock joints but are out of the scope of this study, for example [Jing, 2003; Boulon et al., 1993].

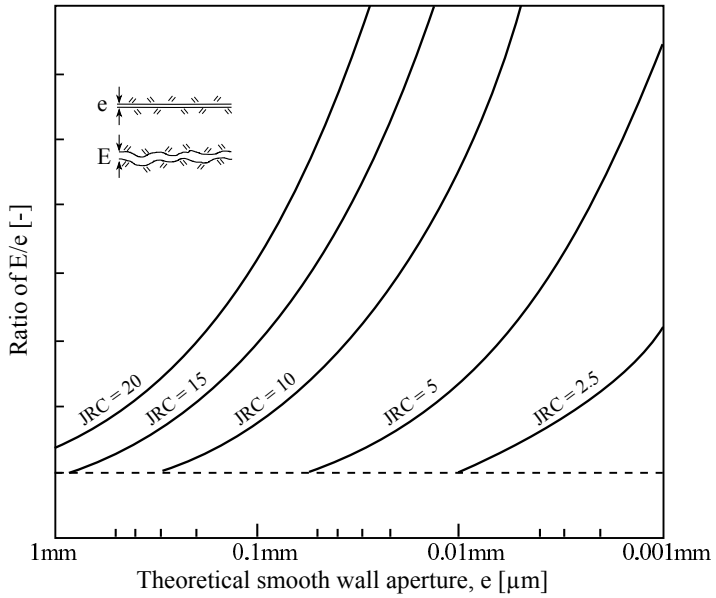

FIGURE 6.11: Relation between hydraulic aperture e and mechanical aperture E of a fault, depending of the joint roughness JRC, after [Olsson and Barton, 2001]

6.3 1D Hydro-mechanical interface element in LAGAMINE

This section aims at describing the 1D zero-thickness hydro-mechanical finite element actually implemented in the finite element code LAGAMINE. The discretisation of the domain, mechanical and hydraulic constitutive laws, the energetically equivalent nodal forces and the derived stiffness matrix as well are addressed. This summary is mainly based on the work of Charlier [1987], Habraken et al. [1998] and Barnichon [1998].

6.3.1 Discretisation

The continuum interface $\partial\mathcal{B}$ is approximated by the discretised n_e^c finite elements (see Figure 6.12)

$$\partial\mathcal{B}^h = \bigcup_{e=1}^{n_c^e} \Gamma_e. \tag{6.26}$$

The 1D element developed possesses three nodes. Thus shape functions are parabolic, [Zienkiewicz and Taylor, 2000]. The primary unknowns are the nodal generalised coordinates $\mathbf{u}$, interpolated along the element through

$$\mathbf{u}^e(\xi) = \sum_{i=1}^{n_c} \phi_i(\xi) \cdot \mathbf{u}_i \qquad \text{and} \qquad \boldsymbol{\Delta}\mathbf{u}^e(\xi) = \sum_{i=1}^{n_c} \phi_i(\xi) \cdot \boldsymbol{\Delta}\mathbf{u}_i. \tag{6.27}$$

In the finite element code LAGAMINE, designations *structure* and *foundation* replace *master* and *slave* to denote the both sides of the interface[3]. Interface elements (foundation and structure as well) are merged with the external segments of volume elements Ω_e (see Figure 6.13c). Thence they use the same nodal unknowns and create a coupling between the two solids.

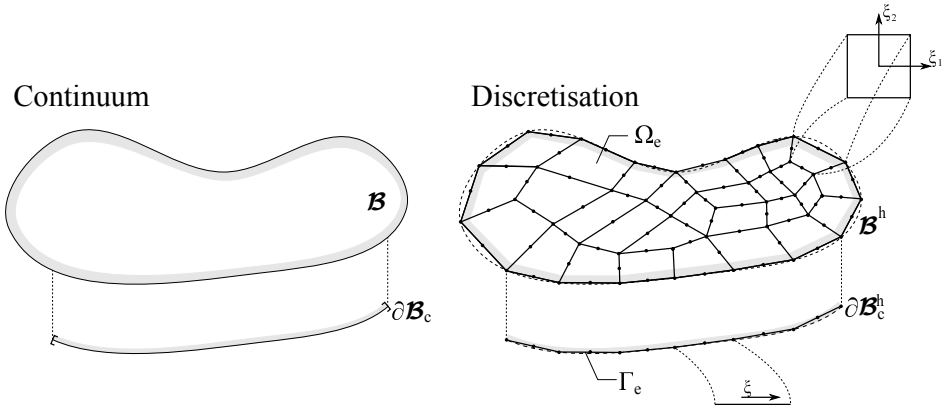

FIGURE 6.12: Discretisation of the continuum, inspired by [Wriggers, 2006]. $\mathcal{B}^1$ and Γ^1 stand for the continuum volume and contact boundary respectively. $\mathcal{B}^{1,h}$ and $\Gamma^{1,h}$ are their discrete counterparts composed by finite elements Ω^e and Γ^e.

It has been shown in Section 6.2.5 that interior of the fault has also to be modelled. Therefore, degrees of freedom have to be added between the sides of the interface. Since the hypothesis of a laminar flux between two parallel plates is adopted, the longitudinal flux depends only on the longitudinal pressure gradient. Therefore only pressure degrees of freedom are necessary in between. A three node formulation is adopted, i.e. the fluid flow through the interface is

[3]No gods, no masters.

modelled by three successive nodes (foundation, interior, structure) [Segura and Carol, 2004]. If parabolic elements are assumed in front of each other (see Figure 6.13b), the discretisation leads to

- three nodes on the structure side, associated to three DOFs : x^S, y^S, u_w^S ;
- three nodes in between the interface, associated to a single DOF : u_w^I ;
- three nodes on the foundation side, associated to three DOFs : x^F, y^F, u_w^F.

Interpolation functions for mechanical and hydraulic degrees of freedom are of equal order. Fields of pressure are discretised on both walls of the interface and inside. Therefore, gradients of pressure exists longitudinally and transversally.
However, structure and foundation are free to slip relatively and nodes are not aligned *a priori*. Thence the treatment of geometry is not an easy job. For a given time step, one has to find the current foundation segment *vis-à-vis* the structure element. The geometrical and algorithmic implications are out of the scope of this study, since special search algorithms are required. However the interested reader should refer to [Cescotto and Charlier, 1993] or [Habraken et al., 1998] or [Wang and Nakamachi, 1997] to dig into the wonderland of algorithmic tricks.

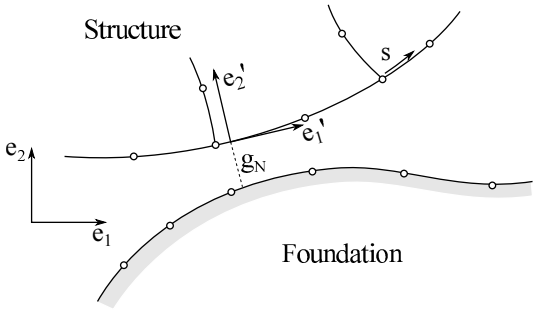

(a) Mechanical discretisation :(e_1, e_2) is the global current basis, (e_1', e_2') is the local current basis, g_N is the gap function and s is the convective coordinate.

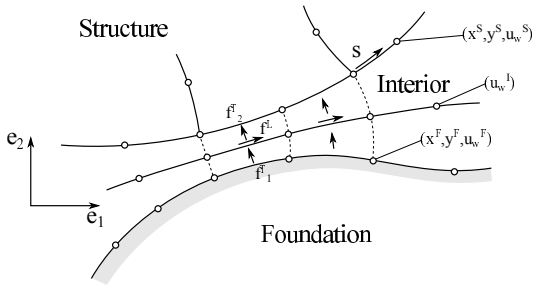

(b) Hydraulic discretisation : $(x^{S/F}, y^{S/F}, u_w^{S/F})$ are the generalised coordinates of body nodes, u_w^I are the internal pressure of interior nodes, f_1^T and f_2^T are the transversal fluxes and f^l is the longitudinal flux.

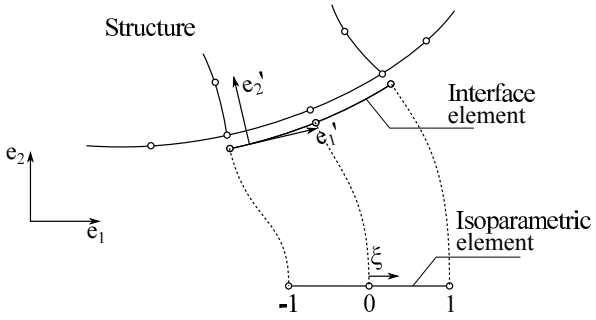

(c) Isoparametric element

FIGURE 6.13: 1D Hydro-mechanical interface element in `LAGAMINE` code.

Mechanical constitutive laws for contact elements must be defined depending on normal and tangential stresses at the current contact interface. Consequently a corotational Lagrangian formulation is adopted in the following and a local basis (e_1', e_2') evolving with the structure has to be defined. A mapping $\varphi : \mathbb{R}^2 \to \mathbb{R}$ relates global to local coordinates. The

global coordinates of the structure (x_1^S, x_2^S) are interpolated from nodal coordinates over the element with,

$$\mathbf{x}^S = \begin{bmatrix} x_1^S \\ x_2^S \end{bmatrix} = \begin{bmatrix} \phi_i^S(\xi) \cdot x_{1,i}^S \\ \phi_i^S(\xi) \cdot x_{2,i}^S \end{bmatrix}, \tag{6.28}$$

where $\phi^s(\xi)$ are the shape function of the structure side of the interface element and $x_{1,i}^S$ the nodal coordinates. The Jacobian of the transformation and its norm are easily computed based on

$$\mathbf{J}^S = \begin{bmatrix} \frac{\partial x_1^S}{\partial \xi} \\ \frac{\partial x_2^S}{\partial \xi} \end{bmatrix} = \begin{bmatrix} \frac{\partial \phi_i^S}{\partial \xi} \cdot x_{1,i}^S \\ \frac{\partial \phi_i^S}{\partial \xi} \cdot x_{2,i}^S \end{bmatrix} \qquad \text{and} \qquad |\mathbf{J}^S| = \sqrt{\left(\frac{\partial x_1^S}{\partial \xi}\right)^2 + \left(\frac{\partial x_2^S}{\partial \xi}\right)^2}. \tag{6.29}$$

The Jacobian matrix is nothing but a vector tangent to the element at any point (x_1^S, x_2^S) belonging to the element. Therefore, a local basis of two orthonormal vectors (e_1', e_2') is easily constructed. The so-called *rotation matrix* is composed of these two unit vectors

$$\mathbf{R} = \begin{bmatrix} e_1' & e_2' \end{bmatrix} = \frac{1}{|\mathbf{J}^S|} \cdot \begin{bmatrix} \frac{\partial x_1^S}{\partial \xi} & -\frac{\partial x_2^S}{\partial \xi} \\ \frac{\partial x_2^S}{\partial \xi} & \frac{\partial x_1^S}{\partial \xi} \end{bmatrix} = \frac{1}{|\mathbf{J}^S|} \cdot \begin{bmatrix} \frac{\partial \phi_i^S}{\partial \xi} \cdot x_{1,i}^S & -\frac{\partial \phi_i^S}{\partial \xi} \cdot x_{2,i}^S \\ \frac{\partial \phi_i^S}{\partial \xi} \cdot x_{2,i}^S & \frac{\partial \phi_i^S}{\partial \xi} \cdot x_{1,i}^S \end{bmatrix} = \begin{bmatrix} D_{X1} & -D_{X2} \\ D_{X2} & D_{X1} \end{bmatrix}. \tag{6.30}$$

The local basis is subsequently defined at each point of the element and a unique relation exists between local (e_1', e_2') and global coordinates (e_1, e_2), as shown in Figure 6.13a,

$$\begin{bmatrix} e_1 & e_2 \end{bmatrix} = \mathbf{R} \cdot \begin{bmatrix} e_1' & e_2' \end{bmatrix}^T \tag{6.31}$$

$$\begin{bmatrix} e_1' & e_2' \end{bmatrix} = \mathbf{R}^T \cdot \begin{bmatrix} e_1 & e_2 \end{bmatrix}. \tag{6.32}$$

6.3.2 Mechanical constitutive law

The *Lagrange multiplier* method involves a continuously changing number of unknowns (due to the activation or not of contact constraint), which is crafty and cumbersome [Zavarise et al., 1998]. On the other hand the *Penalty method* is easily implemented in any finite element code and is stable if the ill-conditioning risk is kept in mind by a careful user. Consequently the latter has been implemented in the LAGAMINE code many years ago [Charlier, 1987].

Defining absolute deformation is senseless since both bodies may encounter very large relative displacements. Therefore, the algorithm is incrementally defined and the purpose of the mechanical constitutive law consists in relating effective stress rate $(\dot{\mathbf{t}}')$ to relative velocities $(\dot{\mathbf{g}})$ by means of the local compliance tensor $\mathbf{C}^{st}$. The stiffness parameters that are identified to the penalty coefficients are rate independent. There is consequently no viscosity effect in the behaviour of the interface,

$$\dot{\mathbf{t}}' = \mathbf{C}^{st} \cdot \dot{\mathbf{g}}, \tag{6.33}$$

where the two components of relative velocities $\dot{\mathbf{g}}$ are

- $\dot{g}_T$: the relative tangential velocity.
- $\dot{g}_N$: the normal relative velocity.
  It's noteworthy that if both sides are close enough, the absolute displacement g_N makes sense and may be used to distinguish between contact and no contact conditions.

The two components of the local effective stresses are

- $\dot{t}_T$: the variation of local shear stress.
- $\dot{p}'_N$: the variation of normal effective stress.
  The total normal stress is computed according to the Terzaghi postulate for saturated soils : $p_N = p'_N + u_w$. The normal effective stress is positive in compression and cannot be negative unless cohesion is allowed in the interface. In the finite element code `LAGAMINE`, the contact condition is
  $$p'_N > 0. \tag{6.34}$$

The compliance tensor $\mathbf{C}^{st}$ remains undetermined. As previously defined in Section 6.2.3 and summarized in Table 6.14a, the state of the interface is either stick (st), slip (^{sl}) or without contact (^{nc}). All these states are gathered within the framework of elastoplasticity [Gens et al., 1988] or [Sheng et al., 2005].
Obviously, when there is no contact, the compliance tensor as well as stresses are null, such as

$$\mathbf{C}^{st} = \mathbf{0} \tag{6.35}$$

	No contact	Stick	Slip
p'_N	$= 0$	> 0	> 0
$\lvert t_T \rvert$	$= 0$	≥ 0	$= \mu \cdot p'_N$
g_N	≥ 0	< 0	< 0
$\mathbf{C}^{st}$	$\mathbf{0}$	Equation(6.36)	Equation(6.46)
E-P	Apex	Elastic	Elastoplastic

(a) Relation between elastoplastic parameters and stick/slip/no contact state.

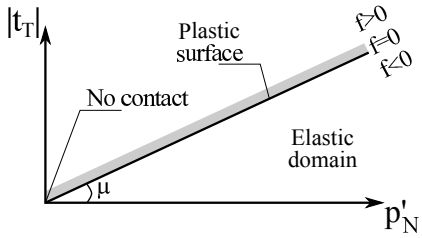

(b) Representation of the yield Mohrt-Coulomb criterion.

FIGURE 6.14: Elastoplastic formalism for the mechanical behaviour of the interface.

The exact stick state (no relative displacement either normal or tangential) is regularised by penalty parameters (K_T, K_N) in order to be more numerical-friendly to deal with. This condition corresponds to an elastic state and the aforementioned compliance tensor becomes

$$\mathbf{C}^{st} = \begin{bmatrix} K_T & 0 \\ 0 & K_N \end{bmatrix} \tag{6.36}$$

The Mohr-Coulomb yield criterion is widely used in soil mechanics either for describing volume or interface behaviours. Although it was shown by Mortara et al. [2002] that more accurate constitutive laws have to be adopted in order to accurately capture monotonic or cyclic behaviour of interfaces, the Mohr-Coulomb criterion with perfect plasticity was adopted hereafter for the sake of simplicity. The justification is twofold. Firstly, only few parameters are necessary to run computations. Secondly, in a suction caisson application, the suction is the major source of resistance and the degradation of the friction along the shaft, although existing, might be neglected as a first approximation.

A 2D representation of the Mohr-Coulomb criterion is depicted in Figure 6.14b and its mathematical formulation reads

$$f = |t_T| - \mu \cdot p'_N \leq 0, \tag{6.37}$$

where $f < 0$ indicates a stick (elastic) state and $f = 0$ stands for slip (plastic) state. The total relative velocity is split into its stick $\dot{\mathbf{g}}^{st}$ and slip $\dot{\mathbf{g}}^{sl}$ components, such as

$$\dot{\mathbf{g}} = \dot{\mathbf{g}}^{st} + \dot{\mathbf{g}}^{sl}. \tag{6.38}$$

Therefore the effective stress variation inside the interface is computed through

$$\dot{\mathbf{t}}' = \mathbf{C}^{st} \cdot \left(\dot{\mathbf{g}} - \dot{\mathbf{g}}^{sl} \right). \tag{6.39}$$

The slip component is defined as

$$\dot{\mathbf{g}}^{sl} = \dot{\lambda} \cdot \frac{\partial h}{\partial \mathbf{t}'}, \tag{6.40}$$

where $\dot{\lambda}$ is the plastic multiplier and h stands for the plastic potential, which could be non associated ($\alpha \neq \mu$)

$$h = |t_T| - \alpha \cdot p'_N \tag{6.41}$$

When the slip state is activated, the so-called *consistency condition* must be enforced, i.e.

$$\dot{f} \equiv \frac{\partial f}{\partial \mathbf{t}'} \cdot \dot{\mathbf{t}}' + \frac{\partial f}{\partial \mu} \cdot \dot{\mu} = 0 \tag{6.42}$$

where $\dot{\mu}$ allows the hardening of the yield function f. It can be described by the general equation

$$\dot{\mu} = \dot{\lambda} \cdot h_\mu \tag{6.43}$$

where h_μ is the hardening direction of the internal variable μ.

Introducing Equations(6.39), (6.40) and (6.43) into Equation(6.42) leads to the plastic multiplicator Equation (6.44)

$$\begin{aligned} & \frac{\partial f}{\partial \mathbf{t}'} \cdot \mathbf{C}^{st} \cdot \left(\dot{\mathbf{g}} - \dot{\lambda} \cdot \frac{\partial h}{\partial \mathbf{t}'} \right) + \frac{\partial f}{\partial \mu} \cdot \dot{\mu} = 0 \\ \Leftrightarrow \quad & \dot{\lambda} = \frac{\dfrac{\partial f}{\partial \mathbf{t}'} \cdot \mathbf{C}^{st} \cdot \dot{\mathbf{g}}}{\dfrac{\partial f}{\partial \mathbf{t}'} \cdot \mathbf{C}^{st} \cdot \dfrac{\partial h}{\partial \mathbf{t}'} - \dfrac{\partial f}{\partial \mu} \cdot h_\mu}. \end{aligned} \tag{6.44}$$

Thence, the explicit computation of the final stress state is straightforward

$$\dot{\boldsymbol{\sigma}}_c = \mathbf{C}^{st} \cdot \left(\dot{\mathbf{g}} - \dot{\lambda} \cdot \frac{\partial h}{\partial \mathbf{t}'} \right) = \mathbf{C}^{sl} \cdot \dot{\mathbf{g}} \tag{6.45}$$

In this document, two hypotheses are formulated

- $\alpha = 0$ meaning that no coupling exists between the shearing of the interface and the normal relative displacement. A non-zero α parameter is more suited for the simulation of rock joints, which is not the purpose of this thesis.
- $\dot{\mu} = 0$ meaning that the resistance of the interface does not vary. This hypothesis is more subject to caution, since the friction available along the interface, particularly during cyclic loading, is prone to evolve [Ho et al., 2011]. Different causes are likely to explain these changes [White and Lehane, 2004; Lings and Dietz, 2005]:
  - crushing of the sand grains ;
  - hardening or softening of the soil close to the structure ;
  - polishing of the structure due to the abrasive effect of the sand.

Therefore, combining Equation(6.45) and Equation(6.44), the local elastoplastic compliance tensor is eventually computed

$$\mathbf{C}^{st} = \mathbf{C}^{sl} = \begin{bmatrix} 0 & K_N \cdot \mu \cdot \dfrac{t_T}{|t_T|} \\ 0 & K_N \end{bmatrix} \tag{6.46}$$

A summary of the different states is provided in Figure 6.14.

6.3.3 Hydraulic constitutive laws

Similarly to the mechanical laws, hydraulic constitutive laws relate the fluid flux f_w to the gradient of pressure $\boldsymbol{\nabla} u_w$ and the gap function variations

$$\mathbf{f}_w = \mathbf{h}(\boldsymbol{\nabla} u_w, \dot{g}_N) \tag{6.47}$$

As stated before, fluxes are of threefold natures

- longitudinal f_w^l; due to the preferential path created by any fault, fracture or interface;
- transversal f_w^t; exchange between sides of the interface and the fracture, fault, interface;
- storage f_w^s; due to the mechanical opening/closing of the fracture and/or to the variation of $\rho_w(u_w)$. This term is necessary to ensure the mass conservation and creates a hydro-mechanical coupling.

6.3.3.1 Transversal fluxes

Whatever the nature of the interior of the interface, filled with altered material or open fracture, a fluid flow occurs within it, unless the interface is impermeable. Therefore, the interior flow is connected with the flows in both solids surrounding it. They only depend on the pressure gradient between each of the solid volume and the interior medium. They are proportional to a transverse transmissivity T_w^t. This transmissivity finds its physical meaning in the hydraulic head loss encountered by the fluid flow, when the medium changes,

$$f_{w,1}^t = T_{w,1}^t \cdot \left(u_w^F - u_w^I\right) \cdot \rho_w, \tag{6.48}$$

$$f_{w,2}^t = T_{w,2}^t \cdot \left(u_w^I - u_w^S\right) \cdot \rho_w, \tag{6.49}$$

where u_w^F is the pore pressure on the foundation side, u_w^I the pore pressure inside and u_w^S on the structure side. Obviously, this transmissivity differs if a fracture is open (fluid flow trough the solid and atmosphere) or if the fracture is filled with water or altered material. These particular cases have to be differentiated.

6.3.3.2 Longitudinal flux

Since the assumption of 1D laminar flux between two parallel plates was deemed valid, the generalised Darcy flow law is adopted to describe the longitudinal flux, Section 6.2.6.2. This hypothesis is valid for both filled or empty interior medium. Indeed, if an open fracture is modelled, this law can be applied with an equivalent intrinsic permeability equal to $e^2/12$,

where e is the hydraulic aperture. On the other hand, if the fault is filled with a material, its actual permeability can be adopted,

$$f_w^l = \frac{-k^l}{\mu_w} \cdot \left(\boldsymbol{\nabla}_{\mathbf{n}_\xi} u_w + \rho_w \cdot g \cdot \boldsymbol{\nabla}_{\mathbf{n}_\xi} x_2\right) \cdot \rho_w, \tag{6.50}$$

where k^l [m^2] is the permeability in the direction of $\mathbf{n}_\xi$ and g the gravity acceleration. The full developments of $\boldsymbol{\nabla}_{\mathbf{n}_\xi} u_w$ and $\boldsymbol{\nabla}_{\mathbf{n}_\xi} x_2$ are given in appendix C.

6.3.3.3 Storage

It was shown in Section 6.2.1 that walls of the interface can be unstuck, e.g. during horizontal loading of a pile or tension of a suction anchor. Therefore, the interior medium is a void that must be filled. As a main hypothesis, it is assumed the vacuum is fully saturated with water (see Figure 6.15). It makes sense in the particular case of offshore engineering. Moreover, the suction effect appearing in the case of offshore foundation in tension, generates a drop of pore water pressure that may affect the specific mass of the fluid.

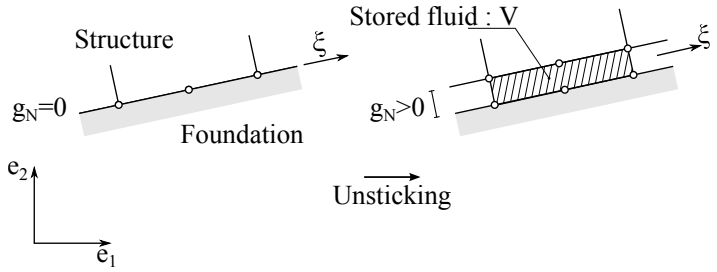

FIGURE 6.15: Unsticking of the interface element. Stored fluid between two neighbouring elements.

Consequently, a storage flux $\dot{S}$ is necessary to verify the mass conservation equation, defined in the weak formulation of the virtual power Eq (6.22). Let us consider a volume of interior medium (see Figure 6.15), i.e. a space V between the walls of the interface filled with water. The storage flux is equal to the variation of mass fluid stored in between, i.e.

$$\begin{aligned}
\dot{S} &= \frac{d}{dt}\left(\rho_w \cdot V\right) \\
&= \dot{\rho}_w \cdot g_N \cdot L + \rho_w \cdot \left(\dot{g}_N \cdot L + \cancel{g_N \cdot L}\right) \\
&= \frac{\partial \rho_w}{\partial u_w} \cdot \frac{\partial u_w}{\partial t} \cdot g_N \cdot L + \rho_w \cdot \dot{g}_N \cdot L \\
&= \frac{\rho_{w,0}}{\chi_w} \cdot \dot{u}_w \cdot g_N \cdot L + \rho_w \cdot \dot{g}_N \cdot L
\end{aligned} \tag{6.51}$$

where

- V is the volume of the void to be filled in;
- L is the length of the void considered, its variation $\dot{L}$ is deemed negligible ;
- $g_N > 0$ is the gap between both sides ;
- ρ_w is the fluid specific mass which is assumed be pressure dependant through the linearised relation

$$\rho_w = \rho_{w,0} \cdot \left(1 + \frac{u_w - u_{w,0}}{\chi_w}\right) \tag{6.52}$$

where

- $\rho_{w,0}$ and $u_{w,0}$ are the reference fluid specific mass and pressure, respectively ;
- χ_w is the water compressibility.

The storage flux per unit of surface is then obtained readily in dividing the storage expression $\dot{S}$ Equation (6.51) by L. This flux is positive for storage and negative for emptying,

$$f_w^s = \frac{\rho_{w,0}}{\chi_w} \cdot \dot{u}_w \cdot g_N + \rho_w \cdot \dot{g}_N. \tag{6.53}$$

6.3.4 Contribution of the interface element to the energetically equivalent nodal forces

6.3.4.1 Internal energetically equivalent nodal forces (hydraulic part)

Energetically equivalent nodal forces were derived in Section 2.5 from the weak formulation of the continuum equations. Contributions of the interface elements to equivalent forces can be derived in the same fashion. Let us consider the contribution to internal power of the contact, i.e. Equation (6.22), for an arbitrary element of the discretised interface Γ_e. If both solids are close enough, the space between them is prone to develop fluid flow. Therefore the following equation holds on $\varphi^3(\mathcal{B}^3)$, i.e. the equivalent medium created inside the interface,

$$\begin{aligned}
\delta\dot{W}_I^{\Gamma_e} &= \int_{\varphi^3(\mathcal{B}^3(\Gamma_e))} f_w^s \cdot \delta u_w^{\Gamma_e} - f_w^l \cdot \boldsymbol{\nabla}_{\mathbf{n}_\xi}(\delta u_w^{\Gamma_e})\,\mathrm{d}V \\
&= \sum_{i=1}^{n_n^c} \left[\int_{\varphi^3(\mathcal{B}^3(\Gamma_e))} f_w^s \cdot \phi_i - f_w^l \cdot \boldsymbol{\nabla}_{\mathbf{n}_\xi}\phi_i \,\mathrm{d}V \right] \cdot \delta u_{w,i}^{\Gamma_e} \\
&= \sum_{i=1}^{n_n^c} F_{I,i}^{\Gamma_e} \cdot \delta u_{w,i}^{\Gamma_e} \qquad (6.54) \\
&= \left[\mathbf{F}_I^{\Gamma_e}\right]^T \cdot \delta \mathbf{u}_w^{\Gamma_e}, \qquad (6.55)
\end{aligned}$$

where Equation (6.55) is the vectorial form of Equation (6.54), n_n^c is the number of nodes of the interface element, $\boldsymbol{\nabla}_{\mathbf{n}_\xi}$ is the directional gradient of u_w and $\mathbf{F}_I^{\Gamma_e}$ is the vector of internal energetically equivalent nodal forces associated to the element Γ_e.

A generalised midpoint rule may be adopted to take into account the fluxes in the element such as in mechanical integration of a constitutive law [Mira et al., 2009]. It means fluid fluxes are evaluated a time $t+\theta\Delta t$, $\theta \in [0,1]$, in which $\theta = 0$ holds for an explicit integration of the law and $\theta = 1$ stems for implicit integration. Therefore, storage and longitudinal fluxes are obtained by a linear combination

$$f_w^l\Big|_{t+\theta\Delta t} = -\frac{k}{\mu_f} \cdot \left[\theta \cdot \left(\frac{\partial u_w}{\partial \xi}\right)\Big|_{t+\Delta t} + (1-\theta) \cdot \left(\frac{\partial u_w}{\partial \xi}\right)\Big|_t + \gamma_w \cdot \frac{\partial x_2}{\partial \xi} \right] \cdot \rho_w \tag{6.56}$$

$$f_w^s|_{t+\theta\Delta t} = \theta \cdot f_w^s|_{t+\Delta t} + (1-\theta) \cdot f_w^s|_t\,. \tag{6.57}$$

Therefore, the expanded expression of $F_{I,i}^{\Gamma_e}$ reads

$$\begin{aligned}
F_{I,i}^{\Gamma_e} &= \int_{\varphi^3(\mathcal{B}^3(\Gamma_e))} \left(f_w^s \cdot \phi_i - \frac{f_w^l}{|\mathbf{J}|} \cdot \frac{\partial \phi_i}{\partial \xi} \right)\Big|_{t+\theta\Delta t} \mathrm{d}V \\
&= \int_{\varphi^3(\mathcal{B}^3(\Gamma_e))} \left(\left\{ \frac{\rho_{w,0}}{\chi_w} \cdot \dot{u}_w \cdot g_N + \rho_w \cdot \dot{g}_N \right\} \cdot \phi_i - \frac{f_w^l}{|\mathbf{J}|} \cdot \frac{\partial \phi_i}{\partial \xi} \cdot \right)\Big|_{t+\theta\Delta t} \mathrm{d}V
\end{aligned} \tag{6.58}$$

where the derivation of $\boldsymbol{\nabla}_{\mathbf{n}_\xi} u_w$ is given in appendix C.1. The gap variation $\dot{g}_N$ is developed to depend on the global coordinates

$$\begin{aligned}
\dot{g}_N &= \begin{bmatrix} 0 & 1 \end{bmatrix} \cdot \mathbf{R}^T \cdot \begin{bmatrix} \dot{x}_1^S - \dot{x}_1^F \\ \dot{x}_2^S - \dot{x}_2^F \end{bmatrix} \\
&= \frac{1}{|\mathbf{J}|} \cdot \begin{bmatrix} -\dfrac{\partial x_2^S}{\partial \xi} & \dfrac{\partial x_1^S}{\partial \xi} \end{bmatrix} \cdot \begin{bmatrix} \dot{x}_1^S - \dot{x}_1^F \\ \dot{x}_2^S - \dot{x}_2^F \end{bmatrix} \\
&= \frac{1}{|\mathbf{J}|} \cdot \left[-\frac{\partial x_2^S}{\partial \xi} \cdot \left(\dot{x}_1^S - \dot{x}_1^F \right) + \frac{\partial x_1^S}{\partial \xi} \cdot \left(\dot{x}_2^S - \dot{x}_2^F \right) \right].
\end{aligned} \tag{6.59}$$

Since the global discretised interface is composed of n_e^c elements, they have to be assembled together using Equation(6.26) to form the vector of hydraulic nodal forces associated to interface elements $\mathbf{F}_I^c$

$$\mathbf{F}_I^c = \bigcup_{e=1}^{n_e^c} \mathbf{F}_I^{\Gamma_e}. \tag{6.60}$$

6.3.4.2 External energetically equivalent nodal forces (hydraulic part)

External energetically equivalent nodal forces due to the transversal fluid fluxes can be derived in the same way from the weak formulation Equation(6.23), if the source term on $\varphi^3(\mathcal{B}^3)$ is deemed null, such that

$$\begin{aligned}
\delta \dot{W}_E^{\Gamma_e} &= \int_{\varphi(\Gamma^e)} \tilde{q} \cdot \delta u_w^{\Gamma_e} \, \mathrm{d}\Gamma \\
&= \sum_{i=1}^{n_n^c} \left[\int_{\varphi(\Gamma^e)} \tilde{q} \cdot \phi_i \, \mathrm{d}\Gamma \right] \cdot \delta u_{w,i}^{\Gamma_e} \\
&= \sum_{i=1}^{n_n^c} F_{E,i}^{\Gamma_e,f} \cdot \delta u_{w,i}^{\Gamma_e} \\
&= \left[\mathbf{F}_E^{\Gamma_e,f} \right]^T \cdot \delta \mathbf{u}_w^{\Gamma_e}
\end{aligned} \tag{6.61}$$

where $\mathbf{F}_E^{\Gamma_e,f}$ is the vector of hydraulic external energetically equivalent loads associated to the element Γ_e and $\tilde{q}$ is the non-classic boundary condition that holds on the sides of the interface. The same midpoint rule is used to integrate the transversal fluxes

$$\tilde{q} = f_w^t\big|_{t+\theta\Delta t} = \theta \cdot f_w^t\big|_{t+\Delta t} + (1-\theta) \cdot f_w^t\big|_t \tag{6.62}$$

However the expression of $\tilde{q}$ depends on the side of the interface considered.

- Structure side

$$F_{E,i}^{\Gamma_e,f} = \int_{\varphi(\Gamma^e)} \left(T_{w,2}^t \cdot (u_w^I - u_w^S) \cdot \rho_w \right)\big|_{t+\theta\Delta t} \cdot \phi_i \, \mathrm{d}\Gamma \tag{6.63}$$

- Foundation side

$$F_{E,i}^{\Gamma_e,f} = -\int_{\varphi(\Gamma^e)} \left(T_{w,1}^t \cdot (u_w^F - u_w^I) \cdot \rho_w \right)\big|_{t+\theta\Delta t} \cdot \phi_i \, \mathrm{d}\Gamma \tag{6.64}$$

- Interior

$$F_{E,i}^{\Gamma_e,f} = \int_{\varphi(\Gamma^e)} \left(T_{w,1}^t \cdot (u_w^F - u_w^I) - T_{w,2}^t \cdot (u_w^I - u_w^S) \cdot \rho_w\right)\big|_{t+\theta\Delta t} \cdot \phi_i \, \mathrm{d}\Gamma \tag{6.65}$$

Finally the vectors $\mathbf{F}_E^{\Gamma_e}$ are assembled together as

$$\mathbf{F}_E^{c,f} = \bigcup_{e=1}^{n_e^c} \mathbf{F}_E^{\Gamma_e,f}. \tag{6.66}$$

6.3.4.3 External energetically equivalent nodal forces (mechanical part)

External energetically equivalent nodal forces due to mechanical coupling can be derived in the same way, from the weak formulation Equation(6.23),

$$\begin{aligned}
\delta\dot{W}_E^{\Gamma_e,m} &= \int_{\varphi(\Gamma^e)} \left(p_N \cdot \delta\dot{g}_N^{\Gamma_e} + t_T \cdot \delta\dot{g}_T^{\Gamma_e}\right) \mathrm{d}\Gamma \\
&= \sum_{i=1}^{n_n^c} \left[\int_{\varphi(\Gamma^e)} [t_T, p_N] \cdot \mathbf{R}^T \cdot \phi_i \, \mathrm{d}\Gamma\right] \cdot \delta\dot{\mathbf{x}}_i^{\Gamma_e} \\
&= \sum_{i=1}^{n_n^c} \left[\mathbf{F}_{E,i}^{\Gamma_e,m}\right]^T \cdot \delta\dot{\mathbf{x}}_i^{\Gamma_e} \\
&= \left[\mathbf{F}_E^{\Gamma_e,m}\right]^T \cdot \delta\dot{\mathbf{x}}^{\Gamma_e}
\end{aligned} \tag{6.67}$$

where $\mathbf{F}_E^{\Gamma_e,m}$ is the vector of mechanical external energetically equivalent forces associated to the element Γ_e and $\mathbf{R}$ is the rotation matrix. It is worth noting that the local normal stress p_N is a total stress including the pore water pressure inside the interface u_w^I, creating a coupling between hydraulic and mechanical behaviours

$$p_N = p'_N + u_w^I. \tag{6.68}$$

Consequently, if a pore water pressure exists inside the interface, i.e. $u_w^I \neq 0$, nodal forces are not null even if the contact is lost , i.e. $p'_N = 0$. The relation between $\delta\dot{\mathbf{g}}$ and $\delta\dot{\mathbf{x}}$ is straightforward. For the sake of simplicity, the expression is derived hereafter for any virtual variation of the velocity of the structure node $(\cdot)^S$.

$$\begin{aligned}
\delta\dot{\mathbf{g}}^S &= \dot{\mathbf{g}}(\dot{\mathbf{x}}^S + \delta\dot{\mathbf{x}}^S, \dot{\mathbf{x}}^F) - \dot{\mathbf{g}}(\dot{\mathbf{x}}^S, \dot{\mathbf{x}}^F) \\
&= \begin{bmatrix} \dot{g}_T(\dot{\mathbf{x}}^S + \delta\dot{\mathbf{x}}^S, \dot{\mathbf{x}}^F) - \dot{g}_T(\dot{\mathbf{x}}^S, \dot{\mathbf{x}}^F) \\ \dot{g}_N(\dot{\mathbf{x}}^S + \delta\dot{\mathbf{x}}^S, \dot{\mathbf{x}}^F) - \dot{g}_N(\dot{\mathbf{x}}^S, \dot{\mathbf{x}}^F) \end{bmatrix} \\
&= \left[\mathbf{R}\left(\mathbf{x}^S + \delta\mathbf{x}^S\right)\right]^T \cdot \begin{bmatrix} \left(\dot{x}_1^S + \delta\dot{x}_1^S - \dot{x}_1^F\right) - \left(\dot{x}_1^S - \dot{x}_1^F\right) \\ \left(\dot{x}_2^S + \delta\dot{x}_2^S - \dot{x}_2^F\right) - \left(\dot{x}_2^S - \dot{x}_2^F\right) \end{bmatrix} \\
&= \begin{bmatrix} \dfrac{\partial}{\partial\xi}\left(x_1^S + \delta x_1^S\right) & \dfrac{\partial}{\partial\xi}\left(x_2^S + \delta x_2^S\right) \\ -\dfrac{\partial}{\partial\xi}\left(x_2^S + \delta x_2^S\right) & \dfrac{\partial}{\partial\xi}\left(x_1^S + \delta x_1^S\right) \end{bmatrix} \cdot \begin{bmatrix} \left(\dot{x}_1^S + \delta\dot{x}_1^S - \dot{x}_1^F\right) - \left(\dot{x}_1^S - \dot{x}_1^F\right) \\ \left(\dot{x}_2^S + \delta\dot{x}_2^S - \dot{x}_2^F\right) - \left(\dot{x}_2^S - \dot{x}_2^F\right) \end{bmatrix} \\
&= [\mathbf{R} + \delta\mathbf{R}]^T \cdot \begin{bmatrix} \phi_i^S \cdot \delta\dot{x}_{1,i}^S \\ \phi_i^S \cdot \delta\dot{x}_{2,i}^S \end{bmatrix} \\
&= \mathbf{R}^T \cdot \phi_i^S \cdot \delta\mathbf{x}_i^S + \cancel{\delta\mathbf{R}^T \cdot \phi_i^S \cdot \delta\mathbf{x}_i^S} \\
&= \mathbf{R}^T \cdot \phi_i^S \cdot \delta\mathbf{x}_i^S
\end{aligned} \tag{6.69}$$

where $(\delta\dot{x}^S_{1,i}, \delta\dot{x}^S_{2,i})$ are the nodal velocities of the structure nodes, ϕ^S_i are the shape functions associated to the structural part of the interface and the second order term $\delta\mathbf{R}^T \cdot \phi^S_i \cdot \delta\mathbf{x}^S_i$ can be neglected.

Finally the $\mathbf{F}^{\Gamma_e}_E$ are assembled together as

$$\mathbf{F}^{c,m}_E = \bigcup_{e=1}^{n^c_e} \mathbf{F}^{\Gamma_e,m}_E. \tag{6.70}$$

6.3.4.4 Assembling

In this section, all the energetically equivalent nodal vectors were only computed for the contact contribution, i.e. $\mathbf{F}^c_I$, $\mathbf{F}^{c,m}_E$ and $\mathbf{F}^{c,f}_E$. They still have to be assembled into the global internal and external force vectors, i.e. $\mathbf{F}_I$ and $\mathbf{F}_E$ respectively. These vectors contain the nodal forces associated to every discretised node of the structure. This step is carried out using the classic assembling operator $\mathfrak{R}$, that adds the contact contributions to the global vectors

$$\mathbf{F}_I = \mathfrak{R}\mathbf{F}^c_I \tag{6.71}$$

$$\mathbf{F}_E = \mathfrak{R}\mathbf{F}^{c,m}_E + \mathfrak{R}\mathbf{F}^{c,f}_E \tag{6.72}$$

The integration is numerically performed using the Gauss quadrature method, as it was stated in Section 2.5.

6.3.5 Assembling of the stiffness matrix

The last step is the computation of the stiffness matrix defined in Section 2.5

$$\mathbf{F}_{OB,i} = \mathbf{F}_{I,i} - \mathbf{F}_{E,i} \tag{6.73}$$

$$[\mathbf{K}]_{ij} = -\frac{\partial \mathbf{F}_{OB,i}}{\partial \mathbf{u}_j}, \tag{6.74}$$

where $\mathbf{F}_{OB,i}$ are the out of balance forces at node i and $\mathbf{u}_j$ the generalised displacement at node j. Therefore, if both sides of an interface are perfectly matched, i.e. perfectly in front of each other, the stiffness tensor associated to the interface is a 21×21 matrix,

$$\mathbf{K} = \begin{bmatrix} [\mathbf{K}]^{SS}_{9\times9} & [\mathbf{K}]^{SI}_{9\times3} & [\mathbf{K}]^{SF}_{9\times9} \\ [\mathbf{K}]^{IS}_{3\times9} & [\mathbf{K}]^{II}_{3\times3} & [\mathbf{K}]^{IF}_{3\times9} \\ [\mathbf{K}]^{FS}_{9\times9} & [\mathbf{K}]^{FI}_{9\times3} & [\mathbf{K}]^{FF}_{9\times9} \end{bmatrix}_{21\times21}, \tag{6.75}$$

associated with the nodal generalised coordinates vector,

$$\begin{aligned} \mathbf{u}^T = \Big[& x^{S,1}_1\, x^{S,1}_2\, u^{S,1}_w\, x^{S,2}_1 x^{S,2}_2 u^{S,2}_w x^{S,3}_1 x^{S,3}_2 u^{S,3}_w \\ & u^{I,1}_w\, u^{I,2}_w\, u^{I,3}_w \\ & x^{F,1}_1\, x^{F,1}_2\, u^{F,1}_w\, x^{F,2}_1\, x^{F,2}_2\, u^{F,2}_w\, x^{F,3}_1\, x^{F,3}_2\, u^{F,3}_w \Big], \end{aligned} \tag{6.76}$$

where x_1 and x_2 are the geometrical coordinates, u_w the pore water pressure. The superscripts $(\cdot)^S$, $(\cdot)^I$ and $(\cdot)^F$ stand for structure, interior and foundation respectively; the superscripts $(\cdot)^1$, $(\cdot)^2$, $(\cdot)^3$ hold for the first, second and third node of the side considered. Full developments to obtain the stiffness matrix are given in Appendix C.4. It must be pointed out that if discretised elements are not perfectly matched, the size of the matrix increases.

6.4 Basic features of the model : 1D example

In the previous sections, a 1D coupled finite element of interface has been described. Particularly, the capability of unsticking has been introduced by means of a storage flux. In the following, a simple 1D example is provided to emphasise the main phenomena induced by unsticking effect. Many references devoting to classic finite elements are already available in the literature about mechanical behaviour of zero thickness finite elements [Habraken et al., 1998]. However, it remains mainly unexplored when dealing with its hydromechanical behaviour [Segura and Carol, 2004]. A pull-out test is already provided to check the potential instabilities and oscillating issues, notably observed in [Gens et al., 1988].

6.4.1 Definition of the case study

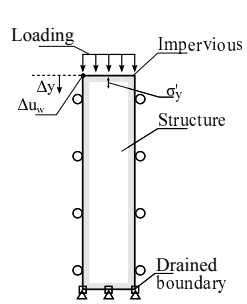

(a) Geometry without interface and definition of measured values

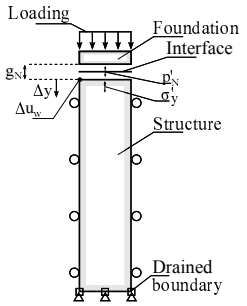

(b) Geometry with interface and definition of measured values

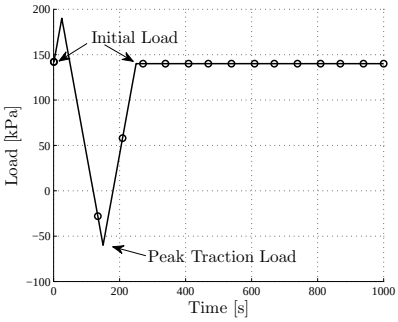

(c) Stress-controlled loading

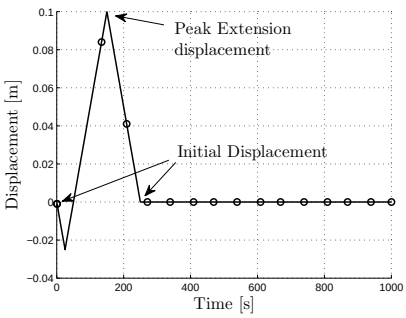

(d) Displacement-controlled loading

FIGURE 6.16: Basic features of the 1D column example of transient consolidation test.

A 8m-high column of elastic soil which parameters are given in Table 6.1 is studied. Hydraulic boundary conditions are drained at the bottom of the column and impervious elsewhere. Two geometries are considered : the first one without interface element at the top (see Figure 6.16a) and the second one with it (see Figure 6.16b). In the latter case, an element represents the foundation that lies on the soil column. The soil column is initially equilibrated by an effective stress in the interface of 40kPa and a pore water pressure of 100kPa.

E [Pa]	ν [-]	ρ_s [kg/m^3]	n [-]	k [m^2]
$2 \cdot 10^8$	0.3	2650	0.36	10^{-12}

TABLE 6.1: Basic parameters employed for the 1D case study

Both stress-controlled and displacement-controlled are considered in order to highlight

different behaviours. However, whatever the driving strategy, the loading is composed of four distinct phases whose the rate of variation is identical (see Figures 6.16c and 6.16d)

- phase 1 : short compressive phase (25s) ;
- phase 2 : strong extension phase in order to highlight the effect of unsticking (125s) ;
- phase 3 : compressive phase back to initial load/displacement (100s) ;
- phase 4 : dissipation of pore water pressure at constant load/displacement (up to the end).

Results analysed are (see Figures 6.16a and 6.16a for their positions in the soil column) :

- Δy : the displacement at the top of the soil column ;
- p'_N : the contact effective pressure in the interface ;
- Δu_w : the pore water pressure variation at the top of the column ;
- σ'_y : effective stress in the soil (first integration point of the first element of the soil, near the top of the column) ;
- g_N : distance which describes either a gap or an interpenetration between both walls of the interface.

6.4.2 Stress-driven simulations

6.4.2.1 Without Interface element

A series of simulations without interface element (corresponding to Figure 6.16a) of the soil column is firstly provided in order to progressively dive into the problem. An insight in Figure 6.17 highlights the non-linearities of these behaviours due to the transient behaviour. The pore water pressure u_w-displacement Δy curve is depicted in Figure 6.17a whilst time evolution of displacement, pore water pressure variation and effective vertical stress are given in Figure 6.17b.

Limit cases

In the former Figure 6.17a, it can be observed that drained and undrained behaviours bound the intermediate solutions, i.e. configurations in which the permeability is not zero nor infinite. These two limit cases are depicted by straight lines. Obviously, there is no variation of pore water pressure in the drained behaviour and the displacement is maximum. On the other hand, no deformation occurs in the undrained[4] case but the pore water pressure variation is maximum.

In Figure 6.17b, the drained behaviour is depicted by the maximum instantaneous displacement while it is null for the undrained curve. Evolutions of pore water pressure variations and effective stress are a kind of yin and yang, both symmetrical and opposite. In the undrained case, the loading is entirely equilibrated by a pore pressure variation. Therefore, the loading curve merges with the $t - u_w$ curve. In the drained case, the loading is fully withstood by the solid skeleton. Consequently the loading curve is identical to the $t - \sigma'_y$ curve. Tensile stress is induced accordingly with the loading, which is non-physical if a sand is considered.

[4] In this case study, the compressibility of the water in infinite.

Simulation $k = 10^{-11}m^2$

If the response curve with $k = 10^{-11}m^2$ is now considered in the Figure 6.17a, it can be observed that it is stretched from the drained curve. Extreme displacements are very close and pore pressure variations are moderate. However, different phases of loading are now differentiated. The first compressive phase is marked by a positive u_w and a negative Δy, i.e. a settlement of the column. Then a load reversal occurs and the curve exhibits a decreasing u_w and a positive Δy, i.e. an extension of the column. During the third phase, the loading is brought back to its initial value which is depicted by a new increasing u_w and decreasing Δy. Finally the loading reaches its initial value and the soil column recovers progressively its initial configuration u_w and Δy.

The first three phases display linear and non-linear parts. The non-linear parts reveal a transient state whilst the linear parts express a stationary behaviour. The observed plateaux emphasise an equilibrium sets up between variations of effective stress, pore water pressure and total load.

It can be observed in the Figure 6.17b that pore water pressure variation is not reinitialised to zero simultaneously with the loading, i.e. there is a slightly delayed effect between loading and soil behaviour. This is due to the partial consolidation encountered by the soil and is a purely transient effect.

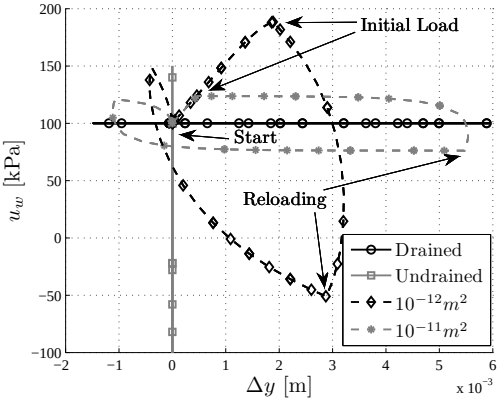

(a) Pore water pressure u_w and displacement Δy at the top of the soil.

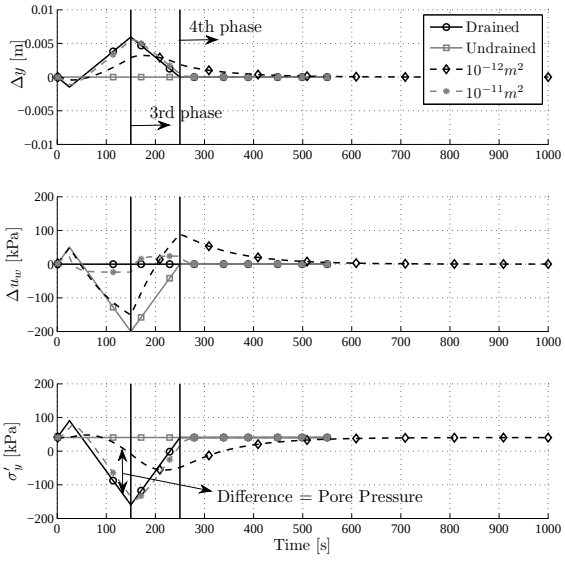

(b) Displacement Δy, pore water pressure variation Δu_w and vertical effective stress σ'_y at the top of the soil.

FIGURE 6.17: Stress-driven simulation without interface element for four drainage conditions (drained, undrained, $k = 10^{-11}m^2$, $k = 10^{-12}m^2$.)

Comparison between all the simulations

Result curves with $k = 10^{-12}m^2$ and $k = 10^{-11}m^2$ can be compared in Figure 6.17a. The former curve is much stiffer than the latter one, the plateaux disappear and extreme pore water pressures increase. Actually, the $k = 10^{-12}m^2$ response tends to the undrained one, which is trivial since the permeability decreases. As a corollary effect, stationary part disappears.

Consequently, the major part of the external loading is balanced by the pore water pressure which can be observed on the $t - \Delta u_w$ curve in Figure 6.17b. Due to the low permeability, this overpressure is slowly dissipated and the total load is only partially transferred to the

soil skeleton. Therefore, the difference between the drained and $t - \sigma'_y$ curves is equal to the pore pressure variation depicted in the $t - \Delta u_w$ curve.
The delayed drainage effect is clearer for the $t - \Delta u_w$ curve with $k = 10^{-12} m^2$ in Figure 6.17b. This fact can be viewed as a memory effect of the past loading. When the total load is reinitialised, $u_w = 90$ kPa. This effect is of paramount importance, since it allows the fluid to participate to the global resistance in both compression and tension. The latter is much more interesting if a sand is considered, since it can only sustain very low tensile drained loading.
Another avatar of the delayed effect is that extreme effective stress σ'_y are postponed after the peak of total load. Indeed, the fate of overpressures Δu_w is dissipated. However, if the permeability is low, it requires a longer time and the effect on σ'_y is deferred.
Actually any point of a drained curve at time t can be seen as a long time state that any permeable material would reach at time $t + \Delta t$ if the loading conditions remained identical.

6.4.2.2 Interface element

In this section, interface element is added at the top of the column (see Figure 6.16b) and material parameters are identical to those given in Table 6.1. Three simulations are proposed hereafter to evaluate its effect on the results (see Figures 6.18a and 6.18b).

- Simul 1 : interface element modified taken the storage into account;
- Simul 2 : no interface element, the loading is directly applied at the top of the column (the foundation is deactivated, see Figure 6.16a);
- Simul 3 : interface element without storage possibility.

Firstly it is worth noting that all the curves are merged at the early beginning of the simulation (see Figure 6.18). This outcome is pretty comforting since only the tensile behaviour of the interface element was modified. The Simul 3 curve diverges from the other ones after a small extension displacement, as shown in the Figure 6.18a. Actually, the contact is lost between foundation and structure. The simulation is stress-driven and unsticking is not taken into account. Thence equilibrium cannot be reached and the computation stops.

The two other curves fit very well up to the unsticking of the soil and the foundation (see Figure 6.18a). From this point, the gap is filled with water since both sides of the interface move away. Therefore, the fluid flux is greater, involving more negative pore pressure at the top of the caisson.
After reloading (start of the third phase) results strongly diverge. The Simul 2 curve without interface element in Figure 6.18a was commented.
The plateau that can be observed in all the Figures 6.18a and 6.18b is an interesting outcome. It starts when the total load is brought back to its initial value. Structure and foundation keep unstuck during the whole third phase (the effective contact pressure p'_N is equal to 0, in Figure 6.18b). Consequently, the total load applied must be equal to the pore pressure inside the caisson in order to ensure the equilibrium of the foundation element (see Figure 6.19). When the initial load is restored, the pressure u_w is constant and equal to 140 kPa[5].

This plateau lasts until the contact is restored. Therefore effective normal stress in the interface rises up and pore pressure is drained simultaneously (see Figure 6.18b, Δu_w and p'_N).
Vertical effective is never in tension, due to the unsticking, which is more physical if a sand is considered (see Figure 6.18b).

[5]The pressure measured u_w is actually different from u_w^I inside, but the gradient is very low and both value are nearly identical.

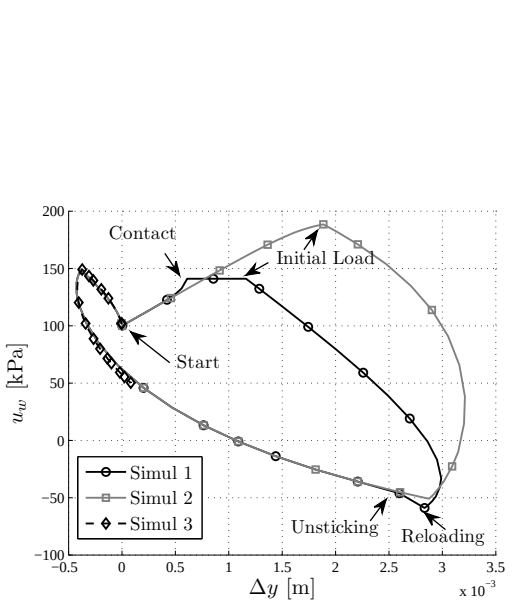

(a) Pore water pressure u_w and displacement Δy at the top of the soil.

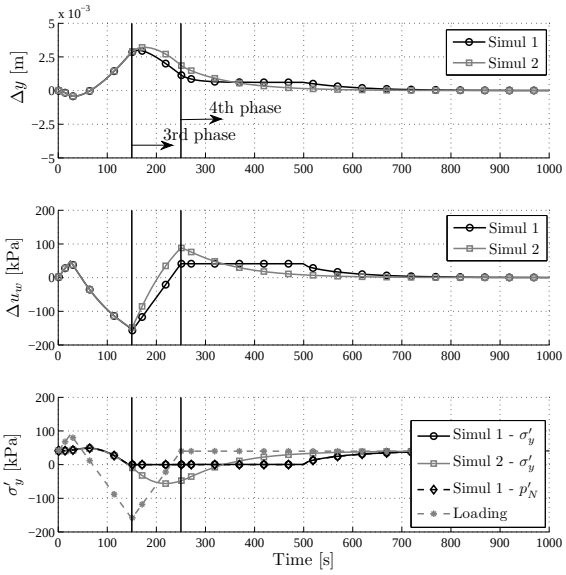

(b) Displacement Δy, pore water pressure variation Δu_w; p'_N is the effective normal stress within the interface and vertical effective stress σ'_y at the top of the soil.

FIGURE 6.18: Stress-driven simulations for 3 configuration : Simul 1 (Interface element with storage), Simul 2 (no interface element), Simul 3 (Interface element without storage).

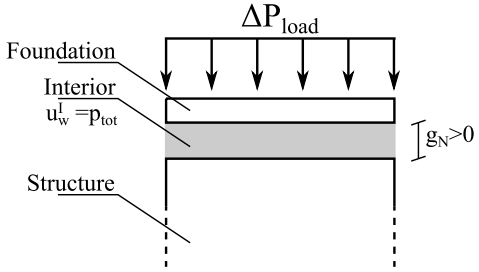

FIGURE 6.19: Unsticking of the interface : creation of a filled void between structure and foundation. The pore water pressure inside is equal to the applied total load.

6.4.3 Displacement-driven simulations

Three identical configurations (Simul 1, Simul 2, Simul 3) are provided for a displacement-driven loading (see Figure 6.20). Once again, three curves of Figure 6.20a fit perfectly for the first stages of the loading. The Simul 3 curve diverges when the contact is lost between structure and foundation. However in this case, the computation does not stop because the simulation is displacement controlled. Indeed, when the contact is lost, a convective exchange with the atmosphere is assumed and u_w tends to 100 kPa.

The reference curve without interface element (Simul 2) has now a symmetric shape in compression and extension because of the displacement loading (see Figure 6.20a). A very high pore water pressure holds when the initial displacement is restored. This one must be dissipated progressively for a fixed Δy. Obviously, extreme pore water pressures are either too high or too low to be physical. For instance, cavitation of the fluid should occur a long time before reaching the minimum [Byrne and Houlsby, 2002].

The Simul 1 curve fits perfectly the reference curve in Figure 6.20a up to the unsticking

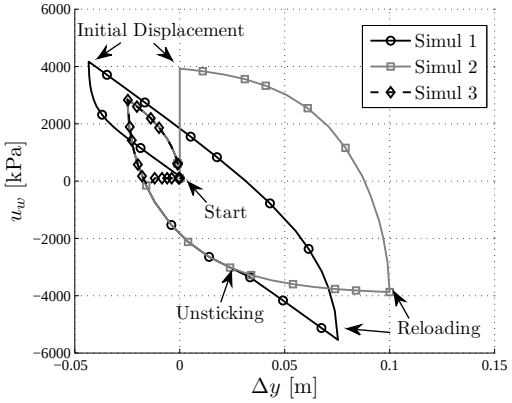

(a) Pore water pressure u_w and displacement Δy at the top of the soil.

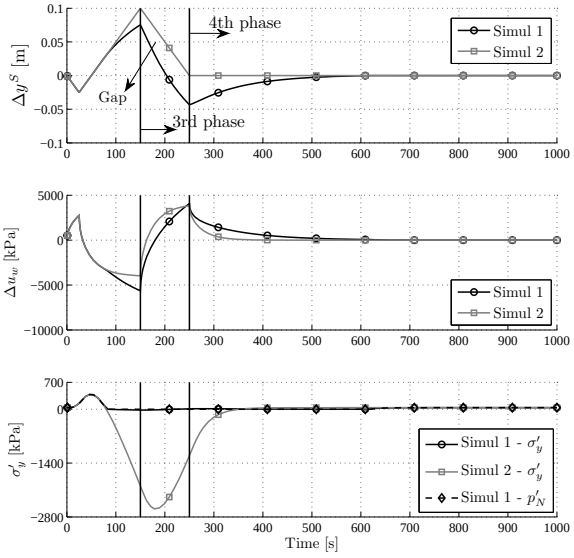

(b) Displacement Δy, pore water pressure variation Δu_w and vertical effective stress σ''_y at the top of the soil.

FIGURE 6.20: Displacement-driven simulations for 3 configuration : Simul 1 (Interface element with storage), Simul 2 (no interface element), Simul 3 (Interface element without storage)

between structure and foundation. Thence variation of pore water pressure is more negative and an equilibrium sets up between the storage and transversal fluxes at the top of the caisson by simply equilibrating the fluid mass fluxes

$$\begin{aligned} f_w^t &= f_w^s \\ \cancel{\rho_w} \cdot T_{w,2}^t \cdot (u_w^I - u_w^S) &= \cancel{\rho_w} \cdot \Delta g_N \\ \Delta u_w &= \frac{\Delta y^F - \Delta y^S}{T_{w,2}^t} \end{aligned} \tag{6.77}$$

where $\dot{y}^F$ is given but $\dot{y}^S$ depends on the consolidation rate of the soil column. The direct consequence is a lower vertical tensile displacement of the soil, which can be observed in both Figures 6.20a and 6.20b. It must be pointed out that in Figure 6.20b, the Simul 2 curve (without interface element) of $t - \Delta y$ corresponds to the displacement imposed curve. Therefore, the difference between Simul 2 and Simul 1 curve over the time is the measure of the gap created between structure and foundation.
Interestingly, this gap enlarges during the re-compressive third phase. This is due to the different distribution of effective vertical stresses and pore water pressures along the cross-section (see Figure 6.21). Finally, both sides of structure and foundation come into contact and all the excess pore pressures are dissipated.

6.4.4 Influence of parameters

The first parameter that influencing the results is the transmissivity T_w^t between the soil and the vacuum (see Figure 6.22a). This parameter eventually influences the $u_w - \Delta y$ curve only if it is very small. Otherwise, the limiting quantity is the permeability of the soil that bounds the flow escaping to fill in the void during unsticking.

The permeability of the soil has a very strong effect on the results observed (see Figure

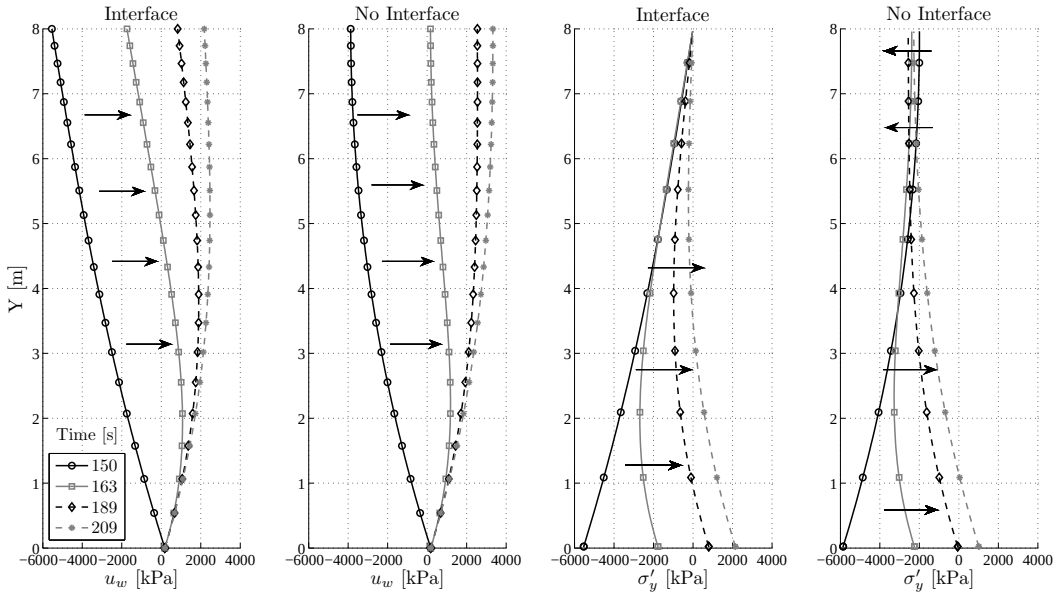

FIGURE 6.21: Comparison of cross sections in the soil column during re-compressive third phase : pore water pressure (u_w) and vertical effective stress (σ'_y).

6.22b). Obviously, the lower the permeability the higher the water pore pressure and the stiffness. As previously stated, a higher permeability induces a stationary phase that is longer. Moreover, the unsticking occurs earlier in that case. The effect of unsticking is also very distinct, marked by nearly straight parts of the curves and the absence of a plateau. Theses phenomena highlight the equilibrium of vertical forces: if no contact holds, the applied load is totally equilibrated by the pore water pressure of the fluid trapped inside the interface, then variations of loading and interior pressure are identical

$$\Delta P_{load} = \Delta u_w^I \tag{6.78}$$

where $\dot{p}^{tot}$ is the rate of variation of loading applied. If the permeability is very high, the vacuum is very quickly filled or emptied and no plateau occurs. If the permability is very low, no unsticking occurs and the response curve tends to the undrained response curve, i.e. a vertical straight line.

These conclusions are directly transposable to analyse the effect of loading rate (see Figure 6.22c). Results present exactly the same features as the effect of permeability but in a more progressive fashion. When the loading rate decreases, the stiffness descreases and the unsticking occurs earlier.

Finally, if the constitutive law, describing the soil is the elastoplastic model of Prevost (see Figure 6.22d and Chapter 4), the effect on displacement is very strong. However, the effect on pore pressure variation is quite identical, whatever the constitutive law. Strong permanent deformations occur because of the stress state that might approach very close to the apex of the resistance cone, i.e. the liquefaction state, where the plastic effects are important.

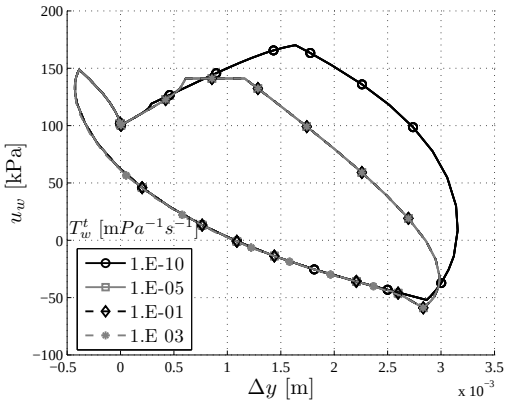

(a) Influence of the transmissivity T_w^t.

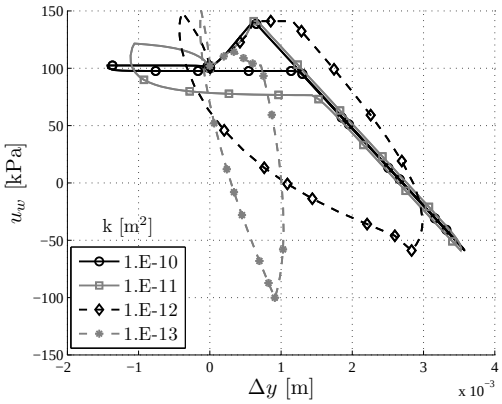

(b) Influence of the permeability k of the soil.

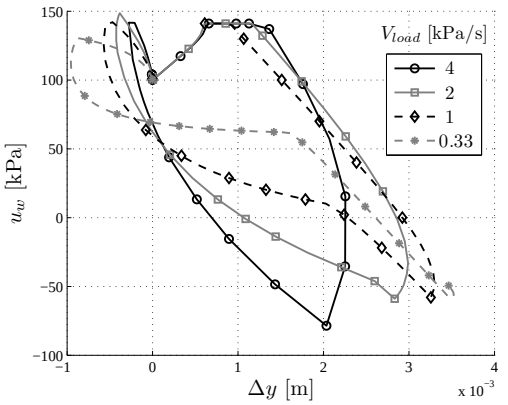

(c) Influence of the loading rate.

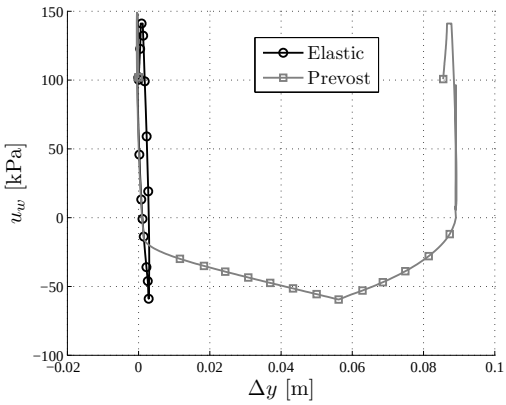

(d) Influence of constitutive law : Prevost model.

FIGURE 6.22: Influence of the main parameters : stress-driven simulations

6.5 From 1D to 2D

1D simulations are of uttermost importance to well-understand basic concepts. However, they neglect the spatial effects such as fluid and stresses diffusion which strongly influence the results. A comparison is provided in Figure 6.23 between the previous 1D 8m column, a 1D 16m column and a 2D axisymmetric suction caisson. The latter is a 4m diameter caisson with a 4m depth plug. The entire domain modelled is 24×26m. All the boundaries are drained except the axis of symmetry. There is no friction resistance available along the shaft of the caisson. Material parameters are obviously identical.

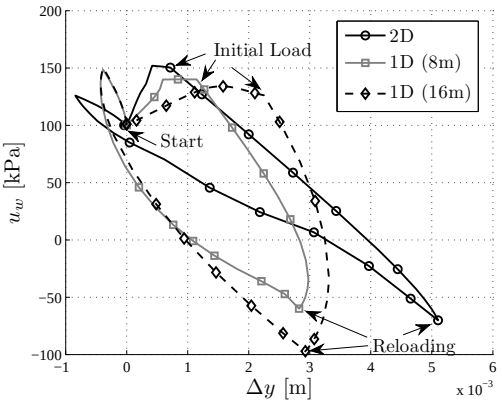

(a) u_w and Δy are respectively the pore water pressure and the vertical displacement at the top of the soil column.

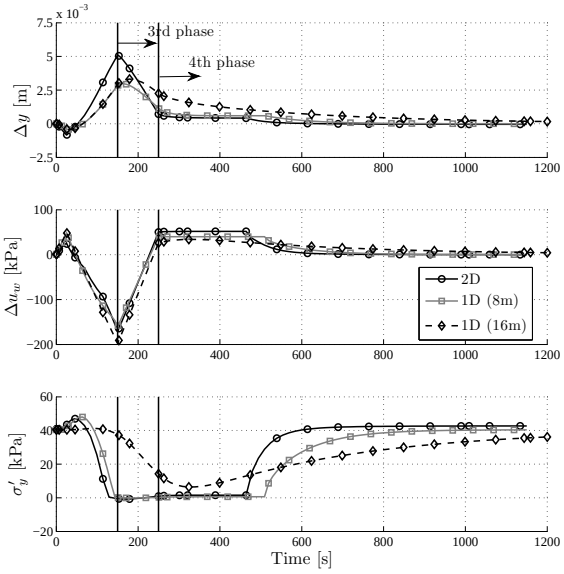

(b) Variations of displacement, pore water pressure and vertical effective stress.

FIGURE 6.23: Comparison between 1D and 2D axisymmetric geometry. The soil column is 16m high whilst the domain size of the 2D simulation is 24×26m.

The height of the 1D soil column influences the results (see Figure 6.23a). They are similar for the compression phase but diverge in extension. As a matter of fact, the height of the column modifies the hydraulic conductivity, since the distance between the top of the caisson and the drained boundary is higher. Therefore, drainage effects are modified. The first compressive phase is too short to observe a difference but the following unloading phase is not. Thence, no unsticking can be noted : the effective stress never reaches zero (see Figure 6.23b) and no plateau can be observed (see Figure 6.23a). This notion of drainage path is a key factor in the understanding of partially drained behaviour of offshore foundations.

1D and 2D curves present a $\Delta y - u_w$ curve different from each others (see Figure 6.23a) even if their time evolution is close (see Figure 6.23b). Actually, pore water pressures generated are quite identical but the displacement is higher, which stretches the curve in the Figure 6.23a. The drainage path does not explain entirely the difference.

The generation of pore water pressure over a cross section is different for 1D and 2D cases (see Δu_w curve in Figure 6.24). The graphs provided depict cross section during the first

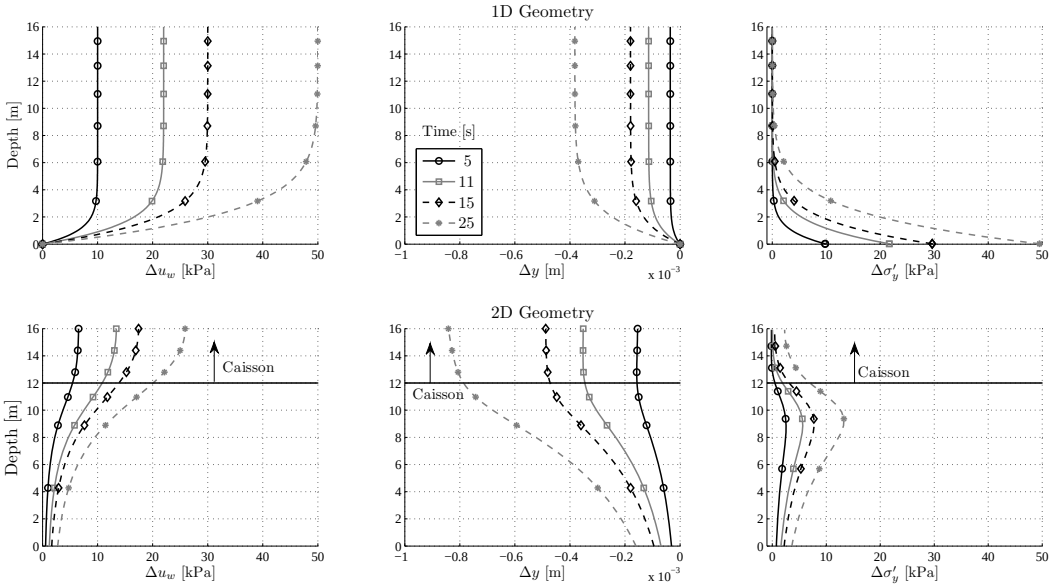

FIGURE 6.24: Comparison between 1D and 2D axisymmetric geometry. The soil column is 16m high whilst the domain size of the 2D simulation is 24×26m. Cross sections at time $[5, 11, 15, 25]$s during compressive phase.

compressive phase. For the 1D geometry, it can be observed that a drainage front propagates towards the top of the column. The uniform pore water pressure is equal to the applied load and delineates the undrained zone. On the other hand, the 2D curve is nearly entirely partially drained and the undrained zone is limited to the very top of the soil column. Actually, the whole 2D domain[6] contributes to the drainage of the pore pressure generated inside the caisson (see Figure 6.25), which is much faster.
The pore pressure distribution directly affects the variation of $\Delta\sigma'_y$ (see Figure 6.23b). Variations of σ'_y are more important for the 1D curve, at the bottom of the soil column, where drainage occurs. On the other hand, for the 2D geometry, variation of σ'_y holds in a zone concentrated under the caisson. This different repartition affects the displacement of the top column since the consolidation is proportional to

$$\Delta y \div \frac{\Delta\sigma'_y}{\sigma'_y}. \tag{6.79}$$

Consequently a variation of $\Delta\sigma'_y$ where σ'_y is higher has less consequences on settlement Δy than a variation where σ'_y is lower. This is illustrated in Figure 6.24.

The loading applied to the caisson (2D results) is distributed between the top of the soil inside and the end-bearing resistance of the shaft. Consequently, pore water pressures generated inside are lower. However this effect might be insignificant since the width of the shaft sidewall is thin.
Moreover, the 2D effect must no be neglected from the diffusion of effective stress. Due to the axisymmetric geometry, effective stresses diffuse under the caisson, implying a stress at the bottom weaker that the applied load $= 50kPa$ (see $\Delta\sigma'_y$ in Figure 6.23b).

Last but not least, if the loading was kept constant after the compressive phase, the final settlement after dissipation of pore pressures would be higher for the 1D geometry ($1.48 \cdot 10^{-3}$m) than for the 2D one ($1.12 \cdot 10^{-3}$m). However, the Δu_w curve in Figure 6.23a

[6]For an axisymmetric case, the implicit 3D effect reinforces this conclusion.

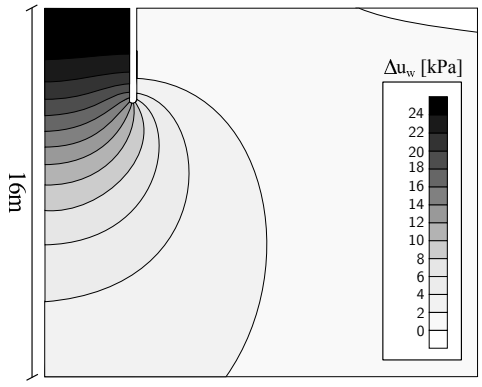

FIGURE 6.25: Variation of pore water pressure under the suction caisson at the end of the compressive phase ($t = 25s$, $\Delta P_{load} = 50kPa$).

yields to the paradoxical conclusion than 1D geometry is stiffer than 2D one. That outcome highlights the inherently transient behaviour of the soil and remind the engineer not to forget the fourth dimension in his/her interpretation.

6.6 Oscillations and ill-conditioning

Accuracy of the solution is one of the main concern when dealing with numerical methods. Different authors brought to light two inaccuracy sources :

- ill-conditioning of the global stiffness matrix [Pande and Sharma, 1979; Wriggers, 2006];
- oscillations of the solution [Kaliakin and Li, 1995; Gens et al., 1988; J.C.J. and De Borst, 1993].

The former issue is the natural consequence of the penalty method introducing very high order terms in the stiffness matrix. The solution is very simple and consists in limiting the value of the penalty parameters to one or two order of magnitude higher than the Young modulus, for example.

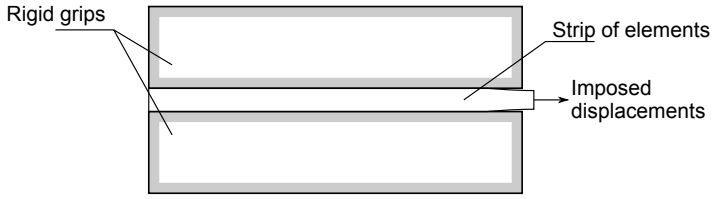

FIGURE 6.26: Pull out test of a strip of elements between two rigid grips. The friction coefficient is equal to 0.3 and the initial normal stress is initiated at 100 kPa.

The latter issue is more pernicious. Some authors tried to develop much accurate elements [Kaliakin and Li, 1995] or to use different numerical integration schemes such as the Newton-Cotes one [Gens et al., 1988] to overcome oscillations. However, it was stated in the latter paper that oscillations cause lies within the concept of finite elements. Indeed, the field of displacement is described by shape functions $\phi(\xi)$ that are most of the time parabolic or linear. If the maximum shear resistance is reached, a front of sliding propagates in the interface as well as a front of shear stress. Actually, this front might be too sharp to be accurately modelled over a single finite element.
A pull test of a strip of solid elements (without water) out of two rigid blocks is carried out in order to illustrate this phenomenon (see Figure 6.26). Displacements are imposed at the end of the strip inside the grips. Parameters adopted for the test are given in Table 6.2. A normal pressure of 100 kPa is assumed initially between the strip and the grips. A coarse mesh of 10 elements over 2m of interface and a fine mesh of 40 elements are compared.

E [Pa]	ν [-]	μ [-]	K_N [N/m^3]
$2 \cdot 10^8$ or $2 \cdot 10^7$	0.3	0.3	$1 \cdot 10^{10}$

TABLE 6.2: Parameters adopted for the pull test

An example of pull test is provided in Figure 6.27. Cross sections of tangential and normal stresses are given for different time steps[7]. Propagation of the sliding front is obvious. The decrease of normal stress is due to the Poisson's effect implying a lateral deformation of the elongated strip material. Therefore, the maximum shear stress decreases as well since it is computed as

$$t_{t,max} = \mu \cdot p_N. \tag{6.80}$$

Coarse and fine meshes provide a similar solution.

[7]The reference to time is just a reference to a given imposed displacement at the end of the strip, since the behaviour of the interface is not rate dependent.

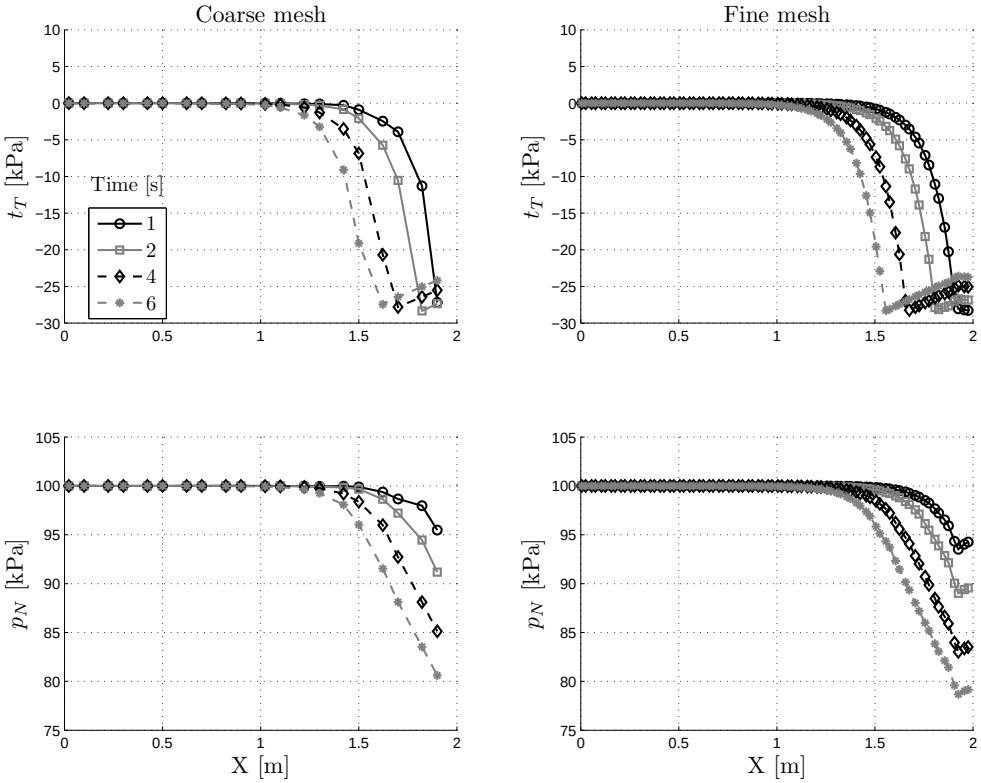

FIGURE 6.27: Pull test for a young modulus of $2 \cdot 10^8$ Pa. Cross sections of both normal and tangential stresses p_N and t_T along the strip. Comparison between fine and coarse meshes.

If the young modulus of the strip is decreased to $E = 2 \cdot 10^7$ Pa, oscillations occur at the beginning (see Figure 6.28) and are attenuated with time. It is noteworthy that these oscillations are slightly attenuated if the mesh is finer.
Actually, the cause of these discrepancies do not lie within the integration scheme but in the shape function order. Let us consider the early beginning of the pull out test ($F > 0$, see Figure 6.29). Sliding occurs over a small part of the strip whilst the other part remains stuck. Let us consider now that the interface was discretised with finite elements which the length is greater than the physical sliding length. Therefore, the discretised distribution of tangential displacement should be represented over the element by a parabolic function,

$$u_x = \sum_{i=1}^{n_n} \phi_i(\xi) \cdot u_{x,i}. \tag{6.81}$$

However, the parabolic approximation is not able to perfectly reproduce the sharp distribution of displacement. Therefore the final solution is nothing but the set of nodal displacements that minimise the error between actual and discretised field of displacement (see Figure 6.29), leading to an oscillating solution. This phenomenon is also encountered when dealing with consolidation of soils, see for example [White and Borja, 2008].
This was eventually established in [Day and Potts, 1994]. The only solution to overcome oscillations is either to refine the mesh or to adopt higher order shape functions.

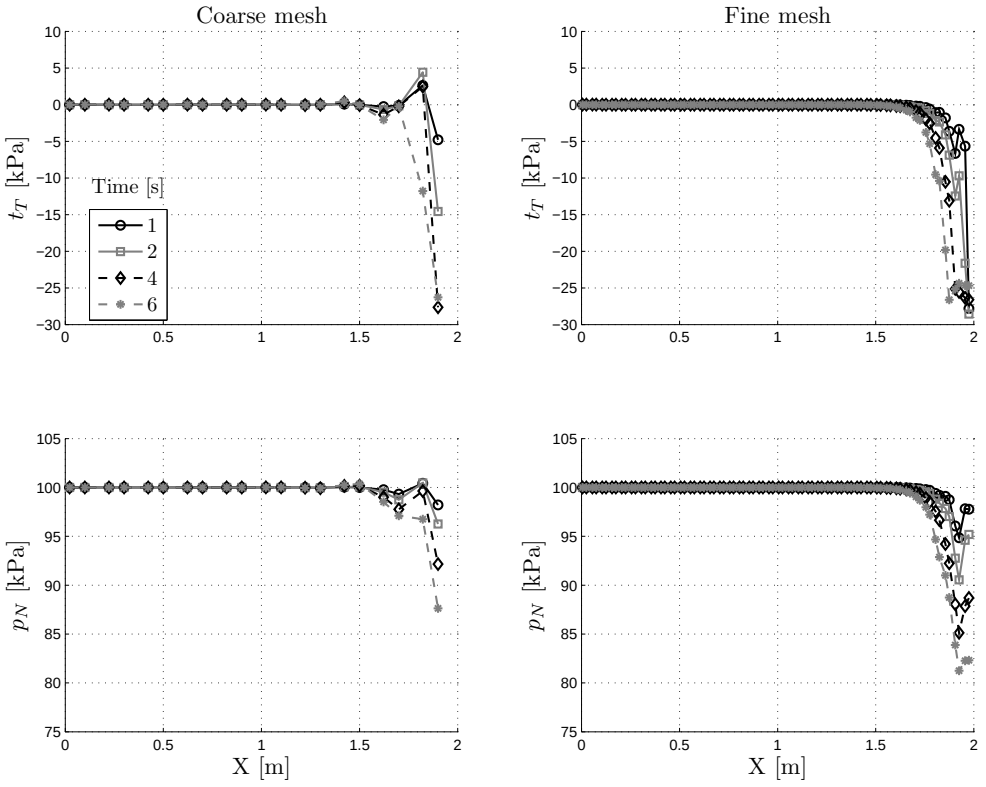

FIGURE 6.28: Pull test for a Young modulus of $2 \cdot 10^7$ Pa. Cross sections of both normal and tangential stresses p_N and t_T along the strip. Comparison between fine and coarse meshes.

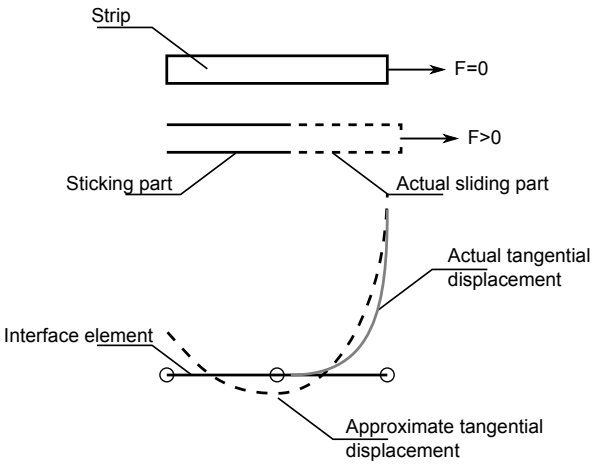

FIGURE 6.29: Partial deformation of a strip element

6.7 Conclusion

In this chapter, the general concept of contact problem is described in the case of mechanical contact and extended to hydro-mechanical couplings. Indeed, when solids in contact are porous media, fluid flow takes place inside. Their proximity induces fluid flow through the interface which must be taken into account. This is achieved by the discretisation of an equivalent porous medium between the two solids in contact if a gap exists between them.

A 1D hydro-mechanical interface finite element already implemented in the finite element code `LAGAMINE` is improved. The unsticking capacity of the two sides of the interface is developed and implemented. Consequently, the finite element is capable of taking into account

- sliding ;
- fluid flow parallel to the interface ;
- fluid flow from the solids through the interface ;
- unsticking and storage of water inside the interface.

A transient consolidation test is carried out on a 1D soil column. It is shown that the behaviour of the soil is partially drained, i.e. pore water pressures generated instantaneously are partially dissipated during the loading, resulting in particular $u_w - \Delta_y$ paths. If the permeability is low, the pore water pressure generated participates to a large part of the equilibrium of external loading. Consequences are twofold : effective stresses in the soil are weaker, then likely tensile effective stresses are weaker in extension. As a corollary effect, settlement encountered during the loading is also lower.

Using an interface element involves no tensile vertical stresses applied to the soil, which is more physical if a sand is modelled. Moreover, when unsticking occurs, the total load is fully balanced by pore water pressure inside the interface, creating a suction effect in tension.
Influence of parameters is also observed. The transmissivity between soil and interface is only important if it is very low. On the other hand, permeability of the soil is the limiting factor of the fluid flux available to fill in the void created by unsticking. This permeability is of uttermost importance since it strongly affects the dissipation of overpressures and therefore the capacity of partially drained resistance. The loading rate has the same consequence. The use of an elastoplastic model has strong consequences on displacements. Since the generated pore water pressure decrease the effective stresses, plastic deformation are greater.

Transition from 1D to 2D highlights effect of actual geometry. Dissipation of pore water pressure is faster and the response curve tends to a more drained behaviour. This outcome coupled with a diffusion effect of the stress involves a lower stiffness of the 2D geometry, for the short-term behaviour. Results highlight that the time effect on the coupling is of great importance.

Perspective of development are multitudinous. The formulation of interface elements can be extended to multi-physical couplings, where gas phases of both air and water can be taken into account. Therefore cavitation and partially saturated behaviours of the soil would be accurately modelled. The constitutive law implemented is very limited and should be extended to cyclic loading or viscosity effects. Finally, 3D finite elements of interface should be very interestingly used to model more complex loading cases, such as the horizontal loading of a suction caisson for example.

Chapter 7

Application to a case study

When we have eliminated the impossible, whatever remains however improbable, must be the truth.

Sir Arthur Conan Doyle

Contents

7.1 Introduction

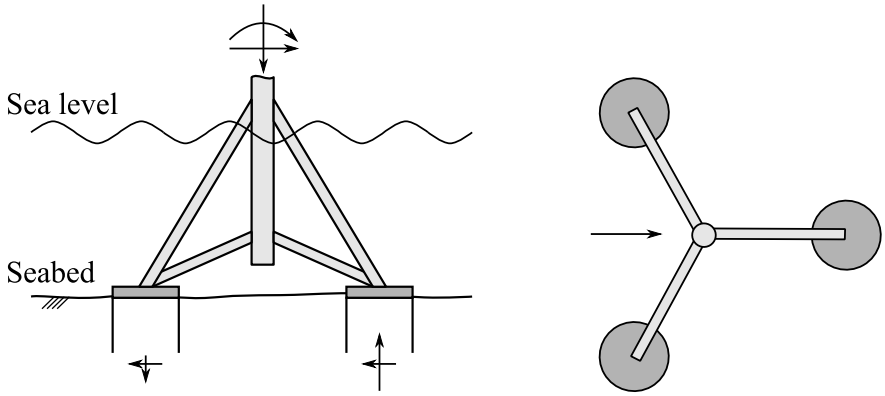

(a) Elevation view (b) Plan view

FIGURE 7.1: Sketch of a tripod foundation structure, inspired by [Kelly et al., 2006b; Houlsby et al., 2005].

In this chapter, all the topics previously developed are integrated into an application in offshore geotechnics. This consists in the modelling of a foundation that is a part of a multipod support for wind turbines, e.g. a tripod foundation (see Figure 7.1). Such structures are particularly used in deep waters where large moment is imposed on the foundation. This global moment created by wind and waves is sustained by a push/pull action on the foundation whatever its nature [Senders and Randolph, 2009].
In the following, this hypothesis on the prevalence of vertical loads is advanced to justify an axisymmetric analysis. The modelling of the superstructure is out of the scope of this study. Thence, interactions between wind turbine, its support and the environment are supposed to be known. Interested reader should refer to [Leblanc, 2009] for more information. The analysis is quasi-static. Thence inertial forces are neglected. This can be justified by the relative low frequency of the loading.
These structures give birth to interesting loading conditions of the foundations. Indeed, they are very light with regard to the overturning moment they have to sustain. For example, Byrne and Houlsby [2003] provide an example of a 3.5MW turbine, which weights 6MN, has to sustain 4MN of horizontal load and a maximum of 120MN of overturning moment. In that case, the wind component represents 25% of the total horizontal loading but 75% of the overturning moment since it is applied at the top of the mast.
The typical design loading case of offshore wind turbines consists of a storm. Such an event is inherently transient. The corresponding loading signal can be generated by special techniques, out of the scope of this study. It must correspond to a given climate, characterised by a wave height and a given return period. That is, the signal embeds a given frequency content and an extreme event, corresponding to the highest wave the structure must resist. Further information about the generation of such a loading, is available in [Taylor et al., 1997; Jonathan and Taylor, 1997; Van Der Tempel, 2006]

The foundation type investigated in this paper is a suction caisson, also termed skirt or bucket foundations, suction anchors or suction piles, [Iskander et al., 2002]. It consists of a hollow cylinder open towards the bottom (see Figure 7.2). The top of the caisson can either be a stiffened plate or a dome, [Tran, 2005]. Stiffeners are often added inside to avoid buckling of the skirt during installation. The wall thickness to diameter ratio lies generally in the range 0.3-0.6%, [Byrne and Houlsby, 2002; Kelly et al., 2006a; Tran, 2005]. Examples of documented suction caissons already installed in sand are provided in Table 7.1.

(a) During installation.

(b) After installation.

FIGURE 7.2: Installation of a prototype foundation at the test site of Fredereikshavn, [Houlsby et al., 2005].

Site	H_w [m]	D [m]	H [m]	Reference
Wilhelmshaven	6.0	16.0	15.0	[Houlsby et al., 2005]
Frederikshavn	1.0	12.0	6.0	[Ibsen, 2004]
Frederikshavn	0.2	2.0	2.0	-
		4.0	4.0	
Sandy Haven	0.5	4.0	2.5	[Houlsby and Byrne, 2005]
Tenby	2.0	2.0	2.0	
Burry Port	0.5	2.0	2.0	-
Luce Bay	0.2	3.0	1.5	[Houlsby et al., 2006]
		1.5	1.0	

TABLE 7.1: Examples of documented suction caissons installed in shallow water, from [Houlsby et al., 2005]. H_w, design wave height; D, diameter of the caisson; H, its height.

The concept of suction caisson covers a large variety of situations and geometries. The idea of suction anchor popped up in the early sixties, [Goodman et al., 1961], to replace inefficient weight anchors, [Tran, 2005]. They were used mainly as temporary anchorages [Senpere and Auvergne, 1982]. The geometry of such anchors have most of the time an aspect ratio H/D higher than one, up to five. In 1989, the Gullfaks C was the first structure employing suction caissons as a permanent foundation system [Tjelta et al., 1990]. This concrete gravity based structure was founded on 16 concrete compartments (16m high, 28m in diameter) in a soft clay (see Figure 7.3a). Structures corresponding to high H/D ratios were also used as deep anchors for buoyant platforms in the Gulf of Mexico [Equihua Anguiano, 2008].
Draupner E and Sleipner T platforms, built in the early nineties marked the first time suction caissons were used as permanent foundations in sand (see Figure 7.3b). They also demonstrate that this method was feasible in very dense sand [Tjelta, 1994]. The success of these projects started the increase of suction caisson use around the world. They are now applied to a large variety of soil conditions and are utilised alone or as part of a multipod foundation [Byrne and Houlsby, 2003; Houlsby et al., 2005].

Installation of suction caissons is quite straightforward [Houlsby et al., 2005]. Initially the caisson is laid down on the ground and penetrates the seabed under its own weight. Water trapped inside is allowed to escape during this phase by an opening. Afterwards, inner water is pumped, creating a differential pressure at the top of the caisson and pushing it down (see Figure 7.4). The pressure gradient generates a seepage flow within the soil, reducing the penetration resistance at the tip and along the inner skirt [Senders and Randolph, 2009].

(a) Gravity based platform, Gullfaks, [Tran, 2005]

(b) Draupner E platform. Source NGI.

FIGURE 7.3

Although the outer friction resistance is increased, the caisson encounters a global reduction of resistance.
However, attention must be paid not to exceed the critical gradient. Indeed, this may generate erosion channels along the skirts (pipping), the excessive loosening of the soil or a ground failure [Andersen et al., 2008]. The partial liquefaction that might appear during the installation phase is prone to create a soil heave (see Figure 7.4), preventing the caisson to be installed at the required depth [Iskander et al., 2002].
The foundation part in the global cost of an offshore wind turbine may reach up to 35% of the total cost [Byrne and Houlsby, 2003]. The main advantage of suction caissons is their low cost of installation. They require a basic equipment (no need for large barge cranes or heavy hammer) and the duration of the installation process lasts less than 24 hours [Tran, 2005]. Furthermore they can be readily retrieved by reverse pumping and reused.

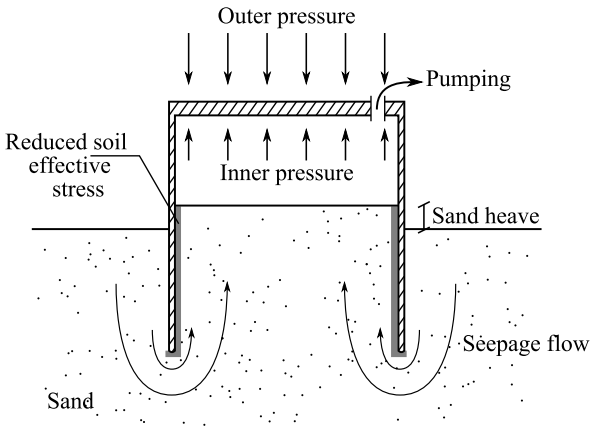

FIGURE 7.4: Installation of a suction caisson by pumping.

Suction caissons have received a special attention in the literature over the last decade. Papers have mainly focused on laboratory [Byrne and Houlsby, 2002; Houlsby et al., 2005; Kelly et al., 2006b] and *in situ* tests [Kelly et al., 2006a; Houlsby et al., 2006]. They aim at defining work-hardening plastic surfaces, where the rupture is reached for a combination of normal and horizontal forces and a moment [Mangal and Houlsby, 1999; Byrne and Houlsby, 2004; Coffman and El-sherbiny, 2004]. Their behaviour is inherently partially drained but the purely drained behaviour is also investigated [Byrne and Houlsby, 1999; Villalobos et al., 2009]. Simplified methods have also been developed to describe the installation of the caisson [Senders, 2008]. Simplified methods and recommendations are also available in [Veritas, 2011],

which is a world-famous standard.
Nowadays, design is more and more facilitated by the use of cyclic stability diagrams. These diagrams relate average and cyclic loads to the state of serviceability of the foundation, [Puech, 2013; Stuyts et al., 2011]. However such diagrams require a large number of computations/-experimental tests. Many papers are devoted to the modelling of offshore foundations, e.g. [Cuéllar et al., 2014]. However, a fully transient modelling of such a structure requires many numerical tools that are not available in each finite element code, [Andresen et al., 2011; Versteele et al., 2013].

This chapter aims at modelling the fully transient vertical behaviour of a suction caisson. The final purpose is not the design of a foundation, neither with simplified formulae nor analytical methods. Indeed, information about real site and in place wind turbine is very scarce. Moreover data corresponding to described experiments and necessary to calibrate a complex constitutive model are often not available. Therefore, this chapter focuses on an extended description of the phenomena ruling the modes of resistance of the suction caissons during both monotonic and cyclic loading.
Initially, the vertical response of the caisson is investigated either in drained and partially drained conditions. The influence of salient parameters (friction coefficient, permeability...) is investigated. A pseudo random cyclic loading is then applied. It consists of a 600s part of a storm loading that includes an extreme event. The pseudo-random behaviour is compared with an sinusoidal equivalent signal. A final full storm is then computed in order to test the behaviour of the model onto a long duration loading sequence.

7.2 Definition of the case study

7.2.1 Reference geometry

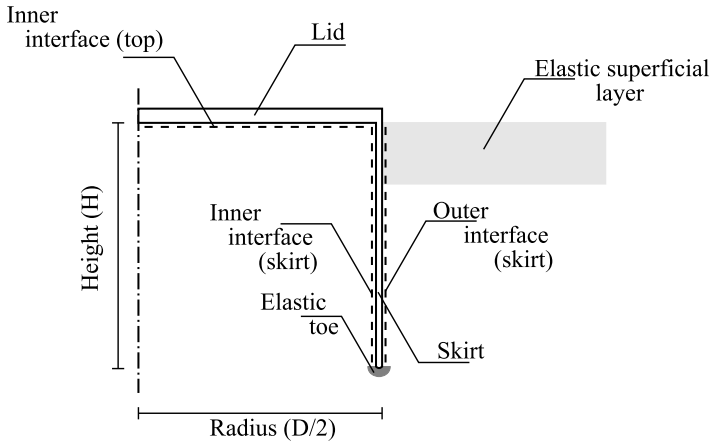

FIGURE 7.5: Sketch of the geometry of the reference caisson and definitions of structural elements.

A sketch of the axisymmetric reference case study is provided in Figure 7.5. The structure is defined by its diameter D, its height H and the thickness of its skirt e. It is assumed to have a circular cross-section. Actual geometries are more complex. However stiffeners along the skirt of the caisson are not taken into account. The lid of the caisson is considered very rigid in order to homogeneously distribute the loading and its thickness is equal to 0.4m. Geometric parameters of the reference case study and the mesh as well are provided in Table 7.2. The mesh is sufficiently refined under the tip of the caisson, but the number of elements is kept acceptable for the simulations to be launched on a laptop. Volume elements used are Q8P8 elements.
The thickness of the skirt is a key factor. Indeed, a non-negligible component of the overall resistance is mobilised under the tip of the caisson. However, for numerical purpose[1] the thickness of the structure was kept artificially large with regards to actual geometries. Real e/D ratios are in the range 0.3-0.6% [Byrne and Houlsby, 2002; Kelly et al., 2006b; Tran, 2005], but the adopted geometries has a ratio e/D= 1.2%. Consequently, the reaction sustained by the tip might be unrealistic. An elastic toe (one element width) is defined underneath the tip which can reduce its relative stiffness. A complete justification is provided in section 7.2.4.
A superficial elastic layer (0.8m) is also established at the top of the soil. Indeed, this layer has a low contribution to the global resistance and is prone to liquefaction, since its confinement is very low. Therefore, an elastic model allows to overcome local failures.

D [m]	H [m]	e [m]	Elements [-]	Nodes [-]
7.8	4	0.1	2364	7085

TABLE 7.2: Geometric and mesh parameters of the reference case study.

Interface elements are distributed inside and outside the caisson between the skirt and the soil. Horizontal elements allow unsticking between soil and the caisson with development of

[1]The structure is to be modelled with solid elements which can not be too narrow and do not take into account flexural behaviour, contrary to shell elements. Furthermore, a too sharp tip would involve a deep perforation of the structure into underneath finite elements, which would be tricky to manage.

suction but are frictionless, *i.e.* $\mu = 0$, in order to facilitate the convergence of the code. On the other hand, vertical elements resist essentially by friction. Elements under the tip are very localised. They are frictionless and no suction effect is taken into account. Indeed, the rounded geometry induces a very painful convergence in case of unsticking.
Finally, the caisson is supposed *in place* and its installation is not modelled. The modelling of this installation would require special numerical techniques, e.g. material point method or remeshing, in order to manage the plug of the caisson. As a consequence, local perturbation of soil density inside the caisson, initial stress distribution or scour under the tip are not investigated.

7.2.2 Material parameters

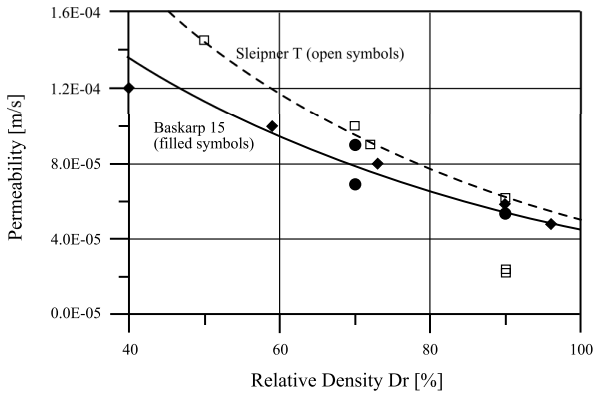

FIGURE 7.6: Evolution of permeability with density, after [Andersen et al., 2008].

Parameters of the Dr= 90% Lund sand are adopted to represent the soil behaviour. They are defined in Section 4.4.4 and only salient parameters are remembered in Table 7.3. The elastic limit is reached for a mobilised friction angle of 1.7°. The phase transformation ratio $\bar{\eta}$ corresponds to an angle of 29°. Failure in both compression and extension corresponds to 44° and 30° respectively.
Data concerning the permeability of this material are not available. More generally, data in the literature are scarce and sparse and the permeability strongly depends on the granulometric curve and the density of the sand. An example of such a relation is illustrated in Figure 7.6 for Baskarp and Sleipner sands. They seem to converge to a similar value at high density.
Therefore, a permeability k= $5 \cdot 10^{-12}$m^2 is adopted although Lund sand does not present the same granulometry distribution. This parameter is crucial and the effect of its sensitivity is to be characterised cautiously. Furthermore, the modelled soil domain is assumed homogeneous while actual configurations are most of the time heterogeneous. Thence, all the efforts made to determine an "exact" permeability of the soil, must be nuanced by its inherent heterogeneity. Finally, a small cohesion of 5 kPa is added for numerical purpose, in order to avoid very local failure.

Elastic parameters of the superficial layer and the elastic toe are provided in Table 7.4. Justification of this choice for the elastic toe is provided hereafter. The caisson is assumed to be made of steel. The friction angle at the interface is strongly affected by the density of the sand, the state of the steel (corrosion) and local conditions. In this work, a friction coefficient μ equal to 0.5 is adopted, corresponding to an angle of 26.6°. It seems to be a reasonable assumption with regard to sparse data provided in the literature [Taiebat, 1999; Lings and Dietz, 2005; Andersen et al., 2008; Senders, 2008].

Physical			Prevost model				
γ_s [kN/m^3]	k [m^2]	n [-]	G_{ref} [MPa]	K_{ref} [MPa]	$\bar{\eta}$ [-]	Ψ [-]	c [kPa]
26.5	$5 \cdot 10^{-12}$	0.36	47	65	1.15	1.0	5

TABLE 7.3: Parameters adopted for the Dr= 90% Lund sand. γ_s, density of the solid grains; k, permeability; n, porosity; G_{ref} and K_{ref}, elastic reference parameters; $\bar{\eta}$, phase transformation line ratio; Ψ, plastic volumetric parameter; c, cohesion.

Elastic soil		Caisson	
G [MPa]	K [MPa]	G [MPa]	K [MPa]
4.36	4.72	$7.6 \cdot 10^4$	$1.66 \cdot 10^5$

TABLE 7.4: Parameters of elastic soil and caisson.

The initial state of the soil is deemed isotropic, i.e. $K_0 = 1$. Indeed, this is a strong assumption, although it is reported to consider $K_0 = 0.8$ in [Andersen et al., 2008]. The main reason is purely numerical. A non isotropic initial state induces, by definition, deviatoric stresses. Thence, since the elastic yield surface is very narrow, the initial state might lie outside it, which is not admissible. A remedy to this situation is the building of the soil domain layer by layer, which is, at least, cumbersome. It would be also possible to carry out oedometric simulation up to a given state of stress and to use the final state of parameters to approach a realistic state of stress.

7.2.3 Loads

A sketch of the loads applied to the reference geometry is represented in Figure 7.7. A confinement of 10kPa exists at the top of the domain. Indeed, it is assumed that the seabed is not well defined, i.e. the limit between a solid soil and water, and then not explicitly modelled. This confinement also increases the overall stability of the computation in limiting the risk of local failure, i.e $p' = 0$. The stress controlled loading is applied at the top of the caisson. It still remains arbitrary and will be defined for both monotonic and cyclic loads.
Effective stresses corresponding to this loading and to the buoyant weight are initialised over the whole domain. So are the initial stresses in the interface elements. The sea water level is assumed to be ten meters higher than the seabed and initial pore water pressures (PWP) are set up accordingly. It must be pointed out that this level has no effect on the results. However, it would have if cavitation were taken into account in case of pulling out of the caisson. This phenomenon bounds the most negative pressure that might be reached within the soil.

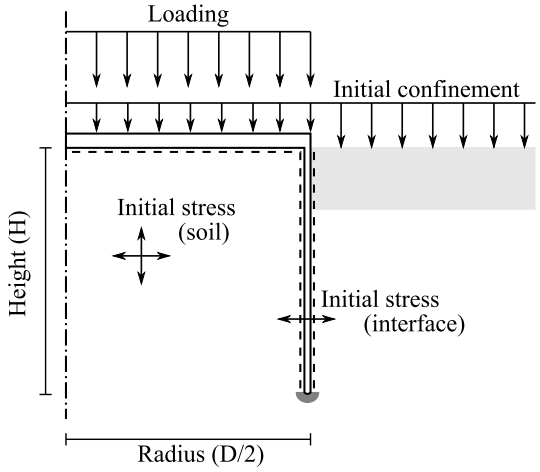

FIGURE 7.7: Sketch of the loading applied to the reference caisson.

7.2.4 Elastic toe

An elastic zone was introduced below the tip of the caisson. It is termed "elastic toe" in Figure 7.5. The elastic modulus characterising it is softer than the modulus of the soil. The purpose of such a zone is manifold.

1. The insertion of the narrow stiff tip of the caisson into the soils creates high stress concentrations that are not easy to manage. Moreover, the mesh should be very refined in this zone, increasing the computational cost. The main advantage of elastic constitutive laws is that a solution always exists even at very large deformations.

2. The corollary effect of stress concentration is the occurrence of local liquefaction of the soil. This local failure of few single elements affects the global convergence of the code but is not an indication of an overall physical failure.

3. For numerical purpose, the skirt of the caisson is numerically wider that it is in reality. Therefore, a softer underlying soil decreases the part of the global load that is sustained by the tip, decreasing its relative stiffness with regard to the top of the caisson or the friction.

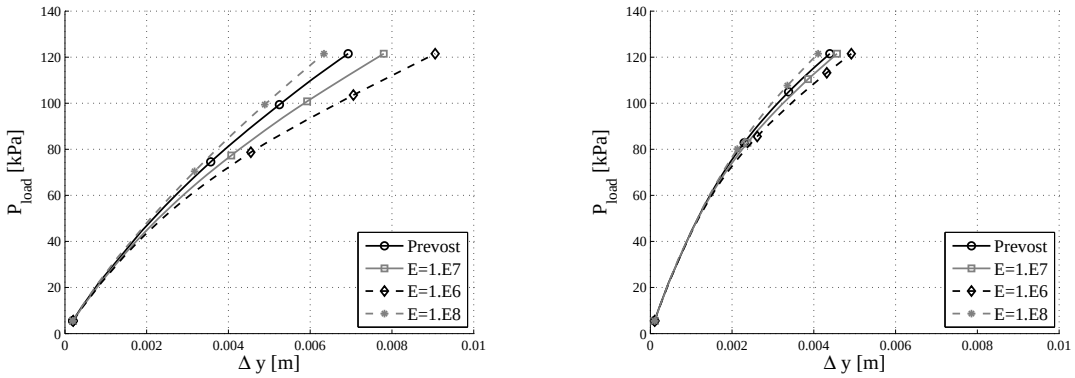

(a) Drained simulation

(b) Partially drained simulation

FIGURE 7.8: Influence of the elastic toe (E in Pa) on the load-displacement curve.

Figure 7.8 summarises the global influence of this zone on the displacement-load curve. Δ_y is the vertical displacement measured in the centre of the lid of the caisson. A simulation

without elastic toe (Prevost model under the tip) is compared with three elastic moduli (in Pa) for both drained and partially drained simulations. Obviously, the lower the elastic modulus, the higher the displacement. The drained Prevost simulation is equally close to E= 10^7Pa and E= 10^8Pa simulations (see Figure 7.8a). However, it is interesting to observe that the results dispersion for the partially drained simulations is very narrow, i.e. it nearly does not affect the final result.
Thence an elastic modulus of E= 10^7Pa is finally adopted for two main reasons. Firstly, such a modulus attenuates the too stiff skirt of the caisson. Secondly, using E= 10^8Pa appears to transfer stress concentration further in the soil which induces non convergent simulations.

7.3 Monotonic behaviour

7.3.1 Components of reaction

In this section, P_{load} denotes the total pressure applied at the top of the suction caisson. F_{tot} is the total vertical force applied to the caisson and ΔF_{tot} is its variation. Different components of reactions can be distinguished (see Figure 7.9a). In the following, variations of pressures and shear mobilised along the caisson are integrated and their resultants are represented:

- ΔF_{int}, variation of total shear mobilised along the skirt, inside the caisson ;
- ΔF_{ext}, variation of total shear mobilised along the skirt, outside the caisson ;
- ΔF_{top}, variation of total vertical effective reaction under the top of the caisson ;
- ΔF_{uw}, variation of total vertical reaction due to pore pressure variation, inside the caisson ;
- ΔF_{tip}, variation of total vertical reaction under the tip.

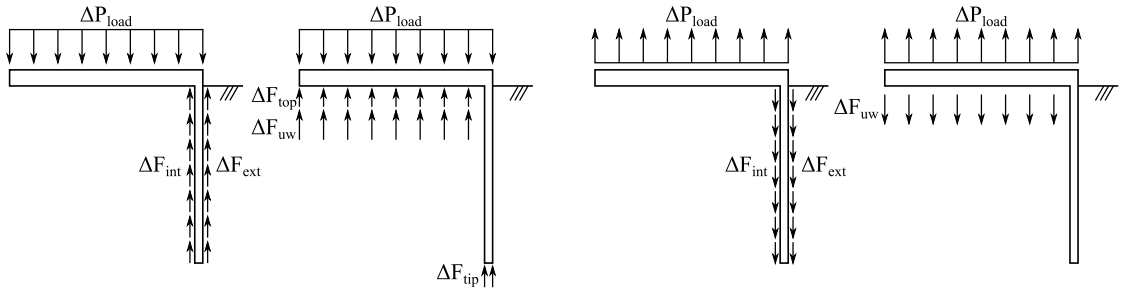

(a) Reaction involved during push tests. (b) Reaction involved during pull tests.

FIGURE 7.9

These reactions are not primary unknowns of the FE code. Therefore, they must be reconstituted. Shear reactions along the skirt and vertical reactions under the lid are integrated using the shear and normal stresses which are known at integration points. The numerical integration is carried out with a Gauss scheme. The amount of PWP within the caisson is obtained through the integration of the pressures, known at each node. The tip reaction is the residual reaction that balances ΔF_{tot}. Indeed, due to the complex geometry of the tip, it was deemed unwieldy to integrate the stresses known at its interface.
The rate of loading adopted is 8kPa/s. It does not influence the drained simulations since no viscous effect is taken into account. However it influences the partially drained simulations. Modifying the rate of loading or the permeability have similar consequences and only the latter will be modified for monotonic simulations.

7.3.2 Push test

7.3.2.1 Drained

A drained monotonic compressive test was carried out on the reference geometry of the caisson reaching to the non convergence of the code, corresponding to 160kPa. Displacement-load curves are provided in Figure 7.10 where both total and normalised variations of reactions

are illustrated. In Figure 7.10b, variations of reaction components ΔF are normalised by the variation of total loading at step t ΔF_{tot}. Therefore, it is possible to understand the contribution of each component to the global resistance. Consequently, the sum of all normalised components is equal to one.

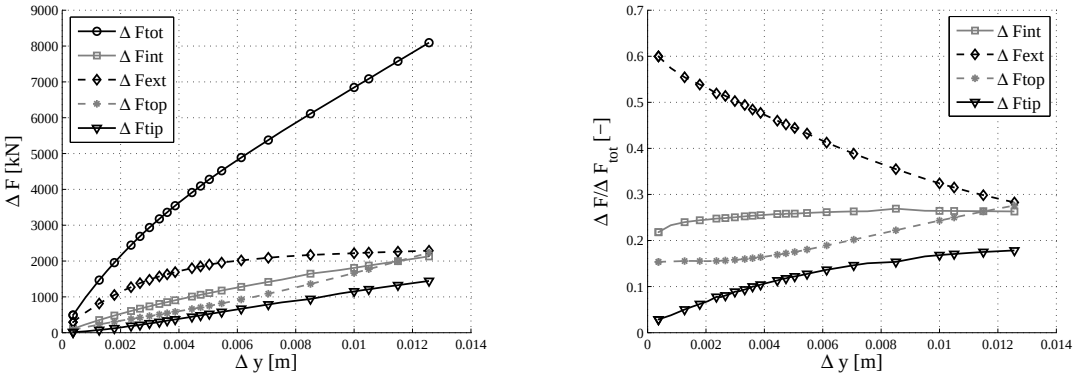

FIGURE 7.10: Drained compressive simulation

In this configuration, the greatest reaction component is the external shear mobilised (ΔF_{ext}, see Figure 7.10a). However, it can be observed that ΔF_{ext} initiates a plateau. Actually this plateau corresponds to the maximum mobilisation of the friction along the external side of the caisson. Furthermore, it is not purely horizontal but slightly inclined, since the confinement increases with the load, the maximum available friction increases as well. The contribution of the outer shear mobilised in the overall resistance monotonically decreases since it is bounded, as shown in Figure 7.10b.

The shear reaction inside the caisson, ΔF_{int}, is low at the beginning and increases with displacement (see Figure 7.10a). However, its contribution to the global reaction is nearly constant (see Figure 7.10b).

The distinct evolution of ΔF_{ext} and ΔF_{int} depends on the different settlement and stress conditions. Inside the caisson, the soil approaches oedometric conditions. It is vertically loaded and the relative displacement between the soil and the skirt is low (see Figure 7.11). On the contrary, there is a large relative displacement between the skirt and the outer sand, which fully mobilises friction.

In this Figure 7.11, the deformation mode appears clearly. The caisson settles monolithically and brings the surrounding soil with it. There is a clear slip outside but it is less marked inside. The isocurves of vertical displacement also give an idea of the diffusion of the shear stress within the soil.

Loads transferred to the top ΔF_{top} or the tip of the caisson ΔF_{tip} increase almost linearly (see Figure 7.10a) and their relative contribution gain importance (see Figure 7.10a). However the curvature of the plot is convex for the top and concave for the tip evolutions. The soil inside the caisson is confined, increasing its stiffness and reducing the deviatoric stress, i.e. the stress state is kept away from the failure line. On the other hand, material around the tip is submitted to a high deviatoric stress, i.e. the stress state around approaches the failure line.

The distribution of the reaction between these components only depends on their relative stiffness, which is not straightforward to determine since the problem considered is far from beam-column structures. The stiffness of each reaction component depends on many parameters, such as permeability, Young modulus of the caisson, plastic moduli of the soil, permeability, length of the skirt... The caisson structure has also a great influence. Indeed,

the lid is assumed very rigid which tends to transfer a large part of the total load to the skirt[2]. A less stiff caisson's top would induce a greater ΔF_{top}. Furthermore, ΔF_{int} diffuses inside the caisson. Therefore ΔF_{top} and ΔF_{int} can be gathered inside a common interior component for the design.

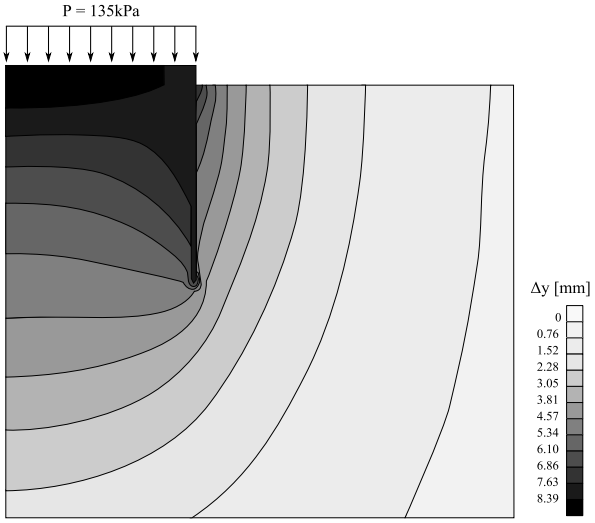

FIGURE 7.11: Vertical displacement, monotonic drained compressive test, during simulation.

7.3.2.2 Partially drained

A partially drained push test is presented in Figure 7.12. It is composed of a compressive phase with the increasing load pressure followed by a consolidation phase, i.e. $\Delta P_{load} = cst$. In this case, results exhibit features similar to the drained simulations. However, the pore water pressure generated inside the caisson, ΔF_{uw}, represents the main contribution to the total reaction during the push phase (see Figure 7.12a). As a consequence, the displacement at the end of this phase ($\sim$ 6mm) is lower than the drained one.
During the push phase, outer shear component ΔF_{ext} presents a plateau (see Figure 7.12a). However, this maximum reaction is slightly lower than the drained resistance. Indeed, the pore pressure variation reduces the normal effective stress inside the caisson and at the interface. The maximum friction available is then decreased.
ΔF_{int} and ΔF_{uw} are correlated. It can be observed that for a displacement between 0 and 1 mm, the ratio $\Delta F_{uw}/\Delta F_{tot}$ decreases but increases afterwards (see Figure 7.12b). The decreasing slope of the PWP component is due to the progressive drainage of the soil. The slope change corresponds to the beginning of the plateau of ΔF_{ext}, i.e. a new load increment can not be sustained by exterior shear and is dispatched between other reaction components, e.g. ΔF_{uw}.

Interestingly, the inner shear ratio, $\Delta F_{int}/\Delta F_{tot}$, appears to be negative at the beginning. However, its absolute value is nearly negligible. The difference might be understood in comparing the patterns[3] of vertical displacements between Figures 7.13 and 7.11. Isocurves of displacements inside the caisson for a drained simulation present a concave curvature. It means that deformation is higher near the skirt of the caisson due to the diffusion of the shear

[2] A parallel can be drawn between this application and a foundation lying over an elastic soil. The skirt creates a "hard spot".

[3] A comparison between the amount of displacement is meaningless since these two snapshots do not corresponds to an identical time step !

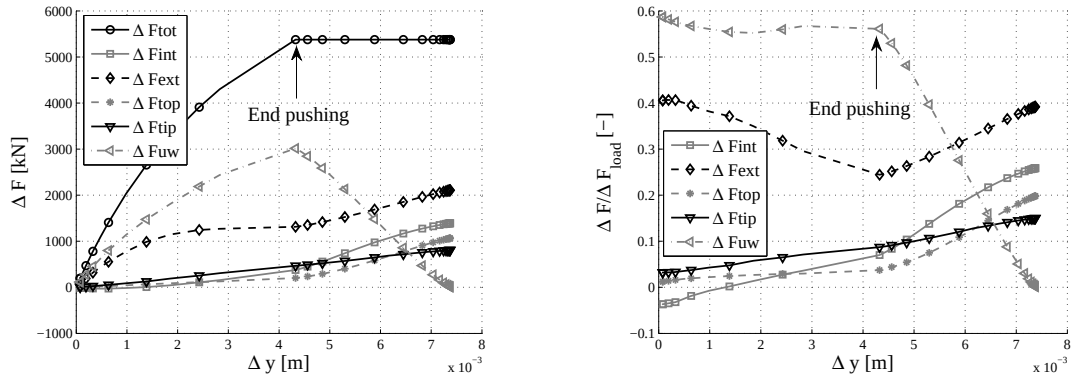

FIGURE 7.12: Partially drained compressive simulation, k= $5 \cdot 10^{-5}$m/s.

stresses. On the other hand, isocurves of the partially drained case inside and under the caisson present a convex curvature, i.e. settlement is higher near the centre. This distribution of settlement affects the relative displacement between the soil plug and the caisson, explaining the negative ΔF_{int} at the beginning.
At the end of the push phase, pore pressures are allowed to dissipate. Therefore, the pore pressure component continuously decreases and the vertical displacement increases accordingly. This load is redistributed between the other reactions components and the ΔF_{ext} one recovers its drained final value ($\sim$ 2200kN in Figure 7.10a). The final displacement achieved is also close to the drained one but not identical since plastic effects are path dependent.

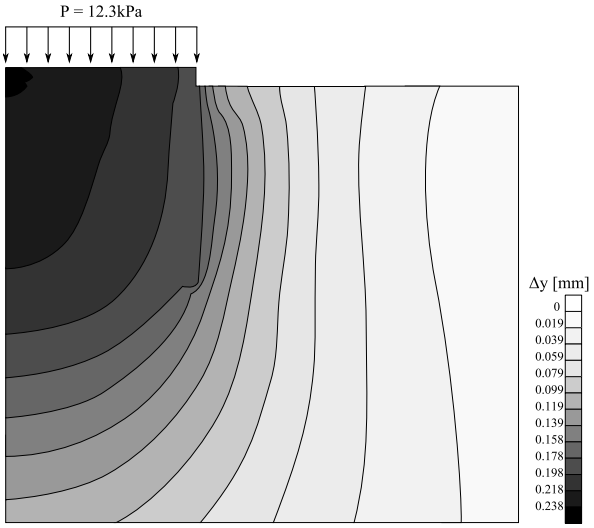

FIGURE 7.13: Vertical displacement, monotonic undrained compressive test at the beginning, k= $5 \cdot 10^{-12}$m^2.

7.3.2.3 Influence of permeability and Prevost model

Figure 7.14 illustrates the influences of the model (elastic or Prevost) and the permeability on the push test. The comparison is limited to the first compressive phase, without consolidation.
Obviously, it can be observed for both models that the lower the permeability, the higher the pore pressure contribution, $\Delta F_{uw}/\Delta F_{tot}$, to the reaction (see Figure 7.14a). Consequently,

the final displacement at the end of the push phase is lower too. Moreover the elastic constitutive law used does not take into account the confinement dependency of the stiffness. The comparison between displacement-load curves is then limited.
Furthermore, the results presented for the Prevost model indicate a higher pore pressure generation inside the caisson. This directly results from the plastic contractive behaviour of the soil. The gap between elastic and Prevost results enlarges with increasing permeability. Indeed, a higher drainage involves a transfer of the total load from the PWP to the solid skeleton. Therefore, variation of deviatoric stress, plastic contractancy and PWP generation are higher. An example of the distribution of η = q/p values is illustrated in Figure 7.15. The whole domain lies within the contractive range, i.e. $\eta < 1.15$.

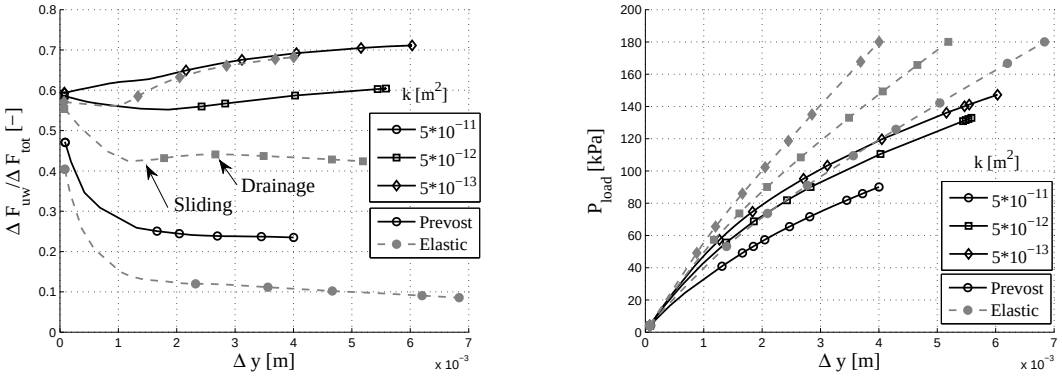

(a) (b)

FIGURE 7.14: Influence of permeability (k) and model type on the displacement-load curve. Black curves (Prevost model) - gray curves (elastic model).

Elastic results better highlight the decreasing ratio $\Delta F_{uw}/\Delta F_{tot}$ with increasing permeability. They also mark more strongly the slope breakage accompanying the beginning of the plateau of outer shear, ΔF_{ext}, highlighting the initiation of sliding. On the other hand, this transition is smoothed when considering the Prevost model. The limit case of k= 10^{-13}m^2 does not even exhibit the decreasing ratio $\Delta F_{uw}/\Delta F_{tot}$ nor the slope breakage. The PWP accumulates continuously and the soil plug might reach a liquefaction state.

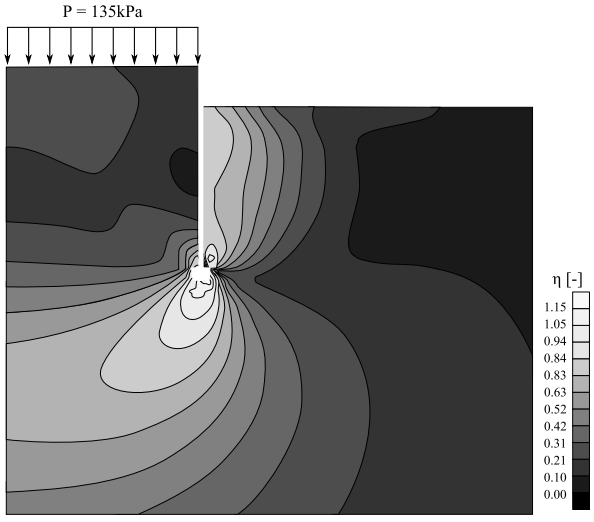

FIGURE 7.15: Reduced deviatoric stress during a push undrained simulation, k= $5 \cdot 10^{-12}$m^2.

7.3.2.4 Influence of friction coefficient

Special interface conditions are illustrated in Figure 7.16 for both drained and undrained simulations. The first limit case depicts a friction angle of the steel-soil interface equal to 0. Thence, the caisson slips along the soil without any resistance. The stuck condition presents an infinite angle of friction of the interface, i.e. there is no limitation of τ.
The difference between stuck and normal conditions is very slight, indicating the shear mobilised nearly does not reach its maximum value along the skirt. However, the gap between results increases, which indicates the inner shear is progressively mobilised. The absence of friction strongly affects the results. In this case, only two reaction components balance the total load : ΔF_{top} and ΔF_{tip}. The former bears the major part of the load which induces a uniform settlement of the soil inside and under the caisson.
The physical global failure is not reached for these simulations. Indeed, the computations stops when local failure are attained.

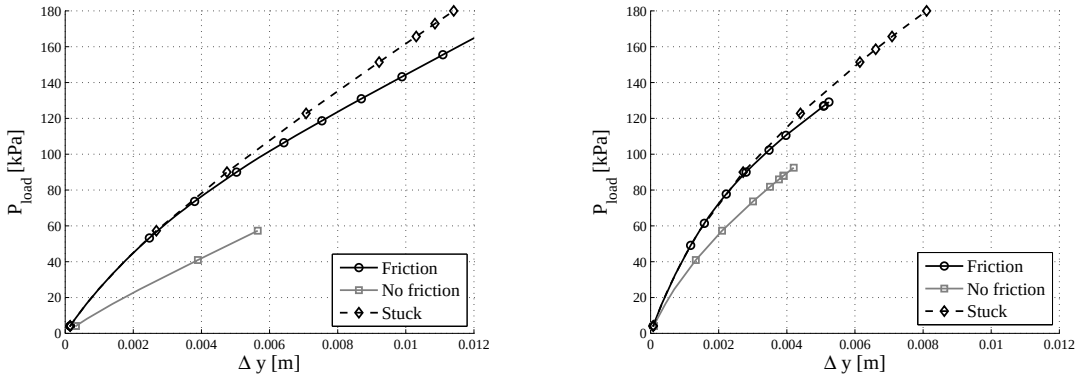

(a) Drained simulation

(b) Partially drained simulation

FIGURE 7.16: Influence of interface conditions during push test. "Friction", sliding is allowed; "No friction", steel-soil friction angle equal to 0; "Stuck", friction angle is infinite.

7.3.2.5 Influence of the caisson height

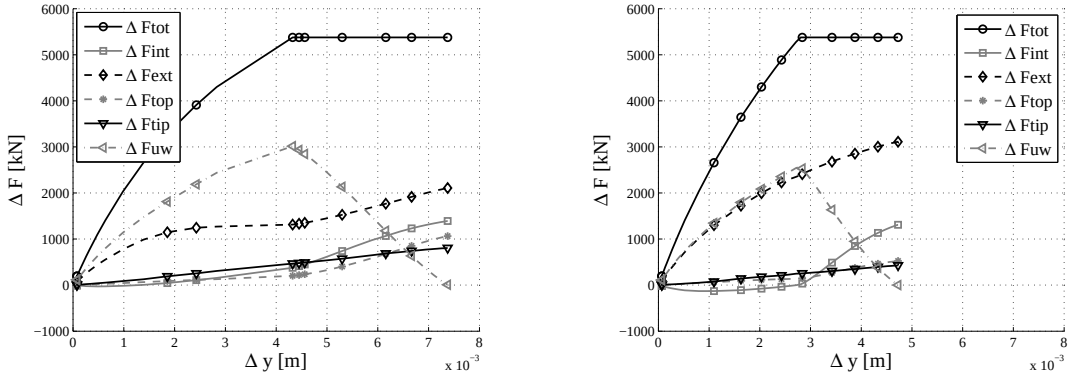

(a) H4 : caisson height is equal to 4m

(b) H6 : caisson height is equal to 6m

FIGURE 7.17: Undrained push test.

Two caissons which are 4m and 6m long were subject to an identical push loading. Their displacement-load results are illustrated in Figure 7.17. The increase of the caisson height has at least three consequences :

- the global outer shear resistance is increased due to the greater surface ;
- the drainage path is increased between the top of the caisson and the seabed ;
- the tip zone is shifted deeper, which increases p'.

The consequence of the increase of friction available is clearly visible in Figure **??**. The H4 component of outer shear, ΔF_{ext}, presents a plateau that is absent of the H6 results. Obviously, such a plateau would also appear in the latter case if the pushing was further continued.
The increase of the drainage path can not be observed merely in Figure 7.17. A longer path reduces the rate of dissipation of the pore water pressure inside. Moreover, in the H=4m case, the soil skeleton is more loaded, generating in turn higher pore pressure. Therefore, a clear consequence of increasing H is not obvious.
So is the consequence of a deeper tip. The component ΔF_{tip} is lower in the H= 6m case, since the maximum outer friction is not yet attained. It is worth noting that if the tip lies deeper, the stress concentration that might result from the plug of the caisson benefits from the higher mean effective stress and decreases the liquefaction risk.

7.3.3 Pull test

7.3.3.1 Drained

Shear along the shaft of the caisson is the only mode of resistance of the caisson during drained pull tests. Results of such a simulation are illustrated in Figure 7.18 (initial point is on the right of the graph). Computation is carried out up to failure, i.e. the caisson pops out. ΔF_{ext} and ΔF_{int} represent 80% of the total reaction component and the exterior shear reaction weights initially 60% of the total (see Figure 7.18b). Afterwards both components converge towards each other. The slope change in the monotonically decreasing $\Delta F_{ext}/\Delta F_{tot}$ ratio corresponds to the maximum available outer friction. It corresponds to a simultaneous rise of $\Delta F_{int}/\Delta F_{tot}$ since further increments of loading are reported on this component.

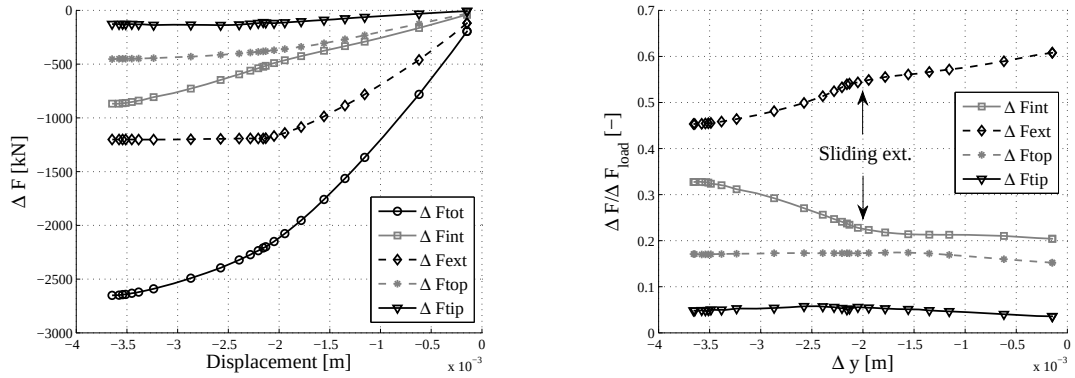

FIGURE 7.18: Drained extension simulation. Results start on the right and negative displacements stand for extension.

It might seem strange to represent ΔF_{tip} and ΔF_{top} since these components can not hold the caisson by surface tractions. However the global resultants F_{tip} and F_{top} are not represented, but their variations. Therefore the non-null plateau of ΔF_{tip} and ΔF_{top}, corresponds to null values of F_{tip} and F_{top}, i.e. it indicates a loss of contact between the soil and the caisson.
Interestingly, although the interface friction angle is identical on both sides of the caisson, the reaction component associated to each of them is different. Final reactions especially are close but not identical. Indeed, the traction applied to the top of the caisson modifies the stress state within the soil. Hence, the normal stress on the skirt, σ'_n. This directly affects the maximum available shear since it reads

$$t_{T,max} = \mu \cdot p'_N. \tag{7.1}$$

The distribution of shear along the shaft is described in Figure 7.19b at the end of the simulation and is homothetic to the distribution of normal stress (see Figure 7.19d), i.e. sliding occurs. The difference between outer and inner resistance is due to the traction loading which deconfines the soil inside and then the normal stress on the skirt.
At the beginning of the pulling, however, the maximum resistance is not reached inside nor outside the caisson. Thence the normal stress does not influence the shear distribution (see Figure 7.19c). The difference between ΔF_{ext} and ΔF_{int} is simply due to the difference of relative soil-interface displacement. Indeed, the soil plug is deconfined which increases its upward movement. As a consequence the relative displacement caisson/soil is lower than outside where the confinement does not change.

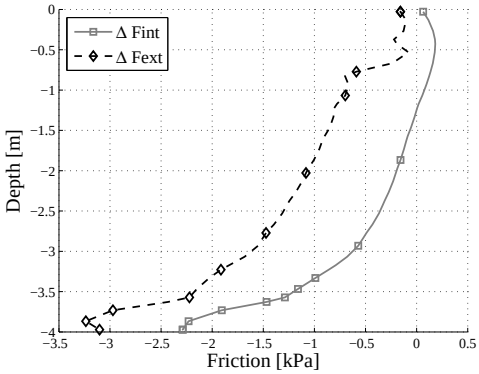

(a) First step (displacement = −0.1mm)

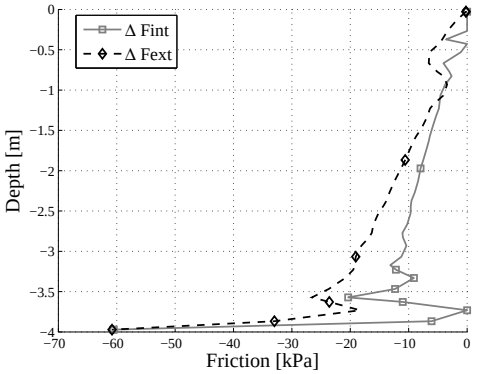

(b) Last step (displacement = −3.6mm)

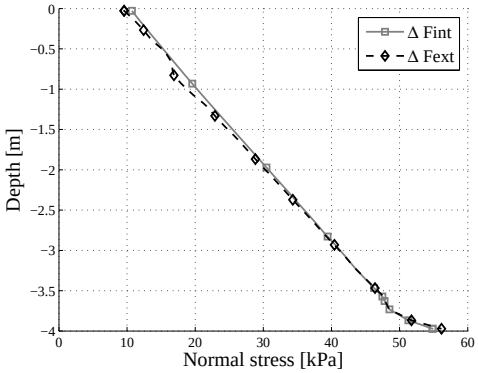

(c) First step (displacement = −0.1mm)

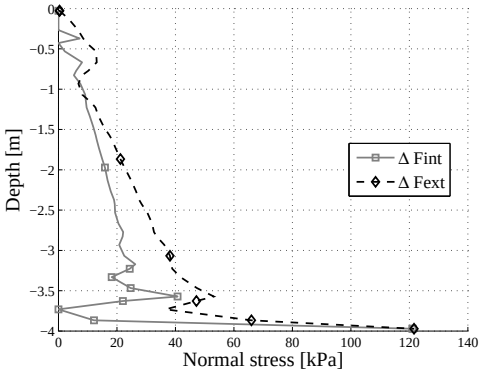

(d) Last step (displacement = −3.6mm)

FIGURE 7.19: Drained extension simulation, distribution of shear along the shaft.

7.3.3.2 Partially drained

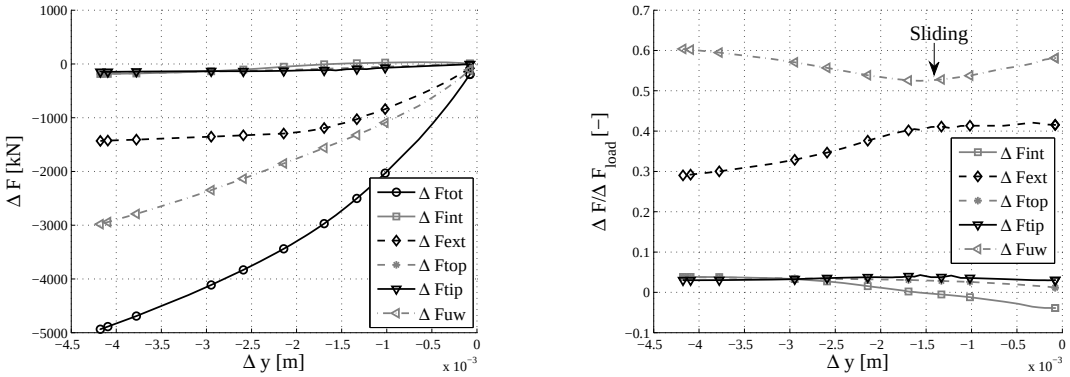

(a) (b)

FIGURE 7.20: Partially drained extension simulations, k= $5 \cdot 10^{-12}$m^2. Results start on the right and negative displacements stand for extension.

Extension partially drained simulation of a pull test is illustrated in Figure 7.20. Results present features already observed. Outer shear mobilised increases up to the initiation of sliding (see Figure 7.20a). Variation of pore water pressure inside the caisson ΔF_{uw}, represents the major component of the reaction. It decreases up to the initiation of sliding and increases afterwards (see Figure 7.20b).
The inner shear is initially positive in absolute value (and negative in relative one). This has little effect on the global result but might be questionable. An hypothesis that could explain this phenomenon, is the non uniform displacement of the soil within the caisson. The suction effect induces a larger displacement in the middle of the soil plug than near the skirt. Thence the relative displacement involves shear stresses tending to pull the caisson (see Figure 7.21b)). The soil can be considered as stuck to the caisson since the relative sliding is very limited. This was already observed at failure in laboratory experiments, [Byrne and Houlsby, 2002; Kelly et al., 2006b]

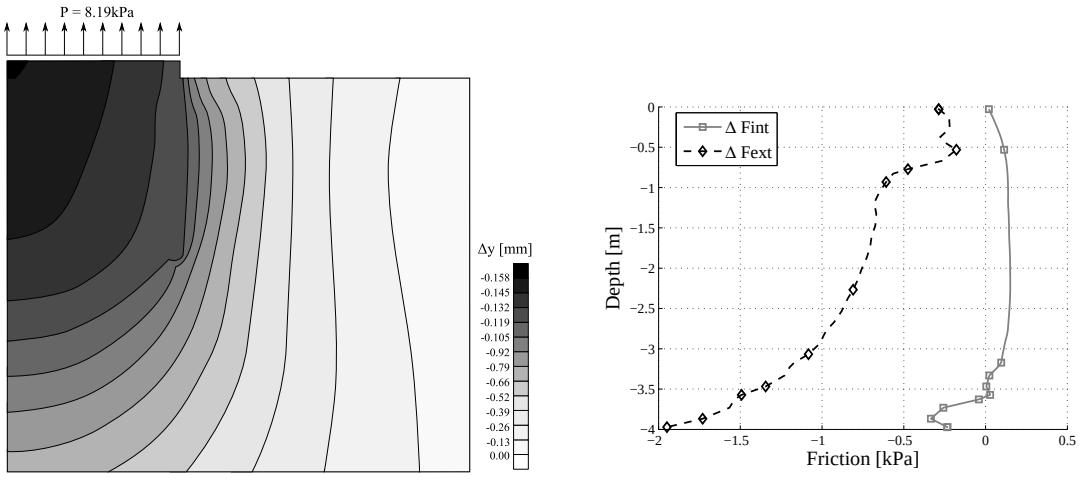

(a) Vertical displacement (negative if upward).

(b) Cross section of the shear mobilised inside and outside the caisson. Positive shear implies stresses pointing upward.

FIGURE 7.21: Extension partially drained test, beginning of the simulation, k= $5 \cdot 10^{-12}$m^2.

Distribution of PWP at the end of the pull test is illustrated in Figure 7.22. It demonstrates the usefulness of the skirt of the caisson. Indeed, pore pressure inside is negative,

inducing a high suction that prevents the pulling out of the caisson. It appears that these under-pressures are very quickly dissipated outside the caisson. Therefore, such an effect could not be mobilised without the skirt or would be significantly less pronounced.
The partially drained effect and the suction pressure generated double the total resistance of the caisson, with regard to a drained simulation. However this resistance is purely transient and depends on the rate of loading. If the load applied is kept constant during a long period, the final total resistance in traction is the drained resistance.

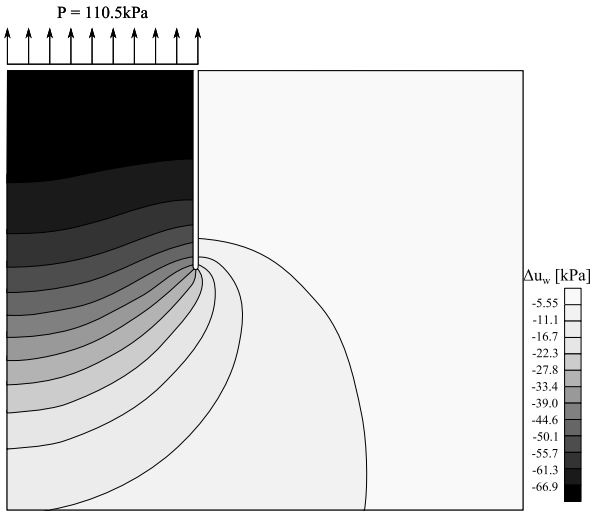

FIGURE 7.22: Pore water pressure distribution around the caisson at the end of the pull test, k= $5 \cdot 10^{-12}$m^2.

7.3.3.3 Influence of permeability

It is interesting to observe the effect of permeability on the displacement-load curve, presented in Figure 7.23. Obviously, the higher the permeability, the higher the flexibility and the displacements reached for a given traction load (see Figure 7.23a). Observations are similar for both the permeability or the rate of loading. Thence only the influence of the former is investigated. Furthermore, the influence of k does not only affect the magnitude of ΔF_{uw} but also its shape, as shown in Figure 7.23b.

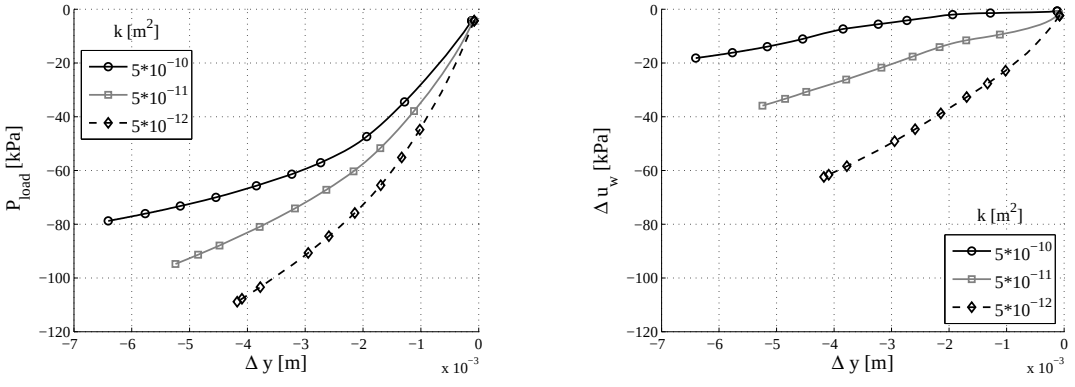

FIGURE 7.23: Comparison of results for k= $[5 \cdot 10^{-10}; 5 \cdot 10^{-11}; 5 \cdot 10^{-12}]$m^2.

The highest permeability results, i.e. k= $5 \cdot 10^{-10}$m^2, are interesting since they summarise all the behaviours that might happen in such a test. They are depicted in Figure 7.24. The

major component of reaction is the outer shear, ΔF_{ext}, since there is a very high drainage (see Figure 7.24b). ΔF_{ext} increases up to reach the plateau of fully mobilised friction. Simultaneously, the contribution of the PWP $\Delta F_{uw}/\Delta F_{tot}$ decreases, due to the drainage (see Figure 7.24b).
The beginning of sliding between the outer soil and the caisson reports additional increments of load onto ΔF_{uw} and ΔF_{int} creating a change of slope (see Figure 7.24b). Thence, the contribution of the internal shear rises up to attain its maximum. A second slope change occurs for the F_{uw} curve which becomes the only mode of resistance of the caisson. Finally, the contact is lost between the top of the caisson and the soil, ΔF_{top} reaches its plateau in Figure 7.24a and the pore pressure becomes more negative. It is also interesting to note that the inner shear decreases slightly after its maximum. This is due to the continuous reduction of normal effective stress acting on the skirt with deconfinement.
This simulation illustrates sequentially all the limits of resistance of each mode. However, it is provided only for pedagogic purpose since it corresponds to either a high permeability or a low stress rate.

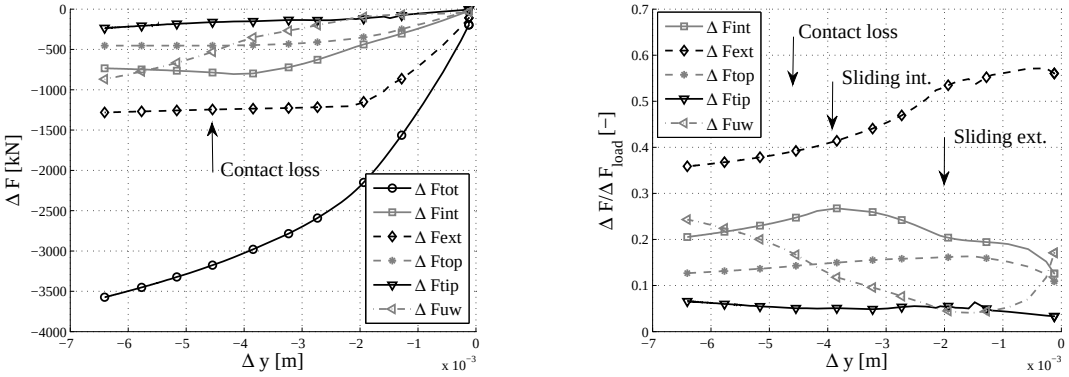

(a) (b)

FIGURE 7.24: Partially drained extension simulation, k= $5 \cdot 10^{-11}$m^2. Results start on the right and negative displacements stand for extension.

7.3.3.4 Influence of friction coefficient

The influence of friction coefficient on the overall results is depicted in Figure 7.25a. Two limit cases are presented. Obviously if no friction is allowed, the results are uninteresting and correspond to the decompression of the initial confinement. On the other hand, if the soil and the caisson are stuck together, the computation stops since the soil locally reaches failure. These interface conditions imply a true traction of the soil, i.e. the caisson pulls the soil, which is non-physical.
Partially drained simulations obviously present a higher stiffness and resistance than drained simulations (see Figure 7.25b). Indeed, they can not reach full failure of the soil since local failure or liquefaction are attained and the computation was not able to continue. However, although this sharp stop is disappointing, it is not a big deal. Indeed, this state of local failure involves a high loading level and has to be avoided in the design of such a structure. Therefore it will not be modelled in the following.

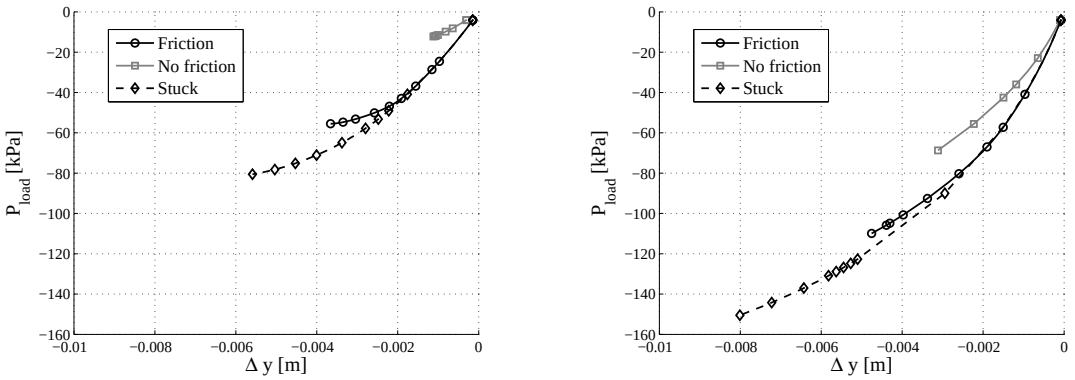

(a) Drained simulation (b) Partially drained simulation

FIGURE 7.25: Influence of interface conditions during pull test. "Friction", sliding is allowed; "No friction", steel-soil friction angle equal to 0; "Stuck", friction angle is infinite.

7.3.3.5 Influence of the caisson height

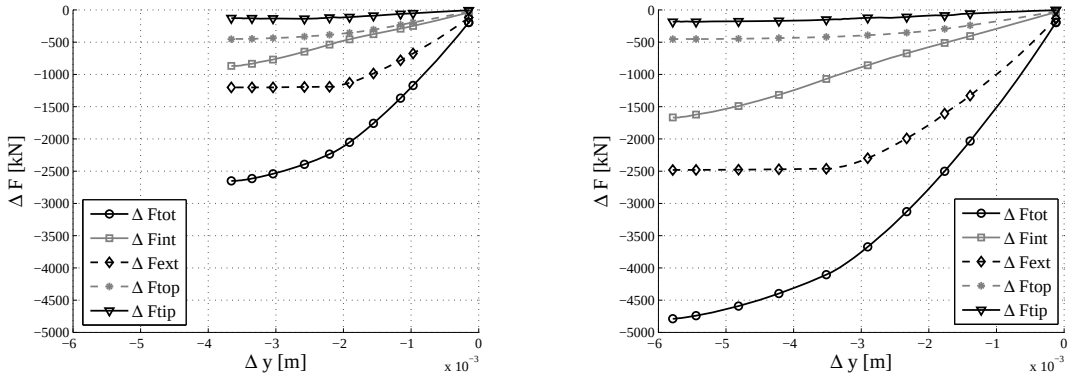

(a) caisson height : 4m (b) caisson height : 6m

FIGURE 7.26: Drained pull test

Drained pull test performed up to failure are provided in Figure 7.26. Not surprisingly, final displacement, inner shear and maximum outer shear as well are greater if H is greater.

It is worth noting that the caisson height is increased of 50% but the total resistance rises up to 80%. This illustrates the varying maximum shear available with depth.

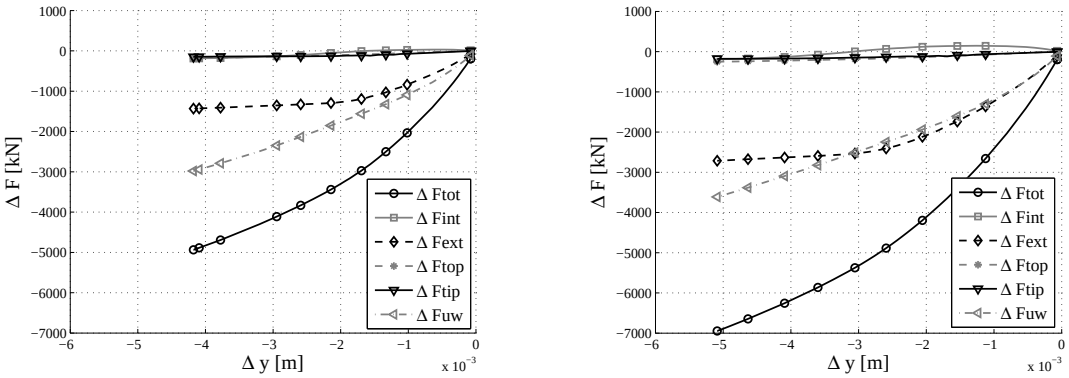

(a) caisson height : 4m (b) caisson height : 6m

FIGURE 7.27: Unrained pull test

Undrained pull tests were carried out up to the loss of convergence of the code. It is not a mandatory sign of physical failure. Indeed, local failure can influence the overall stability of the computation process. For instance, when the contact is lost at the tip, the physical material crumbles and filled in the void. The continuum description of the material is not able to reproduce such a phenomenon.
Once again in Figure 7.27, it appears the shear increases with the length of the caisson. Moreover, the coupling between the pore water pressure and the shear is more apparent in Figure 7.27b, where the plateau of ΔF_{ext} is not constant but slightly evolves. The decrease of PWP inside the caisson increases the normal effective stress on the skirt, hence the maximum resistance to sliding.

7.3.3.6 Influence of the Prevost model

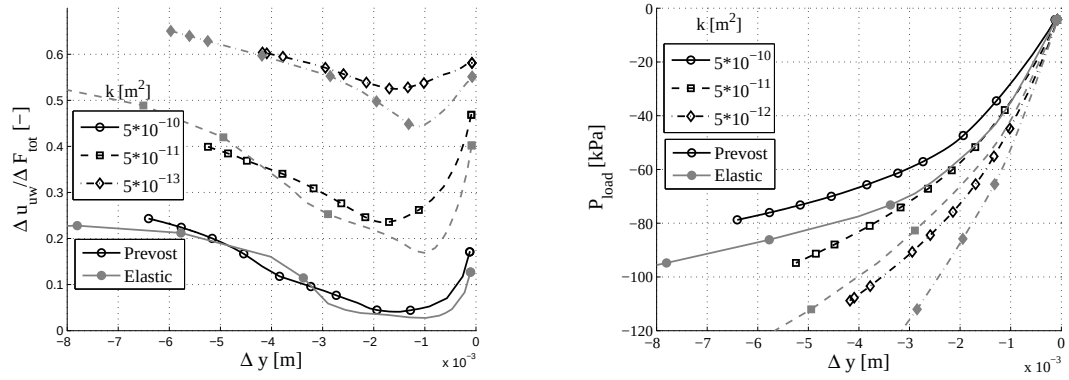

(a) (b)

FIGURE 7.28: Influence of the model type on the displacement-load curve. Black curves (Prevost model) - gray curves (elastic model).

A comparison between elastic and Prevost models is illustrated in Figure 7.28. Variations of pore water pressure inside the caisson are quite similar between both models (see Figure 7.28a). The displacement-load curve is stiffer for elastic results, which is partly due to the non-dependency of the elastic moduli on the confinement. Furthermore, a pull test consists

mainly in unloading the caisson, generating less plastic effects. However these plasticity effects might affect the distribution of normal stresses along the inner and outer interfaces, then the maximum shear stress.

7.4 Cyclic behaviour

7.4.1 Load signal

Nature is in essence irregular and untidy. So is the loading acting on a suction caisson. Initially, a first static drained loading is assumed to represent the dead weight of the wind turbine and its support (20kPa). Afterwards, the cyclic loading is applied to a partially drained soil and arises from the action of wind and waves on the structure. Variation around the mean value is ±40.5kPa.
An example of vertical load signal that represents the action of a storm on foundation (leg of a tripod structure) is provided in Figure 7.29. This example is a classic output result of the analysis of the tripod structure for given climate conditions in the North sea (current, waves and wind). This signal is the assembly of 11 pseudo-random sequences of 600s generated independently. One of them includes an extreme event, i.e. it represents the worst wave that is expected to hit the structure. They correspond to a storm characterised by a wave height $H_w = 10.8$m.

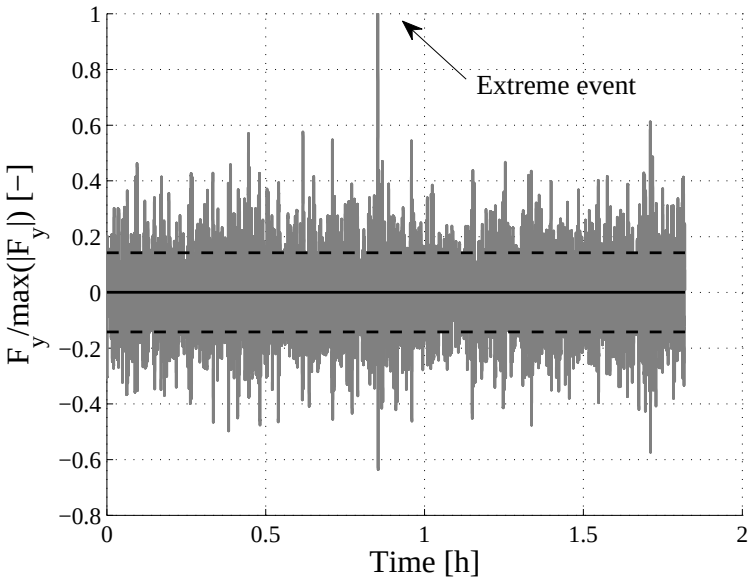

FIGURE 7.29: Storm signal including an extreme event. The signal is normalised by its maximum value.

Lee and Ficht [1975]; Rahman et al. [1977] coined the concept of equivalent storm. The entire signal is decomposed into its salient waves characterised by a height and a period. The basic idea was to relate each wave type to an equivalent loading, such as a cyclic stress ratio τ_{cycl}/σ'_v, which is the amount of shear loading divided by the vertical effective stress. This ratio can then be compared to a measured resistance, which depends on *in situ* measurements.
The sampling frequency of the pseudo-random signal is 20Hz. However this frequency is unnecessary and non practical from a numerical point of view. Indeed, the high frequency content does not influence the results, since its effect is purely undrained. Furthermore, it is very costly to use so small size steps.

A relation between pore pressure variations and a number of shear cycles (of a given

amplitude) was elaborated by [Seed and Idriss, 1971], as shown for instance in Figure 7.30b,

$$\frac{\Delta u_w}{p'_0} = \frac{2}{\pi} \sin^{-1} \left[\left(\frac{N}{N_l} \right)^{\frac{1}{2\alpha}} \right], \tag{7.2}$$

where Δu_w is the variation of PWP, p'_0 is the initial mean effective stress, N_l the number of equivalent cycles necessary to reach liquefaction and N the current number of equivalent cycles. This relation was adapted by [Taiebat, 1999] in order to be implemented into a finite element code. For a given state of the material, the relation provides the increment of pore pressure induced by a additional number of equivalent waves.

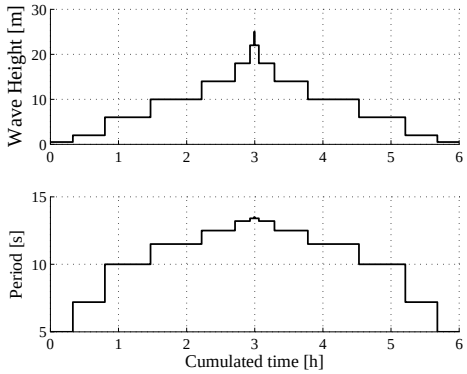

(a) Equivalent storm, from [Taiebat, 1999].

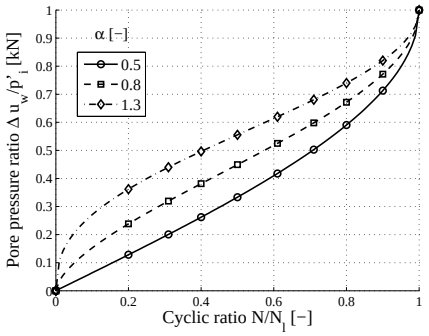

(b) Graphical representation of pore pressure generation function, [Seed and Idriss, 1971; Taiebat and Carter, 2000]

FIGURE 7.30

In the following, two types of load signals are considered : pseudo-random and equivalent. The former is the result of a complex environment-structure interaction and the second is sinusoidal equivalent and deduced from the former pseudo-random signal. The basic working of the foundation is described firstly by a short simulation of a 600s loading of either pseudo-random or equivalent signals. Their sampling frequencies are respectively 3.33Hz and 5Hz.
A simulation of the full storm (6600s) remains very costly at this sampling frequency. Therefore, the full loading signal only considers the local peaks of vertical stresses and the signal is linearly interpolated between them. This leads to an average sampling frequency of 0.5Hz. Equivalent loading signals are discretised by 9 defined points. Their average sampling frequency is around 1Hz.

7.4.2 Half cycle analysis

In this work, a fully coupled transient analysis is carried out. Therefore, a time signal must be entirely taken into account. However, such a signal is not always easy to derive. Moreover, results are sometimes more comprehensive to analyse if they are grouped into packets of waves of similar amplitudes and periods. Such a method highlights the effect of each wave type on the results.
The half cycle analysis, applied by [Byrne and Houlsby, 2002] to reduce the amount of information contained in a signal is adopted here to transform the pseudo-random signal, obtained from the structural analysis, into an equivalent sinusoidal signal. The first step is to establish the mean value of the load signal, P_{mean}. A half cycle is the part of the signal that is included between two successive crosses of $\sigma_{y,mean}$ (see Figure 7.31). Corresponding half period ΔT and amplitudes ΔP are then easily obtained.

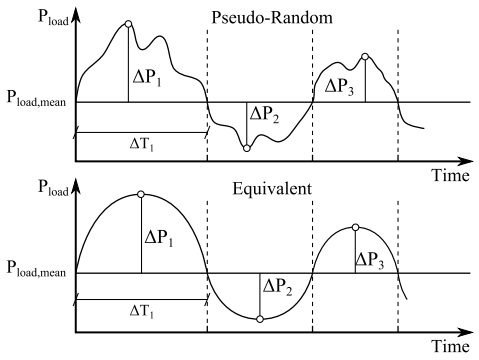

FIGURE 7.31: Half cycle analysis, after [Byrne and Houlsby, 2002]

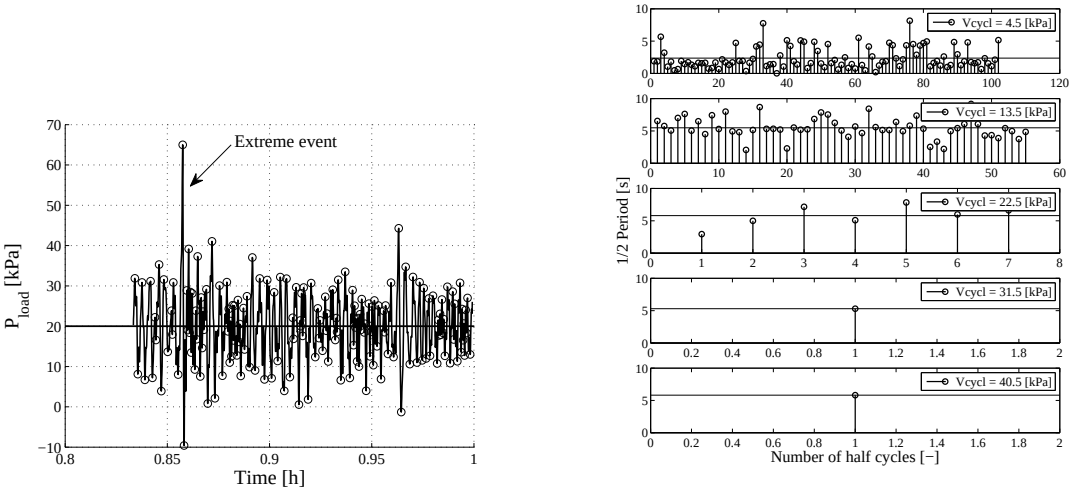

(a) Temporal signal

(b) Half cycle analysis outcomes.

FIGURE 7.32: Short storm load signal containing the extreme event (see Figure 7.29).

The method is applied to the sequence of the storm signal containing the extreme event (600s, short load signal). The adimensional signal provided in Figure 7.29 is scaled to correspond to a mean vertical stress of 20kPa and a maximum cyclic amplitude of ±40.5kPa. This signal is illustrated in Figure 7.32a where the markers denote the peak values of each half cycle.

Half cycle amplitudes are classified into five categories which median values are provided in Figure 7.32b. For each of these categories, a corresponding mean half period $T/2$ is computed. The two greatest amplitudes correspond to the extreme event and are grouped together. Then a complete sinusoidal load signal is reconstituted by gathering waves packets (characterised by their periods and amplitudes) into a full transient signal. Characteristics of equivalent signal are provided in Table 7.5. Two periods of loading clearly exist, 5s and 11s. The latter can be compared to a typical wave period of around 10s. The relatively long duration of such a loading is an argument for dropping inertial effects in the simulation.

	A1	A2	A3	A4
Number of cycles [-]	50	28	4	1
ΔP [kPa]	4.5	13.5	22.5	40.5
T [s]	4.6	11	11.6	11.1

TABLE 7.5: Number of equivalent cycles, associated amplitude and periods (short signal).

The last step is the assembly of the signal. Equivalent cycles might be reorganised randomly but such an order loses the advantages of the method, i.e. an improved readability of the results. In this work, three types of arrangements are considered and are presented in Figure 7.33. The former arranges the cycles in increasing order of amplitude up to the extreme event, in the middle of the signal. Afterwards, cycles are assembled in decreasing order of period and amplitude. This follows the pattern of equivalent storm defined previously in Figure 7.30a. The two last configurations place extreme event respectively at the early beginning or at the end of the simulation.
In the following, these signal types are compared in order to validate or invalidate their equivalence. If they are equivalent, the knowledge of a pseudo-random signal becomes not mandatory and an equivalent signal can be obtained by readily assessing a number of cycles of given amplitude and periods. Moreover, it might be less costly to employ an equivalent signal, which is regular and might require less time steps.

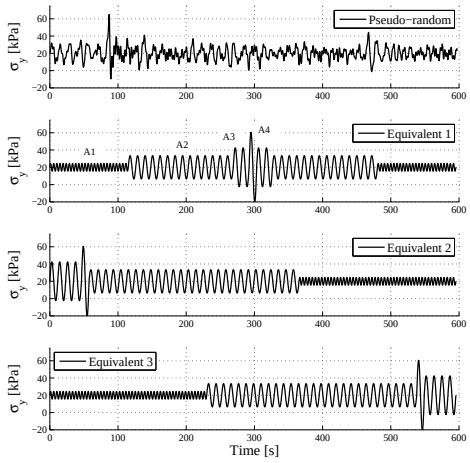

FIGURE 7.33: Reconstituted equivalent short storm signals.

The same procedure was applied to the full storm load signal. Packets of waves are characterised by amplitudes and periods provided in Table 7.6.

	A1	A2	A3	A4	A5
Number of cycles [-]	380	344	58	4	1
ΔP [kPa]	3.7	11.25	18.76	26.23	45
T [s]	6.4	9.9	11.4	11.7	11.7

TABLE 7.6: Number of equivalent cycles, associated amplitude and periods (long signal).

The half cycle analysis method can also be used to analyse and reduce the amount of information embedded in result signals. If an arbitrary response signal X, e.g. displacement or PWP evolution, corresponding to the load signal P was perfectly linear, it would recover its initial mean value when $P = P_{mean}$. However, a deviation from this initial value is most of the time observed (see Figure 7.34) and the deviation is termed δ_{perm}. Thence if δ_{perm} corresponding to each crossing of the mean load are collected, a tendency curve can be established. The tendency for a single cycle is defined as the mean value of the two successive δ_{perm}. It often marks an accumulation, e.g. pore pressure or displacement. Peak values corresponding to each half cycle either over or under the mean value can be collected to delineate envelop curves, i.e. the range of variation of the signal (see Figure 7.34).

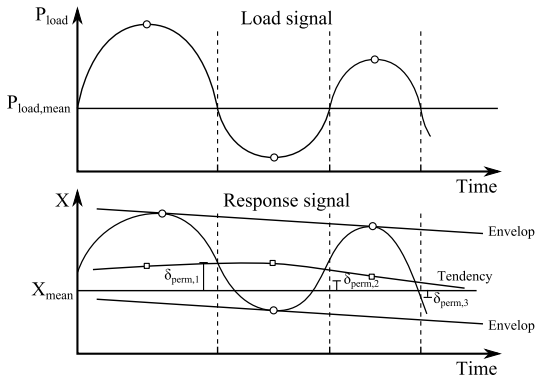

FIGURE 7.34: Half cycle analysis of the results.

7.4.3 Short signal

7.4.3.1 Reference case

A comparison between equivalent and pseudo-random short loading signals is commented hereafter. A consolidation phase is finally simulated where $P = P_{mean}$. It is impossible to compare the stress distributions or the pore pressure variations over the whole domain for each time step. Therefore, the displacement of the centre of the caisson and an average pore pressure variation under its lid are chosen to be representative data. In order to increase the readability of the results, a half cycle analysis is carried out on the outcomes.

Let us first consider a comparison between equivalent and pseudo-random signals, as shown in Figure 7.35. Variations of PWP and total loading are plotted together. It can be observed that the major part of the loading is sustained by inner PWP. Thence, the behaviour is partially drained and even close to the undrained one. It is difficult to draw a clear tendency when analysing the pseudo-random response.
On the other hand, equivalent signal clearly indicates that small amplitude waves (A_1, between 0 and 100s) induce nearly no accumulation, i.e. PWP generated over a half cycle is dissipated during the following. This phase of the loading is quasi stationary. Afterwards a very slow accumulation rate holds and less than 1kPa of PWP is accumulated over 160s, for the second batch of cyclic amplitude. The major part of the pore pressure accumulated then appears for A_3 and A_4 cyclic amplitudes. It is about 4kPa over 30s. This accumulated PWP exists during the next 300s and dissipates gently.

Figure 7.36 compares tendency curves of Δu_w and Δy for the four types of loading signals (Equivalent 1-2-3 and pseudo-random). The tendency are computed using the half-cycle analysis method. Both sub-figures must be analysed in parallel. Indeed, displacement and pore pressure are inherently linked. The initial displacement of 0.8mm corresponds to the settlement due to the static loading.
Each displacement variation can clearly be separated into two phases (see Figure 7.36b). During the first one, a quasi-linear increase of displacement takes place. Then the extreme event occurs and a sharp variations of displacement holds. It is followed by a second phase of settlement (concave curve) up to the final value. This latter corresponds to the consolidation (with varying load) due to the progressive pore pressure dissipation.
It is interesting to note that the final settlement is nearly identical for all load signals even if the "path" followed to reach this final value is different. However, the maximum displacement encountered is slightly different. It is obvious since it corresponds to the extreme event. This latter might affect the design of a structure, which is very sensitive to its rotation and then

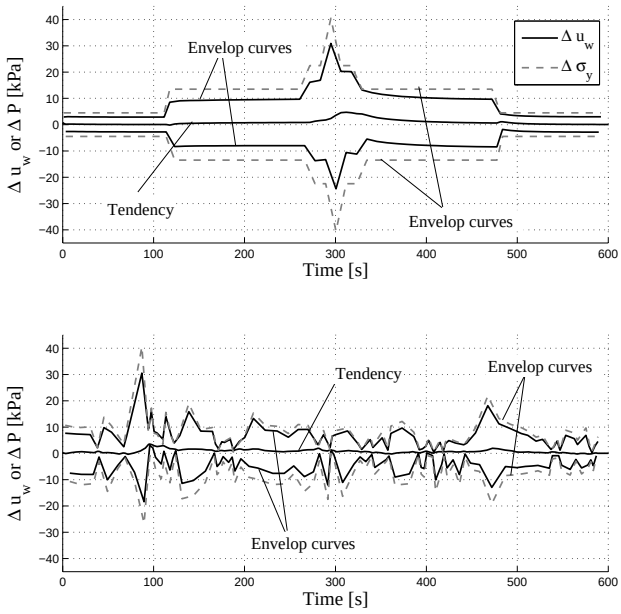

FIGURE 7.35: Comparison between Equivalent 1 (top) and pseudo-random (bottom) loading signals

to a differential settlement of the parts of the foundation.
The maximum accumulated pore pressure is not identical for each load signal. Indeed the highest maximum corresponds to the soonest occurrence of the extreme event. This might indicate that low amplitude cycles "prepare" the soil and make it less sensitive to further loading.
Finally, the pseudo-random response exhibits the lowest final settlement and pore pressure accumulated. Indeed, during equivalent loading, cycles that generate PWP accumulation are grouped together, which amplified this effect. On the other hand, the pseudo-random signal consists of a succession of cycles that are prone to accumulate (high amplitude) or dissipate (low amplitude) PWP. Thence the maximum accumulation is attenuated.

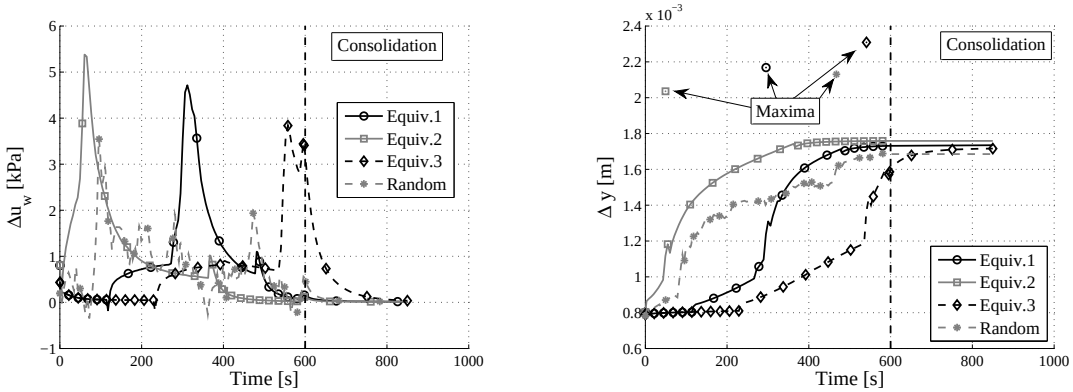

(a) Tendency of pore water pressure (PWP).

(b) Tendency of vertical displacement.

FIGURE 7.36: Comparison between signal types.

7.4.3.2 Influence of the model

A comparison of the cyclic behaviour of respectively purely elastic and Prevost models is illustrated in Figure 7.37. Results are quite distinct in both cases. Elastic results also present an accumulation of pore water pressure, as shown in Figure 7.37a. At the beginning of each new packet of cycles, the flow regime is perturbed and a transient flow variation of pore water pressure occurs, which is fast reduced.
Accumulated settlement is very limited with elastic constitutive law. It is due to sliding of the steel-soil interface, which is nearly negligible. Indeed, an elastic constitutive law can not accumulate deformation, by definition.

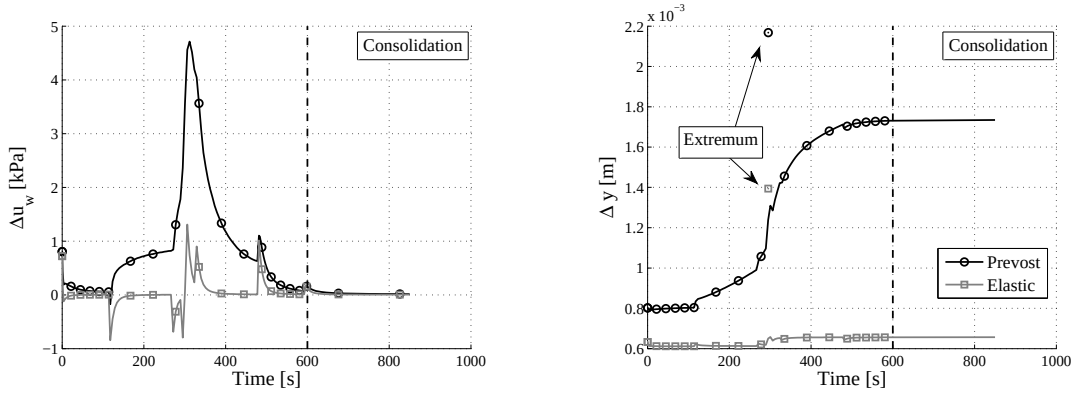

(a) Tendency of pore water pressure (PWP). (b) Tendency of vertical displacement.

FIGURE 7.37: Comparison of the effect of the constitutive law.

7.4.3.3 Influence of permeability

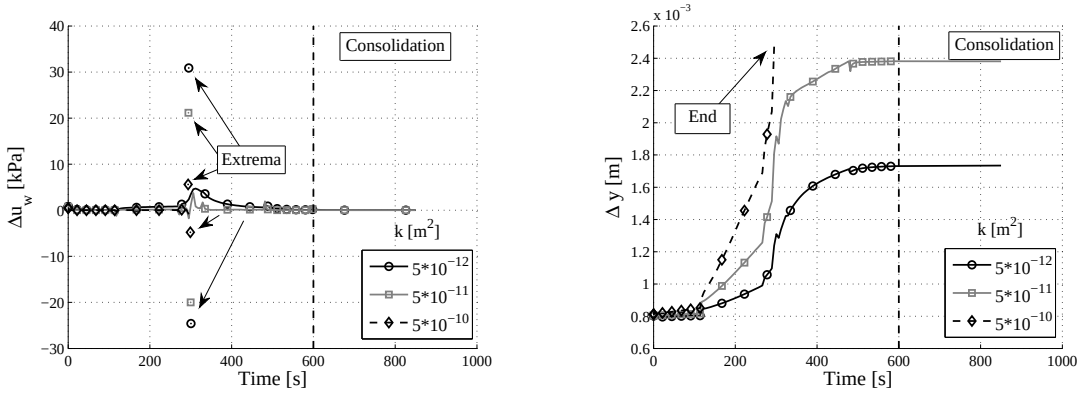

(a) Tendency of pore water pressure (PWP). (b) Tendency of vertical displacement.

FIGURE 7.38: Comparison of the effect of permeability along the skirt.

The influence of permeability is summarised in Figure 7.38. Evidently, the higher the permeability, the lower the extreme PWP generated within the caisson and the PWP accumulated. This can be observed in Figure 7.38a. The corollary effect is the transfer of the total load onto the effective stresses. This implies a greater loading of the soil inside, then a greater settlement (see Figure 7.38b).
It must be pointed out that the highest permeability simulation could not be continued up to the end of the loading. Indeed, it can be observed in Figure 7.38b that the settlement starts increasing sharply when the extreme event is reached. It actually appears that a great part

of the soil is brought to zero mean effective stress state under the lid and near the outer skirt (see Figure 7.39a). The sand fails which can not be reproduced by the model.
The comparison of the stress path under the centre of the lid confirms this observation in each case (see Figure 7.39b). Only the tendencies of q and p' are represented for the sake of readability. It clearly appears the stress path corresponding to k= $5 \cdot 10^{-3}$m/s converges towards the origin of the axes, then to initial liquefaction (point D). On the other hand, the k= $5 \cdot 10^{-4}$m/s result follows the same direction but does not cross the PT-line (point C). A longer load signal may have led to the same conclusion. Finally, the last stress path moves away from that states (point B), which is stabilising.

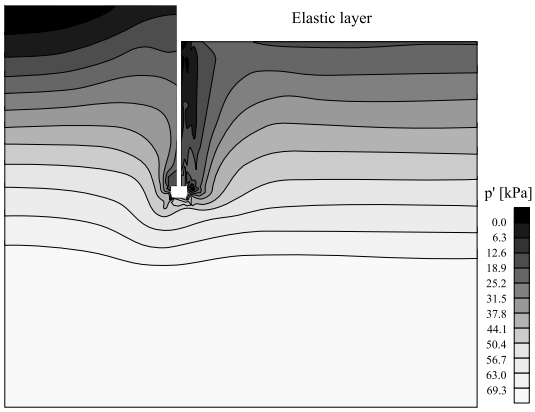

(a) Mean effective stress if k= $5 \cdot 10^{-12}$m^2, when computation stops.

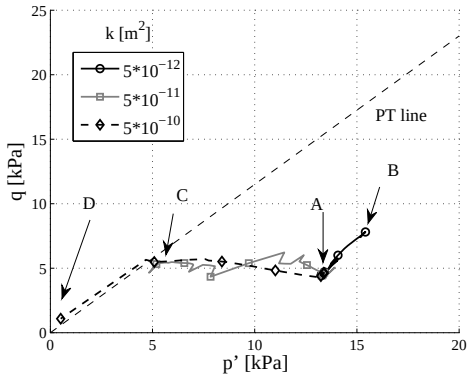

(b) Stress path for a material point just under the lid of the caisson. Starting point, A; End point for k= $5 \cdot 10^{-10}$m^2, B; for k= $5 \cdot 10^{-11}$m^2, C; for k= $5 \cdot 10^{-10}$m^2, D.

FIGURE 7.39: Permeability effect

7.4.3.4 Influence of friction coefficient

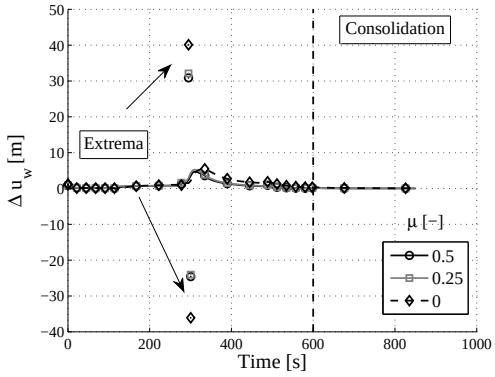

(a) Tendency of pore water pressure (PWP).

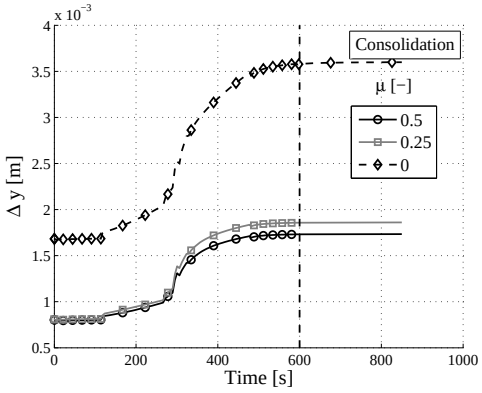

(b) Tendency of vertical displacement.

FIGURE 7.40: Comparison of the effect of friction coefficient along the skirt.

The influence of the friction coefficient on cyclic results is illustrated in Figure 7.40. Obviously, the lower the friction, the higher the pore pressure generated within the caisson. Indeed, the entire loading is only sustained by vertical effort at the top, i.e. effective ΔF_{top} and pore water pressures ΔF_{uw}. Thence the maximum PWP is greater if $\mu = 0$ (see Figure 7.41a).

The PWP accumulation inside the caisson is also greater (see Figure 7.41a). If the entire loading is borne by the total pressure under the lid of the caisson, the effective stress variation within it is greater, involving a higher plastic contraction and then pore pressure generation. The total vertical displacement also highlights the larger amount of plasticity. Firstly, the initial vertical displacement, due to static loading, V_{mean} is higher. The shear stresses along the skirt diffuse the loading within the surrounding soil, relieving the soil under. On the other hand, if no friction is allowed, the entire load is reported on the soil within and under the caisson. Finally, there is almost no difference between $\mu = 0.25$ and $\mu = 0.5$ results. This induces that friction limit is hardly attained.
The settlement variation during cyclic loading with frictionless caisson ($\sim$ 2mm) is twice the other ones ($\sim$ 1mm). The reason of this result is again greater plastic effects inside and under the caisson. Distributions of displacements within the soil in both cases are portrayed in Figures 7.41. They highlight the inherently distinct modes of resistance of the caisson and the different diffusion patterns of the stresses within the soil.
Where friction is not null, the soil and a layer of soil around it settle monolithically. It means shear stresses along the shaft are diffused within the soil around, which contributes to the global resistance of the soil-structure system. Material under the centre settle much less. On the other hand, if the friction coefficient is equal to zero, the load is transferred to the soil only where the contact zones are horizontal (under the lid and under the tip). Therefore, the highest settlement is located in these zones. The volume of soil contributing to the global resistance is lower. Thence it is much loaded and settles more.

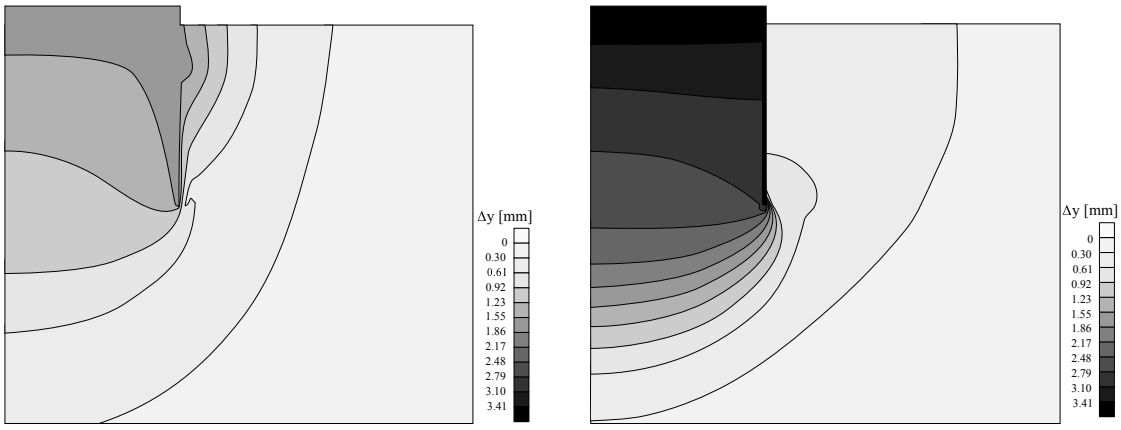

(a) Friction coefficient $\mu = 0.5$ (b) Friction coefficient $\mu = 0.0$

FIGURE 7.41: Vertical displacement at the end of the extreme event batch.

7.4.3.5 Influence of PT ratio

The influence of the phase transformation ratio, $\bar{\eta}$, is illustrated in Figure 7.42. This parameter rules the contractivity of the soil, thence the lower this parameter, the lower the PWP generated and accumulated during the simulation. For the same reason, the settlement is lower (see Figure 7.42b). Results and especially settlement at the end of the simulation, appear to be very sensitive to this parameter. Therefore, if it is reminded $\bar{\eta}$ was a bit tricky to determine from laboratory tests, it seems judicious to always assess its influence on simulations.

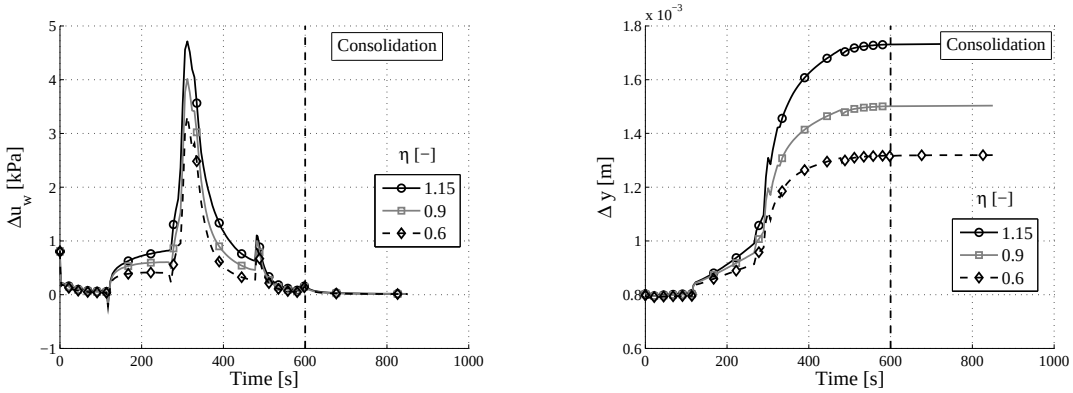

(a) Tendency of pore water pressure (PWP). (b) Tendency of vertical displacement.

FIGURE 7.42: Comparison of the effect of phase transformation ratio.

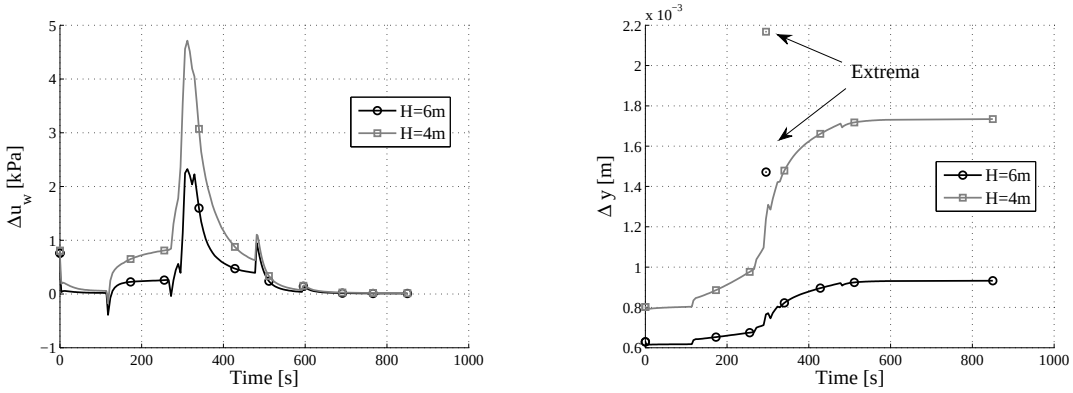

(a) Tendency of pore water pressure (PWP). (b) Tendency of vertical displacement.

FIGURE 7.43: Comparison of the effect of the length of the caisson.

7.4.3.6 Influence of the caisson height

It can be observed in Figure 7.43 that the increase of the caisson height strongly reduces the accumulated displacement. Indeed, the greatest friction that can be mobilised reduces the level of loading of the solid skeleton, hence the amount of settlement and PWP accumulation. Moreover, the increase of the height increases the drainage path. Pore pressures dissipate more slowly and the partially drained effect is increased, meaning less settlement.

7.4.3.7 Influence of K_0

As stated before, the introduction of non isotropic stresses within the soil implies initial deviatoric stresses that might lie outside the yield surface. For a given effective initial state of stress $[\sigma'_x = K_0 \cdot \sigma'_y; \sigma'_y; \sigma'_z = K_0 \cdot \sigma'_y]$, the initial reduced deviatoric stress ratio reads

$$\frac{\mathrm{q}}{\mathrm{p}'} = 3 \cdot \frac{1 - K_0}{1 + 2 \cdot K_0} \tag{7.3}$$

which is depicted in Figure 7.44. A coefficient equal to 0.9 is adopted hereafter, which corresponds to $\eta_0 = 0.1071$. This value lies outside the yield surface. Therefore, parameters of the laws were adapted and the first surface was dropped, i.e. the set of parameters encompasses only 15 surfaces instead of 16. A comparison of cyclic results obtained for either $K_0 = 1$ and

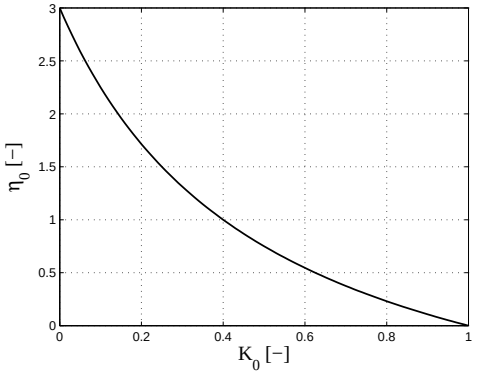

FIGURE 7.44: Relation between the coefficient of earth pressure at rest and the initial reduced deviatoric stress ratio.

$K_0 = 0.9$ is provided in Figure 7.45.
K_0 mostly influences the final displacement accumulated rather than the pore pressure accumulation inside the caisson. Actually, the effect of this parameter is twofold. On one hand, the final η value reached in each point is higher, since the initial state is shifted up. Therefore, surfaces of lower plastic moduli are activated which induces more settlement. On the other hand, $K_0 < 1$ reduces the normal effective stress acting on the skirt of the caisson, then the maximum friction available, which might increase the skirt-soil slip.
Interestingly, the number of surfaces strongly influences the final settlement (see circle and diamond curves in Figure 7.45b). Indeed, the swap between 16-surface and 15-surface configuration enlarges the elastic domain. As a consequence, a large part of the domain, which is weakly loaded does not encounter any plastic effect, hence a weaker settlement.

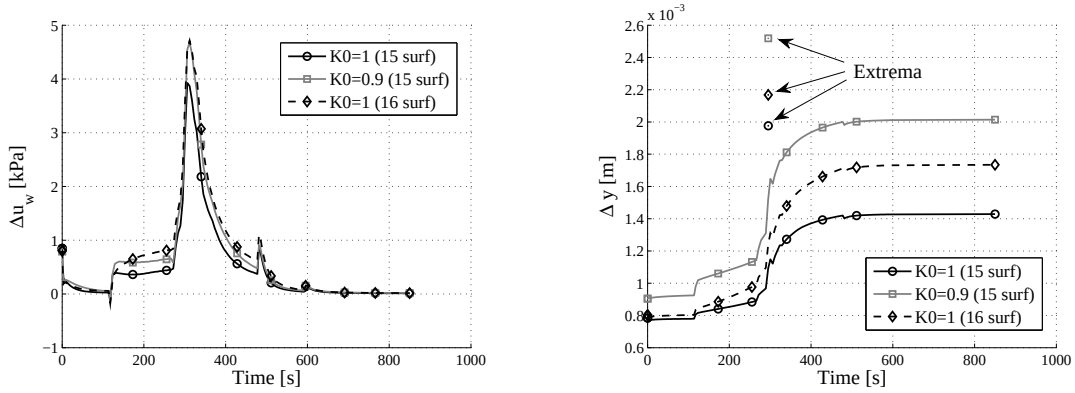

(a) Tendency of pore water pressure (PWP).

(b) Tendency of vertical displacement.

FIGURE 7.45: Comparison of the effect of K_0. (16 surf) stands for the reference model with 16 nested surfaces while (15 surf) holds for the modified set of parameters.

Another possibility to take K_0 into account would have been to modify the initial $\boldsymbol{\alpha}_i$ values. The consolidation process of the sample could have been modelled from an isotropic material up to the η-value corresponding to the K_0 condition.

7.4.3.8 Cyclic diagram

It would be interesting for designers to assess the effect of a storm event onto the final displacement encountered by a foundation, without any complex simulation. Cyclic diagrams presented in Figure 7.47 allow a quick estimation of the total settlement for a given combination of mean ($\sigma_{y,mean}$) and cyclic ($\sigma_{y,cyc,max}$) amplitudes characterising the cyclic load applied to the caisson.
This diagram is based on 32 simulations for a single caisson geometry and identical initial conditions. They are subject to the same equivalent short storm signal but scaled and shifted to correspond to each combination of vertical loads, as shown in Figure 7.46. The cyclic amplitude represents the maximum variable vertical load applied during the extreme event.

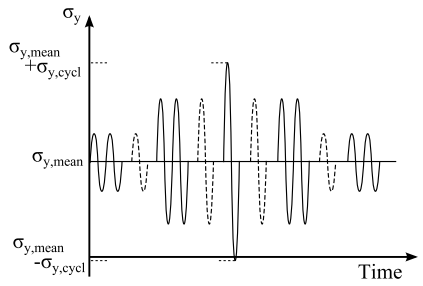

FIGURE 7.46: Short storm signal applied. The mean vertical stress ($\sigma_{y,mean}$) and the cyclic amplitude ($\sigma_{y,cycl}$) are adjusted for each simulation.

The first diagram (see Figure 7.47a) depicts the addition of the settlement encountered during static and cyclic loadings. Settlement accumulates faster in the direction of static variable, since this loading is fully drained. Figure 7.47b represents the settlement accumulated only during the storm event. In this case, if the maximum displacement is imposed, the higher the mean vertical stress, the lower the admissible variable stress. However, this relation is definitely not linear.
Most of the time, such diagrams relate a combination of static and cyclic loads to the number of cycles required to reach failure. However, failure must be defined for that purpose and there is no clear criterion. Moreover, the finite element code encountered problems of convergence when approaching local failure of the material. For both reasons, a representation of the displacement after a given event was preferred.

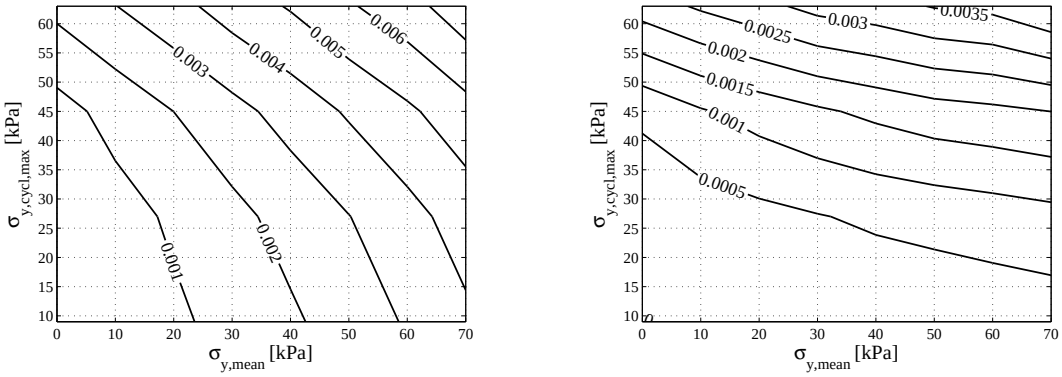

(a) Static and storm

(b) Storm only

FIGURE 7.47: Vertical displacement [m] for a combination of mean ($\sigma_{y,mean}$) and maximum cyclic ($\sigma_{y,cyc,max}$) amplitudes.

7.4.4 Complete storm

A complete storm which has a duration of 1h50 has been modelled for both pseudo-random and first equivalent signals. In both cases, the extreme event occurs in the middle of the loading. The cpu time required to perform the full computation is more or less 30 hours.
The averaged pore water pressure accumulation is depicted in Figure 7.48a. In both cases, the maximum accumulated pore water pressure observed within the caisson is lower than during the short load signal. The low amplitude sequences of the long duration loading seem to "prepare" the soil and the effect of the extreme event on the PWP is attenuated.
It is worth noting in Figure 7.48b the remarkably identical settlements accumulated during the storm, for both signal. This figure demonstrates the half-cycle analysis is pertinent to generate load signals equivalent to pseudo-random ones. The overall final settlement is obviously greater for the long duration storm than for the short one. However it is not proportional to the duration of the storm. Indeed, the settlement accumulation over 6550s of storm is equal to 2.9mm. On the other hand, the settlement accumulated during the short storm (600s) is equal to 0.9mm. The sharp increase of settlement is close to 0.2mm during the short simulation and equal to 0.5mm during the long simulation.
Moreover, considering the equivalent signal, it appears that the main part of the total settlement occurs during the first half storm (2.5mm), encompassing the greater amplitude cycles. More precisely, a settlement of 1.8mm is accumulated at the end of the extreme event. Indeed, it can be observed that the settlement monotonically increases but its concavity is negative, i.e. the slope of the increase of settlement decreases during the storm.
Results of accumulation of settlement for short and long duration storm exhibit similar patterns. Therefore it could be interesting to investigate whether a relation exists between the duration of the storm and the settlement accumulation. Thence, the final settlement could be extrapolated for any given duration of a storm.

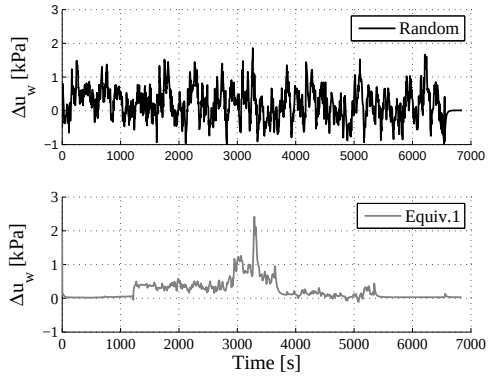

(a) Tendency of pore water pressure (PWP).

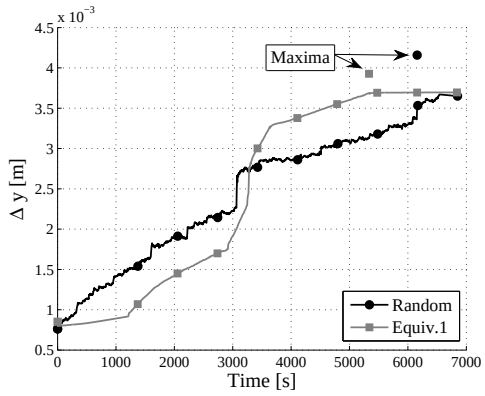

(b) Tendency of vertical displacement.

FIGURE 7.48: Comparison of pseudo-random and first equivalent signals.

Figure 7.49 exhibits the residual stresses within the soil. It distinguishes the deviatoric reduced stress ratio before and after the storm. This representation is only an indirect indicator of the plasticity, since it does not represent cumulated deformation. However, the higher η, the higher the activated surface, hence the lower the plastic modulus.
Strong plastic effects are located near the outer skirt of the caisson over a width of one meter. This fact implies that the use of a complex interface constitutive law and a classic Drucker-Prager model for the solid elements would probably have not been sufficient, i.e. deformation is not only localised near the interface. The representation of η shows the zone of soil influenced by the loading. It is roughly limited to a length close to the caisson height H around the caisson.

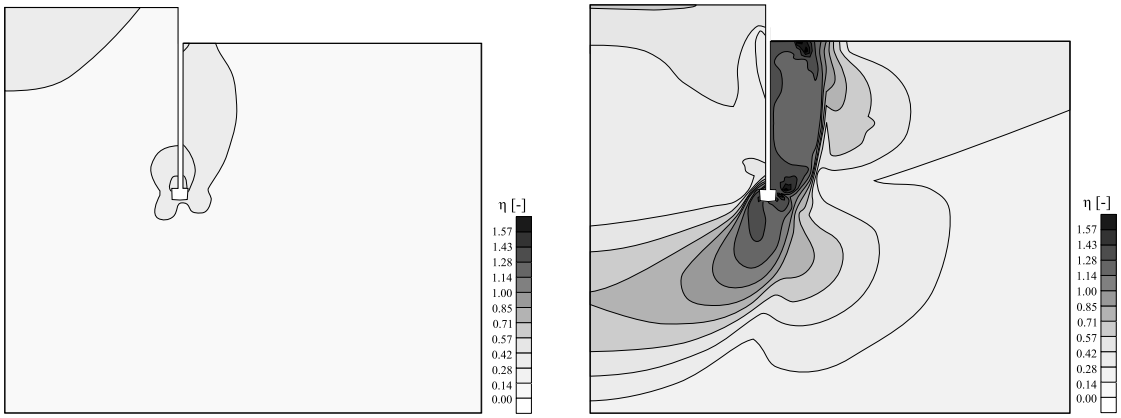

(a) After static loading. (b) After the storm.

FIGURE 7.49: Comparison of the reduced deviatoric stress ratio before and after the long duration storm, for the pseudo-random signal.

The vertical displacement distribution around the caisson after the storm is represented in Figure 7.50. The strong gradient of vertical displacement near the skirt highlights the shear deformation due to soil-steel interface shearing. Finally, the settlement observed is mainly located inside the caisson.

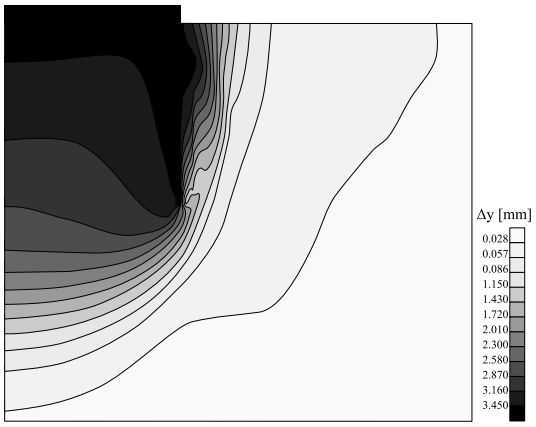

FIGURE 7.50: Vertical displacement at the end of the long duration storm (pseudo-random signal).

7.5 Conclusion

This chapter aims at describing the salient features of suction caissons in dense sand. A fully transient analysis of such a foundation was carried out, taking into account plasticity of the soil (Prevost model) and of the steel-sand interface (Mohr-Coulomb criterion). The geometry adopted consists of a 7.8m diameter and 4m height caisson. It is assumed that vertical loads are preponderant. Thence the mesh is axisymmetric and the loading consists of a push-pull action.
Monotonic drained and undrained simulations highlight the role of the different components of resistance during both push and pull simulations. Unsurprisingly, friction plays a major role in the global resistance. During drained simulations, inner and outer friction are mobilised. However, sliding of the outer interface occurs sooner than the inner one, due to a greater relative displacement. Deformation of the soil is concentrated around the skirt of the caisson. During undrained simulations, the inner friction is hardly mobilised. The suction effect involves a quasi-monolithic movement of the soil plug and the caisson, which is consistent with experimental observations. This suction effect is strongly dependent on the permeability of the soil. Pull simulations highlight the inherently transient behaviour of such a foundation system. Indeed, for a similar drained resistance, the higher the permeability, the lower the maximum traction load sustained. Therefore, long term and short term resistances must be distinguished during design.

Typical load design in offshore geotechnics corresponds to a storm. The signal of vertical loading onto the foundation is not easy to derive since it depends on a complex interaction between the structure and the environment. Complex pseudo-random signals can be furnished by specialised software. An example of such a signal is used to highlight the influence of salient parameters during cyclic loading.
A half cycle analysis was carried out to construct a sinusoidal-equivalent load signal. This simpler signal is compared to the pseudo random one and all of them converge to an identical final settlement. This leads to the conclusion that it is not mandatory to resort to complex pseudo-random load signals. Equivalent sinusoidal ones can be used instead. They are easier to determine since the major part of the cycles is characterised by a typical period of around 10s.
The partially drained behaviour of the caisson is obvious and the pore water pressure generated sustains the main part of the loading. This implies the solid skeleton is hardly loaded which in turn reduces the final settlement observed. Evolution of the settlement clearly highlights the progressive accumulation of plasticity. Small cycles have nearly no effect but the extreme event involves a large settlement coupled with a large pore pressure accumulation.
Permeability is a key factor. Indeed, a higher permeability involves a greater loading of the solid skeleton. Therefore, plastic effects are stronger and the final settlement is larger. On the other hand, depending on the characteristics of the soil, a higher permeability might lead to a greater accumulation of pore water pressure, hence to a liquefaction of the soil around.
The friction parameter also plays a major role in the resistance. Indeed, friction along the skirt allows the diffusion of the vertical loading to the soil around, reducing the loading inside and under, then decreasing the final settlement, either after the static loading and the cyclic one.
The caisson height influences the amount of maximum friction and the length of the drainage path as well. It is worth mentioning the available shear stresses do not increase linearly with the caisson height, due to the increasing confining stress. The coefficient of lateral earth pressure at rest also influences the maximum friction and the amount of plasticity generated within the soil. Finally, a cyclic diagram is elaborated, relating the settlement accumulated during a short storm event to mean and cyclic amplitudes. Such a diagram can be used during

pre-design phases.
A comparison of long duration storm events, for both pseudo-random and equivalent load signals is carried out. The total settlement accumulated at the end of the storm is identical in both cases. It justifies the use of half-cycle analysis to build to build an equivalent load signal.

THe cpu time necessary on a standard laptop lies between 2.5h and 3h. From a technical and cost point of view, such computations are affordable for design offices. The difficulty lies in the calibration of parameters and the sometimes lack of robustness of the constitutive law, especially near the liquefaction state.

Chapter 8

Conclusion

Success consists of going from failure to failure without loss of enthusiasm.

Winston Churchill

8.1 Summary

The cyclic behaviour of sands, widely studied in laboratories is quite complex. Pertinent features of their behaviour are highlighted and are the basic ingredients any constitutive law should reproduce. The most pertinent are the occurrence of plasticity in both loading and unloading; the phase transformation line, delineating contractive from dilative volumetric behaviours; the triggering of flow deformation; accumulation of plastic deformations; asymmetric stress paths in extension and compression.
Other phenomena are assumed to be less pertinent. They correspond to failure and post-failure behaviours, e.g. steady state and cyclic mobility. Indeed, simulations consist mainly in designing a foundation to service loading. The triggering of failure provides a limit resistance that should not be reached. Therefore, the residual resistance does not really matter. Furthermore such phenomena observed macroscopically in laboratory correspond to a loss of homogeneity of the soil samples.

The Prevost model is adopted in order to represent the cyclic behaviour of soils. It belongs to the family of multi-surfaces. The basic formulation of this model has two main advantages: its conceptual simplicity and its physically related parameters. It is able to reproduce salient features of the cyclic behaviour of soils. On the other hand, the post-failure behaviour can be depicted, but the price to pay is a more complex volumetric plastic potential and additional parameters. There is no dependency of the parameters on the void ratio of the material. Therefore, a new set of parameters should be defined for each density range.
Three sets of parameters are calibrated based on experiments (triaxial tests) available in the literature. Detailed and free data are scarce. Thence the calibration process focuses on two distinct materials, the Nevada and Lund sands. A unique set of parameters is obtained for each density. Monotonic drained and undrained triaxial tests are correctecly represented, with regard to the scattered data.
On the other hand, cyclic simulations do not perfectly match the laboratory experiments. Indeed, these tests are quite complex to carry out and are subject to instabilities since they are stress-controlled. However the general trend of the cyclic behaviour is well reproduced. A pore water pressure is accumulated and the stress path is translated towards the origin of the axes, i.e. towards liquefaction.

An implicit integration scheme was developed to implement the constitutive law in the finite element code `LAGAMINE`. The scheme corresponds to a midpoint rule, ensuring a second order accuracy for reasonable sizes of time steps. A local iterative process must be solved, requiring a line search procedure to improve the efficiency and the robustness of the algorithm. Derivatives of the local Newton process are computed analytically.
An implicit hardening rule must be adopted in order to avoid the intersection of successive nested surfaces. Both Mroz and Prager translation rules are compared. It is shown they correspond to distinct models since their response are divergent when subject to a multi-axial loading. The Prager rule is finally adopted.
The verification step ensures the implemented algorithm corresponds to the "analytical" solution. This solution is obtained either from an explicit simplified integration of the model (triaxial simulations), or from the implicit algorithm (multiaxial simulations)), using very small time step. It is highlighted that a substepping scheme should be included to improve the efficiency and the accuracy of the algorithm when a large variation of η holds over a small variation of deformation. This corresponds to the quasi-steady state.
The convergence of the local iterative process is quadratic, ensuring the analytical derivatives are correctly computed. Isoerror maps are elaborated to assess the accuracy of the algorithm.

An interface element is developed to better take into account the soil-structure interaction.

The efficiency of an existing hydro-mechanical interface element is improved. The unsticking capability is added, i.e. the loss of contact between both sides of an interface involves a suction of the fluid inside. Therefore, a resistance to traction exists even if contact is lost. An example of partially drained consolidation of a soil column is investigated and the consequences of an unsticking are highlighted.

The cyclic behaviour of a suction caisson as a part of a wind turbine offshore foundation is investigated. The adopted material is a very dense sand and employed parameters correspond to the Lund sand at a relative density of 90%. The overall loading is assumed mainly vertical and the mesh is axisymmetric.
Monotonic simulations up to failure highlight the modes of resistance of the caisson. Friction along the skirt plays a major role during drained simulations. Only the outer friction is mobilised during partially drained simulations and the soil plug is considered as stuck to the caisson.
The partially drained behaviour of the foundation is a key feature to sustain transient loads. Indeed, the pore water pressure generated inside the caisson is progressively dissipated. However, it sustains the major part of the total transient load. Consequently, the permeability and the rate of loading of the caisson are of paramount importance.
A transient load signal corresponding to a storm, including an extreme event, is applied to the caisson. Firstly a pseudo-random signal resulting from the complex interaction of the wind turbine structure and the environment is utilised. It is compared to a sinusoidal equivalent load signal, encompassing the same number of main cycles. Accumulated settlement at the end of a storm are identical. A cyclic diagram relating a final displacement to a combination of average and cyclic loading is finally elaborated.

The methodology embraced in this work echoes the opening quote of Socrates, *the only true wisdom is in knowing you know nothing*. Indeed, presumed ideas and obviousness are discarded. Continuous questioning on the origin of observed or modelled phenomena sequentially reveals the physics hidden behind the rough results. An extensive knowledge and mastering of the complexity of reality is the first step to simplification, then to the creation of design methods.

8.2 Contributions

The main objective of this thesis is to introduce a cyclic constitutive law in the finite element code `LAGAMINE`. It can be deemed fulfilled. This achievement is the final outcome of a sequence of scientific steps. The first step consists in a deep understanding of the constitutive law. Influence of each parameter on the model is extensively described and explained. Three sets of parameters are calibrated and compared for both monotonic and cyclic simulations.
An original implicit scheme is created to implement the constitutive law in the finite element code. This apparently straightforward step is actually not obvious. It requires the understanding of the `LAGAMINE` environment, the development of an efficient algorithm, its implementation and its verification. A 3D formulation is now available for any type of cyclic loading.

The second main contribution is the update and the improvement of the 2D hydro-mechanical interface element. The efficiency of the already existing element is considerably improved. A "suction effect" is introduced, allowing the unsticking of two solids. This additional feature is dedicated to transient modelling of offshore foundation, where the loss of contact of soil and foundations is not a synonym of global failure.

The third main contribution is related to the dissection of the transient behaviour of suction caissons. This offshore application is extensively investigated. Its salient features and the influence of main parameters are abundantly described and explained. The comparison of pseudo-random and equivalent load signals is also an interesting outcome that might have practical implications. A diagram representing the displacement at the end of a storm event for different combinations of mean and cyclic loadings can be derived.

Finally, the scientific path followed to achieve this work is paved with minor contributions. They consist of all the tools developed either for debugging or post-processing the results. The global experience of the research team about cyclic loading has also been increased.

8.3 Perspectives

Whatever the topic, a thesis always sows the seeds of following ones. Each progress induces new problems; each answer new questions. Science is continuously moving and our knowledge is perpetually perfectible. This thesis paves the way for the complex cyclic modelling of cohesionless material in `LAGAMINE`. Improvements and perspectives concern three main axes : constitutive law, tools and applications. These topics are obviously closely interrelated and depend on each other.

8.3.1 Constitutive law

The constitutive law is the basic component required to model any practical example. Its development and implementation are complex and sometimes cumbersome but lead to a very flexible mean of modelling material in any conditions. The Prevost model is adopted in this work for its conceptual simplicity and its physically-based parameters. It is suitable for the modelling of cyclic behaviour of sand. However, calibration process highlights a need for a more accurate volumetric plastic hardening rule. Such improvements should be a compromise between the accurate modelling of a complex reality and the number of new parameters to calibrate.
Furthermore, it would be interesting to extend a unique set of parameters to all initial states of the material, i.e. to any initial void ratio. Indeed, up to now, a set of parameters must be calibrated for each relative density of a given material, which is cumbersome and non practical. A state dependency should be inspired by the bounding surface models already embedding such features.
It appears *a posteriori*, that some others models would have been interesting. Recent advances in bounding surface models make them very attractive and their structure seems easier to implement. However, only the intensive use and the implementation of a model can reveal all its advantages and drawbacks. Therefore it is impossible to peremptorily assert another model would have been more suitable or not. The liquefaction and post-liquefaction behaviours are still an ongoing topic. It is definitely illusory to model a failure behaviour accurately with classic methods. However, it should be possible to develop a trick that overcomes local failure and mitigates it. Indeed, liquefaction reached at a very local point strongly deteriorates the convergence of the global numerical process, even if it does not correspond to a physical global failure of a structure. Cavitation is a mode of failure that should be integrated to the model since it limits the maximum suction resistance. Furthermore, the soil should desaturate in this case. Thus a retention curve should be modelled accordingly.
Interface plays a major role in soil-structure interaction. It might seem contradictorily to employ an elementary Mohr-Coulomb criterion for the interface and a complex constitutive

law for the surrounding soil. Indeed, a large field of development is opened concerning the cyclic behaviour of interfaces (degradation, dilatancy...). Many experimental studies exist but their numerical counterparts are much more scarce and remain unexplored.
Last but not least, a vulgarisation effort should be undertaken in order to make such models suitable for day to day projects. Indeed the gap between scientists using very complex models and industry is deep and large. The key factors of these models, more than their inherent intrinsic complexity is the calibration and mastering of parameters. An extensive amount of work is still necessary to produce correlations and explanations that would relate both sides of the chasm. Science should not be constrained by industry but scientists can not live in an ivory tower.

8.3.2 Tools

Theoretical models must be converted to practical software in order to be employed in practice. However simple and elegant ideas might be tricky and cumbersome to implement. So is the Prevost model. Many improvements consist in increasing the robustness, the accuracy or the efficiency of the algorithm. These perspectives are limited to a very narrow field of research but may lead to a substantial gain of practicability and a cost reduction.
The implemented algorithm might be enhanced in many ways since only a basic version is available. The effect of the Lode angle and a complex plastic potential can be taken into account. More numerical improvements concern the control of the accuracy that should be managed by a suitable sub-stepping technique. Analytical derivation of the tangent stiffness operator is a key issue for reducing the cpu time spent during integration of the law by a factor five in 2D and seven in 3D.

All the conditions are nearly fulfilled to move to 3D modelling. Only interface elements with suction effect should be extended to 3D. They already exist in their basic formulation but they should be improved. Furthermore, the unsticking effect must be taken into account. As a corollary effect, special resolution techniques must be employed to solve very large systems of equations. The iterative GMRES method is already implemented and available for that purpose.

8.3.3 Applications

The tools developed throughout this thesis coupled with the finite element code `LAGAMINE` offer a very flexible toolbox. The capability of reproducing cyclic behaviour of sand opens up new horizons.
Indeed, the studying of suction caissons can be pushed forward. The main improvement would be to confront numerical modelling with laboratory results. Several obstacles should be overcome. Firstly, data representative of the soil conditions should be at least available to perform a pertinent comparison. Secondly, limit analysis and failure laboratory tests are not easily modelled. Indeed, they involve many local failures before reaching a state of global collapse. These phenomena are, by essence, non-continuous and unstable. Representing exactly post-failure should be put into question. Indeed, the purpose of the design is to avoid the occurrence of a rupture.
The natural next step is the 3D simulation. Indeed, loading is never purely vertical but consists of a combination of vertical, horizontal and moment loads. Validating such simulations should open the door to the study of a large variety of geometry and soil conditions. Indeed, laboratory and numerical experiments should not be viewed as rivals but partners. The former are the only possibility to measure reality. However numerical simulations are much

more flexible and cheaper. Only a comparison between laboratory experiments and numerical simulations can provide reliable design procedures. The extensive understanding of complex phenomena is the first step to simplification. The final outcome should be design charts and diagrams adapted to given soil conditions and geometries.

Perspectives should not be restricted to suction caissons. Indeed, tools developed can be applied to the numerical modelling of many fields of offshore geotechnics such as piles or gravity based foundations. In the former the effect of initial stress distribution is a key issue while local failure (near the top of the seabed) is of major importance for the latter.
Obviously, a suitable constitutive law is the first step towards dynamic and earthquake engineering. However, additional tools have to be implemented before. Absorbing boundaries are the most important tools since they avoid spurious reflections of the loading in the soil domain. Any kind of cyclic modelling might then be tackled.

Bibliography

Alarcon-Guzman, A., Leonards, G.A. & Chameau, J.L. (1988). Undrained monotonic and cyclic strength of sands. *Journal of Geotechnical Engineering* **114**, No. 10, 1089–1109.

Alonso, E.E., Zandarín, M.T. & Olivella, S. (2013). Joints in unsaturated rocks: Thermo-hydro-mechanical formulation and constitutive behaviour. *Journal of Rock Mechanics and Geotechnical Engineering* **5**, No. 3, 200–213.

Andersen, K.H. (2009). Bearing capacity under cyclic loading-offshore, along the coast, and on land. *Canadian Geotechnical Journal* **46**, No. 5, 513–535.

Andersen, K.H., Jostad, H.P. & Dyvik, R. (2008). Penetration Resistance of Offshore Skirted Foundations and Anchors in Dense Sand. *Journal of Geotechnical and Geoenvironmental Engineering* **134**, No. June 2001, 106–116.

Andersen, K.H., Puech, A.A & Jardine, R.J. (2013). Cyclic resistant geotechnical design and parameter selection for offshore engineering and other applications. In *Proceedings of TC 209 Workshop - 18th ICSMGE, Paris.*

Andresen, L., Jostad, H.P. & Andersen, K.H. (2011). Finite element analyses applied in design of foundations and anchors for offshore structures. *International Journal of Geome* **11**, No. December, 417–430.

Andrianopoulos, K.I., Papadimitriou, A.G. & Bouckovalas, G.D. (2010). Bounding surface plasticity model for the seismic liquefaction analysis of geostructures. *Soil Dynamics and Earthquake Engineering* **30**, No. 10, 895–911.

Armero, F. (1999). Formulation and finite element implementation of a multiplicative model of coupled poro-plasticity at finite strains under fully saturated conditions. *Computer methods in applied mechanics and engineering* **171**, No. 3, 205–241.

Armero, F. & Perez-Foguet, A. (2002, January). On the formulation of closest-point projection algorithms in elastoplasticity, part I: The variational structure. *International Journal for Numerical Methods in Engineering* **53**, No. 2, 297–329.

Arulmoli, K., Muraleetharan, K.K., Hossain, M.M. & Fruth, L.S. (1992). Velacs: Verification of liquefaction analyses by centrifuge studies, laboratory testing program, soil data report. *Research Report*.

Barber, J.R. & Ciavarella, M. (2000). Contact mechanics. *International Journal of Solids and Structures* **37**, No. 1, 29–43.

Barnichon, J.D. (1998). *Finite element modelling in structural and petroleum geology.* Ph. D. thesis, University of Liège.

Bart, M. (2006). *Contributions à la modélisation du comportement hydromécanique des massifs rocheux avec fractures.* Ph. D. thesis, Univ. des Sciences et Technologies de Lille.

Bathe, K.-J., Ramm, E. & Wilson, E.L. (1975). Finite element formulations for large deformation dynamic analysis. *International Journal for Numerical Methods in Engineering* **9**, No. 2, 353–386.

Bauer, E. (1996). Calibration of a comprehensive hypoplastic model for granular materials. *Soils and Foundations* **36**, No. 1, 13–26.

Bauschinger, Johann (1886). Über die veränderung der elastizitätsgrenze und der festigkeit des eisens und stahls durch strecken und quetschen, durch erwärmen und abkühlen und durch oftmals wiederholte beanspruchung. *Techn. Lab. K. Techn. Hochsch. München* **13**, 1–116.

Been, K. & Jefferies, M.G. (1985, December). State parameter for sands. *International Journal of Rock Mechanics and Mining Sciences & Geomechanics Abstracts* **22**, No. 6, 198.

Been, K. & Jefferies, M.G. (2004). Stress dilatancy in very loose sand. *Canadian Geotechnical Journal* **41**, 972–989.

Been, K., Jefferies, M.G. & Hachey, J. (1991). The critical state of sands. *Géotechnique* **41**, No. 3, 365–381.

Beer, G. (1985). An isoparametric joint/interface element for finite element analysis. *International Journal for Numerical Methods in Engineering* **21**, 585–600.

Bell, James F & Truesdell, Clifford (1984). *The experimental foundations of solid mechanics.* Springer-Verlag.

Belytschko, T. & Neal, M.O. (1991). Contact impact by the pinball algorithm with penalty and lagrangian methods. *International Journal for Numerical Methods in Engineering* **31**, 547–572.

Bierlaire, M. (2006). *Introduction à l'optimisation différentiable.* PPUR presses polytechniques.

Biot, M.A. (1977). Variational lagrangian-thermodynamics of nonisothermal finite strain mechanics of porous solids and thermomolecular diffusion. *International Journal of Solids and Structures* **13**, No. 6, 579–597.

Bjerrum, L. (1973, January). Geotechnical problems involved in foundations of structures in the North Sea. *Géotechnique* **23**, No. 3, 319–358.

Bolton, M.D. (1986). The strength and dilatancy of sands. *Géotechnique* **36**, No. I, 65–78.

Borja, R.I. (2013). *Plasticity : Modeling & Computation.*

Boulanger, R.W. & Idriss, I.M. (2006). Liquefaction Susceptibility Criteria for Silts and Clays. *Journal of Geotechnical and Geoenvironmental Engineering* **132**, No. November, 1413–1426.

Boulon, M.J., Selvadurai, A.P.S., Benjelloun, H. & Feuga, B. (1993). Influence of rock joint degradation on hydraulic conductivity. *International Journal of Rock Mechanics and Mining Sciences* **30**, No. 7, 1311–1317.

Bourgeois, E & Dormieux, L (1996). Consolidation of a nonlinear poroelastic layer in finite deformations. *European Journal of Mechanics - A/Solids* **15**, No. 4, 575–598.

Boussinesq, J. (1868). Mémoire sur l'influence des frottements dans les mouvements réguliers des fluides. *Journal de Mathématiques Pures et Appliquées*.

Bray, J.D. & Sancio, R.B. (2006). Assessment of the Liquefaction Susceptibility of Fine-Grained Soils. *Journal of Geotechnical and Geoenvironmental Engineering* **9**, No. September, 1165–1177.

Brinkgreve, R.B.J. (2013). *Validating numerical modelling in geotechnical engineering*. United-Kingdom: NAFEMS.

Burger, A. (1985). *Thermique des nappes souterraines*. Presses polytechniques romandes.

Byrne, B.W. & Houlsby, G.T. (1999). Drained behaviour of suction caisson foundations on very dense sand. In *Offshore Technology Conference*.

Byrne, B.W. & Houlsby, G.T. (2002). Experimental investigations of response of suction caissons to transient vertical loading. *Journal of the Geotechnical and Geoenvironmental Engineering* **128**, No. 11, 926–939.

Byrne, B.W. & Houlsby, G.T. (2003, December). Foundations for offshore wind turbines. *Philosophical transactions. Series A, Mathematical, physical, and engineering sciences* **361**, No. 1813, 2909–30.

Byrne, B.W. & Houlsby, G.T. (2004). Experimental investigations of the response of suction caissons to transient combined loading. *Journal of the Geotechnical and Geoenvironmental Engineering* (March).

Canor, T. (2014). *New perspectives on probabilistic methods for nonlinear transient dynamics in civil engineering*. Ph. D. thesis, University of Liege.

Caprace, J.-D., Petcu, C., Velarde, M. & Rigo, P. (2012). Toward a Risk Based Simulation for the Erection of an Offshore Windmill Park. In *Proceedings of the 11th International Conference on Computer Applications and Information Technology in the Maritime Industries*.

Casagrande, A. (1936). Characteristics of cohesionless soils affecting the stability of slopes and earth fills. *Contributions to Soils Mechanics, 1925-1940*.

Casagrande, A. (1971). On liquefaction phenomena. *Gï¿½otechnique* **21**, No. 3, 197–202.

Casagrande, A. (1976). Liquefaction and cyclic deformation of sands: A critical review. In *Proceedings of the Pan-American Conference on Soil Mechanics and foundation Engineering, Buenos Aires*, Volume 5, pp. 79–113.

Castro, G. (1969). *Liquefaction of sands*. Harvard Univ., Div. of Engineering and Applied Mechanics.

Castro, G. (1975). Liquefaction and cyclic mobility of saturated sands. *ASCE Journal of Geotechnical Engineering Division* **101**, No. 6, 551–569.

Castro, G. & Poulos, S.J. (1977). Factors affecting liquefaction and cyclic modbility. *ASCE Journal of Geotechnical Engineering Division* **103**, No. 6, 501–516.

Cerfontaine, B. & Charlier, R. (2014). Implicit implementation of the prevost model. In *Proceedings of NUMGE2014*.

Cerfontaine, B., Levasseur, S., Collin, F. & Charlier, R. (2014). Axisymmetric transient modelling of a suction caisson in dense sand. In *Proceedings of NUMGE2014*.

Cescotto, S (1992). Finite deformation of solids. In *Numerical Modelling of Material Deformation Processes*, pp. 20–67. Springer.

Cescotto, S. & Charlier, R. (1993). Frictional contact finite elements based on mixed variational principles. *International Journal for Numerical Methods In Engineering* **36**, No. 10, 1681–1701.

Cetin, K.O., Der Kiureghian, A. & Seed, R.B. (2002, January). Probabilistic models for the initiation of seismic soil liquefaction. *Structural Safety* **24**, No. 1, 67–82.

Charlier, R. (1987). *Approche unifiée de quelques problèmes non linéaires de mécanique des milieux continus par la méthode des éléments finis (grandes déformations des métaux et des sols, contact unilatéral de solides, conduction thermique et écoulements en milieu poreux).* Ph. D. thesis, University of Liège.

Charlier, R. & Cescotto, S. (1988). Modélisation du phénomène de contact unilatéral avec frottement dans un contexte de grandes déformations. *Journal de Mécanique Théorique et Appliquée* **7**, No. Suppl. 1.

Christensen, P.W., Klarbring, A., Pang, J.S. & Omberg, N.S.T.R. (1998). Formulation and comparison of algorithms for frictional contact problems. *International Journal for Numerical Methods in Engineering* **173**, No. November 1996, 145–173.

Coffman, R.A. & El-sherbiny, R.M. (2004). Measured Horizontal Capacity of Suction Caissons. In *Offshore Technology Conference*, pp. 1–10.

Cosserat, E. & Cosserat, F. (1896). Sur la théorie de l'élasticité. premier mémoire. **10**, No. 3-4.

Coulomb, C.A. (1773). Essai sur une application des rï¿½gles des maximis et minimis ï¿½ quelques problï¿½mes de statique relatifs ï¿½ l'architecture. *Mï¿½moires de Mathï¿½matique et de Physique, Acadï¿½mie des Sciences de Paris* **7**.

Coulomb, C.A. (1821). *Théorie des machines simples.* Bachelier.

Coussy, O. (1991). *Mécanique des milieux poreux.* Editions Technip.

Cuéllar, P., Mira, P., Pastor, M., Fernández Merodo, J.A., Baeß ler, Ma. & Rücker, W. (2014, June). A numerical model for the transient analysis of offshore foundations under cyclic loading. *Computers and Geotechnics* **59**, 75–86.

Curnier, A. (1984). A theory of friction. *International Journal for Solids and Structures* **20**, No. 7, 637–647.

Dafalias, Y.F. (1986). Bounding surface plasticity. I : Mathematical foundation and hypoplasticity. *Journal of Engineering Mechanics* **112**, No. 9, 966–987.

Dafalias, Y.F. & Manzari, M.T. (2004). Simple plasticity sand model accounting for fabric change effects. *Journal of Engineering Mechanics* **130**, No. 6, 622–634.

Dafalias, Y.F. & Popov, E.P. (1975, October). A model of nonlinearly hardening materials for complex loading. *Acta Mechanica* **21**, No. 3, 173–192.

Darve, F. & Labanieh, S. (1982). Incremental constitutive law for sands and clays : simulations of monotonic and cyclic tests. *International Journal for Numerical and Analytical Methods in Geomechanics* **6**, 243–275.

Das, B.M. & Ramana, G.V. (2010, January). *Principles of Soil Dynamics* (Second ed.). CL-Engineering.

Day, R.A. & Potts, D.M. (1994). Zero thickness interface elements - numerical stability and application. *International Journal for Numerical and Analytical Methods in Geomechanics* **18**, 689–708.

de Borst, R & Heeres, O.M. (2002, September). A unified approach to the implicit integration of standard, non-standard and viscous plasticity models. *International Journal for Numerical and Analytical Methods in Geomechanics* **26**, No. 11, 1059–1070.

De Gennaro, V., Canou, J., Dupla, J.C. & Benahmed, N. (2004). Influence of loading path on the undrained behaviour of a medium loose sand. *Canadian Geotechnical Journal* **41**, No. 1, 166–180.

De Montleau, P., Habraken, A.-M. & Duchene, L. (2008). A new finite element integration scheme. application to a simple shear test of anisotropic material. *International journal for numerical methods in engineering* **73**, No. 10, 1395–1412.

DeJong, J.T., White, D.J. & Randoph, M.F. (2006). Microscale observation and modeling of soil structure interface behavior using particle image velocimetry. *Soils and Foundations* **46**, No. 1, 15–28.

Desai, C.S. & Nagaraj, T.K. (1988). Modeling for cyclic normal and shear behaviour of interfaces. *Journal of Engineering Mechanics* **114**, No. 7, 1198–1217.

Desai, C S, Drumm, E. C. & Zaman, M.M. (1985). Cyclic Testing and Modelling of Interfaces. *Journal of Geotechnical Engineering - ASCE* **I**, No. 6, 793–815.

Desrues, J., Chambon, R., Mokni, M. & Mazerolle, F. (1996). Void ratio evolution inside shear bands in triaxial sand specimens studied by computed tomography. *Géotechnique* **3**, No. 3.

Desrues, J. & Viggiani, G. (2004, April). Strain localization in sand: an overview of the experimental results obtained in Grenoble using stereophotogrammetry. *International Journal for Numerical and Analytical Methods in Geomechanics* **28**, No. 4, 279–321.

Detournay, E. & Cheng, A.H.-D. (1993). Fundamentals of poroelasticity.

Di Prisco, C. & Zambelli, C. (2003, August). Cyclic and dynamic mechanical behaviour of granular soils: experimental evidence and constitutive modelling. *Revue française de génie civil* **7**, No. 7-8, 881–910.

Donea, J., Huerta, A., Ponthot, J.-Ph. & Rodríguez-Ferran, A. (2004). Arbitrary lagrangian–eulerian methods. *Encyclopedia of computational mechanics*.

Dowson, D. (1998). *History of tribology* (second ed.). Longman London.

Drucker, D.C. & Prager, W. (1952). Soil mechanics and plastic analysis or limit design. *Quarterly of applied mechanics* **10**, No. 2, 157–165.

Elgamal, A., Yang, Z. & Parra, E. (2002, June). Computational modeling of cyclic mobility and post-liquefaction site response. *Soil Dynamics and Earthquake Engineering* **22**, No. 4, 259–271.

Elgamal, A., Yang, Z., Parra, E. & Ragheb, A. (2003). Modeling of cyclic mobility in saturated cohesionless soils. *International Journal of Plasticity* **19**, No. 6, 883–905.

Eliadorani, A. & Vaid, Y.P. (2005). Liquefaction of Dilating Sand. *Earthquake Engineering & Soil Dynamics*.

Equihua Anguiano, L.N. (2008). *Modélisation des ancrages de structures offshore flottantes dans les grands fonds marins*. Ph. D. thesis, Institut polytechnique de Grenoble.

Euler, L. (1750). Sur le frottement des corps solides. *Memoires de l'academie des sciences de Berlin*.

European Committee for Standardization (2003). *Eurocode 8: Design of structures for earthquake resistance*. CEN Brussels.

Finn, W.D.L., Bransby, P.L. & Pickering, D. J. (1970). Effect of strain history on liquefaction of sand. *Journal of the Soil Mechanics and Foundations Division* **96**, No. November.

Finno, R.J., Harris, W.W., Mooney, M.A & Viggiani, G. (1996). Strain localization and undrained steady state of sand. *Journal of Geotechnical Engineering* **122**, No. 6, 462–473.

Foucault, A. (2010). *Modï¿½lisation du comportement cyclique des ouvrages en terre intï¿½grant des techniques de rï¿½gularisation*. Ph. D. thesis, Ecole centrale Paris.

Galilei, G. (1638). *Discorsi e dimostrazioni matematiche, intorno ï¿½ due nuove scienze*. Lodewijk Elzevir.

Gens, A., Carol, I. & Alonso, E.E. (1988). An interface element formulation for the analysis of soil reinforcement interaction. *Computers and Geotechnics* **7**, 133–151.

Gens, A, Carol, I. & Alonso, E.E. (1990). A constitutive model for rock joints formulation and numerical implementations. *Computers and Geotechnics* **9**, 3–20.

Georgiannou, V. N., Tsomokos, A. & Stavrou, K. (2008, January). Monotonic and cyclic behaviour of sand under torsional loading. *Géotechnique* **58**, No. 2, 113–124.

Ghaboussi, J., Wilson, E.L. & Isenberg, J. (1973). Finite element for rock joints and interfaces. *Journal of the Soil Mechanics and Foundations Division* **99**, 933–848.

Giannakopoulos, A.E. (1989). The return mapping method for the integration of friction constitutive relations. *Computers & Structures* **32**, No. 1, 157–165.

Goodman, L.J., Lee, C.N. & Walker, F.J. (1961). The feasibility of vacuum anchorage in soil. *Géotechnique* **11**, No. 4, 356–359.

Goodman, R.E., Taylor, R.L. & Brekke, T.L. (1968). A model for the mechanics of jointed rock. *Journal of the Soil Mechanics and Foundations Division* **94**.

Green, R.A., Mitchell, J.K. & Polito, C.P. (2000). An energy-based excess pore pressure generation model for cohesionless soils. In *Proceedings of the John Booker Memorial Symposium*, Sydney, New South Wales, Australia, pp. 1–9.

Gudehus, G. (1996). A comprehensive constitutive equation for granular materials. *Soils and Foundations* **36**, No. 1, 1–12.

Guiducci, C., Collin, F., Radu, J.-P., Pellegrino, A. & Charlier, R. (2002). Numerical modeling of hydro-mechanical fracture behavior. In *Proc. of the Eight Int. Symp. on Num. Models in Geomechanics*. International Society for Rock Mechanics. Roma.

Habraken, A.M., Cescotto, S. & Banning, Q. (1998). Contact between deformable solids: The fully coupled approach. *Mathematical and Computer modelling* **28**, No. 4, 153–169.

Hashiguchi, K. (2009). *Elastoplasticity theory*. Springer Verlag Berlin Heidelberg.

Hashiguchi, K. & Chen, Z.-P. (1998). Elastoplastic constitutive equation of soils with the subloading surface and rotation hardening. *International Journal for Numerical and Analytical Methods in Geomechanics* **22**, 197–227.

Hashiguchi, K. & Ueno, M. (1977). Elastoplastic constitutive laws of granular materials, constitutive equations of soils. In Murayama, S. and Schofield, A.N. (Eds.), *Proceedings of the 9th International Conference on Soil Mechanics and Foundation Engineering*, Tokyo, Japan.

Hazen, A. (1920). Hydraulic-fill dams. *Transactions of the American Society of Civil Engineers* **83**, No. 1, 1713–1745.

Hertz, H. (1881). Ueber die Berührung fester elastischer Körper. *Journal für die reine und angewandte Mathematik* **92**, 156–171.

Hicher, P.-Y. & Shao, J.-F. (2002). *Elastoplasticitï¿½ des sols et des roches*, Volume 1. Lavoisier.

Hill, R. (1950). *The mathematical theory of plasticity.* Oxford: Calrendon Press.

Ho, T.Y.K., Jardine, R.J. & Anh-Minh, N. (2011, March). Large-displacement interface shear between steel and granular media. *Géotechnique* **61**, No. 3, 221–234.

Holeyman, A. & Kikuchi, Y. (2005). Technical session 2h: Pile foundations (ii): Installation, quality control, performance, and case histories. In *Proceedings of the 16th International Conference on Soil Mechanics and Geotechnical Engineering: Geotechnology in Harmony with the Global Environment*, Volume 5, pp. 3197–3200.

Hooke, R. (1678). *De potentia restitutiva or Of spring.* London: Royal Society.

Houlsby, G.T. & Byrne, B.W. (2005). Design procedures for installation of suction caissons in sand. In *Proceedings of ICE, Geotechnical Engineering*, Number July, pp. 135–144.

Houlsby, G.T., Ibsen, L.B. & Byrne, B.W. (2005). Suction Caissons for Wind Turbines. *International Symposium on Frontiers in Offshore Geotechnics* **75**, No. September, 94.

Houlsby, G.T., Kelly, R.B. & Byrne, B.W. (2005). The tensile capacity of suction caissons in sand under rapid loading. In *Frontiers in offshore geotechnics*, Number 1, pp. 405–410.

Houlsby, G.T., Kelly, R.B., Huxtable, J. & Byrne, B.W. (2006). Field trials of suction caissons in sand for offshore wind turbine foundations. *Géo* **56**, No. 1, 3–10.

Hujeux, J.C. (1985). Une loi de comportement pour le chargement cyclique des sols. *Génie parasismique*, 278–302.

Hyodo, M., Hyde, A.F.L., Aramaki, N. & Nakata, Y. (2002). Undrained monotonic and cyclic shear behaviour of sand under low and high confining stress. *Soils and Foundations* **42**, No. 3, 63–76.

Hyodo, M., Murata, H., Yasufuku, N. & Fujii, T. (1991). Undrained cyclic shear strength and residual shear strain of saturated sand by cyclic triaxial tests. *Soils and Foundations* **31**, No. 3, 60–76.

Hyodo, M., Tanimizu, H., Yasufuku, N. & Murata, H. (1994). Undrained cyclic and monotonic triaxial behaviour of saturated loose sand. *Soils and Foundations* **34**, No. 1, 19–32.

Iai, S. & Ozutsumi, O. (2005, April). Yield and cyclic behaviour of a strain space multiple mechanism model for granular materials. *International Journal for Numerical and Analytical Methods in Geomechanics* **29**, No. 4, 417–442.

Iai, S., Tobita, T., Ozutsumi, O. & Ueda, K. (2011). Dilatancy of granular materials in a strain space multiple mechanism model. *International Journal for Numerical and Analytical Methods in Geomechanics* **35**, No. March 2010, 360–392.

Ibsen, L.B. (1998). The mechanism controlling static liquefaction and cyclic strength of sand. In *Proceedings of International Workshop on physics and mechanics of soil liquefaction, Baltimore*.

Ibsen, L.B. (2004). Design of a new foundation for offshore wind turbines. In *Proceedings of the 22nd International modal analysis conference (IMAC)*, Detroit, Michigan.

Ibsen, L.B. & Jacobsen, F.R. (1996). Lund sand no. 0. Technical report, Aalborg University.

Ishihara, K. (1993). Liquefaction and flow failure during earthquakes. *Gï¿½otechnique* **43**, No. 3, 351–415.

Ishihara, K. (1996, September). *Soil Behaviour in Earthquake Geotechnics*. Oxford University Press, USA.

Ishihara, K., Tatsuoka, F. & Yasuda, S. (1975). Undrained deformation and liquefaction of sand under cyclic stresses. *Soils and Foundations* **15**, No. 1, 29–44.

Ishihara, K., Verdugo, R. & Acacio, A.A. (1991). Characterization of cyclic behavior of sand and post-seismic stability analysis. In *Proccedings of the Asian Regional Conference on Soil Mechanics and Foundation Engineering, Bangkok, Thailand*, Volume 2, pp. 45–68.

Iskander, M., El-gharbawy, S. & Olson, R. (2002). Performance of suction caissons in sand and clay. *Canadian Geotechnical Journal* **584**, No. may, 576–584.

Iwan, Wilfred D (1967). On a class of models for the yielding behavior of continuous and composite systems. *Journal of Applied Mechanics* **34**, No. 3, 612–617.

J.C.J., Schellekens & De Borst, R. (1993). On the numerical integration of interface element. *International Journal for Numerical Methods in Engineering* **36**, 43–66.

Jing, L. (2003, April). A review of techniques, advances and outstanding issues in numerical modelling for rock mechanics and rock engineering. *International Journal of Rock Mechanics and Mining Sciences* **40**, No. 3, 283–353.

Jonathan, P. & Taylor, P.H. (1997). On irregular, nonlinear naves in a spread sea. *Journal of Offshore Mechanics and Artic Engineering* **119**, No. February.

Kaliakin, V.N. & Li, J. (1995). Insight into deficiencies associated with commonly used zero-thickness interface elements. *Computers and Geotechnics* **17**, 225–252.

Kelly, R.B., Houlsby, G.T & Byrne, B.W. (2006a). A comparison of field and laboratory tests of caisson foundations in sand and clay. *Géotechnique* **56**, No. 9, 617–626.

Kelly, R. B., Houlsby, G. T. & Byrne, B. W. (2006b, January). Transient vertical loading of model suction caissons in a pressure chamber. *Géotechnique* **56**, No. 10, 665–675.

Khalili, N., Habte, M.A. & Valliappan, S. (2005, August). A bounding surface plasticity model for cyclic loading of granular soils. *International Journal for Numerical Methods in Engineering* **63**, No. 14, 1939–1960.

Koiter, W.T. (1953). Stress-strain relations, uniqueness and variational theorems for elastic plastic materials with a singular yield surface. *The quarterly of applied mathematics* **11**, No. 3.

Kolymbas, D. (1991). An outline of hypoplastieity. *Archive of Applied Mechanics* **61**, 143–151.

Lade, P.V. (1984). *Failure criterion for frictional materials*, Chapter 20. John Wiley and Sons Ltd.

Lade, P.V. & Duncan, J.M. (1975). Elastoplastic stress-strain theory for cohesionless soil. *Journal of the Geotechnical Engineering Division* **101**, No. 10, 1037–1053.

Lade, P.V. & Yamamuro, J.A. (1997, December). Effects of nonplastic fines on static liquefaction of sands. *Canadian Geotechnical Journal* **34**, No. 6, 918–928.

Lamé, G. (1866). *Leçons sur la théorie mathématique de l'élasticité des corps solides par G. Lamé*. Gauthier-Villars.

Laursen, T.A. & Simo, J.C. (1993). A continuum-based finite element formulation for the implicit solution of multibody, large deformation-frictional contact problems. *International Journal for Numerical Methods in Engineering* **36**, No. 20, 3451–3485.

Leblanc, C. (2009). *Design of Offshore Wind Turbine Support Structures Selected topics in the field of geotechnical engineering*. Ph. D. thesis, Technical university of Denmark.

Lee, K.L. & Ficht, J.A. (1975). Liquefaction potential at Ekofisk tank in north sea. *Journal of the Geotechnical Engineering Division* **101**.

Lee, K.L. & Seed, H.B. (1967). Cyclic stress conditions causing liquefaction of sand. *Journal of Soil Mechanics & Foundations Div* **93**, 47–70.

Lemaitre, J. (2001). Petite Histoire de l'Experimentation en Mecanique des Solides. *Mecanica* **36**, 13–35.

Lewis, R.W. & Schrefler, B.A. (1998). *The finite element method in the static and dynamic deformation and consolidation of porous media*. John Wiley.

Li, X.S. & Dafalias, Y.F. (2000). Dilatancy for cohesionless soils. *Géotechnique* **50**, No. 4, 449–460.

Li, X.S. & Dafalias, Y.F. (2012). Anisotropic critical state theory: role of fabric. *Journal of Engineering Mechanics* **138**, No. 3, 263–275.

Li, X.-S., Dafalias, Y.F & Wang, Z.-L. (1999). State-dependent dilatancy in critical-state constitutive modelling of sand. *Canadian Geotechnical Journal* **36**, No. 1993, 599–611.

Lings, M.L. & Dietz, M.S. (2005). The peak strength of sand steel interfaces and the role of dilation. *Soils and Foundations* **45**, No. 6, 1–14.

Lubliner, J. (1975). On loading, yield and quasi-yield surfaces in plasticity theory. *International Journal of Solids and Structures* **11**, No. 9, 1011–1016.

Luenberger, D.G. & Ye, Y. (2008). *Linear and nonlinear programming* (third ed.), Volume 116. Springer.

Ma, J., Wang, D. & Randolph, M.F. (2014). A new contact algorithm in the material point method for geotechnical simulations. *International Journal for Numerical and Analytical Methods in Geomechanics*.

Majumdar, A. & Bushan, B. (1991). Fractal model of elasti-palstic contact between rough surfaces. *Journal of Tribology* **113**, No. 1.

Malvern, L.E. (1969). *Introduction to the Mechanics of a Continuous Medium*. Prentice-Hall: Englewood Cliffs.

Mangal, J.K. & Houlsby, G.T. (1999). Partially-drained loading of shallow foundations on sand. In *Offshore Technology Conference*, Houston, Texas.

Manzari, M.T. & Prachathananukit, R. (2001, May). On integration of a cyclic soil plasticity model. *International Journal for Numerical and Analytical Methods in Geomechanics* **25**, No. 6, 525–549.

Marcuson, W.F. (1978). Definition of terms related to liquefaction. *Journal of the Geotechnical Engineering Division* **104**, No. 9, 1197–1200.

Matsuoka, H. & Nakai, T. (1974). Stress-deformation and strenght characteristics of soil under three different principal stresses. *Proceedings of the Japanese Society of Civil Engineers* **232**, 59–70.

Miner, M.A. (1945). Cumulative damage in fatigue. *Journal of Applied Mechanics* **12**, No. 3, 159–164.

Mira, P, Pastor, M, Li, T & Liu, X (2003). A new stabilized enhanced strain element with equal order of interpolation for soil consolidation problems. *Computer Methods in Applied Mechanics and Engineering* **192**, No. 37, 4257–4277.

Mira, P., Tonni, L., Pastor, M. & Fernandez-Merodo, J.A. (2009). A generalized midpoint algorithm for the integration of a generalized plasticity model for sands. *International Journal for Numerical Methods in Geomechanics* (September 2008), 1201–1223.

Miura, S. & Toki, S. (1982). Sample preparation method and its effect on static and cyclic deformation - strength properties of sand. *Soils and Foundations* **22**, No. 1, 61–77.

Mohamad, R. & Dobry, R. (1986). Undrained monotonic and cyclic triaxial strength of sand. *Journal of Geotechnical Engineering - ASCE* **112**, No. 10, 941–958.

Mohr, O. (1882). Ueber die darstellung des spannungszustandes und deformationszustandes eines körperelementes und über die anwendung derselben in der festigkeitslehre. *Der Civilingenieur* **28**.

Montáns, F.J. (2000). Implicit algorithms for multilayer j2-plasticity. *Computer methods in applied mechanics and engineering* **189**, No. 2, 673–700.

Montáns, F.J. (2001). Implicit multilayer J2-plasticity using Prager's translation rule. *International Journal for Numerical Methods in Engineering* **50**, 347–375.

Montáns, F.J. (2004). Implicit plane stress lagorithm for multilayer J2-Plasticity using the Prager-Ziegler translation rule. *International Journal for Numerical Methods in Engineering* **59**, 409–418.

Montáns, F.J. & Caminero, M.A. (2007). On the consistency of nested surfaces models and their kinematic hardening rules. *International journal of solids and structures* **44**, No. 14, 5027–5042.

Mooney, M.A, Finno, R.J. & Viggiani, M.C. (1998). A unique critical state for sand. *Journal of Geotechnical and Geoenvironmental Engineering* **124**, No. 11, 1100–1108.

Mortara, G., Boulon, M. & Ghionna, V.N. (2002, September). A 2-D constitutive model for cyclic interface behaviour. *International Journal for Numerical and Analytical Methods in Geomechanics* **26**, No. 11, 1071–1096.

Mroz, Z. (1967). On the description of anisotropic workhardening. *Journal of the Mechanics and Physics of Solids* **15**, 163–175.

Nadai, A. (1931). *Plasticity, a mechanics of the plastic state of matter.* McGraw-Hill Book Company, inc.

National Research Council (1985). *Liquefaction of soils during earthquakes. National Research Council Report CETS-EE-001.* National Academies.

Nemat-Nasser, B.S. & Takahashi, K. (1985). Liquefaction and fabric of sand. *Mechanics of Materials* **110**, No. 9, 1291–1306.

Newton, I. (1686). *Philosophiae naturalis principia mathematica.*

Niemunis, A., Wichtmann, T. & Triantafyllidis, T. (2005, June). A high-cycle accumulation model for sand. *Computers and Geotechnics* **32**, No. 4, 245–263.

Oda, M., Koishikawa, I. & Higuchi, T. (1978). Experimental study of anisotropic shear strength of sand by plane strain test. *Soils and Foundations* **18**, No. 1, 25–38.

Oden, J.T. & Pires, E.B. (1983). Nonlocal and nonlinear friction laws and variational principles for contact problems in elasticity. *Journal of Applied Mechanics* **50**.

Odqvist, F.K.G. (1933). Die verfestigung von flusseisenihnlichen kï¿½rpern. *Zeitschrift fiï¿½r Angewandte Mathematik und Mechanik* **13**, 360.

Oka, F., Tateishi, A., Yashima, A., Taguchi, Y. & Yamashita, A. (1999, January). A cyclic elasto-plastic constitutive model for sand considering a plastic-strain dependence of the shear modulus. *Géotechnique* **49**, No. 5, 661–680.

Olsson, R. & Barton, N. (2001, April). An improved model for hydromechanical coupling during shearing of rock joints. *International Journal of Rock Mechanics and Mining Sciences* **38**, No. 3, 317–329.

Ortiz, M. & Popov, E.P. (1985). Accuracy and stability of integration algorithms for elasto-plastic constitutive equations.pdf. *International Journal for Numerical Methods in Engineering* **21**, 1561–1576.

Osakada, K. (2010, August). History of plasticity and metal forming analysis. *Journal of Materials Processing Technology* **210**, No. 11, 1436–1454.

Pande, G.N. & Sharma, K.G. (1979). On joint/interface elements and associated problems of numerical ill-conditioning. *International Journal for Numerical Methods in Engineering.*

Papadimitriou, A.G. & Bouckovalas, G.D. (2002, April). Plasticity model for sand under small and large cyclic strains: a multiaxial formulation. *Soil Dynamics and Earthquake Engineering* **22**, No. 3, 191–204.

Papadimitriou, A.G, Bouckovalas, G.D. & Dafalias, Y.F. (2001). Plasticity model for sand under small and large cyclic strains. *Journal of the Geotechnical and Geoenvironmental Engineering* **3**, No. November, 973–983.

Park, I.-J. & Desai, C.S. (2000). Cyclic behaviour and liquefaction of sand using disturbed state concept. *Journal of the Geotechnical and Geoenvironmental Engineering* **126**, No. September, 834–846.

Pastor, M. & Zienkiewicz, O.C. (1986). A generalied plasticity hierarchical model for sand under monotonic and cyclic loading. In *2nd International Symposium on Numerical Models in Geomechanics*.

Pastor, M., Zienkiewicz, O.C. & Chan, H.C. (1990). Generalized plasticity and the modelling of soil behaviour. *International Journal for Numerical Methods in Geomechanics* **14**, 151–190.

Peacock, J. D. & Seed, H. Bolton (1968). Sand liquefaction under cyclic loading simple shear conditions. *Journal of the Soil Mechanics and Foundations Division* **94**, No. 3, 689–708.

Pecker, A. (1984). *Dynamique des sols*. Presses de l'Ecole Nationale des Ponts et Chaussï¿½es.

Pecker, A., Prevost, J.-H. & Dormieux, L. (2001, October). Analysis of pore pressure generation and dissipation in cohesionless materials during seismic loading. *Journal of Earthquake Engineering* **5**, No. 4, 441–464.

Perez-Foguet, A. & Armero, F. (2002). On the formulation of closest-point projection algorithms in elastoplasticity. Part II : globally convergent schemes. *International Journal for Numerical Methods in Engineering* **53**, No. 2.

Perez-Foguet, A., Rodriguez-ferran, A. & Huerta, A. (2001). Consistent tangent matrices for substepping schemes. *Computer Methods in Applied Mechanics and Engineering* **190**, 4627–4647.

Poisson, S.D. & Garnier, J.G. (1838). *Traitï¿½ de Mï¿½canique*. Société belge de librairie.

Polito, C.P., Green, R.A. & Lee, J. (2008). Pore Pressure Generation Models for Sands and Silty Soils Subjected to Cyclic Loading. *Journal of the Geotechnical and Geoenvironmental Engineering* **134**, No. October, 1490–1500.

Ponthot, J.-P. (2002). Unified stress update algorithms for the numerical simulation of large deformation elasto-plastic and elasto-viscoplastic processes. *International Journal of Plasticity* **18**, No. 1, 91–126.

Poulos, S.J. (1981). The steady state of deformation. *Journal of the Geotechnical Engineering Division, ASCE* **107**, No. GT5, Proc. Paper, 16241, 553–562.

Prager, W. (1949). Recent Developments in the Mathematical Theory of Plasticity. *Journal of Applied Physics* **20**, No. 3, 235.

Prandtl, L. (1920). Über die Härte plastischer Körper. *Nachrichten von der Gesellschat der Wissenschaften zu Göttingen, Mathematisch-Physikalische Klasse*, 74–85.

Prevost, J.H. (1977). Mathematical modelling of monotonic and cyclic undrained clay behaviour. *International Journal for Numerical and Analytical Methods in Geomechanics* **1**, No. 2, 195–216.

Prevost, J.H. (1985). A simple plasticity theory for frictional cohesionless soils. *International Journal of Soil Dynamics and Earthquake Engineering* **4**, No. 1, 9–17.

Prevost, J.-H. (1978). Anisotropic Undrained Stress-Strain Behavior of Clays. *Journal of the Geotechnical Engineering Division*.

Prevost, J.-H. (1982). Two surface versus multi-surface plasticity theories : a critical assessment. *International Journal for Numerical and Analytical Methods in Geomechanics* **6**, 323–338.

Puech, A. (2013). Design for cyclic loading: piles and other foundations. In *Proceedings of the 18th ISSMGE, TC209 Workshop*.

Rahman, M.S., Seed, H.B. & Booker, J.R. (1977). Pore pressure development under offshore gravity structures. *Journal of the Geotechnical Engineering Division* **103**, No. December 1977.

Rascol, E. (2009). *Cyclic Properties of Sand: Dynamic Behaviour for Seismic Applications*. Ph. D. thesis, École Polytechnique Fédérale de Lausanne.

Reuss, A. (1930). Berücksichtigung der elastischen formänderung in der plastizitätstheorie. *ZAMM-Journal of Applied Mathematics and Mechanics/Zeitschrift für Angewandte Mathematik und Mechanik* **10**, No. 3, 266–274.

Reynolds, O. (1885, december). On the dilatancy of media composed of rigid particles in contact. *Philosophical Magazine and Journal of Science* **20**, No. 5, 469–481.

Riemer, M.F. & Seed, R.B. (1997). Factors affecting apparent position of steady-state line. *Journal of Geotechnical and Geoenvironmental Engineering* **123**, No. 3, 281–288.

Rojek, J. & Telega, J.J. (2001). Contact problems with friction, adhesion and wear in orthopaedic biomechanics. Part 1 - general developments. *Journal of the theoretical and applied mechanics* **39**, No. 2001.

Roscoe, K.H. & Burland, J.B. (1968). On the generalized stress-strain behaviour of wet clay. *Engineering plasticity*, 535–609.

Roscoe, K.H., Schofield, A.N. & Wroth, C.P. (1958). On the Yielding of soils. *Géotechnique* **8**, No. 1, 22–53.

Rouainia, M.R. & Wood, D.M. (2001). Implicit numerical integration for a kinematic hardening soil plasticity model. *International Journal for Numerical and Analytical Methods in Geomechanics* **1325**, No. May, 1305–1325.

Rowe, P.W. (1962). The stress-dilatancy relation for static equilibrium of an assembly of particles in contact. *Proceedings of the Royal Society, Lodon, Series A*.

Sadrekarimi, A. (2013). Influence of fines content on liquefied strength of silty sands. *Soil Dynamics and Earthquake Engineering* **55**, 108–119.

Sasitharan, S., Robertson, P.K., Sego, D.C. & Morgenstern, N.R. (1993). Collapse behavior of sand. *Canadian Geotechnical Journal* **30**, No. 4, 569–577.

Schofield, A.N. & Wroth, C.P. (1968). *Crititcal state soil mechanics*. London : McGraw-Hill.

Schrefler, B.A. & Lewis, R.W. (1998). *The finite element method in the static and dynamic deformation and consolidation of porous media* (second ed.).

Seed, B. & Lee, K.L. (1966). Liquefaction of saturated sands during cyclic loading. *Journal of Soil Mechanics & Foundations Div* **92**.

Seed, H.B. (1979). Soil liquefaction and cyclic mobility evaluation for level ground during earthquakes. *ASCE J Geotech Eng Div* **105**, No. 2, 201–255.

Seed, H.B. & Booker, J.R. (1977). Stabilization of potentially liquefiable sand deposits using gravel drains. *Journal of the Geotechnical Engineering Division* **103**, No. 7.

Seed, H.B. & Idriss, I.M. (1971). Simplified procedure for evaluating soil liquefaction potential. *Journal of the Soil Mechanics and Foundations Division* **97**, No. 9.

Seed, H.B., Tokimatsu, K., Harder, L.F. & Chung, R.M. (1985). Influence of SPT procedures in soil liquefaction resistance evaluations. *Journal of Geotechnical Engineering - ASCE* **111**, No. 12, 1425–1445.

Seed, R.B., Cetin, K.O., Moss, R.E.S, Kammerer, A.M., Wu, J., Pestana, J.M., Riemer, M.F., Kayen, R.E. & Faris, A. (2003). Recent advances in soil liquefaction engineering: a unified and consistent framework. In *Keynote presentation, 26th Annual ASCE Los Angeles Geotechnical Spring Seminar*, Long Beach, California.

Segura, J.M. & Carol, I. (2004). On zero-thickness interface elements for diffusion problems. *International journal for numerical and analytical methods in geomechanics* **28**, No. 9, 947–962.

Senders, M. (2008). *Suction caissons in sand as tripod foundations for offshore wind turbines.* Ph. D. thesis, University of western Australia.

Senders, M. & Randolph, M.F. (2009). CPT-Based Method for the Installation of Suction Caissons in Sand. *Journal of Geotechnical and Geoenvironmental Engineering* **135**, No. January, 14–25.

Senpere, D. & Auvergne, G.A. (1982). Suction anchor piles-a proven alternative to driving or drilling. In *Offshore Technology Conference*. Offshore Technology Conference.

Shahrour, I. & Rezaie, F. (1997, January). An elastoplastic constitutive relation for the soil-structure interface under cyclic loading. *Computers and Geotechnics* **21**, No. 1, 21–39.

Sharma, K.G. & Desai, C.S. (1993). Analysis and implementation of thin-layer element for interfaces and joints. *Journal of Engineering Mechanics* **118**, No. 27005, 2442–2462.

Sheng, D., Eigenbrod, K.D. & Wriggers, P. (2005, January). Finite element analysis of pile installation using large-slip frictional contact. *Computers and Geotechnics* **32**, No. 1, 17–26.

Simo, J.C. & Hughes, T.J.R. (1998). Computational inelasticity.

Simo, J.C. & Laursen, T.A. (1992). An augmented Lagrangian treatment of contact problems involving friction. *Computers & Structures* **42**, No. 1, 97–116.

Simo, J.C. & Taylor, R.L. (1985). Consistent tangent operators for rate-independent elastoplasticity. *Computer methods in applied mechanics and engineering* **48**, No. 1, 101–118.

Skempton, A.W. (1986). Standard penetration test procedures and the effects in sands of overburden pressure, relative density, particle size, ageing and overconsolidation. *Géotechnique* **36**, No. 3, 425–447.

Skopek, P., Morgenstern, N.R., Robertson, P.K. & Sego, D.C. (1994). Collapse of dry sand. *Canadian Geotechnical Journal* **31**, No. 6, 1008–1014.

Sladen, J.A., D'Hollander, R.D. & Krahn, J. (1985). The liquefaction of sands, a collapse surface approach. *Canadian Geotechnical Journal* **22**, No. 4, 564–578.

Sloan, W.S. (1987). Substepping schemes for the numerical integration of elastoplastic stress-strain relations. *International Journal for Numerical Methods in Engineer* **24**, No. September 1986, 893–911.

Stuyts, B., Irvine, J. & Cathie, D. (2011). Assessing the stability of piled tripod foundations for offshore wind turbines under cyclic loading. In *Proceedings of the 8th International Conference on Structural Dynamics, EUDORYN 2011*, Leuven.

Symes, M.J., Gens, A. & Hight, D.W. (1984). Undrained anisotropy and principal stress rotation in saturated sand. *Géotechnique* **34**, No. 1, 11–27.

Taiebat, H.A. (1999). *Three dimensional liquefaction alaysis of offshore foundations*. Ph. D. thesis, University of Sydney.

Taiebat, H.A.R & Carter, J.P.S (2000). A semi-empirical method for the liquefaction analysis of offshore foundations. *International Journal for Numerical and Analytical Methods in Geomechanics* **24**, 991–1011.

Taylor, D.W. (1948). *Fundamentals of soil mechanics*. Wiley.

Taylor, P.H., Jonathan, P. & Harland, L.A. (1997). Time Domain Simulation of Jack-up Dynamics Witli the Extremes of a Gaussian Process. *Transactions of the American Society of Mechanical Engineering* **119**, No. October.

Timoshenko, S. (1983). *History of strength of materials: with a brief account of the history of theory of elasticity and theory of structures*. Courier Dover Publications.

Tjelta, T.I., Aas, P.M., Hermstad, J. & Andenaes, E. (1990). The skirt piled gullfaks c platform installation. In *Offshore Technology Conference*.

Tjelta, T.-I. (1994). Geotechnical aspects of bucket foundations replacing piles for the europipe 16/11-e jacket. In *Offshore Technology Conference*.

Toyota, H., Nakamura, K. & Kazama, M. (2004). Shear and liquefaction characteristics of sandy soils in triaxial tests. *Soils and Foundations* **44**, No. 2, 117–126.

Tran, M.N (2005). *Installation of Suction Caissons in Dense Sand and the Influence of Silt and Cemented Layers*. Ph. D. thesis, The university of Sydney.

Tsang, Y.W. & Witherspoon, P.A. (1981). Hydromechanical behavior of a deformable rock fracture subject to normal stress. *Journal of Geophysical Research: Solid Earth* **86**, No. B10, 9287–9298.

Tsukamoto, Y., Ishihara, K. & Sawada, S. (2004). Settlement of silty sand deposits following liquefaction during earthquakes. *Soils and Foundations* **44**, No. 5, 135–148.

Vaid, Y.P. & Chern, J.C. (1983). Effect of static shear on resistance to liquefaction. *Soils and Foundations* **23**, No. 1, 47–60.

Vaid, Y.P. & Chern, J.C. (1985). Cyclic and monotonic undrained response of saturated sands. pp. 120–147.

Vaid, Y.P., Chung, E.K.F. & Kuerbis, R.H. (1990). Stress path and steady state. *Canadian Geotechnical Journal* **27**, No. 1, 1–7.

Vaid, Y.P. & Sasitharan, S. (1992). The strength and dilatancy of sand. *Canadian Geotechnical Journal* **29**, No. 3, 522–526.

Vaid, Y.P. & Sivathayalan, S. (2000). Fundamental factors affecting liquefaction susceptibility of sands. *Canadian Geotechnical Journal* **37**, No. 3, 592–606.

Vaid, Y.P., Stedman, J.D. & Sivathayalan, S. (2001). Confining stress and static shear effects in cyclic liquefaction. *Canadian Geotechnical Journal* **38**, No. 3, 580–591.

Vaid, Y.P. & Thomas, J. (1995). Liquefaction and postliquefaction behavior of sand. *Journal of Geotechnical Engineering - ASCE* **121**, No. 2, 163–173.

Van Der Tempel, J. (2006). *Design of support structures for wind turbines.* Ph. D. thesis, TU Delft.

Van Eekelen, H.A.M. (1980). Isotropic yield surfaces in three dimensions for use in soil mechanics. *International Journal for Numerical and Analytical Methods in Geomechanics* **4**, No. 1, 89–101.

Verdugo, R. & Ishihara, K. (1996). The steady state of sandy soils. *Soils and foundations - Japanese Geotechnical Society* **36**, No. 2, 81–91.

Veritas, Det Norske (2011). *Design of offshore wind turbine structures, Offshore Santdard DNV-OS-J101.* Norway.

Verkest, M. (2013). Introduction to offshore wind in belgium, challenges overcome and ahead. Belgian Geotechnical Experiences related to Offshore Wind Energy.

Versteele, H., Stuyts, B., Cathie, D. & Charlier, R. (2013). Cyclic loading of caisson supported offshore wind structures in sand. In *Proceedings of the 18th International Conference on Soil Mechanics and Geological Engineering.*

Villalobos, F., Byrne, B.W. & Houlsby, G.T. (2009). An experimental study of the drained capacity of suction caisson foundations under monotonic loading for offhsore application. *Soils and Foundations* **49**, No. 3, 477–488.

von Mises, R. (1913). Mechanik der festen Körper im plastisch- deformablen Zustand. *Nachrichten von der Gesellschat der Wissenschaften zu Göttingen, Mathematisch-Physikalische Klasse* **4**, 582–592.

von Wolffersdorff, P.A. (1996). A hypoplastic relation for granular materials with a predefined limit state surface. *Mechanics of Cohesive - Frictional Materials* **1**, No. March, 251–271.

Wang, J.G., Ichikawa, Y. & Leung, C.F. (2003, January). A constitutive model for rock interfaces and joints. *International Journal of Rock Mechanics and Mining Sciences* **40**, No. 1, 41–53.

Wang, Q. & Lade, P.V. (2001). Shear banding in true triaxial tests and its effect on failure in sand. *Journal of Engineering Mechanics* **127**, No. 8, 754–761.

Wang, R., Zhang, J.M. & Wang, G. (2014). A unified plasticity model for large post-liquefaction shear deformation of sand. *Computers and Geotechnics*, 54–66.

Wang, S.P. & Nakamachi, E. (1997). The inside-outside contact search algorithm for finite element analysis. *International Journal for Numerical Methods in Engineering* **40**, No. December, 5–16.

Wang, X. & Wang, L.B. (2006). Continuous interface elements subject to large shear deformations. *International Journal of Geomechanics* **6**, No. April, 97–107.

Wang, Z.L., Dafalias, Y.F. & Shen, C.-K. (1990). Bounding surface hypoplasticity model for sand. *Journal of Engineering Mechanics* **116**, No. 5, 983–1001.

White, D. J. & Lehane, B. M. (2004, January). Friction fatigue on displacement piles in sand. *Géotechnique* **54**, No. 10, 645–658.

White, J.A. & Borja, R.I. (2008, September). Stabilized low-order finite elements for coupled solid-deformation/fluid-diffusion and their application to fault zone transients. *Computer Methods in Applied Mechanics and Engineering* **197**, No. 49-50, 4353–4366.

Wichtmann, T., Niemunis, A. & Triantafyllidis, T. (2005, December). Strain accumulation in sand due to cyclic loading: drained triaxial tests. *Soil Dynamics and Earthquake Engineering* **25**, No. 12, 967–979.

Wichtmann, T., Niemunis, A. & Triantafyllidis, T. (2010, August). Strain accumulation in sand due to drained cyclic loading: On the effect of monotonic and cyclic preloading (Miner's rule). *Soil Dynamics and Earthquake Engineering* **30**, No. 8, 736–745.

Wichtmann, T., Rojas, B., Niemunis, A. & Triantafyllidis, T. (2011). Prediction of drained and undrained cyclic behaviour of a fine sand using a high cycle accumulation model. In *5th International Conference on Earthquake Engineering*, Santiago.

Wilkins, M.L. (1964). *Calculation of elastic-plastic flow.* New-York: Academic Press.

Wriggers, P. (1995). Finite element algorithms for contact problems. *Archives of Computational Methods in Engineering* **2**, No. 4, 1–49.

Wriggers, P. (2006). *Computational contact mechanics* (Second ed.). Wiley : Chichester.

Wriggers, P. & Zavarise, G. (2004). *Encyclopedia of Computational Mechanics*, Volume 2: Solids and Structures, Chapter 6: Computational Contact Mechanics.

Yamamuro, J.A. & Lade, P.V. (1997). Static liquefaction of very loose sands. *Canadian Geotechnical Journal* **34**, No. 1993, 905–917.

Yang, Z. & Elgamal, A. (2008). Multi-surface cyclic plasticity sand model with lode angle effect. *Geotechnical and Geological Engineering* **26**, No. 3, 335–348.

Yang, Z., Elgamal, A., Adalier, K. & Sharp, M.K. (2004). Earth Dam on Liquefiable Foundation and Remediation : Numerical Simulation of Centrifuge Experiments. *Journal of Engineering Mechanics* **130**, No. 10, 1168–1176.

Yang, Z., Elgamal, A. & Parra, E. (2003). Computational model for cyclic mobility and associated shear deformation. *Journal of Geotechnical and Geoenvironmental Engineering* **129**, No. 12, 1119–1127.

Yoshimine, M. & Ishihara, K. (1998). Flow potential of sand during liquefaction. *Soils and Foundations* **38**, No. 3, 189–198.

Yoshimine, M, Ishihara, K. & Vargas, W. (1998). Effects of principal stress direction and intermediate principal stress on undrained shear behaviour of sand. *Soils and Foundations* **38**, No. 3, 179–188.

Youd, T.L. & Idriss, I.M. (2001). Liquefaction resistace of soils : summary report. *Journal of the Geotechnical and Geoenvironmental Engineering* **127**, No. 4, 297–313.

Young, T. (1845). *A Course of Lectures on Natural Philosophy and the Mechanical Arts: pt. I. Mechanics. pt. II. Hydrodynamics. pt. III. Physics.* Taylor and Walton.

Yu, H.S. (2006). Multi-surface and bounding surface plasticity. In *Plasticity and Geotechnics*, Chapter 7, pp. 153–196.

Yu, H.-S., Khong, C. & Wang, J. (2007, March). A unified plasticity model for cyclic behaviour of clay and sand. **34**, No. 2, 97–114.

Zavarise, G., Wriggers, P. & Schrefler, B.A. (1998). A method for solving contact problems. *International Journal for Numerical Methods in Engineering* **42**, No. 3, 473–498.

Zerfa, Z. & Loret, B. (2003). Coupled dynamic elastic-plastic analysis of earth structures. *Soil Dynamics and Earthquake Engineering* **23**, No. 6, 435–454.

Zhang, H. & Garga, V.K. (1997). Quasi-steady state: a real behaviour? *Canadian Geotechnical Journal* **34**, No. 5, 749–761.

Zhong, Z. & Mackerle, J. (1992). Static Contact Problems - A review. *Engineering computations* **9**, 3–37.

Zienkiewicz, O.C. & Cheung, Y.C (1967). *The Finite element method in structural and continuum mechanics*. New-York: Mc-Graw-Hill.

Zienkiewicz, O.C. & Mroz, Z. (1984). *Mechanics of engineering materials*, Chapter 33, pp. 655–673. Wiley, New York.

Zienkiewicz, O. C. & Taylor, R. L. (2000, September). *Finite Element Method: Volume 1, Fifth Edition*. Butterworth-Heinemann.

Appendix A

Simplified Prevost model for triaxial test

Zorro est le seul héros qu'on reconnait grâce à son masque.
(Zorro is the only hero that can be recognised thanks to its mask.)

Pierre Cerfontaine

Contents

The Prevost model was degenerated into two simplified Equations (A.1) and (A.2) adapted to the modelling of triaxial tests, [Prevost, 1985]. Only two deformation and two stress variables are then necessary. Deviatoric deformation and stress invariants are denoted by e and q respectively. Volumetric deformation and stress are termed ϵ_v and p[1].

$$\frac{\dot{e}}{\dot{\mathrm{q}}} = \frac{1}{2G} + \frac{1}{H'} \cdot \frac{1 - \eta \dot{\mathrm{p}}'/\dot{\mathrm{q}}}{1 + \frac{2}{9}\eta^2} \tag{A.1}$$

$$\frac{\dot{\epsilon_v}}{\dot{\mathrm{p}}'} = \frac{1}{K} \pm \frac{1}{H'} \cdot \frac{2}{\sqrt{6}} \cdot \frac{1 - (\eta/\bar{\eta})^2}{1 + (\eta/\bar{\eta})^2} \cdot \frac{\dot{\mathrm{q}}/\dot{\mathrm{p}}' - \eta}{\sqrt{1 + \frac{2}{9}\eta^2}} \tag{A.2}$$

where the $\pm$ sign distinguishes between loading and unloadig cases. These equations can be adapted to the specific cases of triaxial test :

- drained ;
- drained ($\mathrm{p}' = \text{constant}$) ;
- undrained.

The purpose of such a formulation is an easier calibration of parameters. This couple of equations can be straightforwardly implemented apart from any finite element code. Simulations are assumed stress driven and depend on the evolution of e. An explicit integration is adopted. The following equations stand for original developments of the Prevost model. Therefore the flow rule is modified according to [Elgamal et al., 2002], *i.e.*

$$P" = \psi \cdot \frac{1 + (\eta/\bar{\eta})^2}{1 - (\eta/\bar{\eta})^2}. \tag{A.3}$$

[1] Effective stress.

A.1 Drained triaxial test

During a triaxial test, the total stress is equal to the effective one and the variation of the mean stress reads

$$\begin{aligned} \dot{\mathrm{p}}^{tot} = \dot{\mathrm{p}}' &= \left(\frac{\dot{\sigma_1} + 2\cdot\dot{\sigma}}{3}\right) \\ &= \left(\frac{\dot{\sigma_1} - \dot{\sigma_3} + 3\cdot\dot{\sigma}}{3}\right) \\ &= \frac{\dot{\mathrm{q}}}{3} + \cancel{\dot{\sigma_3}} \end{aligned} \tag{A.4}$$

where σ_1 and $\sigma_3 = cst$ are the principal stresses. Therefore the ratio $\dot{q}/\dot{\mathrm{p}} = 3$ is constant during the simulation. Equations A.1 and A.2 are then rewritten

$$\dot{e} = \overbrace{\left(\frac{1}{2G} + \frac{1}{H'}\cdot\frac{1-\eta/3}{1+\frac{2}{9}\eta^2}\right)}^{C_1}\cdot\dot{\mathrm{q}} \tag{A.5}$$

$$\dot{\epsilon}_v = \overbrace{\left(\frac{1}{K} \pm \frac{1}{H'}\cdot\frac{2}{\sqrt{6}}\cdot\frac{1-(\eta/\bar{\eta})^2}{1+(\eta/\bar{\eta})^2}\cdot\frac{3-\eta}{\sqrt{1+\frac{2}{9}\eta^2}}\right)}^{C_2}\cdot\dot{\mathrm{p}}'. \tag{A.6}$$

The final set of equations allows for an explicit simulation of drained tests as a function of the deviatoric deformation

$$\begin{cases} \dot{\mathrm{q}} &= \dfrac{\dot{\mathrm{e}}}{C_1} \\ \dot{\mathrm{q}} &= 3\cdot\dot{\mathrm{p}}' \\ \dot{\epsilon}_v &= C_2\cdot\dot{\mathrm{p}}'. \end{cases} \tag{A.7}$$

A.2 Drained triaxial test (p'=constant)

In that particular case, the mean effective stress is kept constant along the simulation. Therefore, Equations A.1 and A.2 are reorganised

$$\dot{e} = \frac{\dot{\mathrm{q}}}{2G} + \frac{1}{H'}\cdot\frac{\dot{\mathrm{q}} - \overbrace{\eta\cdot\dot{\mathrm{p}}'}^{=0}}{1+\frac{2}{9}\eta^2} \tag{A.8}$$

$$\dot{\epsilon}_v = \overbrace{\frac{\dot{\mathrm{p}}'}{K}}^{=0} \pm \frac{1}{H'}\cdot\frac{2}{\sqrt{6}}\cdot\frac{1-(\eta/\bar{\eta})^2}{1+(\eta/\bar{\eta})^2}\cdot\frac{\dot{\mathrm{q}} - \overbrace{\eta\cdot\dot{\mathrm{p}}'}^{=0}}{\sqrt{1+\frac{2}{9}\eta^2}} \tag{A.9}$$

which finally lead to

$$\dot{e} = \overbrace{\left(\frac{1}{2G} + \frac{1}{H'} \cdot \frac{1}{1+\frac{2}{9}\eta^2}\right)}^{C_1} \cdot \dot{\mathrm{q}} \tag{A.10}$$

$$\dot{\epsilon}_v = \overbrace{\left(\pm\frac{1}{H'} \cdot \frac{2}{\sqrt{6}} \cdot \frac{1-(\eta/\bar{\eta})^2}{1+(\eta/\bar{\eta})^2} \cdot \frac{1}{\sqrt{1+\frac{2}{9}\eta^2}}\right)}^{C_2} \cdot \dot{\mathrm{q}} \tag{A.11}$$

and then

$$\begin{cases} \dot{\mathrm{p}}' = 0 \\ \dot{\mathrm{q}} = \dfrac{\dot{e}}{C_1} \\ \dot{\epsilon}_v = C_2 \cdot \dot{\mathrm{q}}. \end{cases} \tag{A.12}$$

A.3 Undrained triaxial test

During undrained triaxial simulation, the following equations can be stated that

$$\begin{aligned} \dot{\mathrm{p}}^{tot} &= \dot{\mathrm{p}}' + \dot{u}_w \\ &= \frac{\dot{\mathrm{q}}}{3} + \cancel{\dot{\sigma}_3} + \dot{u}_w \end{aligned} \tag{A.13}$$

$$\tag{A.14}$$

$$\dot{u}_w = \frac{\dot{\mathrm{q}}}{3} - \dot{\mathrm{p}}. \tag{A.15}$$

Moreover, the volume remains constant during undrained triaxial test, i.e. $\dot{\epsilon}_v = 0$. Therefore, Equation A.2 is recast into

$$0 = \frac{1}{K} \pm \frac{1}{H'} \cdot \frac{2}{\sqrt{6}} \cdot \frac{1-(\eta/\bar{\eta})^2}{1+(\eta/\bar{\eta})^2} \cdot \frac{\dot{\mathrm{q}}/\dot{\mathrm{p}}' - \eta}{\sqrt{1+\frac{2}{9}\eta^2}} \tag{A.16}$$

$$\Leftrightarrow \frac{\dot{\mathrm{q}}}{\dot{\mathrm{p}}'} = \overbrace{\mp\frac{H'}{K} \cdot \frac{\sqrt{6}}{2} \cdot \frac{1+(\eta/\bar{\eta})^2}{1-(\eta/\bar{\eta})^2} \cdot \sqrt{1+\frac{2}{9}\eta^2} + \eta}^{C_1}. \tag{A.17}$$

If the ratio C_1 is introduced into Equation A.1, one gets

$$\dot{e} = \overbrace{\left(\frac{1}{2G} + \frac{1}{H'} \cdot \frac{1-\eta \cdot C_1}{1+\frac{2}{9}\eta^2}\right)}^{C_2} \cdot \dot{q} \tag{A.18}$$

and the following set of equations holds

$$\begin{cases} \dot{\mathrm{q}} = \dfrac{\dot{\mathrm{e}}}{C_2} \\ \dot{\mathrm{p}}' = \dfrac{\dot{\mathrm{q}}}{C_1} \\ \dot{u}_w = \dfrac{\dot{\mathrm{q}}}{3} - \dot{\mathrm{p}}' \end{cases} \tag{A.19}$$

A.4 From triaxial to tensorial backstress

It is worth noting that α is a scalar provided from calibration on triaxial tests. Therefore, the corresponding tensor $\boldsymbol{\alpha}$ that is used in the tensorial formulation can be reconstituted readily

$$\alpha = \alpha_{22} - \alpha_{33} \tag{A.20}$$

$$\alpha_{22} + 2 \cdot \alpha_{33} = 0 \tag{A.21}$$

$$\Rightarrow \quad \boldsymbol{\alpha} = \frac{1}{3} \cdot \begin{bmatrix} -\alpha & & \\ & 2 \cdot \alpha & \\ & & -\alpha \end{bmatrix} \tag{A.22}$$

where α_{22} and α_{33} diagonal components of the backstress tensor $\boldsymbol{\alpha}$. Equation (A.20) holds by definition and Equation (A.21) expresses that the backstress tensor if purely deviatoric, i.e. its trace is null.

Appendix B

Analytical derivatives

Science sans conscience n'est que ruine de l'âme
(Science without conscience is nothing but ruin of the soul.)

François Rabelais

Contents

In the following and for the sake of readability, $M'^i = \sqrt{\frac{2}{3}} \cdot M^i \qquad \forall i.$

B.1 Preamble

Proposition B.1.1. *Derivative of a unit second order tensor is self-orthogonal.*

Proof. Let us assumed that a second order tensor $\mathbf{n}$ depends on ξ

$$\mathbf{n} = \begin{bmatrix} n_{11}(\xi) & n_{12}(\xi) \\ n_{21}(\xi) & n_{22}(\xi) \end{bmatrix} \tag{B.1}$$

and $\hat{\mathbf{n}}$ the corresponding unit tensor, using the Frobenius norm.

$$\hat{\mathbf{n}} = \begin{bmatrix} n_{11} & n_{12} \\ n_{21} & n_{22} \end{bmatrix} \cdot \frac{1}{\sqrt{n_{11}^2 + n_{12}^2 + n_{21}^2 + n_{22}^2}} = \frac{\mathbf{n}}{\sqrt{\mathbf{n} : \mathbf{n}}} \tag{B.2}$$

$$\frac{\partial \hat{\mathbf{n}}}{\partial \xi} = \frac{\dfrac{\partial \mathbf{n}}{\partial \xi} \cdot \|\mathbf{n}\| - \dfrac{\partial \|\mathbf{n}\|}{\partial \xi} \cdot \mathbf{n}}{\|\mathbf{n}\|^2} \tag{B.3}$$

$$= \frac{\dfrac{\partial \mathbf{n}}{\partial \xi} \cdot \|\mathbf{n}\| - \dfrac{1}{2} \cdot \dfrac{1}{\sqrt{\mathbf{n} : \mathbf{n}}} \cdot \left(\mathbf{n} : \dfrac{\partial \mathbf{n}}{\partial \xi} + \dfrac{\partial \mathbf{n}}{\partial \xi} : \mathbf{n} \right) \cdot \mathbf{n}}{\|\mathbf{n}\|^2} \tag{B.4}$$

$$= \frac{\dfrac{\partial \mathbf{n}}{\partial \xi} \cdot \|\mathbf{n}\| - \dfrac{1}{\|\mathbf{n}\|} \cdot \dfrac{\partial \mathbf{n}}{\partial \xi} : \mathbf{n} \cdot \mathbf{n}}{\|\mathbf{n}\|^2} \tag{B.5}$$

$$\frac{\partial \hat{\mathbf{n}}}{\partial \xi} : \mathbf{n} = \frac{\dfrac{\partial \mathbf{n}}{\partial \xi} : \mathbf{n} \cdot \|\mathbf{n}\| - \dfrac{1}{\|\mathbf{n}\|} \cdot \dfrac{\partial \mathbf{n}}{\partial \xi} : \mathbf{n} \cdot \mathbf{n} : \mathbf{n}}{\|\mathbf{n}\|^2} \tag{B.6}$$

$$= \frac{\dfrac{\partial \mathbf{n}}{\partial \xi} : \mathbf{n} \cdot \|\mathbf{n}\| - \dfrac{1}{\cancel{\|\mathbf{n}\|}} \cdot \dfrac{\partial \mathbf{n}}{\partial \xi} : \mathbf{n} \cdot \|\mathbf{n}\|\cancel{^2}}{\|\mathbf{n}\|^2} = 0 \tag{B.7}$$

□

B.2 Derivative of $\hat{\mathbf{n}}_{n+1}$

$$
\begin{aligned}
\mathbf{n}_{n+1} &= \mathbf{s}_{tr} - p'_{n+1} \cdot \boldsymbol{\alpha}^a_n - H^*_{a,n+1} \cdot \Delta\gamma^a_{n+1} \cdot \hat{\boldsymbol{\mu}}^a \\
\frac{\partial \mathbf{n}_{n+1}}{\partial H^*_{a,n+1}} &= -\Delta\gamma^a_{n+1} \cdot \hat{\boldsymbol{\mu}}^a \\
\frac{\partial \mathbf{n}_{n+1}}{\partial \Delta\gamma^a_{n+1}} &= -H^*_{a,n+1} \cdot \hat{\boldsymbol{\mu}}^a \\
\frac{\partial \mathbf{n}_{n+1}}{\partial \mathrm{p}_{n+1}} &= -\boldsymbol{\alpha}^a_n \\
\frac{\partial \mathbf{n}_{n+1}}{\partial \|\mathbf{Q}'_{n+1}\|} &= \mathbf{0}
\end{aligned}
$$

$$
\begin{aligned}
\hat{\mathbf{n}}_{n+1} &= \frac{\mathbf{n}_{n+1}}{\|\mathbf{n}_{n+1}\|} \\
\frac{\partial \hat{\mathbf{n}}_{n+1}}{\partial \xi} &= \frac{\frac{\partial \mathbf{n}_{n+1}}{\partial \xi} \cdot \|\mathbf{n}_{n+1}\| - \frac{\partial \|\mathbf{n}_{n+1}\|}{\partial \xi} \cdot \mathbf{n}_{n+1}}{\|\mathbf{n}_{n+1}\|^2} = \frac{\frac{\partial \mathbf{n}_{n+1}}{\partial \xi} - \frac{\partial \mathbf{n}_{n+1}}{\partial \xi} : \hat{\mathbf{n}}_{n+1} \cdot \hat{\mathbf{n}}_{n+1}}{\|\mathbf{n}_{n+1}\|} \\
\frac{\partial \hat{\mathbf{n}}_{n+1}}{\partial H^*_{a,n+1}} &= \frac{-\Delta\gamma^a_{n+1} \cdot \hat{\boldsymbol{\mu}}^a + \Delta\gamma^a_{n+1} \cdot \hat{\boldsymbol{\mu}}^a : \hat{\mathbf{n}}_{n+1} \cdot \hat{\mathbf{n}}_{n+1}}{\|\mathbf{n}_{n+1}\|} = \Delta\gamma^a_{n+1} \cdot \frac{-\hat{\boldsymbol{\mu}}^a + \hat{\boldsymbol{\mu}}^a : \hat{\mathbf{n}}_{n+1} \cdot \hat{\mathbf{n}}_{n+1}}{\|\mathbf{n}_{n+1}\|} \\
\frac{\partial \hat{\mathbf{n}}_{n+1}}{\partial \Delta\gamma^a_{n+1}} &= \frac{-H^*_{a,n+1} \cdot \hat{\boldsymbol{\mu}}^a + H^*_{a,n+1} \cdot \hat{\boldsymbol{\mu}}^a : \hat{\mathbf{n}}_{n+1} \cdot \hat{\mathbf{n}}_{n+1}}{\|\mathbf{n}_{n+1}\|} = H^*_{a,n+1} \cdot \frac{-\hat{\boldsymbol{\mu}}^a + \hat{\boldsymbol{\mu}}^a : \hat{\mathbf{n}}_{n+1} \cdot \hat{\mathbf{n}}_{n+1}}{\|\mathbf{n}_{n+1}\|} \\
\frac{\partial \hat{\mathbf{n}}_{n+1}}{\partial \mathrm{p}_{n+1}} &= \frac{-\boldsymbol{\alpha}^a_n + \boldsymbol{\alpha}^a_n : \hat{\mathbf{n}}_{n+1} \cdot \hat{\mathbf{n}}_{n+1}}{\|\mathbf{n}_{n+1}\|} \\
\frac{\partial \hat{\mathbf{n}}_{n+1}}{\partial \|\mathbf{Q}'_{n+1}\|} &= \mathbf{0}
\end{aligned}
$$

B.3 Derivative of $\|\mathbf{Q}'_{n+1}\|$

$$
\begin{aligned}
\|\mathbf{s}_{n+1} - \mathrm{p}_{n+1} \cdot \boldsymbol{\alpha}^a_{n+1}\| &= \sqrt{\left(\mathbf{s}_{n+1} - \mathrm{p}_{n+1} \cdot \boldsymbol{\alpha}^a_{n+1}\right) : \left(\mathbf{s}_{n+1} - \mathrm{p}_{n+1} \cdot \boldsymbol{\alpha}^a_{n+1}\right)} \\
\frac{\partial}{\partial \xi}\|\cdot\| &= \frac{\cancel{1}}{\cancel{2}} \cdot \frac{1}{\|\cdot\|} \cdot \cancel{2} \cdot \left[\frac{\partial}{\partial \xi} \cdot \left(\mathbf{s}_{n+1} - \mathrm{p}_{n+1} \cdot \boldsymbol{\alpha}^a_{n+1}\right)\right] : \left(\mathbf{s}_{n+1} - \mathrm{p}_{n+1} \cdot \boldsymbol{\alpha}^a_{n+1}\right) \\
&= \frac{1}{\|\cdot\|} \cdot \left[\frac{\partial}{\partial \xi} \cdot \underbrace{\left(\mathbf{s}_{tr} - 2 \cdot G \cdot \Delta\gamma_{n+1} \cdot \|\mathbf{Q}'_{n+1}\| \cdot \hat{\mathbf{n}}_{n+1} - \mathrm{p}_{n+1} \cdot \boldsymbol{\alpha}^a_n - \Delta\gamma^a_{n+1} \cdot H^*_{a,n+1} \cdot \hat{\boldsymbol{\mu}}^a\right)}_{\mathbf{A}}\right] : (\cdot) \\
\frac{\partial \mathbf{A}}{\partial H^*_{a,n+1}} &= -2 \cdot G \cdot \|\mathbf{Q}'_{n+1}\| \cdot \left(\frac{\partial \Delta\gamma_{n+1}}{\partial H^*_{a,n+1}} \cdot \hat{\mathbf{n}}_{n+1} + \Delta\gamma_{n+1} \cdot \frac{\partial \hat{\mathbf{n}}_{n+1}}{\partial H^*_{a,n+1}}\right) - \Delta\gamma^a_{n+1} \cdot \hat{\boldsymbol{\mu}}^a \\
\frac{\partial \mathbf{A}}{\partial \Delta\gamma^a_{n+1}} &= -2 \cdot G \cdot \|\mathbf{Q}'_{n+1}\| \cdot \left(\frac{\partial \Delta\gamma_{n+1}}{\partial \Delta\gamma^a_{n+1}} \cdot \hat{\mathbf{n}}_{n+1} + \Delta\gamma_{n+1} \cdot \frac{\partial \hat{\mathbf{n}}_{n+1}}{\partial \Delta\gamma^a_{n+1}}\right) - H^*_{a,n+1} \cdot \hat{\boldsymbol{\mu}}^a \\
\frac{\partial \mathbf{A}}{\partial \mathrm{p}_{n+1}} &= -2 \cdot G \cdot \|\mathbf{Q}'_{n+1}\| \cdot \left(\frac{\partial \Delta\gamma_{n+1}}{\partial \mathrm{p}_{n+1}} \cdot \hat{\mathbf{n}}_{n+1} + \Delta\gamma_{n+1} \cdot \frac{\partial \hat{\mathbf{n}}_{n+1}}{\partial \mathrm{p}_{n+1}}\right) - \boldsymbol{\alpha}^a_n \\
\frac{\partial \mathbf{A}}{\partial \|\mathbf{Q}'_{n+1}\|} &= -2 \cdot G \cdot \|\mathbf{Q}'_{n+1}\| \cdot \left(\frac{\partial \Delta\gamma_{n+1}}{\partial \|\mathbf{Q}'_{n+1}\|} \cdot \hat{\mathbf{n}}_{n+1} + \cancel{\Delta\gamma_{n+1} \cdot \frac{\partial \hat{\mathbf{n}}_{n+1}}{\partial \|\mathbf{Q}'_{n+1}\|}}\right) - 2 \cdot G \cdot \Delta\gamma_{n+1} \cdot \hat{\mathbf{n}}_{n+1}
\end{aligned}
$$

$$\frac{\partial f}{\partial \boldsymbol{\sigma}} = 2 \cdot \underbrace{\left(\mathbf{s}_{n+1} - \mathrm{p}_{n+1} \cdot \boldsymbol{\alpha}^a_{n+1}\right)}_{\mathbf{A}} + \frac{2}{3} \cdot \underbrace{\left[\mathrm{p}_{n+1} \cdot \boldsymbol{\alpha}^a_{n+1} : \boldsymbol{\alpha}^a_{n+1} - \mathrm{p}_{n+1} \cdot \left(M'^a\right)^2 - \mathbf{s}_{n+1} : \boldsymbol{\alpha}^a_{n+1}\right]}_{B} \cdot \boldsymbol{\delta}$$

$$\left\| \frac{\partial f}{\partial \boldsymbol{\sigma}} \right\| = \sqrt{4 \cdot \mathbf{A} : \mathbf{A} + \frac{4}{9} \cdot B^2 \cdot 3}$$

$$\frac{\partial}{\partial \xi} \cdot \left\| \frac{\partial f}{\partial \boldsymbol{\sigma}} \right\| = \frac{1}{\sqrt{4 \cdot \mathbf{A} : \mathbf{A} + 4/3 \cdot B^2}} \cdot \frac{1}{2} \left(4 \cdot \cancel{2} \cdot \frac{\partial \mathbf{A}}{\partial \xi} : \mathbf{A} + \frac{4}{3} \cdot \cancel{2} \cdot B \cdot \frac{\partial B}{\partial \xi} \right)$$

$$\frac{\partial B}{\partial \xi} = \frac{\partial}{\partial \xi} \cdot \left[\mathrm{p}_{n+1} \cdot \boldsymbol{\alpha}^a_{n+1} : \boldsymbol{\alpha}^a_{n+1} - \mathrm{p}_{n+1} \cdot (M'^a)^2 - \mathbf{s}_{n+1} : \boldsymbol{\alpha}^a_{n+1} \right]$$

$$\frac{\partial B}{\partial \xi} = \left[\frac{\partial \mathrm{p}_{n+1}}{\partial \xi} \cdot \boldsymbol{\alpha}^a_{n+1} : \boldsymbol{\alpha}^a_{n+1} + 2 \cdot \mathrm{p}_{n+1} \cdot \frac{\partial \boldsymbol{\alpha}^a_{n+1}}{\partial \xi} : \boldsymbol{\alpha}^a_{n+1} - (M'^a)^2 \cdot \frac{\partial \mathrm{p}_{n+1}}{\partial \xi} - \frac{\partial \mathbf{s}_{n+1}}{\partial \xi} : \boldsymbol{\alpha}^a_{n+1} - \mathbf{s}_{n+1} : \frac{\partial \boldsymbol{\alpha}^a_{n+1}}{\partial \xi} \right]$$

$$\mathbf{s}_{n+1} = \mathbf{s}_{tr} - 2 \cdot G \cdot \Delta\gamma_{n+1} \cdot \mathbf{Q}'_{n+1} = \mathbf{s}_{tr} - 2 \cdot G \cdot \Delta\gamma_{n+1} \cdot \|\mathbf{Q}'_{n+1}\| \cdot \hat{\mathbf{n}}_{n+1}$$

$$\frac{\partial \mathbf{s}_{n+1}}{\partial \xi} = -2 \cdot G \cdot \left(\frac{\partial \Delta\gamma_{n+1}}{\partial \xi} \cdot \|\mathbf{Q}'_{n+1}\| \cdot \hat{\mathbf{n}}_{n+1} + \Delta\gamma_{n+1} \cdot \frac{\partial \|\mathbf{Q}'_{n+1}\|}{\partial \xi} \cdot \hat{\mathbf{n}}_{n+1} + \Delta\gamma_{n+1} \cdot \|\mathbf{Q}'_{n+1}\| \cdot \frac{\partial \hat{\mathbf{n}}_{n+1}}{\partial \xi} \right)$$

$$\frac{\partial \boldsymbol{\alpha}^a_{n+1}}{\partial \xi} = \frac{\partial}{\partial \xi} \left(\boldsymbol{\alpha}^a_n + \frac{\Delta\gamma^a_{n+1} \cdot H^*_{a,n+1}}{\mathrm{p}_{n+1}} \cdot \hat{\boldsymbol{\mu}}^a \right)$$

$$= \frac{\left(\frac{\partial \Delta\gamma^a_{n+1}}{\partial \xi} \cdot H^*_{a,n+1} + \Delta\gamma^a_{n+1} \cdot \frac{\partial H^*_{a,n+1}}{\partial \xi} \right) \cdot \mathrm{p}_{n+1} - \frac{\partial \mathrm{p}_{n+1}}{\partial \xi} \cdot \Delta\gamma^a_{n+1} \cdot H^*_{a,n+1}}{(\mathrm{p}_{n+1})^2} \cdot \hat{\boldsymbol{\mu}}^a$$

B.4 Derivative of $\Delta\gamma_{n+1}$

$$
\begin{aligned}
\Delta\gamma_{n+1} &= \Delta\gamma^a_{n+1} + \sum_{i=1}^{a-1} \Delta\gamma^i_{n+1} \\
\Delta\gamma^i_{n+1} &= \frac{\mathbf{Q}'_{n+1} : \boldsymbol{\mu}^i_{n+1}}{\bar{H}^i} = \frac{\|\mathbf{Q}'_{n+1}\| \cdot \hat{\mathbf{n}}_{n+1} : \boldsymbol{\mu}^i_{n+1}}{\bar{H}^i} \\
\boldsymbol{\mu}^i_{n+1} &= \mathrm{p}_{n+1} \cdot \left[\boldsymbol{\alpha}^a_n - \boldsymbol{\alpha}^i_n + \left(M'^a - M'^i \right) \cdot \hat{\mathbf{n}}_{n+1} \right] + \Delta\gamma^a_{n+1} \cdot H^*_{a,n+1} \cdot \hat{\boldsymbol{\mu}}^a
\end{aligned}
$$

$$
\begin{aligned}
\frac{\partial \Delta\gamma_{n+1}}{\partial \xi} &= \frac{\partial \Delta\gamma^a_{n+1}}{\partial \xi} + \sum_{i=1}^{a-1} \frac{\partial \Delta\gamma^i_{n+1}}{\partial \xi} \\
&= \begin{cases} 1 + \displaystyle\sum_{i=1}^{a-1} \frac{\partial \Delta\gamma^i_{n+1}}{\partial \Delta\gamma^a_{n+1}} & \text{if} \quad \xi = \Delta\gamma^a_{n+1} \\ \displaystyle\sum_{i=1}^{a-1} \frac{\partial \Delta\gamma^i_{n+1}}{\partial \xi} & \text{otherwise} \end{cases} \\
\frac{\partial \Delta\gamma^i_{n+1}}{\partial \xi} &= \frac{\partial \|\mathbf{Q}'_{n+1}\|}{\partial \xi} \cdot \frac{\hat{\mathbf{n}}_{n+1} : \boldsymbol{\mu}^i_{n+1}}{\bar{H}^i} + \frac{\|\mathbf{Q}'_{n+1}\|}{\bar{H}^i} \cdot \left(\frac{\partial \hat{\mathbf{n}}_{n+1}}{\partial \xi} : \boldsymbol{\mu}^i_{n+1} + \hat{\mathbf{n}}_{n+1} : \frac{\partial \boldsymbol{\mu}^i_{n+1}}{\partial \xi} \right)
\end{aligned}
$$

$$
\begin{aligned}
\frac{\partial \boldsymbol{\mu}^i_{n+1}}{\partial H^*_{a,n+1}} &= \mathrm{p}_{n+1} \cdot \left(M'^a - M'^i \right) \cdot \frac{\partial \hat{\mathbf{n}}_{n+1}}{\partial H^*_{a,n+1}} + \Delta\gamma^a_{n+1} \cdot \hat{\boldsymbol{\mu}}^a \\
\frac{\partial \boldsymbol{\mu}^i_{n+1}}{\partial \Delta\gamma^a_{n+1}} &= \mathrm{p}_{n+1} \cdot \left(M'^a - M'^i \right) \cdot \frac{\partial \hat{\mathbf{n}}_{n+1}}{\partial \Delta\gamma^a_{n+1}} + H^*_{a,n+1} \cdot \hat{\boldsymbol{\mu}}^a \\
\frac{\partial \boldsymbol{\mu}^i_{n+1}}{\partial \mathrm{p}_{n+1}} &= \boldsymbol{\alpha}^a_n - \boldsymbol{\alpha}^i_n + \left(M'^a - M'^i \right) \cdot \hat{\mathbf{n}}_{n+1} + \mathrm{p}_{n+1} \cdot \left(M'^a - M'^i \right) \cdot \frac{\partial \hat{\mathbf{n}}_{n+1}}{\partial \mathrm{p}_{n+1}} \\
\frac{\partial \boldsymbol{\mu}^i_{n+1}}{\partial \|\mathbf{Q}'_{n+1}\|} &= \mathbf{0}
\end{aligned}
$$

B.5 Derivative of P"

$$
\begin{aligned}
P" &= \frac{1}{3}\cdot\frac{\eta^2-\bar{\eta}^2}{\eta^2+\bar{\eta}^2}\\
\frac{\partial P"}{\partial \xi} &= \frac{1}{3}\cdot\frac{2\cdot\eta\cdot\frac{\partial\eta}{\partial\xi}\cdot\left(\eta^2+\bar{\eta}^2\right)-2\cdot\eta\cdot\frac{\partial\eta}{\partial\xi}\cdot\left(\eta^2-\bar{\eta}^2\right)}{\left(\eta^2+\bar{\eta}^2\right)^2}\\
&= \frac{4}{3}\cdot\frac{\eta\cdot\bar{\eta}^2}{\left(\eta^2+\bar{\eta}^2\right)^2}\cdot\frac{\partial\eta}{\partial\xi}
\end{aligned}
$$

$$
\begin{aligned}
\eta &= \sqrt{\frac{3}{2}}\cdot\frac{\sqrt{\mathbf{s}_{n+1}:\mathbf{s}_{n+1}}}{\mathrm{p}_{n+1}}\\
\frac{\partial\eta}{\partial H^*_{a,n+1}} &= \sqrt{\frac{3}{2}}\cdot\frac{1}{2}\cdot\frac{1}{\sqrt{\mathbf{s}_{n+1}:\mathbf{s}_{n+1}}}\cdot\frac{1}{\mathrm{p}_{n+1}}\cdot\left(\frac{\partial\mathbf{s}_{n+1}}{\partial H^*_{a,n+1}}:\mathbf{s}_{n+1}+\mathbf{s}_{n+1}:\frac{\partial\mathbf{s}_{n+1}}{\partial H^*_{a,n+1}}\right)\\
&= \sqrt{\frac{3}{2}}\cdot\frac{1}{\sqrt{\mathbf{s}_{n+1}:\mathbf{s}_{n+1}}}\cdot\frac{1}{\mathrm{p}_{n+1}}\cdot\frac{\partial\mathbf{s}_{n+1}}{\partial H^*_{a,n+1}}:\mathbf{s}_{n+1}\\
\frac{\partial\eta}{\partial\Delta\gamma^a_{n+1}} &= \sqrt{\frac{3}{2}}\cdot\frac{1}{\sqrt{\mathbf{s}_{n+1}:\mathbf{s}_{n+1}}}\cdot\frac{1}{\mathrm{p}_{n+1}}\cdot\frac{\partial\mathbf{s}_{n+1}}{\partial\Delta\gamma^a_{n+1}}:\mathbf{s}_{n+1}\\
\frac{\partial\eta}{\partial\mathrm{p}_{n+1}} &= \sqrt{\frac{3}{2}}\cdot\frac{\frac{1}{2}\cdot\frac{1}{\sqrt{\mathbf{s}_{n+1}:\mathbf{s}_{n+1}}}\cdot\left(\frac{\partial\mathbf{s}_{n+1}}{\partial\mathrm{p}_{n+1}}:\mathbf{s}_{n+1}+\mathbf{s}_{n+1}:\frac{\partial\mathbf{s}_{n+1}}{\partial\mathrm{p}_{n+1}}\right)\cdot\mathrm{p}_{n+1}-\sqrt{\mathbf{s}_{n+1}:\mathbf{s}_{n+1}}}{(\mathrm{p}_{n+1})^2}\\
&= \sqrt{\frac{3}{2}}\cdot\frac{\frac{\mathrm{p}_{n+1}}{\sqrt{\mathbf{s}_{n+1}:\mathbf{s}_{n+1}}}\cdot\frac{\partial\mathbf{s}_{n+1}}{\partial\mathrm{p}_{n+1}}:\mathbf{s}_{n+1}-\sqrt{\mathbf{s}_{n+1}:\mathbf{s}_{n+1}}}{(\mathrm{p}_{n+1})^2}\\
\frac{\partial\eta}{\partial\|\mathbf{Q}'_{n+1}\|} &= \sqrt{\frac{3}{2}}\cdot\frac{1}{2}\cdot\frac{1}{\sqrt{\mathbf{s}_{n+1}:\mathbf{s}_{n+1}}}\cdot\frac{1}{\mathrm{p}_{n+1}}\cdot\left(\frac{\partial\mathbf{s}_{n+1}}{\partial\|\mathbf{Q}'_{n+1}\|}:\mathbf{s}_{n+1}+\mathbf{s}_{n+1}:\frac{\partial\mathbf{s}_{n+1}}{\partial\|\mathbf{Q}'_{n+1}\|}\right)\\
&= \sqrt{\frac{3}{2}}\cdot\frac{1}{\sqrt{\mathbf{s}_{n+1}:\mathbf{s}_{n+1}}}\cdot\frac{1}{\mathrm{p}_{n+1}}\cdot\frac{\partial\mathbf{s}_{n+1}}{\partial\|\mathbf{Q}'_{n+1}\|}:\mathbf{s}_{n+1}
\end{aligned}
$$

B.6 Derivative of $e\left(H^*_{a,n+1}, \Delta\gamma^a_{n+1}, \mathrm{p}_{n+1}, \|\mathbf{Q}'_{n+1}\|\right)$

$$
\begin{aligned}
e &= \frac{H^*_{a,n+1}}{\bar{H}_a} \cdot \|\mathbf{Q}'_{n+1}\| \cdot \hat{\mathbf{n}}_{n+1} : \hat{\boldsymbol{\mu}}^a - 1 \\
\frac{\partial e}{\partial H^*_{a,n+1}} &= \frac{1}{\bar{H}_a} \cdot \|\mathbf{Q}'_{n+1}\| \cdot \left(\hat{\mathbf{n}}_{n+1} : \hat{\boldsymbol{\mu}}^a + H^*_{a,n+1} \cdot \frac{\partial \hat{\mathbf{n}}_{n+1}}{\partial H^*_{a,n+1}} : \hat{\boldsymbol{\mu}}^a \right) \\
\frac{\partial e}{\partial \Delta\gamma^a_{n+1}} &= \frac{H^*_{a,n+1}}{\bar{H}_a} \cdot \|\mathbf{Q}'_{n+1}\| \cdot \frac{\partial \hat{\mathbf{n}}_{n+1}}{\partial \Delta\gamma^a_{n+1}} : \hat{\boldsymbol{\mu}}^a \\
\frac{\partial e}{\partial \mathrm{p}_{n+1}} &= \frac{H^*_{a,n+1}}{\bar{H}^a} \cdot \|\mathbf{Q}'_{n+1}\| \cdot \frac{\partial \hat{\mathbf{n}}_{n+1}}{\partial \mathrm{p}_{n+1}} : \hat{\boldsymbol{\mu}}^a \\
\frac{\partial e}{\partial \|\mathbf{Q}'_{n+1}\|} &= \frac{H^*_{a,n+1}}{\bar{H}^a} \cdot \hat{\mathbf{n}}_{n+1} : \hat{\boldsymbol{\mu}}^a
\end{aligned}
$$

B.7 Derivative of $g\left(H^*_{a,n+1}, \Delta\gamma^a_{n+1}, \mathrm{p}_{n+1}, \|\mathbf{Q}'_{n+1}\|\right)$

$$
\begin{aligned}
g &= \mathbf{s}_{tr} : \hat{\mathbf{n}}_{n+1} - 2 \cdot G \cdot \Delta\gamma_{n+1} \cdot \|\mathbf{Q}'_{n+1}\| \cdot \overbrace{\hat{\mathbf{n}}_{n+1} : \hat{\mathbf{n}}_{n+1}}^{1} - \mathrm{p}_{n+1} \cdot \boldsymbol{\alpha}^a_n : \hat{\mathbf{n}}_{n+1} \\
&\quad - H^*_{a,n+1} \cdot \Delta\gamma^a_{n+1} \cdot \hat{\boldsymbol{\mu}}^a : \hat{\mathbf{n}}_{n+1} - \mathrm{p}_{n+1} \cdot M'^a \\
\frac{\partial g}{\partial H^*_{a,n+1}} &= \mathbf{s}_{tr} : \frac{\partial \hat{\mathbf{n}}_{n+1}}{\partial H^*_{a,n+1}} - 2 \cdot G \cdot \frac{\partial \Delta\gamma_{n+1}}{\partial H^*_{a,n+1}} \cdot \|\mathbf{Q}'_{n+1}\| - \mathrm{p}_{n+1} \cdot \boldsymbol{\alpha}^a_n : \frac{\partial \hat{\mathbf{n}}_{n+1}}{\partial H^*_{a,n+1}} - \Delta\gamma^a_{n+1} \cdot \hat{\boldsymbol{\mu}}^a : \hat{\mathbf{n}}_{n+1} \\
&\quad - H^*_{a,n+1} \cdot \Delta\gamma^a_{n+1} \cdot \hat{\boldsymbol{\mu}}^a : \frac{\partial \hat{\mathbf{n}}_{n+1}}{\partial H^*_{a,n+1}} \\
&= \overbrace{\frac{\partial \hat{\mathbf{n}}_{n+1}}{\partial H^*_{a,n+1}} : \underbrace{\left(\mathbf{s}_{tr} - \mathrm{p}_{n+1} \cdot \boldsymbol{\alpha}^a_n - H^*_{a,n+1} \cdot \Delta\gamma^a_{n+1} \cdot \hat{\boldsymbol{\mu}}^a\right)}_{\mathbf{n}_{n+1}}}^{=0} - 2 \cdot G \cdot \frac{\partial \Delta\gamma_{n+1}}{\partial H^*_{a,n+1}} \cdot \|\mathbf{Q}'_{n+1}\| - \Delta\gamma^a_{n+1} \cdot \hat{\boldsymbol{\mu}}^a : \hat{\mathbf{n}}_{n+1} \\
&= -2 \cdot G \cdot \frac{\partial \Delta\gamma_{n+1}}{\partial H^*_{a,n+1}} \cdot \|\mathbf{Q}'_{n+1}\| - \Delta\gamma^a_{n+1} \cdot \hat{\boldsymbol{\mu}}^a : \hat{\mathbf{n}}_{n+1} \\
\frac{\partial g}{\partial \Delta\gamma^a_{n+1}} &= -2 \cdot G \cdot \frac{\partial \Delta\gamma_{n+1}}{\partial \Delta\gamma^a_{n+1}} \cdot \|\mathbf{Q}'_{n+1}\| - H^*_{a,n+1} \cdot \hat{\boldsymbol{\mu}}^a : \hat{\mathbf{n}}_{n+1} \\
\frac{\partial g}{\partial \mathrm{p}_{n+1}} &= -2 \cdot G \cdot \frac{\partial \Delta\gamma_{n+1}}{\partial \mathrm{p}_{n+1}} \cdot \|\mathbf{Q}'_{n+1}\| - \boldsymbol{\alpha}^a_n : \hat{\mathbf{n}}_{n+1} - M'^a \\
\frac{\partial g}{\partial \|\mathbf{Q}'_{n+1}\|} &= -2 \cdot G \cdot \left(\frac{\partial \Delta\gamma_{n+1}}{\partial \|\mathbf{Q}'_{n+1}\|} \cdot \|\mathbf{Q}'_{n+1}\| + \Delta\gamma_{n+1}\right)
\end{aligned}
$$

B.8 Derivative of $h\left(H^*_{a,n+1}, \Delta\gamma^a_{n+1}, \mathrm{p}_{n+1}, \|\mathbf{Q}'_{n+1}\|\right)$

$$
\begin{aligned}
h &= \mathrm{p}_{n+1} - p'^{tr} - 3 \cdot B \cdot P\text{”} \cdot \Delta\gamma_{n+1} \\
\frac{\partial h}{\partial H^*_{a,n+1}} &= -3 \cdot B \cdot \left(\frac{\partial P\text{”}}{\partial H^*_{a,n+1}} \cdot \Delta\gamma_{n+1} + P\text{”} \cdot \frac{\partial \Delta\gamma_{n+1}}{\partial H^*_{a,n+1}}\right) \\
\frac{\partial h}{\partial \Delta\gamma^a_{n+1}} &= -3 \cdot B \cdot \left(\frac{\partial P\text{”}}{\partial \Delta\gamma^a_{n+1}} \cdot \Delta\gamma_{n+1} + P\text{”} \cdot \frac{\partial \Delta\gamma_{n+1}}{\partial \Delta\gamma^a_{n+1}}\right) \\
\frac{\partial h}{\partial \mathrm{p}_{n+1}} &= 1 - 3 \cdot B \cdot \left(\frac{\partial P\text{”}}{\partial \mathrm{p}_{n+1}} \cdot \Delta\gamma_{n+1} + P\text{”} \cdot \frac{\partial \Delta\gamma_{n+1}}{\partial \mathrm{p}_{n+1}}\right) \\
\frac{\partial h}{\partial \|\mathbf{Q}'_{n+1}\|} &= -3 \cdot B \cdot \left(\frac{\partial P\text{”}}{\partial \|\mathbf{Q}'_{n+1}\|} \cdot \Delta\gamma_{n+1} + P\text{”} \cdot \frac{\partial \Delta\gamma_{n+1}}{\partial \|\mathbf{Q}'_{n+1}\|}\right)
\end{aligned}
$$

B.9 Derivative of $i\left(H^*_{a,n+1}, \Delta\gamma^a_{n+1}, \mathrm{p}_{n+1}, \|\mathbf{Q}'_{n+1}\|\right)$

$$
\begin{aligned}
i &= \|\mathbf{Q}'_{n+1}\| - 2 \cdot \frac{\|\mathbf{s}_{n+1} - \mathrm{p}_{n+1} \cdot \boldsymbol{\alpha}^a_{n+1}\|}{\left\|\dfrac{\partial f}{\partial \boldsymbol{\sigma}}\right\|} \\
\frac{\partial i}{\partial \xi} &= \frac{\partial \|\mathbf{Q}'_{n+1}\|}{\partial \xi} - 2 \cdot \frac{\dfrac{\partial}{\partial \xi}\|\mathbf{s}_{n+1} - \mathrm{p}_{n+1} \cdot \boldsymbol{\alpha}^a_{n+1}\| \cdot \left\|\dfrac{\partial f}{\partial \sigma}\right\| - \|\mathbf{s}_{n+1} - \mathrm{p}_{n+1} \cdot \boldsymbol{\alpha}^a_{n+1}\| \cdot \dfrac{\partial}{\partial \xi}\left\|\dfrac{\partial f}{\partial \sigma}\right\|}{\left\|\dfrac{\partial f}{\partial \sigma}\right\|^2}
\end{aligned}
$$

Appendix C

2D Hydro-mechanical interface element in the finite element code LAGAMINE

Le désert est la seule chose qui ne puisse être détruite que par construction.
(Desert is the only thing which can only be destroyed by building.)

Boris Vian

Contents

C.1 Constitutive laws

The gradients of u_w in the direction $\mathbf{n}_\xi$ is obtained from

$$\begin{aligned}
\boldsymbol{\nabla}_{\mathbf{n}_\xi} u_w &= \boldsymbol{\nabla}^T u_w \cdot \mathbf{n}_\xi \\
&= \left[\frac{\partial u_w}{\partial x_1} \quad \frac{\partial u_w}{\partial x_2}\cdot\right] \cdot \frac{1}{|\mathbf{J}^S|} \begin{bmatrix} \dfrac{\partial x_1}{\partial \xi} \\ \dfrac{\partial x_2}{\partial \xi} \end{bmatrix} \\
&= \frac{1}{|\mathbf{J}^S|} \cdot \left[\frac{\partial u_w}{\partial x_1}\frac{\partial x_1}{\partial \xi} + \frac{\partial u_w}{\partial x_2}\frac{\partial x_2}{\partial \xi}\right] \\
&= \frac{1}{|\mathbf{J}^S|} \cdot \frac{\partial u_w}{\partial \xi} \cdot \left[\frac{\partial \xi}{\partial x_1}\frac{\partial x_1}{\partial \xi} + \frac{\partial \xi}{\partial x_2}\frac{\partial x_2}{\partial \xi}\right] \\
&= \frac{1}{|\mathbf{J}^S|} \cdot \frac{\partial u_w}{\partial \xi} \cdot \mathbf{J}^{-1} \cdot \mathbf{J} \\
&= \frac{1}{|\mathbf{J}^S|} \cdot \frac{\partial \phi_i}{\partial \xi} \cdot u_{w,i} \qquad \text{(C.1)}
\end{aligned}$$

where $\mathbf{J}$ and $\mathbf{J}^{-1}$ and the Jacobian and inverse Jacobian respectively ; $u_{w,i}$ is the nodal pore water pressure. The directional gradient of x_2 can be derived accordingly

$$\begin{aligned}
\boldsymbol{\nabla}_{\mathbf{n}_\xi} x_2 &= \boldsymbol{\nabla}^T x_2 \cdot \mathbf{n}_\xi \\
&= \frac{1}{|\mathbf{J}^S|} \cdot \frac{\partial \phi_i}{\partial \xi} \cdot x_{2,i} \qquad \text{(C.2)}
\end{aligned}$$

C.2 Derivation of the principle of virtual powers

For any porous medium, equilibrium of internal and external powers can be derived from

$$\begin{aligned}
\delta \dot{W}_E &= \int_{\varphi(\mathcal{B})} \bar{Q} \cdot \delta u_w \,\mathrm{d}V + \int_{\varphi(\partial\mathcal{B})} \bar{q} \cdot \delta u_w \,\mathrm{d}A \qquad \text{(C.3)} \\
&\quad \bar{Q} = \dot{S} + \operatorname{div} \mathbf{f}_w \qquad \text{strong equilibrium equation} \qquad \text{(C.4)} \\
&= \int_{\varphi(\mathcal{B})} \left(\dot{S} + \operatorname{div} \mathbf{f}_w\right) \cdot \delta u_w \,\mathrm{d}V + \int_{\varphi(\partial\mathcal{B})} (-\mathbf{n} \cdot \mathbf{f}_w) \cdot \delta u_w \,\mathrm{d}A \qquad \text{(C.5)} \\
&\quad \iiint_V \operatorname{div} \mathbf{F} \,\mathrm{d}V = \oiint_{\partial V} \mathbf{F} \,\mathrm{d}\mathbf{S} \qquad \text{(C.6)} \\
&= \int_{\varphi(\mathcal{B})} \dot{S} \cdot \delta u_w + \operatorname{div} \mathbf{f}_w \cdot \delta u_w - \operatorname{div}\left(\mathbf{f}_w \cdot \delta u_w\right) \mathrm{d}V \qquad \text{(C.7)} \\
&\quad \operatorname{div}\left(\mathbf{f} \cdot \mathbf{A}\right) = \mathbf{f} \cdot \operatorname{div}\mathbf{A} + \boldsymbol{\nabla}\mathbf{f} \cdot \mathbf{A} \qquad \text{(C.8)} \\
&= \int_{\varphi(\mathcal{B})} \dot{S} \cdot \delta u_w - \mathbf{f}_w^T \cdot \boldsymbol{\nabla}(\delta u_w) \,\mathrm{d}V \qquad \text{(C.9)} \\
&= \int_V \dot{S} \cdot \delta u_w - \frac{f_w^l}{|\mathbf{J}^S|} \cdot \frac{\partial \delta u_w}{\partial \xi} \,\mathrm{d}V = \delta \dot{W}_I \qquad \text{(C.10)}
\end{aligned}$$

C.3 Equivalent nodal forces

The continuum formulation of the equivalent nodal forces was given in section 6.3.4. The numerical expressions for each component are derived hereafter. It is reminded to the reader

that

- t is the thickness of the element ;
- $\mathbf{R}$ is the rotation matrix ;
- $|\mathbf{J}^S|$ the the determinant of the Jacobian matrix ;
- W_G are the Gauss weights associated to the integration points.

C.3.1 Structure side

The mechanical part of the equivalent nodal forces is derived from

$$\mathbf{F}^S_{i,m} = \sum_{IP} \begin{bmatrix} t_T & \mathrm{p}_N \end{bmatrix} \cdot \mathbf{R} \cdot \phi^S_i \cdot |\mathbf{J}^S| \cdot t \cdot W_G \qquad i \in [1,3]. \tag{C.11}$$

The hydraulic part of the equivalent nodal forces is derived from

$$F_{i,f} = \sum_{IP} f^{t,2}_w \cdot \phi^S_i \cdot |\mathbf{J}^S| \cdot t \cdot W_G \qquad i \in [1,3]. \tag{C.12}$$

C.3.2 Interior of the interface

Inside the foundation, only hydraulic equivalent nodal forces are taken into account

$$F_{i,f} = \sum_{IP} \left(f^{t,1}_w - f^{t,2}_w + f^l_w \cdot g_N - f^s_w \right) \cdot \phi^I_i \cdot |\mathbf{J}^S| \cdot t \cdot W_G \qquad i \in [1,3]. \tag{C.13}$$

C.3.3 Foundation side

The mechanical part of the equivalent nodal forces is derived from

$$\mathbf{F}^F_{i,m} = -\sum_{IP} \begin{bmatrix} t_T & \mathrm{p}_N \end{bmatrix} \cdot \mathbf{R} \cdot \phi^F_i \cdot |\mathbf{J}^S| \cdot t \cdot W_G \qquad i \in [7,9]. \tag{C.14}$$

The hydraulic part of the equivalent nodal forces is derived from

$$F_{i,f} = -\sum_{IP} f^{t,1}_w \cdot \phi^F_i \cdot |\mathbf{J}^S| \cdot t \cdot W_G \qquad i \in [7,9]. \tag{C.15}$$

It must be pointed out that although the shape function of the structure is considered, the integration is carried out over the surface of the structure side, *i.e.* the determinant of the Jacobian used is $|\mathbf{J}^S|$.

C.4 Tangent matrix

In the general case where two sides of an interface are perfectly in front of each other, 9 nodes and 21 degrees of freedom are involved in the stiffness matrix :

- 3 nodes for the structure, associated to 3 degrees of freedom : x^S_1, x^S_2, u^S_w ;

- 3 nodes for the interior, associated to 1 degree of freedom : u_w^I ;
- 3 nodes for the foundation, associated to 3 degrees of freedom : x_1^F, x_2^F, u_w^F.

The vector of generalised displacements associated to that matrix is

$$\begin{aligned}\mathbf{u}^T &= \Big[x_1^{S,1}\, x_2^{S,1}\, u_w^{S,1}\, x_1^{S,2} x_2^{S,2} u_w^{S,2} x_1^{S,3} x_2^{S,3} u_w^{S,3} \\ &\qquad u_w^{I,1}\, u_w^{I,2}\, u_w^{I,3} \\ &\qquad\quad x_1^{F,1}\, x_2^{F,1}\, u_w^{F,1}\, x_1^{F,2}\, x_2^{F,2}\, u_w^{F,2}\, x_1^{F,3}\, x_2^{F,3}\, u_w^{F,3}\Big], \end{aligned} \tag{C.16}$$

where x_1 and x_2 are the geometrical coordinates; u_w the pore water pressure; the superscripts ^{S}, ^{I} and ^{F} stand for structure, interior and foundation respectively; the subscripts $_1$, $_2$, $_3$ hold for the first, second and third node of the side considered.

Each component of the matrix is computed through

$$[\mathbf{K}]_{ij} = \frac{\partial \mathbf{F}_{OB,i}}{\partial \mathbf{u}_j}, \tag{C.17}$$

i.e. the variation of the nodal out of balance forces at node i $\mathbf{F}_{OB,i}$ due to the variation of generalised coordinates at node j, $\mathbf{u}_j$, with $i, j \in [1, 9]$. All the components can be summarised in

$$\mathbf{K} = \begin{bmatrix} [\mathbf{K}]_{9\times9}^{SS} & [\mathbf{K}]_{9\times3}^{SI} & [\mathbf{K}]_{9\times9}^{SF} \\ [\mathbf{K}]_{3\times9}^{IS} & [\mathbf{K}]_{3\times3}^{II} & [\mathbf{K}]_{3\times9}^{IF} \\ [\mathbf{K}]_{9\times9}^{FS} & [\mathbf{K}]_{9\times3}^{FI} & [\mathbf{K}]_{9\times9}^{FF} \end{bmatrix}_{21\times21} \tag{C.18}$$

and the general topology of the matrix is given in Figure C.1.

C.4.1 $\mathbf{K}^{SS}$

The stiffness component $[\mathbf{K}]_{9\times9}^{SS}$ of the local matrix is defined for $i \in [1, 3]$ and $j \in [1, 3]$,

$$[\mathbf{K}]_{9\times9}^{SS} = \begin{bmatrix} \mathbf{K}_{i=1,j=1}^{SS} = \begin{bmatrix} K_{1,1} & K_{1,2} & 0 \\ K_{2,1} & K_{2,2} & 0 \\ & & K_{3,3} \end{bmatrix} & \mathbf{K}_{i=1,j=2}^{SS} & \mathbf{K}_{i=1,j=3}^{SS} \\ \mathbf{K}_{i=2,j=1}^{SS} & \mathbf{K}_{i=2,j=2}^{SS} & \mathbf{K}_{i=2,j=3}^{SS} \\ \mathbf{K}_{i=3,j=1}^{SS} & \mathbf{K}_{i=3,j=2}^{SS} & \mathbf{K}_{i=3,j=3}^{SS} \end{bmatrix} \tag{C.19}$$

1. The **mechanical part** of $\mathbf{K}_{ij}^{SS}$, corresponds to the terms : $K_{1,1}, K_{1,2}, K_{2,1}, K_{2,2}$.

$$\begin{aligned}[\mathbf{K}_{1:2,1:2}]_{ij}^{SS} &= -\frac{\partial \mathbf{F}_i^S}{\partial \mathbf{x}_j^S} \\ &= -\sum_{IP}\left[\mathbf{R}\cdot\frac{\partial \mathbf{t}}{\partial \mathbf{x}_j^S}\cdot|\mathbf{J}^S|\cdot\phi_i^S + \frac{\partial}{\partial \mathbf{x}_j^S}\left(\mathbf{R}\cdot|\mathbf{J}^S|\right)\cdot\mathbf{t}\cdot\phi_i^S\right]\cdot t\cdot W_G \\ &= -\sum_{IP}\left[-\mathbf{R}\cdot\mathbf{C}_{loc}\cdot\mathbf{R}^T\cdot|\mathbf{J}^S|\cdot\phi_j^S + \mathbf{R}'\cdot\begin{bmatrix} t_T \\ \mathrm{p}_N\end{bmatrix}\right]\cdot\phi_i^S\cdot t\cdot W_G \\ &= \sum_{IP}\left[\mathbf{C}_{glob}\cdot|\mathbf{J}^S|\cdot\phi_j^S - \begin{bmatrix} t_T & -\mathrm{p}_N \\ \mathrm{p}_N & t_T\end{bmatrix}\cdot\frac{\partial\phi_j^S}{\partial\xi}\right]\cdot\phi_i^S\cdot t\cdot W_G \end{aligned} \tag{C.20}$$

	x	y	uw	x	y	uw	x	y	uw	uw	uw	uw	x	y	uw	x	y	uw	x	y	uw
Fx	M	M		M	M		M	M		HM	HM	HM	M	M		M	M		M	M	
Fy	M	M		M	M		M	M		HM	HM	HM	M	M		M	M		M	M	
fw			H			H			H	H	H	H									
Fx	M	M		M	M		M	M		HM	HM	HM	M	M		M	M		M	M	
Fy	M	M		M	M		M	M		HM	HM	HM	M	M		M	M		M	M	
fw			H			H			H	H	H	H									
Fx	M	M		M	M		M	M		HM	HM	HM	M	M		M	M		M	M	
Fy	M	M		M	M		M	M		HM	HM	HM	M	M		M	M		M	M	
fw			H			H			H	H	H	H									
fw	HM	HM	H	HM	HM	H	HM	HM	H	H	H	H	HM	HM	H	HM	HM	H	HM	HM	H
fw	HM	HM	H	HM	HM	H	HM	HM	H	H	H	H	HM	HM	H	HM	HM	H	HM	HM	H
fw	HM	HM	H	HM	HM	H	HM	HM	H	H	H	H	HM	HM	H	HM	HM	H	HM	HM	H
Fx	M	M		M	M		M	M		HM	HM	HM	M	M		M	M		M	M	
Fy	M	M		M	M		M	M		HM	HM	HM	M	M		M	M		M	M	
fw										H	H	H			H			H			H
Fx	M	M		M	M		M	M		HM	HM	HM	M	M		M	M		M	M	
Fy	M	M		M	M		M	M		HM	HM	HM	M	M		M	M		M	M	
fw										H	H	H			H			H			H
Fx	M	M		M	M		M	M		HM	HM	HM	M	M		M	M		M	M	
Fy	M	M		M	M		M	M		HM	HM	HM	M	M		M	M		M	M	
fw										H	H	H			H			H			H

FIGURE C.1: Topology of the stiffness matrix. M stands for mechanical term, H for hydraulical and HM hydro-mechanical couplings. Fx, Fy and fw are equivalent nodal forces in x and y direction and the flux, respectively. x, y and pw are the dof associated to each node.

where

$$\dot{\mathbf{t}}' = -\mathbf{C}_{loc}\cdot\begin{bmatrix}\dot{g}_N\\ \dot{g}_T\end{bmatrix} = -\mathbf{C}_{loc}\cdot\mathbf{R}^T\cdot\begin{bmatrix}\dot{x_1}^S - \dot{x_1}^F\\ \dot{x_2}^S - \dot{x_2}^F\end{bmatrix} = -\mathbf{C}_{loc}\cdot\mathbf{R}^T\cdot\begin{bmatrix}\phi_j^S\cdot\dot{x}_{1,j}^S - \phi_j^F\cdot\dot{x}_{1,j}^F\\ \phi_j^S\cdot\dot{x}_{2,j}^S - \phi_j^F\cdot\dot{x}_{2,j}^F\end{bmatrix} \quad \text{(C.21)}$$

and

$$\frac{\partial\mathbf{t}}{\partial\mathbf{x}_j^S} = \frac{\partial\dot{\mathbf{t}}}{\partial\mathbf{x}_j^S} = \frac{\partial\dot{\mathbf{t}}'}{\partial\mathbf{x}_j^S} + \cancel{\frac{\partial u_w^I}{\partial\mathbf{x}_j^S}\cdot\begin{bmatrix}0\\1\end{bmatrix}} = \frac{\partial}{\partial\mathbf{x}_j^S}\left\{-\mathbf{C}_{loc}\cdot\mathbf{R}^T\cdot\begin{bmatrix}\phi_j^S\cdot\dot{x}_{1,j}^S - \phi_j^F\cdot\dot{x}_{1,j}^F\\ \phi_j^S\cdot\dot{x}_{2,j}^S - \phi_j^F\cdot\dot{x}_{2,j}^F\end{bmatrix}\right\} = -\mathbf{C}_{loc}\cdot\mathbf{R}^T\cdot\phi_j^S \quad \text{(C.22)}$$

The derivative of $\mathbf{R}\cdot|\mathbf{J}^S|$ yields to the order 3 tensor (C.23)

$$\mathbf{R}'\big|_{[2\times2\times2]} = \frac{\partial}{\partial\mathbf{x}_j^S}\cdot\begin{bmatrix}\frac{\partial\phi_i^S}{\partial\xi}\cdot x_{1,i}^S & -\frac{\partial\phi_i^S}{\partial\xi}\cdot x_{2,i}^S\\ \frac{\partial\phi_i^S}{\partial\xi}\cdot x_{2,i}^S & \frac{\partial\phi_i^S}{\partial\xi}\cdot x_{1,i}^S\end{bmatrix} = \frac{\partial\phi_j}{\partial\xi}\cdot\begin{bmatrix}\delta_{1,k} & -\delta_{2,k}\\ \delta_{2,k} & \delta_{1,k}\end{bmatrix} \qquad \text{k=1,2} \quad \text{(C.23)}$$

The local compliance tensor is rotated to global coordinates through the relation (C.24)

$$\begin{aligned}\mathbf{C}_{glob} &= \mathbf{R}\cdot\mathbf{C}_{loc}\cdot\mathbf{R}^T \qquad \text{(C.24)}\\ &= \begin{bmatrix}D_X & -D_Y\\ D_Y & D_X\end{bmatrix}\cdot\begin{bmatrix}C_{UU} & C_{UV}=0\\ C_{VU} & C_{VV}\end{bmatrix}\cdot\begin{bmatrix}D_X & D_Y\\ -D_Y & D_X\end{bmatrix}\\ &= \ldots\\ &= \begin{bmatrix}C_{UU}D_{XX} - C_{UV}D_{XY} + C_{VV}D_{YY} & C_{UU}D_{XY} + C_{UV}D_{XX} - C_{VV}D_{XY}\\ C_{UU}D_{XY} - C_{VV}D_{XY} - C_{UV}D_{YY} & C_{UU}D_{YY} + C_{VV}D_{XX} + C_{UV}D_{XY}\end{bmatrix}\end{aligned}$$

In the `LAGAMINE` code, due to other sign convention and order of unknowns, the local compliance tensor is written

$$\begin{aligned} C_{UU} &\Rightarrow C_{VV} \\ C_{VV} &\Rightarrow C_{UU} \\ C_{UV} &\Rightarrow C_{VU} \end{aligned}$$

which leads to another final rotated global compliance tensor

$$\mathbf{C}_{glob} = \begin{bmatrix} C_{VV}D_{XX} - C_{VU}D_{XY} + C_{UU}D_{YY} & C_{VV}D_{XY} + C_{VU}D_{XX} - C_{UU}D_{XY} \\ C_{VV}D_{XY} - C_{UU}D_{XY} - C_{VU}D_{YY} & C_{VV}D_{YY} + C_{UU}D_{XX} + C_{VU}D_{XY} \end{bmatrix} \tag{C.25}$$

2. The hydraulic part of of $\mathbf{K}_{ij}^{SS}$, corresponds to the term : $K_{3,3}$.

$$\begin{aligned} [K_{3,3}]_{ij}^{SS} &= -\frac{\partial F_i^S}{\partial u_{w,j,(t+\Delta t)}^S} \\ &= -\sum_{IP} \frac{\partial f_{w,2,(t+\theta\Delta t)}^t}{\partial u_{w,j,(t+\Delta t)}^S} \cdot \phi_i^S \cdot |\mathbf{J}^S| \cdot t \cdot W_G \\ &= \sum_{IP} \theta \cdot T_w^t \cdot \phi_j^S \cdot \rho_w \cdot \phi_i^S \cdot |\mathbf{J}^S| \cdot t \cdot W_G \end{aligned} \tag{C.26}$$

where

$$\begin{aligned} \frac{\partial f_{w,2,(t+\theta\Delta t)}^t}{\partial u_{w,j,(t+\Delta t)}^S} &= \frac{\partial}{\partial u_{w,j,(t+\Delta t)}^S} \left(\theta \cdot f_{w,1/2}\big|_{t+\Delta t} + (1-\theta) \cdot f_{w,2}|_t \right) \\ &= \theta \cdot \frac{\partial f_{w,2}^t}{\partial u_{w,j,(t+\Delta t)}^S} \\ &= \theta \cdot \frac{\partial}{\partial u_{w,j,(t+\Delta t)}^S} \left[T_w^t \cdot \left(\phi_j^I \cdot u_{w,j}^I - \phi_j^S \cdot u_{w,j,(t+\Delta t)}^S \right) \cdot \rho_w \right] \\ &= -\theta \cdot T_w^t \cdot \phi_j^S \cdot \rho_w \end{aligned} \tag{C.27}$$

C.4.2 $\mathbf{K}^{FF}$

The $\mathbf{K}^{FF}$ matrix is calculated the same way as $\mathbf{K}^{SS}$ and has the same topology as Eq. (C.19) for $i \in [7,9]$ and $j \in [7,9]$. However, the rotation matrix is a function of structure coordinates only, i.e. a function of $\mathbf{x}^S$. In this case, Eq. (C.23) yields to

$$\mathbf{R}'\big|_{[2\times 2\times 2]} = \frac{\partial}{\partial \mathbf{x}_j^F} \cdot \begin{bmatrix} \frac{\partial \phi_i^S}{\partial \xi} \cdot x_{1,i}^S & -\frac{\partial \phi_i^S}{\partial \xi} \cdot x_{2,i}^S \\ \frac{\partial \phi_i^S}{\partial \xi} \cdot x_{2,i}^S & \frac{\partial \phi_i^S}{\partial \xi} \cdot x_{1,i}^S \end{bmatrix} = \begin{bmatrix} 0 & 0 \\ 0 & 0 \end{bmatrix} \qquad \text{k=1,2} \tag{C.28}$$

The mechanical components of the matrix change accordingly

$$[\mathbf{K}_{1:2,1:2}]_{ij}^{FF} = \sum_{IP} \mathbf{C}_{glob} \cdot |\mathbf{J}^S| \cdot \phi_j^F \cdot \phi_i^F \cdot t \cdot W_G \tag{C.29}$$

since

$$\frac{\partial \mathbf{t}}{\partial \mathbf{x}_j^F} = \mathbf{C}_{loc} \cdot \mathbf{R}^T \cdot \phi_j^F \tag{C.30}$$

The hydraulic term is computed easily from

$$[K_{3,3}]_{ij}^{FF} = \sum_{IP} \theta \cdot T_w^t \cdot \phi_j^F \cdot \rho_w \cdot \phi_i^F \cdot |\mathbf{J}^S| \cdot t \cdot W_G \tag{C.31}$$

C.4.3 $\mathbf{K}^{II}$

The stiffness component $[\mathbf{K}]_{3\times3}^{II}$ of the local matrix is defined for $i \in [4,6]$ and $j \in [4,6]$, where each nodes has only a hydraulical dof $(u_{w,j}^I)$

$$[\mathbf{K}]_{3\times3}^{II} = \begin{bmatrix} \mathbf{K}_{i=4,j=4}^{II} = \begin{bmatrix} K_{1,1} \end{bmatrix} & \mathbf{K}_{i=4,j=5}^{II} & \mathbf{K}_{i=4,j=6}^{II} \\ \mathbf{K}_{i=5,j=4}^{II} & \mathbf{K}_{i=5,j=5}^{II} & \mathbf{K}_{i=5,j=6}^{II} \\ \mathbf{K}_{i=4,j=6}^{II} & \mathbf{K}_{i=6,j=5}^{II} & \mathbf{K}_{i=6,j=6}^{II} \end{bmatrix} \tag{C.32}$$

Each flow type contributes to the stiffness matrix of interior nodes. Therefore, each $[\mathbf{K}]_{ij}^{II}$ term is the assembling of : transversal flows $\mathbf{K}_{ij}^{II}\Big|_t$, longitudinal flow $\mathbf{K}_{ij}^{II}\Big|_l$ and storage flow $\mathbf{K}_{ij}^{II}\Big|_s$. The first transversal flow component is computed the same way as Eq.(C.26), but two transversal flows have to be taken into account

$$[\mathbf{K}]_{ij}^{II}\Big|_t = -\sum_{IP} \theta \cdot \left(T_w^{t,1} + T_w^{t,2}\right) \cdot \phi_j^I \cdot \rho_w \cdot \phi_i^I \cdot |\mathbf{J}^S| \cdot t \cdot W_G \tag{C.33}$$

The longitudinal flow component is obtained from

$$[\mathbf{K}]_{ij}^{II}\Big|_l = -\frac{\partial}{\partial u_{w,j,(t+\delta t)}^I} \sum_{IP} \left[\frac{f_w^l}{|\mathbf{J}^S|}\Big|_{t+\theta\cdot\Delta t} \cdot \frac{\partial \phi_i^I}{\partial \xi} \right] \cdot g_N \cdot |\mathbf{J}^S| \cdot t \cdot W_G \tag{C.34}$$

$$= -\theta \sum_{IP} \left[\frac{\partial f_w^l}{\partial u_{w,j}^I} \cdot \frac{1}{|\mathbf{J}^S|} \cdot \frac{\partial \phi_i^I}{\partial \xi} \right] \cdot g_N \cdot |\mathbf{J}^S| \cdot t \cdot W_G \tag{C.35}$$

$$= -\theta \sum_{IP} \left[\frac{-k_w}{\mu_w} \cdot \rho_w \cdot \frac{\partial \boldsymbol{\nabla} u_w^I}{\partial u_{w,j}^I} \cdot \frac{1}{|\mathbf{J}^S|} \cdot \frac{\partial \phi_i^I}{\partial \xi} \right] \cdot g_N \cdot |\mathbf{J}^S| \cdot t \cdot W_G \tag{C.36}$$

$$= \theta \sum_{IP} \left[\frac{k_w}{\mu_w} \cdot \rho_w \cdot \frac{1}{|\mathbf{J}^S|} \cdot \frac{\partial \phi_j^I}{\partial \xi} \cdot \frac{1}{|\mathbf{J}^S|} \cdot \frac{\partial \phi_i^I}{\partial \xi} \right] \cdot g_N \cdot |\mathbf{J}^S| \cdot t \cdot W_G \tag{C.37}$$

And finally, the storage component depends on the pressure dependency of the fluid specific mass.

$$K_{ij}^{II,s} = \frac{\partial F_i^{I,s}}{\partial p_{w,j}^I} \tag{C.38}$$

$$= \sum_{IP} \frac{\rho_{w,0}}{\chi_w} \cdot \frac{1}{\Delta t} \cdot g_N \cdot \phi_j \cdot \phi_i \cdot |\mathbf{J}^S| \cdot t \cdot W_G \tag{C.39}$$

C.4.4 $\mathbf{K}^{SI}$ and $\mathbf{K}^{FI}$

Components $\mathbf{K}^{SI}$ and K^{FI} contain coupling hydro-mechanical terms due to the Terzaghi postulate. They are defined for $i \in [1,3]$ and $j \in [4,6]$ in the former case and $i \in [7,9]$ and $j \in [4,6]$ in the latter. The pressure applied on both sides of the bodies in contact is the sum of the effective contact pressure and inside water pressure

$$\mathrm{p}_N = \mathrm{p}'_N + u^I_w \tag{C.40}$$

$$[\mathbf{K}]^{SI}_{9\times 3} = \begin{bmatrix} \mathbf{K}^{SS}_{i=1,j=4} = \begin{bmatrix} K_{1,1} \\ K_{2,1} \\ K_{3,1} \end{bmatrix} & \mathbf{K}^{SI}_{i=1,j=5} & \mathbf{K}^{SI}_{i=1,j=6} \\ \mathbf{K}^{SI}_{i=2,j=4} & \mathbf{K}^{SI}_{i=2,j=5} & \mathbf{K}^{SI}_{i=2,j=6} \\ \mathbf{K}^{SI}_{i=3,j=4} & \mathbf{K}^{SI}_{i=3,j=5} & \mathbf{K}^{SI}_{i=3,j=6} \end{bmatrix} \tag{C.41}$$

1. The **mechanical part** of $\mathbf{K}^{SI}_{ij}$ and $\mathbf{K}^{FI}_{ij}$, corresponds to the terms : $K_{1,1}, K_{2,1}$.

$$[\mathbf{K}_{1:2,1}]^{SI}_{ij} = -\frac{\partial \mathbf{F}^S_i}{\partial p^I_{w,j}} \tag{C.42}$$

$$= -\frac{\partial}{\partial p^I_{w,j}} \sum_{IP} \begin{bmatrix} t_T \cdot D_{X1} - (p' + p^I_w) \cdot D_{X2} \\ t_T \cdot D_{X2} + (p' + p^I_w) \cdot D_{X1} \end{bmatrix} \cdot \phi^S_i \cdot |\mathbf{J}^S| \cdot W_G \tag{C.43}$$

$$= \sum_{IP} \begin{bmatrix} D_{X2} \\ -D_{X1} \end{bmatrix} \cdot \phi^S_i \cdot \phi^I_j \cdot |\mathbf{J}^S| \cdot W_G \tag{C.44}$$

$$\tag{C.45}$$

and easily

$$[\mathbf{K}_{1:2,1}]^{FI}_{ij} = \sum_{IP} \begin{bmatrix} D_{X2} \\ -D_{X1} \end{bmatrix} \cdot \phi^F_i \cdot \phi^I_j \cdot |\mathbf{J}^S| \cdot W_G \tag{C.46}$$

2. The **hydraulic part** of $\mathbf{K}^{SI}_{ij}$, corresponds to the term : $K_{3,1}$. It's computed the same way as Eq.(C.26).

$$[K_{3,3}]^{SI}_{ij} = \sum_{IP} \theta \cdot T^t_w \cdot \phi^I_j \cdot \rho_w \cdot \phi^S_i \cdot |\mathbf{J}^S| \cdot t \cdot W_G \tag{C.47}$$

Terms of $\mathbf{K}^{FI}_{ij}$ are computed accordingly.

C.4.5 $\mathbf{K}^{SF}$ and $\mathbf{K}^{FS}$

The stiffness component $[\mathbf{K}]^{FS}_{9\times 9}$ of the local matrix is defined for $i \in [7,9]$ and $j \in [1,3]$, where each nodes has 3 dofs $(x^S_j, y^S_j, p^S_{w,j})$

$$[\mathbf{K}]^{SS}_{9\times 9} = \begin{bmatrix} \mathbf{K}^{FS}_{i=1,j=1} = \begin{bmatrix} K_{1,1} & K_{1,2} & 0 \\ K_{2,1} & K_{2,2} & 0 \\ & & 0 \end{bmatrix} & \mathbf{K}^{FS}_{i=1,j=2} & \mathbf{K}^{FS}_{i=1,j=3} \\ \mathbf{K}^{FS}_{i=2,j=1} & \mathbf{K}^{FS}_{i=2,j=2} & \mathbf{K}^{FS}_{i=2,j=3} \\ \mathbf{K}^{FS}_{i=3,j=1} & \mathbf{K}^{FS}_{i=3,j=2} & \mathbf{K}^{FS}_{i=3,j=3} \end{bmatrix} \tag{C.48}$$

There are only mechanical components since there is no coupling between hydraulical dof of both sides. They are identical to Eq.(C.20) and Eq.(C.29).

$$\begin{aligned}
[\mathbf{K}_{1:2,1:2}]_{ij}^{FS} &= -\frac{\partial \mathbf{F}_i^F}{\partial \mathbf{x}_j^S} \\
&= -\sum_{IP} \left[\mathbf{C}_{glob} \cdot |\mathbf{J}^S| \cdot \phi_j^S - \begin{bmatrix} t_T & -p \\ p & t_T \end{bmatrix} \cdot \frac{\partial \phi_j^S}{\partial \xi} \right] \cdot \phi_i^F \cdot W_G \qquad \text{(C.49)} \\
[\mathbf{K}_{1:2,1:2}]_{ij}^{SF} &= -\frac{\partial \mathbf{F}_i^S}{\partial \mathbf{x}_j^F} \\
&= -\sum_{IP} \mathbf{C}_{glob} \cdot |\mathbf{J}^S| \cdot \phi_j^F \cdot \phi_i^S \cdot W_G \qquad \text{(C.50)}
\end{aligned}$$

C.4.6 $\mathbf{K}^{IS}$ and $\mathbf{K}^{IF}$

The stiffness component $[\mathbf{K}]_{3\times 9}^{IS}$ of the local matrix is defined for $i \in [4,6]$ and $j \in [1,3]$, where each nodes has 3 dofs $(x_j^S, y_j^S, u_{w,j}^S)$.

$$[\mathbf{K}]_{9\times 9}^{IS} = \begin{bmatrix} \mathbf{K}_{i=4,j=1}^{IS} = \begin{bmatrix} K_{1,1} & K_{1,2} & K_{1,3} \end{bmatrix} & \mathbf{K}_{i=4,j=2}^{IS} & \mathbf{K}_{4=1,j=3}^{IS} \\ \mathbf{K}_{5=2,j=1}^{IS} & \mathbf{K}_{i=5,j=2}^{IS} & \mathbf{K}_{i=5,j=3}^{IS} \\ \mathbf{K}_{i=6,j=1}^{IS} & \mathbf{K}_{i=6,j=2}^{IS} & \mathbf{K}_{i=6,j=3}^{IS} \end{bmatrix} \qquad \text{(C.51)}$$

1. The **mechanical components** $K_{1,1}, K_{1,2}$ are due to the mechanical coupling from the geometric storage. In the structure it yields to

$$\begin{aligned}
[\mathbf{K}_{1:2,1:2}]_{ij}^{IS} &= -\frac{\partial F_i^{I,s}}{\partial \mathbf{x}_j^S} \\
&= -\sum_{IP} \rho_w \cdot \frac{\partial}{\partial \mathbf{x}_j^S} \left(\dot{g}_N \cdot |\mathbf{J}^S| \right) \cdot \phi_i^I \cdot t \cdot W_G \\
&= \sum_{IP} \rho_w \cdot \left[\frac{\partial \phi_j^S}{\partial \xi} \cdot \left(\dot{x}_2^S - \dot{x}_2^F \right) - \frac{\partial x_2^S}{\partial \xi} \cdot \frac{\phi_j^S}{\Delta t}, \right. \\
&\qquad \left. - \frac{\partial \phi_j^S}{\partial \xi} \cdot \left(\dot{x}_1^S - \dot{x}_1^F \right) + \frac{\partial x_1^S}{\partial \xi} \cdot \frac{\phi_j^S}{\Delta t} \cdot \phi_i^I \cdot t \cdot W_G \right] \qquad \text{(C.52)}
\end{aligned}$$

   and for the foundation

$$\begin{aligned}
[\mathbf{K}_{1:2,1:2}]_{ij}^{IF} &= -\frac{\partial F_i^{I,s}}{\partial \mathbf{x}_j^F} \\
&= \sum_{IP} \rho_w \cdot \frac{\partial}{\partial \mathbf{x}_j^F} \left(\dot{g}_N \cdot |\mathbf{J}^S| \right) \cdot \phi_i^I \cdot t \cdot W_G \\
&= \sum_{IP} \rho_w \cdot \left[\frac{\partial x_2^S}{\partial \xi} \cdot \frac{\phi_j^F}{\Delta t} \quad , - \frac{\partial x_1^S}{\partial \xi} \cdot \frac{\phi_j^F}{\Delta t} \right] \cdot \phi_i^I \cdot t \cdot W_G \qquad \text{(C.53)}
\end{aligned}$$

Variation of global coordinates in Eq.(C.52) are obtained from the expression of local

variables

$$\begin{bmatrix} \dot{x}_1^S - \dot{x}_1^F \\ \dot{x}_2^S - \dot{x}_2^F \end{bmatrix} = \mathbf{R} \cdot \begin{bmatrix} \dot{g}_T \\ \dot{g}_N \end{bmatrix} = \begin{bmatrix} DX_1 \cdot \dot{g}_T - DX_2 \cdot \dot{g}_N \\ DX_2 \cdot \dot{g}_T + DX_1 \cdot \dot{g}_N \end{bmatrix} \tag{C.54}$$

2. The **hydraulical component** $K_{1,3}$ is simply derived from the transversal flows, equally to Eq.(C.26)

$$[K_{3,3}]_{ij}^{IS} = -\sum_{IP} \theta \cdot T_w^{t,2} \cdot \phi_j^I \cdot \rho_w \cdot \phi_i^S \cdot |\mathbf{J}^S| \cdot t \cdot W_G \tag{C.55}$$

Abstract

The main objective of this thesis is the studying of the cyclic behaviour of dense sand. Its centre of gravity is the implementation of a convenient constitutive law in the finite element code `LAGAMINE`.

The first step consists in summarising the salient features of the cyclic behaviour of sand observed in laboratory tests. Undrained monotonic and cyclic experiments are addressed. The phase transformation line is a key parameter in the description of its behaviour. The plasticity effects in both loading and unloading, the progressive pore pressure accumulation coupled with the degradation of the stiffness of the soil are of uttermost importance in the cyclic behaviour.

The Prevost model is adopted for its conceptual simplicity and its physically related parameters. The basic equations of the model are described and its variants are illustrated. Calibration of the required parameters is carried out by means of simplified routines implemented in Matlab. A unique set of parameters is determined for each soil at a given relative density. Monotonic experiments are well reproduced. The model also replicates satisfactorily the trend of cyclic experiments.

An implicit scheme is embraced in order to implement the model in the finite element code `LAGAMINE`. The implicit Prager translation rule is adopted for that purpose. It is ensured the discrete formulation reproduces exactly the analytical model. Accuracy, efficiency and robustness of the model are addressed throughout triaxial and multi-axial numerical examples.

A hydro-mechanical interface finite element is developed. It consists in a three-node 1D isoparametric element. It is able to reproduce fluid flows across and along the interface. The unsticking of both walls of the interface is coupled with a suction effect due to the filling of the vacuum created. The behaviour of the element is illustrated by simple 1D examples of transient consolidation of a soil column.

A final application consists in the modelling of a suction caisson, part of a tripod structure for wind turbines. An axisymmetric representation of this foundation is carried out. It is assumed embedded into dense Lund sand described by the Prevost model. Monotonic and cyclic simulations are performed in both drained and partially drained conditions. The salient features of the resistance of such foundations are highlighted. Their partially drained behaviour strongly increases their transient resistance. A storm including an extreme event is employed to simulate a cyclic loading. A pseudo-random short signal and its sinusoidal equivalent representation finally lead to an identical vertical settlement. This is confirmed by a long duration storm. Finally, a cyclic diagram summarising the final settlement attained for combinations of average and cyclic vertical loads is elaborated.

Keywords : Numerical modelling - Cyclic behaviour - Sand - Offshore Geotechnics - Constitutive modelling - Interfaces